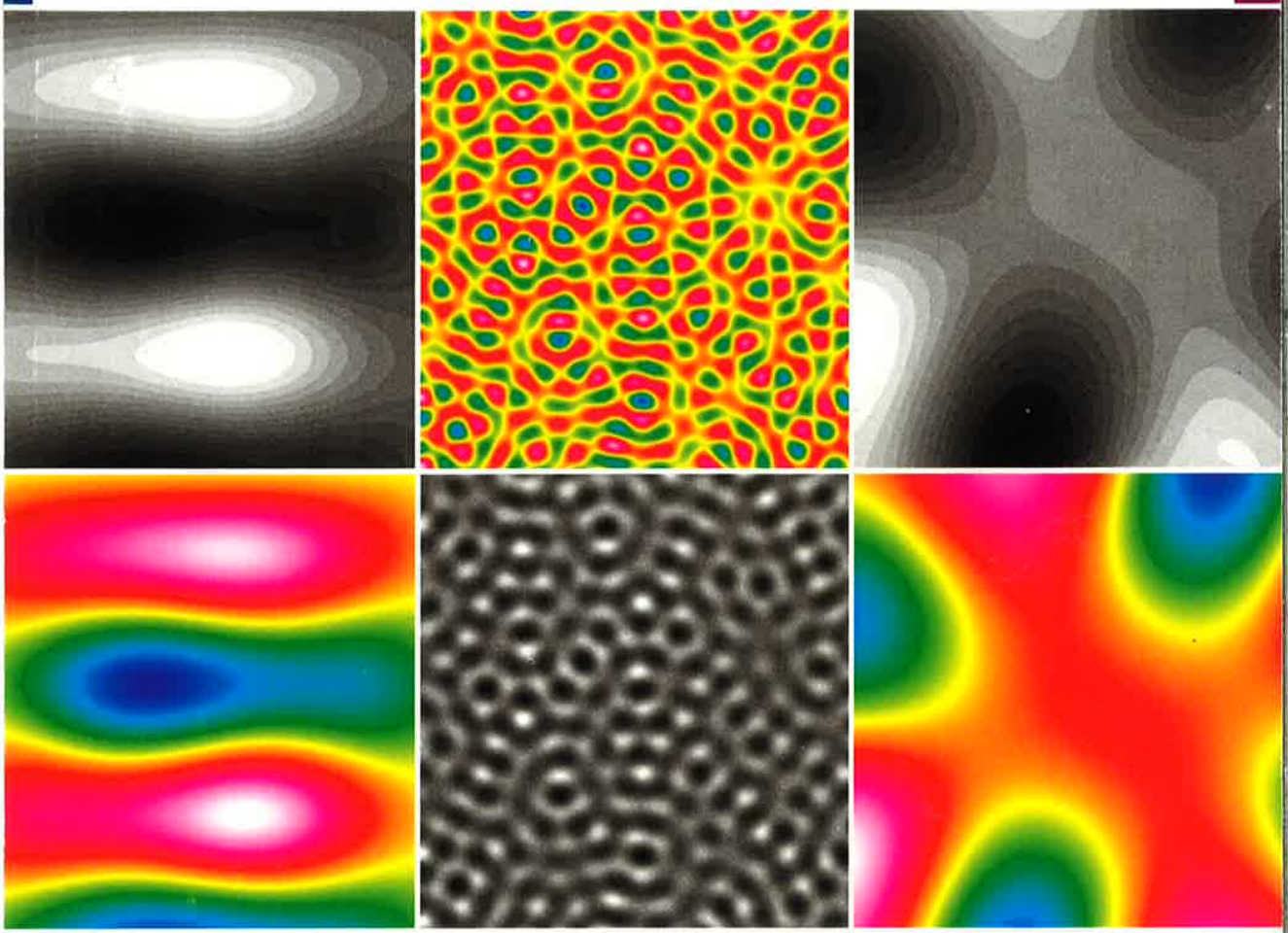

VIII Suomen mekaniikkapäivät

Espoossa 12.-13. kesäkuuta 2003

1. Kokouspäivän esitelmät

Peter Råback, Kari Santaoja ja Rolf Stenberg (toim.)

Helsinki University of Technology Laboratory for Mechanics of Materials Research Reports
Teknillisen korkeakoulun Lujuusopin laboratorion julkaisuja
Espoo, Kesäkuu 2003 TKK-LO-36

VIII SUOMEN MEKANIIKKAPÄIVÄT

Espoossa 12.-13.6.2003

NIDE 1
1. Kokouspäivän esitelmät

Toimittajat
Peter Råback, Kari Santaoja ja Rolf Stenberg

TEKNILLINEN KORKEAKOULU
TEKNISKA HÖGSKOLAN
HELSINKI UNIVERSITY OF TECHNOLOGY
TECHNISCHE UNIVERSITÄT HELSINKI
UNIVERSITE DE TECHNOLOGIE D´HELSINKI

Tieteellinen neuvosto

Jukka Aalto, TKK
Tuomo Kärnä, VTT
Juha Paavola, TKK
Mauri Määttänen, TKK
Peter Råback, CSC
Kari Santaoja, TKK
Timo Siikonen, TKK
Rolf Stenberg, TKK
Jukka Tuhkuri, TKK

Järjestelytoimikunta

Tuula Donskoi
Irina Forsman
Kirsi Hepolehto
Katri Luostarinen
Peter Råback
Kari Santaoja
Rolf Stenberg
Heli Tuomela

TEKNILLINEN KORKEAKOULU
Lujuusopin laboratorio
PL 4100
02015 TKK

Puh. (09) 451 3445
fax. (09) 451 3443

ISBN 951-22-6569-9

ESIPUHE

Suomen mekaniikkapäivät on järjestetty vuodesta 1982 lähtien joka kolmas vuosi. Nyt vuorossa oli Otaniemi, jossa kahdeksannet päivät pidettiin 12.-13.6.2003. Käytännön järjestelyistä vastasivat tieteen tietotekniikan keskus CSC sekä Teknillinen korkeakoulu.

Kutsuttuina esitelmöitsijöinä olivat professorit *Ben Leimkühler,* University of Leicester, *Arthur Rizzi*, Kungliga Tekniska högskolan, ja *Juhani Koski*, Tampereen Teknillinen Yliopisto, sekä toimitusjohtaja *Mauno Paavola*, Teollisuuden Voima Oy. Pääosa päivien ohjelmasta koostui tarjotuista esitelmistä, joita hyväksyttiin yhteensä 63. Esitelmiin liittyvät artikkelit on koottu tähän niteeseen.

Edellisten mekaniikkapäivien jälkeen ovat kaksi alamme johtohahmoa, professorit

Martti Mikkola ja **Eero-Matti Salonen**

saaneet lisätittelin "*Emeritus*". Suomen mekaniikan tutkijat ja opettajat haluavat sekä kiittää että kunnioittaa Marttia ja Eero-Mattia omistamalla tämän kirjan heille.

Lopuksi esitämme lämpimät kiitoksemme kaikille niille, jotka ovat myötävaikuttaneet päivien onnistumiseen; osallistujille, artikkelien kirjoittajille, tieteelliselle neuvostolle sekä ennen kaikkea niille henkilöille, jotka ovat osallistuneet järjestelytyöhön.

Peter Råback
Kari Santaoja
Rolf Stenberg

ENGLISH SUMMARY

These two volumes contain the Proceedings of the VIII Finnish Mechanics Days, held in Otanemi, Espoo, June 12-13, 2003. The conference was organized by CSC, the Finnish IT center for science and Helsinki University of Technology.

The invited speakers were professors *Ben Leimkühler,* University of Leicester, *Arthur Rizzi*, Royal Instute of Technology, *Juhani Koski*, Tampere University of Technology, and *Mauno Paavola,* President and CEO of the electricity generation company Teollisuuden Voima Oy.

The volumes are dedicated to professors *Martti Mikkola* and *Eero-Matti Salonen*, who both recently retired from Helsinki University of Technology.

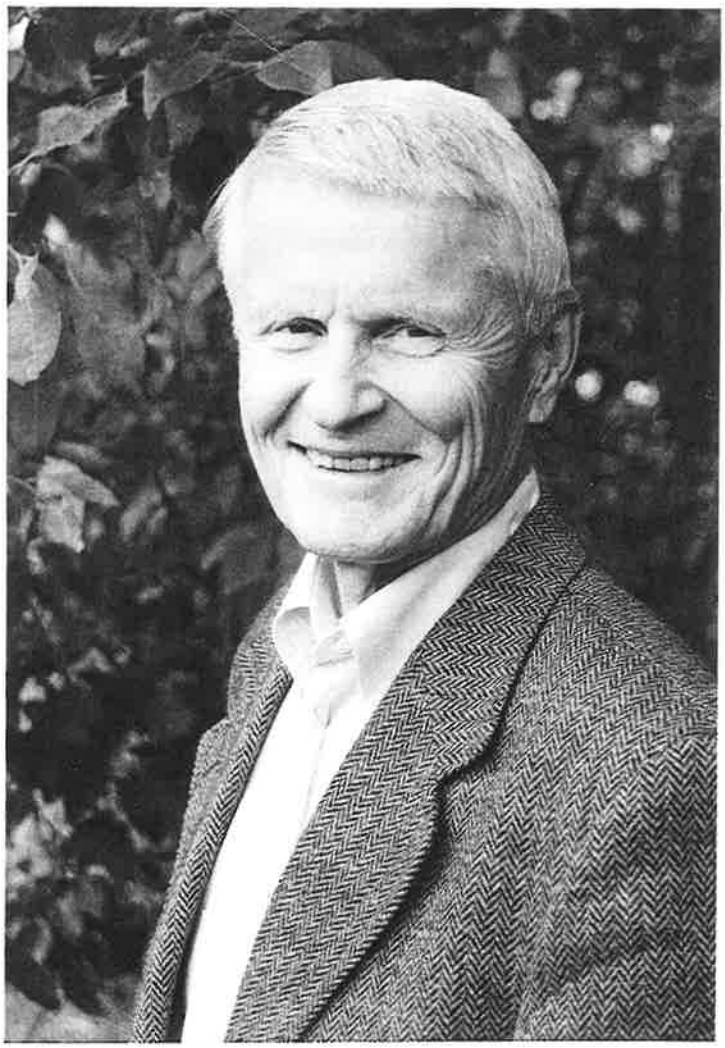

Martti Mikkola
s. 6.9.1936 Oulainen

DI TKK R 1961, TkL TKK R 1964, TkT TKK R 1967, FK HY mat/luonn 1963

TVH siltaosasto toimistoinsinööri 1961-65, TKK laboratorioinsinööri 1965-67, rakenteiden mekaniikan apulaisprofessori ja professori 1967-97, rakennusinsinööriosaston osastonjohtaja 1976-77, 1987-89, 1994-95, mekaniikan professori 1997-2001, SA tutkijaprofessori 1977-80, Virginia Polytechnic Institute and State University vieraileva professori 1980-81, Laboratorie Central des Ponts et Chaussées Pariisi vieraileva tutkija 1989-90, Ecole Polytechnique Laboratorie Mécanique des Solides vieraileva professori 1992, 2001

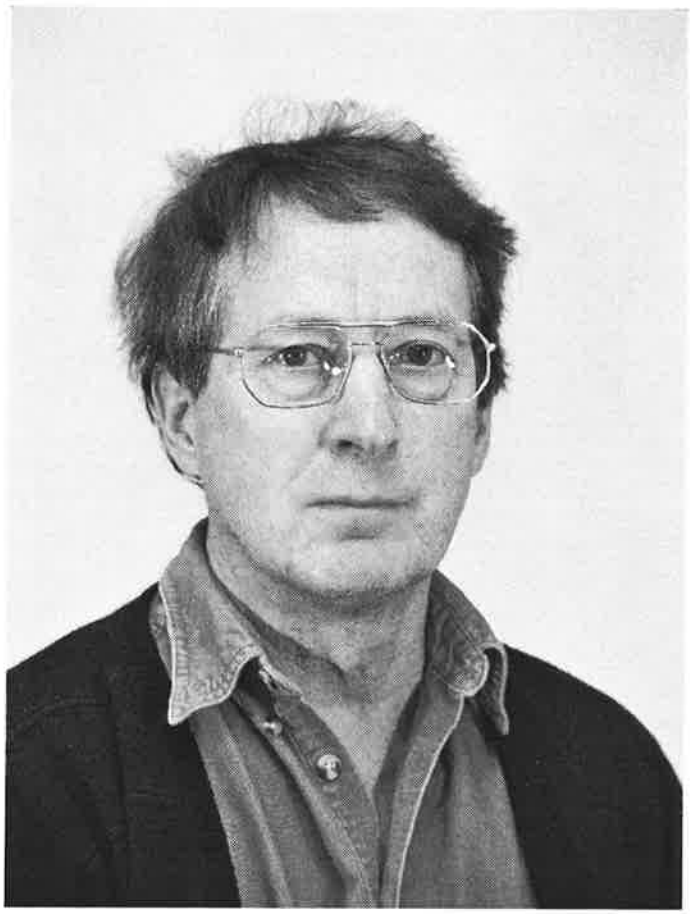

Eero-Matti Salonen
s. 14.12.1937 Helsinki

DI TKK R 1963, TkL TKK R 1967, TkT TKK R 1970,
MSc University of Wales Swansea Civil Engineering 1974

TVH siltaosasto nuorempi insinööri 1964-65, Teknillisten tieteiden toimikunnan tutkimusassistentti 1965-70, nuorempi tutkija 1970-73, TKK apulaisprofessori 1974-98, professori 1998-2002

SISÄLLYSLUETTELO

Värähtelymekaniikka

Kokeellinen mekaniikka

Virtauksen ja rakenteen vuorovaikutus

Murtumismekaniikka

Rakenteiden mekaniikka I

Maa- ja jäämekaniikka

Laskentamenetelmiä opetukseen

Mekaniikan ohjelmistokehitys

NIDE 2

Optimointi II

Rakenteiden mekaniikka II

Materiaalien käyttäytyminen

Elementtimenetelmän teoria

Mekaniikan erityisongelmia

Virtauslaskenta II

THINGS THAT GO "BUMP"

BEN LEIMKUHLER
Centre for Mathematical Modelling
University of Leicester
Leicester LE1 7RH
UK

From ghoulies and ghosties
And long-leggedy beasties
And things that go bump in the night,
Good Lord, deliver us!
-- Traditional Scottish Prayer

ABSTRACT

The author discusses ongoing work on a simple class of methods for simulating the dynamics of rigid bodies subject to hard impacts. These methods have primarily been developed and tested in the setting of hard sphere molecular dynamics simulation, but they are much more general and powerful than this. This article describes generalizations of the basic scheme to treat constraints, thermostatic control and structured nonlinear dissipation, which should allow the methods to be used much more widely.

1. INTRODUCTION

By collisional rigid body dynamics, we mean the simulation of a system of rigid bodies interacting under the forces of nature and subject to purely elastic impacts. We assume that the dynamics between impacts satisfy Newton's laws of motion,

(1) $$M\,q'' = F(q, q', t),$$

possibly augmented by constraints ($q: R \to R^d$ positions or configurations, q' the velocity vector, q'' acceleration, $M \in R^{d \times d}$ a mass matrix, and $F: R^{2d+1} \to R^d$ the vector of forces). Impacts are defined by nonempty solutions of a contact condition

(2) $$W(q) = 0.$$

It is assumed that, at impact, available physical laws (energy and momentum) allow determination of a unique continuation of the solution and that the motion of the system is well-defined by these principles for all forward time beginning with any suitable initial data $q^0 = q(t_0)$, $v^0 = q'(t_0)$. We may assume that, at the point of impact, the position remains unchanged while the velocity v undergoes a reflection determined by the exact nature of the impulse, thus

$$v \to R(q)\, v.$$

We distinguish between the conservative cases for which the motion, between collisions, can be given a Hamiltonian formulation and for which energy is conserved everywhere along solutions, and nonconservative cases (for which energy may dissipate or increase during simulation). This framework is not completely general, but it is adequate to describe a wide range of important applications problems, including systems arising in:

- Multibody Mechanical Simulation
- Biodynamics
- Computer Gaming and Virtual Reality
- Powder and Granular flows
- Die-Filling/Injection Moulding
- Paint Spraying, Particle-Laden Flows
- Polymer Modelling
- Molecular Dynamics Simulation

In molecular dynamics, the hard sphere model was the first to be studied in computer simulation [1]. The hard sphere model remains important because it allows for exact determination of the equilibrium statistical mechanics of the system. Hard sphere models represent important reference points for studying properties of systems and for analyzing theories and methods. An example of such system is the restricted primitive model [2], which also typically incorporates long-ranged Coulombic forces. In polymer models, constraint chains or spring-linked bead models are very commonly treated with a variety of bead-bead interactions: hard sphere, soft sphere, or lump. A very popular recently proposed scheme is the dissipative particle dynamics method [3] which may also include hard bodies [4]. The models typically include nonlinear structured momentum-preserving dissipation forces and stochastic perturbations as well as conservative forces. According to [4], "The use of **hard spheres** with the DPD algorithm is complicated by the mixture of continuous and impulsive forces...and the need to unravel the correlated motions of the rigid bodies."

While our focus in this discussion is on fine-scale models of molecular and polymer chemistry, we believe that many of the ideas discussed here will eventually carry over to other simulations, such as granular flows. The goal in this work is to develop methods which are at once very efficient in terms of force computations (since force computations are typically the standard measure of work) and stable (so that largest possible timesteps can be used). One of the exciting recent developments in numerical simulation of conservative systems has been the concept of geometric integration. Unfortunately, geometric integration for collisional systems is still in its infancy, despite our own work in this area and that of a few other authors [5,6]. The key obstacle here is the development of a useful backward error analysis extending the approach used for smooth systems [7,8,9]. The presence of dissipative forces only complicates the situation still further, as the structural issues are currently poorly understood even for smooth dissipative systems. This article does not purport to examine the full range of GI issues associated to collisional dynamics, but the methods proposed here have some important GI elements.

The seed of the approach described here was put forward for standard form N-body systems as the Collisional Verlet method of Houndonougbo, Laird and Leimkuhler [10], a second-order scheme which uses a symplectic (and therefore volume preserving) and angular momentum conserving map between collisions. There are some important basic challenges to the rational treatment of more general classes of collisional models by numerical simulation. The systems typically incorporate constraints of one form or another. While nonholonomic constraints (such as slipping) might be interesting in larger scale regimes, the emphasis in fine-scale models is on

holonomic constraints which can be thought of as constraints on the positions of the bodies. The treatment of holonomic constraints in geometric integration [11,12,13] is by now at a fairly well-developed position, including rigid body systems [14,15,16] and these schemes are important in molecular simulation [17,18]. We will briefly explain here how these constraint-preserving schemes can be combined with the Collisional Verlet method.

Another important challenge at the molecular/polymer level is the incorporation of a temperature control in simulation. Dynamic thermostatting is an important subject in itself, and we only touch on this here in order to explain its treatment in the context of collisional dynamics. We exhibit a simple technique for this based on the recently proposed separated approach to Nosé dynamics [19].

Finally, as we are interested in the extension of these approaches for polymer modelling, we wish to explore the treatment of nonconservative forcing, particularly damping. Some work has been undertaken on developing geometric formulations and numerical treatments for damping, but either (i) they are very qualitative in nature or (ii) they are focussed on linear models of dissipation. Here we explain how the dissipative forces arising in DPD can be treated so that the underlying systems rate of dissipation is matched by the numerical method. We show how this type of dissipation handling can be mated with collisional dynamics techniques, although the additional complexity that it introduces probably limits the practical order of the method to one.

2. SPLITTING METHODS AND GEOMETRIC INTEGRATION

A broad family of one-step methods can be developed for integrating differential equation initial value problems of the form $dz/dt=f(z)$, $z(0)=z^0$ based on the concept of splitting. Given $f=f^{(1)}+f^{(2)}$, the idea is to solve the system in two steps: first $f^{(1)}$ for time h, then $f^{(2)}$ for the same interval. The result is an approximation of the evolution of the original system on $[0,h]$. For this to be useful, the two vector fields $f^{(1)}$ and $f^{(2)}$ should be individually integrable, or, at least they should be much easier to solve by some other methods (e.g. further splitting). More generally, if $f=\Sigma_i f^{(i)}$, then the evolution of $dz/dt=f(z)$ can be approximated by solving successively $dz/dt=f^{(i)}(z)$, $i=1,2,....$ To illustrate, consider a smooth vector field $f: R^N \rightarrow R^N$ with components $f_1, f_2,...,f_N$. A splitting method is obtained by setting

$$f^{(1)}=f_1, f^{(2)}=f_2, ...f^{(N)}=f_N$$

since, e.g. $dz/dt=f^{(1)}(z)$ gives

$$dz_1/dt=f_1(z_1, z_2, .., z_N)$$

$$dz_i/dt=0,\ i=2..N$$

Clearly components $2..N$ of the solution are constants of motion of the vector field $f^{(1)}$, whereas z_1 can in principle be recovered by quadrature. A similar situation exists for each of the other terms. This suggests the following algorithm:

$Z_0 = z_n$

for $i=1..N$

  solve $d\zeta/dt=f^{(i)}(\zeta)$, $\zeta(0)=Z_{i-1}$ *on* $[0,h]$

  set $Z_i=\zeta(h)$

end

$z^{n+1}=Z_N$

The algorithm computes $z^{n+1}=\Phi(z^n; h)$, which can be shown to be a first order accurate numerical

method. By iterating this map, we can approximate to $O(h)$ accuracy the solution of the original differential equation on any desired finite time interval. The flow-map of a given system can be denoted by $exp(hL_f)$, where L_f is the Lie-derivative along the vector field f. It is convenient to shorten this to $exp(hf)$, in which case the splitting method above can be denoted by $z^{n+1} = \Phi(z^n; h) = \Pi_i \, exp(hf^{(i)}) \, z^n$. Splitting methods are also referred to as "composition methods" as they replace the flow map by an approximation based on the composition of the flow maps of each of the terms of the splitting.

Splitting methods prove most useful when we need to conserve some symmetry or invariant structure of the flow of the system. For example, if f and the terms of a given splitting all preserve a first integral, then the corresponding composition method is automatically integral-preserving. If f is a Hamiltonian vector field, $f=J\nabla H$, $J=-J^T$, the flow-map on f is *symplectic*. A splitting of the Hamiltonian $H=H_1 + H_2$ induces a vector field splitting

$$f = f_1 + f_2, \qquad f_1 = J\nabla H_1 \qquad f_2 = J\nabla H_2$$

and the composition $exp(hJ\nabla H_2)exp(hJ\nabla H_1)$ defines a first order "symplectic integrator".

For example, if H=T(p) +V(q), we can integrate first T, then V or, alternatively first V then T, defining a pair of 1st order symplectic methods. Since the differential equations on T and V are

$$T: \qquad dq/dt = \nabla_p T; \qquad dp/dt = 0$$

$$V: \qquad dq/dt = 0; \qquad dp/dt = -\nabla_q V$$

we see that these systems are individually integrable. We can also solve first V for half a step, then T, then V for another half-step, resulting, after some simplification, in the following method:

$$p^{n+1/2} = p^n - (h/2)\,\nabla V(q^n)$$

$$q^{n+1} = q^n + h\,\nabla_p T\,(p^{n+1/2});$$

$$p^{n+1} = p^{n+1/2} - (h/2)\,\nabla V(q^{n+1})$$

This method is symplectic, second order accurate, angular momentum conserving, and time-reversible, and it requires just a single force evaluation at each timestep. It is referred to as the leapfrog or Stoermer-Verlet method and is by far the most popular scheme for standard molecular dynamics.

The repertoire of composition methods for ODEs has been developed extensively over the past several years, and now includes high-order schemes, and schemes specially adapted for quantum dynamics, molecular dynamics, celestial mechanics, and various types of partial differential equations. A forthcoming book by the author together with S. Reich (Imperial College) will present a general approach to geometric integration, including splitting, and many application examples in detail.

3. COLLISIONAL VERLET

We next describe the basic collisional Verlet method as proposed in [10]. The idea of this method is based on the Verlet method applied to N-body systems with energy function (expressed in terms of velocity and position):

(3) $$E(q,q') = q'^T M q'/2 + V(q)$$

and equations of motion

$$q' = v; \quad Mv' = -\nabla V(q)$$

The leapfrog/Verlet method computes a step from time t_n to $t_{n+1} = t_n + h$ taking (q^n, v^n) to $(q^{n+1}, v^{n+1}) = \Phi^{LF}((q^n, v^n); h)$:

(4) $v^{n+1/2} = v^n - (h/2)\, M^{-1} \nabla V(q^n)$

(5) $q^{n+1} = q^n + h\, v^{n+1/2}$

(6) $v^{n+1} = v^{n+1/2} - (h/2)\, M^{-1} \nabla V(q^{n+1})$

It is easily seen that

(7) $q^{n+1} = q^n + hv^n - (h^2/2)\, M^{-1} \nabla V(q^n)$

hence $q^{n+1} = q^{n+1}(h)$ is a quadratic polynomial of the stepsize. It is natural to use this as the basis for a collisional dynamics technique:

1. Set $h_C = min\ \{h>0 \mid W(\ q^n + hv^n - (h^2/2)\, M^{-1} \nabla V(q^n)\ ) = 0\ \}$
2. Set $h = min\ \{\ h_C,\ h_{max}\ \}$
3. $(q^{n+1}, \underset{\sim}{v}^{n+1}) = \Phi^{LF}((q^n, v^n);\ h)$
4. $v^{n+1} = R(\ q^{n+1})\ \underset{\sim}{v}^{n+1}$
4. $t_{n+1} = t_n + h$

Here h_{max} represents a suitable stepsize for the system in the absence of collisions. The timestep is simply chosen so that collision points are associated to collisions in the quadratic approximations. If we think of hard spheres with centres q_i and q_j and radii R_i and R_j, then the collisions correspond to points h where

$$|| q_i - q_j || = R_i + R_j$$

or

$$|| q_i - q_j ||^2 = (R_i + R_j)^2$$

which is a quartic polynomial in h, so in this case the collisions can be resolved exactly. If there are many bodies, we must determine the times of collision for all pairs (or we must eliminate some pairs from consideration by some device) and then we choose the smallest of these to compare against h_{max}. Of course it is not essential that these equations are exactly solvable. If they are not, we need to compute the solutions by Newton's method or some other appropriate numerical scheme, being careful not to miss any collisions (e.g. by use of continuation methods). There is undeniable benefit to working with the exactly solvable case.

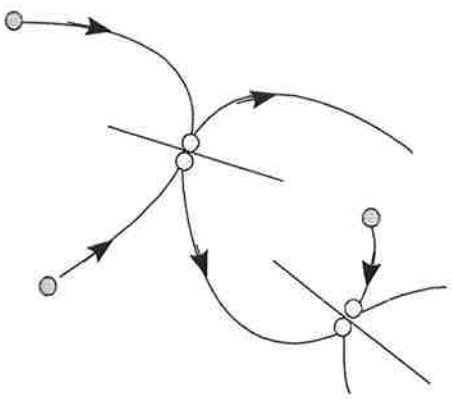

4. SOFT FORCE SPLITTING

In many molecular systems, the frequency of collision will be very great indeed. It was pointed out in [10] that collisional systems do not allow the use of potential splitting techniques in general. In potential splitting, we simply divide the potential energy of the system into two terms, $V = V_0 + V_{weak}$, say, and we propagate the system by first applying an impulse $\underset{\sim}{v}^n = v^n - h\, \nabla V_{weak}(q^n)$ then integrate the system with energy $E_0(q,q') = q'^T M q'/2 + V_0(q)$ for the same time interval h. This can also be done in a symmetric way, a la leapfrog/Verlet, by first applying an impulse scaled by half the stepsize, next propagating the system, then applying another half-impulse, yielding a method which is reversible and giving second order accuracy. In practice, we actually evolve the system with energy E_0 using a small timestep, say h/M. This can be a very useful tool

for systems subject to weakly perturbing forces, since the weak forces are evaluated relatively rarely compared to the strong one.

However, if we attempt to combine this idea of potential splitting with our hard sphere algorithm, so that we first apply a weak impulse, then apply some sequence of collisional steps, then apply another weak impulse, we find that what was a second order method in the noncollisional setting becomes *first order* (and it is virtually impossible to recover the 2nd order accuracy). This is just one of many ways that our intuition from understanding of smooth systems (which is justified only by the previously mentioned "backward error analysis" of numerical integrators) can lead us astray when dealing with nonsmooth systems.

A fix for this problem was explained in [10]. It was shown that potential splitting methods will retain their order provided the weak force vanishes at impacts, i.e. on the contact set. Of course we cannot expect this to hold in general, but if it is not the case, we can induce it. Specifically, consider a system of spheres of constant radius R, and suppose the potential energies are sums of pair potentials between bodies, thus V_0, V_{weak} *are* associated with pair potentials of the form $\phi_0(r)$, $\phi_{weak}(r)$, respectively, where

$$V_0(q) = \sum_{i<j} \phi_0(||q_i - q_j||); \qquad V_{weak}(q) = \sum_{i<j} \phi_{weak}(||q_i - q_j||)$$

Then the necessary condition can be induced by introducing an artificial additive splitting of ϕ_{weak},

$$\phi_{weak} = \phi^{(1)} + \phi^{(2)}$$

where $\phi^{(1)}$ is short-ranged (gradient has zero support outside a compact interval near zero) and

$$(d/dr)\,\phi^{(2)}(2R) = 0.$$

Finally we lump $\phi_0 + \phi^{(1)}$ and use this to describe a modified $V_0(q)$, while $\phi^{(2)}$ is used in place of ϕ_{weak} to define the new weak potential V_{weak}.

The method that results from this device is a relatively efficient scheme for molecular dynamics with hard sphere, and has been used in several recent simulations in the physical literature.

What can we say about the properties of the collisional Verlet method? Because it is based on Verlet, the Impulsive Verlet method inherits some of its appealing properties. For example it is second order. It generates a symplectic map between collisions and is therefore volume preserving. However, like all currently available schemes, including the "variational methods" described in [5], the method exhibits secular energy drift with a stochastic character. (We do not exclude the possibility that the scheme of [10] is "variational" in the sense of [5].) An advantage of the collisional Verlet method as compared to the schemes in [5] is that it only requires one force evaluation per collisional step. This will be a major difference between the schemes in the setting of models such as the restricted primitive model which involve long-range Coulombic forces.

5. TREATMENT OF CONSTRAINTS

The extension of the collisional dynamics method to constrained systems is work currently in progress with S. Bond (UCSD). Here we outline the basic ideas, leaving the thorny implementation issues aside. For a holonomic system, we introduce a vector of m constraints $g(q)=0$ and Lagrange multiplier vector $\lambda \in R^m$ and write the Euler-Lagrange equations:

$$dq/dt = v; \quad dv/dt = -M^{-1}\nabla V - M^{-1} g'(q)^T\lambda; \quad g(q) = 0 \tag{8}$$

The natural extension of Störmer-Verlet is RATTLE (after SHAKE [RCB97]):

$$q^{n+1} = q^n + h\, v^{n+1/2} \tag{9}$$

(10) $v^{n+1/2} = v^n - (h/2)\, M^{-1}\nabla V(q^n) - (h/2)\, M^{-1} g'(q^n)^T\lambda^n$

(11) $g(q^{n+1}) = 0$

(12) $v^{n+1} = v^{n+1/2} - (h/2)\, M^{-1}\nabla V(q^{n+1}) - (h/2)\, M^{-1} g'(q^{n+1})^T \xi^{n+1}$

(13) $g'(q^{n+1})v^{n+1} = 0$

These equations are solved as follows: equations (9)-(11) can be reduced to

(14) $g(q^{LF}(h) + G^T \mu) = 0$

where $G = -\ M^{-1} g'(q^n)^T$, and $\mu = h\lambda/2$. $q^{LF}(h)=^{n+1} = q^n + h\, v^n - (h^2/2)\, M^{-1}\nabla V(q^n)$ represents the unconstrained leapfrog step with the given potential field. This is a system of m equation in m unkowns (the scaled Lagrange multipler vector) and can be solved by Newton iteration in general. In some cases the equations are exactly solvable. After Although implicit, this scheme still only requires a single applied force (∇V)evaluation per timestep, so it has a characteristic of an explicit method. This is very important in the setting of molecular systems, and it is for this reason that the SHAKE discretization is the standard in biomolecular simulation. The SHAKE discretization (with its RATTLE [13] variant) was studied in [11] and shown to be symplectic.

The trajectories are now seen to be quadratics projected obliquely onto the constraint manifold. If we are willing to search in this geometry for collisions, then we can define a numerical method analogous to Collisional Verlet for the constrained case. Specifically, we propose to solve the combined system in h, μ

(15) $g(q^{LF}(h) + G^T \mu) = 0;$ $\qquad W(q^{LF}(h) + G^T \mu\ ) = 0$

The first of these solutions (i.e. the solution with smallest positive h) then is taken as the point of first collision. We illustrate this approach with a couple of examples:

Example 1: N spherical bodies on the surface of a sphere

The constraint manifold is defined by $||q_i||^2 = 1,\ i=1..N$. We assume unit masses and uniform radii R for the bodies. The contact conditions are taken to be $||q_i - q_j||^2 = (2R)^2$. For each i, write $q_i^{LF}(h) = q_i^n + h\, v_i^n - (h^2/2)\, a_i(q^n)$ where each of the coefficients is a vector in R^3. The projection in (15) takes the form

$$|| q_i^{\ LF}(h) + q_i^n \mu_i ||^2 = 1$$

or

$$|| q_i^{\ LF}(h)||^2 + 2\mu_i\, q_i^n \bullet q_i^{\ LF}(h) \ + \mu_i^2\ ||q_i^n||^2 = 1$$

This is a quadratic equation for μ_i. The equations can be simplified by using the fact that the previous step can be assumed to lie on the constraint manifold. Once the multipliers for each body are determined as functions of h, the equations of contact must be solved for each pair of bodies (e.g. by Newton's method). A similar approach could be used for billiards problems on *any* smooth algebraically defined surface, although generally not allowing all the simplifications seen here for the case of a sphere.

Example 2: A Rigid Body

Consider a single rigid body moving in a potential field. The equations of motion can be written in the form

(16) $dQ/dt = PJ^{-1}\ ;\ dP/dt = -\nabla_Q V(Q,q) - Q\Lambda;\ \ Q^T Q = I$

(17) $dq/dt = M^{-1}p\ ;\ dp/dt = -\nabla_q V(Q,q);$

Q is a 3×3 orthogonal matrix which defines the orientation of the rigid body in space, and $q\in R^3$ its centre of mass. P,p are the associated canonical momenta. J is a (typically diagonal) matrix related to the inertial tensor. M is the mass of the body, and Λ is a symmetric matrix of Lagrange multipliers which must be

determined to maintain the constraint of orthogonality.

A very useful concept in discussing implementation of algorithms for rough-shaped rigid bodies is that of a bounding sphere. The idea is to define a sphere whose centre is located at the body centre of mass, and such that the entire body is contained within. As an illustration of how this can be useful, consider a single odd-shaped rigid body experiencing collisions with a plane. Discretizing (16)-(17) for the motion using RATTLE leads to a decoupled system, in effect equivalent to applying RATTLE to (16) and leapfrog/Verlet to (17). Thus the motion of the centre mass under discretization follows a quadratic arc in the stepsize. Collisions are very near to collisions of the corresponding bounding spheres. We know that these collisions can be determined by solving a quadratic equation. (In the case of two colliding rigid bodies, their bounding sphere impacts are determined by solving a quartic polynomial.) We can thus use the bounding spheres to determine initial conditions for continuation in order to find the exact time of impact taking into account the precise body geometry.

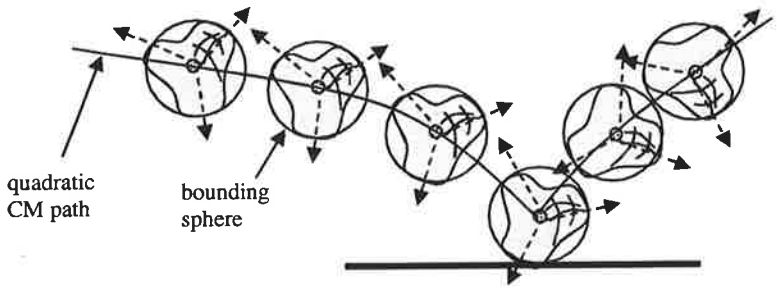

6. COMBINATION WITH CONSTANT TEMPERATURE MOLECULAR DYNAMICS

Important in molecular dynamics is the simulation of systems in the canonical (constant temperature) ensemble. While there are several means of computing sampling trajectories with the density *exp(-H/kT)*, the most popular is undeniably the Nose formulation which replaces the system Hamiltonian *H(q,p)* by an extended Hamiltonian augmented by certain thermostatting variables,

$$H^{nose}(q,p,\ s,p_s) = H(q,p/s) + p_s^2/2\mu + gkT\ ln\ s$$

It can be shown that averages of a given function with respect to constant Nose energy ("microcanonical" averages) can be reduced to canonical averages with respect to the original energy, i.e.

$$\iiint f(q,p)\ \delta[H^{Nose} - E]\ dqdpds\ dp_s = \iint f(q,p)\ exp(-H/kT)\ \ dqdp$$

Assuming that the Nose system is sufficiently strongly mixing so that the microcanonical average on the left can be replaced by the temporal average of *f(q(t),p(t))*, along constant Nose energy trajectories, we can recover canonical averages by computing molecular dynamics trajectories.

More recently, a broader class of thermostats was introduced in [20] termed generalized Nose:

$$H^{GN}(q,p,\ s,p_s,\ \theta,\ \pi) = H(q,p/s) + a(\theta)\ p_s^2/2\mu + gkT\ ln\ s\ \ + G(\theta,\ \pi)$$

Here G is an essentially arbitrary auxiliary "bath" whose properties can be tuned to enhance ensemble convergence. A "real-time" formulation can also be given based on use of a Poincare transformation of the form $H^{GN} \rightarrow s[H^{GN}-E]$ [21].

These techniques can be combined with the concepts of the collisional verlet method, but their implementation becomes substantially more challenging. In particular we know longer obtain

quadratic paths. An approach to constant temperature hard sphere dynamics based on Nose-Poincare methods [21] was given in [22].

If we consider just the standard Nose method, however, there is an alternative which is very attractive and retains the simplicity of collisional Verlet method. Note that for a simple mechanical form Hamiltonian

$$H(q,p) = p^T M^{-1} p/2 + V(q)$$

we have

$$H^{nose}(q,p,s,p_s) = p^T M^{-1} p/2s^2 + p_s^2/2\mu + V(q) + gkT \ln s$$

substituting, as in [19] the canonical coordinate change

$$s = exp(x) \qquad p_x = exp(-x)\, p_s$$

the Nose Hamiltonian is mapped to

$$H^*(q,p,x,p_x) = exp(-2x)\,(p^T M^{-1} p/2 + p_x^2/2\mu) + V(q) + gkT\, x$$

hence a Poincare transformation of the form $H^* \rightarrow exp(2x)[H^* - E]$ reduces the system to simple mechanical form:

$$H^{**}(q,p,x,p_x) = p^T M^{-1} p/2 + p_x^2/2\mu + exp(2x)\,(V(q) + gkT\, x - E)$$

This transformation is useful for understanding the nature of Nose's method, but it is also very handy for developing numerical methods. In particular if we use this formulation and discretize with Verlet, the trajectories are again quadratic paths in the stepsize, and identification of collisions is simplified. Because the separated formulation is not a real time formulation, an interpolation of the data, or alternatively a reweighting in the computation averages, will be needed, see [19].

7. STRUCTURED NONLINEAR DISSIPATION

Linear and nonlinear dissipation have been discussed by several authors in the context of geometric integration. However, an important type of "radial" dissipation seems to have been overlooked in the existing literature. This is the topic of current work by the author and T. Arponen (HUT/Leicester).

When introducing geometric integration ideas for dissipative models, it is natural to treat first the case of weak damping in an otherwise conservative model. But a rod is sometimes modelled by a strongly damped stiff spring with rest length. For example the equations of motion for a simple pendulum with spring constant k, damping coefficient d, and natural length L are:

$$dq/dt = p/m$$

$$dp/dt = -k(1 - L/|q|)q - d(qq^T/|q|^2)\, p$$
$$= F(q) + D(q)p$$

If $k,d >> 1$, it is difficult to introduce vibrational energy. At the same time any vibrations that are introduced are rapidly damped out. As a perfectly rigid rod introduces a holonomic constraint, it is natural in this setting to view the strongly damped system as "close" in some sense to Hamiltonian.

The pendulum model has interesting geometric features. In particular, the flow conserves angular

momentum. This raises a first GI problem for structured dissipative systems: construction of momentum-conserving integrators. But the system has another layer of geometric structure: observe that the divergence of the vector field is $tr[D(q)] = -d$, hence the phase space volume dissipates uniformly. A second natural GI question is therefore raised. *Can we find Uniformly Dissipative Integrators (UDIs)?*

Somewhat surprisingly, the generalized leapfrog method (Lobatto IIIA/B) and implicit midpoint method, both of which are uniformly dissipative for systems with linear dissipative forces, are not uniformly dissipative when applied to the pendulum model. Yet is easy to get a momentum conserving uniformly dissipative integrator for the pendulum, or for the closely related model of a pair of particles linked by a damped spring.

Since $D = -d\,R$ where R is a projector, we have $D^2 = (-d)^2R^2 = d^2R$, $D^3=-d^3R$, ...and

$$exp(hD) = exp(-hdR) = I - hdR + h^2d^2\,R/2 - h^3d^3R/6 + \ldots = I + (exp(-hd)-1)R$$

The splitting of the pendulum equations into

$$dq/dt = p/m \qquad\qquad dp/dt = F(q)$$

and

$$dq/dt = 0 \qquad\qquad dp/dt = D(q)p$$

defines a method which is uniformly dissipative and explicit, and conserves angular momentum. (Some method such as leapfrog/Verlet would have to be used to integrate the conservative part, in general.). Of course the pendulum is of limited interest so we must look to apply these ideas in more general settings.

Can we get UDIs for more general classes of problems? In particular we would wish to treat N-body models arising in dissipative particle dynamics, smoothed particle hydrodynamics, and elsewhere which have pairwise conservative and dissipative forces:

$$dq_i/dt = p_i/m$$
$$dp_i/dt = F_i(q) + \Sigma_j D_{ij}(q_i-q_j)(p_i-p_j)$$

Here F is assumed to be a conservative force field based on pairwise (distance dependent) interactions. If $D_{ij}(u) = d_{ij}\; u\,u^T/\,|u|^2$, then the flow of this system is angular/linear momentum conserving and uniformly dissipative. In this case, it is possible to build a momentum-preserving UDI by splitting the dissipative term into pairwise components and integrating each in succession.

In realistic cases, we will usually have short-ranged potentials and short-ranged damping between bodies

$$D_{ij}(u) = d(|q_i-q_j|)\; uu^T/|u|^2$$

where e.g. $d(r) \sim 1/r^{\alpha}$, $\alpha \geq 1$. In this more complicated case, dissipation is no longer uniform but we can design momentum conserving integrators based on splitting. At the same time we can develop schemes that *preserve the essential character of the dissipation.*

Collisional integrators can be designed to incorporate these techniques for handling structured dissipation. In a first order splitting, the positions still move along quadratic trajectories defined by the leapfrog (or symplectic Euler) splitting of the conservative part, with the damping only

applied *at impact points.* For methods with order 2, however, we now must include in the trajectory determination the complicated formulas coming from integrating the damping term based on splitting. For this reason the currently available higher-order dissipative collisional methods are probably impractical for most realistic applications.

[1] Alder B.J. and Wainwright, T.E., Phase transition for a hard sphere system, *J. Chem. Phys.* **27**, 1957.

[2] Luijten, E., Fisher, M.E., Panagiotopoulos, A., Universality class of criticality in the restricted primitive model electrolyte, *Physical Review Letters* **88**, 2002.

[3] P.J. HoogerBrugge and J.M.V.A. Koelman, Simulating microscopic hydrodynamic phenomena with dissipative particle dynamics, *Europhysics.Lett.* 19 1992.

[4] Elliott, J.A. and Windle, A.H. A dissipative particle dynamics method for modelling the geometrical packing of filler particles in polymer composites, *J. Chem. Phys.* **113**, 2000.

[5] Pandolfi, A., C.Kane, J.E. Marsden, and M. Ortiz, Time-discretized variational formulation of nonsmooth frictional contact *Int. J. Num. Methods in Engineering* **53**, 2002.

[6] D.E. Stewart, Rigid-body dynamics with friction and impact, *SIAM Review*. **42**, 2000.

[7] G. Benettin and A. Giorgilli, On the Hamiltonian Interpolation of Near to the Identity Symplectic Mappings with Application to Symplectic Integration Algorithms, *J. Stat. Phys.* **74,** 1994.

[8] S. Reich, Backward error analysis for numerical integrators, *SIAM J. Numer. Anal.* **36** , 1999

[9] Ernst Hairer, Christian Lubich, The life-span of backward error analysis for numerical integrators, *Numer. Math.* **76**, 1997.

[10] Y.A. Houndonougbo, B.B. Laird and B.J. Leimkuhler, Molecular dynamics algorithms for mixed hard-core/continuous potentials, *Molecular Physics,* **98,** 1999.

[11] Leimkuhler, B. and Skeel, R.D., Symplectic numerical integrators in constrained Hamiltonian systems, *Journal of Computational Physics* **112**, 1994.

[12] J.P.Ryckaert, G.Ciccotti and H.J.C.Berendsen, Numerical integration of the Cartesian equation of motion of a system with constraints: molecular dynamics of N-alkanes, *J. of Computational Physics* **23**, 1977.

[13] HC Andersen. Rattle: a `velocity' version of the shake algorithm for molecular dynamics calculations. *J. Comput. Phys.*, **52**, 1983

[14] Barth, E., and Leimkuhler, B., Symplectic methods for conservative multibody systems, *Communications of the Fields Institute,* **10,** 1996

[15] R. I. McLachlan, Explicit Lie-Poisson integration and the Euler equations, *Phys. Rev. Lett.* **71**, 1993.

[16] S. Reich, Momentum conserving symplectic integrators, *Physica D* **76,** 1994.

[17] A. Kol, B. Laird and B. Leimkuhler, A symplectic method for rigid-body molecular simulation, *J. Chem. Phys.* **107**, 1997.

[18] Dullweber, A., Leimkuhler, B., and McLachlan, R., Split-Hamiltonian methods for rigid-body molecular dynamics, *Journal of Chemical Physics* **107**, 1997.

[19] Leimkuhler, B., A separated form of Nose dynamics for constant temperature and pressure simulation, *Computer Physics Communications* **148**, 2002.

[20] B.B. Laird and B.J. Leimkuhler, Generalized dynamical thermostatting , *Phys. Rev. E,* to appear, 2003.

[21] S.D. Bond, B.J. Leimkuhler and B.B. Laird, The Nose-Poincare method for constant temperature molecular dynamics, *J. Comp. Phys.* **151**, 1999.

[22] A. Houndonougbo and B.B. Laird, Constant-temperature molecular-dynamics algorithms for mixed hard-core/continuous potentials *J. Chem. Phys.* **117** , 2002.

UNSTEADY CFD SIMULATIONS OF VORTEX INTERACTIONS OVER DELTA WINGS

ARTHUR RIZZI, STEFAN GÖRTZ and YANN LE MOIGNE
Royal Institute of Technology (KTH)
100 44 Stockholm, Sweden

INTRODUCTION

Modern high-performance fighter aircraft like Saab's JAS39 "Gripen"(Fig.1) make use of highly swept, slender, sharp-leading-edge delta wings. The high-angle-of-attack aerodynamics of such delta-wing configurations is dominated by the lift-enhancing effects of the vortices generated by the roll up of the shear layer emanating from the wing's leading edge.

The current research on delta-wing aircraft is focused on the unsteady nature of the complicated flow field at very high angle of attack and dynamic flight conditions where the generally very stable and lift enhancing leading-edge vortices may lag in motion and/or burst (Fig2) producing in either case dynamic effects in the aerodynamic loading. It is important to predict these dynamic effects because they dramatically change the flight characteristics of the aircraft and are often difficult to measure in wind tunnel tests.

Figure 1: Saab Aerospace/BAe system Gripen

Figure2: Smoke visualization of vortex breakdown above NASA F18-HARV

The first part of the presentation presents the state of the art of time-accurate Navier-Stokes simulations of three-dimensional vortex breakdown above a full-span, stationary delta wing using the Navier-Stokes Multi Block (NSMB) code. Analysis of this complex problem remains challenging and computationally expensive, mainly because of very small time steps and large number of grid points

required to resolve the physical time and length scales of the inherent flow unsteadiness time accurately.

The second part of the presentation treats a half-span delta wing in sinusoidal pitch oscillation and captures the dynamic formation and burst of the leading-edge vortices over the wing causing dynamic lift overshoot and hysteresis loops in the load history. A moving grid is used to reproduce the motion of the wing and the time-dependent flow equations are integrated with the dual timestepping method. The main testcase is a 70°-swept delta wing oscillating around a mean angle of attack of 22 degrees with a semi-amplitude of 18 degrees at a Mach number of 0.2. The hysteresis behaviour is reproduced and good agreement with experimental data is obtained. Flow visualizations show the expected formation, burst and disappearance of the vortices.

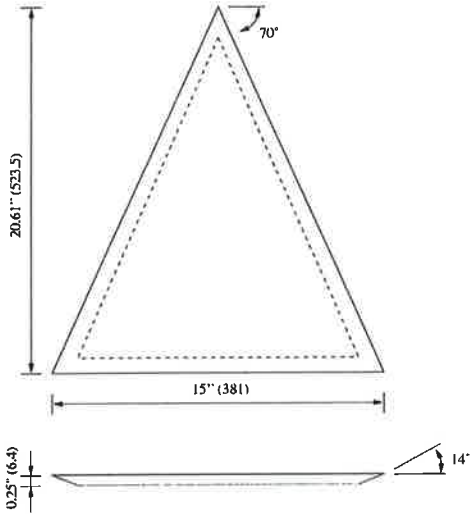

Figure 3: Wing geometry

Figure 4: Top view of the wing surface mesh for the full span wing

1. NUMERICAL PROCEDURE

The Navier-Stokes Multi Block (NSMB) code is used throughout this numerical study. It is being developed in a joint research project between universities and industry, among them KTH, EPFL, CERFACS, Saab Aerospace and Aérospatiale-Matra Airbus. The cell-centered finite volume method using block-structured grids is employed to discretize the full unsteady, three-dimensional Navier-Stokes equations. The equations are solved using the dual time-stepping technique presented by Jameson.

In the present study, a second order implicit backward scheme is used for the outer timestepping, and a very efficient matrix version of the semi-implicit LU-SGS scheme is employed for the inner loop. Multi grid is used to accelerate the convergence to "steady state" in the inner loop. A fourth-order skewsymmetric central scheme with fourth-order artificial dissipation is used for the spatial discretization. The newly available patched grid capability of the flow solver is made use of to refine

the vortical flow field in regions of interest in an effort to reach grid resolution for this complex problem.

2. MODEL GEOMETRY AND GRID

Initially only stand-alone delta-wing planforms are investigated. The delta-wing model treated here is a flat plate delta wing of 70° leading-edge sweep with a bevel on the bottom surface (Fig.3). Both half span and full span wings have computed. The sharp leading edge fixes the primary separation line of the primary vortex and makes it Reynolds number independent

An H-H-C type grid was generated for this model to ensure maximum consistency with model geometry. Three blocks were placed above the wing in an effort to avoid a singular line at the wing's apex (Fig.4). Several other grid topologies have also been tried but were less successful.

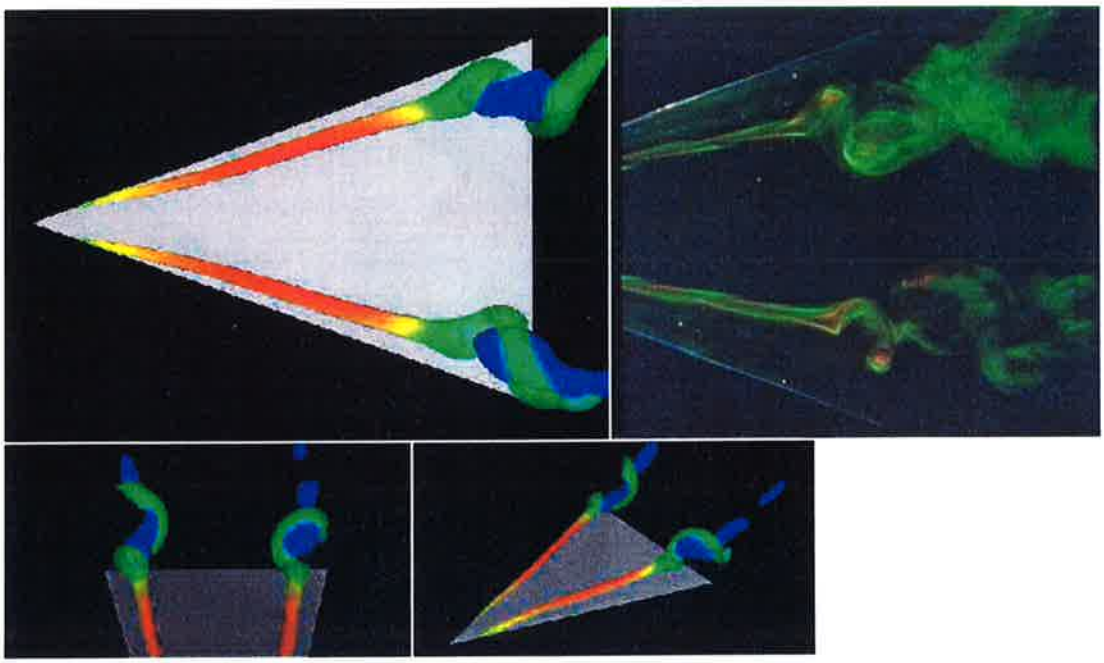

Figure 5: Assymetric vortex breakdown over full-span delta wing (Euler simulations (left) and water tunnel visualization (right))

3. SELECTED RESULTS STATIONARY DELTA

The full-span model time-accurate Euler simulations capture vortex interactions - the numerical solutions exhibit asymmetry as well as streamwise fluctuations in the port and starboard vortex breakdown locations, despite symmetric boundary conditions and a symmetric computational grid. Flow visualization reveals that spiral-type breakdown is predicted over both sides of the wing for the predominant part of the simulations. The rotation of the port and starboard post-breakdown helical structures is shown to be out of phase at certain times (compare Fig.5). Intermittent bubble-type breakdown is also observed to occur periodically over one side or the other of the wing and related to

the occurrence of asymmetry in the vortex breakdown location. For Detached-Eddy Simulation (DES), a time step study and a grid sensitivity study are conducted on semi-span grids to verify time accuracy and grid resolution. The full-span DES results are compared to detailed LDV and pressure measurements for the same geometry. The breakdown location is shown to be grid sensitive. Agreement between the measured and computed breakdown locations is shown to be good on the refined grid. The surface pressure distribution is underestimated, even on the refined grid, maybe due to excessive wind-tunnel blockage effects.

4. SELECTED RESULTS PITCHING DELTA

Fig.6 shows the different shape of the vortex at an angle of attack of 22° with and without vortex breakdown in the pitching case. The difference is due to the history of the motion of the wing before reaching this angle of attack i.e. if the angle of attack is increasing, decreasing or is maintained constant.

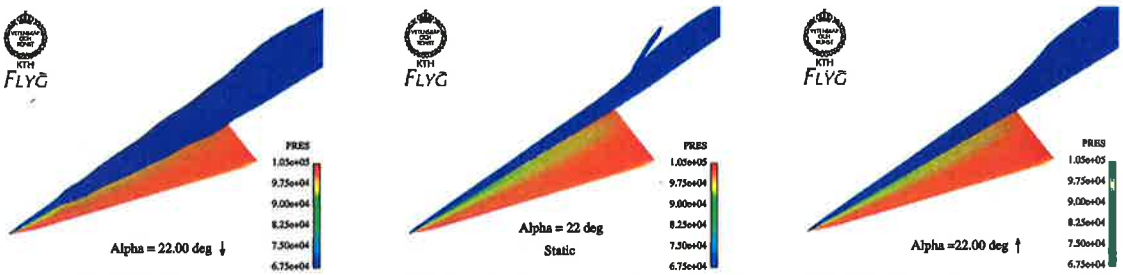

(a): Pitching up (b): Static (constant α) (c): Pitching down

Figure 6: Vortex visualization (Euler) above a semispan delta wing at α=22°,

5. HISTORICAL PERSPECTIVE ON HPC PERFORMANCE

CFD simulations of the flow around delta wings have been undertaken during the past 20 years or more, and hence it is a good subject matter to gauge the progress made in high performance computing during this period. The presentation will survey the advances made in processor speed, in memory size and in CFD methods together with software implementation and visualization techniques that have materialized during this time frame. This then provides us with some perspective of where we have come from, and where we are today, and gives some idea of where we may be in the near future.

SENSITIVITY ANALYSIS IN STRUCTURAL OPTIMIZATION

J. KOSKI
Institute of Applied Mechanics and Optimization
Tampere University of Technology
P.O. Box 589
FIN-33101 Tampere
FINLAND

ABSTRACT

The purpose of this article is to present different sensitivity analyses used in structural optimization. First, the sensitivities of the objective and the constraint functions with respect to design variables are considered. Next the sensitivity of an optimal design with respect to any fixed parameter is presented. Finally, the global sensitivity analysis of the chosen criteria, which is needed in the decision-making process, is briefly discussed in the context of multicriterion optimization.

1. INTRODUCTION

Structural optimization problem is usually formulated by choosing convenient design variables x_i, $i = 1,2,\ldots,n$, imposing required equality and inequality constraints, and forming an objective function which a designer wants to minimize or maximize. The following finite dimensional standard formulation in the design space is obtained by using nondimensional variables and functions. Because every maximization problem can be converted into a minimization problem, the latter is applied here. By using notation $\mathbf{x} \in R^n$ for the design vector, which includes all the design variables as components, notation $g_i: R^n \to R$ for inequality constraint functions, notation $h_j: R^n \to R$ for equality constraint functions and notation $f: R^n \to R$ for the scalar objective function or criterion, a standard nonlinear optimization (NLP) problem has the form

$$\min f(\mathbf{x}) \tag{1}$$

$$g_i(\mathbf{x}) \le 0 \quad , \quad i = 1,2,\ldots,r \tag{2}$$

$$h_j(\mathbf{x}) = 0 \quad , \quad j = 1,2,\ldots,s\,. \tag{3}$$

This is called briefly problem P in the continuation to separate it from multicriterion problem P_m discussed later in the text. In structural design usually most of the functions are nonlinear, but particularly in limit load problems of plasticity they all may be linear. The above formulation includes the linear programming (LP) problem as a special case, but in this article nonlinear optimization problems associated with linear structural analysis are considered.

Typical objective functions in structural design are the material volume and the cost, including material and manufacturing as well as the running costs. Other frequently used criteria are quantities associated with strength, stiffness, stability, vibration, reliability and fatigue life, just to mention a few. In the case of several conflicting criteria the multicriterion approach is applied.

Using compact vector notations $\mathbf{g}(\mathbf{x}) = \left[g_1(\mathbf{x})\, g_2(\mathbf{x}) \ldots g_r(\mathbf{x})\right]^T$ and $\mathbf{h}(\mathbf{x}) = \left[h_1(\mathbf{x}) h_2(\mathbf{x}) \ldots h_s(\mathbf{x})\right]^T$ for the constraint functions a feasible set

$$\Omega = \left\{\mathbf{x} \in R^n \mid \mathbf{g}(\mathbf{x}) \le \mathbf{0},\ \mathbf{h}(\mathbf{x}) = \mathbf{0}\right\} \tag{4}$$

is obtained. The most seen constraints in structural design are stress, displacement, natural frequency and stability constraints, but any restrictions given by standards or manufacturing process as well as all other wanted requirements can be added to the constraint set. Those inequality constraints, which are fulfilled as equalities at the current design point, are called active.

Different sensitivity considerations are an essential part of the design process. Their purpose is to determine how some chosen design quantities change when certain parameters are varied. According to this definition, the sensitivity analysis is a broad concept including several tasks even in the context of one design problem. Assuming that functions are sufficiently differentiable, some basic types of the most used sensitivity analyses in structural optimization are briefly described in the sequel.

2. SENSITIVITY WITH RESPECT TO DESIGN VARIABLES

2.1 Analytical approach

Most optimization algorithms use a gradient information at each iteration step during the line search or in order to find a feasible direction in which the objective function improves. Also optimality conditions include the gradients of the objective and constraint functions. Karush-Kuhn-Tucker conditions

$$\nabla f(\mathbf{x}^*) + \lambda^T \nabla \mathbf{g}(\mathbf{x}^*) + \mu^T \nabla \mathbf{h}(\mathbf{x}^*) = \mathbf{0} \tag{5}$$

$$\lambda_i g_i(\mathbf{x}^*) = 0 \quad , \quad i = 1,2,\ldots,r \tag{6}$$

$$\lambda_i \ge 0 \quad , \quad i = 1,2,\ldots,r \tag{7}$$

represent the necessary conditions for vector $\mathbf{x}^* \in \Omega$ to be a local optimum of problem P, provided that certain constraint qualifications are met. These conditions should be checked for any optimum candidate before accepting it to the design process. Furthermore, some algorithms like optimality criteria methods in structural design are based on an iterative solution of these equations. Here the gradients include the partial derivatives with respect to design variables, whereas λ and μ represent the vectors of Lagrange multipliers.

In structural optimization typical design variables are cross-sectional properties for beams, plate or shell thicknesses, nodal coordinates of a truss or frame, locations of control nodes in shape optimization, topology parameters, and fiber orientations together with layer thicknesses in laminated composite design. In the case of a linear static analysis the derivates of the objective function and the response functions like stresses and displacements should be computed at certain design points several times during the iteration by keeping the finite element equilibrium equation

$$\mathbf{K}(\mathbf{x})\mathbf{u} = \mathbf{p}(\mathbf{x}) \tag{8}$$

satisfied. In order to simplify the notation it assumed here that instead of $\mathbf{x}$ only one design variable x exists. By differentiating eq. (8) with respect to x sensitivity equation

$$\mathbf{K}\frac{d\mathbf{u}}{dx} = \frac{d\mathbf{p}}{dx} - \frac{d\mathbf{K}}{dx}\mathbf{u} \tag{9}$$

is obtained. This is called a "direct method" for determining the derivatives of nodal displacements $d\mathbf{u}/dx$, from which the stress derivatives can be computed by applying kinematic and constitutive equations. Using the chain rule the constraint function $g(\mathbf{u}(x),x)$ can be differentiated to give

$$\frac{dg}{dx} = \frac{\partial g}{\partial x} + \mathbf{z}^T\frac{d\mathbf{u}}{dx} \tag{10}$$

where

$$\mathbf{z} = \left[\frac{\partial g}{\partial u_1}\ \frac{\partial g}{\partial u_2}\ \ldots\ \frac{\partial g}{\partial u_N}\right]^T \tag{11}$$

represents the vector of partial derivatives with respect to all nodal displacements. Another alternative is to apply a so called "adjoint method" where the displacement derivatives need not be computed. Here an adjoint equation

$$\mathbf{K}\mathbf{y} = \mathbf{z}\ , \tag{12}$$

which is similar to eq. (8), must be solved to get vector $\mathbf{y}$ needed in the constraint derivative expression

$$\frac{dg}{dx} = \frac{\partial g}{\partial x} + \mathbf{y}^T\left(\frac{d\mathbf{p}}{dx} - \frac{d\mathbf{K}}{dx}\mathbf{u}\right). \tag{13}$$

Vector $\mathbf{z}$ can be interpreted as another loading condition, so called "dummy load", in addition to the real loading $\mathbf{p}$. Thus the numerical solution of eq. (12) is far cheaper than the solution of eq. (8), which is needed at each design point for both the direct and adjoint method. It can be noticed that the direct method requires the solution of eq. (9) once for each design variable, whereas the adjoint method requires the solution of (12) once for each constraint. Consequently, in the case where the number of design variables is smaller than the number of constraints for which gradients are needed, the direct method is more efficient. Correspondingly, the adjoint method is cheaper when the number of constraints to be differentiated is smaller than the number of design variables.

Sometimes the Hessian matrix is needed at a certain design point, as may be the case in some numerical algorithms or in more general sensitivity calculations (see chapter 3). For simplicity, it is assumed here that g does not depend explicitly from x or y. Then eqs. (9) and (10) can further be differentiated with respect to another design variable y to yield equation

$$\mathbf{K}\frac{d^2\mathbf{u}}{dx\,dy} = \frac{d^2\mathbf{p}}{dx\,dy} - \frac{d^2\mathbf{K}}{dx\,dy}\mathbf{u} - \frac{d\mathbf{K}}{dx}\frac{d\mathbf{u}}{dy} - \frac{d\mathbf{K}}{dy}\frac{d\mathbf{u}}{dx} \tag{14}$$

for the second derivatives of the displacements and equation

$$\frac{d^2 g}{dx\, dy} = \mathbf{z}^T \frac{d^2 \mathbf{u}}{dx\, dy} + \left(\frac{d\mathbf{u}}{dx}\right)^T \mathbf{U} \left(\frac{d\mathbf{u}}{dy}\right) \tag{15}$$

for the constraint function derivative. These equations, where matrix **U** includes the second partial derivates of function g with respect to the nodal displacements, represent the direct method. It is possible to derive the adjoint method equations for the second derivatives as well, but they are not shown here.

For linear eigenvalue problems, associated with the undamped free vibration and the linear buckling analysis, the governing equations

$$\left(\mathbf{K} - \omega^2 \mathbf{M}\right)\mathbf{u} = \mathbf{0} \tag{16}$$

can be differentiated to give the derivative of a certain natural frequency with respect to design variable x as follows

$$\frac{d\omega^2}{dx} = \frac{\mathbf{u}^T \left(\dfrac{d\mathbf{K}}{dx} - \omega^2 \dfrac{d\mathbf{M}}{dx}\right)\mathbf{u}}{\mathbf{u}^T \mathbf{M} \mathbf{u}} \tag{17}$$

Here the natural frequency and the corresponding eigenvector are first computed from eq. (16). If the derivatives of the eigenvectors are needed, they can be obtained by differentiating the normalization condition (for example $\mathbf{u}^T \mathbf{M}\, \mathbf{u} = 1$) and combining the result with eq. (17).

If repeated eigenvalues appear, as may happen for example in maximizing the fundamental frequency, they are no more differentiable. Several approaches for this nonsmooth situation have been developed in the literature, but they are not considered here. Similar sensitivity formulae, which were shown here for a linear static analysis, can be derived for different finite element based problems like for example linear damped vibration, transient response and nonlinear static analysis.

2.2 Difference and semi-analytical methods

Perhaps the simpliest way to calculate gradients for criteria and constraint functions is to use finite difference approximations. If commercial finite element packages are used, the code is usually hidden from the user, and it is necessary to perform the sensitivity analysis outside the program. Then for example the forward difference approximation

$$\frac{dg}{dx} \approx \frac{g(x+\Delta x) - g(x)}{\Delta x} \tag{18}$$

can be used to calculate constraint gradients. In order to obtain the required gradients at the current design point n+1 finite element analyses are needed. If instead of eq. (18) the central difference is applied the number of analyses becomes 2n+1 and the higher order approximations still increase

the computational effort. In addition to the high cost serious accuracy problems may arise in the finite difference approach due to both truncation and condition errors.

Sometimes it is advantageous to use the finite difference approximation to calculate the derivatives of the stiffness matrix and the load vector. The forward difference formula

$$\frac{d\mathbf{K}}{dx} \approx \frac{\mathbf{K}(x+\Delta x)-\mathbf{K}(x)}{\Delta x} \tag{19}$$

is useful for example in shape optimization, where it may be difficult to calculate the derivatives with respect to shape design variables which control the geometry of elements. The approach that uses analytic formulae given in eqs. (9) ... (13), but compute some derivatives using finite differences, is called a semianalytical method.

2.3 Shape optimization

In optimizing the shape of a two dimensional structural component B-splines or Bezier-curves are often used to describe the boundary of the body. Instead of using nodal coordinates as design variables the locations of the control nodes of the parametric curves (or surfaces in three dimensional problems) are usually applied. In this way it is possible to avoid accuracy problems which may result in a very disturbed and unpractical saw edge boundary. The sensitivity analysis becomes more complicated because both kinematic matrix **B** and Jacobian determinant $|\mathbf{J}|$ in the master element expression

$$\mathbf{K}_e = \iint_{A_e} \mathbf{B}^T \mathbf{D}\mathbf{B}\, t\,|\mathbf{J}|\, d\xi d\eta \,, \tag{20}$$

where **D** is a material property matrix and t is a thickness of the element, depend on design variables. Before solving $d\mathbf{u}/dx$ from eq. (9) it is necessary to calculate the derivatives of the load vector and the stiffness matrix. The derivation of the analytic expressions is a lengthy process and it is not shown here. Different approximations may become necessary in the calculations and often the shape sensitivity analysis is based on the semi-analytical or even on the difference method. After the displacement derivatives have been determined, the corresponding element stress derivatives can be computed from equation

$$\frac{d\sigma^e}{dx} = \mathbf{D}\left(\mathbf{B}\frac{d\mathbf{u}^e}{dx} + \frac{d\mathbf{B}}{dx}\mathbf{u}^e\right) , \tag{21}$$

where matrix **D** associated with Hooke's law is assumed constant.

A more sophisticated approach for the shape sensitivity analysis may be the application of so-called material derivative

$$D_p g = \frac{\partial g}{\partial p} + \nabla g\left(\mathbf{x}_\phi(\mathbf{x},p),p\right)^T \frac{\partial \mathbf{x}_\phi}{\partial p} \,, \tag{22}$$

where ∇ denotes the gradient in the two or three dimensional space and term $\partial \mathbf{x}_\phi / \partial p$ is called the velocity field, because parameter p here is similar to the time variable. The material derivative is popular in shape optimization applications, but also new approaches to generate the sensitivity information are constantly developed.

Variational methods in sensitivity analysis differentiate the governing structural equations before they are discretized. The sensitivity equations obtained in this way can be solved by using FEM-analysis or a corresponding program. This rigorous approach is especially suitable in situations where the finite element package is used and the code is not available.

3. SENSITIVITY WITH RESPECT TO FIXED PROBLEM PARAMETERS

In structural optimization many design parameters, like allowed stresses or displacements and member lengths or other dimensions, are fixed during optimization. Still it may be interesting to see, how the optimal solution changes when these fixed parameters are varied. It is assumed here that only inequality constraints are present and that vector $\bar{\mathbf{g}}$ represents those constraints which are active at the optimal point $\mathbf{x}^*$. Optimization problem is now formulated as

$$\min f(\mathbf{x}, \varepsilon) \tag{23}$$

$$g_i(\mathbf{x}, \varepsilon) \le 0 \qquad i = 1,2,\ldots,r \tag{24}$$

where both the objective function and all the constraint functions may depend on certain parameter ε, which was fixed in the original problem (1).

The differentiation of KKT-conditions (5) and the equalities

$$\bar{g}_i(\mathbf{x}^*) = 0 \qquad i = 1,2,\ldots,r_a \tag{25}$$

of the active inequality constraints yields a system of simultaneous equations in the form

$$\frac{\partial}{\partial \varepsilon}(\nabla f) + \frac{\partial \mathbf{G}}{\partial \varepsilon}\lambda + \mathbf{G}\frac{d\lambda}{d\varepsilon} + (\mathbf{H} + \Lambda)\frac{d\mathbf{x}^*}{d\varepsilon} = \mathbf{0} \tag{26}$$

$$\frac{\partial \bar{\mathbf{g}}}{\partial \varepsilon} - \mathbf{G}^T \frac{d\mathbf{x}^*}{d\varepsilon} = \mathbf{0} \ . \tag{27}$$

Here $\mathbf{G}$ is the matrix including gradients $\nabla \bar{g}_i$ as columns, $\mathbf{H}$ is the Hessian of the objective function and matrix Λ is defined componentwise by

$$\Lambda_{kl} = \sum_j \frac{\partial^2 \bar{g}_j}{\partial x_k \partial x_l}\lambda_j \ . \tag{28}$$

From eqs. (26) and (27) the derivatives of the design variables and of the Lagrange multipliers can be computed.

In the case where only the derivative of the objective function $f^*(\varepsilon)$ is needed, equation

$$\frac{df^*}{d\varepsilon} = \frac{\partial f^*}{\partial \varepsilon} + \lambda^T \frac{\partial \overline{\mathbf{g}}}{\partial \varepsilon} \tag{29}$$

can be derived by using the chain rule and eq. (27) together with KKT-condition (5). For example if in the case of a stress constraint the sensitivity of the optimal objective function with respect to the allowable stress $\overline{\sigma}$ is wanted, nice result

$$\Delta f^* = -\lambda_j \Delta \overline{\sigma} \tag{30}$$

is obtained. It should be stressed, however, that these sensitivity equations based on derivatives are valid only if the set of active constraints remains the same in the perturbated optimal solution. Thus only small changes in the fixed parameters are allowed and if larger variations are needed, the original optimization problem with new fixed parameter values must be solved.

4. MULTICRITERION OPTIMIZATION

Most design problems include several conflicting and noncommensurable criteria which should be optimized simultaneously in the feasible set. If each criterion $f_i(\mathbf{x})$, i = 1,2,...,*m*, is optimized separately in Ω usually *m* different optimal solutions appear. It is evident that if one compromise solution is wanted, some decisions concerning the mutual importance of different criteria must be made. If the criteria are combined into one scalar objective function by using suitable weights, standard problem *P* given in (1) ... (3) is obtained. Instead of choosing the weights beforehand it is advantageous to use a multicriterion approach, where the decisions concerning the importance of each criterion are postponed after the optimization problem has been solved.

Multicriterion (multicriteria, multiobjective, vector) optimization problem P_m differs from scalar problem *P* only in the objective function which is vector valued, i.e. $f: R^n \rightarrow R^m$. It includes the conflicting criteria as components and is denoted by

$$\mathbf{f}(\mathbf{x}) = \left[f_1(\mathbf{x})\ f_2(\mathbf{x}) \ldots f_m(\mathbf{x})\right]^T . \tag{31}$$

Using the minimization form and the notations given in chapter 1 multicriterion problem P_m can be stated as

$$\min_{\mathbf{x} \in \Omega} \mathbf{f}(\mathbf{x}) . \tag{32}$$

The solution of this optimization problem is a Pareto optimum (nondominated, noninferior or efficient point). Vector $\mathbf{x}^* \in \Omega$ is called Pareto optimal for problem P_m if no criterion can be improved without worsening at least one other criterion. This definition implies that a Pareto optimal set rather than one optimal point is typical for the multicriterion problem. The corresponding optimal solution $\mathbf{z}^* = \mathbf{f}(\mathbf{x}^*)$ is called a minimal solution. It belongs to criterion space R^m and is an element of attainable set

$$\Lambda = \left\{ \mathbf{z} \in R^m \,|\, \mathbf{z} = \mathbf{f}(\mathbf{x}),\ \mathbf{x} \in \Omega \right\} . \tag{33}$$

This is the image of the feasible set and in continuous problems minimal points locate on its boundary.

In multicriterion decision-making the criterion space becomes important after the Pareto optimal set, which represents the collection of the best solutions in a mathematical sense, has been generated. The minimal curve in a bicriterion case or the minimal hypersurface in the m-dimensional case, both given in the criterion space, represent global sensitivity results for the optimal design criteria. As a matter of fact, multicriterion optimization may be viewed as a systematic sensitivity analysis with respect to the most important value judgements.

5. CONCLUSION

The sensitivity analysis in structural optimization has been discussed here in a broad sense by introducing three different categories: local sensitivity with respect to design variables and fixed parameters as well as global sensitivity of several conflicting criteria. Also a local sensitivity analysis, called trade-off calculation, appears in multicriterion optimization. The important topic of nonsmooth optimization, where subgradients or generalized gradients are applied to the sensitivity analysis, was not discussed here. Furthermore, sensitivity studies of discrete or mixed variable problems were not considered in this article. These both problem types, discrete and continuous but nonsmooth, often appear in optimizing load carrying structures.

REFERENCES

1. Belegundu, A. D. and Arora, J. S., A sensitivity theorem for adjoint variable in optimal design. Computer Methods in Applied Mechanics and Engineering, **48**, pp. 81-89, 1985.
2. Choi, K. K., Shape design sensitivity analysis and optimal design of structural systems. Computer Aided Optimal Design (ed. C. A. Mota Soares), Springer-Verlag, 1987, pp. 439-492.
3. Eschenauer, H., Koski, J. and Osyczka, A. eds., Multicriteria design optimization, Springer-Verlag, 1990.
4. Haftka, R. T., Sensitivity calculations for iteratively solved problems. International Journal for Numerical Method in Engineering, **21**, pp. 1535-1546, 1985.
5. Haslinger, J. and Mäkinen, R., Introduction to shape optimization: theory, approximation and computation, SIAM, 2003.
6. Haug, E. J., Choi K. K. and Komkov. V., Design sensitivity analysis of structural systems, Academic Press, 1986.
7. Miettinen, K., Nonlinear multiobjective optimization, Kluwer, 1999.
8. Nack. W. V. and Belegundu, A. D., Shape design sensitivities. General Motors Technical Center, Warren, MI, 1985.
9. Ojalvo, I. U., Efficient computation of mode-shape derivatives for large dynamic systems, AIAA Journal, **25**, No 10, pp. 1386-1390, 1987.
10. Suffer, T.R., Camarda, C.J. Walsh, J.L. and Adelman, H. M., Comparison of several methods for calculating vibration mode shape derivatives, AIAA Journal, **26**, No. 12, pp. 1506-1511, 1988.

MINIMUM WEIGHT DESIGN OF COMPOSITE LAMINATION WITH AN INTERACTIVE DESCENT METHOD

P. KERE[a,*], M. LYLY[b], J. OJALA[a]

[a] Tampere University of Technology, Institute of Applied Mechanics and Optimization
P.O. Box 589, FIN - 33101 Tampere, Finland

[b] CSC – Scientific Computing Ltd., P.O. Box 405, FIN - 02101 Espoo, Finland

ABSTRACT

Using multicriterion optimization methods for weight minimization of failure strength controlled composite structures is described. A composite lay-up design problem for minimizing the number of layers under strength constraints with respect to multiple loading conditions is formulated. The constrained problem is transferred into a sequence of unconstrained problems and solved with an interactive descent method. A typical design cycle that comprises the finite element mesh generator and solver as well as the laminate analysis and optimization modules is illustrated with a numerical example.

1. INTRODUCTION

When loads vary with the point position or different loading conditions occur at different times under in-service conditions, the decision-maker needs to consider laminate minimum weight designs that are capable of carrying various conflicting loading conditions. A natural formulation for a problem with several competing criteria is the multi-criteria optimization formulation, where the conflicting design objectives are introduced as a vector objective function and so-called Pareto optima [12, 13] are sought.

In this paper, using an interactive descent method [1] for weight minimization of failure strength controlled composite laminates made from orthotropic fiber-reinforced layers is represented. The laminate is subjected to multiple loading conditions that may be due to the different in-service conditions at particular point of the finite element model of the structure or they may be the loads at the representative points of the critical areas of the structure. In both cases the different loading conditions are finally represented in terms of layer stress resultants integrated through the thickness of a laminate [2]. Conventions for these so-called in-plane force and moment resultants for an N-layered laminate are shown in Figure 1a.

Each loading condition may involve simultaneously applied external mechanical loads and internal loads caused by the temperature difference between the stress-free temperature and the operating temperature and by moisture absorption or desorption. The temperature and moisture content differences are assumed to vary linearly through the thickness of the laminate (Figure 1b). In the

* Corresponding author. Fax: +358-3-3115-2107.
E-mail address: petri.kere@tut.fi.

laminate failure analysis, the hygrothermal loads are assumed to stay fixed in the constant load part while the external mechanical loads are varied in the variable load part.

In failure analyses of composite structures, failure margin measuring the criticality of the effective load (the nominal load multiplied by the factor of safety FoS) with respect to the failure load is often indicated in terms of a reserve factor $RF \in R$, $RF > 0$, failure being defined by an appropriate failure criterion. According to the constant and variable load approach [3, 4], the laminate initial failure (First Ply Failure, FPF) occurs with the failure load defined as

$$\begin{pmatrix} \mathbf{N} \\ \mathbf{M} \end{pmatrix}_{xy}^{FPF} = FoS^{c} \begin{pmatrix} \mathbf{N} \\ \mathbf{M} \end{pmatrix}_{xy}^{c} + RF^{FPF} FoS^{v} \begin{pmatrix} \mathbf{N} \\ \mathbf{M} \end{pmatrix}_{xy}^{v} \tag{1}$$

where the constant (superscript c) and variable (superscript v) load vectors may be due to combined loading of external load expressed as resultant forces and moments and internal load expressed as equivalent thermal and moisture forces and moments determined as in [5].

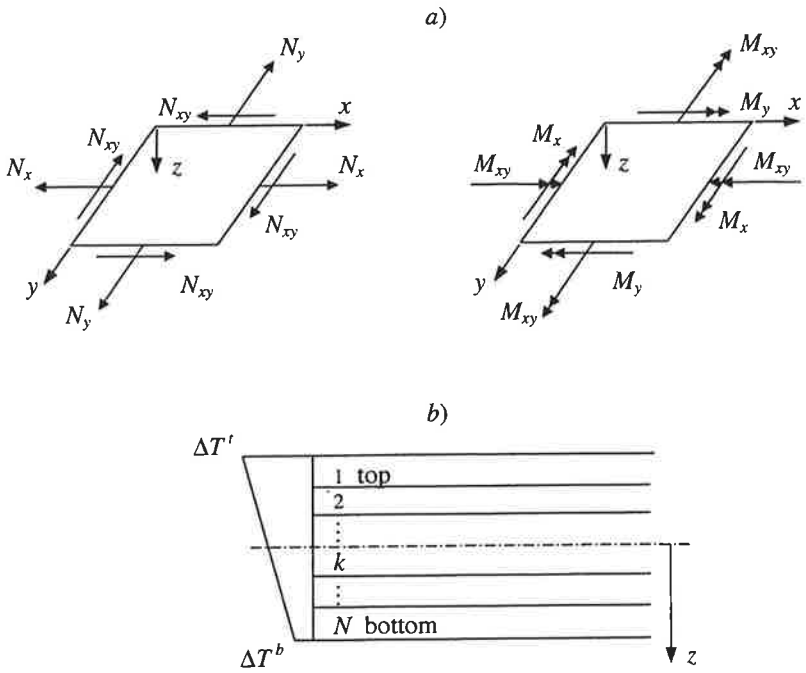

Figure 1. a) Laminate resultant in-plane forces $\mathbf{N}_{xy}$ and moments $\mathbf{M}_{xy}$ on a flat laminate. b) The temperature difference between the operating temperature and the constant stress-free temperature of a laminate. The moisture distribution can be defined analogously.

The minimum of the layer reserve factors on the top (superscript t) and bottom (superscript b) surfaces of the layer defines margin to laminate initial failure with respect to the applied loads as

$$RF^{\text{FPF}} = \min RF_k^{t,b}, \quad k = 1,2,\ldots,N \tag{2}$$

2. THE STRUCTURAL OPTIMIZATION PROBLEM

Let the symmetric and balanced laminate structure be defined so that the laminate thickness can only be multiples of the layer thickness. Let a set of initial allowable angles for layer orientations of a symmetric laminate $\theta(l)$, l=1, 2,..., N/2, be defined as $\Theta(s)$=(0, 90, +θ, −θ) degrees, s=1, 2, 3, 4, where $\theta \in [0, 90]$ degrees. Alternative symmetric and balanced laminate lay-up configurations (Figure 2) are represented as

$$\mathbf{x} = (x_{11}, x_{12}, \ldots, x_{ls}), x_{ls} \in \{0,1\}, \sum_s x_{ls} = 1, \sum_l (x_{l3} - x_{l4}) = 0 \tag{3}$$

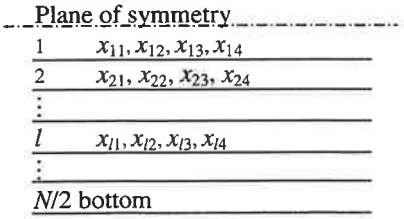

Figure 2. Discrete design variables for laminate lay-up definition.

The structural weight minimization problem can be stated in discrete form such that the laminate total number of layers N is minimized over the feasible lay-up configurations.

$$\overline{\Omega} = \{\mathbf{x} \mid \arg\min_{\mathbf{x}\in\Omega} N(\mathbf{x})\} \tag{4}$$

$$\Omega = \{\mathbf{x} \mid g_i(\mathbf{x}) = 1 - RF_i^{\text{FPF}}(\mathbf{x}) \le 0, i = 1,2,\ldots,m\} \tag{5}$$

The solution for weight minimization problem is not unique, i.e., there might be several feasible laminate lay-up configurations with the minimum number of layers. Since we want to find the lay-up configurations that maximize the failure margins with respect to the applied loading conditions, it is meaningful to introduce failure margins as criteria so that the alternative laminates can be partially ordered. The objective is to find such symmetric and balanced laminate lay-up configurations with constant ply properties and given allowable angles for layer orientations that the laminate margins to initial failure with respect of the given loading conditions are maximized with the minimum feasible number of layers. Formally, the structural optimization problem is stated as follows.

$$\max_{\mathbf{x}\in\Omega} \mathbf{f}(\mathbf{x}) \qquad \mathbf{f}(\mathbf{x}) = \begin{pmatrix} RF_1^{\text{FPF}}(\mathbf{x}) \\ RF_2^{\text{FPF}}(\mathbf{x}) \\ \vdots \\ RF_m^{\text{FPF}}(\mathbf{x}) \end{pmatrix} \tag{6}$$

In problem Eq. 6 $\mathbf{f}$ is a vector objective function where the components $f_i : \overline{\Omega} \to R$, $i = 1, 2, \ldots, m$ are called criteria and they represent the design objectives by which the performance of the laminate is measured.

The image of the feasible set in the criterion space, that is, the attainable set, is defined as

$$\Lambda = \{ \mathbf{z} \in Z \mid \mathbf{z} = \mathbf{f}(\mathbf{x}),\ \mathbf{x} \in \overline{\Omega} \} \tag{7}$$

Definition 1. A solution $\mathbf{x}^*$ is Pareto optimal for problem Eq. 6 if and only if there exists no $\mathbf{x} \in \overline{\Omega}$ such that $f_i(\mathbf{x}) \geq f_i(\mathbf{x}^*)$ for all $i = 1, 2, \ldots, m$ and $f_i(\mathbf{x}) > f_i(\mathbf{x}^*)$ for at least one $i = 1, 2, \ldots, m$. The points $\mathbf{z}^* = \mathbf{f}(\mathbf{x}^*) \in \Lambda$ in the criterion space are called the maximal points.

Definition 2. A solution $\mathbf{x}^*$ is weakly Pareto optimal for problem Eq. 6 if there does not exist another solution $\mathbf{x} \in \overline{\Omega}$ such that $f_i(\mathbf{x}) > f_i(\mathbf{x}^*)$ for all $i = 1, 2, \ldots, m$. The corresponding points in the criterion space are called the weakly maximal points.

3. ACHIEVEMENT FUNCTION APPROACH

Let $\overline{\mathbf{z}} \in \mathbf{R}^m$ be arbitrary reference objectives characterizing aspiration levels for the given criterion vector and let $s_{\overline{z}} : \Lambda \to R$ be a continuous achievement function. The achievement problem to be solved is

$$\min_{\mathbf{z}\in\Lambda} s_{\overline{z}}(\mathbf{z}) \tag{8}$$

Definition 3. A function $s_{\overline{z}}$ is *strictly decreasing* if for $\mathbf{z}^{(j)}, \mathbf{z}^{(j+1)} \in \mathbf{R}^m$ $z_i^{(j)} < z_i^{(j+1)}$ for all $i = 1, \ldots, m$ imply $s_{\overline{z}}(\mathbf{z}^{(j)}) > s_{\overline{z}}(\mathbf{z}^{(j+1)})$.

Definition 4. A continuous achievement function $s_{\overline{z}} : \Lambda \to R$ is *order-representing* if it is strictly decreasing as a function of $\mathbf{z} \in \Lambda$ for any $\overline{\mathbf{z}} \in \mathbf{R}^m$ and if $\{ \mathbf{z} \in \mathbf{R}^m \mid s_{\overline{z}}(\mathbf{z}) < 0 \} = \overline{\mathbf{z}} + \operatorname{int} \mathbf{R}^m$ for all $\overline{\mathbf{z}} \in \mathbf{R}^m$. For a continuous order-representing achievement function $s_{\overline{z}} : \Lambda \to R$ we have $s_{\overline{z}}(\overline{\mathbf{z}}) = 0$.

Based on the results represented by Wierzbicki [14, 15, 16], Miettinen (1999) [11] has given the following conditions concerning the solutions of an achievement function to be Pareto optimal. The proof for a vector minimization problem can be found in Miettinen (1999) [11], for instance.

Sufficient condition for a solution of an achievement function to be weakly Pareto optimal. If the achievement function $s_z : \Lambda \to R$ is order-representing, then, for any $\bar{\mathbf{z}} \in \mathbf{R}^m$, the solution of problem Eq. 8 is weakly Pareto optimal.

Necessary condition for a solution of an achievement function to be weakly Pareto optimal. If the achievement function $s_z : \Lambda \to R$ is order-representing and $\mathbf{z}^* \in \Lambda$ is weakly Pareto optimal or Pareto optimal, then it is a solution of problem Eq. 8 with $\bar{\mathbf{z}} = \mathbf{z}^*$ and the value of the achievement function is zero.

4. THE REDUCED PROBLEM FORMULATION

The problem to be solved is

$$\min_{\mathbf{z} \in Z} \max_{i=1,2} \{ w_i (\bar{z}_i - z_i) \} \tag{9}$$

where some of the criteria might be combined linearly as

$$\begin{aligned} z_1 &= f_i(\mathbf{x}) \text{ for one } i = 1, 2, \ldots, m \\ z_2 &= \sum_r \lambda_r f_r(\mathbf{x}) \text{ for } r = 1, 2, \ldots, m-1, r \neq i \end{aligned} \tag{10}$$

Here the subscript r is the index of the combined criteria and $\lambda_r \in \boldsymbol{\lambda}$, $\lambda_r > 0$, $\sum_r \lambda_r = 1$.

The normalizing coefficients $w_i \in \mathbf{w}$, $w_i > 0$ are used to make the criteria commensurable.

Reducing the original multiple criteria problem into a bicriteria problem has been suggested by Koski and Silvennoinen (1982, 1987) [17, 18], for instance. By fixing the parameters used to reduce the number of the criteria, it is possible to control the evolution of the sequence generated by the optimization procedure towards some subset of Pareto optima. Pareto optimal solutions found with particular parameter values in the reduced criterion space are also Pareto optimal solutions in the original criterion space. Koski and Silvennoinen (1987) [18] have shown that by using the reduced problem formulation, the decision-maker always operates on the maximal set of the original problem. The reverse relation is not generally true, but in any case, at least a subset of Pareto optima of the original problem is obtained with the reduced problem formulation.

We employ an optimization procedure where the problem is solved iteratively by transferring the constrained problem into a sequence of unconstrained problems. The state of a sequence $\mathbf{x}^{(j)}$ corresponds to the selected lay-up configuration at that cycle of the iterative procedure. Convergence of the algorithm is measured with an achievement function called the descent function

$$s_z(\mathbf{x}^{(j)}) = \max \{ \bar{z}_i - f_i(\mathbf{x}^{(j)}) \}, \quad i = 1, 2, \ldots, m \tag{11}$$

Termination condition for the algorithm is defined as

$$\max \{ 0, s_z(\mathbf{x}^{(j)}) \} \leq \delta \tag{12}$$

where $\delta > 0$ is a small predefined scalar.

5. NUMERICAL EXAMPLE

To illustrate the design optimization technique, we consider the weight minimization problem of a clamped Z-profile elastic beam shown in Figure 3. The beam is composed of layers having the mechanical properties of in plane 23 transversely isotropic Carbon/epoxy ply listed in Table 1.

Table 1. Mechanical properties of the ply.

Carbon/epoxy, $t = 0.2$ mm, $\rho = 1550$ kg/m^3			
$E_1 = 155$ GPa	$\nu_{12} = 0.3$	$X_t = 1950$ MPa	$Y_t = 48$ MPa
$E_2 = 8.5$ GPa	$\nu_{23} = 0.28$	$X_c = 1480$ MPa	$Y_c = 200$ MPa
$G_{12} = 5.5$ GPa	$G_{23} = 3.32$ GPa	$S_{12} = 79$ MPa	

The length of the beam is 1 m, the height of the web and the width of the flanges are 0.1 m. The beam is subjected to its own weight and to two external forces $F_y = 7000$ N at the mid length of the beam and $F_z = -5000$ N at the free end of the beam as shown in Figure 3. The objective is to find a minimum weight solution for the beam without failure, failure being predicted according to the Tsai-Hill failure criterion [2]. The web and flanges should have identical laminate lay-up configuration.

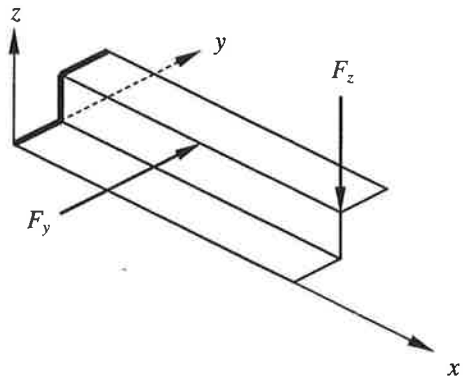

Figure 3. The clamped Z-profile elastic beam.

The beam is analyzed with the initial [0/±45/90]SE (SE denotes symmetric even laminate structure) lay-up employing the ELMER [9] software. ELMER is a software package for solving Partial Differential Equations (PDEs). It has been developed at CSC – Scientific Computing Ltd. in collaboration with Finnish universities, research laboratories, and industry. ELMER includes physical models of fluid dynamics, structural mechanics, electromagnetics, vibroacoustics, and heat transfer, for instance. These are described by PDEs which ELMER solves by FEM. Recently the software capabilities have been extended to cover orthotropic laminated structures as well.

The beam is analyzed using the shell model based on a facet approximation of the midsurface, standard plane stress equations (discretized by the standard FEM), and the plate model of Reissner and Mindlin (discretization by the stabilized MITC-technique [6, 7, 8]). As a result, there are six degrees of freedom per node. The FE model used for the ELMER solver is shown in Figure 4.

Based on the laminate level stress-strain state at nodes of the FE model, the laminate FPF analysis is performed with the composite analysis and design software ESAComp [10, 19]. In the laminate failure analysis, the Tsai-Hill failure criterion and FoS^{v}=1.0 have been used. The two critical points in the FE model, LC_1: (N, M)=(−1565000, −46158, 81086, −147.52, −18.79, −12.49) N/m, Nm/m and LC_2: (N, M)=(694300, 499450, −563490, −30.33, 1.53, 0.97) N/m, Nm/m producing $RF_1^{FPF} = 0.486$ and $RF_2^{FPF} = 0.485$, respectively, have been selected interactively as the representative points for the optimization phase.

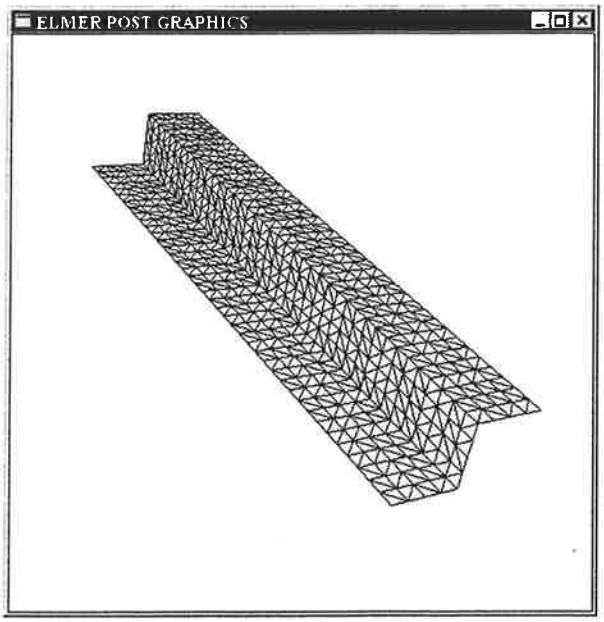

Figure 4. The FE model of the beam.

The bicriteria optimization problem is formulated as

$$\max_{\mathbf{x}\in\Omega} \begin{pmatrix} RF_1^{FPF}(\mathbf{x}) \\ RF_2^{FPF}(\mathbf{x}) \end{pmatrix} \tag{13}$$

$$\overline{\Omega} = \{ \mathbf{x} \mid \arg\min_{\mathbf{x}\in\Omega} N(\mathbf{x}) \} \tag{14}$$

$$\Omega = \{ \mathbf{x} \mid g_i(\mathbf{x}) = 1 - RF_i^{\text{FPF}}(\mathbf{x}) \le 0,\ i = 1,2 \tag{15}$$

The constrained problem is transferred into a sequence of unconstrained problems

$$\min_{\mathbf{x} \in X^{(j)}} \max_{i=1,2} \{1 - \tilde{f}_i(\mathbf{x})\} \tag{16}$$

where $\tilde{f}_i(\mathbf{x}) = RF_i^{\text{FPF}}(\mathbf{x}) / \max_{\mathbf{x} \in X^{(j)}} RF_i^{\text{FPF}}(\mathbf{x})$.

At the initial step all permutations of the symmetric and balanced lay-ups with N=8 and initial allowble layer orientations are created. A set of new design points is defined at each cycle on the basis of the preceding point $\mathbf{x}^{(j)}$ as

$$\mathbf{x}^{(j+1)} \in X^{(j)} = \begin{Bmatrix} (\mathbf{x}^{(j)},0,0),(0,\mathbf{x}^{(j)},0),(0,0,\mathbf{x}^{(j)}), \\ (\mathbf{x}^{(j)},0,90),\ (0,\mathbf{x}^{(j)},90),(0,90,\mathbf{x}^{(j)}), \\ (\mathbf{x}^{(j)},90,0),(90,\mathbf{x}^{(j)},0),(90,0,\mathbf{x}^{(j)}), \\ (\mathbf{x}^{(j)},90,90),(90,\mathbf{x}^{(j)},90),(90,90,\mathbf{x}^{(j)}), \\ (\mathbf{x}^{(j)},+\theta,-\theta),\ (\mathbf{x}^{(j)},-\theta,+\theta), \\ (+\theta,-\theta,\mathbf{x}^{(j)}),(-\theta,+\theta,\mathbf{x}^{(j)}) \end{Bmatrix} \tag{17}$$

where for each new design point in $X^{(j)}$, the layer orientations of additional layers in a half laminate are for clarity denoted in degrees. Hence, for instance the $(\mathbf{x}^{(j)},0,0)$ design point corresponds to the $[\mathbf{x}^{(j)}/0/0]$SE laminate lay-up where $\mathbf{x}^{(j)}$ is half of the selected symmetric laminate at the jth cycle. To avoid the generation of undesirable thick $(+\theta)$ or $(-\theta)$ sublaminates, the $(+\theta, \mathbf{x}^{(j)}, -\theta)$ and $(-\theta, \mathbf{x}^{(j)}, +\theta)$ permutations are neglected in the set.

Convergence of the algorithm is measured with the descent function

$$s_z(\mathbf{x}^{(j)}) = \max\{1 - RF_i^{\text{FPF}}(\mathbf{x}^{(j)})\}, \quad i = 1,2 \tag{18}$$

Termination condition is defined as in Eq. 12.

The solution for problem Eq. 13 is found with the initial allowable layer orientations Θ=$(0, 90, +\theta, -\theta)$, θ=$\{42,49\}$ degrees. Improvement of the descent function value for the $[(0)3/+\theta/-\theta/(90)2/-\theta/+\theta]$SE stacking sequence with θ=42 degrees is represented in Figure 5.

Pareto optimal $[(0)3/+\theta/-\theta/(90)2/-\theta/+\theta]$SE and $[(0)4/+\theta/-\theta/90/-\theta/+\theta]$SE stacking sequences with N=18 have been found as a solution of the problem. The $(\pm\theta)$ layers are varied with θ=$\{1, 2,..., 90\}$ degrees and the maximal points are identified. Maximal points in the criterion space are shown in Figure 6.

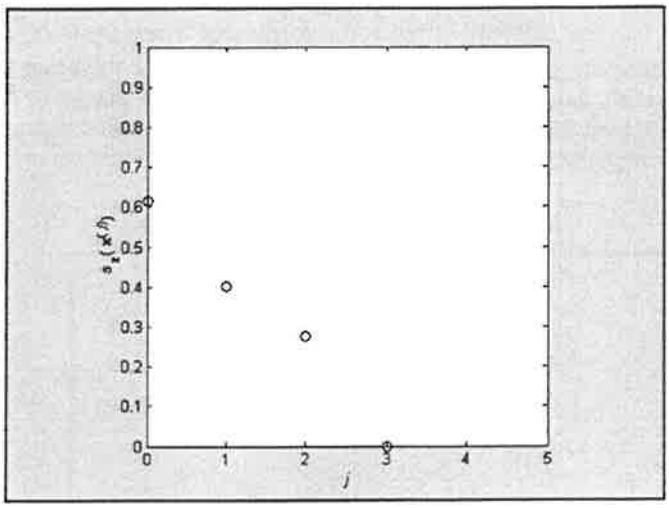

Figure 5. Improvement of the descent function value for the [(0)3/+θ/−θ/(90)2/−θ/+θ]SE stacking sequence with θ=42 degrees.

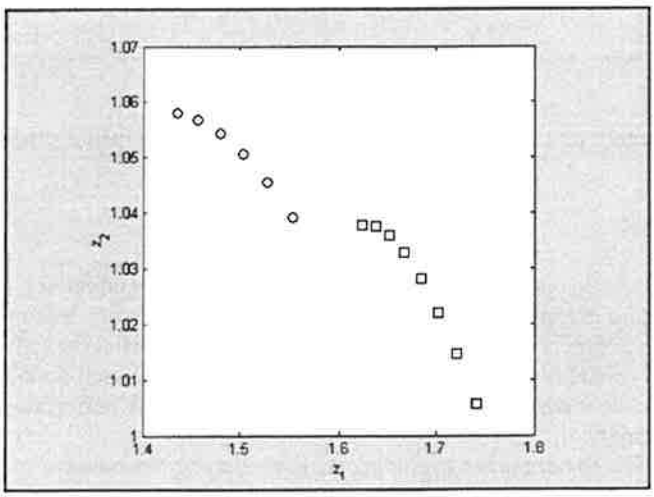

Figure 6. Maximal points in the criterion space for problem Eq. 13 with the Tsai-Hill failure criterion. Circle corresponds to the [(0)3/+θ/−θ/(90)2/−θ/+θ]SE stacking sequence with θ={44, 43,..., 39} degrees and square to the [(0)4/+θ/−θ/90/−θ/+θ]SE stacking sequence with θ={50, 49,..., 43} degrees.

The [(0)3/+44/–44/(90)2/–44/+44]SE lay-up with N=18 is selected as the minimum weight solution and returned into the ELMER software for conducting a reanalysis of the structure. The failure analysis gives now the positive failure margin $RF^{FPF} = 1.35$ for the beam with the Tsai-Hill failure criterion. As a result, thus, for the optimized beam we have 35 % margin of safety with respect to the first layer failure. First failure is expected to occur at the uppermost 0 degree layer at the free end of the beam. An example of the beam analysis results with ELMER is shown in Figure 7.

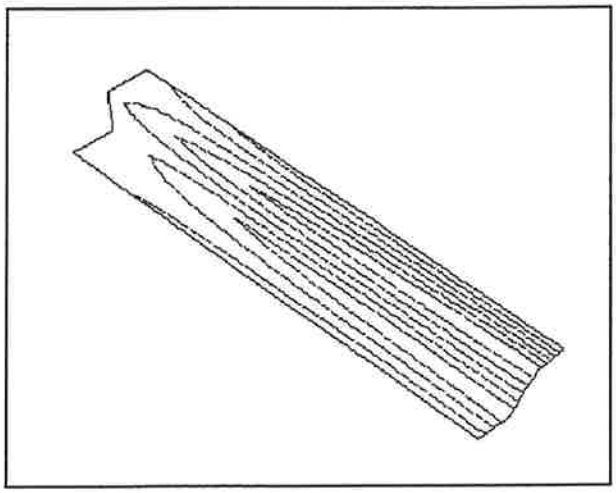

Figure 7. A contour plot of the longitudinal deflection for a clamped Z-profile elastic beam.

6. CONCLUSIONS

The design optimization approach considered in this work can be effectively used in the minimum weight design of failure strength controlled laminated structural elements. The optimization procedure is independent of the failure criterion internal formulation used to predict the failure of a laminate. The laminate level stress or strain state at preselected or interactively selected nodes of the FE model are taken as input to the laminate analysis and optimization modules for performing the laminate failure analysis and optimization.

Since the set of Pareto optima may be large, it is beneficial to formulate the multi-criteria problem computationally as economically as possible. Instead of computing all Pareto optima, it is usually sufficient to determine only a relevant subset of Pareto optima. The more appropriately the subset of Pareto optima is determined, the easier it is for the decision-maker to deal with the results. For that reason, a reduced problem where parameters are introduced to combine linearly some criteria has been formulated. The decision-maker can interact in computation by setting the parameters on the basis of his preferences and the information available on the past computations.

7. REFERENCES

[1] Kere P, Koski J. Multicriterion Optimization of Composite Laminates for Maximum Failure Margins with an Interactive Descent Algorithm. Structural and Multidisciplinary Optimization 2002; 23: 436–447.

[2] Jones RM. Mechanics of Composite Materials. New York: Hemisphere Publishing Corporation, 1975.

[3] Palanterä M, Klein M. Constant and Variable Loads in Failure Analyses of Composite Laminates. In: Brebbia M, editors. Computer Aided Design in Composite Material Technology IV (CADCOMPIV). Southampton: Computational Mechanics Publication, 1994; 221–228.

[4] Kere P, Palanterä M. A Method for Solving Margins of Safety in Composite Failure Analysis. In: Aalto J, Salmi T, editors. Proceedings of the 6th Finnish Mechanics Days. Oulu: University of Oulu, Structural Engineering Laboratory, 1997; Publication 56: 187–197.

[5] Humphreys EA, Rosen BW. Properties Analysis of Laminates. In: Engineered Materials Handbook,Vol. 1, Composites. Metals Park, OH: ASM International, 1987; 218–235.

[6] Brezzi F, Fortin M, Stenberg R. Error analysis of mixed-interpolated elements for Reissner-Mindlin plates. Mathematical Models and Methods in Applied Sciences 1991; 1: 125–151.

[7] Lyly M. On the connection between some linear triangular Reissner-Mindlin plate bending elements. Numerische Mathematik 2000; 85: 77–107.

[8] Hughes TJR, Brezzi F. On drilling degrees of freedom. Computer Methods in Applied Mechanics and Engineering 1989; 72: 105–121.

[9] ELMER web site at www.csc.fi/elmer.

[10] Katajisto H, Palanterä M. Post Processing of FE Results Using Laminate Analysis Software. In: Proceedings of the 13th International Conference on Composite Materials (ICCM/13), Beijing, 25-29 June 2001. Paper 1449.

[11] Miettinen K. Nonlinear Multiobjective Optimization. Boston: Kluwer Academic Publishing, 1999.

[12] Edgeworth FY. Mathematical Physics. London: Kegan-Paul & Co., 1881.

[13] Pareto V. Manual of Political Economy (Cours d'Economie Politique, 1896). New York: The Macmillan Press Ltd., 1971.

[14] Wierzbicki AP. The Use of Reference Objectives in Multiobjective Optimization. In: Fandel G, Gal T, Eds. Multiple Criteria Decision Making Theory and Application. Lecture Notes in Economics and Mathematical Systems; 177: 468–486.

[15] Wierzbicki AP. A Mathematical Basis for Satisficing Decision Making. In: Morse JN, Ed. Organizations: Multiple Agents with Multiple Criteria. Lecture Notes in Economics and Mathematical Systems; 190: 465–485.

[16] Wierzbicki AP. A Methodological Approach to Comparing Parametric Characterizations of Efficient Solutions. In: Fandel G, Grauer A, Kurzhanski A, Wierzbicki AP, Eds. Large-Scale Modelling and Interactive Decision Analysis. Lecture Notes in Economics and Mathematical Systems; 273: 27–45.

[17] Koski J, Silvennoinen R. Pareto Optima of Isostatic Trusses. Computer Methods in Applied Mechanics and Engineering 1982; 31: 265–279.

[18] Koski J, Silvennoinen R. Norm Methods and Partial Weighting in Multicriterion Optimization of Structures. International Journal for Numerical Methods in Engineering 1987; 24: 1101–1121.

[19] ESAComp web site at www.componeering.fi/esacomp.

Optimointialgoritmien käyttö epälineaarisen tasapainopolun määrityksessä

MIKKO KAUTTO, SAMI PAJUNEN[#]

Tampereen teknillinen yliopisto
Teknillisen mekaniikan ja optimoinnin laitos
PL 589 33101 TAMPERE

TIIVISTELMÄ

Kaarenpituusmenetelmän eri versiot ovat kolmen viimeisen vuosikymmenen aikana vakiintuneet standardityökaluiksi epälineaaristen statiikan tehtävien numeerisessa ratkaisemisessa. Laajan kehitystyön tuloksena kaarenpituusmenetelmät ovat muokkautuneet nykyiseen asuunsa ja lähes kaikki uusi tutkimus kohdistuukin menetelmien yhä parempaan luotettavuuteen ja tehokkuuteen. Tästä poiketen tässä tutkimuksessa on kajottu kaarenpituusmenetelmän yhteen keskeiseen osaan ja tutkittu mitä etuja voitaisiin saavuttaa jos perinteinen Newton-Raphson iterointiin perustuva tasapainopolulle palautus muotoiltaisiinkin rajoitetuksi minimointitehtäväksi ja ratkaistaisiin se tehokkaalla SQP-optimointialgoritmilla.

1. JOHDANTO

Elementtimenetelmällä diskretoitujen rakenteiden epälineaarisen statiikan tehtävien ratkaisemiseen on kehitetty erilaisia polunseurantamenetelmiä. Näistä käytetyin on kaarenpituusmenetelmä, joka perustuu tasapainopolun kaarenpituuden rajoitusyhtälöllä laajennetun tasapainoyhtälöryhmän inkrementaaliseen ja iteratiiviseen ratkaisemiseen. Toisin sanoen kaarenpituusmenetelmällä saadaan määritettyä rakenteen tasapainopolku kasvattamalla kontrolliparametrin eli tasapainopolkua pitkin kulkevan koordinaatin arvoa askeleittain ja iteroimalla rakenne tasapainotilaan kunkin askeleen lopussa. Jokainen polunseuranta-askel koostuu tasapainopolun tangentin suuntaan otetusta ennustaja-askeleesta sekä lukuisista korjaaja-askeleista, joiden suunnan ja suuruuden määrää käytössä oleva kaarenpituuden rajoitusyhtälö sekä käytetty Newton-Raphson iteroinnin versio.

Kaarenpituusmenetelmällä voidaan määrittää epälineaarisia yksikäsitteisiä tasapainopolkuja joissa voi esiintyä kuvan 1 mukaisia rajapisteitä, eli pisteitä joissa kuormakertoimella λ on ääriarvo. Kuvan 1 mukainen tasapainopolku syntyy esimerkiksi läpilyöntitilanteessa.

Tässä työssä tarkastellaan polunseurantamenetelmää, jossa korjaaja-askeleiden määrittämiseen sovelletaan totutusta Newton-Raphson iteroinnista poiketen optimointialgoritmia. Ratkaisu saatetaan ennustaja-askeleen jälkeen tasapainopolulle muodostamalla rajoitettu minimointitehtävä

[#] Yhteyshenkilö, nykyinen s-posti: sami.pajunen@patria.fi

siten, että kohdefunktiona on epätasapainovektorin normi. Rajoitusyhtälö muodostetaan siten, että etsittävä tasapainopolun piste on edelliseen tasapainopolun pisteeseen piirretyn tietyn säteisen pallon pinnalla. Näin saadaan menetelmän askelpituus määrättyä kaarenpituusmenetelmää vastaavaksi. Syntyneeseen rajoitettuun minimointitehtävään sovelletaan SQP-minimointialgoritmia (Sequential Quadratic Programming). Samantyylistä lähestymistapaa on käytetty tasapainopolkujen etsimiseen myös moninkertaisen haarautumispisteen ympäristössä [5].

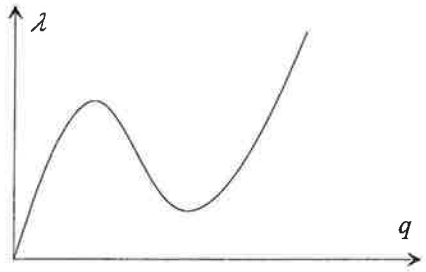

Kuva 1 Esimerkki läpilyöntitehtävän epälineaarisesta tasapainopolusta.

Työssä esitellään yksi laskentaesimerkki, jossa vertaillaan SQP-menetelmän toimivuutta nykyisin monissa ohjelmistoissa käytettyihin Riksin normaalitasomenetelmään [1] ja Crisfieldin pallorajoitusmenetelmään [2].

2. POLUNSEURANTA MINIMOINTILÄHESTYMISTAVALLA

Lähdetään liikkeelle laajennetusta tasapainoyhtälöryhmästä

$$\mathbf{G}(\mathbf{q},\lambda)=\begin{Bmatrix}\mathbf{r}(\mathbf{q})-\lambda\mathbf{p}_{\text{ref}}\\ \mathbf{c}(\mathbf{q},\lambda)\end{Bmatrix}=\mathbf{0};\qquad \mathbf{G}:\mathbf{R}^{n+1}\rightarrow\mathbf{R}^{n+1} \tag{1}$$

jossa $\mathbf{q}$ on solmusiirtymävektori, λ on kuormitusparametri, $\mathbf{r}$ on sisäisten voimien solmuvoimavektori, $\mathbf{p}_{\text{ref}}$ on ulkoinen referenssikuormitusvektori ja c=0 on kaarenpituuden rajoitusyhtälö. Yhtälöryhmä (1) ratkaistaan kahdessa vaiheessa. Annetaan ensin ohjausparametrille eli kaarenpituuskoordinaatille s määrätty inkrementti Δs ja lasketaan sitä vastaavat siirtymä- ja kuormakerroininkrementit. Sen jälkeen minimoidaan SQP-menetelmällä epätasapainovektorin $\mathbf{r}(\mathbf{q})$-$\lambda\mathbf{p}_{\text{ref}}$ euklidista normia rajoitusyhtälöllä $c(\mathbf{q},\lambda)$=0 jotta ratkaisu saadaan palautettua tasapainopolulle. Ratkaisun yksityiskohtaisempi kulku on esitetty seuraavassa.

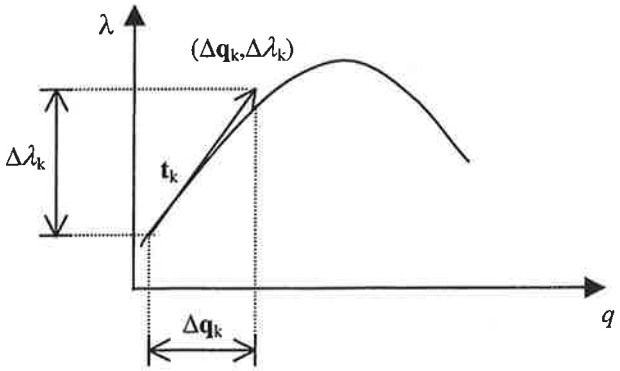

Kuva 2 Tasapainopolun tangentin suuntaan otettu ennustaja-askel.

Saavutettussa tasapainopisteessä ($\mathbf{q}_k$, λ_k) otetaan tasapainopolun tangentin suuntaan ennustaja-askel $\mathbf{t}_k$ (kuva 2), jonka pituus on (ainakin likimain) ohjausparametrin inkrementin Δs suuruinen. Ennustaja-askel voidaan jakaa komponentteihin

$$\mathbf{t}_k = \begin{bmatrix} \Delta\mathbf{q}_k \\ \Delta\lambda_k \end{bmatrix} \qquad \mathbf{t}_k \in \mathbf{R}^{n+1} \tag{2}$$

jossa skalaari $\Delta\lambda_k$ on kuormakertoimen λ inkrementaalinen lisäys pisteessä ($\mathbf{q}_k$, λ_k) ja vektori $\Delta\mathbf{q}_k$, sisältää vastaavan inkrementaalisen siirtymän. Nämä inkrementaaliset lisäykset voidaan laskea esimerkiksi kaavoilla

$$\mathbf{K}_{T_k}\Delta\mathbf{q}_p = \mathbf{p}_{ref} \tag{3}$$

$$\Delta\mathbf{q}_i = \frac{\Delta s}{\|\Delta\mathbf{q}_p\|}\Delta\mathbf{q}_p \tag{4}$$

$$\Delta\lambda_i = \frac{\Delta s}{\|\Delta\mathbf{q}_p\|} \tag{5}$$

Jolloin on vielä määrättävä suurin sallittu kuormakertoimen inkrementti ja tarkistettava, että se ei ylity. Ennustaja-askeleella on näin siirrytty pisteeseen ($\mathbf{q}_k+\Delta\mathbf{q}_k$, $\lambda_k+\Delta\lambda_k$). Ratkaisun palauttamiseksi tasapainopolulle muodostetaan minimointitehtävä, jossa rajoitusehto määrää ratkaisun pysyvän pisteeseen ($\mathbf{q}_k$, λ_k) piirretyn Δs-säteisen pallon pinnalla. Rajoitusehto on siis sama kuin Crisfieldin menetelmässä. Yhtälörajoitettu minimointitehtävä yleisessä muodossa on [3]

$$\begin{aligned} \min \quad & f(\mathbf{x}) \\ & h(\mathbf{x}) = 0 \end{aligned} \tag{6}$$

Tarkasteltavassa tehtävässä minimointiongelma kirjoitetaan muodossa

$$\min \quad \left\| \mathbf{r}(\mathbf{q}_k^i) - \lambda_k^i \mathbf{p}_{ref} \right\| \tag{7}$$

$$\left(\Delta\mathbf{q}_k^i\right)^T \Delta\mathbf{q}_k^i + \left(\Delta\lambda_k^i\right)^2 \psi^2 \mathbf{p}_{ref}{}^T \mathbf{p}_{ref} - \Delta s^2 = 0 \tag{8}$$

jossa suunnittelumuuttujat $\Delta\mathbf{q}_k^i$ sekä $\Delta\lambda_k^i$ sisältävät siirtymä- ja kuormakerroininkrementit askeleella k ja iteraatiokierroksella i, $\mathbf{q}_k^i$ ja λ_k^i ovat siirtymävektorin ja kuormakertoimen vastaavat kokonaisarvot. Parametrillä ψ saadaan termien dimensiot täsmäämään sekä saadaan painotettua kuormakerrointa halutulla tavalla. Valitaan nyt parametrin arvo siten, että

$$\psi^2 = \frac{1}{\mathbf{p}_{\text{ref}}{}^{\text{T}}\mathbf{p}_{\text{ref}}} \tag{9}$$

SQP-menetelmää varten generoidaan tehtävä kvadraattiseen muotoon. Otetaan käyttöön Lagrangen funktio

$$L(\mathbf{q},\lambda,\mu) = f(\mathbf{q},\lambda) + \mu h(\mathbf{q},\lambda) \tag{10}$$

joka tarkasteltavassa tapauksessa on

$$L(\mathbf{q},\lambda,\mu) = \left\| \mathbf{r}_k^i - \lambda_k^i \mathbf{p}_{\text{ref}} \right\| + \mu\left(\left(\Delta\mathbf{q}_k^i\right)^{\text{T}} \Delta\mathbf{q}_k^i + \left(\Delta\lambda_k^i\right)^2 \psi^2 \mathbf{p}_{\text{ref}}{}^{\text{T}}\mathbf{p}_{\text{ref}} - \Delta s^2 \right) \tag{11}$$

jossa μ on Lagrangen kerroin. Tällöin tehtävänä on ratkaista yhtälö $\nabla L(\mathbf{q},\lambda,\mu) = 0$. Kun tähän sovelletaan Newton-Raphson menetelmää tehtävä saadaan muotoon

$$\begin{cases} \mathbf{H}_k\mathbf{d}_k^i + \nabla h(\mathbf{x}_k^i)\mu_k^{i+1} = \nabla f(\mathbf{x}_k^i) \\ \nabla h(\mathbf{x}_k^i)^{\text{T}}\mathbf{d}_k^i = -h(\mathbf{x}_k^i) \end{cases} \tag{12}$$

Saatu yhtälöryhmä edustaa kvadraattisen probleeman

$$\begin{aligned} \min \quad & \nabla f(\mathbf{x}_k^i)^{\text{T}}\mathbf{d}_k^i + \frac{1}{2}\mathbf{d}_k^i\mathbf{H}_k^i\mathbf{d}_k^i \\ & h(\mathbf{x}_k^i) + \nabla h(\mathbf{x}_k^i)^{\text{T}}\mathbf{d}_k^i = \mathbf{0} \end{aligned} \tag{13}$$

Kuhn-Tucker ehtoja. Vektori

$$\mathbf{x}_k^i = \begin{bmatrix} \mathbf{q}_k^i \\ \lambda_k^i \end{bmatrix} \tag{14}$$

on ennustaja-askeleella saavutettu SQP-menetelmän aloituspiste. Kvadraattisen probleeman ratkaisuna saadaan SQP-menetelmällä hakusuunta $\mathbf{d}_k^i$ ja Lagrangen kerroin μ_k^{i+1}. Menetelmän seuraava iteraatiopiste saadaan kaavasta $\mathbf{x}_k^{i+1} = \mathbf{x}_k^i + t^i\mathbf{d}_k^i$, jossa t^i on laskettu optimaalinen askelpituus. Minimointia jatketaan kunnes kohdefunktion arvo alittaa annetun toleranssin. Tehokkuuden takia Hessen matriisia $\mathbf{H}_k$ päivitetään BFGS-menetelmällä [4].

SQP-menetelmää varten määritetään kohdefunktion ja rajoitusyhtälön analyyttiset gradientit

$$\nabla f(\mathbf{q},\lambda)=\begin{bmatrix}\dfrac{\mathbf{r}_{,q}{}^{T}(\mathbf{r}-\lambda\mathbf{p}_{ref})}{\|\mathbf{r}-\lambda\mathbf{p}_{ref}\|}\\ \dfrac{-\mathbf{p}_{ref}{}^{T}(\mathbf{r}-\lambda\mathbf{p}_{ref})}{\|\mathbf{r}-\lambda\mathbf{p}_{ref}\|}\end{bmatrix} \qquad \nabla h(\mathbf{q},\lambda)=\begin{bmatrix}2\Delta\mathbf{q}\\ 2\Delta\lambda\psi^{2}\mathbf{p}_{ref}{}^{T}\mathbf{p}_{ref}\end{bmatrix} \tag{15}$$

Gradientteja voidaan approksimoida myös numeerisesti esimerkiksi differenssimenetelmällä. Esimerkiksi Matlab (optimazation toolbox) käyttää differenssimenetelmää mikäli analyyttisiä gradientteja ei anneta syötteenä.

3. NUMEERINEN ESIMERKKI

Tarkastellaan kuvan 3 mukaista yhden vapausasteen tapausta. Kuvan 3 rakenteessa stabiilisuuden menetys tapahtuu läpilyöntinä kuormituksen P vaikutuksesta, ja rakenteen tasapainopolku on kuvan 1 mukainen.

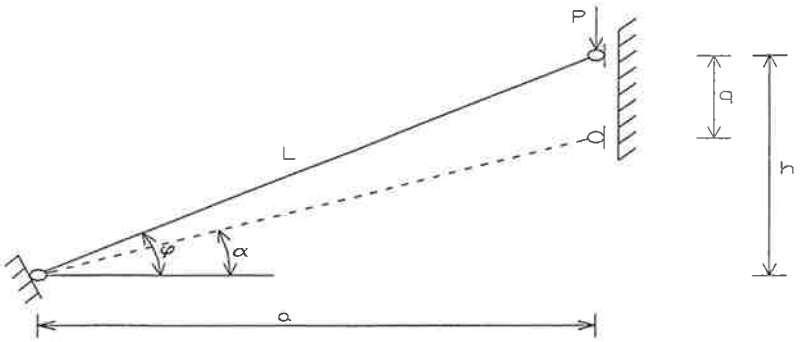

Kuva 3 Yhden vapausasteen sauvarakenne.

Kyseinen tapaus voidaan ratkaista analyyttisestikin käyttäen apuna sisäisten voimien vektorin tarkkaa lauseketta

$$r(q)=EA\frac{h-q}{L}\left(-1+\frac{L}{\sqrt{a^{2}+(h-q)^{2}}}\right) \tag{16}$$

Sovelletaan kuitenkin edellä esitettyä polunseurantamenetelmää ja annetaan alkuarvoiksi $E=200N/m^{2}$, $A=1m^{2}$, $L=5m$, $a=L\sqrt{3}/2$, $h=L/2$. Valitaan ensimmäisen ennustaja-askeleen Δs pituudeksi 2 ja aloitetaan laskenta pisteestä (q_k,λ_k) = (0,0). Laskennan tuloksena saadaan kuvan 4 mukainen tasapainopolku, jossa kaarenpituusmenetelmällä lasketut pisteet on esitetty tähtimerkinnällä.

Residuaalivektorin normin minimipistettä haettaessa iteraatio lopetetaan, kun kohdefunktion arvo on pienempi kuin 0.005. Tutkitaan iteraatioiden lukumäärää eri pisteissä ja tarkastellaan ensimmäiseksi pistettä $(\Delta q,\ \Delta\lambda)$ = (0.19,1.99) , joka on origosta Δs = 2 pituisella ennustaja-askeleella saatu piste. Taulukossa 1 on esitetty kohdefunktion arvon muuttuminen liikuttaessa kohti minimiä.

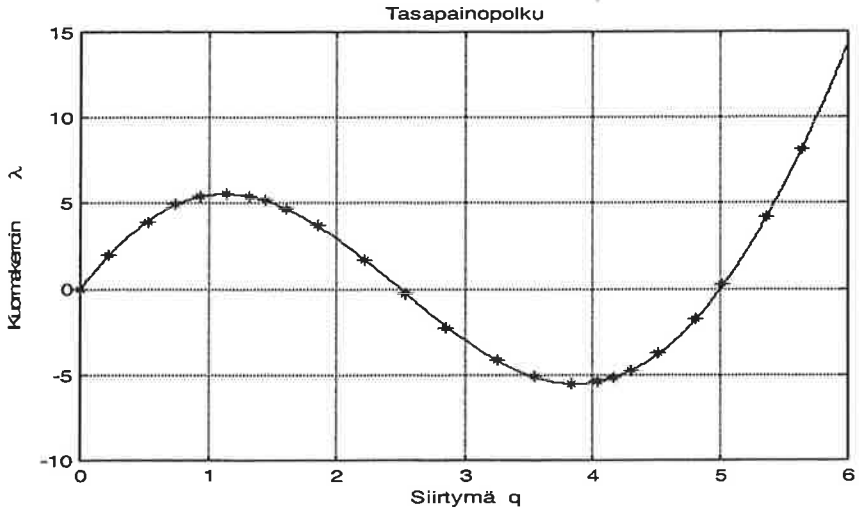

Kuva 4 Polunseurantamenetelmällä saatu tasapainopolku.

Taulukko 1 Kohdefunktion f arvo ensimmäisen askeleen eri korjaaja-askelilla.

Iteraatio	1	2	3	4	5	6
f	0.1792	0.0821	0.0450	0.0194	0.0126	0.0034

Kuudella iteraatiokierroksella saatu minimipiste on $(q, \lambda) = (0.22,1.98)$. Mikäli ollaan käyrän osalla, jossa tasapainopolun tangentin suunta muuttuu nopeasti, on ennustaja askeleen pituutta lyhennettävä, jotta menetelmä suppenisi. Tutkitaan pistettä $(\Delta q, \Delta\lambda) = (1.06,5.59)$, joka on saatu ottamalla $\Delta s = 0.25$ pituinen ennustaja-askel edellisestä tasapainopisteestä. Taulukossa 2 on saadut kohdefunktion arvot.

Taulukko 2 Kohdefunktion f arvo kuudennella askeleella eri korjaaja-askelilla.

Iteraatio	1	2	3	4	5
f	0.0798	0.0068	0.0251	0.0136	0.0009

Viidellä iteraatiolla saadaan minimipiste $(q, \lambda) = (1.13,5.52)$. Jos ennustaja-askel on liian pitkä paikassa, jossa tasapainopolku muuttuu nopeasti, niin haluttua kohdefunktion minimiarvoa ei välttämättä löydetä.

Lasketaan vertailutuloksia käyttäen Riksin ja Crisfieldin menetelmiä, joissa paluu tasapainopolulle tehdään modifioidulla Newton-Raphson iteraatiolla. Modifioidussa Newton-Raphson menetelmässä ei päivitetä tangenttijäykkyysmatriisia jokaisella iteraatiokierroksella vaan käytetään samaa tangenttijäykkyysmatriisia jokaisessa korjaaja-askeleen iteraatiossa. Modifioitua Newton-Raphson menetelmää käytetään vertailuna, koska tässä tapauksessa SQP-menetelmän Hessen matriisin päivitys ei tapahdu jokaisella iteraatiokierroksella. Käytetään iteraation aloituspisteenä pistettä $(\Delta q, \Delta\lambda) = (0.39,3.98)$, joka on saatu ottamalla $\Delta s = 4$ pituinen ennustaja-askel pisteestä (0,0). Kuvassa 5 ja taulukoissa 3-6 on esitetty kuinka vertailtavat menetelmät suppenevat kohti tasapainopolkua.

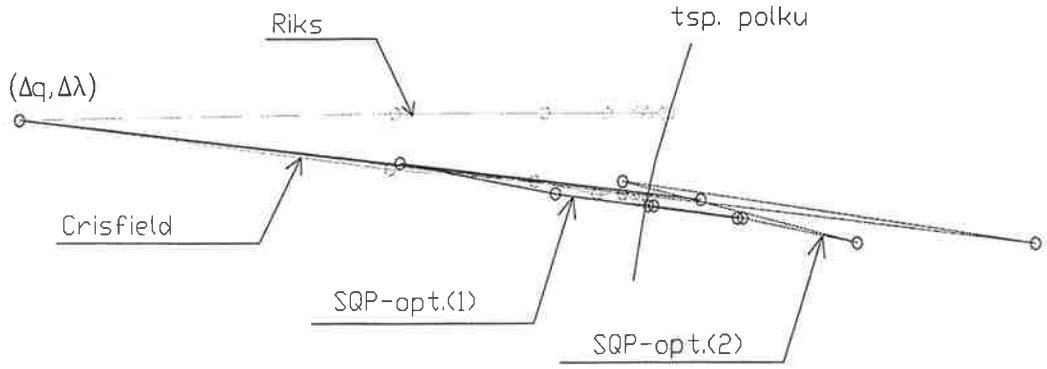

Kuva 5 Riksin, Crisfieldin ja minimointimenetelmän suppeneminen kohti tasapainopolkua. SQP-opt.(1) käyttää analyyttisiä derivaattoja ja SQP-opt.(2) differenssimenetemän antamia derivaattoja.

Taulukko 3 Riksin menetelmä (modifioidulla Newton-Raphson iteroinnilla).

Iteraatio	1	2	3	4	5	6	7
q	0.470	0.499	0.511	0.517	0.519	0.521	0.522
λ	3.980	3.981	3.981	3.981	3.981	3.981	3.981

Seitsemännellä iteraatiokierroksella kohdefunktion f arvo on 0.0014.

Taulukko 4 Crisfieldin menetelmä (modifioidulla Newton-Raphson iteroinnilla).

Iteraatio	1	2	3	4	5	6	7
q	0.469	0.497	0.509	0.514	0.517	0.58	0.519
λ	3.972	3.970	3.968	3.968	3.987	3.967	3.967

Seitsemännellä iteraatiokierroksella kohdefunktion f arvo on 0.0029.

Taulukko 5 SQP-menetelmä (SQP-opt.(2)), jossa kohdefunktion ja rajoitusehdon gradientit on laskettu käyttäen differenssimenetelmää.

Iteraatio	1	2	3	4	5	6
q	0.593	0.514	0.559	0.537	0.521	0.519
λ	3.960	3.967	3.961	3.964	3.966	3.966

Kuudennella iteraatiokierroksella kohdefunktion f arvo on 0.00069.

Taulukko 6 SQP-menetelmä (SQP-opt.(1)), jossa kohdefunktion ja rajoitusehdon gradientit on laskettu analyyttisesti.

Iteraatio	1	2	3	4	5
q	0.529	0.471	0.501	0.536	0.519
λ	3.967	3.973	3.967	3.964	3.966

Viidennellä iteraatiokierroksella kohdefunktion f arvo on 0.0029.

Kuvasta 5 ja taulukoista 5 ja 6 nähdään, että SQP-menetelmällä minimoitu tehtävän epätasapainovektorin normi suppenee kohti tasapainopolkua kuudella iteraatiokierroksella, kun gradientit on laskettu differenssimenetelmällä. Viiteen iteraatiokierrokseen päästään kun gradientit on laskettu analyyttisesti. Taulukoista 3 ja 4 nähdään, että Riksin ja Crisfieldin menetelmät saavuttavat tasapainopolun seitsemällä iteraatiokierroksella.

4. YHTEENVETO

Käsitellyn numeerisen esimerkin perusteella nähdään, että menetelmällä pystytään määrittämään kuvan 3 yksinkertaisen mallin tasapainopolku varsin tehokkaasti. Menetelmän vaatimien iteraatiokierrosten lukumäärä vaihtelee viiden ja kuuden kierroksen välillä ennustaja-askeleen pituudesta riippuen. Ennustaja-askeleen pituus tuli merkittäväksi lähestyttäessä tasapainopolun rajapisteitä, joissa tasapainopolun tangentin kulmakerroin muuttuu nopeasti. Esimerkkitehtävässä jouduttiin lyhentämään ennustaja-askelta alkuarvosta $\Delta s = 4$ arvoon $\Delta s = 0.25$ kyseisellä tasapainopolun osalla, jotta ratkaisu olisi supennut tasapainopolulle. Esimerkissä on käytetty huomattavan suuria ennustaja-askeleen arvoja verrattuna käytännön tehtäviin, joissa ennustaja-askeleen pituus ei nouse kuitenkaan ongelmaksi.

Esimerkissä tehtiin myös vertailua eri menetelmien välillä, joissa vertailtiin korjaaja-askeleiden iteraatiokierroksia. Vertailussa käytetyt Riksin normaalitasomenetelmä ja Crisfieldin pallorajoitusmenetelmä käyttivät molemmat seitsemän iteraatiokierrosta tasapainopolulle pääsyyn, kun iterointiin käytettiin modifioitua Newton-Raphsonia. SQP-menetelmä käytti viisi tai kuusi iteraatiokierrosta riippuen siitä oliko kohdefunktion ja rajoitusehdon gradientit laskettu differenssimenetelmällä vai analyyttisesti. Kuvasta 5 nähdään, että SQP-menetelmä ottaa suuria askelia ensimmäisillä iteraatiokierroksilla. Iteraatioiden käyttäytymistä kuvaa hyvin se, että ensimmäisellä askeleella mennään tasapainopolun yli ja seuraavalla palataan taas takaisin. Yhteensä tasapainopolun ylityksiä esimerkkilaskun tapauksessa tulee kolme kappaletta. Lähellä minimipistettä SQP-menetelmä ottaa taas hyvin lyhyitä askeleita, jotka lisäävät iteraatioiden määrää optimipisteen ympäristössä. Tätä voidaan kontrolloida halutulla pysäytyskriteerillä. Esimerkin tapauksessa iteraatio pysäytettiin mikäli kohdefunktion arvo oli pienempi kuin 0.005. Riksin ja Crisfieldin menetelmillä lasketut iteraatiot taas lähestyvät tasapainopolkua siltä puolelta,

johon ennustaja-askel on otettu. Eli näillä menetelmillä ei tasapainopolun ylitystä tapahdu. SQP-menetelmä otti alussa suuria askeleita ja se suppeni nopeasti kohti optimia. Suppeneminen oli hieman nopeampaa kuin Riksin ja Crisfieldin menetelmissä.

Työssä esitetyllä numeerisella esimerkillä on pyritty selvittämään ja havainnollistamaan kuinka epälineaarisen tehtävän polunseurannassa voidaan käyttää perinteisten kaarenpituusmenetelmien sijaan minimointilähestymistapaan perustuvaa menetelmää. Esimerkin valossa menetelmä näyttää lupaavalta, mutta menetelmän toimivuutta ja jalostamista suuremmille tehtäville ei ole tutkittu.

LÄHTEET

1. Riks E., The application of Newtons method to the problem of elastic stability, *J. Appl. Mech.*, **39**, 1060-1066 (1972).
2. Crisfield M.A., A fast incremental/iterative solution procedure that handles 'snap-through', *Computers & Structures*, **13**, 55-62 (1981).
3. Kaleva O., *Matemaattinen Optimointi* 1, Opintomoniste, TTKK (2002).
4. Powell M.J.D., A fast algorithm for nonlinearly constrained optimization calculus, In: Watson G.A. (ed.), *Lecture Notes in Mathematics*, **630**, Springer-Verlag (1978).
5. Pajunen S. & Tuomala M., Branch switching from coincident bifurcation points, *Mech. Struct. & Mach.*, **28**, 339-353 (2000).

OPTIMUM DESIGN OF COLD-FORMED Σ-SHAPE STEEL PURLIN USING GENETIC ALGORITHMS

W. LU, P. MÄKELÄINEN

Laboratory of Steel Structures,
Department of Civil and Environmental Engineering
Box 2100, FIN-02015, HUT, Espoo
e-mail: luwei@cc.hut.fi, pentti.makelainen@hut.fi

ABSTRACT

A Genetic Algorithm (GA) is applied to optimize the dimensions of cold-formed Σ-shape purlin continuously over two spans under gravity loads. The objective is to maximize the load efficiency. Purlins are designed in accordance with Eurocode 3, Part 1.3 and the modified Eurocode 3 method, in which the numerical elastic buckling stresses calculated using Finite Strip Method (FSM) are integrated into the calculation of the effective section properties. Via this integration, it is shown that such numerical method as the finite strip method may also be integrated into the genetic algorithm optimization process.

1. INTRODUCTION

An important advantage of cold-formed steel is the great flexibility of cross-sectional shapes and sizes available to the structural steel designer. However, the lack of standard optimized shapes makes the selection of the most economical shape very difficult. This task is further complicated by the complex and highly nonlinear nature of the rules that govern their designs. In this paper, a GA is used to optimize the dimensions of the Σ-shaped purlins over two spans under gravity load.

GA is a general-purpose, derivative-free, stochastic search algorithm [1, 2] and starts with randomly choosing an initial population that consist of candidate solutions to the problem at hand. Each individual in the population is characterized by a fixed length binary bit string, which is called chromosome. These chromosomes are evaluated by means of a fitness function. Combining the fittest individuals from the previous population, a new generation of chromosomes is created. Evolutionary operators such as selection, crossover, and mutation are used to create this new population. Besides, Elitism, which is a method that copies the best chromosome or a few better chromosomes to the new population, may be incorporated into the algorithm to avoid losing the best individual. This process continues until the specified level of fitness is reached.

Purlins are designed in accordance with Eurocode 3, Part 1.3 [3]. In addition, the modified Eurocode 3 method, in which the elastic local buckling stress and distortional buckling stress are calculated using FSM, is used to determine the effective section properties. The results calculated using these two design methods are compared.

2. GA-BASED DESIGN

The cross-section of the Σ-shaped purlin continuously over two spans under gravity loads is shown in Figure 1. In the figure, b is width of the flange; c is the depth of the lip; h is the height of the cross-section; h_1 and h_5 are the distances of the web stiffener to the top and bottom flange, respectively; h_2 and h_4 are the depths of the stiffener along the web in the direction of the web height; d_s is the depth of the stiffener along the web perpendicular the web height, and h_3 is the distance between the stiffeners along the web.

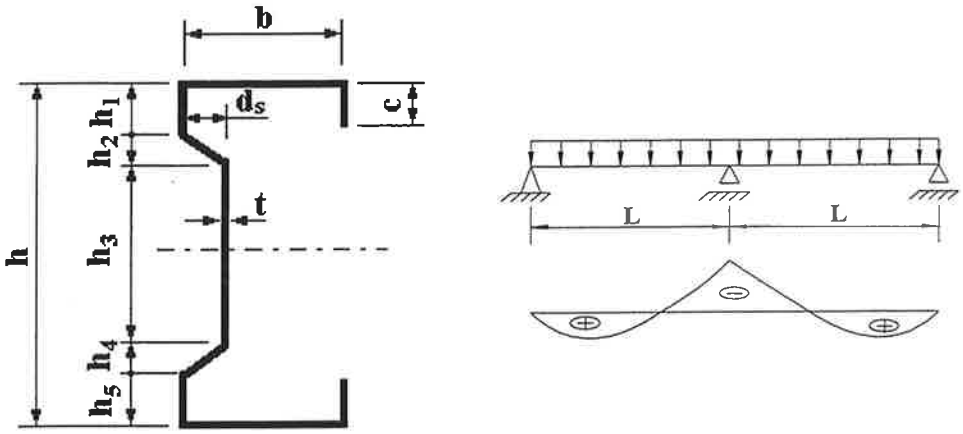

Figure 1 Dimensions of Σ-shape purlin continuously over two spans under gravity loads

In Eurocode 3, Part 1.3, the free flange is considered as a beam on an elastic foundation. When the purlin is continuous over two spans, the resistance of the cross-section of the restrained flange should satisfy:

$$M_{y,Sd}/W_{eff,y} \le f_y/\gamma_M \qquad (1)$$

and that of the free flange should satisfy:

$$M_{y,Sd}/W_{eff,y} + M_{fz,Sd}/W_{fz} \le f_y/\gamma_M \qquad (2)$$

The stability of the free flange at the internal support should be checked by:

$$1/\chi \cdot M_{y,Sd}/W_{eff,y} + M_{fz,Sd}/W_{fz} \le f_y/\gamma_{M1} \qquad (3)$$

where $M_{y,Sd}$ is the in-plane bending moment; $W_{eff,y}$ is the effective section modulus of the cross-section for bending about y-y axis; M_{fz} is the bending moment in the free flange due to the lateral load; W_{fz} is the gross elastic section modulus of the free flange plus 1/6 of the web height, for bending about the z-z axis; χ is the reduction factor for flexural buckling of the free flange and γ_M, γ_{M1} are the partial safety factors.

Since the bending moments in the above formulas are functions of distributed load q, the objective of the optimization is to obtain the maximum distributed load per cross section area, A_g, when the material reaches its yield strength, f_y, i.e.

$$q/A_g \rightarrow \max \tag{4}$$

subjected to the following constraints according to Eurocode 3, Part 1.3:

$$h/t \le 500, \quad b/t \le 60 \tag{5}$$

Besides, from the manufacture point of view, the sum of flanges, lips and the web, L_{Strip}, should be in the range of the given length of the strip and the height of the web part above the web stiffener is not less than 35 mm, i.e.

$$200 \le L_{strip} = 2 \cdot b + 2 \cdot c + 2 \cdot d + 2 \cdot h_1 + 2 \cdot h_3 + 2 \cdot \sqrt{h_2^2 + d_s^{\,2}} \le 625, \quad h_1 \ge 35 \tag{6}$$

In addition, due to the shape requirements, the following constraint should be satisfied

$$d_s < b \tag{7}$$

Since the GA is directly used for solving an unconstrained optimization problem, the constrained problem mentioned above should be transformed into an unconstrained problem by including a penalty function [4]. In this analysis, a quadratic penalty function is used, and the corresponding unconstrained optimization problem becomes:

$$\textit{Maximize} \quad F = \begin{cases} q/A_g - KK \cdot n \cdot CC & \textit{if } q/A_g > KK \cdot n \cdot CC \\ 0 & \textit{otherwise} \end{cases} \tag{8}$$

where $CC = \Sigma c_i$ is the sum of constraint violations, c_i, which is given by:

$$c_i = \begin{cases} 0 & \textit{if } \alpha_i \le 0 \\ \alpha_i^{\,2} & \textit{otherwise} \end{cases} \tag{9}$$

where α_i are the normalized constraints provided by:

$$\alpha_1 = \frac{h/t}{500} - 1, \quad \alpha_2 = \frac{b/t}{60} - 1, \quad \alpha_3 = \frac{c/b}{0.6} - 1, \quad \alpha_4 = 1 - \frac{c/b}{0.2},$$
$$\alpha_5 = L_{strip}/625 - 1, \quad \alpha_6 = 1 - L_{strip}/200 \tag{10}$$

In equation (8), n is the coefficient that makes the values of q/A_g and CC at the same order so as to avoid one value dominating over the other. In this analysis, the value of n is defined as $10^{L_f - 1 - L_c}$ to keep the order of CC one degree lower than that of q/A_g, in which L_f and L_c are the orders of q/A_g and CC, respectively. Moreover, $KK \ge 0$ is a coefficient and the solution of the penalty problem can be made arbitrarily close to the solution of the original problem by choosing KK sufficiently large [5]. In GA terminology, equation (8) is called fitness function that is used in the reproduction phase in order to guide the genetic search.

According to Eurocode 3 Part 1.3, the ratio of c to b should satisfy $0.2 \le c/b \le 0.6$. Assuming $\alpha = c/b$, thus, α can be selected as one of design variables instead of c. Moreover, the ratio of the value of h_1 to the length of the flange is chosen as the design variable instead of the value of h_1.

The height of the web, h, the thickness of cross section, t, and the length of the single span, L, are given values. The design variables and their possible values are listed in Table 1.

Table 1 Values for the design and given variables

Design variables	Possible values
Length of the flange b	from 40 to 100 with step 1 mm
Ratio of c to b	0.2 to 0.6 with step 0.01
Ratio of h_1 to b	0.45 to 1 with step 0.01
Values of h_2	from 5 to 40 mm with step 1 mm
Values of d_s	from 5 to 40 mm with step 1 mm

Figure 2 shows how the purlin design is integrated into the GA optimization process. GA-based design starts from randomly generating an initial population that is composed of candidate solutions to the current problem. Each individual in the population is a bit string of fixed length. After decoding, these individuals that represent the dimensions of the purlins are sent to the purlin design program. The constraints are checked and if the constraints are violated, the penalty is applied and the fitness function is calculated. After the evaluation of the fitness for each individual, a new generation is created using such operators as selection, crossover and mutation. In order to keep the best individuals in each generation, the elitism may also be used. This process is continued until the specified stopping criteria are satisfied.

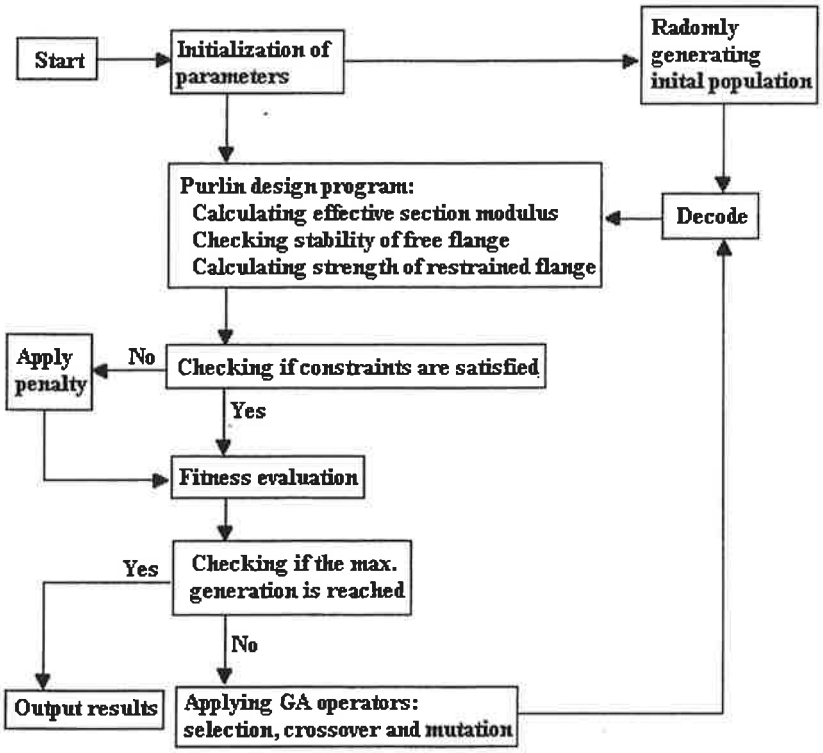

Figure 2 Integrating purlin design into GA optimization

3. OPTIMIZATION RESULTS BASED ON EUROCODE 3 METHOD

The GA, which is based on bit representation, two-point crossover, bit-flip mutation, and tournament selection with elitism, is used to optimize the Σ-shape purlin with a height of 350 mm, a thickness of 2.0 mm and a span of 6 m. Such parameters as the population size, the crossover rate and the mutation rate in genetic algorithms are set to 50, 0.8 and 0.001, respectively.

The optimization results are presented in Table 2. Besides the value of q/A_g, Table 2 also lists the value of M_y/A_g, in which M_y is the minimum moment that causes the yielding of the material and is defined as $M_y=W_{eff,y}f_y/\gamma_M$. Table 2 shows that the optimized dimension for the cross-section is *b=83 mm, c=33.20 mm*, i.e. *c/b=0.4*, h_1 = *68.06 mm*, h_2=*28 mm* and d_s=*30 mm*.

Table 2 Optimization results of 10 runs

No.	*b (mm)*	*c (mm)*	h_1 *(mm)*	h_2 *(mm)*	d_s *(mm)*	q/A_g *(N/mm/mm²)*	M_y/A_g *(N·mm/mm²)*	A_g *(mm²)*
1	83	36.52	66.40	18	29	0.004216	26379.73	1199.033
2	83	34.03	68.06	30	31	0.004200	26511.13	1178.393
3	83	36.52	66.40	18	29	0.004216	26379.73	1199.033
4	83	33.20	68.06	28	30	0.004241	26451.04	1174.677
5	83	33.20	68.06	28	30	0.004241	26451.04	1174.677
6	83	33.20	68.06	28	30	0.004241	26451.04	1174.677
7	83	34.03	68.06	30	31	0.004200	26511.13	1178.393
8	83	36.52	66.40	18	29	0.004216	26379.73	1199.033
9	84	35.28	72.24	31	32	0.004213	26414.51	1188.838
10	82	30.34	63.96	21	27	0.004160	26202.89	1159.877

4. INTEGRATING THE MODIFIED EUROCODE 3 METHOD INTO OPTIMIZATION

The modified Eurocode 3 method integrates elastic local and distortional buckling stresses calculated using the FSM analysis into the design procedure. In this process, the reduction factor, ρ, is calculated according to the elastic local buckling stress from the FSM analysis. The effective width of the lip, flange and web are all calculated based on this value. Similarly, the reduction factor, χ, for reduced thickness due to the partially effective of edge or intermediate stiffener is calculated using the distortional buckling stress from the FSM analysis. By doing so, the interaction among the lip, the flange and the web are integrated due to the treatment of the section as a whole.

In this paper, the elastic local and distortional buckling stresses and modes are calculated using the computer program CUFSM, which is developed by Schafer [6]. The buckling modes can be classified into four types. The first type is the local buckling of the flange, the lip and the element above the web stiffener (Figure 3 (a)). In this mode, the buckling may be initiated by any one of the above-mentioned elements. The second type is the local buckling of the compression part under the web stiffener (Figure 3 (b)). The third type is the web distortional buckling mode (Figure 3 (c)), in which the web stiffener is moved with other elements along the web. The last type is the distortional buckling mode (Figure 3 (d)).

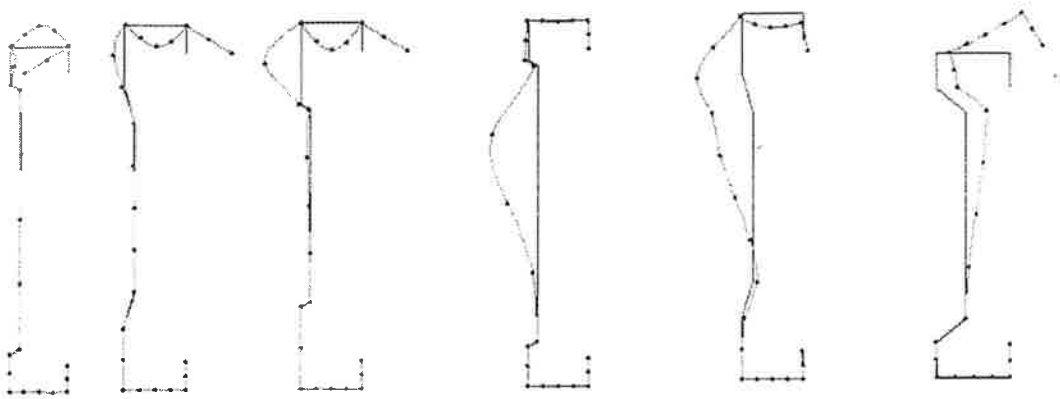

Figure 3 Typical buckling modes (a) Local buckling of flange, lip and element above the web stiffener; (b) Local buckling of the element under the web stiffener; (c) Web distortional buckling mode; (d) Conventional distortional buckling mode

When calculating elastic buckling stresses, there might exist an indistinct buckling mode for some cross-sections, i.e. there is no obvious minimum in the buckling curve for the local buckling mode or the distortional buckling mode. Thus, in either of these cases the design procedure is based on Eurocode 3.

A demonstration example is used to show how the modified Eurocode 3 method can be integrated into the GA optimization process for Σ-shape purlins. The objective of the optimization is to maximize the value of q/A_g for a cross-section with $h=350$ mm, $t=2.0$ mm and $L=6000$ mm. Table 3 lists the comparisons of optimization results designed based on the Eurocode 3 method (EC3) to those based on the modified Eurocode 3 method (MEC3). Table 3 indicates that for this specific cross-section, the optimal dimensions based on 'MEC3' are the same as those based on 'EC3'; and the values of q/A_g and M_y/A_g calculated using 'MEC3' are about 0.12 % and 0.13 % lower than those calculated using 'EC3', respectively.

Table 3 Comparisons of optimization results based on the Modified Eurocode 3 method (MEC3) with those based on the Eurocode 3 method (EC3)

Methods	*b (mm)*	*c (mm)*	h_1 *(mm)*	h_2 *(mm)*	d_s *(mm)*	q/A_g *(N/mm/mm²)*	M_y/A_g *(N·mm/mm²)*
EC3	83	33.20	68.06	28	30	0.004241	26451.04
MEC3	83	33.20	68.06	28	30	0.004236	26421.06

5. CONCLUSIONS

As demonstrated in this paper, GA can be used as an optimization tool to obtain the optimum dimensions of the Σ-shape purlins under gravity load. This GA-based design method can also be applied to the optimization of other shapes of cold-formed steel purlins and other cold-formed steel members. In addition, the comparison of the modified Eurocode 3 method to the Eurocode 3 method for the specific case indicates that the optimum dimensions are the same using these two methods. For other cross-sections, further analyses need to be carried out.

6. REFERENCES

[1] Mitchell M. (1998). An introduction to genetic algorithms. Cambridge (MA) MIT Press.

[2] Cogan B. (2001). The evolution of genetic algorithms. Scientific Computing World, May/June, 28-31.

[3] ENV 1993-1-3, Part 1.3 (1996): General rules. Supplementary rules for cold-formed thin gauge members and sheeting.

[4] Koumousis V. K. and Georgion P. G. (1994). Genetic algorithms in discrete optimization of steel truss roofs. Journal of Computing in Civil Engineering, 8, 309-325.

[5] Bazaraa M. S., Sherali H. D. and Shetty C. M. (1993). Nonliner programming: theory and algorithms, second edition, John Wiley & Sons, Inc.

[6] Schafer, B.(2002). Elastic Buckling of Thin-Walled Structures. *http://www.ce.jhu.edu/bschafer/.*

OPTIMUM DESIGN OF A POWER TRANSMISSION USING ELECTRO-RHEOGICAL ,VISCOUS AND HYDRODYNAMIC FLUID CONTROL OF TORQUE AND SPEED FOR MACHINES

H. MARTIKKA* and M. KUOSA#
*Professor, Department of Mechanical Engineering,
#Department of Energy and Environmental Engineering,
Lappeenranta University of Technology,
P.O.Box 20, FIN-53851 Lappeenranta, FINLAND

ABSTRACT

The goal of this paper is to present results of analysing the functionality of a power transmission system. In the present case study the power is input from a motor to a hydrodynamic torque converter. It actuates a machinery consisting of a variator, a compound gear train, a planetary gear train, clutch alternatives and a load machine. The purpose of the converter is to obtain high startup torque. The aim of the variator is to obtain stepless speed transmission. Various clutch alternatives are considered and possibilities of an optimal synthesis to obtain optimal transmission of power and speed. Electro-rheological fluid power and clutch components are studied for obtaining optimal torque transmission. The design variables of the ER-clutch are number of activated plates, disk spacing and the shear stress of the fluid. The torque capacity of the ER-clutch depends on the ER-shear stress of the fluid which depends on the electric field and temperature. Dry and wet friction clutches are considered and also a viscoelastic clutch. One conclusion is that this model is useful for starting a conceptual concurrent design to obtain an optimal power transmission with a novel hybrid clutch.

1. INTRODUCTION

There is a constant need for better mechanical and electrical power transmissions and optimal control. Conventionally they are designed sequentally as separate groups. Modern trend is to strive for integration already at the concept design stage as discussed by Cochin & al [1]. Power transmission can be effected using a large combination of components. Rules of combining and designing are needed. Basic component choices are conventional shafts, gear trains and variators. Also rigid and flexible clutches, dry and wet friction clutches are available. New choices are emerging. Viscolelastic clutches are discussed by Peschke [2]. More complex electro-rheological clutches are discussed by Papadopoulos [3]. An established group are hydraulic clutches and hydrodynamic torque converters as discussed by Juvinall et al [4] and produced by Voith [5]. One example of this trend is stepless drive system for new Mini [6]. The aim in this study is to consider design ideas and design rules, basic theory and methodology in combining these to a case study. Further aim is to create innovative combinations using these modules.

2. THE POWER TRANSMISSION SYSTEM STUDIED

The general overview of the system is shown in Figure 1.

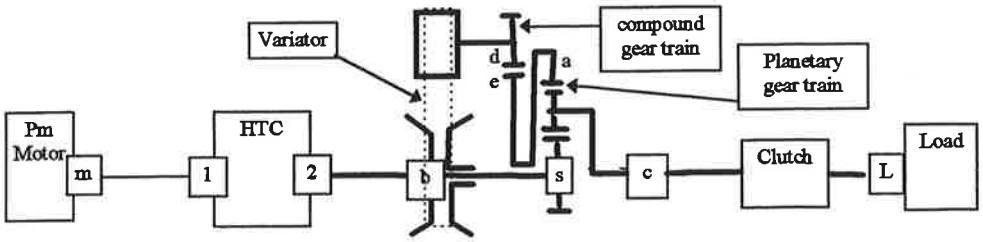

m, motor	1	2	b	s, sun	c, carrier	clutch options
$P_m = T_m\omega_m$	$P_1 = T_1\omega_1$	$P_2 = T_2\omega_2$	$P_b = T_b\omega_b$	$P_s = T_s\omega_s$	$P_c = T_c\omega_c$	-ER-clutch
T_m	T_1	T_2	T_b	T_s	T_c	-viscous clutch
ω_m	ω_1	ω_2	ω_b	ω_s	ω_c	-frictional clutch

a)

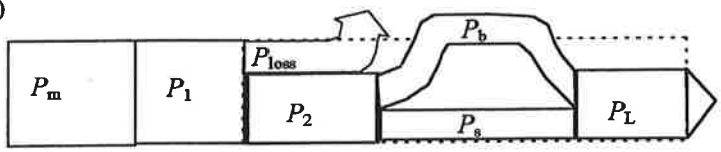

b)

Figure 1. Overview of the system studied. Power is input from the motor m to a hydrodynamic torque converter (HTC) which is used to get high initial startup torque when the loaded system is not yet moving. A belt variator is used and a compound gear train with a constant ratio gear ratio. Planetary gear train is connected to load via clutch and feed back to variator.
b) Power flows are illustrated in principle.

2.1 Transmission ratios

The transmission ratios are the following.

$x = \frac{\omega_L}{\omega_b} = K_{Lb}$ is transmission ratio of speed of load L to speed on shaft b at variator

$V = \frac{\omega_b}{\omega_{bb}} = K_{b,bb}$ is transmission ratio of speed of wheel b to to speed on wheel bb at variator

$i = \frac{\omega_d}{\omega_e} = K_{de}$ is transmission ratio of speed pf wheel d to speed of wheel e at reduction gear

$\nu = \frac{\omega_2}{\omega_1} = K_{21}$ is transmission ratio of pump impeller speed to turbine shaft speed at HTC

The relative transmission ratio between annulus and sun gears is obtained as

$$\frac{\omega_a - \omega_c}{\omega_s - \omega_c} = \frac{\frac{\omega_a}{\omega_c} - 1}{\frac{\omega_s}{\omega_c} - 1} = \frac{K_{ac} - 1}{K_{sc} - 1} = R_{a/s} = -\frac{z_s}{z_a} \quad (1)$$

Loops a-c and s-c are traced and the transmission ratio x of the inner machinery is solved

$$\frac{K_{ac}-1}{K_{sc}-1}=R_{a/s}=\frac{K_{ac}K_{ed}K_{d,bb}K_{bb,b}K_{bL}K_{Lc}-1}{K_{sb}K_{bL}K_{Lc}-1} \tag{2}$$

$$R_{a/s}=\frac{1\bullet\frac{1}{i}\bullet1\bullet\frac{1}{V}\bullet\frac{1}{x}\bullet1-1}{1\bullet\frac{1}{x}\bullet1-1}=\frac{\frac{1}{Vi}\frac{1}{x}-1}{\frac{1}{x}-1}=\frac{\frac{1}{Vi}-x}{1-x}\quad\Rightarrow\quad x=\frac{\frac{1}{Vi}-R_{a/s}}{1-R_{a/s}}=\frac{\omega_L}{\omega_b}=K_{Lb}$$

Some details of the system are shown in Figure 2.The motivation of choosing this combination is that with HTC high startup torque is obtained and with a variator and gear trains even reversed output rotations are obtained.

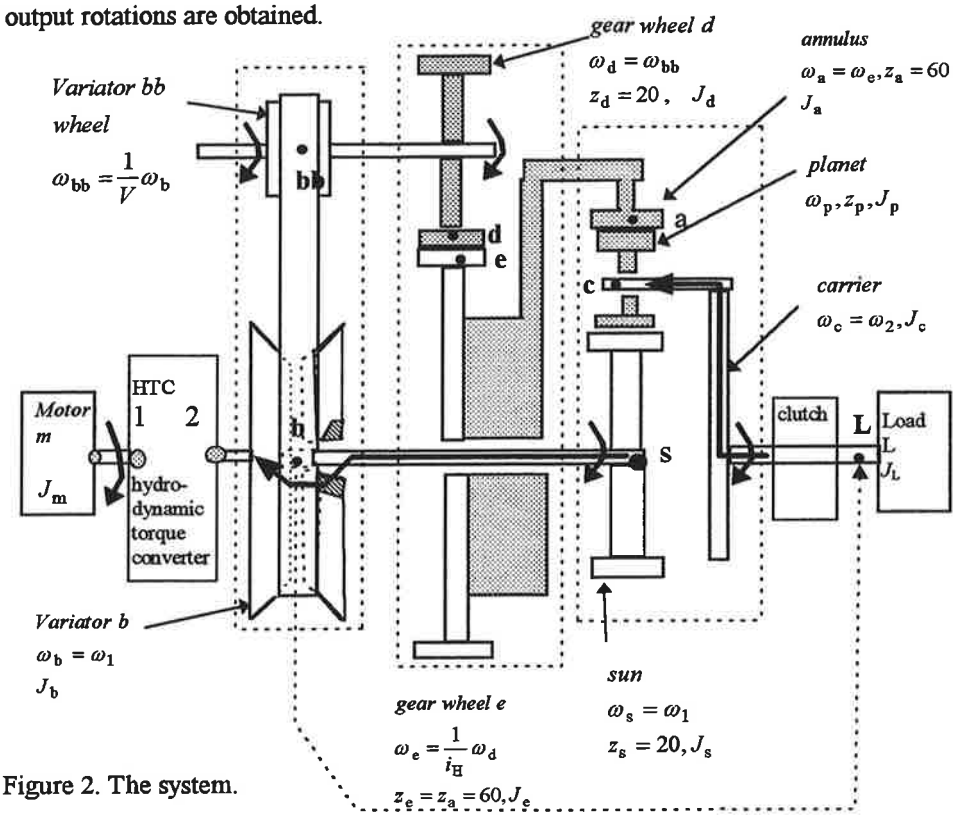

Figure 2. The system.

2.2 Planetary gear train

The kinematic operational principle of the planetary gear train is illustrated in Figure 3.

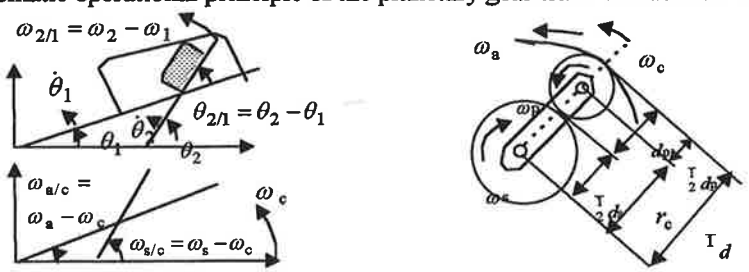

Figure 3. The kinematic operational principle of a planetary gear train.

Some details of a planetary gear train are shown in Figure 4.

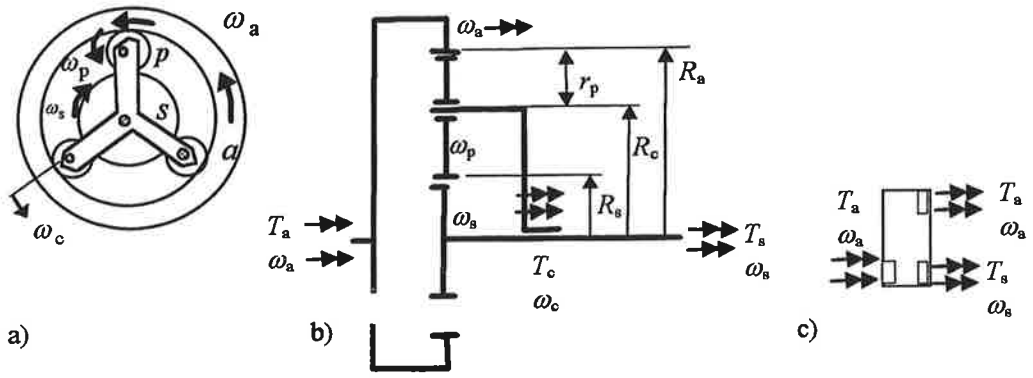

Figure 4. Details of a planetary gear train. a) Cross sectional view showing the main components, *s* is the sun wheel, *p* is the planet wheel, *a* is the annulus wheel and *c* is the carrier conveying the planets .b) Side view showing the interconnections. c) Freebody model showing the applied torques and assumed rotations.

The torque and power balances for the planetary gear train can be formulated by assuming that the rotations and torques all act in the same positive direction

$$\begin{aligned}
&\Sigma T = T_a + T_s + T_c = 0 \quad , \\
&\qquad \Rightarrow \quad , \Rightarrow \quad , \Rightarrow \\
&\Sigma P = T_a\omega_a + T_s\omega_s + T_c\omega_c = 0 \\
&\quad + \omega_a \Rightarrow \quad , + \omega_s \Rightarrow \quad , + \omega_c \Rightarrow \\
&\Sigma P = P_a + P_s + P_c = 0
\end{aligned} \tag{3}$$

The componentwise powers can be expressed relative to the carrier velocity

$$\begin{aligned}
P_a &= +T_a\omega_a \quad = +T_a\omega_c + T_a(\omega_a - \omega_c) \\
P_s &= +T_s\omega_s \quad = +T_s\omega_c + T_s(\omega_s - \omega_c) \\
P_c &= +T_c\omega_c \quad = +T_c\omega_c \\
\Sigma P &= 0 = \Sigma T \cdot \omega_c + T_a(\omega_a - \omega_c) + T_s(\omega_s - \omega_c) = 0
\end{aligned} \tag{4}$$

From this one obtains a internal torque ratio between the sun and the annulus wheels

$$+T_a(\omega_a - \omega_c) + T_s(\omega_s - \omega_c) = 0 \quad \rightarrow \quad \frac{\omega_a - \omega_c}{\omega_s - \omega_c} = -\frac{T_s}{T_a} = R_{as} = -\frac{z_s}{z_a} \tag{5}$$

2.3 Clutch alternatives

Several alternatives are considered and their possible combinations, too. They are ER clutch, frictional clutches, dry or wet clutches and a viscoelastic clutch. Possibility of an innovative synthesis of these is discussed shortly. In creating a synthesis one may synergically combine the advantages of each clutch and hopefully leave out some undesirable features.

2.3.1 A typical electro-rheological clutch

Torque model

Torque model for this clutch is obtained using the models shown in Fig.5.

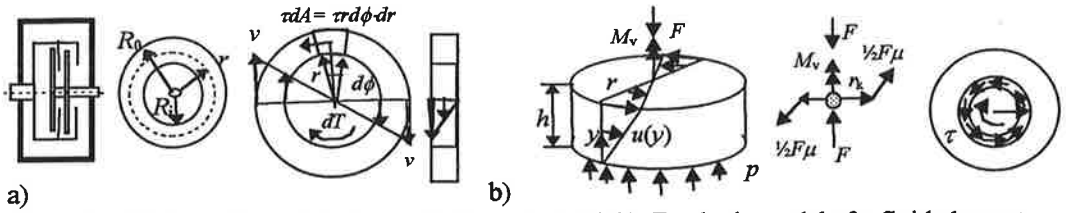

a) b)

Figure 5. a) Schematic model of a multi-disk ER clutch.b) Freebody model of a fluid element

In calculations the following values are used: outer diameter D_o = 0.19m = 2 R_o. A recommended radius ratio range by Juvinall [4] for inner radius is $0.45R_o < R_i < 0.8\,R_o$. Using this the value $R_i = 0.5\,R_o$ is chosen as reasonable. Typical values give a mean radius as $r_k = (2/3)\,R_o$.

Now the Bingham model for the fluid is applicable according to most researchers [3]

$$\tau = \tau_0 + \mu\frac{du}{dy} \tag{6}$$

Using through the fluid film thickness integrated values for the velocity gradient gives

$$v = \Delta\omega r \quad , \quad h = \int dh \quad , \quad \tau = \tau_0 + \mu\frac{\Delta\omega r}{h} \tag{7}$$

Here n is the number of active clutch plate surfaces, h is their separation, $\Delta\omega$ is the angular velocity difference between the plates. A freebody model for the fluid element gives

$$dT' = nr\left(\tau\cdot rd\phi dr\right) = gd\phi \quad , \quad dT = nr\left(\tau\cdot 2\pi dr\right) = \int_0^{2\pi} gd\phi$$
$$dT = 2\pi nr^2\left(\tau_0 + \mu\frac{\Delta\omega r}{h}\right)dr \tag{8}$$

Integration within the radial range of the fluid surface gives

$$T = 2\pi n\cdot\int_{R_i}^{R_o} r^2\left(\tau_0 + \mu\frac{\Delta\omega r}{h}\right)dr = T = \frac{2}{3}\pi n\tau_0\left(R_o{}^3 - R_i{}^3\right) + \frac{1}{2}\pi n\mu\Delta\omega\frac{1}{h}\left(R_o{}^4 - R_i{}^4\right) \tag{9}$$
$$T = T_o + T_\mu$$

Principle of the behaviour of the ER clutch

Experimental test data by Papadopoulos [3] showing the behaviour of a typical electro-rheological fluid clutch is shown in Figure 6. Two models for describing shear stress are formulated:
A An empirical shear stress model and B. Bingham viscosity based shear stress model.

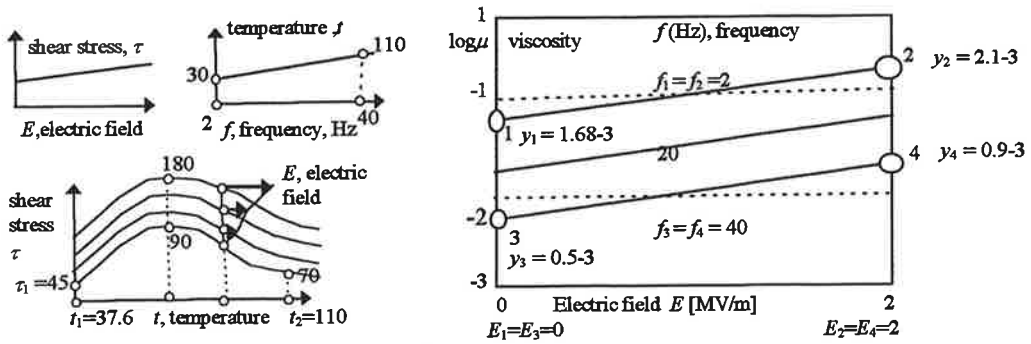

a) b)

Figure 6. Principle of the behaviour of a typical electro-rheological fluid. a) Shear stress increases with electric field and changes nonlinearly with temperature .b) Viscosity depends on the electric field and decreases with frequency of operation due to heating.

A. An empirical shear stress model

Temperature vs frequency model is linear within the studied range [3].

$$t = t_1 + (f - f_1)\frac{t_2 - t_1}{f_2 - f_1} = 30°C + (f - 2Hz)\frac{110-30}{40-2} \quad ,f_1 = 2, \quad t_1 = 30°C, \quad f_2 = 40, \quad t_2 = 110 \tag{10}$$

Now using the frequency of operation $f = \frac{\Delta\omega}{2\pi}[Hz] = \frac{100-50}{2\pi} = 8Hz$ gives $t = 46C$.

The viscosity depends on the temperature via frequency of rotation in the specified system. According to Papadopoulos [3] the shear stress depends on the electric field E and on the temperature t . A simple model is roughly

$$\tau = \tau_1 f(t)g(E) \quad , \quad \tau = \tau_1\left[1 + b(t - t_1')e^{-c(t-t_1)}\right]\cdot\left[1 + a(E - E_1)\right] \quad ,[Pa] \tag{11}$$

Here $a = 10^{-6}$, E_1=0, E=1MV/m,b= 0.05,c=0.0163,t_1'=37.6C, τ_1=45Pa. These give τ = **156Pa**

B.Bingham viscosity based shear stress model

A model can be fitted to experimental data by [3]. Three parameters for three points are used

$$\log\mu = y = W(E)\cdot F(t) \quad , \quad y(E,f) = y_1\left(1 + e(E - E_1)\right)\left(1 + u(t - t_1)\right)$$
$$y_i = W(E_i)\cdot F(t_i) \quad , \quad i = 1,2... \tag{12}$$

Here y_1= 1.68-3, e=-0.8·10^{-8}, u = 0.011, t_1= 30C, t =46C, E_1=0 MV/m. The viscosity model is

$$\mu = \mu_1^{\,K} = \mu_1^{\,1+K'} \quad ,K = \left(1 + b(E - E_1)\right)\left(1 + u(f - f_1)\right) \tag{13}$$

Substituting input values here gives $\mu = 0.03^{1.1} = 0.022$ Pas. The calculations give shear stress

$$\tau = \tau_0 + \mu\frac{\Delta\omega r}{h} = 45 + 0.022\,\frac{50\cdot 0.067}{0.001} = 114Pa$$

Average value of the shear stress at these conditions can be calculated as

$$\bar{\tau} = \frac{T}{r_k A\cdot n} = \frac{2Nm}{0.067m\cdot 0.021m^2\cdot 10} = 148Pa \tag{14}$$

2.3.2 Viscoelastic clutch

The viscolelastic clutch model has been studied by Peschke [2]. The following model is obtained

$$T_v = \frac{1}{2}\pi n \mu_v \Delta\omega \frac{1}{h}\left(R_o{}^4 - R_i{}^4\right) = \frac{1}{2}\pi n \mu_v \Delta\omega \frac{1}{h} R_o{}^4 \left(1 - \left(\frac{R_i}{R_o}\right)^4\right) \tag{15}$$

Using typical input values $\Delta\omega$ = 100-50=50 rad/s , μ_v = 0.1 m^2/s, distance between plates h = 0.00025m, number of active plates n = 10 in this model gives for the torque capacity

$$T_v = \frac{1}{2}\pi \cdot 10 \cdot \left[01\frac{m^2}{s}\right]\left[50\frac{rad}{s}\right]\frac{1}{\left[0.00025m\right]}\left[0.095m\right]^4\left(1 - \left(\frac{0.0047}{0.095}\right)^4\right) = 120Nm \tag{16}$$

The heat dissipation capacity is however a constraint which limits this torque capacity.

2.3.3 Friction clutch with constant pressure

The operation of the friction clutches requires external normal force N to generate pressure on the clutch friction plates.The interfacial shear stress transmitting the torque is generated by dry friction which is roughly independent of the sliding velocity

$$p = \frac{N}{A} = \frac{N}{\pi\left(R_o{}^2 - R_i{}^2\right)} \quad , \quad \tau_r = f_r p \tag{17}$$

The torque transmission capacity is

$$T_r = \frac{2}{3}\pi n \tau_r \left(R_o{}^3 - R_i{}^3\right) = n \cdot f_r N \cdot r_k \quad , \quad r_k = \frac{2}{3}\frac{R_o{}^3 - R_i{}^3}{R_o{}^2 - R_i{}^2} \tag{18}$$

Dry clutches of cast iron,steel plate pairs give dynamic friction coefficient f_r = 0.15...0.25, p_{max} = 0.69..1.72MPa, max bulk temperature 260C [4]. Wet clutches operate in oil. With cast iron- hard steel pairs f_r = 0.03-0.06 [4]. Choosing reasonable values f_r = 0.03 and p = 0.1MPa gives an estimate for torque T_r = 40Nm.

2.4 Hydrodynamic torque converter

Principles and sketches of the hydrodynamic torque converter are shown in Figure 8.

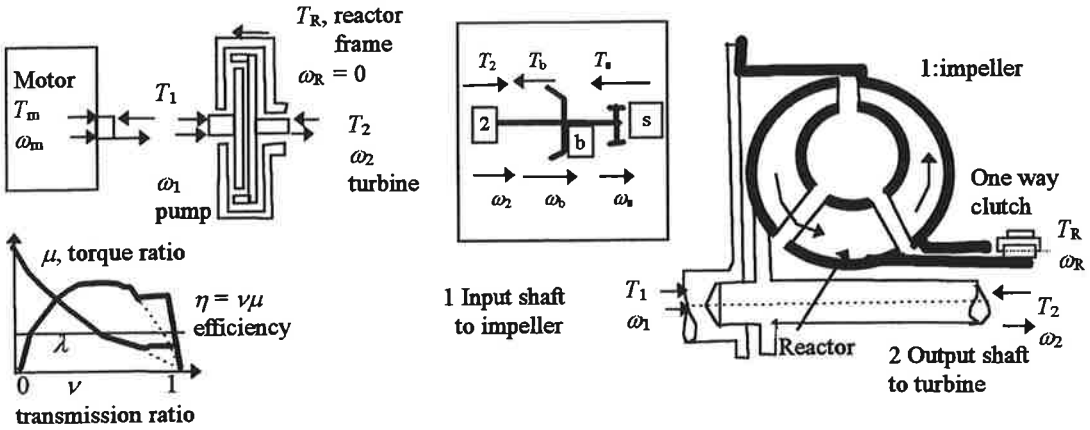

Figure 8.Principles of the hydrodynamic torque converter.

According to the models by Voith [5] at small output speeds the torque is high at start-ups. The power from the motor is inputted to the HTC [5]. Here λ is a structural parameter.

$$T_1 = \lambda \cdot \rho D^5 {\omega_1}^2 = t_{11}{\omega_1}^2 \quad , \quad \omega_1 = \omega_m \quad , \quad D \approx 2R_o \quad , \quad T_m \omega_m = T_1 \omega_1 \tag{19}$$

Torque balance gives [5]

$$\Sigma T = T_1 - T_R - T_2 = 0 \tag{20}$$

Power balance. Input power equals the output power plus the losses

$$\begin{aligned} &\Sigma P = P_1 - P_2 - P_{loss} = 0 \\ &\mu = \frac{T_2}{T_1} \quad , \quad \nu = \frac{\omega_2}{\omega_1} \quad , \quad \eta = \frac{P_2}{P_1} = \frac{T_2}{T_1}\frac{\omega_2}{\omega_1} = \mu\nu \\ &P_1 = P_2 + P_{loss} = \eta P_1 + P_{loss} \quad , \quad P_{loss} = (1-\eta)P_1 \end{aligned} \tag{21}$$

The efficiency can be approximated as a parabolic curve by assuming simply $\eta(½) = 1$.

$$\begin{aligned} &\eta \approx 4\nu(1-\nu) \Rightarrow \eta \equiv \mu\nu \quad \rightarrow \nu = \frac{\omega_2}{\omega_1} \\ &T_2 = T_1 \cdot 4\left(1 - \frac{\omega_2}{\omega_1}\right) = \mu T_1 \quad , \mu = 4\left(1 - \frac{\omega_2}{\omega_1}\right) \end{aligned} \tag{22}$$

Some advantages and disadvantages of using HTC

1. High start up torque is often needed using the torque multiplication of the HTC
2. After startup the equality of torques is obtained at a certain speed transmission ratio

$$T_2 = T_1 \cdot 4\left(1 - \frac{\omega_2}{\omega_1}\right) \rightarrow T_1 \quad , K_{21} = \frac{\omega_2}{\omega_1} = \frac{\omega_b}{\omega_m} = \frac{3}{4} \tag{23}$$

3. Then the transmission ratio is changed by using the variator variable V

$$K_{tot} = K_{Lm} = \frac{\omega_L}{\omega_m} = \frac{\omega_L}{\omega_b}\frac{\omega_b}{\omega_m} = x\frac{\omega_2}{\omega_1} = x(V)K_{21} = x(V)\tfrac{3}{4} \tag{24}$$

One disadvantage is power loss.

2.5 Torques within the machine and dimensioning principles

Information of the torques within the machine are needed for dimensioning of the machine elements.Power and torque balance of the shaft HTC -variator wheel b, and sun s are

$$T_2\omega_2 + (-T_b)\omega_b + (-T_s)\omega_s = 0 \quad , \quad \omega_2 = \omega_b = \omega_s \rightarrow \quad T_2 - T_b - T_s = 0 \tag{25}$$

Power flow from output of HTC arrives at the load L

$$P_2 = P_L \quad , \quad T_2\omega_2 = T_L\omega_L \quad , \quad T_b\omega_b + T_s\omega_s = T_L\omega_L \tag{26}$$

The wheels 2 ,b and s are on the same shaft so that their angular velocities are equal

$$\omega_2 = \omega_b = \omega_s \rightarrow x = \frac{\omega_L}{\omega_b} = \frac{\omega_L}{\omega_2} = \frac{1}{K_{2L}} \tag{27}$$

Using this in the power balance equation gives

$$T_b + T_s \frac{\omega_s}{\omega_b} = T_L \frac{\omega_L}{\omega_b} \quad \rightarrow \quad T_2 = T_b + T_s = T_L x \tag{28}$$

Here the torque ratios are known

$$T_s = t_{sa} \cdot T_a \quad , \quad T_a = 1 \cdot T_e \tag{29}$$

The power flows form gear wheel e to d and gives

$$\begin{aligned} T_e \omega_e = T_d \omega_d \rightarrow T_e = T_d \frac{\omega_d}{\omega_e} = K_{de} T_d = i T_d, \quad T_d = 1 \cdot T_{bb} \\ T_{bb} \omega_{bb} = T_b \omega_b \rightarrow T_{bb} = T_b \frac{\omega_b}{\omega_{bb}} = K_{b,bb} T_b = V T_b \end{aligned} \tag{30}$$

The input torque from HTC at output point 2 results in the output torque as follows

$$T_s = t_{sa} \cdot i \cdot T_{bb} = t_{sa} \cdot i \cdot V \cdot T_b \quad , \quad T_2 = T_b \left(1 + t_{sa} \cdot i \cdot V\right) = T_L x \tag{31}$$

The power balance for the PL can be used to calculate internal torques

$$T_a \omega_a + T_s \omega_s + T_c \omega_c = 0 \quad , \quad \omega_c = \omega_L, \quad T_c = T_L, \quad T_a = T_s \cdot t_{as} \tag{32}$$

These results on torques and velocities are needed for dimensioning of the machinery.

3. RESULTS AND CONCLUSIONS

The following results are obtained:

The functionality of a multi component power transmission machinery can rather well be estimated using basic theory. The problems in this approach are lack of reasonable models and reliable data on strength and constraints especially at fast dynamic and loadings and at long term loadings. The machinery generally needs a clutch functioning at the output part before the load. Several clutch types are considered. For comparison purposes the main dimensions , plate numbers and load conditions were set the same. The torque of a conventional wet clutch is about 40 Nm. The viscous clutch could give about 120 Nm but the temperature dissipation is a limiting constraint. The ER clutch can transmit only 2Nm before slipping. It is tentatively suggested that a synergic combination of various clutch types could result in a novel innovation. One conceivable option is a wet clutch with electro-rheological fluid .With plates pressed together it operates as a normal wet clutch. Then with increasing separation it can be operated as a viscous clutch. By applying electric field a fine tuning control could be obtained.

The following conclusions can be drawn

1. The motivation of choosing this combination is that with HTC high startup torque is obtained and with the variator and gear trains even reversed of rotations are obtained.
2. The shear models and viscosity models gave a complex but controllable dependence on temperature and electric field but these effects can be modelled using simple design rules.
3. Many power transmission combinations can be realized using conventional and new transmission components

4. Hybrid combination can be obtained by synergic use best characteristics of various clutches based on various physical principles of transmitting torque, like dry and wet friction, viscous and electro-rheological transmission principles.
5. Technical development and optimization design is needed when the optimal concept has been found.

4. REFERENCES

[1] Cochin Ira,Cadwallender W, Analysis and Design of Dynamic Systems, Addison Wesley, 1997

[2] Peshcke ,Wolfgang, Die Wirkungsweise einer Visco-Kupplung und ihr Einfluss auf die Traktion eines Allradfahrzeugs, Dissertation, Hannover, 1989 .

[3] Papadopoulos Chris A., Brakes and clutches using ER fluids.Mechatronics 8 (1998) 719-726

[4] Juvinall, Robert C., Marshek, Kurt M., Fundamentals of machine component design, John Wiley & Sons, Inc, New York, 1999.

[5] Voith.Hydrodynamik in der Antriebstechnik.Wandler,Wandlergetriebe ,Kupplungen, Bremsen.Vereinigte Fachverlage.Krauskopf, Ingenieur Digest,Mainz, 1987,ISBN 3-7830-0227-3

[6] Hall W,Pour R.,Mathiek D.,and Gueter C.,Das stufenlose Automatikgetriebe für den neuen Mini, ATZ 5/2002, 458-463.

CFD Simulation of Fiber Suspensions

David Hammarström, Process Flow Ltd Oy,
fax: +358-2-2759580
email: david.hammarstrom@processflow.fi
Jari P. Hämäläinen, Metso Paper Inc.
Anders Dahlkild, Faxén Laboratory, KTH, Sweden

Abstract
Fiber suspensions are present at many dry contents in the fiber line in the paper making process. Proper fiber handling is of vital importance to maintain the quality of the individual fibers and to optimise each unit process of the fiber line. In order to optimise the process, thorough knowledge of the suspension flow is necessary, both on the level of suspension, fiber networks and individual fibers. Knowledge of the fiber suspension flow behaviour combined with commercial CFD (Computational Fluid Dynamics) provides an efficient design tool for unit processes of the pulp and paper industry.

In this paper the general validity of a pulp flow model presented in a previous paper is demonstrated. The simulation method has been developed in pipe flow, but the method allows the flow of fiber suspensions to be simulated in any industry geometry. The model is presented with one set of measured head loss data for a pipe flow for which the fluid specific parameters are fitted. Numerical solution using the model is compared to experimental head loss data from the literature. The most significant result presented in this paper is that pulp suspension can be modelled using flow models for homogenous fluids, despite what has been argumented in the literature.

1. Introduction

The head losses in pipe flow of pulp suspensions has been measured for many decades. The study of fiber suspension flow must be done in fully controlled environments, such as, pipe flow. Pipe flow of pulp fiber suspensions do not follow the head loss curve of neither the laminar nor the fully turbulent flow curve, but usually show a very characteristic "S"-shaped curve for the head loss plotted against the flow rate. The head loss measurements presented in the literature are based on many different pipe diameters and using many different pulp types. Different pipe diameters can be taken into account when developing flow models for pulp flow, but different pulp types cannot be combined due to the significant differences in behaviour. Several old measurement series have used too short calming lengths for the pulp flow, but a good source is the thesis of Möller [1], from which the reference data presented in this paper is taken.

Earlier only the first, laminar, part of the flow could be properly modelled. Shear thinning viscosity models have been used for slow velocities, but they fail as the velocity increases resulting eventually in decreasing head losses. Myréen [2] demonstrated the use of the power-law viscosity model for pulp flow modeling for the laminar plug-flow region. Duffy [3], on the other hand, arguments that the flow of fiber suspensions cannot be modeled using non-Newtonian laminar flow models. Several important flow features are neglected when using homogenous flow models, for instance, the tendency to form fiber netwoks and agglomerates, flocs.

The region where the head losses decrease with increasing flow rate has been attributed to the formation of a water annulus at the pipe walls. The thickness of this slip layer has been analytically calculated by Soszynski [4] and Hämäläinen [5]. Both authors showed that the water annulus thickness is negligible compared to the other dimensions of the flow. A mathematical model presented by Hammarström et al [6] is capable of describing both flow regimes, that is, increasing and decreasing head losses as a function of increasing velocity. The model is an effective wall slip model, which does not model the slip phenomenon, but only the effects on the flow.

The current results show that the wall slip phenomenon is independent of pipe diameter and that the laminar flow models can be used for simulating complex pulp flows, based on relatively simple head loss measurements in pipe flows.

2. Suspension Rheology

The fiber suspension is modelled as a homogeneous shear-thinning fluid. The power-law viscosity model, equation {1} is used, where τ is the shear stress, μ is the viscosity, K is the consistency coefficient and n is the fluid behaviour index and $\dot{\gamma}$ is the strain rate.

$$\tau = \mu\dot{\gamma} = K(\dot{\gamma})^{n-1}\dot{\gamma} \qquad \{1\}$$

There are also other generalized Newtonian models, for example, Wikström and Rasmusson [7] used the Bingham model (a yield-stress model) for an industrial screening application. The viscosity model is not a key issue of this paper, the power-law model was chosen in order to demonstrate a new method, with which the same model can be used to describe both the plug-flow regime and the wall-slip regime.

3. Wall slip model

The model derived for the plug-flow regime is assumed valid for the suspension, and that the head loss reduction is due to slip on the wall. This is illustrated in Picture 1. The pulp plug is assumed intact, and the slip velocity is setting the correct flow rate.

By introducing a slip term, the shear stress at the wall is given by {2}

$$\mu\dot{\gamma} + Fu_{slip} = 0 \qquad \{2\}$$

where the first term is the shear stress near the wall, and the second term is a constant multiplied by the wall slip velocity, u_{slip}. At the pipe wall, the velocity is always zero, but as the current model is not modelling the flow down to the wall, the velocity at the boundary between the pulp core plug and the water layer is used.

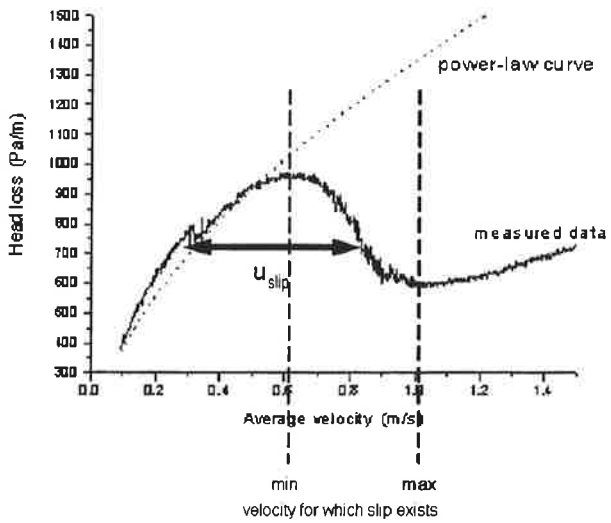

Picture 1. The lower and upper limits of the validity of the wall slip assumption is given by the dashed lines. The region at lower flow rates than the wall slip region is referred to as the plug flow region.

By inserting expression {2} into the axially symmetric two-dimensional Navier-Stokes equation, and solving for the velocity profile in the pipe, the mean flow rate in the pipe is obtained. The first term on the right hand side in equation {3} is the normal solution for the mean velocity in pipe flow of a fluid of which the viscosity is given by power-law model, equation {1}. The second term is the slip velocity required in order to get the correct flow rate, which is illustrated by picture 1.

$$u_{average} = \left(\frac{\Delta p}{\Delta l \, 2k} \right)^{\frac{1}{n}} \frac{n}{3n+1} R^{\frac{n+1}{n}} + u_{slip} \qquad \{3\}$$

The slip term in equation {2} is modified in order to model the head loss curves correctly. The wall shear stress is described by an exponential and a linear term of the wall slip velocity, of which the exponential term is known as the generalized Navier's law [8]. The simplest wall slip model that is able to describe the head loss curve is given by {4}

$$\mu \dot{\gamma} + \left(f_1 u_{slip}^{e-1} + f_2 \right) u_{slip} = 0 \qquad \{4\}$$

4. Calculations

The measured data of the flow of Hudson Birch pulp was taken from Möller [1]. The measurement series contained three different pipe diameters, and the measurements had been carried out at many dry contents of the pulp. Four of the consistencies were selected, based on the number of measurement points in the flow rate regions of interest.

Table 1 The model parameters fitted for the measured head loss data of Hudson birch pulp.

	k	n	f_1	e	f_2
1.51%	2.1995	0.2250	5.3701	-0.0019	-1.9576
1.97%	3.8691	0.2530	11.9443	-0.0188	-4.0994
2.65%	7.2163	0.2657	26.5436	-0.0108	-4.4447
3.51%	9.0215	0.2670	35.4059	-0.0306	-2.5706

The viscosity parameters, k and n, of each consistency were determined in the plug flow region, see picture 1. The parameters of each consistency have been determined in the 4 inch pipe, the same parameter have been used for the simulation for all pipes in pictures 2-4. In a similar way, the parameters for the wall friction were determined in the wall slip region according to equation {2}. The parameters of both regions are presented in table 1. The wall slip function was implemented in the commercial CFD code FLUENT, version 6.0.20. As the wall slip function is implemented directly as a wall boundary condition, there is no need to specify in which region the flow is, the solver determines this based on the mass and force balances.

The simulations have been carried out in three pipes with inner diameters 2.09, 3.01 and 3.93 inches. The pipes were modelled in 2D with axial symmetry. The computational grids contained 3600-5500 cells. The cell height was reduced towards the pipe wall. The head loss curve of each pipe and consistency was simulated by incrementing the inlet boundary condition with 0.1m/s for each simulated point. The suitability of the numerical scheme and cell size and convergence criteria has been controlled.

5. Results

The simulation results of the pulps are presented in pictures 2-4. The results are presented in the same way as the measurement results, one picture per pipe diameter. As is clearly visible, the agreement between the simulations and the measurements is quite good. There are a few small differences between the data, this is caused by the difficulty of determining the mean head loss curve for the pipe in which the parameters are fitted. The important thing to notice is that it is not important for which pipe diameter the viscosity and slip paremeters have been fitted, but that the same parameters have been used for all pipes. For a more accurate determination of the pulp parameters more measurement points would be required, the current number is a bare minimum. But still, the results show an excellent agreement for all three pipe diameters.

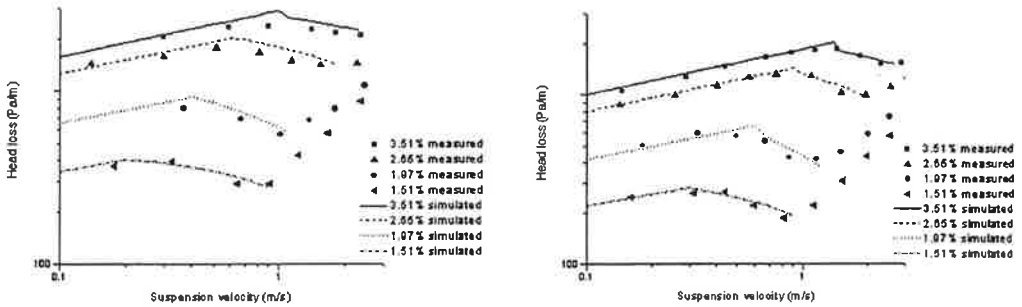

Picture 2-3 Measured and simulated head losses in 2 and 3 inch pipes.

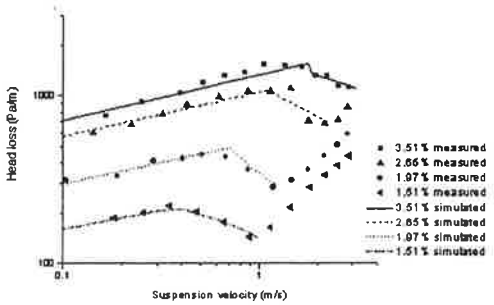

Picture 4 Measured and simulated head losses in 4 inch pipe

The influence of the wall slip model is shown by picture 5. In this picture the resulting velocity profile of four cases are shown. Two velocities, 0.3 and 1.4m/s, from the 3inch pipe at 2.65% consistency were chosen. The velocities were chosen to represent both flow rate region. The lower velocity is in the plug flow region, and the higher is in the wall slip region. For comparison, identical simulation results but without the slip model at the pipe wall have been included in the picture.

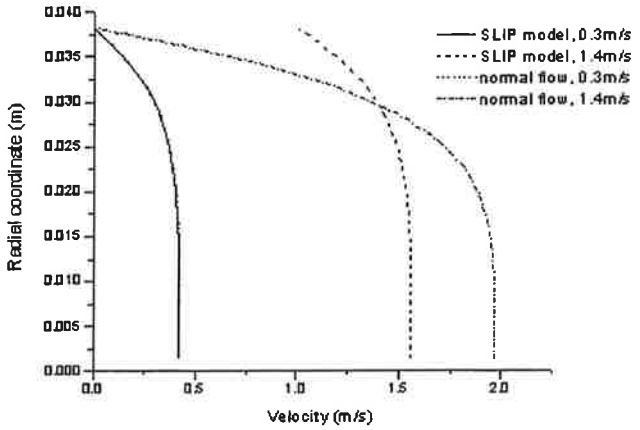

Picture 5 The velocity profile in the pipe. The legends refer to the boundary conditions used at the pipe wall and mean velocity.

In the low velocity cases, both the simulation with the wall slip and the normal no-slip wall boundary condition return identical velocity profiles, which shows that the method can be used for low flow rates as well. In the higher velocity cases, there is a significant slip velocity at the pipe walls. The normal no-slip simulation returns a zero velocity at the pipe wall, the wall slip model returns roughly 1m/s.

This difference is of fundamental importance. If, for instance, the velocity profile in this kind of pipe flow is determined with any kind of instrument, the instrument will need to have a very high resolution near the pipe wall. Otherwise, the instrument will just see one large plug. That the instrument will observe just one large plug has been observed by many authors, for instance, Head and Durst [9] commented that the velocity profile is rectangular. If the viscosity parameters are determined at the higher flow rate case in picture 5 neglecting the wall slip, then the resulting pulp parameters will be incorrect.

5. Discussion

The wall slip has been shown to be a useful and valid method for describing the head loss in laminar pipe flow of fiber suspensions. The method has been shown to be able to correctly describe the flow of several consistencies over a large range of flow rates in three pipe diameters. This quite clearly shows that pulp suspensions can be modelled using laminar flow models for homogenous fluids. The upper limit for the validity of the currently presented wall slip model has been set to the local minimum on the head loss curve. At this point the flow becomes turbulent.

6. Acknowledgements

The financial support from the Finnish National Technology Agency, TEKES, and Faxén Laboratory at the Royal Institute of Technology, Stockholm, Sweden is thankfully acknowledged.

References:

[1] Möller K; **The Plug Flow of Paper Pulp Suspensions**, PhD thesis, University of Auckland, New Zealand, 1972

[2] Myréen B; **Modelling the Flow of Pulp Suspensions in Pipes, Part 1.** Paperi ja Puu, 5/1989.

[3] Duffy G.G; **The Importance of Mechanistic-based Models in Fibre Suspension Flow**, Nordic Pulp and Paper Journal, 2003, in press

[4] Soszynski R; **The Plug Flow of Fiber Suspensions in Pipes. A Case of Clear Water Annulus**, Nordic Pulp and Paper Research Journal, no 3, 1991.

[5] Hämäläinen, J; **Mathematical Modelling and Simulation of Fluid Flows in the Headbox of Paper Machines,** PhD Thesis, University of Jyväskylä, 1993

[6] Hammarström D, Hämäläinen J, Dahlkild A, Jäsberg A; **Modeling of laminar suspension flows**, submitted to JPPS

[7] Wikström T, Rasmusson A; **Transition Modelling of Pulp Suspensions Applied to a Pressure Screen**, Journal of Pulp and Paper Science, vol 28, 2002

[8] **POLYFLOW 3.8 User Guide**, ch 6, Fluent Inc.

[9] Head V.P, Durst R.E; **Stock Slurry Hydraulics**, TAPPI vol 40 no 12, 1957

NUMERICAL SIMULATION OF FREE SURFACE FLOWS IN 2D WITH UNSTRUCTURED FINITE VOLUME BASED PRESSURE CORRECTION METHOD

T. MIKKOLA

Ship Laboratory
Helsinki University of Technology
P.O. Box 4100, FIN-02015 HUT
e-mail: Tommi.Mikkola@hut.fi

ABSTRACT

A 2D unstructured, collocated, pressure correction method is extended for free surface flows. Two free surface solution approaches based on either the kinematic or the dynamic boundary condition, with partial coupling to the pressure correction method, are studied. Two different velocity boundary conditions have been tested in the kinematic approach. Grid updating is implemented with a well known linear spring model. Developed methods have been tested with a flow over a bump and around a submerged hydrofoil. The comparison of the convergence properties of the approaches shows superior stability for the kinematic approach. Computed results for both cases agree well with experimental and numerical reference data.

1 INTRODUCTION

Flow simulations with a free surface are special due the presence of a material interface free to deform following the flow underneath it. The final location of the free surface is not known in advance and has to be solved together with the bulk flow.

Within the field of ship research, viscous free surface flows have commonly been solved using surface tracking methods based on structured boundary fitted grids. Due to the use of structured grids, these methods are, however, not very well suited for cases involving complex geometries and large deformations of the free surface. Unstructured methods, having the capability to cope also with geometrical complexities, are therefore a more suitable choice for these kind of cases. An equally important feature of unstructured grids is adaptivity, i.e. the possibility to regenerate the grid locally during the solution process without affecting the rest of the grid.

The purpose of the on-going research at Helsinki University of Technology Shiplaboratory is the development of an unstructured, finite volume flow solver for free surface flows with surface tracking, adaptive grid reconstruction. The first part of the work was the development of a basic laminar 2D solver without free surface for triangles based on the pressure correction method.[11] In this paper the solver is extended for free surface flows with emphasis on the coupling of free surface solution and pressure correction method. Two approaches for the solution of the free surface deformation, with partial coupling to the bulk flow solution, are presented. As the interest is on the free surface solution approach, only Eulerian flow is considered. The surface tracking is implemented with a well known spring analogy model.

2 GOVERNING EQUATIONS

2.1 Field equations

The flow is assumed to be incompressible, inviscid and isothermal in 2D. The governing equations for the flow are the incompressible 2D continuity and momentum balance equations. In conservation form these are

$$\int_{\partial\Omega} \rho v_i n_i dS = 0 \quad \text{and} \tag{1}$$

$$\int_{\Omega} \rho \frac{\partial v_i}{\partial t} dV + \int_{\partial\Omega} \rho v_i v_j n_j dS = -\int_{\partial\Omega} p n_i dS \tag{2}$$

respectively. Here ρ is the density, v_i are the velocity components and n_i are the components of the outer normal for domain Ω respectively. The piezometric pressure p includes the effect of gravity and is given by

$$p = p^{\mathrm{st}} + \rho g x_2 \,, \tag{3}$$

where p^{st} is the static pressure and gravity points in the negative x_2-direction.

2.2 Free surface boundary conditions

The bulk flow and free surface are connected through boundary conditions, which have to be satisfied on the deforming surface. As a material interface, the free surface introduces two types of conditions on the flow quantities.

The first one of these is the kinematic boundary condition stating that there is no flow through the interface. This requires that

$$\left(v_i - v_i^{\mathrm{fs}}\right) n_i = 0 \qquad \text{, where} \qquad v_i^{\mathrm{fs}} = \frac{\partial h}{\partial t}\delta_{i2} \tag{4}$$

is the velocity of the surface parallel to the x_2-axis. Wave height h is measured from some reference level parallel to the x_1-axis. Writing out Eq. (4) gives the kinematic boundary condition

$$\frac{\partial h}{\partial t} = v_2 + v_1 \frac{n_1}{n_2} \,. \tag{5}$$

The second condition to be satisfied on the free surface is the dynamic boundary condition. This states, that stresses have to be continous across the free surface. In this work, the inviscid approximation of this without surface tension effects is used. For the normal stress, this gives

$$p^{\mathrm{st}} = p^{\mathrm{atm}} \,. \tag{6}$$

Assuming zero atmospheric pressure and taking into account Eq. (3) leads to the dynamic boundary condition

$$p = \rho g h \tag{7}$$

for the piezometric pressure on the free surface.

3 NUMERICAL METHOD

The numerical method used in this work is based on the unstructured finite volume method and the flow equations are solved using a SIMPLE-type [3], collocated pressure correction method.[11] Boundary conditions are taken into account by setting appropriate values for the variables in ghost cells on the boundaries. Velocities and pressures are defined at the centres of the control volumes and wave heights at the centres of the free surface faces.

3.1 Unstructured finite volume method

The finite volume method is based on the fact, that the Navier-Stokes equations in conservation form (1) are valid for any arbitrary domain Ω within the flow field. The computational domain is divided into nonoverlapping subdomains – in this work triangles – creating a computational grid and the equations are applied for each element of the grid separately.

The continuity and momentum balance equations for triangle l of the grid can be written as sums over the sides lm connecting neighbouring triangles l and m leading to

$$\sum_m \dot{m}_{lm} = 0 \quad \text{and} \tag{8}$$

$$\rho V_l \frac{\partial v_{i,l}}{\partial t} = -\sum_m F_{i,lm} \tag{9}$$

respectively. Here

$$\dot{m}_{lm} = \rho \bar{v}_{(lm)} S_{(lm)} \tag{10}$$

is the mass flux through face lm and $\bar{v}_{lm}$ is the convection velocity normal to the face. The fluxes in the momentum balance equations (9) are given by

$$F_{i,lm} = \left(\rho v_{i,(lm)} \bar{v}_{(lm)} + p_{(lm)} n_{i,(lm)}\right) S_{(lm)} \,. \tag{11}$$

3.2 Pressure correction method

The solution process is based on a velocity-pressure decoupling, in which the velocities and pressures are solved separately in an iterative manner. In each iteration, the velocity field is first updated from momentum balance (9) using the current pressure field and corrected after this by altering the pressure according to the mass balance error on the left hand side of the continuity equation (8). This process is repeated until a steady state is reached. Each global iteration can be divided into three parts: the velocity update, calculation of the mass balance error and the pressure correction stage.

3.2.1 Momentum balance

Momentum equations (9) are integrated in time by the implicit Euler scheme. Linearization of the fluxes gives

$$A_{P,l} \Delta v_{i,l} + \sum_{n \neq l} a_{ln} \Delta v_{i,n} = R_{i,l} \,, \tag{12}$$

where

$$A_{P,l} = \frac{\rho V_l}{\Delta t} + a_{(l)(l)} \qquad a_{ln} = \sum_m \frac{\partial F_{i,lm}}{\partial v_{i,n}} \qquad R_{i,l} = -\sum_m F_{i,lm} \,. \tag{13}$$

The convected velocity components $v_{i,lm}$ are upwinded using the extrapolation presented by Frink [7] modified for 2D or by

$$v_{i,lm} = v_{i,l} + \gamma \frac{\partial v_{i,l}}{\partial x_i} \left(x^c_{i,lm} - x_{i,l}\right) \,, \tag{14}$$

where the flow is assumed to be from l to m. Above $x^c_{i,lm}$ are the coordinates of the centre of the face and γ, with a value between 0 and 1, a parameter controlling the amount of upwinding.

The convection velocity $\bar{v}_{lm}$ and the pressure p_{lm} in Eq. (11) are taken as averages of the values at auxiliary points l' and m'. These are projected from points l and m respectively on a line normal to face lm and going through the centre point of this face. The gradient components for velocities

and pressure, required for the extrapolations, are calculated using a least squares based method described in e.g. [4] or iteratively from

$$\frac{\partial p_l^{k+1}}{\partial x_i} = \frac{1}{V_l} \sum_m n_{i,lm} S_{lm} \left\{ f_1 \left[p_l + p_l \frac{\partial p_l^k}{\partial x_j} (x_{j,l'} - x_{j,l}) \right] + (1 - f_1) \left[p_m + \frac{\partial p_m^k}{\partial x_j} (x_{j,m'} - x_{j,m}) \right] \right\} \tag{15}$$

written here for the pressure.

In the implicit stage, i.e. for the calculation of the linearized terms in (13), the fluxes are approximated with first order schemes. This ensures that only the closest neighbours of an element contribute to the linear system.

3.2.2 Mass balance

In order to avoid decoupling of the neighbouring velocities and pressures, some artificial damping must be added into the mass fluxes for the calculation of the mass balance error.[13] In the current method, a simplified damping term or a term similar to the one proposed by Rhie and Chow [13] is used. The simplified term is based directly on an approximation of the third derivative of pressure on a regular grid

$$d_{lm} = \frac{1}{4} (p_{ml}^n - 3p_m + 3p_l - p_{lm}^n) \ . \tag{16}$$

Here p_{lm}^n and p_{ml}^n are the values at the vertices opposite to the face on the left and right hand sides respectively. With the added damping, the mass flux on a face can be written as

$$\dot{m}_{lm}^* = \rho S_{(lm)} \bar{v}_{(lm)}^* + C \frac{\rho S_{(lm)}^2}{A_{P,(lm)}} d_{lm} \ , \tag{17}$$

where the asterisk is a common way to denote uncorrected values in pressure correction methods, C is a parameter controlling the amount of damping and $A_{P,lm}$ is the average of the diagnonal terms $A_{P,l}$ and $A_{P,m}$.

3.2.3 Pressure correction

Corrected velocities can be written as

$$v_i = v_i^* + v_i' \qquad p = p^* + p' \ . \tag{18}$$

Here, v_i^* and p^* are the provisional velocity components and pressure after the solution of the momentum equations and v_i' and p' are the unknown corrections. Continuity condition for the corrected velocities gives a relation between the provisional values and the corrections

$$\sum_m \dot{m}_{lm}' = -\sum_m \dot{m}_{lm}^* \ . \tag{19}$$

The connection between the change of pressure and mass flux on a face can be derived from the momentum equations. Following the approach used in the SIMPLE method [3] gives the pressure correction equation

$$\sum_m \alpha_{lm} p_m' = -\sum_m \dot{m}_{lm}^* \ , \tag{20}$$

where

$$\alpha_{lm} = -\frac{3}{2}\frac{\rho S_{lm}^2}{A_{P,l} + A_{P,m}} \qquad \alpha_{ll} = -\sum_{m \neq l} \alpha_{lm} \tag{21}$$

are the off-diagonal and diagonal elements respectively. Here the geometrical properties of triangles have been utilised. In case there are highly skewed triangles in the grid, the pressure corrections are adjusted with the deferred-correction approach [6].

Updated pressures and velocities are given by

$$p_l^{n+1} = p_l^n + \alpha_p p_l' \qquad v_{i,l}^{n+1} = v_{i,l}^* + \alpha_v v_{i,l}' \,, \tag{22}$$

where α_p and α_v are under-relaxation factors. Velocity corrections are calculated from

$$A_{P,l} v_{i,l}' = -\sum_n S_{ln} p_{ln}' n_{i,ln} \,. \tag{23}$$

3.3 Free surface solution

A common approach to solve free surface problems is to decouple the bulk flow and free surface problems. In that case, the solution of the flow consists of two steps iterated in turns until a converged solution is reached. For each iteration, the bulk flow is updated first with boundary conditions according to the current free surface. This is followed by the solution of the new free surface location based on the updated bulk flow and adjustment of the grid to match the new boundary. Calculation of the new wave height can be based on either the kinematic or dynamic boundary condition. The next bulk flow step is then based on boundary conditions on the updated free surface.

In the current method, the approach above is improved slightly by partially coupling the bulk flow and free surface solutions through the pressure correction equation.

3.3.1 Kinematic free surface approach

In this approach the update of the wave height is based on the kinematic boundary condition. The grid is assumed to be fixed and to coincide with the current instantaneous free surface. Velocity components are updated from the momentum balance (12) using dynamic boundary condition (7) for the pressure and either zeroth or first order extrapolation for the velocities on the free surface.

Full decoupling of the bulk flow and free surface solutions would result into a constant pressure boundary condition on the free surface, implying zero pressure correction on the free surface. On the other hand, the deformation of the free surface combined with the dynamic boundary condition changes the pressure on the free surface. This incompatibility of boundary conditions would lead to a jump in pressure across the free surface during the iteration, affecting the stability of the method. In order to avoid this complication, the deforming free surface is taken into account during the pressure correction stage using the dynamic boundary condition.

After the calculation of the mass balance error, the change of wave height is evaluated by integrating the kinematic boundary condition (5) in time with the explicit Euler scheme, resulting into

$$\Delta h = \left(v_2 + v_1 \frac{n_1}{n_2} \right) \Delta t \,. \tag{24}$$

Pressure on the new free surface has to satisfy the dynamic boundary condition, giving with Eq. (24) relation

$$p'^{\mathrm{fs}} = \rho g \left(v_2 + v_1 \frac{n_1}{n_2} \right) \Delta t \tag{25}$$

between the pressure correction on the free surface and the change of wave height. For the solution of the pressure correction equation (20), linear extrapolation is used for the ghost cell values, so that

Eq. (25) is satisfied exactly on the free surface. Due to the relaxation of the pressure corrections, wave heights have to be updated according to

$$h^{n+1} = h^n + \alpha_p \Delta h \tag{26}$$

in order to get a free surface compatible with the corrected pressure field.

3.3.2 Dynamic free surface approach

In the second approach used in the current method, the calculation of the new wave height is based on the dynamic boundary condition. Each iteration starts with the calculation of the current wave height from the pressure on the surface:

$$h = \frac{p^{\mathrm{fs}}}{\rho g} . \tag{27}$$

As with the kinematic approach, the grid is assumed fixed. Time integration of the momentum equations is done assuming slip condition on the free surface. The pressures are thus extrapolated linearly into the ghost cells and velocity components are mirrored with respect to the surface, resulting into zero mass flux through the surface. This same condition is used for the calculation of the mass balance error as well.

Full decoupling of the solutions would lead to large deformations on the free surface, making the method very unstable, unless considerable under-relaxation of the pressures is applied after the solution of the pressure correction equation. Heavy under-relaxation would, however, have a dramatic effect on the convergence speed of the solution process.

In this approach, the partial coupling of the bulk flow and free surface solutions is in a form of under-relaxation in the pressure correction stage based on the deforming free surface. As in the first method, the pressure correction on the free surface and the change in wave height can be related through the dynamic boundary condition giving

$$\Delta h = \frac{p'^{\mathrm{fs}}}{\rho g} . \tag{28}$$

If the grid is assumed fixed, this movement of the free surface results into a mass flux through the face of the fixed grid given by the kinematic boundary condition as

$$\dot{m}_{lm}^{*\mathrm{fs}} = \frac{f_1 p'_l + (1 - f_1) p'_m}{g \Delta t} S_{lm} n_{2,lm} . \tag{29}$$

Here l is the computational cell with a face on the free surface and m the associated ghost cell. This mass flux is substituted onto the right hand side of the pressure correction equation (20). Using zeroth order extrapolation for the pressure corrections in Eq. (29), i.e. $p'_m = p'_l$ and transfering the contribution on the left hand side, the diagonal term of a computational cell with a face on the free surface can be written as

$$\alpha_{ll}^{\mathrm{fs}} = \alpha_{ll} + \frac{S_{lm} n_{2,lm}}{g \Delta t} . \tag{30}$$

3.3.3 Grid update

The wave heights are given at the centres of the faces on the free surface. Before the grid can be updated, these values have to be transformed to the grid points on the surface. A centred scheme for the transformation leads to decoupling of the neighbouring wave heights, when calculating normal

vectors and therefore an upwind scheme is used instead. Assuming that the flow is from left to right, the wave height at the right hand end point of the face h^r is approximated by a third order scheme

$$h^r = \frac{2\bar{h}^r + 2h - \bar{h}^l}{3} . \tag{31}$$

Here $\bar{h}^r$ and $\bar{h}^l$ are the weighted averages of neighbouring wave heights at the right and left hand ends of the face respectively. An alternative to this scheme is zeroth order extrapolation of wave height, which can be used close to boundaries to damp out transient waves.

The updating of the grid is based on the well known linear spring analogy model first presented by Batina [1], in which the edges of the grid connecting the grid points are assumed to be linear springs. The grid points are moved by searching for the equilibrium of the spring system knowing the displacements on the free surface.

4 NUMERICAL TESTS

The free surface solution approaches described above have been tested with two test cases. These are a flow over a bump on the bottom of an infinitely wide channel [2] and flow over a submerged hydofoil with an angle of attack [5].

Results are presented for three different free surface solution approaches. These are:

a. kinematic free surface approach with zero gradient condition for the velocity components

b. kinematic free surface approach with linear extrapolation for the velocity components

c. dynamic free surface approach

Local time stepping is used for the bulk flow and free surface solutions in order to accelerate the convergence of the solution process. These are controlled separately through nondimensional CFL-numbers given by

$$\mathrm{CFL} = \max_{m=1,3} \frac{v_{i,l} n_{i,lm} S_{lm} \Delta t_l}{V_l} \qquad \mathrm{CFL}^{\mathrm{fs}} = \frac{v_1 \Delta t^{\mathrm{fs}}}{S n_2} \tag{32}$$

for bulk flow and free surface time steps respectively.

4.1 Flow over a bump

This case was chosen for the overall comparison of different approaches during the development of the free surface solution method due to its simplicity and the prior experience [10] with the case. Testing has been preformed with both the unstructured solver decribed in this paper as well as with a structured counterpart. The findings from the test performed with these two different solvers were however very similar and thus only the results for the unstructured versions are presented.

The geometry of the bump on the floor of the channel is given by

$$x_2 = -1 + 0.1e^{-(x_1-10)^2} \tag{33}$$

with a height of 0.1 and the centre at $x_1 = 10$. In x_1-direction the domain extends from -20 to 50, with damping zones from -20 to 0 and from 30 to 50 on the free surface. Undisturbed water level is at $x_2 = 0$. The grid for the case was created with EasyMesh grid generator [12] and has 1533 nodes, 4123 sides and 2591 triangles. The number of points on the free surface is 279. Cell size in the grid increases towards the inflow and outflow boundaries.

Testing has been performed with both a subcritical and supercritical cases, with Froude numbers based on depth below and above unity respectively. The results presented below are for the

subcritical case with Froude number of 0.567. At low inflow velocity, both free surface approaches performed well in terms of convergence. The time step parameters CFL and CFL^{fs} were 5.0 and 1.0 respectively for both approaches. Pressure corrections were under-relaxed slightly more in the case of the dynamic approach, with relaxation factor 0.3 for the kinematic and 0.2 for the dynamic approach. With these choices the residuals converged to machine accuracy after around 6000 iterations for the kinematic approach and after around 8000 iterations for the dynamic approach, where the slower convergence of the latter is probably due to the smaller pressure relaxation factor. For comparison, the case was tested also with fully decoupled approaches. In this case, the dynamic approach was extremely unstable and, even with radical reduction of the pressure under-relaxation factor, computations diverged. For the kinematic approach, the difference was more subtle. With fully decoupled approach, the free surface CFL-number had to be limited to roughly 0.5. As the limiting factor with the above choice of parameters seemed to be the free surface evolution, the reduction of the free surface time step resulted into roughly twice as slow convergence of the total solution.

At higher velocities considerable difference emerged between the approaches. As the inflow velocity was increased, the dynamic approach became highly unstable with large free surface deformations leading to the divergence of the solution, unless the final pressure corrections were heavily under-relaxed. The kinematic approaches on the other hand required very few changes to the input parameters.

Some differences can also be seen in the wave profiles compared in Fig. 1 with results from a previous test with FINFLO flow solver [10]. The damping with the dynamic approach is slightly

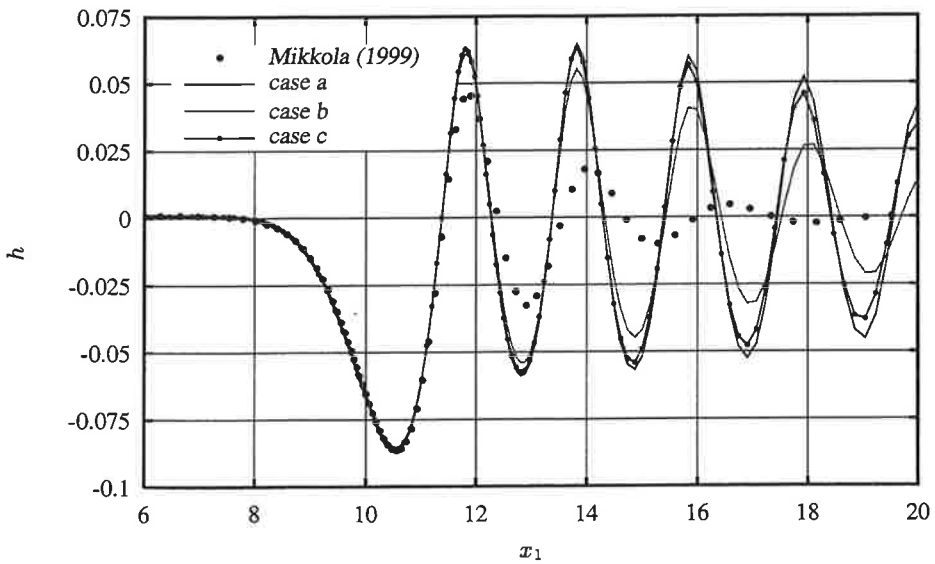

Figure 1: Wave profiles for flow over a bump compared with results for FINFLO [10].

stronger than with the kinematic approach and linear extrapolation for the velocity components. For the kinematic approach with zero gradient condition, the damping is considerably stronger than with cases b and c. The location and depth of the first through as well as the location of the first peak for all cases agree well with the previous results for FINFLO. The strong damping of the wave field in the FINFLO result is partially due to the rapid increase of the cell size towards the outflow boundary, and therefore further away from the obstacle the results are not comparable.

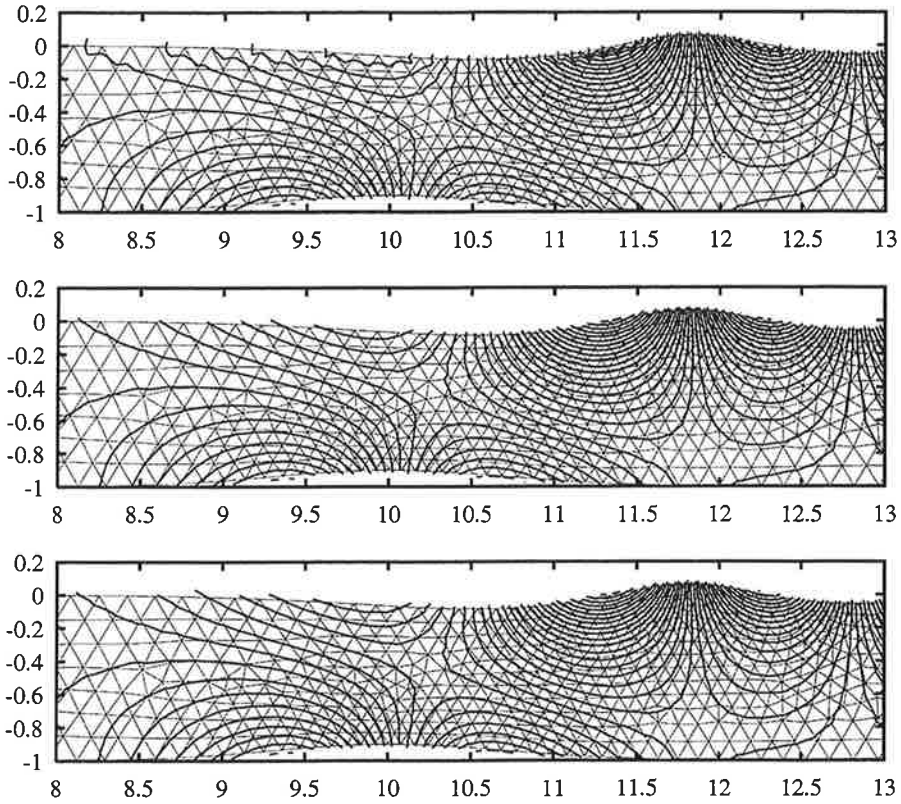

Figure 2: Contours of v_2-velocity for flow over a bump in cases a, b and c respectively. Contour interval is 0.02.

Differences in the flow field are most easily seen from the contours of v_2-velocity shown in Fig. 2 for the three different free surface approaches. Here the contours are drawn based on values at the cell centres and averaged values at the grid points including ghost cells. Cases b and c give relatively smooth and almost identical velocity distributions, whereas the velocity field from case a has some oscillations close to the free surface. It can be seen, that because of the zero gradient condition the contours cross the free surface orthogonally for a large part, which clearly should not be the case. Due to an incompatible boundary condition there is thus a jump in the gradient field close to the free surface.

4.2 Flow over a submerged hydrofoil

The accuracy of the free surface approaches was checked with a flow over a submerged NACA-0012 hydrofoil with an angle of attack of 5 degrees. The Froude number based on the chord length is 0.567. Experimental results for this case have been presented by Duncan [5]. It has also been extensively used for numerical testing, see e.g. [8] and [9].

The chord length of the hydrofoil is 1 and the leading edge is at (0,-0.99). The computational domain and the unstructured grid generated for the case with EasyMesh are presented in Fig. 3. The grid consists of 2996 points, 8699 sides and 5703 triangles. There are damping zones on the free surface from the inflow boundary to -7 and from 6.25 to the outflow boundary. The resolution of the grid is increased around the leading and trailing edges of the foil as well as close to the free surface

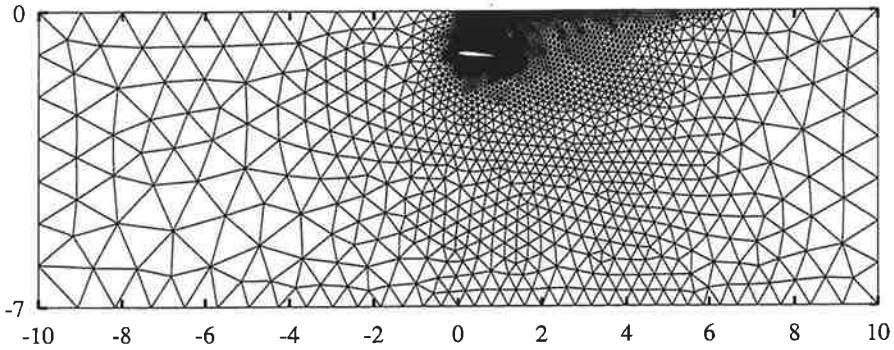

Figure 3: Computational domain and unstructured grid for flow over a submerged hydrofoil.

between $x_1 = 0$ and $x_1 = 6.25$. The number of points on the hydrofoil and on the free surface are 128 and 115 respectively.

The CFL-numbers for the bulk flow and free surface solutions were set to 1.0 and 0.5 respectively. For pressure correction factor 0.2 machine accuracy for the residuals was reached after 4000 to 5000 iterations in all cases, with slightly more iterations required for the dynamic approach.

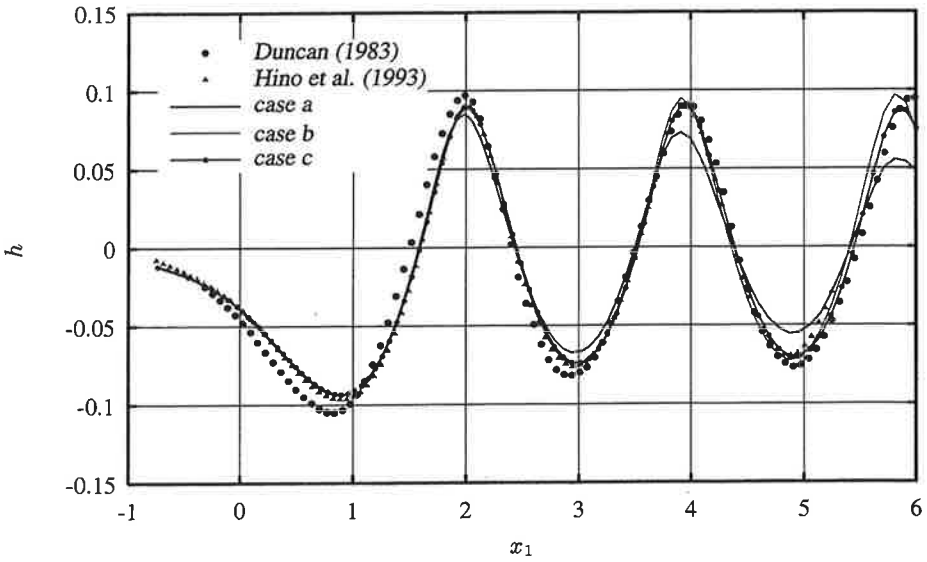

Figure 4: Wave profiles for flow over a submerged hydrofoil compared with measurements [5] and numerical reference data [8].

Wave profiles for different approaches are compared with experimental and numerical references in Fig. 4. Good agreement with the numerical and experimental results can be seen with similar damping to the first test case. Compared to the experiment, the depth of the first through is however under-estimated. This may be due to an insufficient resolution of the grid in front of the through, where the cell size can be seen to increase quite rapidly. There is also a small difference in the wave

length between the computations and the measurement.

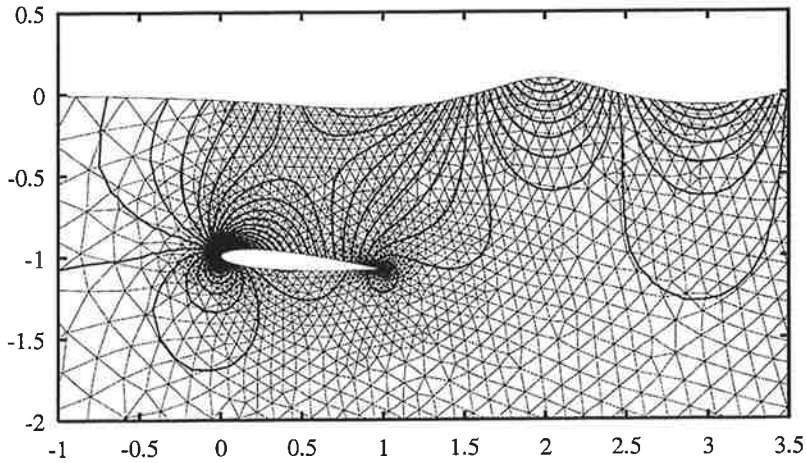

Figure 5: Contours of pressure for flow over a submerged hydrofoil in case b. Contour interval is 100.

Comparison of the contours of velocities and pressure showed again, that cases b and c give practically identical results, while the contours in case a oscillate slightly close to the free surface. Despite the differences close to the free surface, discrepancies close to the hydrofoil are negligible. Pressure contours for case b are shown in Fig. 5.

5 CONCLUSIONS

Unstructured pressure correction solver based on triangle meshes has been extended for free surface flows. Two kind of approaches for free surface solution with partial coupling to the pressure correction method have been studied. In the kinematic approach the updating of the wave field is based on the kinematic boundary condition, whereas in the dynamic approach the new wave height is evaluated from the dynamic boundary condition. Additionally, the kinematic approach has been tested with two different velocity boundary conditions.

Comparison with the fully decoupled approaches showed, that at low inflow velocity the stability of the dynamic approach was greatly improved by the partial coupling of the solutions. Some improvement was also shown for the kinematic approach. Both approaches performed equally well in terms of convergence. At higher velocities partial coupling was effective only in the case of kinematic approach.

Wave profiles agreed well with experimental and numerical reference data. Numerical damping of the wave field was marginally stronger in the dynamic approach, as long as linear extrapolation was used for the velocity components on the free surface with the kinematic approach. Zeroth order extrapolation resulted into considerably stronger damping of the wave field.

The next phase of the research will concentrate on the development of the adaptive, surface tracking grid reconstruction. The proposed approach consists of two parts. The first part is the identification of the areas requiring updating and regridding of these areas, while the second one is the initialization of the solution in the updated parts of the grid. Because the intended approach is very similar to more common forms of adaptivity, it should be possible to make good use of existing research on adaptive methods.

REFERENCES

[1] BATINA, J. T. Unsteady euler algorithm with unstructured dynamic mesh for complex-aircraft aerodynamic analysis. *AIAA Journal 29*, 3 (1991), 327–333.

[2] BET, F., D., H., AND SHARMA, S. D. Simulation of hydrodynamical free-surface flow. In *ECCOMAS'96* (1996), Elsevier.

[3] CARETTO, L. S., GOSMAN, A. D., PATANKAR, S. V., AND SPALDING, D. B. Two calculation procedures for steady, three-dimensional flows with recirculation. In *Proc. Third Int. Conf. Numer. Methods Fluid Dyn.* (Paris, 1972).

[4] DEMIRDŽIĆ, I., AND MUZAFERIJA, S. Numerical method for coupled fluid flow, heat transfer and stress analysis using unstructured moving meshes with cells of arbitrary topology. *Computer methods in applied mechanics and engineering 125* (1995), 235–255.

[5] DUNCAN, J. The breaking and non-breaking wave resistance of a two-dimensional hydrofoil. *Journal of Fluid Mechanics 126* (1983).

[6] FERZIGER, J. H., AND PERIĆ, M. *Computational Methods for Fluid Dynamics*, 2nd ed. Springer, 1997.

[7] FRINK, N. T. Recent Progress Towards a Three-Dimensional Unstructured Navier-Stokes Flow Solver. *AIAA 94-0061* (1994).

[8] HINO, T., MARTINELLI, L., AND JAMESON, A. A finite-volume method with unstructured grid for free surface flow simulations. In 6^{th} *International Conference on Numerical Ship Hydrodynamics* (Iowa, 1993).

[9] LUNGU, A., AND MORI, K.-H. A study on numerical schemes for more accurate and efficient computations of free-surface flows by finite difference method. *Journal of Society of Naval Architects of Japan 173* (1993).

[10] MIKKOLA, T. Testing of Two FINFLO-based Free-surface Codes Using Eulerian Flow Over a Gaussian Ground Elevation. Internal report D-56, Helsinki University of Technology, Ship Laboratory, 1999.

[11] MIKKOLA, T. Development of an unstructured pressure-correction solver based on triangle meshes. In 5^{th} *Numerical Towing Tank Symposium* (Pornichet, France, 2002), G. Delhommeau and M. Visonneau, Eds., Ecole Centrale de Nantes.

[12] NICENO, B. Easymesh. `http://www-dinma.univ.trieste.it/~nirftc/research/easymesh/`.

[13] RHIE, C. M., AND CHOW, W. L. A numerical study of the turbulent flow past an isolated airfoil with trailing edge separation. *AIAA Journal 21* (1983), 1525–1532.

TURBULENT PRANDTL NUMBER THAT MATTERS

M. M. Rahman and T. Siikonen

Helsinki University of Technology, Department of Mechanical Engineering,
Laboratory of Applied Thermodynamics, Sähkömiehentie 4, FIN-02015 HUT
Finland

ABSTRACT

A low-Reynolds number k-$\tilde{\epsilon}$ turbulence model is proposed that incorporates the modeling of turbulent Prandtl numbers $\sigma_{(k,\epsilon,t)}$. The anisotropic production in near-wall regions is accounted for substantially by adding a secondary source term in the $\tilde{\epsilon}$ equation. Hence, it reduces the kinetic energy and length scale magnitudes to improve prediction of adverse pressure gradient flows, involving flow separation and reattachment. Unlike the conventional k-ϵ model, it requires no wall function/distance parameter that bridges the near-wall integration. The model is validated against a few flow cases, yielding predictions in good agreement with the direct numerical simulation (DNS) and experimental data.

1 INTRODUCTION

The eddy viscosity concept is based on an analogy between turbulent transport and molecular diffusion. This analogy simply requires that the turbulent transport of any quantity could be formulated as the gradient of that quantity multiplied by the eddy viscosity. Consequently, alike molecular diffusion, appropriate turbulent Prandtl numbers are needed for each variable to obtain plausible diffusion models. Another flaw seems to be attached to the characteristic scale based on the turbulent kinetic energy k and its dissipation rate $\tilde{\epsilon}$ that enters the model for the diffusivity, appearing to be inadequate in accounting for the near-wall viscous effects. Paradoxically, the precise situation where the turbulence model encounters most difficulties is the turbulent diffusion, dominating the overall balance of the flow. However, the amount of empiricism invoked in the model equations can favor such as not to envisage a failure of the diffusion models. In fact, turbulent Prandtl numbers ranging from $0.68 - 2.0$ can be found for k [1], the most widely used value being $\sigma_k = 1.0$. For $\tilde{\epsilon}$, $\sigma_\epsilon = 1.3$ is the standard choice, but values as low as 0.72 can be found. The commonly used value for $\sigma_t = 0.9$. Nevertheless, it is not precisely correct and there are significant departures from $\sigma_t = 0.9$, particularly in wake/near-wall regions [1, 2].

A wall-distance-free low-Reynolds number k-$\tilde{\epsilon}$ turbulence model is developed. To enhance dissipation in nonequilibrium flow regions, an extra positive source term is included in the $\tilde{\epsilon}$ transport equation, thus reducing the turbulent kinetic energy and length scale magnitudes to improve prediction of adverse pressure gradient flows involving separation and reattachment. The wall singularity is removed by using an appropriate time scale that never falls below the Kolmogorov (dissipative eddy) time scale representing the time scale realizability enforcement accompanied by the near-wall turbulent phenomena. In this way, the introduction of a pseudo-dissipation rate used to remove the singularity in the dissipation equation at the wall, is avoided. A hybrid type eddy viscosity damping function

is designed in terms of the total kinetic energy and invariants of strain-rate and vorticity tensors with no reference to the distance from the wall. It reaches the upper limit value of unity in the logarithmic layer. In addition, the turbulent Prandtl numbers $\sigma_{(k,\epsilon,t)}$ are adjusted such as to provide substantial turbulent diffusion in near-wall regions.

The performance of the new model is demonstrated through the comparison with experimental and DNS data of well documented flows, consisting of fully developed channel flows, a flat plate boundary layer flow with zero pressure gradient and heat transfer from the circular cylinder in cross flow, respectively.

2 GOVERNING EQUATIONS

The two-dimensional Reynolds-averaged Navier-Stokes ($RANS$) equations, including the equations for the kinetic energy k and dissipation $\tilde{\epsilon}$, can be written in the following form:

$$\frac{\partial U}{\partial t} + \frac{\partial (F - F_v)}{\partial x} + \frac{\partial (G - G_v)}{\partial y} = Q \tag{1}$$

where $U = (\rho, \rho u, \rho v, E, \rho k, \rho \tilde{\epsilon})^T$. The inviscid fluxes are

$$F = \begin{pmatrix} \rho u \\ \rho u^2 + p + \frac{2}{3}\rho k \\ \rho uv \\ u(E + p + \frac{2}{3}\rho k) \\ \rho uk \\ \rho u\tilde{\epsilon} \end{pmatrix}, \qquad G = \begin{pmatrix} \rho v \\ \rho vu \\ \rho v^2 + p + \frac{2}{3}\rho k \\ v(E + p + \frac{2}{3}\rho k) \\ \rho vk \\ \rho v\tilde{\epsilon} \end{pmatrix} \tag{2}$$

Here ρ is the density and p is the pressure. The total energy is defined as

$$E = \rho e + \frac{\rho \vec{V} \cdot \vec{V}}{2} + \rho k \tag{3}$$

where e is the specific internal energy and $\vec{V} = u\vec{i} + v\vec{j}$ is the velocity . The viscous fluxes are

$$F_v = \begin{pmatrix} 0 \\ \tau_{xx} + \frac{2}{3}\rho k \\ \tau_{xy} \\ u\tau_{xx} + v\tau_{xy} - q_x \\ \mu_k(\partial k/\partial x) \\ \mu_\epsilon(\partial \tilde{\epsilon}/\partial x) \end{pmatrix}, \qquad G_v = \begin{pmatrix} 0 \\ \tau_{xy} \\ \tau_{yy} + \frac{2}{3}\rho k \\ u\tau_{xy} + v\tau_{yy} - q_y \\ \mu_k(\partial k/\partial y) \\ \mu_\epsilon(\partial \tilde{\epsilon}/\partial y) \end{pmatrix} \tag{4}$$

and the viscous stress tensor can be given as

$$\tau_{ij} = 2\,\mu \left(S_{ij} - \frac{1}{3} S_{kk}\,\delta_{ij} \right) - \rho \overline{u_i u_j} \tag{5}$$

where μ is the laminar viscosity and the Reynolds stresses $\rho \overline{u_i u_j}$ are related to the mean strain-rate tensor S_{ij} through the Boussinesq approximation:

$$-\rho \overline{u_i u_j} = 2\,\mu_T \left(S_{ij} - \frac{1}{3} S_{kk}\,\delta_{ij} \right) - \frac{2}{3}\rho\, k\, \delta_{ij}, \qquad S_{ij} = \frac{1}{2}\left(\frac{\partial u_i}{\partial x_j} + \frac{\partial u_j}{\partial x_i} \right) \tag{6}$$

The heat flux is calculated from

$$\vec{q} = -\left(\mu \frac{c_p}{Pr} + \mu_T \frac{c_p}{\sigma_t} \right) \nabla T \tag{7}$$

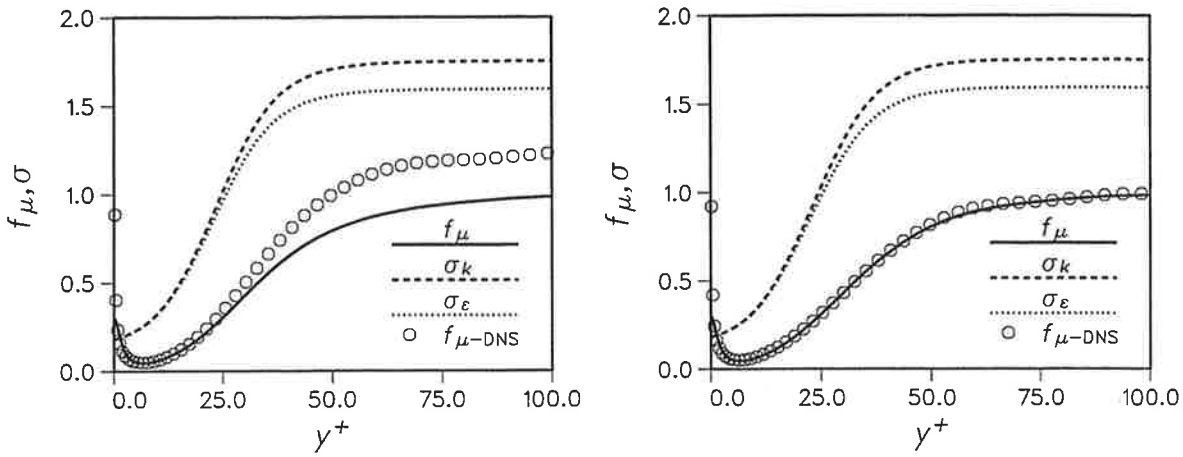

Figure 1: Variations of f_μ and σ with wall distance in channel flow: (a) $Re_\tau = 180$ and (b) $Re_\tau = 395$.

where μ_T is the coefficient of turbulent viscosity, c_p is the specific heat at constant pressure, Pr and σ_t represent the molecular and turbulent Prandtl numbers, respectively, and T implies the temperature. Clearly, the turbulent part of the total heat flux is estimated using the Boussinesq approximation. The diffusion of turbulence is modeled as

$$\mu_k \nabla k = (\mu + \frac{\mu_T}{\sigma_k})\nabla k, \qquad \mu_\epsilon \nabla \tilde{\epsilon} = (\mu + \frac{\mu_T}{\sigma_\epsilon})\nabla \tilde{\epsilon} \tag{8}$$

where σ_k and σ_ϵ are the appropriate turbulent Prandtl numbers. The source term Q for the k and $\tilde{\epsilon}$ equations can be written as

$$Q = \begin{pmatrix} \rho P - \rho\epsilon \\ \dfrac{C_{\epsilon 1}\rho P - C_{\epsilon 2}\rho\tilde{\epsilon} + E_\epsilon}{T_t} \end{pmatrix} \tag{9}$$

where $\epsilon = \tilde{\epsilon} + 2\nu \left(\partial\sqrt{k}/\partial x_j\right)^2$. The turbulent production term $P = -\overline{u_i u_j}(\partial u_i/\partial x_j)$ and E_ϵ is a secondary source term designed to increase the level of $\tilde{\epsilon}$ in nonequilibrium flow regions. The symbolized T_t is the characteristic (mixed or hybrid) time scale, having the asymptotic consistency in the near-wall region. The associated constants are $C_{\epsilon 1} = 1.45$ and $C_{\epsilon 2} = 1.83$.

3 NEAR-WALL TURBULENCE MODELING

In the vicinity of the wall, the molecular viscosity effect is superior to the turbulent mixing, reflecting a strong anisotropic condition. Consequently, an important criterion regarding the appropriateness of the turbulence model is to represent the near-wall behavior of turbulence quantities accompanied by a preferential damping of velocity fluctuations in the direction normal to the wall that reconciles the influence of wall proximity adequately.

The realizable time scale T_t included in Eq. (9) can simply be defined as

$$T_t = \sqrt{\frac{k^2}{\tilde{\epsilon}^2} + C_T^2 \frac{\nu}{\epsilon}} = \frac{k}{\tilde{\epsilon}} \sqrt{1 + \frac{\tilde{\epsilon}}{\epsilon} \frac{C_T^2}{R_T}}, \qquad R_T = \frac{k^2}{\nu \tilde{\epsilon}} \tag{10}$$

where ν denotes the kinematic viscosity and R_T is the turbulent Reynolds number. Equation (10) warrants that the eddy time scale never falls below a compatibility bound deduced from the Kolmogorov time scale $C_T\sqrt{\nu/\epsilon}$. It is dominant in the immediate neighborhood of the solid wall and prevents the singularity in the dissipation equation down to the wall. Alternatively, the turbulence time scale is $k/\tilde{\epsilon}$ at large R_T but approaches the Kolmogorov limit $C_T\sqrt{\nu/\epsilon}$ for $R_T \ll 1$. The empirical constant C_T associated with the Kolmogorov time scale is estimated as follows. In the viscous sublayer $k = y^2/(C_T^2\nu/\epsilon)$, where the basic scale is the Kolmogorov time scale. Besides, the k equation reduces to $\nu\partial^2 k/\partial y^2 = \epsilon$ as the wall is approached. Combining these relations provide $C_T = \sqrt{2}$. Obviously, the inclusion of T_t in the $\tilde{\epsilon}$ equation guarantees near-wall asymptotic consistency without resorting to *ad hoc* damping functions employed in many $k-\epsilon$ models [3].

Since the viscous dissipation presumably dominates near the wall, the eddy viscosity is evaluated from

$$\mu_T = C_\mu\, f_\mu\, \rho\, k\, T_t \tag{11}$$

where $C_\mu = 0.09$ and the dynamic time scale $k/\tilde{\epsilon}$ is replaced by T_t, a distinct turbulence time scale. The damping function is chosen pragmatically as

$$\begin{aligned} f_\mu &= f_\lambda + \frac{\sqrt{C_\mu}}{1+6\,R_\lambda^2} & R_\lambda &= \sqrt{\frac{C_\mu\, K_T}{\nu\,\eta}} \\ f_\lambda &= tanh(C_1\, R_\lambda + C_2\, R_\lambda^2), & K_T &= \vec{V}\cdot\vec{V}/2 + k \end{aligned} \tag{12}$$

where $C_1 = 1\times 10^{-2}$ and $C_2 = 4.5\times 10^{-3}$. The parameter $\eta = max(S, W)$, containing the invariants of strain-rate and vorticity respectively; $S = \sqrt{2S_{ij}S_{ij}}$ and $W = \sqrt{2W_{ij}W_{ij}}$. The mean vorticity tensor W_{ij} is defined as

$$W_{ij} = \frac{1}{2}\left(\frac{\partial u_i}{\partial x_j} - \frac{\partial u_j}{\partial x_i}\right) \tag{13}$$

The empirical function f_μ is valid in the whole flow field, including the viscous sublayer and the logarithmic layer. In the region close to the wall, the Reynolds stress $-\overline{uv} \sim y^3$ and $k \sim y^2$. To preserve the correct cubic power-law behavior of $-\overline{uv}$, the damping function needs to increase proportionally to y in the near-wall region. Equation (12) confirms that as $y \to 0$, $R_\lambda \sim y$ and hence $f_\mu = O(\sqrt{C_\mu})$ at the close proximity of the wall (i.e., f_μ pretends to increase like $f_\mu \sim y^{-1}$). In principle, the construction of f_μ compared to the traditional one [3] augments the potentiality of f_μ to grow particularly in near-wall regions, thereby expediting the viscous dissipation. Alternatively, the adopted form of f_μ reproduces correctly the asymptotic limit, involving the distinct effects of low-Reynolds number and wall proximity. As evinced by Fig. 1 in comparison with the DNS data [4] for fully developed turbulent channel flows, the proposed function $f_\mu = 1$ remote from the wall to ensure the model being compatible to the standard $k-\epsilon$ turbulence model. The use of R_λ (a new parameter with no reference to the distance from the solid surface) confronts the singularity at neither the separating nor the reattaching point in contrast to the adoption of $y^+ = u_\tau y/\nu$, where u_τ is the friction velocity. Consequently, the model is applicable to separated and reattaching flows.

The budgets of k and ϵ from the DNS data approve that the role of turbulent diffusion in the near-wall region is substantial. Accordingly, the Prandtl numbers σ_k and σ_ϵ are modeled, rather than being assigned constant values (unlike the commonly adopted practice with $\sigma_k = 1.0$, and $\sigma_\epsilon = 1.3$):

$$\sigma_\epsilon = C_T\, C_\mu + f_\sigma, \qquad \sigma_k = \frac{\sigma_\epsilon}{1 - C_\mu\, f_\sigma} \tag{14}$$

where $f_\sigma = 2f_\lambda/(1+f_\lambda^2)$. The distribution of σ is depicted in Fig. 1. The model coefficients σ_k and σ_ϵ are developed such that sufficient diffusion is obtained in the vicinity of the wall and in the core region of the flow $\sigma_k/\sigma_\epsilon > 1$ to eliminate the common drawback where the turbulent diffusion of k overwhelms the diffusion of ϵ with $\sigma_k < \sigma_\epsilon$ [5].

The turbulent Prandtl number correlation of Ref. [6] is adopted with a near-wall modification:

$$\sigma_t = \frac{2}{Pr\,(1+\mu_T/\mu)} + 9\,C_\mu \tag{15}$$

The formulation is consistent with the theoretical behavior over a wide range of the molecular Prandtl number Pr, approaching $9\,C_\mu$ as the turbulent Peclet number ($= \mu_T\,Pr/\mu$) is sufficiently large. To this end, it must be stressed that the modification to σ_t (rather than applying $\sigma_t = 0.9$ [2], traditionally) facilitates the avoidance of excessive heat transfer coefficients, particularly in near-wall regions.

The extra source term E_ϵ in Eq. (9) is constructed from the most extensive turbulent diffusion models for k and ϵ equations derived by Yoshizawa [7] with the two-scale direct-interaction approach using the inertial-range simplification. To receive positive benefits from the numerical reliability and to integrate the inertial-range condition directly to the solid wall, the cross-diffusion term is designed with an assistance of Ref. [8] as

$$E_\epsilon = C_\epsilon \frac{\mu_T}{T_t}\, max\left[\frac{\partial(k/\epsilon)}{\partial x_j}\frac{\partial k}{\partial x_j}, 0\right], \qquad C_\epsilon = 1 + C_{\epsilon 2} \tag{16}$$

Obviously, the source term E_ϵ stimulates the energy dissipation in nonequilibrium flows, thereby reducing the departure of the turbulent length scale from its local equilibrium value and enabling improved prediction of adverse pressure gradient flows accompanied by flow separation and reattachment. At this stage, it appears necessary to identify that the quantity E_ϵ is characteristically beneficial in the vicinity of reattachment point and hence, it can be regarded as an attempt at replacing the Yap correction [9].

The transport equations for k and $\tilde{\epsilon}$ are subjected to the following boundary conditions at solid walls:

$$k_w = 0, \qquad \left(\frac{\partial k}{\partial y}\right)_w = 0 \tag{17}$$

$$\tilde{\epsilon}_w = 0, \qquad \left(\frac{\partial \tilde{\epsilon}}{\partial y}\right)_w = 0 \tag{18}$$

Herein, it can be emphasized that reproducing the wall limiting behavior necessitates a fine grid system in near-wall regions.

4 COMPUTATIONS

To ascertain the efficacy of the proposed model, a few applications to two-dimensional turbulent flows consisting of a fully developed channel flow, a flat plate boundary layer flow with zero pressure gradient and heat transfer from a circular cylinder in cross flow are considered. For a comparison purpose, calculations from the original Chien (OCH) model [10] and the modified Chien (MCH) model [8] are included. Note that both the OCH and MCH models assume a constant value for σ (i.e., $\sigma_k = 1.0$, $\sigma_\epsilon = 1.3$ $\sigma_t = 0.9$). A cell centered finite-volume scheme combined with an artificial compressibility approach is employed to solve the flow equations [11, 12]. A fully upwinded second-order spatial differencing is applied to approximate the convective terms. Roe's [13] damping term is

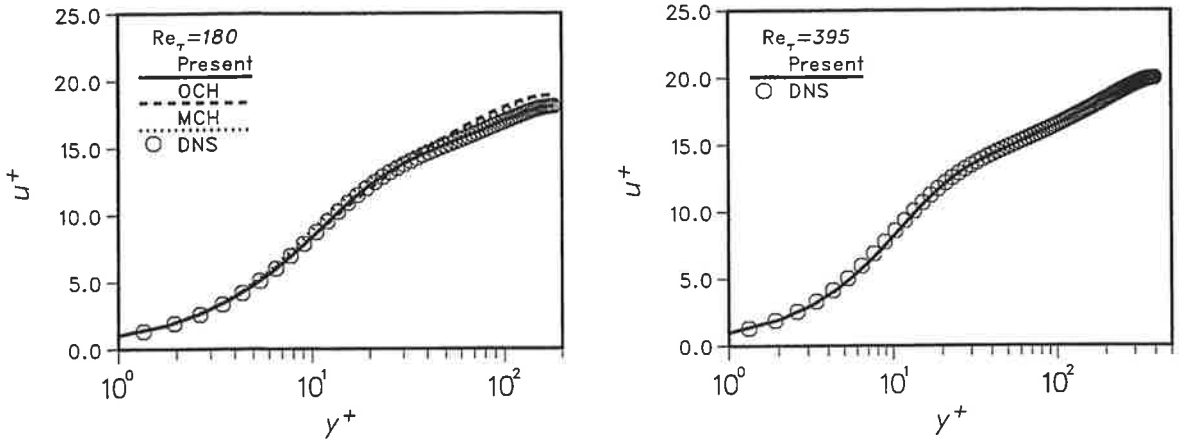

Figure 2: Mean velocity profiles of channel flow.

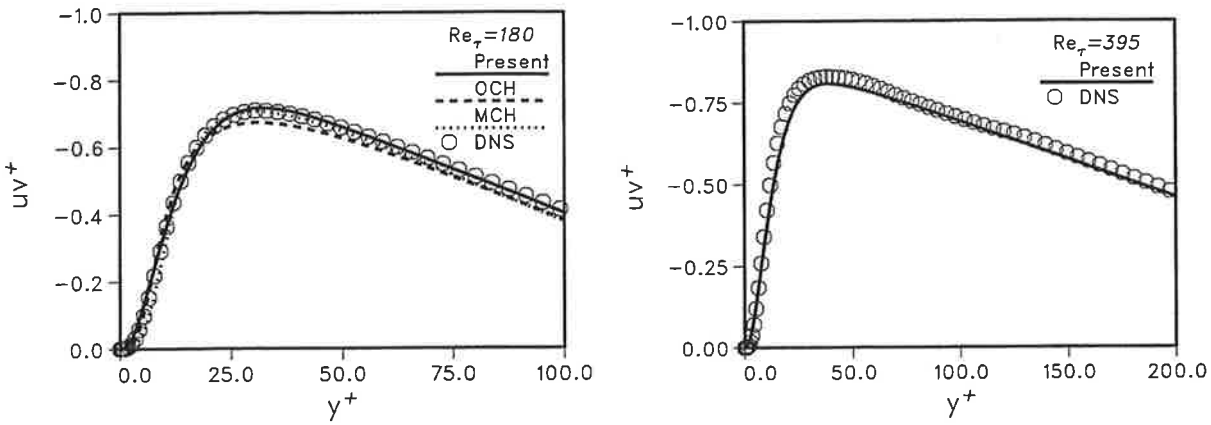

Figure 3: Shear stress profiles of channel flow.

used to calculate the flux on the cell face. A diagonally dominant alternating direction implicit (DDADI) time integration method [14] is applied for the iterative solution to the discretized equations. A multigrid method is utilized for the acceleration of convergence [15]. The basic implementation of the artificial compressibility method and associated features are described in [11, 12, 16].

Channel Flow

Computations are carried out for fully developed turbulent channel flows at $Re_\tau = 180$ and 395, for which turbulence quantities are attainable from the DNS data [4]. Calculations are conducted in the half-width of the channel, imposing periodic boundary conditions, except for the pressure, pertaining to the upstream and downstream boundaries. Computations involving a 48×32 nonuniform grid refinement for $Re_\tau = 180$ and 48×48 for $Re_\tau = 395$ are considered to be sufficiently accurate to describe the flow characteristics. For both cases, the length of the computational domain is 32δ, where δ is the channel half-width. To ensure the resolution of viscous sublayer the first grid node near the wall is

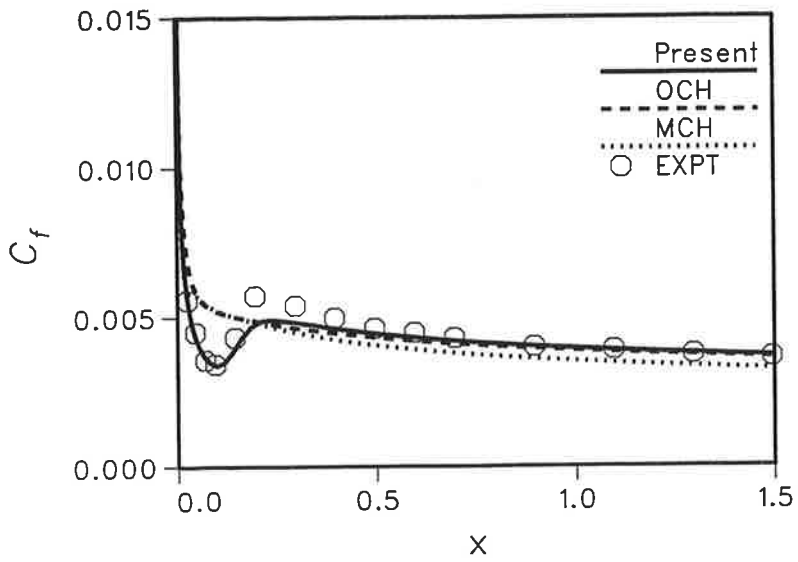

Figure 4: Streamwise skin-friction coefficient of boundary layer flow.

placed at $y^+ \approx 0.4$. Comparisons are made by plotting the results in the form of $u^+ = u/u_\tau$ and $\overline{uv}^+ = \overline{uv}$ versus y^+.

Figure 2 shows the velocity profiles for different models. Predictions of both the present and MCH models agree well with the DNS data. The OCH model slightly overestimates the mean velocity profile in the outer layer. Profiles of turbulent shear stresses are displayed in Figure 3. Agreement of all model predictions with the DNS data seems to be almost perfect.

4.1 Flat Plate Boundary Layer Flow

The performance of the proposed model is further contrasted with the experimental data of the flow over a flat plate with a high free stream turbulence intensity. The test case is taken from "ERCOFTAC" Fluid Dynamics Database WWW Services (http://fluindigo.mech.surrey.ac.uk/) preserved by P. Voke. Measurements down to $x = 1.495m$ which corresponds to $Re_x \approx 94000$, are made by J. Coupland at Rolls-Royce. The inlet velocity is $9.4m/s$ and the pressure gradient is zero. The upstream turbulence intensity $Tu = 6.0\%$, defined as $Tu = \sqrt{\frac{2}{3}k}/U_{ref}$, where U_{ref} indicates the reference velocity. The dissipation is set so that the decay of free stream turbulence is in balance.

Computations begin $16cm$ ahead of the leading edge and symmetric conditions are applied. The length and height of the grid are $1.6m$ and $0.3m$, respectively. The near-wall grid node is located at $y^+ < 1.0$, except the point at the leading edge ($y^+ = 2.1$). The grid size is 96×64 and heavily clustered near the wall.

The predicted skin friction coefficients ($C_f = 2u_\tau^2/U_{ref}^2$) are compared with the experimental data in Figure 4. The overall performance in predicting the friction coefficient is the best for the present model, exhibiting an interesting feature that the transition starts at the right position and it is strong enough. In contrast, both the OCH and MCH models, having the wall distance in the damping functions provide earlier transition than that seen in the experiment, coincident with Savill's investigation [17]. Seemingly, the agreement

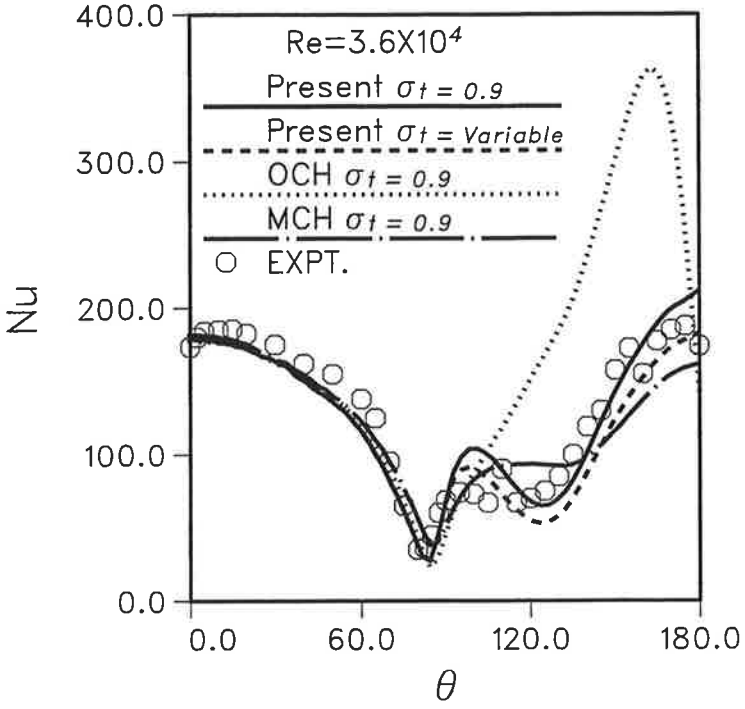

Figure 5: Local Nusselt number distribution over half of tube surface.

between the computations and the experiment is fairly good toward the end of the transition (e.g., beyond $x = 0.195m$). However, the MCH model prediction is somewhat on a lower level than the data show.

4.2 Heat Transfer from Circular cylinder in Cross Flow

The performance of the proposed model is further evaluated by comparing with the experimental data of turbulent heat transfer around a circular cylinder at $Re = 3.6 \times 10^4$ in cross flow [18]. Probably, this is a typical Re for practical heat exchangers. The configuration is geometrically simple but difficult to model. The reasoning is most likely to be attributed to the boundary layer separation, leading to a complex environment. The tested cylinder consists of a tube with $D = 0.025\ m$, where D is the diameter. The reference velocity is $U_{ref} = 22.85m/s$ with an upstream turbulence intensity $Tu = 0.5\%$. An O type grid with 128×96 resolution, clustered heavily near the solid wall, is employed. The radial length of the computational domain is $60D$. External boundary, that is, far field, conditions are applied. A constant temperature is prescribed at the wall, which simulates the experimental boundary conditions.

Figure 5 portrays the variation of the local Nusselt number with the azimuth angle. As can be seen, the distribution exhibits the characteristic feature of a minimum Nusselt Number at the separation that corresponds to $\theta \approx 85°$, followed by an increase in heat transfer in the wake regions. Obviously, the present model prediction maintains good agreement with the experiment. The present model achieve some improvement with a variable σ_t particularly in separation and wake regions.

5 CONCLUSIONS

The proposed turbulent model is wall distance free, tensorially invariant and frame-indifferent. Consequently, it is applicable to arbitrary topology in conjunction with structured or unstructured grids. The model is susceptible to the near-wall and low-Reynolds number effects emanating from the physical requirements. The potential importance of the damping functions is conspicuous. The anisotropic production in the dissipation equation is accounted for substantially by adding a secondary source term, leading to a reduced level of turbulence generation in nonequilibrium flow regions. Consequently, the model is capable of evaluating the flow cases entangling separation and reattachment. In particular, the turbulent Prandtl numbers cannot be considered as constants throughout the flow, leading to examine where an accurate modeling of the diffusion process is required. Contrasting the predicted results with measurements demonstrates that the present model reproduces correctly the skin-friction coefficients and the near-wall heat transfer behavior.

REFERENCES

[1] Cazalbou, J.B., and Bradshaw, P., 1993, Turbulent Transport in Wall-Bounded Flows, Evaluation of Model Coefficients Using Direct Numerical Simulation, *Physics of Fluids A*, 5, pp. 3233-3239.

[2] Jones, W.P., and Launder, B.E., 1973, The Calculation of Low-Reynolds Number Phenomena with a Two-Equation Model of Turbulence, *Int. J. Heat Mass Transfer*, 16, pp. 1119-1130.

[3] Patel, V.C., Rodi, W., and Scheuerer, G., 1985, Turbulence Models for Near-Wall and Low Reynolds Number Flow: A Review, *AIAA J.*, 23, pp. 1308-1319.

[4] Mansour, N.N., Kim J., and Moin, P., 1988, Reynolds-Stress and Dissipation-Rate Budgets in a Turbulent Channel Flow, *J. Fluid Mech.*, 194, pp. 15-44.

[5] Nagano, T., and Tagawa, M., 1990, An Improved $k-\epsilon$ Model for Boundary Layer Flows, *J. Fluids Engrg.*, 112, pp. 33-39.

[6] Kays, W.M., 1994, Turbulent Prandtl Number- Where are We? *ASME J. Heat Transfer*, 116, pp. 284-290.

[7] A. Yoshizawa, A., 1987, Statistical Modeling of a Transport Equation for the Kinetic Energy Dissipation Rate, *Physics of Fluids A*, 30, pp. 628-631.

[8] Rahman, M.M., and Siikonen, T., 2000, Improved Low-Reynolds-Number k-$\tilde{\epsilon}$ Model, *AIAA J.*, 38, pp. 1298-1300.

[9] Yap, C.R., 1987, Turbulent Heat and Momentum Transfer in Recirculating and Impinging Flows, *Ph.D. Thesis*, Faculty of Technology, University of Manchester.

[10] Chien, K.-Y., 1982, Predictions of Channel and Boundary Layer Flows with a Low-Reynolds Number Turbulence Model, *AIAA J.*, 20, pp. 33-38. *Int. J. Heat Fluid Flow*, 18, pp. 209-217.

[11] Rahman, M.M., Rautaheimo P., and Siikonen, T., 1997, Numerical Study of Turbulent Heat Transfer from a Confined Impinging Jet Using a Pseudo-Compressibility Method, *Second Int. Symposium on Turbulence, Heat and Mass transfer*, Delft, The Netherlands, Hanjalic, K., and Peeters, T.W.J., (eds), Delft University Press: Delft, pp. 511-520.

[12] Rahman, M.M., and Siikonen, T., 2001, An Artificial Compressibility Method for Incompressible Flows, *Numer. Heat Transfer, Part B*, 40, pp. 391-409.

[13] Roe, P.L., 1981, Approximate Riemann Solvers, Parameter Vectors, and Difference Schemes, *J. Comput. Physics*, 43, pp. 357-372.

[14] Lombard, C., Bardina, J., Venkatapathy, E., and Oliger, J., 1983, Multi-Dimensional Formulation of CSCM - an Upwind Flux Difference Eigenvector Split Method for the Compressible Navier-Stokes Equations, *Sixth AIAA Comput. Fluid Dynamics Conference* , AIAA Paper 83-1895-CP, pp. 649-664.

[15] Jameson, A., and Yoon, S., 1986, Multigrid Solution of the Euler Equations Using Implicit Schemes, *AIAA J.*, 24, pp. 1737-1743.

[16] Siikonen, T., 1995, An Application of Roe's Flux-Difference Splitting for $k-\epsilon$ turbulence Model, *Int. J. Numer. Meth. Fluids*, 21, pp. 1017-1039.

[17] Savill, A.M., 1993, Some Recent Progress in the Turbulence Modeling of By-pass Transition, *In Near-Wall Turbulent Flows*, So, R.M.C., Speziale, C.G., and Launder, B.E., (eds.), Elsevier, pp. 829-848.

[18] Scholten, J.W., and Murray, D.B., 1998, Unsteady Heat Transfer and Velocity of a Cylinder in Cross Flow –I, Low Free Stream Turbulence, *Int. J. Heat Mass Transfer*, 41, pp. 1139-1148.

A COMPARISON OF TURBULENCE MODELS AND THE CALCULATION OF THE NEAR-WALL AREA IN THE CASE OF A JET IN A CROSSFLOW

A. KARVINEN AND H. AHLSTEDT

Institute of Energy and Process Engineering
Tampere University of Technology
P.O. Box 589, FIN-33101 TAMPERE
email: aku.karvinen@tut.fi

ABSTRACT

A circular jet in a crossflow is simulated numerically using different computational grids, turbulence models and near-wall treatments. A grid resolution study is performed to find a grid that yields a grid-independent solution. The standard k-ϵ model, the RNG k-ϵ model, the realizable k-ϵ model, the standard k-ω model, the shear-stress transport (SST) k-ω model and the Reynolds stress model (RSM) are compared. The three different near-wall treatments (the standard wall functions, the non-equilibrium wall functions and the two-layer zonal model) are used. In all calculations jet to crossflow velocity ratio $R = 2.0$ is used. The Reynolds number of the main flow $\mathrm{Re_h} \approx 417{,}000$ and the jet $\mathrm{Re_D} \approx 96{,}000$, based on the hydraulic diameter and the jet diameter, respectively, are used. Results show that a grid should be very fine to obtain a grid-independent solution. Differences between the turbulence models are much smaller than expected. All near-wall treatments gave very similar results; differences between wall functions are mainly a consequence of the different grids used.

1 INTRODUCTION

The case considered in this paper is turbulent. Turbulent flow can be solved using turbulence models based on Reynolds-averaged Navier-Stokes equations (RANS), large eddy simulation (LES) or direct numerical simulation (DNS). In this work RANS-based turbulence models are used exclusively. In deriving traditional RANS-based models, high Reynolds number is assumed. However, near the wall flow is laminar and classical RANS models are not valid. Hence, some specific near-wall treatment is needed, low-Reynolds-number turbulence models or so-called wall functions.

Jet in crossflow (Fig. 1) occurs in many applications, eg in vertical and/or short take-off and landing (V/STOL) aircraft in transition from vertical to forward flight, in turbomachinery (film cooling of turbine blades, jets into combustors), in combustor chambers, in oil or gas flow into a container and in waste discharge into water bodies and into the atmosphere. Jet in crossflow has been under intensive study for over fifty years. The first studies focused on determining the place of the core of the jet [1, 2]. In the articles [3, 4, 5, 6] the shape of the jet has been studied experimentally. Numerical studies have been done by eg [7, 8, 9, 10]. More extensive review can be found in [11, 12].

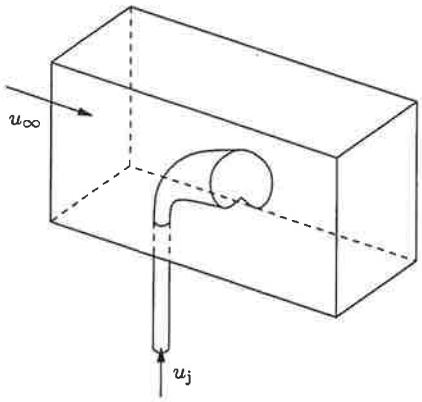

Figure 1: Jet in crossflow.

2 GOVERNING EQUATIONS AND THEIR NUMERICAL SOLUTION

In this work incompressible, steady-state flow is assumed. No body forces or buoyancy are taken to account. Under these assumptions, the Reynolds-averaged Navier-Stokes equations (RANS) are

$$\frac{\partial u_i}{\partial x_i} = 0, \tag{1}$$

$$u_j \frac{\partial u_i}{\partial x_j} = -\frac{1}{\rho}\frac{\partial p}{\partial x_i} + \frac{\partial}{\partial x_j}\nu\frac{\partial u_i}{\partial x_j} + \frac{\partial}{\partial x_j}\left(-\overline{u_i' u_j'}\right), \tag{2}$$

where u_i is the mean velocity component in x_i direction, ρ is the mass density, p is the mean pressure, ν is the kinematic viscosity and the overbar denotes time averaging.

2.1 Turbulence Models

In the k-ϵ models and the k-ω models, the Boussinesq hypothesis [13] is used. The Reynolds stresses, $-\overline{u_i' u_j'}$, are approximated with

$$-\overline{u_i' u_j'} = 2\nu_t S_{ij} - \frac{2}{3}k\delta_{ij}, \qquad S_{ij} = \frac{1}{2}\left(\frac{\partial u_i}{\partial x_j} + \frac{\partial u_j}{\partial x_i}\right), \tag{3}$$

where ν_t is the turbulent (or eddy) viscosity.

Standard k-ϵ Model In the standard k-ϵ model [14] the turbulence kinetic energy, k, and its dissipation rate, ϵ, are obtained from the modeled transport equations:

$$u_j \frac{\partial k}{\partial x_j} = \frac{\partial}{\partial x_j}\left[\left(\nu + \frac{\nu_t}{\sigma_k}\right)\frac{\partial k}{\partial x_j}\right] + \nu_t S^2 - \epsilon, \tag{4}$$

$$u_j \frac{\partial \epsilon}{\partial x_j} = \frac{\partial}{\partial x_j}\left[\left(\nu + \frac{\nu_t}{\sigma_\epsilon}\right)\frac{\partial \epsilon}{\partial x_j}\right] + C_{1\epsilon}\frac{\epsilon}{k}\nu_t S^2 - C_{2\epsilon}\frac{\epsilon^2}{k}, \tag{5}$$

where $S \equiv \sqrt{2S_{ij}S_{ij}}$. The turbulent viscosity is computed from

$$\nu_t = C_\mu \frac{k^2}{\epsilon}, \tag{6}$$

where C_μ is a constant. The model constants have the following values [15]: $C_\mu = 0.09$, $C_{1\epsilon} = 1.44$, $C_{2\epsilon} = 1.92$, $\sigma_k = 1.0$ and $\sigma_\epsilon = 1.3$.

RNG k-ϵ Model In the RNG k-ϵ model [16] the turbulence kinetic energy and its dissipation rate are obtained from the following transport equations:

$$u_j \frac{\partial k}{\partial x_j} = \frac{\partial}{\partial x_j}\left(\alpha_k \nu_t \frac{\partial k}{\partial x_j}\right) + \nu_t S^2 - \epsilon, \tag{7}$$

$$u_j \frac{\partial \epsilon}{\partial x_j} = \frac{\partial}{\partial x_j}\left(\alpha_\epsilon \nu_t \frac{\partial \epsilon}{\partial x_j}\right) + C_{1\epsilon}\frac{\epsilon}{k}\nu_t S^2 - C_{2\epsilon}\frac{\epsilon^2}{k} - \frac{C_\mu \eta^3 (1-\eta/\eta_0)}{1+\beta\eta^3}\frac{\epsilon^2}{k}, \tag{8}$$

where $\eta \equiv Sk/\epsilon$, $\eta_0 = 4.38$, $\beta = 0.012$ and ν_t is obtained in a similar way as in the standard k-ϵ model. The inverse effective Prandtl numbers, α_k and α_ϵ, are computed using the following formula:

$$\left|\frac{\alpha - 1.3929}{\alpha_0 - 1.3929}\right|^{0.6321}\left|\frac{\alpha + 2.3929}{\alpha_0 + 2.3929}\right|^{0.3679} = \frac{\nu}{\nu_t},$$

where $\alpha_0 = 1.0$. The model constants are: $C_\mu = 0.0845$, $C_{1\epsilon} = 1.42$ and $C_{2\epsilon} = 1.68$.

Realizable k-ϵ Model The transport equations for k and ϵ in the realizable k-ϵ model [17] are

$$u_j \frac{\partial k}{\partial x_j} = \frac{\partial}{\partial x_j}\left[\left(\nu + \frac{\nu_t}{\sigma_k}\right)\frac{\partial k}{\partial x_j}\right] + \nu_t S^2 - \epsilon, \tag{9}$$

$$u_j \frac{\partial \epsilon}{\partial x_j} = \frac{\partial}{\partial x_j}\left[\left(\nu + \frac{\nu_t}{\sigma_\epsilon}\right)\frac{\partial \epsilon}{\partial x_j}\right] + C_{1\epsilon} S\epsilon - C_{2\epsilon}\frac{\epsilon^2}{k + \sqrt{\nu\epsilon}}, \tag{10}$$

where $C_{1\epsilon} = \max\left[0.43, \eta/(\eta+5)\right]$ and $\eta = Sk/\epsilon$. The turbulent viscosity is obtained from (6), but now

$$C_\mu = \frac{1}{A_0 + A_s \frac{ku^*}{\epsilon}}, \quad u^* \equiv \sqrt{S_{ij}S_{ij} + \tilde{\Omega}_{ij}\tilde{\Omega}_{ij}}, \quad \tilde{\Omega}_{ij} = \Omega_{ij} - 2\epsilon_{ijk}\omega_k, \quad \Omega_{ij} = \bar{\Omega}_{ij} - \epsilon_{ijk}\omega_k$$

and $\bar{\Omega}_{ij}$ is the mean rate-of-rotation tensor viewed in a rotating reference frame with the angular velocity ω_k. $A_0 = 4.04$ and $A_s = \sqrt{6}\cos\phi$, where

$$\phi = \frac{1}{3}\cos^{-1}\left(\sqrt{6}W\right), \qquad W = \frac{S_{ij}S_{jk}S_{ki}}{(S_{ij}S_{ij})^{3/2}}.$$

The model constants are: $C_{2\epsilon} = 1.9$, $\sigma_k = 1.0$ and $\sigma_\epsilon = 1.2$.

Standard k-ω Model In the standard k-ω model [18] the turbulence kinetic energy, k, and the specific dissipation rate, ω, are obtained from the following transport equations:

$$u_j \frac{\partial k}{\partial x_j} = \frac{\partial}{\partial x_j}\left[\left(\nu + \frac{\nu_t}{\sigma_k}\right)\frac{\partial k}{\partial x_j}\right] + \nu_t S^2 - \beta^*_\infty f_{\beta^*_\infty} k\omega, \tag{11}$$

$$u_j \frac{\partial \epsilon}{\partial x_j} = \frac{\partial}{\partial x_j}\left[\left(\nu + \frac{\nu_t}{\sigma_\omega}\right)\frac{\partial \omega}{\partial x_j}\right] + \frac{\omega}{k}\nu_t S^2 - \beta_i f_{\beta_i}\omega^2, \tag{12}$$

where

$$\nu_t = \frac{k}{\omega}, \qquad f_{\beta^*_\infty} = \begin{cases} 1 & (\chi_k \le 0) \\ \frac{1+680\chi_k^2}{1+400\chi_k^2} & (\chi_k > 0) \end{cases}, \qquad \chi_k \equiv \frac{1}{\omega^3}\frac{\partial k}{\partial x_j}\frac{\partial \omega}{\partial x_j},$$

$$f_{\beta_i} = \frac{1+70\chi_\omega}{1+80\chi_\omega}, \qquad \chi_\omega = \left|\frac{\Omega_{ij}\Omega_{jk}S_{ki}}{(\beta^*_\infty\omega)^3}\right|, \qquad \Omega_{ij} = \frac{1}{2}\left(\frac{\partial u_i}{\partial x_j} - \frac{\partial u_j}{\partial x_i}\right).$$

The model constants are: $\beta_i = 0.072$, $\beta^*_\infty = 0.09$, $\sigma_k = 2.0$ and $\sigma_\omega = 2.0$.

Shear-Stress Transport (SST) k-ω Model The shear-stress transport (SST) k-ω model [19] has a similar form to the standard k-ω model:

$$u_j\frac{\partial k}{\partial x_j}=\frac{\partial}{\partial x_j}\left[\left(\nu+\frac{\nu_t}{\sigma_k}\right)\frac{\partial k}{\partial x_j}\right]+\nu_t S^2-\beta^*_\infty k\omega, \tag{13}$$

$$u_j\frac{\partial \epsilon}{\partial x_j}=\frac{\partial}{\partial x_j}\left[\left(\nu+\frac{\nu_t}{\sigma_\omega}\right)\frac{\partial \omega}{\partial x_j}\right]+S^2-\beta_i\omega^2+D_\omega, \tag{14}$$

where

$$\nu_t=\frac{k}{\omega}\frac{1}{\max\left[1,\frac{\Omega F_2}{a_1\omega}\right]},\qquad \Omega\equiv\sqrt{2\bar{\Omega}_{ij}\bar{\Omega}_{ij}},$$

$$\sigma_k=\frac{1}{F_1/\sigma_{k,1}+(1-F_1)/\sigma_{k,2}},\qquad \sigma_\omega=\frac{1}{F_1/\sigma_{\omega,1}+(1-F_1)/\sigma_{\omega,2}},$$

$$F_1=\tanh\left(\Phi_1^4\right),\qquad \Phi_1=\min\left[\max\left(\frac{\sqrt{k}}{0.09\omega y},\frac{500\nu}{\rho y^2\omega}\right),\frac{4\rho k}{\sigma_{\omega,2}D^+_\omega y^2}\right],$$

$$F_2=\tanh\left(\Phi_2^2\right),\qquad \Phi_2=\max\left[2\frac{\sqrt{k}}{0.09\omega y},\frac{500\nu}{y^2\omega}\right],$$

$$D_\omega=2\left(1-F_1\right)\sigma_{\omega,2}\frac{1}{\omega}\frac{\partial k}{\partial x_j}\frac{\partial \omega}{\partial x_j},\qquad D^+_\omega=\max\left[2\rho\frac{1}{\sigma_{\omega,2}}\frac{1}{\omega}\frac{\partial k}{\partial x_j}\frac{\partial \omega}{\partial x_j},10^{-20}\right],$$

$\beta_i=F_1\beta_{i,1}+(1-F_1)\beta_{i,2}$ and $\bar{\Omega}_{ij}$ is the mean rate-of-rotation tensor. The model constants are: $a_1=0.31$, $\beta^*_\infty=0.09$, $\beta_{i,1}=0.075$, $\beta_{i,2}=0.0828$, $\sigma_{k,1}=1.176$, $\sigma_{\omega,1}=2.0$, $\sigma_{k,2}=1.0$ and $\sigma_{\omega,2}=1.168$.

Reynolds Stress Model In the Reynolds stress model (RSM) there are the exact transport equations for the transport of Reynolds stresses, $-\overline{u_i'u_j'}$ [20, 21]:

$$\underbrace{\frac{\partial}{\partial x_k}\left(u_k\overline{u_i'u_j'}\right)}_{C_{ij}}=\underbrace{-\frac{\partial}{\partial x_k}\left[\overline{u_i'u_j'u_k'}+\overline{\frac{p'}{\rho}\left(\delta_{kj}u_i'+\delta_{ik}u_j'\right)}\right]}_{D^T_{ij}}\underbrace{-\left(\overline{u_i'u_k'}\frac{\partial u_j}{\partial x_k}+\overline{u_j'u_k'}\frac{\partial u_i}{\partial x_k}\right)}_{P_{ij}}+$$

$$\frac{\partial}{\partial x_k}\left[\nu\frac{\partial}{\partial x_k}\left(\overline{u_i'u_j'}\right)\right]+\underbrace{\overline{\frac{p'}{\rho}\left(\frac{\partial u_i'}{\partial x_j}+\frac{\partial u_j'}{\partial x_i}\right)}}_{\phi_{ij}}\underbrace{-2\nu\overline{\frac{\partial u_i'}{\partial x_k}\frac{\partial u_j'}{\partial x_k}}}_{\epsilon_{ij}}\underbrace{-2\Omega_k\left(\overline{u_j'u_m'}\epsilon_{ikm}+\overline{u_i'u_m'}\epsilon_{jkm}\right)}_{F_{ij}}, \tag{15}$$

where D^T_{ij} and ϕ_{ij} are modeled using the following relations:

$$D^T_{ij}=\frac{\partial}{\partial x_k}\left(\frac{\nu_t}{\sigma_k}\frac{\partial\overline{u_i'u_j'}}{\partial x_k}\right),\qquad \nu_t=C_\mu\frac{k^2}{\epsilon},$$

$$\phi_{ij}=\phi_{ij,1}+\phi_{ij,2}+\phi_{ij,w},\qquad \phi_{ij,1}\equiv-C_1\frac{\epsilon}{k}\left[\overline{u_i'u_j'}-\frac{2}{3}\delta_{ij}k\right],$$

$$\phi_{ij,2}\equiv-C_2\left[\left(P_{ij}+F_{ij}-C_{ij}\right)-\frac{2}{3}\delta_{ij}\left(P-C\right)\right],\qquad P=\frac{1}{2}P_{kk},\qquad C=\frac{1}{2}C_{kk},$$

and $\phi_{ij,\mathrm{w}}$ is a so-called wall-reflection term [22]. The dissipation tensor, ϵ_{ij}, is modeled as $\epsilon_{ij} = \frac{2}{3}\delta_{ij}\epsilon$, where ϵ is obtained from (5) in which the second last term is replaced with $C_{1\epsilon}P_{ii}\epsilon/2k$. The turbulence kinetic energy is modeled as $k = \frac{1}{2}\overline{u_i'u_i'}$. The model constants are: $C_1 = 1.8$, $C_2 = 0.60$, $C_{1\epsilon} = 1.44$, $C_{2\epsilon} = 1.92$, $C_\mu = 0.9$, $\sigma_k = 1.0$ and $\sigma_\epsilon = 1.3$.

2.2 Calculation of Near-Wall Area

When using the k-ϵ model or the RSM, the wall functions are needed to connect the fully turbulent core flow with the viscosity-dominated near-wall region.

Standard Wall Functions The standard wall function [15] for mean velocity is

$$u^* = \begin{cases} \frac{1}{\kappa}\ln(Ey^*) & (y^* > 11.225) \\ y^* & (y^* < 11.225) \end{cases}, \tag{16}$$

where

$$u^* \equiv \frac{u_P C_\mu^{1/4} k_P^{1/2}}{\tau_\mathrm{w}/\rho}, \qquad y^* \equiv \frac{C_\mu^{1/4} k_P^{1/2} y_P}{\nu},$$

κ is the von Kármán constant ($= 0.4185$), $E = 9.81$, u_P is the mean velocity of the fluid at point P, k_P is the turbulence kinetic energy at point P, τ_w is the shear stress at the wall and y_P is the distance from point P to the wall.

Non-Equilibrium Wall Functions In the non-equilibrium wall functions [23] there is a log law for mean velocity:

$$\frac{\tilde{u}C_\mu^{1/4}k^{1/2}}{\tau_\mathrm{w}/\rho} = \frac{1}{\kappa}\ln\left(E\frac{C_\mu^{1/4}k^{1/2}y}{\nu}\right), \tag{17}$$

where

$$\tilde{u} = u - \frac{1}{2}\frac{\mathrm{d}p}{\mathrm{d}x}\left[\frac{y_\mathrm{v}}{\rho\kappa k^{1/2}}\ln\left(\frac{y}{y_\mathrm{v}}\right) + \frac{y - y_\mathrm{v}}{\rho\kappa k^{1/2}} + \frac{\rho y_\mathrm{v}^2}{\nu}\right], \qquad y_\mathrm{v} \equiv \frac{\nu y_\mathrm{v}^*}{C_\mu^{1/4}k_P^{1/2}},$$

and $y_\mathrm{v}^* = 11.225$. When calculating the budget of turbulence kinetic energy, the two-layer concept is used. It consists of the following profile assumptions:

$$\tau_t = \begin{cases} 0 & (y < y_\mathrm{v}) \\ \tau_\mathrm{w} & (y > y_\mathrm{v}) \end{cases}, \qquad k = \begin{cases} \left(\frac{y}{y_\mathrm{v}}\right)^2 k_P & (y < y_\mathrm{v}) \\ k_P & (y > y_\mathrm{v}) \end{cases} \qquad \epsilon = \begin{cases} \frac{2\nu k}{y^2} & (y < y_\mathrm{v}) \\ \frac{k^{3/2}}{C_\ell y} & (y > y_\mathrm{v}) \end{cases},$$

where $C_\ell = \kappa C_\mu^{-3/4}$.

Two-Layer Zonal Model In the two-layer zonal model the whole domain is subdivided into two regions, based on $\mathrm{Re}_y \equiv \sqrt{k}y/\nu$, where y is the distance from the wall to the cell centre. In the fully turbulent region ($\mathrm{Re}_y > 200$) the k-ϵ model or the RSM is used. In the area where $\mathrm{Re}_y < 200$ basic model equations are retained, but the turbulent viscosity and the turbulence kinetic energy are computed from the following equations [24, 25]:

$$\nu_t = C_\mu\sqrt{k}\ell_\mu, \qquad \ell_\mu = C_\ell y\left(1 - e^{-\mathrm{Re}_y/A_\mu}\right),$$

$$\epsilon = \frac{k^{3/2}}{\ell_\epsilon}, \qquad \ell_\epsilon = C_\ell y\left(1 - e^{-\mathrm{Re}_y/A_\epsilon}\right),$$

where $A_\mu = 70$ and $A_\epsilon = 2C_\ell$ [25].

2.3 Calculation Procedure

Apart from the calculations which use the k-ω models, all the calculations have been done using FLUENT 5.5, a commercial software based on the finite volume method [26]. The k-ω model calculations have been done using FLUENT 6.0 [22], because FLUENT 5.5 does not contain the k-ω models. All terms in all equations are discretised in space using second-order central differencing, apart from the convection term, which is discretised using a second-order upwind scheme. Pressure-velocity coupling has been done using SIMPLE algorithm.

3 COMPUTATIONAL DOMAIN AND MESH

The schematic of the problem is shown in Figure 2 (I is the turbulence intensity). The Reynolds number of the main flow is $\mathrm{Re_h} \approx 417{,}000$ and jet $\mathrm{Re}_D \approx 96{,}000$, based on the hydraulic diameter and the jet diameter, respectively. The working fluid is air with density $\rho = 1.225\ \mathrm{kg/m^3}$ and dynamic viscosity $\mu = 1.7894 \times 10^{-5}\ \mathrm{kg/ms}$ ($\nu = \mu/\rho$).

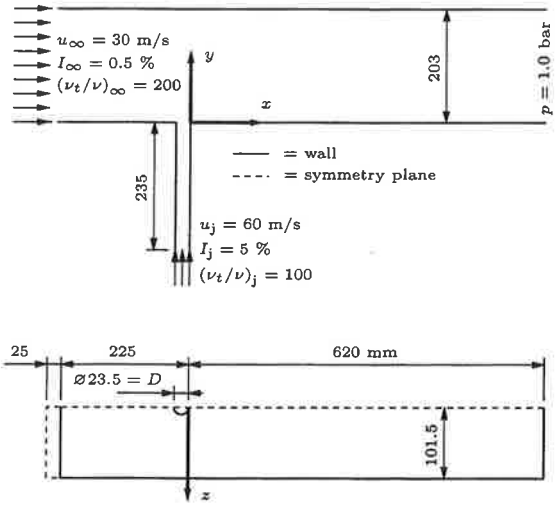

Figure 2: Computational domain and boundary conditions.

All grids used consist of 8-node brick (hexahedral) control volumes. In the coarsest grid (denoted grid I) the length of the edge of a control volume is about 8 mm (Table 1). When grid I is refined in the area of the jet penetration ($-3 \le x/D \le 10$, $y/D \le 7$, $z/D \le 4$), grid II is obtained. Grid III is obtained from grid II by refining in the region $-2 \le x/D \le 9$, $y/D \le 6$, $z/D \le 3$ and grid IV is obtained from grid III by refining in the region $-2 \le x/D \le 7$, $y/D \le 5$, $z/D \le 2.25$. The finest grid (grid V) is obtained using the solution of grid IV and refining only near the core of the jet (cf. [27]).

When using the two-layer zonal model, the grid has been refined near the wall so that the dimensionless distance from the wall is $y^+ \equiv u_\tau y/\nu < 4...5$ ($u_\tau = \sqrt{\tau_\mathrm{w}/\rho}$).

Table 1: Number of control volumes for different grids used.

Grid	I	II	III	IV	V
N_total	35,637	102,466	398,741	1,628,025	2,535,295

4 RESULTS

Figure 3 shows some general results of the calculations. It can be seen from the path lines in Figure 3(a) how the jet divides into two separated counter-rotating vortices. Downstream close to the jet and close to the wall there is a region where mean x-velocity is negative and there is reverse flow (Fig. 3(b)). On the downstream side of the jet there is a region where the turbulence kinetic energy is high (Fig. 3(c)). The viscosity ratio is also high on the downstream side of the jet, but in addition in front of the jet (Fig. 3(d)).

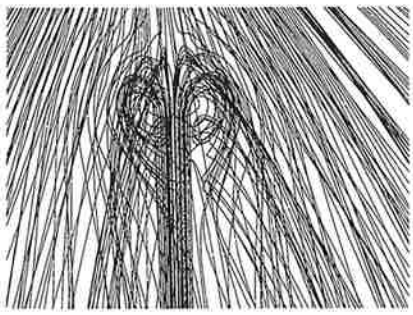

(a) Path lines

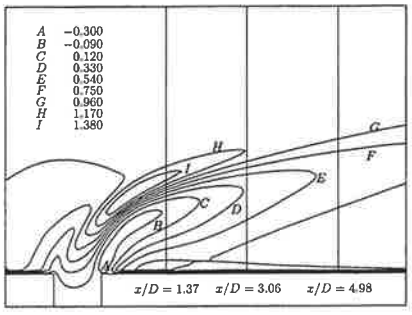

(b) Horizontal velocity, u/u_∞

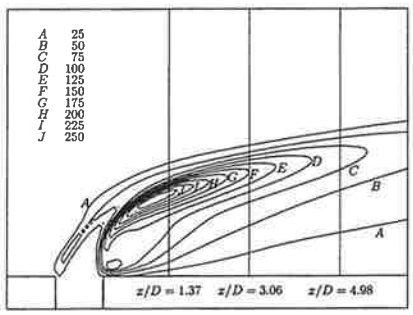

(c) Turb. kinetic energy, $k\,[\mathrm{m}^2/\mathrm{s}^2]$

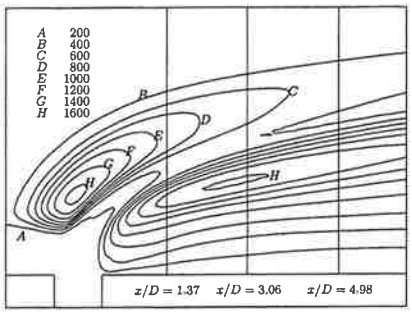

(d) Viscosity ratio, ν_t/ν

Figure 3: General results using grid III, standard k-ϵ model and standard wall functions.

4.1 Grid Resolution Study

The grid resolution study was performed to find a grid that yields a grid-independent solution.

There were no convergence problems and all the cases were performed for the situation where scaled residuals were settled and all the residuals were decreased to the value 10^{-6} (Fig. 4). When using finer grids, the time needed for one iteration is substantially greater. In addition, the needed number of iterations increases noticeably when the grid is refined.

The two coarsest grids (grid I and grid II) do not give good results (Fig. 5). On the other hand, the results of the two finest grids (grid IV and grid V) do not differ much from the results of grid III. Besides that, calculation using grid IV or grid V needs significantly more computer time. Therefore, grid III was used exclusively from here onwards.

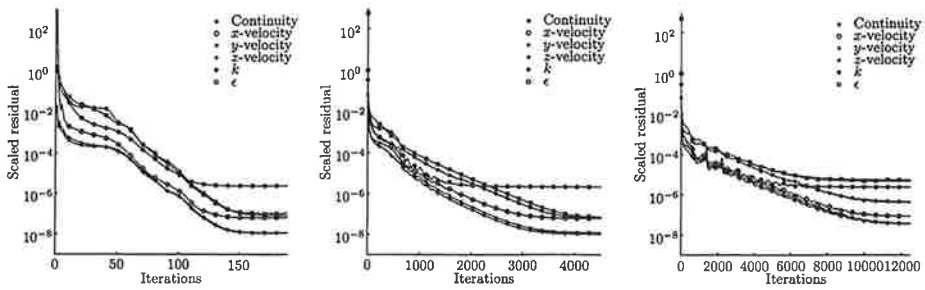

(a) Grid I (b) Grid IV (c) Grid V

Figure 4: Convergence history of scaled residuals using standard k-ϵ model, standard wall functions and different grids.

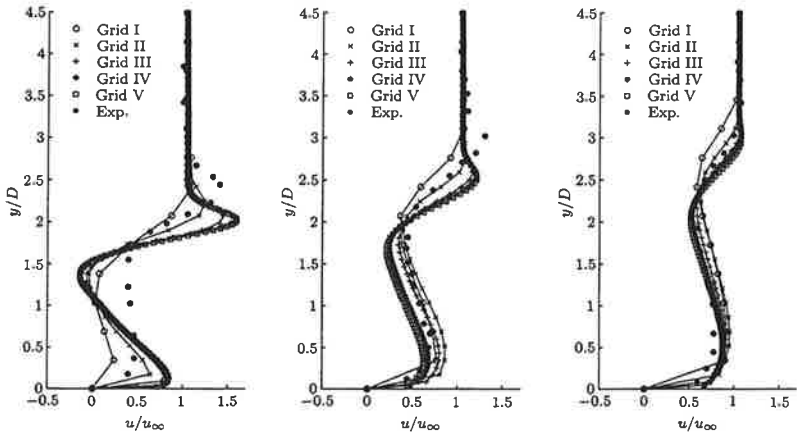

(a) $x/D = 1.37$ (b) $x/D = 3.06$ (c) $x/D = 4.98$

Figure 5: Horizontal dimensionless mean velocity, u/u_∞, in plane $z = 0$ using standard k-ϵ model, standard wall functions and different grids. Measurements [3].

There is no region of reverse flow in the measurements at all, but this can be a consequence of the inability of the hot-wire anemometer to measure the direction of the velocities accurately. In [8] they agree with this opinion.

4.2 Turbulence Model Comparison

In this section the standard k-ϵ model, the RNG k-ϵ model, the realizable k-ϵ model, the standard k-ω model, the SST k-ω model and the RSM are compared. In all these calculations, grid III and the standard wall functions are used, except in k-ω model calculations, where the near-wall region is treated in a different way [22].

In the case of the RNG k-ϵ model there were serious convergence problems; residuals did not settle and they decreased only to the value 10^{-2} (Fig. 6(b)). Reducing the underrelaxation factors did not help. Also calculation using the RSM did not converge. The scaled

residuals settled well, but results changed considerably when iteration was continued. In the case of other turbulence models, convergence problems did not occur and the results did not change if iteration was continued. The standard k-ω model needs about twice as many iterations as other converged models.

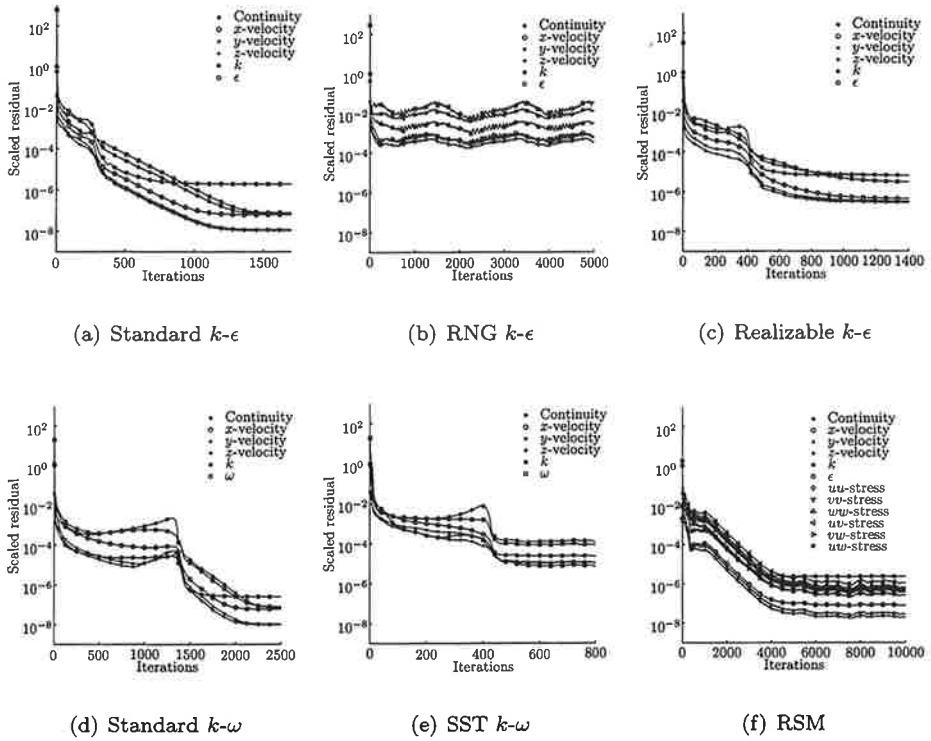

(a) Standard k-ϵ (b) RNG k-ϵ (c) Realizable k-ϵ

(d) Standard k-ω (e) SST k-ω (f) RSM

Figure 6: Convergence history of scaled residuals using grid III, standard wall functions and different turbulence models.

Because of problems in convergence of the RNG k-ϵ model and RSM, the results obtained using these models are useless. Results of other turbulence models are close to each other (Fig. 7). Only results obtained with the standard k-ω model differ considerably from results of other converged models; in the region of the jet the velocities are considerably slower. In the upper part of the jet, the SST k-ω model predicts slower velocities than other models, but the difference is quite small.

4.3 Comparison of Near-Wall Treatments

In this section different near-wall treatments (standard wall functions, non-equilibrium wall functions and two-layer zonal model) are compared. When the two-layer zonal model was used, scaled residuals did not decrease properly (Fig 8(c)), but results did not change when iteration was continued. Hence, it can be assumed that calculation is converged. All wall functions needed about the same number of iterations (Fig 8).

The two-layer zonal model predicted slower velocity in the area where $y/D = 0 \ldots 2.5$ and $x/D \approx 3.06$ (Fig. 9(b)), but this is a consequence of the different grid used (grid was refined near the wall). Differences between other wall functions are quite small (Fig. 9).

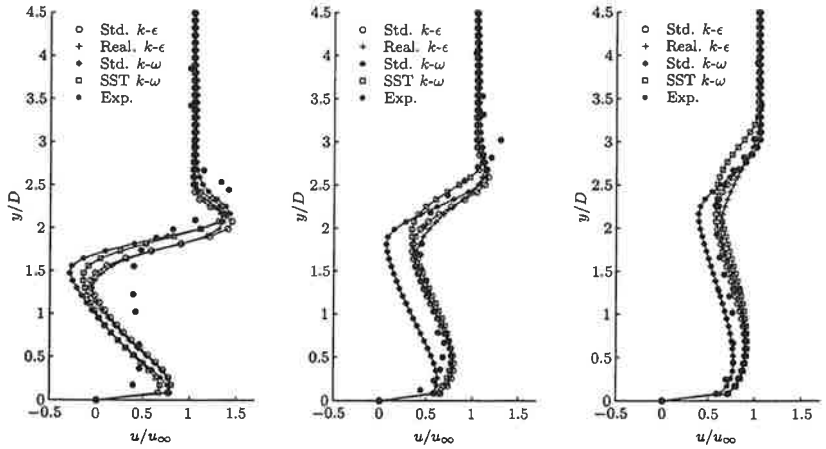

(a) $x/D = 1.37$ (b) $x/D = 3.06$ (c) $x/D = 4.98$

Figure 7: Horizontal dimensionless mean velocity, u/u_∞, in plane $z = 0$ using grid III, standard wall functions and different turbulence models. Measurements [3].

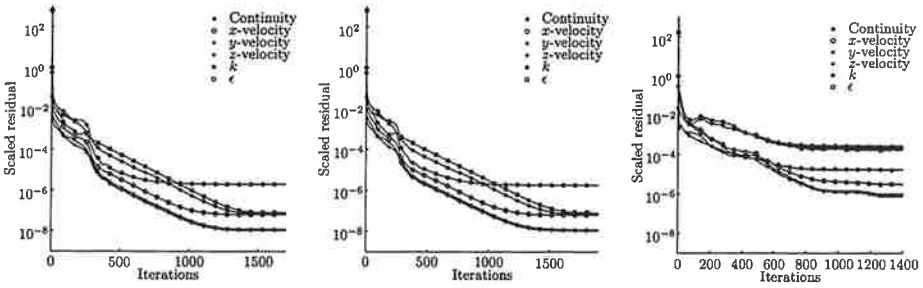

(a) Standard (b) Non-equilibrium (c) Two-layer

Figure 8: Convergence history of scaled residuals using grid III, standard k-ϵ model and different wall functions.

5 CONCLUSIONS

The grid resolution study showed that accurate calculation of the jet in a crossflow requires a very fine grid. However, results change very little when a grid is refined from 1.6 million to 2.5 million cells. A grid with about 400,000 cells gives good enough results in practical applications.

In the comparison of turbulence models it emerged that the RNG k-ϵ model and the RSM do not converge well. There is some fluctuation in scaled residuals and results even after a large number of iterations. All converged models give quite similar results; only the results of the standard k-ω model differ from results of other models and these differences are quite moderate.

The two-layer zonal model predicted slower velocity in some regions, but this is a con-

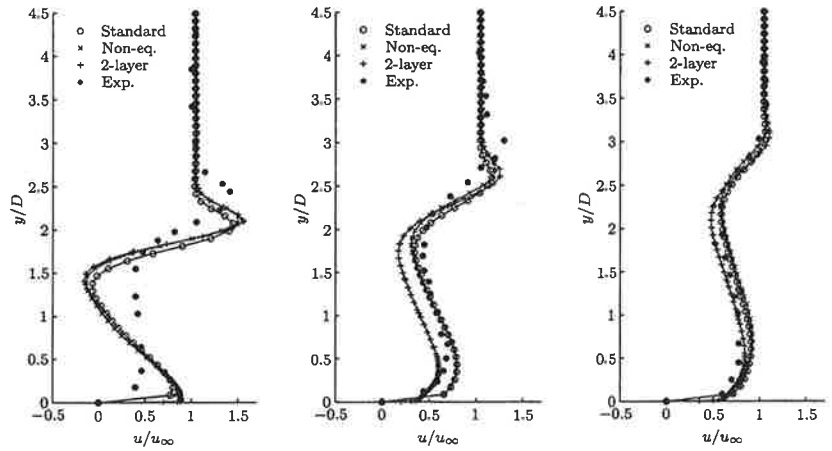

(a) $x/D = 1.37$ (b) $x/D = 3.06$ (c) $x/D = 4.98$

Figure 9: Horizontal dimensionless mean velocity, u/u_∞, in plane $z = 0$ using grid III, standard k-ϵ model and different turbulence models. Measurements [3].

sequence of the different grid used (grid was refined at near the wall). Differences between other wall functions are quite small.

REFERENCES

[1] R. Jordinson. *Flow in a jet directed normal to the wind.* R & M No. 3074, British A.R.C., 1956.

[2] R. J. Margason. *The path of a jet directed at large angles to a subsonic free stream.* Technical Report NASA TN D-4919, 1968.

[3] J. W. Ramsey and R. J. Goldstein. *Interaction of a heated jet with a deflecting stream.* Journal of Heat Transfer, **94**, 365-372 (1971).

[4] J. Andreopoulos and W. Rodi. *Experimental investigation of jets in a crossflow.* Journal of Fluid Mechanics, **138**, 93-127 (1984).

[5] K. C. Kim, S. K. Kim and S. Y. Yoon. *PIV measurements of the flow and turbulent characteristics of a round jet in crossflow.* Journal of Visualization, **3**, 157-164 (2000).

[6] K. E. Meyer, O. Özcan and C. H. Westergaard. *Flow mapping of a jet in crossflow with stereoscopic PIV.* Journal of Visualization, **5**, 225-231 (2002).

[7] S. V. Patankar, D. K. Basu and S. A. Alpay. *Prediction of the three-dimensional velocity field of a deflected turbulent jet.* Journal of Fluids Engineering, **99**, 758-762 (1977).

[8] J. Alvarez, W. P. Jones and R. Seoud. *Predictions of momentum and scalar fields in a jet in cross-flow using first and second order turbulence closures.* In *Computational and Experimental Assessment of Jets in Cross Flow, AGARD-CP-534*, pages 24–1...24–10. 1993.

[9] L. L. Yuan and R. L. Street. *Trajectory and entrainment of a round jet in crossflow*. Physics of Fluids, **10**, 2323-2335 (1998).

[10] L. L. Yuan, R. L. Street and J. H. Ferziger. *Large-eddy simulations of a round jet in crossflow*. Journal of Fluids Engineering, **379**, 71-104 (1999).

[11] J. A. Schetz. *Injection and Mixing in Turbulent Flows*, volume 68 of *Progress in Astronautics and Aeronautics*. AIAA, New York, 1980.

[12] R. J. Margason. *Fifty years of jet in cross flow research*. In *Computational and Experimental Assessment of Jets in Cross Flow, AGARD-CP-534*, pages 1–1...1–33. 1993.

[13] J. O. Hinze. *Turbulence*. McGraw-Hill, New York, 1975.

[14] B. E. Launder and D. B. Spalding. *Lectures in Mathematical Models of Turbulence*. Academic Press, London, 1972.

[15] B. E. Launder and B. I. Sharma. *Application of the energy dissipation model of turbulence to the calculation of flow near a spinning disc*. Letters in Heat and Mass Transfer, **1**, 131-138 (1974).

[16] D. Choudhury. *Introduction to the renormalization group method and turbulence modeling*. Fluent Inc. Technical Memorandum TM-107, 1993.

[17] T.-H. Shih, W. W. Liou, A. Shabbir, Z. Yang and J. Zhu. *A new k-ϵ eddy viscosity model for high Reynolds number turbulent flows*. Computers Fluids, **24**, 227-238 (1995).

[18] D. C. Wilcox. *Turbulence Modeling for CFD*. DCW Industries, Inc., La Canada, California, 1998.

[19] F. R. Menter. *Two-equation eddy-viscosity turbulence models for engineering applications*. AIAA Journal, **32**, 1598-1605 (1994).

[20] M. M. Gibson and B. E. Launder. *Ground effects on pressure fluctuations in the atmospheric boundary layer*. Journal of Fluid Mechanics, **86**, 491-511 (1978).

[21] B. E. Launder, G. J. Reece and W. Rodi. *Progress in the development of a Reynolds-stress turbulence closure*. Journal of Fluid Mechanics, **68**, 537-566 (1975).

[22] Fluent Inc. *FLUENT 6 user's guide*. Lebanon, 2001.

[23] S.-E. Kim and D. Choudhury. *A near-wall treatment using wall functions sensitized to pressure gradient*. In *ASME FED Vol. 217, Separated and Complex Flows*. ASME, 1995.

[24] M. Wolfshtein. *The velocity and temperature distribution of one-dimensional flow with turbulence augmentation and pressure gradient*. International Journal of Heat and Mass Transfer, **12**, 301-318 (1969).

[25] H. C. Chen and V. C. Patel. *Near-wall turbulence models for complex flows including separation*. AIAA Journal, **26**, 641-648 (1988).

[26] Fluent Inc. *FLUENT 5 user's guide*. Lebanon, 1998.

[27] A. Karvinen and H. Ahlstedt. *Turbulenssimallien ja seinän lähialueen laskennan vertailu ristivirtaussuihkun mallinnuksessa*. Tampere University of Technology, Energy and Process Engineering, Report 167, 2002. In Finnish.

DELAY PHENOMENA IN ROLL VIBRATIONS

Marko Jorkama[1] and Raimo von Hertzen[2]
[1]Metso Paper Inc., Winders
[2]Helsinki University of Technology, Institute of Mathematics
P.O.Box 1100, FIN-02015 HUT, FINLAND

ABSTRACT

Nip contact between the wound roll and the winding drum, rider roll or some other nip roller may cause that the wound roll is deformed into a convex polygon. This deformation process is accompanied with a very strong vibration. The conditions under which this phenomenon occurs depend much on the web properties. For example, in the paper industry some bulky grades with a high layer-to-layer COF are known to be prone to this unstable vibration.

In this paper a simple wind up model, capable of capturing quite comprehensively this phenomenon, is developed. The polygonal pattern formation is modeled as a viscoelastic surface deformation. This results in linear delay differential equations. In order to analyze the stability, the Laplace transformation is performed for the system equations. The inspection of the root locus shows several zones of instability during the winding cycle. In an example, it is shown how the model can be utilized to explain some well-known winder vibration phenomena.

The paper is concluded by stating general beneficial trends for the wind up design and by explaining how to determine the susceptibility of certain webs to unstable vibration by simple laboratory measurements.

NOMENCLATURE

$\mathbf{A}$	system matrix in the Laplace-domain
c_1, c_2	viscous damping coefficients of the winding drum and wound roll, respectively
$e(t)$	deviation of the wound roll's shape from circular evaluated at the nip
$\tilde{e}(t)$	evolution of $e(t)$ during one revolution of the roll
f_1, f_2	first and second harmonic of the wound roll rotation frequency
f_{n1}, f_{n2}	first and second natural frequencies of the system
g_i	diagonal terms of $\mathbf{A}$ (i = 1,2,3)
k_1	the spring constant of the winding drum
k_2, k_3	spring constants of the delayed and instant recovery elements of the wound roll, respectively
m_0	core mass per unit length
m_1, m_2	the masses of the winding drum and wound roll, respectively
$r(t)$	the deformed radius of the wound roll evaluated at the nip
$r_0(t)$	the undeformed radius of the wound roll evaluated at the nip
r_d	the winding drum radius
R_0	the average of $r_0(t)$ over one roll revolution

s	the Laplace-variable
s_i	the complex roots of equation det$\mathbf{A} = 0$ ($i = 1,2,3,\ldots$)
t	time variable
T	wound roll rotation period
u	deformation of the delayed recovery element
x_1, x_2	the vertical displacements of the winding drum and wound roll, respectively
$\mathbf{X}$	column vector of the state variables in the Laplace-domain
X_1, X_2	Laplace transforms of x_1 and x_2
z	an internal translational degree-of-freedom of the wound roll
Z	Laplace transform of z
w	delay term in the system equations
α	the recovery coefficient of the wound roll
δ	the nip deformation of the wound roll

INTRODUCTION

Vibration is a common problem for two-drum winders running certain paper grades. Although these "vibrating paper" grades are of quite wide variety, some common features of the vibrations can be stated. Firstly, the frequency of the vibration is without exception equal to the wound roll rotation frequency or its integer multiple. Secondly, the paper and roll properties are such that the nip induced wound roll deformations will not fully recover during one roll revolution. As a consequence of these features, the oscillating nip load will cause the wound roll to become deformed into a convex polygon.

The most common self-excited winder vibration categories are:

a) **Vibration during the initial acceleration**
This vibration mode occurs when the winder speed is accelerated from zero speed to full running speed. Typically, this vibration state develops fast at the very end of the acceleration stage. Typical paper grades for which this type of vibration can occur are rough and bulky grades with high COF - such as book papers. However, also some thin, coated and calendered paper grade can vibrate in this mode. Because of this vibration, the roll edges can become uneven and the web can brake. Although not confirmed, the vibration mode relating to this type of vibration is believed to be the one where the wound roll has the largest amplitude (wound roll eigenmode). Since the rolls are still quite light when the vibration takes place, the corresponding natural frequency is quite high, typically 40 – 150 Hz.

b) **Roll bouncing, resulting to eccentricity**
This is clearly the most serious vibration problem for two-drum winders nowadays. Typically, the grades experiencing this problem are easily wound up to the roll diameter 500 – 700 mm but then, little by little, start increasingly to develop eccentricity. The paper grades with a tendency to the above-mentioned vibration include DIP newsprint and bag paper. This vibration mode occurs always at the roll rotation frequency and is hence not accompanied with audible sound. On a two-drum winder the rolls are seen to bounce in a more or less irregular pattern from drum to drum. Due to the roll eccentricity, also the core chucks are vibrating heavily. The mechanism and mode for this type of vibration is quite complex, involving interplay of the adjacent rolls due to the edge contact and frictional forces.

c) **Wound roll excited drum resonance vibration**
This vibration occurs generally at steady running speed when a multiple of the wound roll rotation frequency matches or is in the vicinity of the drum natural frequency. Depending on the running speed and the value of the natural frequency, the multiple number of the rotation frequency can be 2, 3, 4 or 5. Paper grades vibrating in this mode include uncoated fine paper and sackkraft.

Common for all these above mentioned vibration categories is that they are generated by an oscillating nip load which is synchronous to the wound roll rotation frequency or its multiple. Although a large part of the nip induced roll deformation recovers in one revolution of the roll, some residual deformation is fed back during the reentry into the nip. This results in a self-enforcing vibration state, where the roll surface deformations and nip load oscillations grow hand in hand.

One of the earliest papers where the essential features of this self-excited vibration mechanism were explained was written by Daly [1]. Without any modeling, Daly explained the vibration phenomena using a washboard road analogy. Later Möhle *et al.* [2] studied two-drum winder vibrations and developed a simple one-degree-of-freedom mathematical model based on experimental observations. In their model, the generation of the wavy roll was implemented as a purely plastic residual deformation developed one revolution earlier and reentering the nip. Although the model was simple, they could nicely explain the unstable regions occurring at certain roll rotation frequencies. A more comprehensive two-drum winder model including all interacting structural elements of the wind up was presented by Jorkama [3]. Various eigenmodes of the wind up were presented and requirements for damping the vibrations were studied. However, the self-enforcing development of the wavy roll surface was omitted. Sueoka *et al.* [4] have presented an analogous calender rubber roll-covering polygonalization model. In their model, the development of the roll surface deformation pattern is based on a viscoelastic model of the behavior of the rubber cover. Their model results in a constant coefficient, linear, time delay ordinary differential equation system which stability is extensively studied.

The present paper follows the outline of Ref. [4]. In addition, some characteristic features of winding, such as the time dependence of the coefficients of the differential equations and rotation frequency of the wound roll, are included. The authors believe that even this simple model can elucidate the essential features of the winder vibrations and, hence, lead the way to reduce the costly problems due to winder vibrations.

THEORY

Consider the wind up model of Figure 1 consisting of the winding drum, depicted as the lower uniform circle, and the wound roll, depicted as the wavy upper circle. On the right, the wind up is in its undeformed state and on the left in its deformed state. The winding drum cover is undeformable but has a translational vertical degree of freedom x_1. The deviation of the wound roll's shape from circular is denoted by $e(t)$. In addition, the wound roll has a vertical translational degree-of-freedom, denoted by x_2.

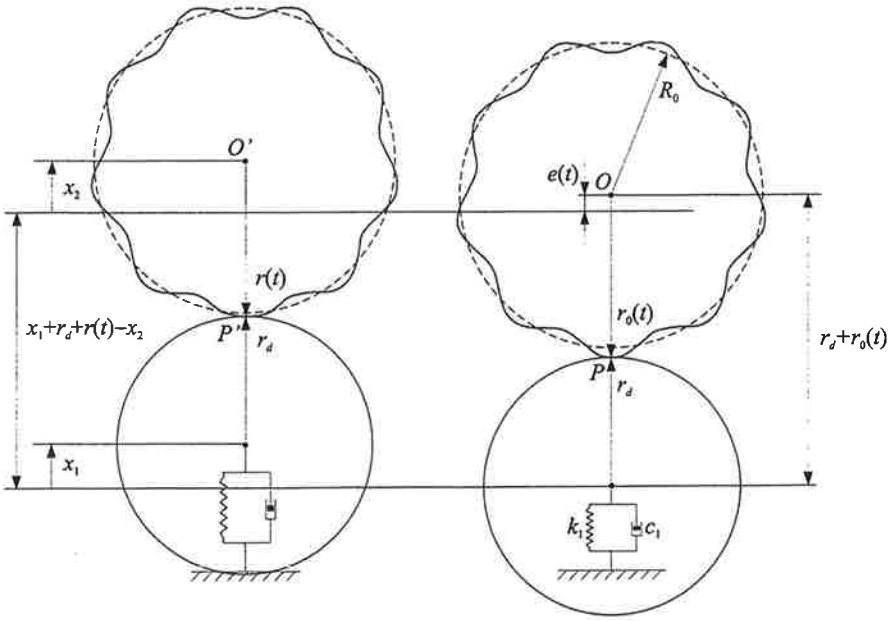

Figure 1. Deformed (left) and undeformed (right) configurations.

From Figure 1 we see the following geometrical relation

$$x_1 + r(t) - x_2 + e(t) = r_0(t)\,. \qquad (1)$$

Denoting the nip compression by δ, the deformed radius $r(t)$ can be represented as

$$r(t) = r_0(t) - \delta\,, \qquad (2)$$

Substituting (2) to (1) yields

$$x_1 - x_2 + e(t) = \delta. \qquad (3)$$

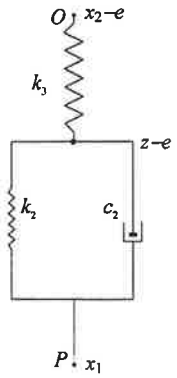

Figure 2. Description of the paper roll deformation element.

This compression occurs between the points O and P. In this simple model, the description of the response of δ to the nip loading constitute the *constitutive equation* of the winding roll and, hence, will determine dominantly the system characteristics. In general, this equation should be formulated so that it reflects the observed deformation characteristics of the paper roll as close as possible. With a high number of internal degrees of freedom, the behavior can be described accurately but the understanding and interpretation of the model predictions become more difficult. In this paper, the emphasis lies in the ease of the interpretation of the qualitative behavior. Hence, a viscoelastic constitutive model of

Figure 2 with only one internal degree of freedom (three independent parameters) is chosen for describing the deformation characteristics of the wound roll.

The equations of motion become

$$\begin{aligned} &m_1\ddot{x}_1 + k_1x_1 + c_1\dot{x}_1 + k_2\left[x_1 - z + e(t)\right] + c_2\left[\dot{x}_1 - \dot{z} + \dot{e}(t)\right] = 0\,, \\ &k_2\left[x_1 - z + e(t)\right] + c_2\left[\dot{x}_1 - \dot{z} + \dot{e}(t)\right] + k_3\left(x_2 - z\right) = 0\,, \\ &m_2\ddot{x}_2 + k_3\left(x_2 - z\right) = 0\,. \end{aligned} \tag{4}$$

Apparently $e(t)$ is a function (or functional) of the nip deformation occurred one revolution earlier. Denoting by $u(t)$ the nip deformation and by T the revolution period, this relation reads

$$e(t) = F(u(t-T)). \tag{5}$$

The nip-induced deformation of the spring element k_3 is instantaneously recovered, whereas the deformation of the element c_2-k_2 is restored only partially during one revolution. The deformation of this element, which is denoted by u, is

$$u = x_1 - z\,, \tag{6}$$

where the sign of u is chosen so that compression is positive. After exiting the nip, this element is free, and hence, the balance equation reads

$$k_2\tilde{e} + c_2\dot{\tilde{e}} = 0\,, \tag{7}$$

where $\tilde{e}$ denotes the position of this element in the course of one revolution. The solution of equation (7) is

$$\tilde{e}(t) = -u(t_1)e^{-\alpha(t-t_1)}\,, \tag{8}$$

where

$$\alpha = \frac{k_2}{c_2} \tag{9}$$

and t_1 the time when the circumferential location under consideration passed the nip last time. Since $e(t)$ is defined as the deviation of the wound roll from circular shape just before entering the nip, the expression

$$e(t) = -u(t-T)e^{-\alpha T} \tag{10}$$

is obtained. Inserting the result (10) to the equations of motion (4) gives

$$
\begin{aligned}
&m_1\ddot{x}_1 + c_1\dot{x}_1 + k_1x_1 + k_2w + c_2\dot{w} = 0\,,\\
&k_2w + c_2\dot{w} + k_3\left(x_2 - z\right) = 0\,,\\
&m_2\ddot{x}_2 + k_3\left(x_2 - z\right) = 0\,,
\end{aligned}
\tag{11}
$$

where

$$
w(t) = u(t) - e^{-\alpha T}u(t-T)\,. \tag{12}
$$

Rearranging Eqs. (11) gives

$$
\begin{aligned}
&m_1\ddot{x}_1 + c_1\dot{x}_1 + (k_1 + k_3)x_1 - k_3(x_1 - z) - k_3x_2 = 0\,,\\
&k_2w + c_2\dot{w} - k_3x_1 + k_3\left(x_1 - z\right) + k_3x_2 = 0\,,\\
&m_2\ddot{x}_2 + k_3x_2 - k_3x_1 + k_3\left(x_1 - z\right) = 0\,.
\end{aligned}
\tag{13}
$$

It should be noted that in the analysis α is taken as an independent parameter since with the current constitutive model it is not possible to describe simultaneously the nip damping and the dent recovery on the roll surface.

In order to analyze the stability of the system, the Laplace transformation is performed for Eq. (13). The revolution period T is treated as a constant when the Laplace transformation is done. During most of the winding cycle, this is a good assumption since the angular frequency of the roll does not change much during one roll revolution. When all initial values are set to zero, the Laplace transformation yields

$$
\mathbf{AX} = \mathbf{0} \tag{14}
$$

where

$$
\begin{aligned}
&\mathbf{X} = (X_1, X_1 - Z, X_2)^t\,,\\
&\mathbf{0} = (0,0,0)^t
\end{aligned}
\tag{15}
$$

and

$$
\mathbf{A} = \begin{bmatrix} g_1 & -k_3 & -k_3 \\ -k_3 & g_2 & k_3 \\ -k_3 & k_3 & g_3 \end{bmatrix}, \tag{16}
$$

where

$$g_1 = m_1 s^2 + c_1 s + k_1 + k_3 ,$$
$$g_2 = k_3 + (c_2 s + k_2)\left[1 - e^{-(\alpha+s)T}\right] , \qquad (17)$$
$$g_3 = m_2 s^2 + k_3 .$$

RESULTS

Characteristic of winder dynamics is that both the excitation and natural frequencies change with time. The change of the excitation frequency stems from the constantly increasing roll diameter and changing running speed, which consists of acceleration, steady running speed and deceleration. The natural frequencies change because the mass of the paper roll increases during winding. According to experimental winder vibration studies [3], it is known that in severe vibration cases the excitation source is almost exclusively the wound roll. Hence, it is instructive to start with determining the situations when the multiples of the roll rotation frequency hit the resonances. Figure 3 depicts the natural frequency curves (solid lines) together with the first and second harmonics of the roll rotation frequency (dashed lines) during one winding cycle. The model parameters are chosen to be representative for a modern wide winder running newsprint grade. These parameters are shown in Table 1. The drum stiffness is determined from a modal measurement and the roll spring constant from a roll compression test. The recovery coefficient α is most accurately measured from the paper roll by indenting it with some "bump" attached onto the winding drum surface and observing the recovery of the dent caused by the indenter. Here, however, a much simpler test set up was used to obtain an estimate for α. A relaxation test was performed for a pile of newsprint (height 4 cm, area 7 cm x 7 cm). Initially 1 MPa pressure was applied and then the compression was kept constant and the decay in the pressure was observed. The data was fitted into a six parameter linear, viscoelastic model. The calculated relaxation time constants corresponded to the following values of α: 0.35, 0.033 and 0.0033 1/s.

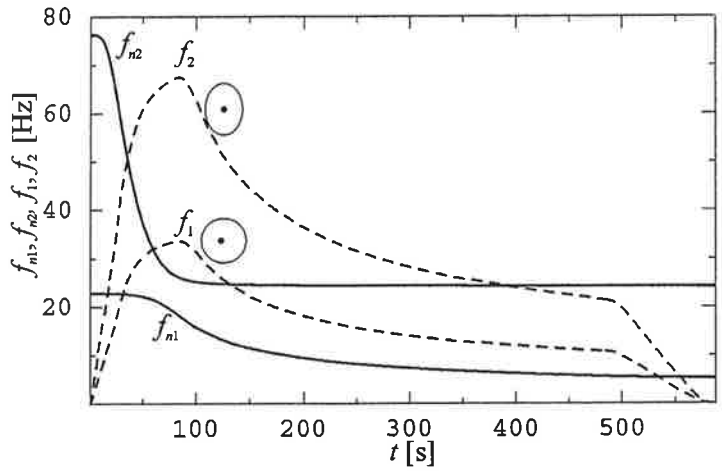

Figure 3. Natural frequencies of the system f_{n1} and f_{n2} (solid lines), the roll rotation frequency f_1 (lower dashed line) and the second harmonic of the roll rotation frequency f_2 (upper dashed line) as a function of time t.

Table 1.

Parameter values used in the calculations

Parameter	Notation	Value
Paper thickness	τ	63 μm
Acceleration	a	0.5 m/s^2
Deceleration	b	0.5 m/s^2
Steady state running speed	v_0	40 m/s
Rounding time in the running speed	t_p	12 s
Core diameter	d_0	0.1 m
Final roll diameter	d_e	1.25 m
Paper density	ρ	750 kg/m^3
Winding drum mass	m_1	4000 kg
Winding drum stiffness	k_1	83.5 MN/m
Winding drum damping	c_1	7 kNs/m
Mass of the core/length	m_0	5 kg/m
Stiffness coefficient of the viscoelement	k_2	100 MN/m
Damping coefficient of the viscoelement	c_2	10 kNs/m
Stiffness coefficient of the roll	k_3	10 MN/m
Recovery coefficient	α	0.1 1/s

During the first 50 seconds, the shapes of the eigenmodes corresponding to these natural frequencies are well localized. Within this time region, the first eigenmode consists of a high amplitude movement of the drum and a negligible movement of the roll whereas in the second mode the opposite movements occur.

In the interval 50 –120 s, when the natural frequencies are closest to each other, the modes are such that the amplitudes of the winding drum and the roll are comparable. In the first eigenmode, the winding drum and the roll move in the same phase and in the second mode in opposite phases.

During the rest of the winding cycle, after 120 s, the modes become again localized. The first eigenmode is the wound roll mode and the second one the winding drum mode.

It can be seen from Figure 3, that the first natural frequency f_{n1} becomes equal to the first or second roll harmonic only during the acceleration ($t \approx$ 20s and 40 s) and deceleration ($t \approx$ 530 s and 560 s). During the steady running speed, the roll rotation frequency at this running speed is always higher than f_{n1}.

The second natural frequency f_{n2} becomes first equal to the second roll harmonic at approximately 40 s and shortly later equal to the first roll harmonic. Both these incidents occur during the acceleration. Later, at $t \approx$ 400 s, during the steady running speed phase, the second roll harmonic becomes again equal to the second natural frequency.

From Eq. (14), the characteristic equation is given by

$$\det \mathbf{A} = 0 . \qquad (18)$$

Since there exists a time lag, there are an infinite number of characteristic roots s_i of Eq. (18). The system is stable if all the real parts of these roots are negative. On the other hand, the system is unstable if one or more real parts are positive.

The evolution of the first and second characteristic roots during the winding cycle are shown in Figs. 4 and 5, respectively. The upper panel shows the imaginary part together with the second natural frequency and the lower panel the real part. The imaginary part of s_1 follows most of the time the f_1–curve. At the end of the acceleration stage and at the beginning of the steady running speed stage, it coincides with the second natural frequency f_{n2}. At this location, there exists a wide unstability region. Although the vibration frequency here is lower than generally in the vibration case a), for this single drum winder model this corresponds to the vibration during the initial acceleration.

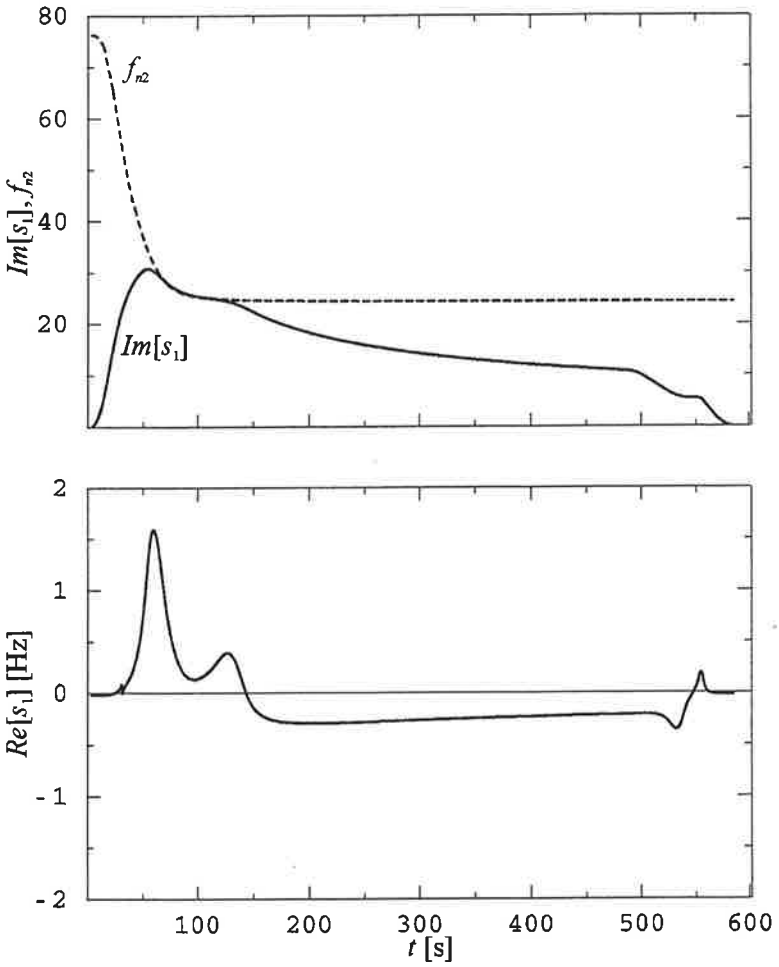

Figure 4. The imaginary (upper panel) and real (lower panel) parts of the first characteristic root.

The imaginary part of the second characteristic root in Fig. 5 follows during the acceleration and deceleration the second harmonic of the roll and during most of the steady running speed stage the second natural frequency. There are short duration unstability regions during the acceleration and deceleration stages and a longer region between 350 s and 430 s. This latter region can be related to vibration category c) since the second harmonic of the roll excites the natural frequency of the winding drum.

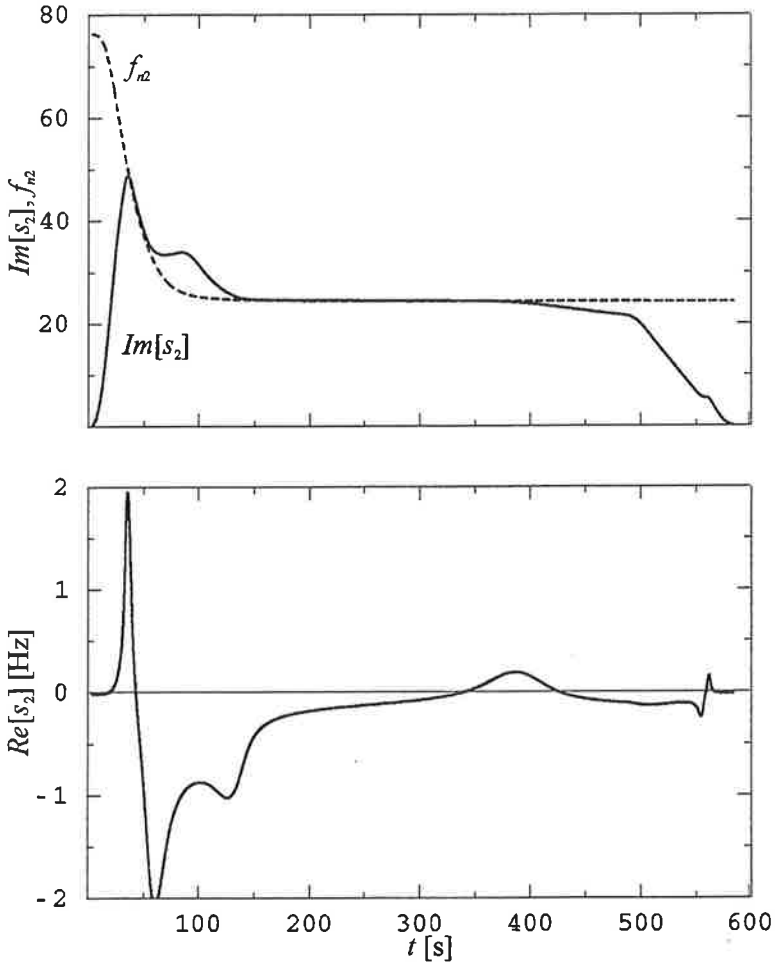

Figure 5. The imaginary (upper panel) and real (lower panel) parts of the second characteristic root.

A parameter study revealed that for values of α larger than 50 1/s, the system is always stable and for values of α smaller than 0.1 1/s the system becomes quite immune for any changes of α. In the viscoelastic measurement of paper, the relative weighting of the estimated α's should also be taken into account. The smaller the weighting of the small values of α is, the stabler the material is.

In this model, the winding drum stiffness does not seem to have any other influence than slightly shifting the unstability zones. Increasing the winding drum damping is beneficial, since it shrinks the unstability regions of all characteristic roots. However, it is not very effective, since doubling, which

might be very difficult to accomplish in practice, of the damping produced only approximately 10 – 20 % shorter unstability regions. Doubling of the roll damping didn't have practically any influence on the stability. This is because the first natural frequency (which activates the roll damping) is excited only during the acceleration and deceleration for short periods. For a two-drum winder, the case would be different since the natural frequencies related to the wound roll movement are higher due to the additional front drum and rider roll nips.

CONCLUSIONS

With the present model, the most common winder vibration cases could be represented. Due to the time lag in the system equations, negative damping is fed into the system and during certain stages along the winding cycle the system becomes unstable. In the studied example, long, unstable zones were found at the end of the acceleration stage and later at steady running speed when the second harmonic of the roll matched the second natural frequency. These unstability zones were identified as "vibration during the initial acceleration" and "wound roll excited drum resonance vibration" which are well known in practice. The non-existence of the third common winder vibration case "roll bouncing" in single drum winders was explained by studying the excitation and natural frequencies.

The are several directions how to further develop the model and analysis. One possibility is to model the winder structure more accurately and extend it to two-drum winding. Another, maybe more challenging possibility, is to improve the constitutive description of the wound roll.

REFERENCES

1. Daly, D., 'How paper rolls on a winder generate vibration and bouncing'. *Paper Trade Journal* **151**, pp. 48-51 (1967).
2. Möhle, H., Buschmann, G. and Müller, G., 'Vibration an Papierrollmaschinen', *Das Papier* **11**, pp. 845-850 (1970).
3. Jorkama, M., 'On the winder vibration analysis', *Licentiate's thesis*, Helsinki University of Technology, 1996.
4. Sueoka, A., Ryu, T., Kondou, T., Tsuda, Y., Katayama, K., Takasaki, K., Yamaguchi, M., Hirooka, H., 'Polygonal deformation of roll-covering rubber,' *JSME International Journal*, Series C, **39**(1), pp. 1-10, 1996.

OUTPUT-ONLY MOODIANALYYSI

P. NURKKALA[1)], H. HAAPANIEMI[2)], P. LUUKKANEN[3)], A. SAARENHEIMO[4)]

1) Fortum Service Vantaa, Pekka.Nurkkala@fortum.com
2) VTT Tuotteet ja tuotanto Espoo, Heikki.Haapaniemi@vtt.fi
3) Fortum Power and Heat Loviisan Voimalaitos, Pekka.Luukkanen@fortum.com
4) VTT Tuotteet ja tuotanto Espoo, Arja.Saarenheimo@vtt.fi

TIIVISTELMÄ

Loviisan ydinvoimalaitoksen syöttövesiputkistolle RL61 on suoritettu pelkkien vasteiden mittaamiseen perustuva output-only moodianalyysi (Ooma). Käytetty menetelmä, mittausjärjestelyt ja saadut tulokset on esitetty tässä artikkelissa. Ooma -menetelmällä määritettyjä tuloksia, ominaistaajuuksia ja -muotoja, on verrattu täristinherätteen avulla saatuihin moodianalyysi tuloksiin.

JOHDANTO

Perinteisessä moodianalyysissä rakenne herätetään käyttäen esimerkiksi iskuvasaraa tai, massiivisten rakenteiden kyseessä ollessa, erilaisia hydraulisia täristimiä. Täristimen asentaminen optimaaliseen herätepisteeseen voi olla erittäin vaikeaa tai jopa mahdotonta. Mittausten suorittaminen perinteisillä menetelmillä saattaa vaatia ainakin laitoksen kyseisen osan toiminnan pysäyttämistä ja aiheuttaa tuotantolaitokselle (tehdas, voimalaitos tms.) taloudellisia menetyksiä tuotannon häiriintyessä.
Output-only moodianalyysissa (Ooma) herätteenä toimivat rakenteen omat käynninaikaiset tai ympäristöstä tulevat (ambient) herätteet. Ooma menetelmää on käytetty mm. siltojen moodiparametrien määrittämiseen, jolloin herätteenä voi olla sillalla kulkeva liikenne ja esimerkiksi tuuli. Meneillään olevassa projektissa on tarkoituksena selvittää Ooma -menetelmän soveltuvuutta teollisuuslaitteiston moodianalysiin tilanteessa, jossa rakenteeseen vaikuttaa voimakas käynninaikainen harmoninen heräte. Ooma -menetelmän etuina teollisuuslaitoksissa tehtävissä mittauksissa on helppo mittaus, mitattavaa järjestelmää ei tarvitse ajaa alas ja lisäksi hankalilta täristimen asennuksilta vältytään. Koska Ooma -mittaukset tehdään käynninaikaisissa olosuhteissa, tulevat moodiparametritkin määritellyiksi todellisten käynninaikaisten reunaehtojen vallitessa.

TARKASTELTAVA RAKENNE

Tarkasteltava putkisto on esitetty kuvassa 1. Kyseessä on Loviisan 1 laitoksen syöttövesilinjan painepuolen putki RL61. RL61 on syöttövesipumpun painepuolen linja, joka alkaa syöttövesipumpusta ja päättyy runkolinjaan. Putkisto sijaitsee lähes yhdessä pystytasossa ja tehden miltei täydellisen silmukan ja sen kokonaispituus on noin 28 metriä. Putkistolinja RL61 on valmistettu hiiliteräksestä ja sen nimellinen ulkohalkaisija 323.9 mm. Nimellinen seinämänpaksuus on 20 mm, paitsi alas laskevalla osuudella 17.5 mm (pisteiden 118 ja 222 välinen osuus kuvassa 2). Putkisto on eristetty 120 mm paksuisella mineraalivilla eristeellä.
Putkisto on pääosin koottu hitsaamalla. Päittäisiä hitsisaumoja on 12 kpl. Kaikki putkistossa olevat mutkat ovat taivutettuja (so. ei esiinny hitsaamalla koottuja mutkia). Putkiston kolme laippaliitosta

sijaitsevat pumpun/takaiskuventtiilin alueella. Linjan alaosan vaakasuoralla osuudella, jousikannakkeen No. 46 molemmin puolin (kuva 1), on kaksi raskasta (978 kg) sulkuventtiiliä V1 ja V2, jotka ovat putkiston käyttäytymisen kannalta merkittäviä pistemassoja.
Putkisto on kannakoitu kolmella jousikannakkeella S1, S2 ja S3 (pisteet 46, 47 ja 48 kuvassa 1 tai pisteet 227, 119 ja 109 kuvassa 2), joiden jousivakiot ovat S1 660 N/mm ja S2 ja S3 446 N/mm. Pystysuorat kannakoinnit S2 ja S3 on toteutettu niin, että putkeen on hitsattu vahvikelevyt vastakkaisille puolille poikkileikkausta. Kumpaankin vahvikelevyyn on hitsattu putken pituusakselin tasossa oleva teräksinen kolmiomainen osa, jonka kautta jousen tukireaktio tuodaan putkeen. Vaakaosalla oleva kannake S1 on toteutettu pulttiliitoksilla kootuista 180 asteen taivutetuista sangoista, jotka on puristettu putken ympärille.

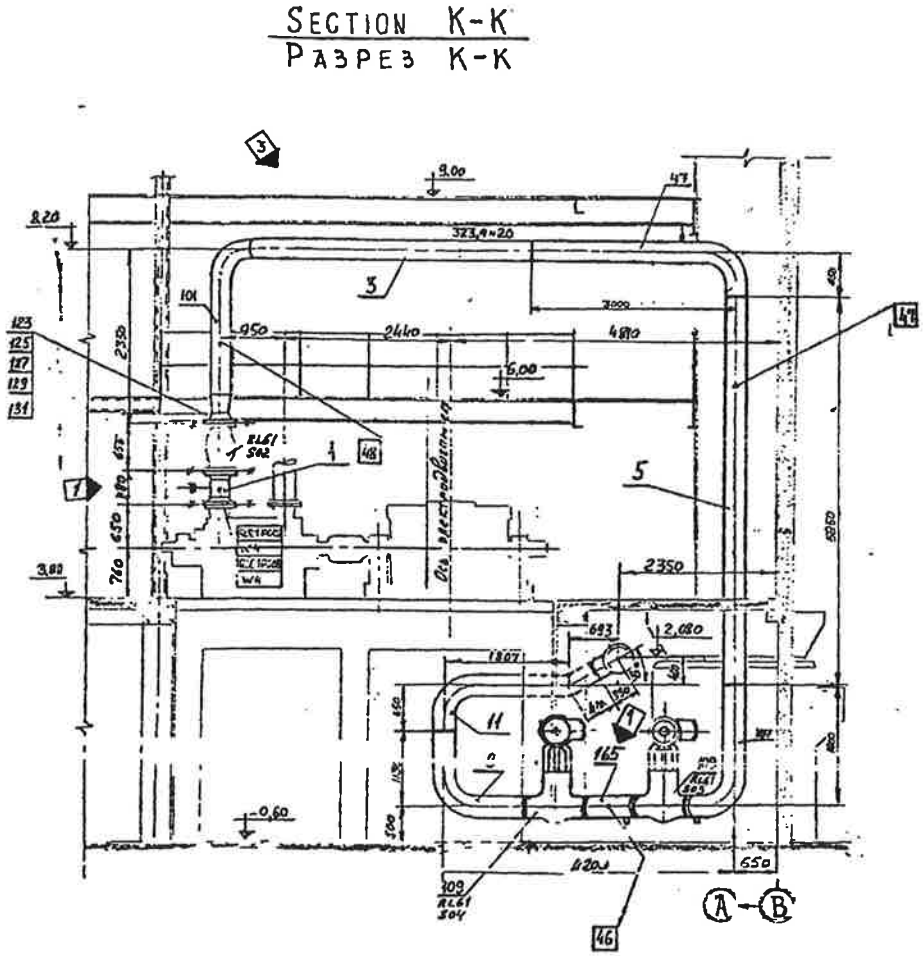

Kuva 1. Loviisan 1 laitoksen syöttövesilinjan painepuolen putki RL61.

KOEJÄRJESTELYT

Täristinmittaus ja moodianalyysi

Antureiden ja herätepisteen optimaalinen sijainti määritettiin numeerisesti ABAQUS elementtimenetelmäohjelmaa [1] ja FEMtools ohjelmaa [2] hyväksi käyttäen. Esilaskenta, sekä iskuvasara-

ja täristinherätteellä mitattujen koetulosten alustava tarkastelu on raportoitu lähteessä [3]. Kuvassa 2 on esitetty moodianalyysissä käytetyt mittausmallin pisteet ja globaali koordinaatisto. Rakenne herätettiin pisteestä 114 kahteen suuntaan: 114Y- ja 114Z+. Kaikista mittauspisteistä, joita on 31 kappaletta, mitattiin kiihtyvyysantureita käyttäen vasteet globaalin koordinaatiston akseleiden suunnissa. Kokeet suoritettiin käyttäen yhtä herätesuuntaa kerrallaan. Rakenne herätettiin servohydraulisella täristimellä, joka tuottaa jatkuvaa herätesignaalia inertiamoodissa. Näin saavutettiin tarvittavat voimatasot (luokkaa 2 kN) sekä tarvittava taajuusresoluutio (0.03125 Hz) taajuusvastefunktio-mittauksissa. Taajuusvastetietokannan analysoimiseen käytettiin SDRC:n IDEAS-ohjelmistoa [4]. Moodiparametrit määritettiin käyttämällä ominaistaajuuksien ja niihin liittyvien vaimennusarvojen ratkaisuun Complex Exponential-menetelmää ja ominaismuodot ratkaistiin Circle-Fit- algoritmilla. Täristinmittaus ja siihen liittyvä moodianalyysi on selitetty yksityiskohtaisesti lähteessä [5].

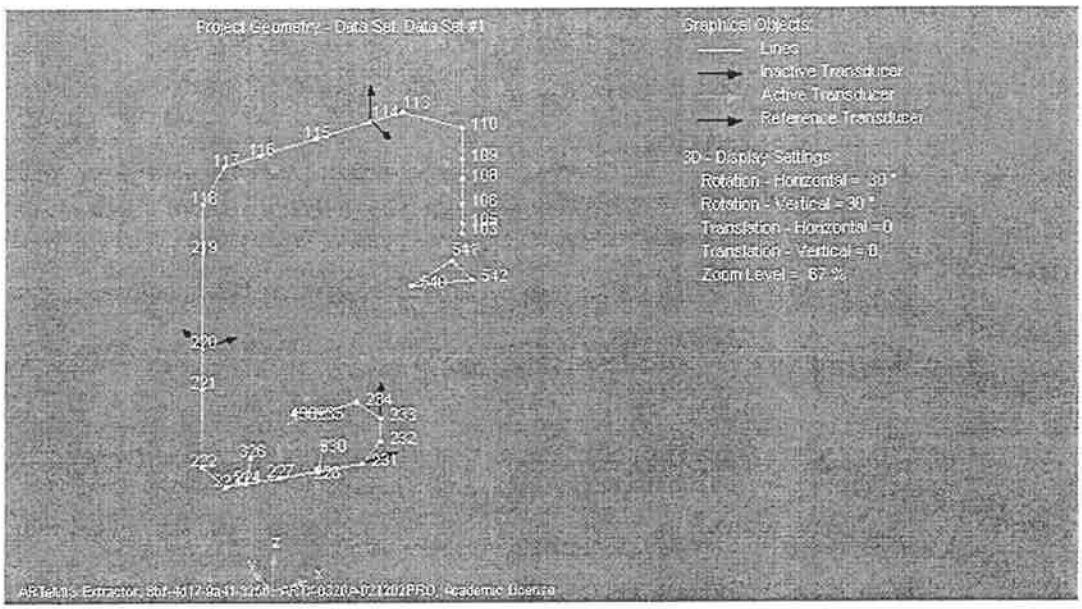

Kuva 2. Putkilinja RL61 kokeellinen malli. Kuvassa esitetty mittapisteryhmä 1 ja käytetyt referenssipisteet.

Käynninaikaiset mittaukset

Käynninaikaiset vasteiden aikasarjamittaukset Ooma-analyysiä varten suoritettiin 16-kanavaisella moodianalysaattorilla. Referenssipisteitä/suuntia oli kuusi (114Y-/Z+, 220X+/Y+, 231X+ ja 234Z+), ja niihin tarvittiin siis jokaiseen anturi. Paikat ja suunnat on esitetty sinisin nuolin kuvassa 2. Kymmentä anturia siirrettiin mittaussuunnitelman mukaisesti mittauskertojen välillä. Suunnitelma mahdollisti mittauksen suorittamisen siirtämällä antureita kymmenen kertaa, eli tuloksena saatiin 10 mittausryhmää. Kuvassa 2 on esitetty mittausryhmä 1 vihrein nuolin. Kuuden referenssipisteen käytöllä varmistettiin mahdollisimman monen rakenteen ominaismuodon löytyminen myöhemmässä moodianalyysissä, sillä edellytys moodin identifioinnille on, että moodi "näkyy" referenssipisteessä. Usean referenssipisteen käyttö tekeekin Ooma menetelmästä todellisen multiple-input multiple-output -menetelmän.
Käynninaikaisissa mittauksissa putkiston herätteenä toimivat pumpulta tulevat mekaaniset herätteet, nesteen virtaus ja virtauksen pulsaatio putkistossa, nesteen turbulenssi putkimutkissa, nesteen mahdollinen paineväräht ely ja muut ulkoiset tukirakenteiden kautta putkistoon välittyvät herätteet. Pumppu on ns. siipipumppu, jonka pyörimisnopeus on 1500 rpm.

Mitattujen aikasarjojen pituus oli 600 sekuntia ja käytetty näytteenottotaajuus oli 1.024 kHz. Näillä asetuksilla pyrittiin varmistamaan riittävän hyvälaatuisen mittausdatan saaminen, jotta harmonisen herätteen tai melun aiheuttamat ongelmat olisivat mahdollisimman vähäiset. Lisäksi näin parannetaan mahdollisuuksia erottaa lähellä toisiaan olevat moodit toisistaan. Mittausdataa ASCII-formaatissa oli noin 1 gigatavu.
Tarvittava aikasarjan pituus T määrittää alimman oletetun ominaistaajuuden f_{min} avulla ja näytteenottotaajuus f_s korkeimman kiinnostavan ominaistaajuuden f_{max} perusteella seuraavasti [6]:

$$T = 1000 / f_{\min} \tag{1}$$

$$f_s \geq 3 f_{\max} . \tag{2}$$

OOMA-ANALYYSI

Ooma-analyysi eli moodien määrittäminen käynninaikaisista aikasarjoista suoritettiin kaupallisella ARTeMIS Extractor [6] ohjelmistolla. Analyysi suoritettiin usealla taajuusviivojen määrällä, viivojen välit 12.5 mHz, 25 mHz, 50 mHz ja 100 mHz. Mitä vähemmän viivoja käytetään sitä enemmän spektriviivojen keskiarvoistuminen vaikuttaa ja sitä helpommin ominaistaajuudet ovat tunnistettavissa. Liian pieni viivamäärä voi kuitenkin johtaa liialliseen keskiarvoistumiseen ja ominaistaajuuden virheelliseen arviointiin ja mahdollisten vierekkäisten moodien huomaamatta jäämiseen. Koska suurin kiinnostus kohdistui mataliin taajuuksiin, mittausdataa desimoitiin 20 kertaa eli vain joka 20. näyte säilytettiin. Tämän seurauksena Nyqvistin taajuudeksi tuli 25.6 Hz. Nyqvistin taajuudella tarkoitetaan tässä taajuutta, joka on puolet käytetystä näytteenottotaajuudesta 51.2 Hz.

Frequency Domain Decomposition (FDD) menetelmä

Moodien identifioimiseksi käynninaikaisesta mittausdatasta käytettiin nyt ns. Frequency Domain Decomposition (FDD) menetelmää, jonka teoria on esitetty lähteessä [7]. Menetelmä pohjautuu Basic Frequency Domain (BFD) tekniikaksi kutsuttuun taajuustason lähestymistapaan, jonka mukaan toisistaan erillään olevat moodit voidaan laskea suoraan tehospektrin tiheysmatriisista [8]. FDD menetelmässä, sen sijaan että käytettäisiin spektrin tiheysmatriisia suoraan kuten BFD menetelmässä, spektrimatriisit hajotetaan jokaisen spektriviivan kohdalla (taajuudella) käyttäen Singular Value Decomposition (SVD) menetelmää. Tällöin spektrimatriisit hajotetaan, mikäli vaimennus on vähäistä, kuormitus puhdasta valkoista kohinaa ja lähekkäin olevien moodien ominaismuodot geometrisesti ortogonaalisia, ryhmäksi yhden vapausasteen systeemiä vastaavia autospektrin tiheysfunktioita. Todellisessa tilanteessa näitä ehtoja ei voida yleensä täyttää, vaan hajotelmaa yhden vapausasteen systeemiksi on pidettävä vain arviona, joka kuitenkin on huomattavasti tarkempi kuin perinteisen BFD menetelmän tulokset.
SVD menetelmällä ratkaistuja singulaarivektoreita voidaan pitää ominaismuotoina ja ominaistaajuudet voidaan ratkaista viemällä yksittäiset yhden vapausasteen autospektrin tiheysfunktiot takaisin aikatasoon käänteismuunnoksen avulla. Taajuus ja vaimennus arvioidaan yhden vapausasteen autokorrelaatiofunktion avulla värähdysajan ja logaritmisen dekrementin perustella [9].

Moodien identifiointi

Mittausten laadun varmistamiseksi ennen varsinaista moodien identifiointia tarkasteltiin saatuja spektrin tiheyksiä ja spektrin tiheysmatriiseja. Kuvassa 3 on esitetty ns. autospektrin tiheys kaikissa eri dataseteissä (10 kpl) referenssipisteen 4 (220Y+) tapauksessa. Kuvan perusteella voi päätellä, että eri mittauskerroilla saatu data on hyvin samanlaista eli kaikki moodit ovat todennäköisesti hyvin edustettuina jokaisessa datasetissä ja että energiatasot ovat myös samankaltaisia kaikissa dataseteissä. Kuvassa 4 on esitetty autospektrin tiheys referenssipisteen 2

(114Z+) tapauksessa, tämän perusteella mittausryhmässä seitsemän referenssipisteen 2 energiataso on alhaisempi kuin muiden, vaikka autospektrin muoto onkin hyvin samanlainen. Lisäksi mittausryhmässä yksi referenssipisteen 2 energiataso on korkeampi kuin muissa tapauksissa. Nämä erot saattavat aiheuttaa ongelmia mittausryhmien yksi ja seitsemän käsittelyssä, vaikkakin erot ovat varsin vähäisiä. Muiden referenssipisteiden tapauksessa tilanne muistuttaa kuvan 3 tilannetta, eli autospektrit ovat hyvin samankaltaisia.

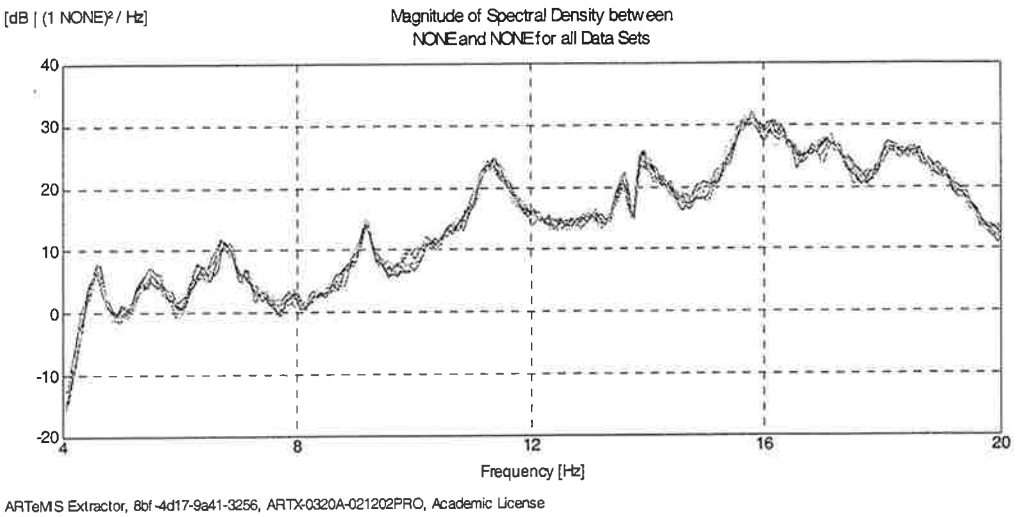

Kuva 3. Autospektrin tiheys kaikissa dataseteissä referenssipisteelle 4 (220Y+).

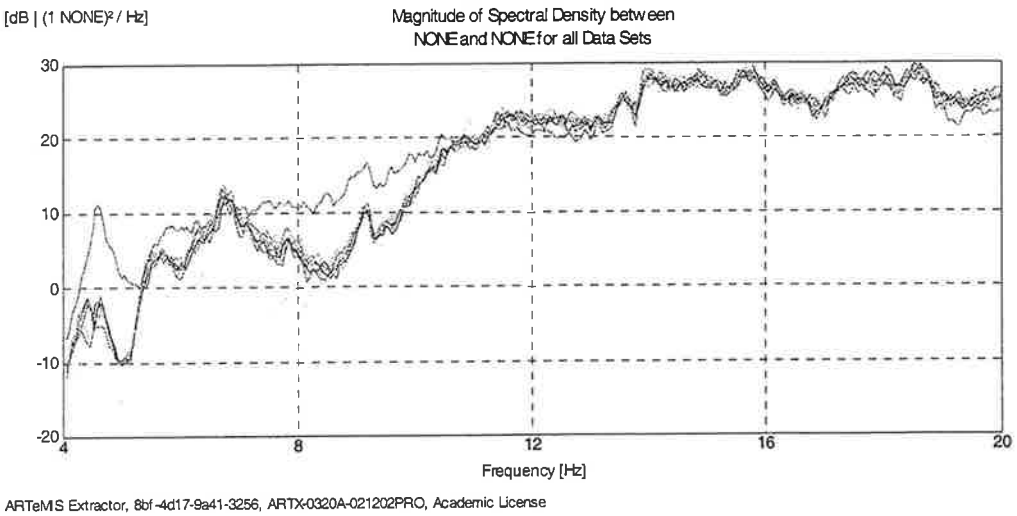

Kuva 4. Autospektrin tiheys kaikissa dataseteissä referenssipisteelle 2 (114Z+).

Kuvan 5 perusteella kaikkien referenssipisteiden autospektrien tiheysfunktioiden keskiarvot ovat hyvin samankaltaisia kaikissa mittausryhmissä. Yleisesti ottaen mittauksia voidaan pitää onnistuneina ja kerätyn datan laatua hyvänä.
Autospektrin tiheysfunktioiden huippujen avulla voidaan päätellä, miltä taajuuksilta moodeja voisi identifioida. Ensimmäiset ominaistaajuudet löytyvät taajuuksien 4.5 Hz ja 7 Hz väliltä. Toinen

menetelmä mahdollisten ominaistaajuuksien tunnistamiseksi on eri kanavien välisen koherenssin tarkastelu (kuva 6), sillä koherenssi saa normaalisti korkeita arvoja resonanssitaajuuksilla.

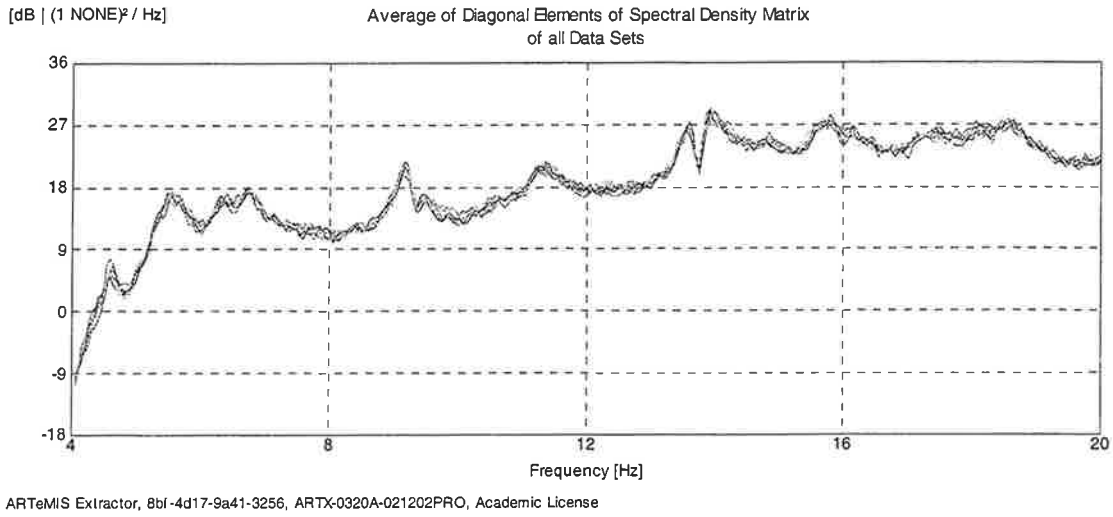

Kuva 5. Kaikkien referenssipisteiden autospektrien tiheysfunktioiden keskiarvot mitatuista dataseteistä.

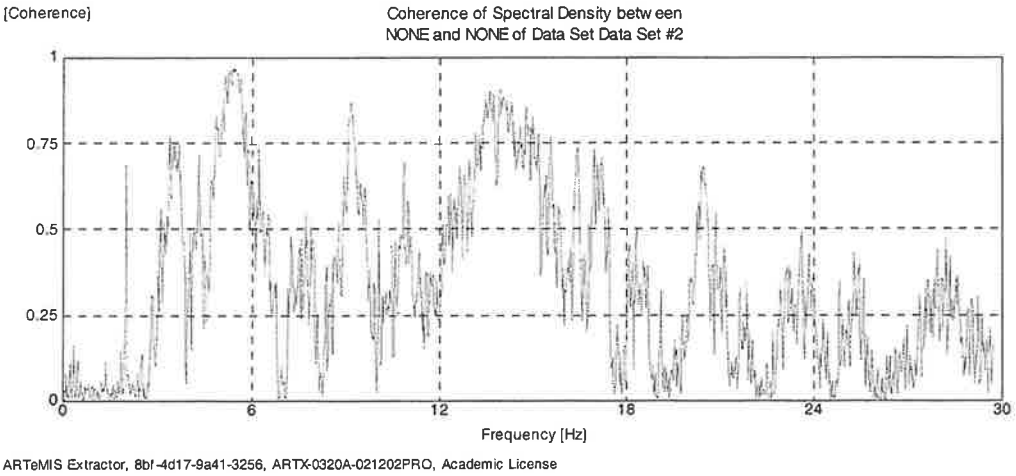

Kuva 6. Koherenssi funktio mittauspisteiden 220X+ ja 233X- välillä.

Varsinainen moodien identifiointi suoritetaan FDD menetelmässä poimimalla ns. piikit kaikkien mittausryhmien spektrien tiheysmatriisien SVD hajotelmien normalisoitujen singulaariarvojen keskiarvoista. Kuvassa 7 on esitetty 11 korkeinta singulaariarvoa (SVD-käyrää) kaikkien eri mittausryhmien spektrin tiheysmatriisien singulaariarvojen keskiarvoista, jotka on normalisoitu ylimmän käyrän (ensimmäinen singulaariarvo) alle jäävään alan suhteen. Kuvassa 7 on nähtävissä, että taajuudella ~4.5 Hz on selvä piikki kolmessa korkeimmassa SVD-käyrässä. Tämä tarkoittaa, että kyseisellä taajuudella on ainakin kolme ns. toistuvaa moodia. Kuvasta voi tunnistaa mahdollisia vierekkäisiä tai kaksoismoodeja esimerkiksi taajuudella 6.7 Hz kolmannella SVD-käyrällä. Lisäksi kuvassa on nähtävissä heikkoja piikkejä kohdissa 4 Hz, 6 Hz ja 8 Hz alimmilla

SVD-käyrillä. Nämä piikit ilmeisesti aiheutuvat heikoista harmonisista herätteistä, joilla on yhteys siipipumpun siipien lukumäärään. Kuvassa mahdolliset ominaistaajuudet on merkitty viivoilla ja neliö viivassa ilmoittaa SVD-käyrän, jonka perusteella kyseinen moodi määritetään.

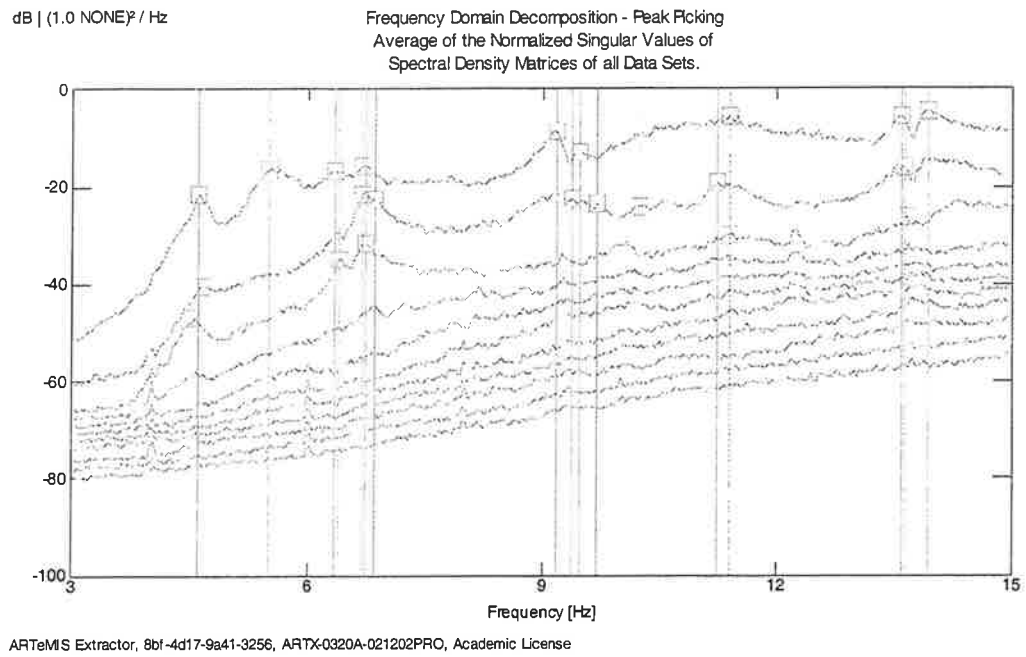

Kuva 7. Mahdollisia ominaistaajuuksia. Käytetty spektriviivojen tiheys 25 mHz.

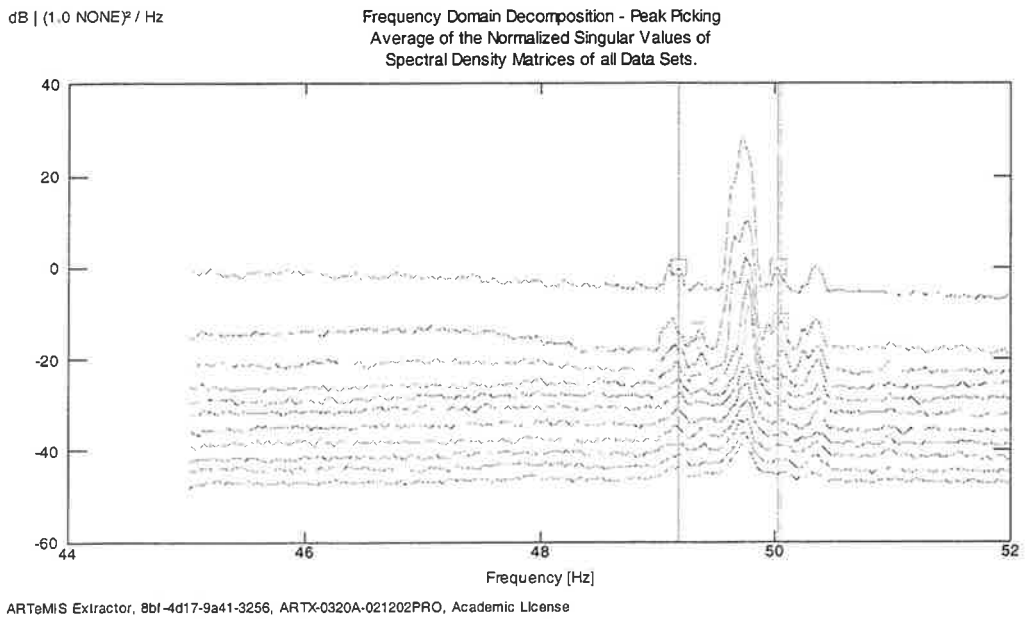

Kuva 8. Harmonisen herätteen aiheuttama piikki SVD-käyrissä 49.9 Hz taajuudella ja mahdollisia ominaistaajuuksia.

Siipipumpun aiheuttama voimakas harmoninen heräte taajuudella ~49.9 Hz on nähtävissä selvästi kuvassa 8. Lisäksi kuvassa näkyy kaksi, ilmeisesti harmonisten muotojen aiheuttamaa, piikkiä taajuuksien 49.1 Hz ja 50.6 Hz kohdalla. Kuvaan 8 on myös merkitty 4 mahdollista ominaistaajuutta harmonisten herätteiden aiheuttamien piikkien läheisyydessä. Näiden moodien verifiointi vaatisi moodien identifiointia ns. Stochastic Subspace Iteration (SSI) menetelmällä.

TULOKSET

Ooma -menetelmällä FDD -tekniikalla määritetyt moodit, käyttäen sekä 25 mHz että 50 mHz spektriviivojen jaottelua ja keskimääräisiä SVD-käyriä, on esitetty taulukossa 1. Moodit 1 - 12 määritettiin käyttäen 25 mHz jaottelua ja moodit 13 - 35 50 mHz jaottelulla. Taulukon sarakkeissa 2 ja 3 on listattu parhaiten vastaavat täristinkokeen perusteella määritellyt moodit. Täristinherätteen avulla määritettyjen moodien ja Ooma-moodien välinen korrelaatio, taajuuseron ja ominaismuotojen korrelaation avulla, on esitetty sarakkeessa 7. Korrelaatio on laskettu käyttäen Modal Assurace Criteria (MAC) menetelmää [10], jossa kahden ominaisvektorin Φ_i ja Φ_j välinen korrelaatio voidaan määrittää seuraavasti:

$$MAC_{ij} = \frac{\left[\{\Phi_i\}^T \{\Phi_j\}^*\right]^2}{\left[\{\Phi_i\}^T \{\Phi_i\}^*\right]\left[\{\Phi_j\}^T \{\Phi_j\}^*\right]}, \qquad (3)$$

missä * merkitsee vektorin kompleksikonjugaattia. Mitä korkeampi MAC arvo on, sitä parempi on ominaisvektoreiden välinen korrelaatio. Usein käytetty kriteeri hyvälle korrelaatiolle on MAC > 0.7 ja heikolle korrelaatiolle MAC < 0.5. Lisäksi taulukossa on ilmoitettu miltä SVD-käyrältä kyseinen moodi on identifioitu.

Moodien keskinäistä korrelaatiota, kuten ominaistaajuuksien erot ja ominaismuotojen korrelaatio, tarkasteltaessa on muistettava, etteivät olosuhteet k.o. mittauksissa ole olleet täysin identtiset. Putkiston käyttöpaine on noin 7,5 MPa ja käyttölämpötila noin 165 °C, täristinmittausten aikana putkisto oli täytetty kuumalla vedellä mutta sekä lämpötila että paine olivat kuitenkin selvästi alhaisempia kuin käyttötilassa. Mittausten välillä oli yli vuosi aikaa, jonka aikana eristeiden ominaisuudet ovat voineet muuttua. Menetelmiä vertailtaessa on myös muistettava, että täristin heräte ei välttämättä herätä kaikkia muotoja kuten todellinen käynninaikainen multiple-input heräte.

Taulukon 1 perusteella on havaittavissa, että Ooma menetelmällä löytyisi selvästi useampia moodeja kuin täristinherätteellä. Osa moodipareista korreloi keskenään kuitenkin varsin hyvin sekä taajuudeltaan että ominaismuodoltaan, kuten esim. ensimmäinen moodi. Matalien taajuuksien omanaismuodot korreloivat paremmin kuin korkeampien taajuuksien muodot. Kaiken kaikkiaan moodien keskinäiseen vastaavuus on varsin hyvä, vaikka vallinneissa olosuhteissa ja käytetyissä herätteissä oli eroja.

Ooma-menetelmällä identifioitujen ominaismuotojen tarkempi vertailu täristinherätteen avulla määriteltyihin ominaismuotoihin osoittaa suurimpien eroavaisuuksien olevan yleensä rakenteen alaosassa sekä venttiileissä erityisesti Y ja Z-suunnissa eli täristyssuunnissa että putkimutkissa, jotka värähtelevät selvästi voimakkaammin käynninaikaisen herätteen tapauksessa. Erityisesti ensimmäisen SVD-käyrän perusteella identifioidut moodit värähtelevät voimakkaasti putkimutkissa varsinkin pisteissä 116 - 219. Syynä tähän ilmiöön on todennäköisesti kyseisessä putkimutkassa tapahtuva turbulentti virtaus, joka aiheuttaa mutkaan erillisen voimakkaan herätteen. Toisen ja kolmannen SVD-käyrän perusteella identifioidut moodit ovat selvästi lähempänä perinteisiä rakenteellisia ominaismuotoja.

Taulukko 1. FDD menetelmällä määritetyt ominaistaajuudet ja -muodot sekä niiden korrelaatio täristinkokeen tulosten kanssa.

OOMA	Taajuus (Hz)	Täristin	Taajuus (Hz)	Erotus (Hz)	Erotus	MAC	SVD
1	4.6	1	4.279	0.321	6.98 %	0.78	3
2	4.6	2	4.510	0.090	1.96 %	0.35	1
3	4.625	3	6.821	-2.196	-47.48 %	0.31	2
4	5.5						2
5	5.525						1
6	6.375						2
7	6.4	4	6.833	-0.433	-6.77 %	0.38	3
8	6.725						2
9	6.725						3
10	6.75						1
11	6.825						2
12	7.225						4
13	8.2	5	9.175	-0.975	-11.89 %	0.56	4
14	9.15						1
15	9.2						2
16	9.25						4
17	9.25						3
18	9.7	6	9.339	0.361	3.72 %	0.65	2
19	10.05						3
20	11.25	7	11.431	-0.181	-1.61 %	0.61	2
21	11.35						1
22	11.4	8	13.514	-2.114	-18.54 %	0.49	3
23	12.25						3
24	13.6	9	13.763	-0.163	-1.20 %	0.37	2
25	13.6						1
26	13.9						1
27	14.3						3
28	15.75						1
29	16.75						3
30	17.15						2
31	18.45						3
32	18.6						1
33	19.2	11	20.299	-1.099	-5.72 %	0.46	2
33	19.2	12	20.506	-1.306	-6.80 %	0.34	2
34	20.95	10	20.124	0.826	3.94 %	0.37	1
34	20.95	13	20.634	0.316	1.51 %	0.42	1
35	21						3

Kuvassa 9 on esitetty moodipari Ooma 4.6 Hz (project A) ja täristin 4.279 Hz (project B), joiden ominaismuotojen korrelaatio on hyvä, MAC = 0.78. Ominaismuotojen suurimmat eroavaisuudet ovat pisteiden 220 ja 227 välillä ja venttiilissä, pisteessä 326. Ooma-moodi on identifioitu kolmannen SVD-käyrän perusteella.

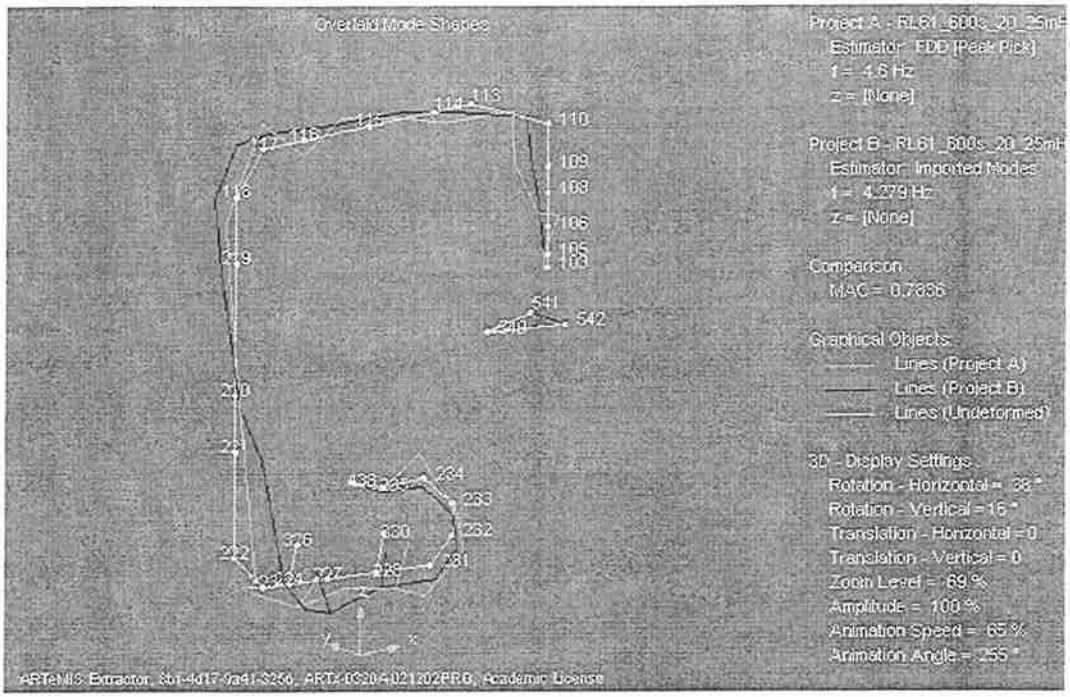

Kuva 9. Moodipari Ooma 4.600 Hz ja täristin 4.279 Hz. Ominaismuotojen korrelaatio MAC 0.78.

Kuvassa 10 on esitetty mahdollinen ominaismuoto, joka on identifioitu harmonisen herätteen aiheuttaman SVD-käyrien piikin vierestä (Kuva 8, piikin oikeapuoli) toisesta SVD-käyrästä. Kyseinen ominaismuoto muistuttaa rakenteellista muotoa, mutta tämän varmistaminen vaatisi lisäanalyysiä esim. SSI -menetelmällä.

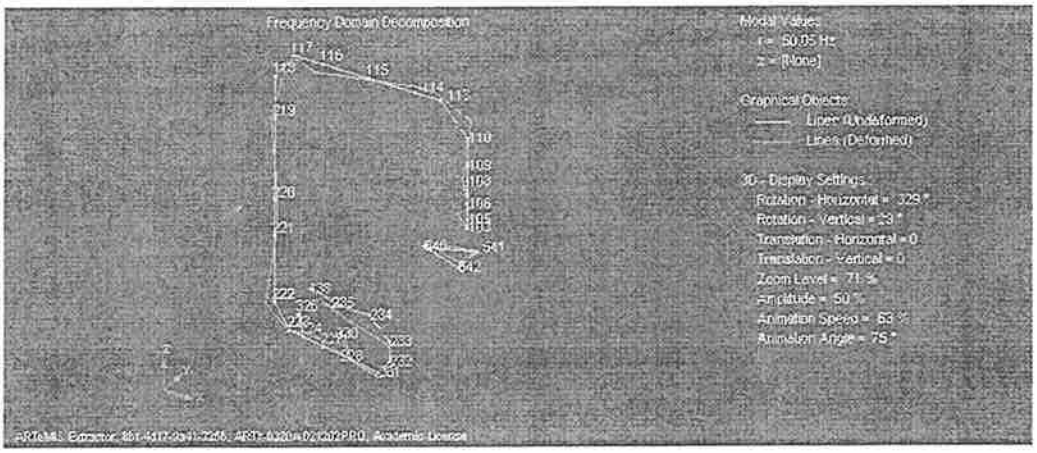

Kuva 10. Ooma-moodi 50.5 Hz. Mahdollinen ominaismuoto harmonisen herätteen tuntumassa.

Taulukossa 2 on esitetty tarkemman moodien identifioinnin tulokset joillekin taulukon 1 perusteella valituille moodipareille. Tarkemmassa identifioinnissa pyrittiin etsimään paremmin

täristinmittausten perusteella ratkaistujen moodien kanssa korreloivia moodeja käyttäen erilaisia spektriviivojen tiheyksiä (12.5 mHz - 100 mHz) ja tarkastelemalla jokaista mittausryhmää erikseen. Tulokset osoittavat, että näin saadut ominaismuodot korreloivat paremmin kuin keskimääräisiä SVD-käyriä käyttämällä saadut muodot, mutta menetelmä on huomattavasti työläämpi. Menetelmän soveltamisen mielekkyys normaalitilanteessa riippuu siitä, kuinka paljon moodien ominaistaajuudet vaeltavat eri mittausryhmien kesken ja muuttuvatko vasteiden energiatasot voimakkaasti eri moodien ja mittausryhmien kesken. Taulukossa 2 moodit, joiden identifiointi onnistuu paremmin käyttäen jotakin muuta menetelmää kuin aiemmin käytettyä 25 mHz spektriviivojen tiheyttä ja keskimääräisiä SVD-käyriä ilman "jatkuvaa" vertailua täristin-moodeihin, on merkitty tähdellä*.

Taulukko 2. Moodien identifioinnin tuloksia erilaisilla asetuksilla.

OOMA Taajuus (Hz)	TÄRISTIN Taajuus (Hz)	Ero (Hz)	Ero (%)	MAC
4.512*	4.279	0.233	5.16 %	0.71
4.592	4.279	0.313	6.82 %	0.79
9.387	9.175	0.212	2.26 %	0.57
9.68*	9.339	0.341	3.52 %	0.67
10.62	9.339	1.281	12.06 %	0.68
10.62	9.175	1.445	13.61 %	0.60
11.2*	11.431	-0.231	-2.06 %	0.67
11.39	13.514	-2.124	-18.65 %	0.52
13.7	13.763	-0.063	-0.46 %	0.44
24.42	24.732	-0.312	-1.28 %	0.44

YHTEENVETO

Mittaamalla vain käynninaikaiset vasteet ja identifioimalla moodit Ooma -menetelmällä Frequency Domain Decomposition (FDD) menetelmää hyödyntäen onnistuttiin löytämään useita moodeja voimalaitosputkistosta, joka oli voimakkaan harmonisen herätteen alaisena. Identifioitujen moodien lähempi tarkastelu ja vertailu täristinmittauksen perusteella määritettyihin moodeihin osoittaa, että vaikka löydettyjen moodien lukumäärässä on selvä ero, niin kuitenkin osa moodeista on varsin samankaltaisia ja saatuja tuloksia voidaan pitää varsin luotettavina. Selvimmät eroavaisuudet Ooma-muotojen ja täristinmuotojen välillä ovat, erityisesti täristyssuunnissa, putkimutkissa ja rakenteen alaosassa. Eroavuuksia analysoitaessa on muistettava, etteivät vallitsevat reunaehdot olleet aivan samat eri mittaustilanteissa.

Mittaustuloksien ja Ooma analyysin perusteella rakenteessa on havaittavissa useita taajuuksia, joilta löytyy ns. toistuvia moodeja (repeated modes), joiden löytäminen muilla menetelmillä saattaa olla vaikeaa. Ensimmäisen SVD-käyrän perusteella identifioidut ominaismuodot olivat usein muotoja, jotka värähtelivät voimakkaasti putkimutkissa. Toisen ja kolmannen SVD-käyrän perusteella identifioidut muodot korreloivat yleensä paremmin täristinmuotojen kanssa kuin ensimmäisen SVD-käyrän perusteella ratkaistut muodot. Syynä tähän saattaa olla putkimutkien voimakas vaste niissä vaikuttavan turbulentin virtauksen aiheuttamaan herätteeseen.

Nyt saatujen tulosten perusteella lähestymistapa vaikuttaa toimivalta ja tulevaisuudessa vastaavan kaltaista putkistoa tarkasteltaessa on todennäköisesti mahdollista tulla toimeen lyhyemmillä aikasarjoilla ja alhaisemmalla näytteenottotaajuudella. Tällöin varsinainen mittaustapahtuma olisi nopeampi ja moodien identifiointi vaatisi pienempien tiedostojen ansioista vähemmän resursseja.

KIITOKSET

Tämä työ on osa Teollisuuden Voiman (TVO) Rakenteiden Kestävyys ja Käyttöiän hallinta projektia (RKK). Tätä osaprojektia ovat rahoittaneet TEKES, TVO, Fortum Loviisan Voimalaitos, Fortum Neste Engineering ja Fortum Nuclear Service, siitä heille kiitokset. Kiitämme myös Aimo Tuomasta ja Timo Krouvia Loviisan Voimalaitokselta hyvästä yhteistyöstä. Kiitokset myös Jaakko Rostedtille/J.Rostedt Oy, joka oli mukana suorittamassa käynninaikaisia mittauksia.

LÄHTEET

1. ABAQUS Theory Manual, Version 5.8. Hibbit, Karlsson & Sorensen Inc. RI, 1998.
2. FEMtools Theoretical Manual Version 2.1.0. Dynamic Design Solutions N.V. (DDS). Leuven, Belgium, 2001.
3. Saarenheimo, A., Haapaniemi, H., Luukkanen, P., Nurkkala, P. ja Rostedt, J. Modal Analysis of feed water pipe line RL61 at the Loviisa NPP. Plant Life Management. VTT SYMPOSIUM 227. Espoo, 2003.
4. I-DEAS Test: Modal Analysis User's Guide. I-DEAS Master Series 7, Structural Dynamics Research Corporation, USA, 1998.
5. Nurkkala, P., Loviisa 1 syöttövesilinjan painepuolen RL61 putkiston moodianalyysi kolmella eri reunaehdolla elokuussa ja lokakuussa 2001, Työseloste Fortum CMC, CMC-155, 2002.
6 ARTeMIS Extractor Pro Release 3.2 Getting Started Manual. Structural Vibration Solutions (SVIBS) ApS. Aalborg, Denmark, 2002.
7. Brincker, R, Zhang, L. and Andersen, P., "Modal Idenfication from Ambient Responses using Frequency Domain Decomposition", Proc. of the 18th International Modal Analysis Conference (IMAC), pp. 625 - 630, 2000.
8. Bendat, J. S. & Piersol, A. G. "Engineering Applications of Correlation and Spectral Analysis", 2nd ed. John Wiley & Sons, 1993, ISBN: 0471570559.
9. Møller, N., Brincker, R. & Andesen, P., "Modal Extraction on a Diesel Engine In Operation", Proc. of the 18th International Modal Analysis Conference (IMAC), pp. 1845 - 1851, 2000.
10. Allemang, R. J. & Brown, D. L. "A Correlation Coefficient for Modal Vector Analysis", Proc. of the 1st International Modal Analysis Conference (IMAC), pp. 110 - 116, 1983.

APPLICATIONS OF FREQUENCY-DOMAIN APPROACH FOR VORTEX-INDUCED VIBRATION OF BRIDGES

Dr R. KIVILUOMA
Consulting Engineers Sormunen & Uuttu Ltd
Kaikukatu 3, FIN-00530 Helsinki
E-mail: risto.kiviluoma@inststo-su.fi

ABSTRACT

In the present paper, analysis of vortex-induced vibrations of two challenging long-span bridges is described. The frequency-domain approach employing spectral analysis and amplitude dependant correlation model is used. An attempt is make, not only to demonstrate features and capabilities of the approach, but also to discuss implications the phenomenon of vortex shedding might enter into the design of modern suspended-span bridges.

1. VORTEX-INDUCED VIBRATIONS OF BRIDGES

In bridge aerodynamics, vortex-induced vibrations are a concern of light-weight deck sections and pylons. In the recent decade, the importance of vortex shedding to cause potential problems is re-discovered. Historically, the phenomena has been well noticed, but the break-through research has been buried under the extensive work on bridge flutter and buffeting in periods 1940-1960 and 1960-1990, respectively. This is partly due to fact that the resulting oscillations, although embarrassing and harmful to users, are usually not destructive regarding overall structural safety and stability. Furthermore, most big suspended-span bridges built in the past have open truss-type stiffening girder, which will usually not initiate problematic vortex shedding actions.

The modern European-style decks of long-span bridges are usually made of steel and have streamlined box or double-I girder design. Optimisation of steel consumption and usage of light-weight road pavements will reduce overall mass further, increasing vulnerability to problematic vortex-induced vibrations. Among recent suspension bridges and in-field situations, it is interesting to note that for example the deck of Great-Belt East Bridge (main span 1624 m) was found suffering form vortex-induced vibrations, although extensive and sophisticated analysis was made in advance. Moreover, typical long-span Norwegian suspension bridges, employing narrow steel box-girder, have possessed embarrassing deck oscillations. In some occasions in moderate wind around 5...15 m/s at deck level, the double amplitudes of these structures have been of order 1 m and accelerations of order 0.5 g. These bridges have been successfully corrected afterwards by mounting guide vanes at lower corners of the cross-section (*Fig. 1*).

Another specific issue is the construction of pylons of cable-stayed and suspension bridges. During the construction, the tallest pylons act as slender towers. Again, steel pylons are more susceptible to vortex-induced vibrations in comparison with concrete ones, due to smaller mass and mechanical damping. In many cases reinforced concrete pylon alternatives are competitive with respect to steel ones. Former mentioned could usually be constructed without notable wind-induced problems. In longest cable-stayed spans built so far, the pylons have exceed heights of 200 m, and at

least upper part of pylon is made of steel to reduce dead load end ease the construction. Another reason to use steel is to avoid winter casting, which might be too complex or expensive.

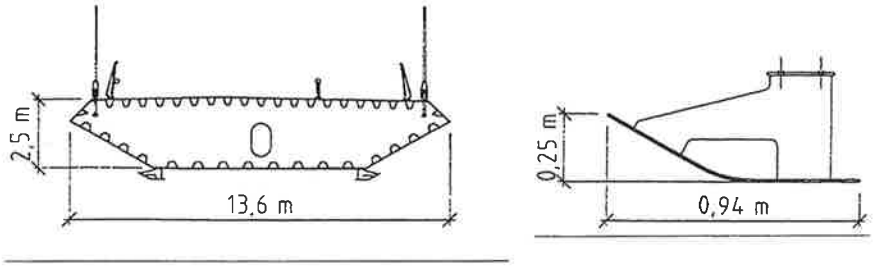

Fig. 1: Guide vane of the Osterøy Suspension Bridge after ISAKSON et al. (2001).

There are some fundamental concerns in reliable analysis of bridge decks for vortex shedding, which follows from the size and elongated shape of the cross-section:

- resonances with mode shapes and lock-in falls usually to the critical Reynolds number range, where at least circular cylinders are known to have marked decrease of drag and disorganised vortex street. Substantial uncertainties could exists in wind-tunnel experiments of scale models due to dissimilarity of Reynolds number
- elongated shape causes vortices shedding from the leading edge to interface and attach to the rest of the body and the vortex trail in a complicated manner. This reflects into the phenomenon that only decks having certain aspect ratio λ (= h/B, where h = reference across-wind dimension and B = width of the cross-section) and shape, will have dominant response and lock-in at or near resonance suggested by the classical Strouhal law. The Strouhal law is expressed as

  $$n_K = S_t \frac{U}{h}, \tag{1}$$

  where n_K = shedding frequency of vortices in the von Kármán vortex street; S_t = Strouhal number (a geometric constant or slowly varying function of Reynolds number) and U = steady wind velocity. Instead, in some wind-tunnel experiments it is found that other forms of periodic vortex excitation, synchronized with oscillation of the body at structural natural frequency, will control the phenomena
- as in analysis of other line-like structures, span-wise correlation of loading vs. vibration amplitude is an important issue. Bridge decks have usually sharp corners, which have been demonstrated to result higher level of correlation with respect to circular cylinders. Consequently, analysis of bridge decks needs additional family of correlation models to be developed. These are also needed for vibrations in torsion mode, which could be important in some cases.

Two widespread analytical models exist for assessments of bridge decks, including the conventional harmonic excitation model and the models inspired by the nonlinear fluid-oscillator model. Both models, to give realistic results, should be extended to include effects of span-wise load correlation. For the former model, this extension could be done by means of spectral analysis and random vibration theory, while for the latter model no definite theory is probably available. In the case of fluid-oscillator models, some authors have proposed, to account effects of correlation loss, that excitation could be modelled to occur only in some portion along the bridge span. In discussing which model type is more useful for bridge design, it could be noted that:

- relative "non-dimensional" amplitudes (z_p/h, where z_p = displacement amplitude) in successful bridge designs could not be big. For example, a deck section of 2...3 m in height, if possessing non-dimensional amplitude around 10 % will probably be classified as unacceptable. Non-linear actions within the phenomena, although important, are not expected to weaken the applicability of linear approaches, provided that open design parameters are tuned to applicable level of non-dimensional amplitudes
- due to Reynolds number range, the excitation process will probably have stronger random character vs. the sub-critical Reynolds number range being the bases of most fluid-oscillator models.

The analysis of vortex-induced vibrations of bridges is usually based on wind-tunnel tests directly or indirectly. Although full and taut-strip models, i.e. 3D scale models, could be used to obtain response estimates directly, 2D "section model" type scale models have several advantages in practical engineering work. In particularly, 2D scale-model results could be used to extract loads on structures to prepare design tables of associated non-dimensional quantities (Strouhal numbers, aerodynamic exciting coefficients etc.). As soon as problematic actions are indicated, original section model could be easily modified to search aerodynamic devices to mitigate excitation. One of the most useful approaches is semi-empirical: to calculate, as accurate as possible, full bridge behaviours by means of measured responses of section models. Once the successful cross-section is found, testing of full models could be optionally conducted to make the final design check.

2. FREQUENCY-DOMAIN APPROACH FOR ANALYSIS OF VORTEX SHEDDING

Application of frequency-domain approach, or the spectral analysis, seems to be not new, but promising branch for developing generally accepted method for analysing vortex-induced vibrations of bridges. For example, the model adopted in EUROCODE (1991), available also analysis of conventional bridges, is in many sense identical to the Correlation model of BLEVINS *et al.* (1976), in which the Correlation model was developed for cylindrical structures in the framework of random vibrations and spectral analysis. More recently, a rigorous frequency-domain model is proposed by KIVILUOMA (2001) for bridges. The model is, despite its mutual simplicity, versatile to take into account key properties of the phenomenon: amplitude dependence of load correlation; turbulence reduction effect on response; and self-limiting nature of the excitation force vs. amplitude. The excitation process is modelled as band-limited white noise, which will have finite variance. While the bandwidth will be dependant on relative amplitude at lock-in vibrations, the excitation load variance is proposed to be invariant. Inspired by the model of VICKERY *et al.* (1983) for circular cylinders, the bandwidth is assumed to be dependent on longitudinal turbulence level of air in a simply and justifiable form. Response calculations follow the standard procedures of spectral analysis and normal mode summation, and are suitable to efficient computer implementations. The core equations of the excitation model are repeated below.

Spectral density of exiting force is modelled as

$$S_K(n) = \begin{cases} \left(\frac{1}{2}\rho \overline{U}^2 h\right)^2 \frac{\widetilde{C}_K^2}{\Delta_n} & ; \quad \left(n_i - \frac{\Delta_n}{2} \le n \le n_i + \frac{\Delta_n}{2}\right) \\ 0 & ; \quad \textit{elsewhere,} \end{cases} \tag{2}$$

where $S_K(n)$ = one-sided spectral density of excitation load acting per unit length; n = frequency; ρ = density of air; $\widetilde{C}_K$ = non-dimensional RMS-exciting coefficient; n_i = structural natural frequency of interest; and Δ_n = bandwidth of dominant excitation. For theoretical zero bandwidth (i.e., harmonic load), relation $C_K = \sqrt{2}\,\widetilde{C}_K$ holds, in which tabulated peak values of C_K could be found in literature. In general, non-dimensional RMS-exciting coefficients are to be determined

experimentally as function of reduced velocity $U/(hn_i)$. Aerodynamic damping is taken as zero when extracting or applying these. The bandwidth is proposed to be dependent on non-dimensional amplitude and turbulence intensity in a convex functional form. The proposed form is

$$\begin{cases} \dfrac{\Delta_{St}}{n_i} = \sqrt{\beta_0^2 + \beta_u^2} \\ \dfrac{\Delta_n}{n_i} = \dfrac{\Delta_{St}}{n_i}\left(1 - \dfrac{\sigma_z}{\sigma_{Cr,z}}\right)^2, \end{cases} \tag{3}$$

where β_0 = non-dimensional constant specifying the bandwidth in smooth flow ($\beta_0 \approx 0.05 \ldots 0.1$); $\beta_u \approx 1.3 I_u$, with I_u = longitudinal turbulence intensity; σ_z = response standard deviation; and $\sigma_{Cr,z}$ = critical standard deviation response. In above formulation at critical amplitude, specified by $\sigma_{Cr,z}$, the bandwidth is zero. Model's extension to actual 3D structures is made by specifying the cross-spectrum through formula

$$S_K(n)\big|_{ij} = \sqrt{S_K(n)\big|_i \; S_K(n)\big|_j}\; e^{C(\Delta r)}, \tag{4}$$

where $C(\Delta_r)$ = non-dimensional decay function; i and j denote coordinates on the structure; and Δ_r = separation between the coordinates i and j. For bridge decks

$$C(\Delta_r) = -\frac{a_1}{a_2 + \dfrac{\sigma_m}{h_m}}\sqrt{\frac{\Delta_r}{h_m}} \;;\; h_m \equiv \frac{h_i + h_j}{2} ; \sigma_m \equiv \frac{\sigma_i + \sigma_j}{2}, \tag{5}$$

where parameters $a_1 \approx 0.001$ and $a_2 \approx 0.019$ have been reported for H-shape cross-sections by other investigators. Alike formulation could be used also for twisting oscillations. For pylon legs, the original model of BLEVINS *et al.* (1976) could be written as

$$C(\Delta_r) = -\frac{2\Delta_r}{h l_c} \;;\; l_c = a_3 + \frac{a_4 \dfrac{\sigma_m}{h}}{a_5 - \dfrac{\sigma_m}{h}} \;;\; a_3 = 5 \;;\; a_4 = \frac{100}{\sqrt{2}} \;;\; a_5 = \frac{0.35}{\sqrt{2}}. \tag{6}$$

The resulting analysis model is nonlinear with respect to non-dimensional amplitude and needs to be solved, e.g., through fixed-point iteration.

3. TWO APPLICATIONS OF THE PRESENT MODEL

Applications of the present model for two internationally notable bridges, with the author being involved in aerodynamic analysis in the years 2000-2002, are described: the world-record span cable-stayed bridge proposal for the Stonecutters design competition in Hong Kong, China; and the Neva Cable-Stayed Bridge in St. Petersburg, Russia. Main designers for the former bridge came from Finnish company ConsultingKORTES Ltd. The latter bridge is designed by Russian consultants Institute Giprostroymost - Saint Petersburg (the cable-stayed part) and Institute Stroi-poect (approach spans and management of the whole project). General views of these bridges, as used in aerodynamic analysis, are illustrated in *Figs 2* and *3*.

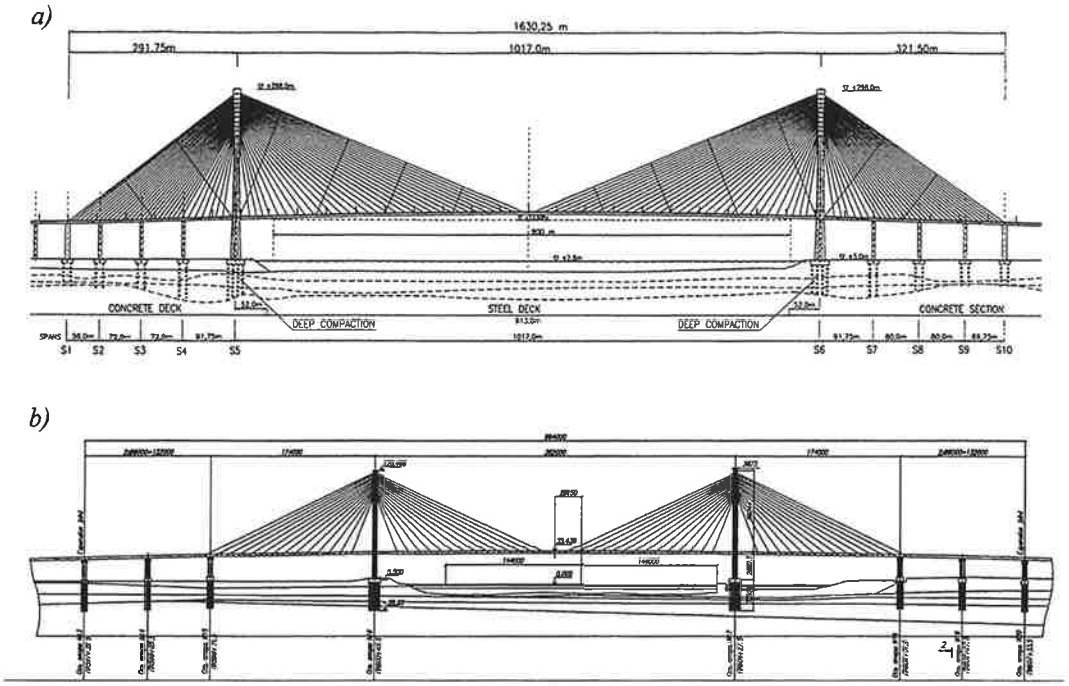

Fig. 2: a) Elevation of the Stonecutters Bridge proposal and b) the Neva Cable-Stayed Bridge.

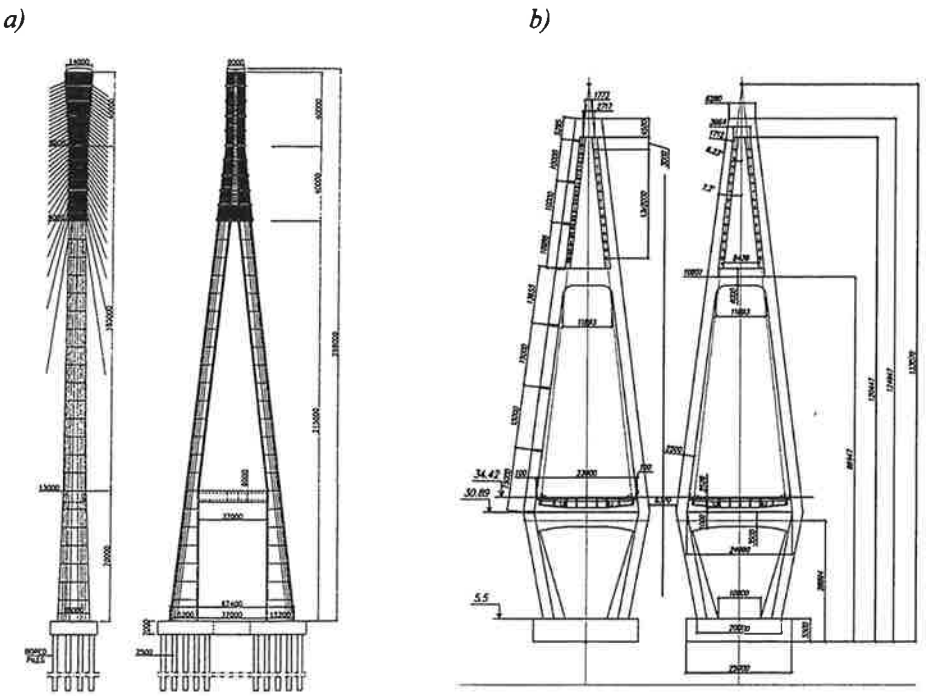

Fig. 3: Pylons of a) the proposed Stonecutters Bridge and b) the Neva Cable-Stayed Bridge.

The Stonecutters bridge competition in the year 2000, promoted bridge engineers around the world to consider breaking a 1 km span-limit among cable-stayed bridges. The Finnish proposal, ranked to 4th prize in the competition, was based on the proven technology and classical-style cable-stayed alternative. The A-shaped pylons, reaching the height 298 m, comprise reinforced concrete legs and steel anchorage upper part about 80 m in height. In aerodynamic analysis, about 50 lowest mode shapes were calculated using the commercial FE-programs FEMAP & CAEFEM for three 3D models of in-service bridge and two construction stages. Extracted natural frequencies lie in range 0.11...2.5 Hz. The modal analysis results were used as input to aerodynamic analysis, assisted with the integrated computer code BWIND-3 developed by the author. Parallel verification calculations were conducted using the simplified models of EUROCODE (1991).

The analysis of vortex shedding indicates that dominant displacements occur in fundamental modes, but the acceleration responses increase with wind speed due to lock-in with higher modes (*Fig. 4*). It was demonstrated that vortex shedding will be the governing aerodynamic excitation mechanism for the deck and pylons under construction. Up to the design wind velocity, accelerations of order 0.5 g and 1 g were predicted to occur at pylon and cantilever tips, respectively. The aerodynamic analysis output static-equivalent wind loads to structural engineers. These include the actions of inertia forces (mass multiplied by acceleration) as one component. The loads were found to be within acceptable limits. At in-service stage, the cables will "fix" the pylons, and asphalt pavement will increase mass to reduce deck oscillations. Furthermore, steel parts at pylon tips have perforated cladding, which will distort formation of regular vortex trail.

It was concluded that calculated pylon responses were in agreement with the simplified model. This was not the case, however, in deck analysis. This was attributed to disparity in correlation models, or correlation lengths, of EUROCODE (1991) and the models deduced for bridge decks. The aerodynamic study as a whole implies that 1 km span length among cable-stayed bridges is quite reachable from aerodynamic point-of-view, if aerodynamic issues are seriously taken into account in design. The most concern is probably the parametric excitation of extremely long and flexible stay-cables at main spans. In the proposed design, stay-cables were fixed with cross-ties (*Fig. 2*).

In the context of Stonecutters design competition, it has been later observed that vortex-induced pylon oscillations were problematic in the winning concept, which has mast-type steel pylon with circular cross-section. This design has been replaced by steel-concrete composite alternative.

The Neva Cable-Stayed Bridge is a big twin bridge (two identical bridges side by side) currently under construction. Planned completion of the 1st and the 2nd bridges are in the years 2005 and 2009, respectively. During the construction, continuous long-term monitoring system is operating to report health of the structure, including recordings of wind-induced vibrations. Deck and pylons are both light-weight steel-box structures. Of special interest in aerodynamic analysis are the vortex-induced vibrations and their possible interaction with fluid coupling. In fluid coupling, adjacent structures can interface with each other over the fluid medium. Generally, windward structure either provides windshield to leeward structure, or magnifies the response of the leeward structure due to highly periodic wake generated from the windward structure. In the present case, both bridges have identical natural frequencies, which could further reinforce the phenomena.

The main aerodynamic analysis is made experimentally using wind-tunnel tests of full models by Danish Maritime Institute and analytically by the author. FE-based modal analysis was done by the main designer for 3 different models, including in-service bridge and two critical construction stages. These results were used as input to the BWIND-3 analysis conducted by the author.

Wind-tunnel experiments indicate that in smooth flow, width of the first lock-in wind-speed range associated to the fundamental bending mode of 0.27 Hz, is very narrow. This reflects into analyti-

cal calculations in a sense that results are sensitive to across-wind dimensions the cross-section (the pylons are slightly tapered in elevation) and height profile of the mean wind velocity. Obviously, lock-in excitation is not encountered simultaneously in all cross-sections at varying altitudes. In turbulent-flow experiments, vortex-induced response of fundamental mode was small and hardly noticeable.

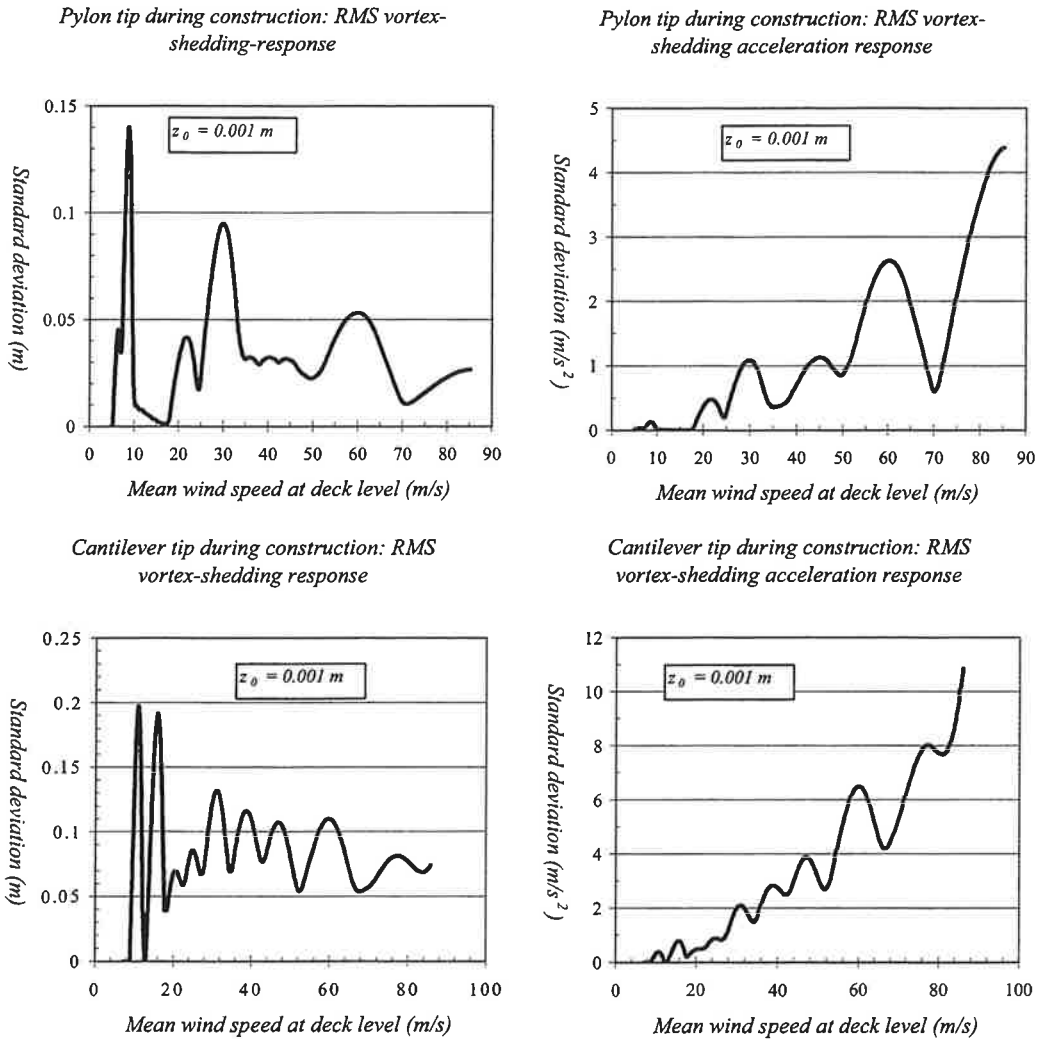

Fig. 4: Calculated vortex-induced vibrations for critical construction stages of the proposed Stonecutters Bridge. Reduction effect of turbulence is neglected by taking $\beta_u = 0$ in Eq. (3). The parameter z_0 refers to surface roughness length used to calculate height profile of the mean wind velocity.

It was found that the pylons could possess problematic oscillations in extreme winds during the construction. After re-analysis of wind tunnel data due to analytical calculations, these were attributed to the vortex shedding with resonance to the 2nd bending mode in direction to bridge span (1.7

Hz). The main disparity between the experimental and analytical results was due to the Strouhal number of the pylon leg. Experiments indicate $S_t \approx 0.2$ while EUROCODE (1991) value $S_t \approx 0.1$ was applied in initial calculations. From designer's point-of-view, uncertainties in S_t are problematic when inspecting whether or not certain higher mode will reach resonance in wind velocity range up to the design value. It is also important to know good initial estimate for minimum lock-in wind speed to detect, if the lowest controllable flow speed in wind tunnel is sufficient to inspect vortex shedding concerning natural frequencies of the scale model.

After matching the Strouhal number with the experimental one, and making some minor changes to analysis model, a good agreement was found between the results (*Figs 5* and *6*). The responses in *Fig. 5* are related to the wind-tunnel experiment conducted in smooth flow and in very low value of mechanical damping. For design value of damping, analytical calculations indicate peak accelerations of order 1.5 g and 0.6 g to occur in smooth and turbulent wind conditions, respectively. Former mentioned "design value" of acceleration is still big concerning inertial loads and static-equivalent wind loads, and will put structural capacity into the "limit". The installation of temporary tuned-mass-dampers was calculated to be sufficient and optimum solution to suppress vibrations of the 2nd mode, if required. Perhaps the most important contribution of analytical calculations was to demonstrate that the high accelerations were due to vortex shedding instead of more serious form of instability called galloping.

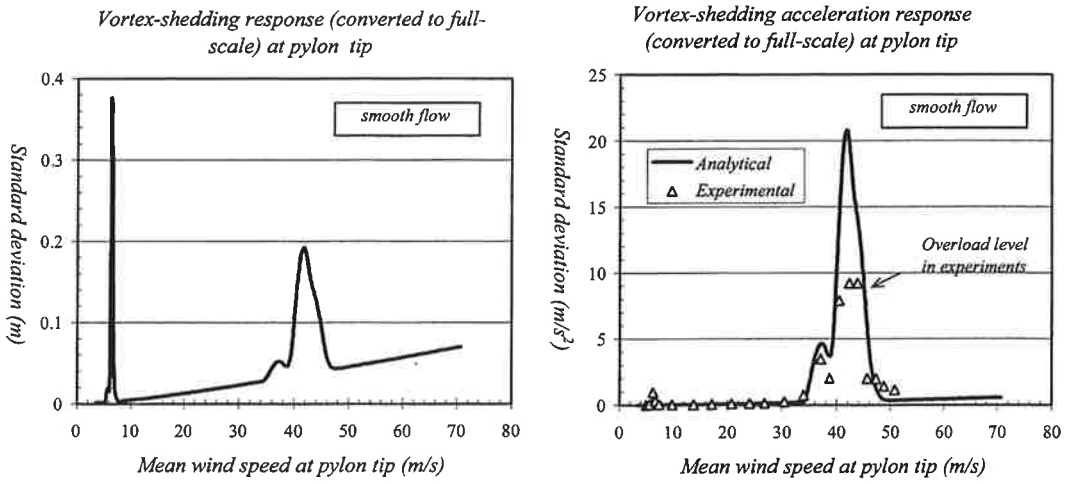

Fig. 5: Smooth-flow responses (I_u = 0) of the pylon tip at construction stage of the Neva Cable-Stayed Bridge in very low mechanical damping. "Overload level" refers to problems in empirical setup, in which the upper measuring range of accelerometers was exceeded.

Wind-tunnel experiments indicate that fluid-coupling in the presence of both bridges will have no remarkable adverse effects into responses of pylons and decks. It seams that the windward structures only provide some shielding to leeward structures. The horizontal clearance between the decks is about 10 m. In the case of two adjacent pylons and wind perpendicular to bridge span, it was even found that the response of the windward pylon was slightly lower than in the single pylon case. A possible explanation of this is that leeward pylon tends to distort regular vortex street generated from the windward pylon (*Fig. 6*).

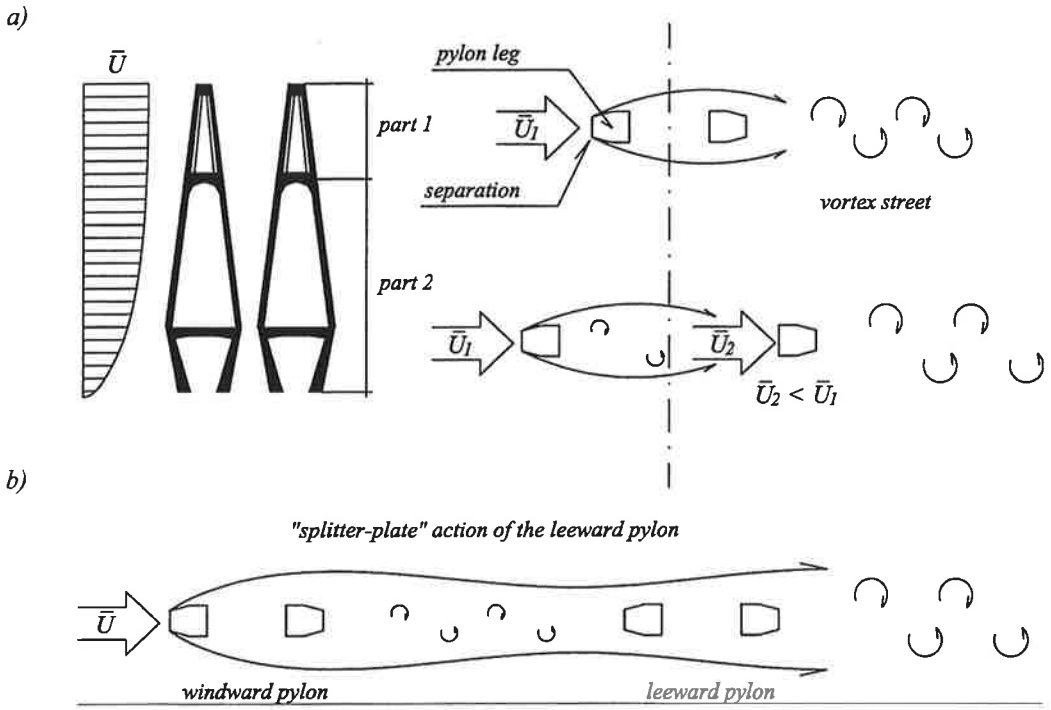

Fig. 6: a) Idealization done in assessments of pylons for vortex shedding. Pylon legs in "part 1" are assumed to act as single body. In "part 2", wind velocity hitting the leeward pylon leg is lower than in the windward leg due to shielding effect. b) Illustration of possible "splitter-plate" action of the leeward pylon. The structures in wake can distort regular vortex trail and reduce the excitation in windward structure.

4. CONCLUSIONS

- vortex-induced vibrations have became of special interest in design of modern bridges with lighter decks, increasing span-lengths and taller pylons. Generally, the most severe problems occur in suspended-span steel bridges due to relatively small mass and damping
- frequency-domain approach provide a promising framework for deducing reliable and generally accepted design method for vortex shedding of bridges, with the present model being one candidate
- separate correlation models are evidently needed for pylons and bridge decks
- vortex-induced vibrations in resonance with very low natural frequency (i.e., fundamental modes of tall pylons during construction) are sensitive to various design parameters, including also simply across-wind dimensions of cross-sections. The height profile of mean wind velocity needs carefully be reproduced in analysis, to ensure correct assessments of lock-in at various altitudes
- study of the proposed Stonecutters Bridge suggests that 1 km span length among cable-stayed bridges is technically reachable from aerodynamic point-of-view, if aerodynamic issues are taken into account when designating the key design solutions. Suppression of stay-cable vibrations will be of special importance in most designs
- aerodynamic analysis of the Neva Cable-Stayed Bridge demonstrated the usefulness of analytical models in purpose of complementing wind-tunnel tests. Analytical models could give

close insight to loading of structures to assist structural engineers to perform stress-check for design. It also helps correct interpretation of wind-tunnel test results
- in wind-tunnel tests of the Neva Cable-Stayed Bridge, fluid coupling was not found initiating problematic interactions between the two identical bridges close to each other.

Acknowledgements

The author expresses his gratitude to Mr Paavo Hassinen and Dr Reijo Kouhia from the Laboratory of Structural Mechanics of Helsinki University of Technology for promoting preparation of this paper. Mr Igor Kolyushev, Chief Engineer from Institute Giprostroymost - Saint Petersburg; and Mr Esko Järvenpää, Director from ConsultingKORTES Ltd; are acknowledged to their consent of using design information of the two bridges dealt in more detail.

References

BLEVINS, R. D. & BURTON, T. E. (1976). Fluid forces induced by vortex shedding. *Journal of Fluids Engineering*, 98(1), pp. 19...24.

EUROCODE 1 (1991): Basis of design and actions on structures, Part 2-4: Wind actions, European prestandard ENV1991-2-4. 157 p.

ISAKSEN, B., STRØMMEN, E. & GJERDING-SMITH, K. (2001). Suppression of vortex shedding vibrations at Osterøy suspension bridge. Krogeborg (ed.), Strait Crossings 2001, A.A.Balkema publishers, Lisse, pp. 99-105.

KIVILUOMA, R. (2001). Frequency-domain approach for calculating wind-induced vibration and aeroelastic stability characteristics of long-span bridges. Acta Polytechnica Scandinavica, Ci 123. The Finnish Academy of Technology, Espoo, p. 112. http://lib.hut.fi/Diss/2001/isbn9512259109

VICKERY, B. J. & BASU, R. I. (1983). Across-wind vibrations of structures of circular cross-section. Part I. Development of a mathematical model for two-dimensional conditions. *Journal of Wind Engineering and Industrial Aerodynamics*, 12(1), pp. 49...73.

BALLISTOKARDIOGRAFIA SYDÄMEN KUNNON SEURANNASSA

Suvi Koskinen[1], Raimo von Hertzen[2] ja Raimo Sepponen[1]
[1]Teknillinen korkeakoulu, Sovelletun elektroniikan laboratorio
[2]Teknillinen korkeakoulu, Matematiikan laitos
PL 1100, 02015 TKK

TIIVISTELMÄ

Työssä tutkittiin kuntoharjoittelujakson yhteydessä ballistokardiografialla (BKG) saatuja mittaustuloksia. Spektrianalyysin ja työssä johdetun matemaattisen muunnoksen avulla etsittiin BKG-signaalista ja sen taajuusspektristä fyysisen kunnon nousun kanssa korreloivia tekijöitä. Osoittautui, että maksimaalisen hapenottokyvyn muutos korreloi skaalatun spektrin painopisteen muutoksen kanssa (r^2 = 0.78) ja muunnetun signaalin I J-amplitudi kasvoi selvästi kunnon kohoamisen myötä.

JOHDANTO

Ballistokardiografia (BKG) on menetelmä, jolla rekisteröidään sydämen pumppauksesta kehoon aiheutuvia rekyylivoimia. Mittaustuloksena saadaan ballistokardiogrammi, jonka huiput vastaavat tiettyjen sydämen aiheuttamien verenkierrollisten muutosten kehoon kohdistamia rekyylivoimia ihmisen ollessa paikallaan mittauslaitteessa. Koska sydämen pumppaus- ja supistuskyky paranevat kuntourheilun tuloksena, pitäisi menetelmällä pystyä seuraamaan sydämen sekä muiden verenkiertoelinten kunnon kehitystä kuntoharjoittelujakson aikana. Sydämen tutkimiseen menetelmä tarjoaa hyvän vaihtoehdon, sillä se on täysin ei-invasiivinen eikä kiinnittämistä tarvittavia elektrodeja ole; koehenkilön tai potilaan tarvitsee vain istua mittaustuolissa. Tässä työssä mittauslaitteena käytetty tuoli antaakin mahdollisuuden mitata sydämen toimintakuntoa helpon rekisteröinnin avulla, jonka vuoksi sitä voitaisiinkin käyttää esimerkiksi kotona tai kuntosaleilla.

Erityisesti aiemmissa tutkimuksissa BKG-signaalin amplitudia ja yksittäisiä huippuja on analysoitu hyvin tarkkaan [1], [2]. Amplitudien vertailuja on tehty muun muassa normaalien ihmisten ja urheilijoiden välillä [1]. Jo näissä tutkimuksissa todettiin sydämen pumppauksesta aiheutuvien rekyylivoimien kasvu kuntourheilun seurauksena [2]. Samassa tutkimuksessa havaittiin lisäksi BKG-signaalin amplitudin olevan suuri juoksulajien urheilijoilla. Myös amplitudien hyvä korrelaatio iskuvolyymin kanssa on löydetty sairaalapotilailla [3]. Itse signaalin spektriä ei ole kuitenkaan aikaisemmin juuri analysoitu kuntourheilun yhteydessä, minkä vuoksi erityisesti spektrin tutkiminen saattaa tuoda uutta tietoa sydämen toiminnan muutoksista kuntoilun seurauksena.

Työn tarkoituksena oli tutkia ballistokardiografisesta tuolimittauksesta saatavaa signaalia sekä signaalin taajuusspektrin muutoksia kuntoharjoittelun seurauksena. Tavoitteena oli löytää ballistokardiogrammin ominaisuuksia, jotka korreloivat fyysisen kunnon muutoksen kanssa.

TUTKIMUSMENETELMÄT JA KOHTEET

Aiemmin suoritetut mittaukset

Paikallisessa sanomalehdessä olleen ilmoituksen perusteella vapaaehtoisia koehenkilöitä ilmoittautui 119. Ilmoittautuneet palauttivat täytetyn kyselykaavakkeen, jonka avulla määritettiin poissulkukriteerit, joita olivat pääpiirteissään yli 65 vuoden ikä, sydän- tai verisuonisairaus, sydämen lyöntitiheyteen vaikuttava lääkitys, astma tai merkittävä ylipaino. Testiohjelmaan yritettiin tällä tavoin saada mahdollisimman terveitä henkilöitä, joilla ei ollut sydämen toimintahäiriöihin liittyvää historiaa. Kaikkien ilmoittautuneiden joukosta tutkimukseen valittiin 64 henkilöä. Lopullisessa koehenkilöiden joukossa keski-ikä oli näin ollen 43,2 vuotta.

Koehenkilöiden tuli harjoitella 3 kertaa viikossa 10 viikon ajan vähintään puoli tuntia kerrallaan sydämen lyöntitiheyden ollessa 120 iskua minuutissa. Tällaisen harjoittelujakson on jo aiemmin todettu aiheuttavan huomattavia muutoksia iskutilavuudessa sekä sydänlihaksen massan määrässä. Koehenkilöille suoritettiin peruskunnon testaus perinteisellä polkupyöräkuormitustestillä ennen kuntoharjoittelujakson alkua sekä 10 viikon kuluttua tutkimusjakson päättyessä. Tällöin mitattiin mm. maksimaalinen hapenottokyky, jota käytettiin mittarina tarkasteltaessa kunnon muutoksia. Ballistokardiografinen tutkimus suoritettiin mittaustuolilla, jossa sydämen kehoon kohdistamat rekyylivoimat mitattiin pystysuorassa suunnassa tuolissa olevien voima-antureiden avulla, jolloin tuloksena saatiin voima-ballistokardiogrammi. Neljältä kanavalta saatujen BKG-sigaalien summaa käytettiin myöhemmässä vaiheessa tehdyssä signaalin analysoinnissa. Polkupyörätestien yhteydessä ennen ja jälkeen harjoittelujakson tehtyjen BKG-mittausten lisäksi rekisteröitiin yksikanavainen elektrokardiogrammi, rintalastan kiihtyvyys-ballistokardiogrammi sekä olkavarren valtimopulssikäyrä mansettimenetelmällä. Näistä EKG:a käytettiin syketaajuuden määrittämiseen kulloisenkin mittauksen kohdalla. Ennen jaksoa sekä sen loputtua 34 koehenkilölle tehtiin myös sydämen magneettikuvaus vasemman kammion lihasmassan, sydämen koon ja ejektiofraktion selvittämiseksi. Ejektiofraktiolla tarkoitetaan iskutilavuuden suhdetta koko kammion täyttötilavuuteen [4], [5].

BKG-signaalin käsittely ja analysointi

Kuvan 1 mukaiselta BKG-tuolilta mitatut signaalit luettiin, suodatettiin ja summattiin yhteen käyttäen J. Ritolan laatimia Matlab-pohjaisia funktioita. Summasignaalille tehtiin Fourier-muunnos käyttäen Matlabin funktioita fft (fast fourier transform), jonka jälkeen signaalin itseisarvoistettu taajuusspektri piirrettiin Matlabilla ja taajuusakseli skaalattiin kunkin mittauksen syketaajuuden mukaan. Näytteistystaajuus oli 1000 Hz, syketaajuus laskettiin BKG-mittausten

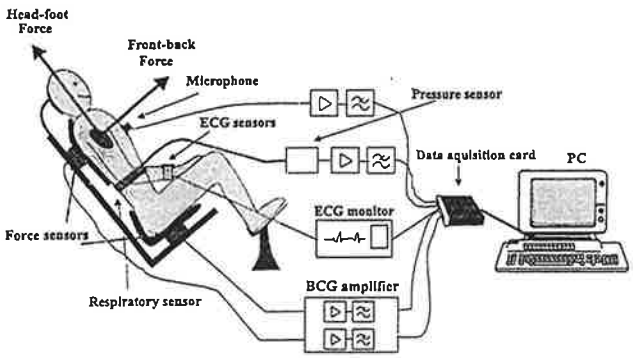

Kuva 1. Ballistokardiografinen mittaustuoli [6].

yhteydessä rekisteröidyistä EKG-signaaleista ja Fourier-muunnokseen otettiin koko minuutin mittainen signaali. Graafisen tarkastelun jälkeen taajuusspektrille laskettiin painopiste integroimalla spektriä ja edelleen tutkimalla, millä taajuudella spektrin pinta-alaintegraali saavutti puolivälinsä.

Suoran graafisen amplitudianalyysin ja spektrianalyysin lisäksi summasignaalille tehtiin matemaattinen muunnos, joka minimoi tuolin vaikutukset alkuperäiseen signaaliin. Muunnoksen avulla pystyasennossa tuolista mitattu signaali voidaan saada muistuttamaan vaaka-asennossa laakeroidulla pöydällä tehtyä BKG-mittausta tai ULF-alueen mittausta. Muunnos johdettiin tarkastelemalla aluksi pöytämallisen mittauslaitteen massakeskipisteitä erikseen keholle, verelle ja pöydälle. Kaavio pöytämallisesta mittauslaitteesta on esitetty kuvassa 2, missä M on kehon kiinteä massa, m veren massa ja m_p pöydän massa. Vastaavasti massakeskipisteiden sijainnit ovat keholle $x_0 + X$, verelle $x_0 + x$ ja pöydälle $x_0 + x_p$. Koko systeemin massakeskipisteeksi saadaan siis

$$X_c = \frac{M(x_0 + X) + m(x_0 + x) + m_p(x_0 + x_p)}{M + m + m_p} = x_0 + \frac{MX + mx + m_p x_p}{M + m + m_p}, \quad (1)$$

joka on vakio, sillä systeemiin ei vaikuta ulkoisia vaakavoimia ja nettosiirtymä on nolla. Derivoimalla systeemin massakeskipisteen lauseke ajan suhteen (X, x_p vakioita) saadaan

$$\dot{X}_c = \dot{x}_0 + \frac{m\dot{x}}{M + m + m_p} = 0, \quad (2)$$

jolloin

$$\dot{x}_0 = -\frac{m}{M + m + m_p}\dot{x} = \dot{X}_{BKG}, \quad (3)$$

missä $X_{BKG} = x_0 + a$ on saatu mittaustulos pöydällä ja a = vakio.

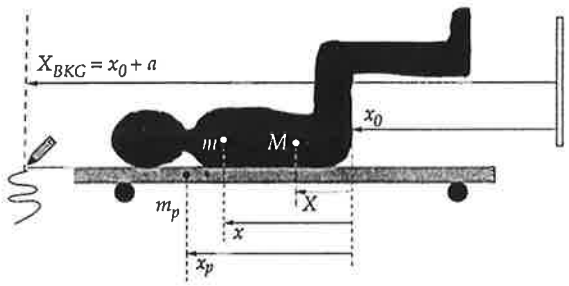

Kuva 2. Kaavio pöytämallisesta mittauslaitteesta systeemin eri osien massakeskipisteet huomioiden. Signaali X_{BKG} on mittaustuloksena saatava siirtymä-BKG pöydällä mitattuna.

Kuvassa 3 on esitetty yhden vapausasteen malli tuolityyppiselle mittauslaitteelle. Tällöin $M + m$ on koko kehon massa, johon lasketaan siis erikseen kiinteä massa ja veri, m_t on mittaustuolin massa, x_c koko kehon massakeskipiste, x_0 tuolin pystykoordinaatti, k tuolin jousivakio ja l jousen pituus venymättömänä. Systeemin resonanssikulmataajuuden neliölle voidaan tällöin muodostaa lauseke

$$\omega_0^2 = \frac{k}{M+m+m_t}. \tag{4}$$

Koko kehon massakeskipisteen lauseke on

$$x_c = x_0 + \frac{MX + mx}{M+m}, \tag{5}$$

josta derivoimalla ja yhtälöä (3) käyttämällä saadaan

$$\dot{x}_c = \dot{x}_0 + \frac{m\dot{x}}{M+m} = \dot{x}_0 - (1 + \frac{m_p}{m+M})\,\dot{X}_{BKG}\ . \tag{6}$$

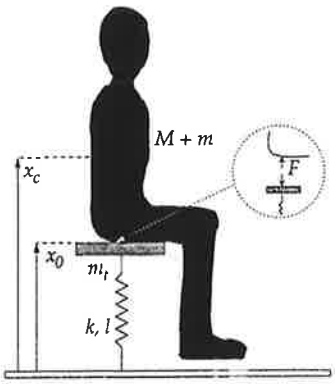

Kuva 3. Yhden vapausasteen malli tuolityyppiselle mittauslaitteelle, jossa tuolin elastisuus on mallinnettu jousella.

Henkilön ja tuolin liikeyhtälöiksi voidaan siis kirjoittaa

$$(M+m)\ddot{x}_c = F - (M+m)g\ , \tag{7}$$

$$m_t\ddot{x}_0 = -F - m_t g - k(x_0 - l)\,. \tag{8}$$

Lasketaan yhtälöt (7) ja (8) puolittain yhteen, jolloin saadaan

$$(M+m)\ddot{x}_c + m_t\ddot{x}_0 = -(M+m+m_t)g - k(x_0 - l)\,. \tag{9}$$

Yhtälöön (9) sijoitetaan vielä

$$x_0(t) = y_0(t) + x_{st}\ , \tag{10}$$

missä

$$x_{st} = l - \frac{M+m+m_t}{k}g \tag{11}$$

on tuolin siirtymä staattisessa tilanteessa (ei värähtelyjä). Yhtälöitä (6), (10) ja (11) käyttämällä saadaan yhtälöstä (9) tuolin värähtelyvasteen $y_0(t)$ differentiaaliyhtälöksi

$$\ddot{y}_0 + 2\zeta\omega_0\dot{y}_0 + \omega_0^2 y_0 = \frac{M+m+m_p}{M+m+m_t}\ddot{X}_{BKG}\,, \tag{12}$$

missä yhtälön vasemmalle puolelle on lisätty tuolin vaimennuksesta aiheutuva termi. Yhtälö (12) ilmaisee tuolilla ja pöydällä mitattujen BKG-signaalien välisen yhteyden. Seuraavaksi muodostetaan BKG-pöytäsignaalit, kun tuolisignaali $y_0(t)$ tunnetaan. Merkitään

$$X = \frac{M+m+m_p}{M+m+m_t}X_{BKG}\,, \tag{13}$$

jolloin yhtälö (12) tulee muotoon

$$\ddot{X}(t) = \ddot{y}_0(t) + 2\zeta\omega_0\dot{y}_0(t) + \omega_0^2 y_0(t)\,. \tag{14}$$

Integroimalla yhtälöä (14) saadaan

$$\dot{X}(t) = \dot{y}_0(t) + 2\zeta\omega_0 y_0(t) + \omega_0^2\int_0^t y_0(\eta)d\eta\,, \tag{15}$$

$$X(t) = y_0(t) + 2\zeta\omega_0\int_0^t y_0(\eta)d\eta + \omega_0^2\int_0^t\int_0^\xi y_0(\eta)d\eta d\xi\,. \tag{16}$$

Yhtälöiden (14)-(16) osoittamalla tavalla voidaan siis pöydällä mitatut kiihtyvyys-, nopeus- ja siirtymä-BKG:t laskea tuolisignaalin $y_0(t)$ avulla. Lausekkeen (14) mukainen kiihtyvyys-ballistokardiogrammi $\ddot{X}(t_i)$ laskettiin keskeisdifferenssiä käyttäen, missä i = 2,..., N-1, signaalin pituus on N merkkiä, h on askelväli, $t_i = ih$ ja $y_i = y_0(t_i)$. Nopeussignaalin $\dot{X}(t_i)$ muodostamiseen käytettiin Matlab-funktiota, joka integroi kiihtyvyyssignaalin trapetsikaavaa käyttäen. Saatu nopeussignaali lisäksi keskiarvoistettiin nollaksi, jotta edelleen laskettavaan siirtymäsignaaliin $X(t_i)$ ei muodostuisi kumuloituvaa komponenttia. Lopuksi vielä siirtymäsignaali keskiarvoistettiin nollatasoon.

TULOKSET

Taajuussiirtymä ja korrelaatio hapenottokyvyn kanssa

Kuvassa 4 nähdään koehenkilön 2021* (katso Taulukko 1) summasignaalien taajuusspektrit sekä ennen harjoittelua että harjoittelun jälkeen. Kuvasta voidaan havaita harjoittelun jälkeisen spektrin siirtymä suurempia taajuuskomponentteja kohti. Kuvan 4 spektrit on kerrottu funktiolla $y = x/5$ painottaen korkeampia taajuuksia ja esitetty logaritmisella y-asteikolla. Spektrien taajuusakselit on lisäksi skaalattu x-suunnassa kunkin mittauksen syketaajuudella. Taulukkoon 1 on kirjattu eri koehenkilöiden kunkin mittauksen syketaajuus, taajuusspektristä laskettu spektrin painopiste sekä rasituskokeella mitattu maksimaalinen hapenottokyky yksiköissä ml/kg/min. Kaikista näistä on myös laskettu prosentuaaliset muutokset alkumittauksen ja loppumittauksen välillä. Näissä tuloksissa negatiivinen muutos ilmentää painopisteen siirtymistä matalammille taajuuksille, positiivinen muutos korkeammille taajuuksille. Taulukon 1 koehenkilöille 2001 ja 2021 on tehty

TAULUKKO 1. Maksimaalinen hapenottokyky ja taajuusspektrin painopiste sekä näiden prosentuaaliset muutokset alku- ja loppumittauksen välillä kullekin koehenkilölle. Lisäksi taulukossa on esitetty syketaajuus jokaisen mittauksen aikana EKG:n avulla laskettuna ja syketaajuuden muutokselle on laskettu prosentuaalinen arvo.

	Ennen harjoittelujaksoa			Harjoittelujakson jälkeen					
Koe-henkilö	Syke-taajuus / Hz	Paino-piste / suht.	$V(O_2)_{max}$ (ml/kg/min)	Syke-taajuus / Hz	Paino-piste / suht.	$V(O_2)_{max}$ (ml/kg/min)	Syketaajuuden muutos / %	Painopisteen muutos / %	$V(O_2)_{max}$ muutos / %
2001*	1,2667	6,3888	36	1,0000	8,6673	37	-21,0547	35,6640	2,7778
2001**	1,0167	7,7900	38	1,0000	8,6673	37	-1,6426	11,2619	2,7778
2010	1,1500	6,3655	43	1,0167	7,8720	49	-11,5913	23,6666	13,9535
2018	1,0333	7,0518	38	0,9333	8,0192	44	-9,6777	13,7185	15,7895
2021*	1,1500	6,2350	37	0,9333	8,2340	47	-18,8435	32,0609	27,0270
2021**	1,0833	6,6528	37	0,9333	8,2340	47	-13,8466	23,7674	27,0270
2026	1,0333	7,4704	44	0,9333	8,1266	45	-9,6777	8,7840	2,2727
2050	1,4167	5,8292	44	1,1833	6,6834	44	-16,4749	14,6538	0,0000
2015	1,5167	5,3680	34	1,3333	6,1125	39	-12,0920	13,8692	14,7059
2053	1,2667	6,6132	31	1,2500	6,7697	33	-1,3184	2,3665	6,4516
2011	1,0667	8,0840	46	0,9833	6,8276	54	-7,8185	12,2222	17,3913
2012	0,9500	9,1700	35	0,8167	10,0776	35	-14,0316	9,8975	0,0000
2013	1,3000	6,6304	34	1,2833	6,9940	42	-1,2846	5,4838	23,5294
2014	1,0833	7,2688	43	1,2000	6,2411	40	10,7726	-14,1385	-6,9767
2019	1,1833	6,2885	41	1,4333	5,1736	40	21,1274	-17,7305	-2,4390
2031	1,3000	7,1040	37	1,3667	7,0394	39	5,1308	-0,9093	5,4054
2047	1,3000	6,7456	39	1,3167	6,2484	42	1,2846	-7,3707	7,6923
2055	0,9500	8,8025	43	1,0000	7,6152	46	5,2632	-13,4882	6,9767

kaksi alkumittausta. Taulukossa yksi tähti (*) ilmentää ensimmäisen alkumittauksen ja kaksi tähteä (**) toisen alkumittauksen vertailua loppumittaukseen. Korrelaatioanalyysi antoi selvän yhteyden ($r^2 = 0.78$) maksimaalisen hapenottokyvyn muutoksen ja spektrin painopisteen muutoksen kanssa.

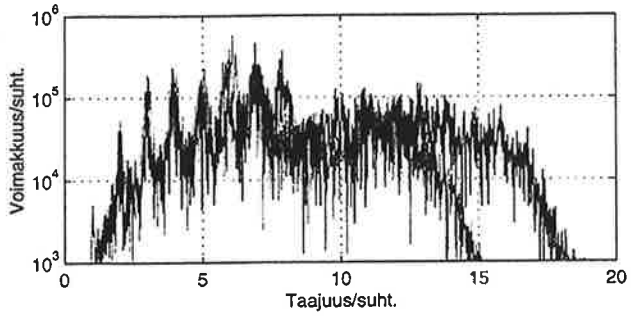

Kuva 4. Taajuusspektrit kerrottuna funktiolla $y = x/5$ ja esitettynä logaritmisella y-asteikolla.

IJ-amplitudin kasvu

Edellä johdetun matemaattisen muunnoksen (yhtälöt (14)–(16)) avulla saatiin alkuperäinen tuolilla mitattu signaali muistuttamaan pöytämallisella laitteella mitattua signaalia. Muunnoksella saadut signaalit siirtymälle, nopeudelle ja kiihtyvyydelle ennen ja jälkeen harjoittelun on esitetty kuvissa 5 ja 6

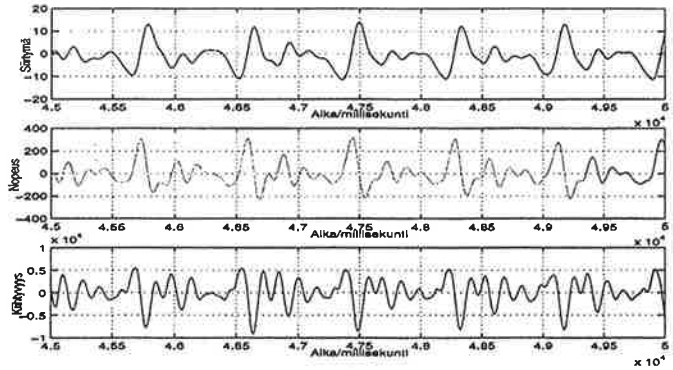

Kuva 5. Muunnoksella saadut ballistokardiogrammit siirtymälle, nopeudelle ja kiihtyvyydelle ennen harjoittelua. Pystyakselien yksiköt ovat suhteellisia.

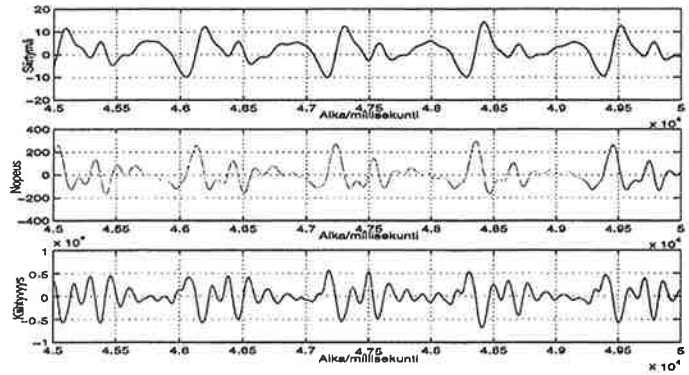

Kuva 6. Kuten kuva 5, mutta harjoittelujakson jälkeen.

koehenkilölle 2021*. Tuolirakenteen suhteellisena vaimennuksena käytettiin arvoa $\zeta = 0.1$ ja resonanssikulmataajuutena tuolin mittauksista saatua arvoa $\omega_0 = 2\pi \cdot 12Hz$. Kuvassa 7 on esitetty muunnoksella saadut siirtymä-ballistokardiogrammit ennen harjoittelua ja harjoittelujakson jälkeen. Signaaleista voidaan helposti havaita I- ja J-huippujen välisen nousun suureneminen.

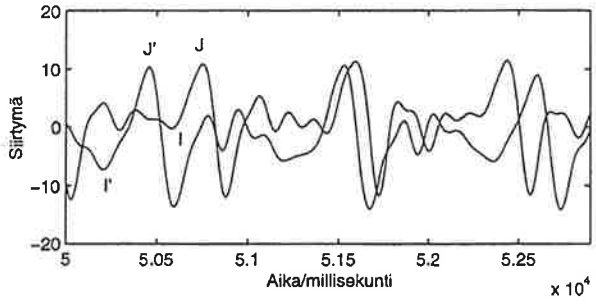

Kuva 7. Muunnoksella saadut siirtymä-ballistokardiogrammit ennen harjoittelujaksoa ja jakson jälkeen. Kuvasta havaitaan selvästi harjoittelun I J-amplitudia kasvattava vaikutus $(I'J' > IJ)$. Siirtymän yksikkö on suhteellinen.

TULOSTEN ANALYSOINTI

Taulukosta 1 nähdään, että painopisteen muutos kohti suurempia taajuuksia ei ole kaikilla koehenkilöillä huomattava ja muutamalla muutos on jopa negatiivinen eli spektri on siirtynyt matalammille taajuuksille. Kuitenkin niillä koehenkilöistä, joilla maksimaalisen hapenottokyvyn kasvu oli merkittävä, havaittiin selvä sydämen supistusvireyden paranemiseen viittaava spektrisiirtymä. Näillä henkilöillä todetut muutokset taajuusspektrissä todennäköisesti aiheutuvat sydämen tehostuneesta pumppauskyvystä, mutta myös ääreisverenkierron vastus sekä autonominen hermosto saattavat vaikuttaa havaittuun siirtymään [5]. Lisäksi on syytä todeta, että syketaajuuden pieneneminen jo sinällään siirtää skaalattua spektriä korkeammille taajuuksille. Tämä ei kuitenkaan suoraan selitä spektrin jakaumassa tapahtuvia selviä muodonmuutoksia.

Kuvissa 5 ja 6 nähdään muunnoksella lasketut siirtymä-, nopeus- ja kiihtyvyys-ballistokardiogrammit koehenkilölle 2021* ennen ja jälkeen harjoittelujakson. Aiemmissa tutkimuksissa [6] on esitetty, että siirtymä-BKG ilmoittaisi sydämen pumppaaman veren määrän eli toisin sanoen iskutilavuuden. Nopeuden ollessa siirtymän ensimmäinen derivaatta ilmentäisi nopeus-BKG tällöin veren virtausta aortassa. Vastaavasti kiihtyvyys-BKG:llä voitaisiin havainnoida veren kiihtyvyyttä aortassa. Tämän veren virtauksen kiihtyvyyden on ehdotettu olevan hyvä sydämen supistuskyvyn mittari [6]. Lisäksi kiihtyvyyttä laskevassa aortassa pidetään hyvänä sydänlihaksen yleisen toiminnan indikaattorina [6]. Kuvista 5 ja 6 huomataan, että siirtymäsignaalin I-huippua vastaa aina kiihtyvyyden maksimi, mikä on todettu jo aikaisemmissa tutkimuksissa [6]. Voidaan siis päätellä muunnoksen toimivan hyvin, sillä alkuperäisistä tuolilla mitatuista BKG-signaaleista muunnetut signaalit vastaavat muodoltaan kirjallisuudessa esiintyviä pöydällä mitattuja ballistokardiogrammeja. Erityisesti siirtymäsignaali vastaa hyvin viitteessä [7] esitettyä signaalia (ks. kuva 8), missä siirtymäsignaalin suurien huippujen ajoitus ja muoto näkyvät erityisen selvästi. Vastaavuus kirjallisuudessa esitettyihin ballistokardiogrammeihin huomataan jo pelkästään tarkastelemalla silmämääräisesti huippujen ajoitusta: jokaisen nopeussignaalin suuremman maksimin jälkeen tulee siirtymän suurin maksimi, jota vastaa kiihtyvyyden pienin minimi.

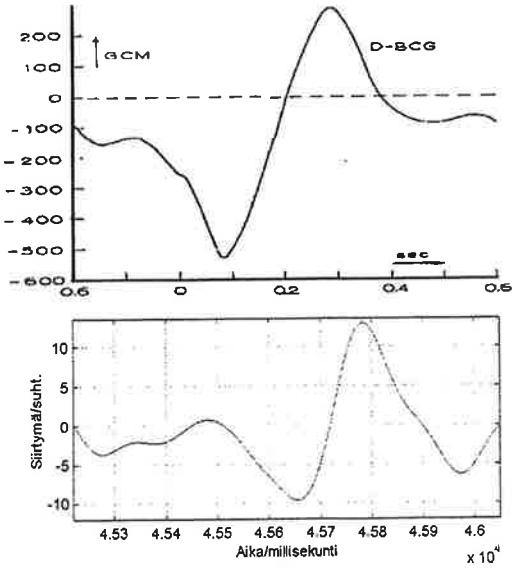

Kuva 8. Viitteen [7] ja tämän työn muunnoksella johdettujen siirtymäsignaalien vertailu. Alkuperäinen BKG-signaali, josta siirtymä-signaali on laskettu, on peräisin koehenkilön 2021* alkumittauksesta.

Vastaavasti jokaista kiihtyvyyden pienintäkin maksimia vastaa siirtymän minimi. Lisäksi kuvien 5 ja 6 siirtymäsignaaleista huomataan pienempien värähtelyjen poistuminen, ts. signaali on 'rauhoittunut'. Jo tämä itsessään tekee signaalin tulkitsemisen helpommaksi. Edellä mainittujen tulosten vastaavuuksien avulla voidaan todeta edellä johdetun matemaattisen muunnoksen toimivan hyvin haluttaessa minimoida tässä työssä mittauslaitteena käytetyn tuolin dynaamisia vaikutuksia primääriin BKG-signaaliin.

JOHTOPÄÄTÖKSET

Tässä työssä johdetulla matemaattisella muunnoksella saadut signaalit vastaavat hyvin kirjallisuudessa esiintyviä pöydällä rekisteröityjä ballistokardiogrammeja. Muunnoksen tarkkuutta voitaisiin kasvattaa lisäämällä systeemiin toinen vapausaste siten, että henkilön ja tuolin väliin mallinnettaisiin jousi ja vaimennin. Tuolin pehmusteet ja ihmisen lihakset sekä rasvakudos saattavat vaimentaa signaalia omalta osaltaan, jolloin vaimennetun kahden vapausasteen systeemin käyttäminen olisi perusteltua. Koehenkilöillä tapahtuneet kunnon muutokset ovat myös nähtävissä taajuusspektristä. Vaikka kuntoharjoittelun aikana kehossa tapahtuvat monimuotoiset muutokset kaikki saattavat vaikuttaa spektrin siirtymiseen, on kuitenkin varmaa, että korkeampitaajuisten värähtelyjen lisääntyminen indikoi fyysisen kunnon nousua.

Tutkimustulosten perusteella ballistokardiografinen tuoli voi toimia helppokäyttöisenä mittausmenetelmänä kuntourheilijoiden sydän- ja verenkiertoelimistön kehityksen seurannassa. Laitteistoa voitaisiinkin kehittää suuntaan, jossa henkilön fyysisen kunnon tasoa kvantisoitaisiin jonkinlaisen laskettavan 'kuntoindeksin' avulla. Mahdollisuudet myös kliiniseen käyttöön ovat olemassa. Mittausmenetelmää voitaisiin käyttää mm. sydämen vajaatoiminnan hoidon seurannassa ja lääkityksen oikeassa mitoituksessa. Tällöin etsittäisiin sellainen lääkityksen määrä, jolla pumppauskyky ei enää huomattavasti vastaa lääkityksen kasvuun. Samantyyppisesti BKG-mittauksia voitaisiin käyttää digitaliksen annostelussa, jossa ongelmana on se, että lääke ei vaikuta kaikilla potilailla, mutta sivuvaikutukset ovat kuitenkin olemassa. Lääkitys voitaisiin tällöin nopeasti lopettaa, jos BKG-mittauksissa ei todettaisi minkäänlaista pumppauskyvyn kasvua. BKG-mittauksilla on myös mahdollisuuksia toimia etälääketieteellisenä menetelmänä esimerkiksi kotihoidon seurannassa: jatkokehityksen avulla voitaisiin tuoliin lisätä verenpainemittari ja muutama EKG-elektrodi käsinojiin. Tällä tavoin lääkäri voisi esimerkiksi verkon välityksellä seurata potilaan tilannetta työpaikaltaan käsin tietyin väliajoin ja pakollisia kontrollikäyntejä voitaisiin näin ollen vähentää. Tässä mielessä ballistokardiografia yhdistettynä muihin seurantamenetelmiin vähentäisi myös sydän- ja verisuonisairauksiin liittyviä kansantaloudellisia kustannuksia.

VIITTEET

[1] S'Jongers J.J., Segers M., "Differences Between the Ballistocardiograph of Athletes and of Sedentary Persons, Preliminary Note", *Ballistocardiography. Proc. 6th Europ. Congr. Ballistocardiography*, London 1967; Bibl. cardiol. 21: 145-151 (Karger, Basel/New York 1968).

[2] Jokl E., "Ballistocardiographic Studies on Athletes", *The American Journal of Cardiology*, Vol. III, No. 1, 1959.

[3] McKay W.P., "Sternal Acceleration Ballistocardiography and Arterial Pressure Wave Analysis to Determine Stroke Volume", *Clin Invest Med*, Vol. 22, 4-13, 1999.

[4] Kettunen R., Heikkinen J., Sepponen R., Sipola P., Anttonen T., Kilpeläinen A., Koskinen S., Ritola J., von Hertzen R., Järvinen E., "Ballistocardiography in Physical Training – a Preliminary Study", *International Journal of Bioelectromagnetism*, Volume 3, Number 2, 2001.

[5] Kettunen R., Heikkinen J., Sepponen R., Sipola P., Anttonen T., Ritola J., Kilpeläinen A., Järvinen E., von Hertzen R., "Ballistokardiografinen sydäntutkimusjärjestelmä kuntourheilijoiden harjoitteluseurannassa", väliraportti 14.8.2001.

[6] Vähärahka T., *Ballistocardiograms at Rest and After Exercise Recorded with a New Chair-type Apparatus. A Preliminary Study*. Master's Thesis, Helsinki University of Technology, 1997.

[7] Noordergraaf A., "Further Studies on a Theory of the Ballistocardiogram", *Circulation*, Vol. XXIII, p. 413-425, March 1961.

MEASUREMENT OF THE ANISOTROPIC ELASTIC PROPERTIES OF THE PAPER WEB IN PLANE STRESS CASE

JORMA KINNUNEN
Metso Paper Inc.
Wärtsilänkatu 100
04400 JÄRVENPÄÄ
FINLAND
jorma.kinnunen@metso.com

ABSTRACT

Paper material is a true anisotropic material. To understand the behavior of the paper web in web handling applications, using the usual orthotropic material assumptions gives inaccurate results. The literature of anisotropic materials is very limited. Most papers handling anisotropy are essentially limited to orthotropic materials.

Paper is not purely elastic material, but in many cases, when the stresses are low, the behavior can be essentially explained by elastic deformations. The methods and devices to measure *all* elastic parameters, even in plane stress case, are not publicly available. In this presentation, a method for measuring full elastic parameter matrix by image deformation analysis is detailed.

Knowing the elastic orientation of the web is essential in web handling. The elastic orientation of paper material is related to the fiber orientation. Some results of measured correlation between fiber orientation and elastic orientation is also described.

1. INTRODUCTION

In most part of the web handling, we can approach the web as two-dimensional material. This leads to assumptions of *generalized plane stress*. We do not assume that the tension is constant over the thickness of the web, we just have very limited information of the tension distribution. In contrary, we know that the paper material is very inhomogenous in the thickness direction, and also the stress distribution might be very inhomogenous. Fortunately, integrating the three-dimensional stress and strain equations over the thickness of the web can derive the generalized plane stress equations (Lekhnitskii 1968). By using two-dimensional approach, we can avoid problems connected to thickness of the web. In the case of paper material the definition of the thickness is problematic. We can measure caliper c instead. Caliper is measured by laying the paper sample between two parallel plates, compressed with certain pressure, and measuring the distance between the plates. The measured caliper depends of the area and pressure of those plates.

2. MEASURES OF ELASTIC PROPERTIES, STRESS AND STRAIN

The routinely measured elastic properties of paper material are tensile stiffness S and bending stiffness[1] B. They are usually measured in machne direction (MD) and in cross-machine direction (CD) of the web. We can not measure directly the modulus of elasticity, because we have very limited information of the distribution of the stresses and strains in the thickness direction. The tensile stiffness can be measured directly. Theoretically tensile stiffness is the modulus of elasticity integrated over the thickness. If we divide the tensile stiffness by the caliper we can get the average modulus of elasticity of the paper. Because we do not know the distribution of the modulus of elasticity and the thickness, we can not calculate the bending stiffness using tensile stiffness of the material, but it has to be measured directly.

In web handling, the web tension $\{T\}$, is the measure of the stress. The word *tension* reminds us of the fact that an unsupported thin web material can not take compression, it buckles at very low compressive tension. Web tension is the force divided by linear length. Also, it can be understood theoretically as the stress integrated over the thickness of the web. In certain coordinate system, the web tension can be divided in normal tensions T_x and T_y and shear tension T_{xy}. In the paper machines, we can measure only the machine direction tension. From this reason, scalar T denotes very often the machine direction normal tension component $T=T_{MD}$.

Paper material is very complicated composite material with fibrous structure. The deformation of paper material, in general, is rather complicated matter. The deformation can be a combination of elastic strain, plastic strain, creep, moisture expansion and temperature expansion. In many cases, when elastic strain is dominating, we can simplify the treatment by dividing the total deformation in two parts: the elastic strain $\{\varepsilon\}$ and the material expansion by other reasons $\{\alpha\}$.

$$\begin{Bmatrix} \partial u/\partial x \\ \partial v/\partial y \\ \partial u/\partial y + \partial v/\partial x \end{Bmatrix} = \begin{Bmatrix} \varepsilon_x \\ \varepsilon_y \\ \gamma_{xy} \end{Bmatrix} + \begin{Bmatrix} \alpha_x \\ \alpha_y \\ \alpha_{xy} \end{Bmatrix} \tag{1}$$

In this equation, u and v are the displacements of material particles in x and y directions. The measures of the strain in the coordinate system x,y are the engineering strains ε_x and ε_y in the direction of the coordinate axes, and the shear strain γ_{xy} in radians. In this work, we concentrate on elastic strain, and in the measurements we try to keep other expansions minimal. Some creep always happens, even at low tension levels, giving some error to the measurements. In these tests, we use small strain assumptions and engineering strains, because dry paper material usually breaks at relatively low 1...2 % strain.

3. UNIAXIAL TENSILE TEST

With the uniaxial tensile test according to figure 1a, we can get information of the tensile stiffness, Poisson's ratio and shear deformation in one direction of the material. Because the paper material is very thin, it is quite difficult to apply shear stresses to the sample, and we can not measure shear modulus directly. The method to define all the elastic parameters of anisotropic materials by simple tensile tests is based on the idea of Salonen (1999). Same kind of method to determine the

[1] Most authors use S_t for tension stiffness and S_b for bending stiffness, but because both are tensor quantities, we do not want to use subindex with basic symbols.

shear modulus of paper has been used by Seo (1999). If we measure the strains under the influence of uniaxial stress in different directions, we can collect information to determine all the terms of the material compliance matrix.

The global X,Y coordinate system is fixed to the material in the reference state. The direction of X-coordinate coincides to the machine direction of the paper machine (MD), and Y-coordinate points to cross-machine direction (CD). The local x,y coordinate system rotates with material sample direction. The angle of the loading direction and the direction of the material sample is denoted by β. Also, the tensions, strains and material parameters referring to certain direction are labeled by superscript β. The matrices and vectors are labeled with subscript. For example $[D]_\beta$ denotes the material compliance matrix rotated to angle β. The symbols and matrices without a reference to rotated coordinate system, refer to global coordinates, where $\beta=0$.

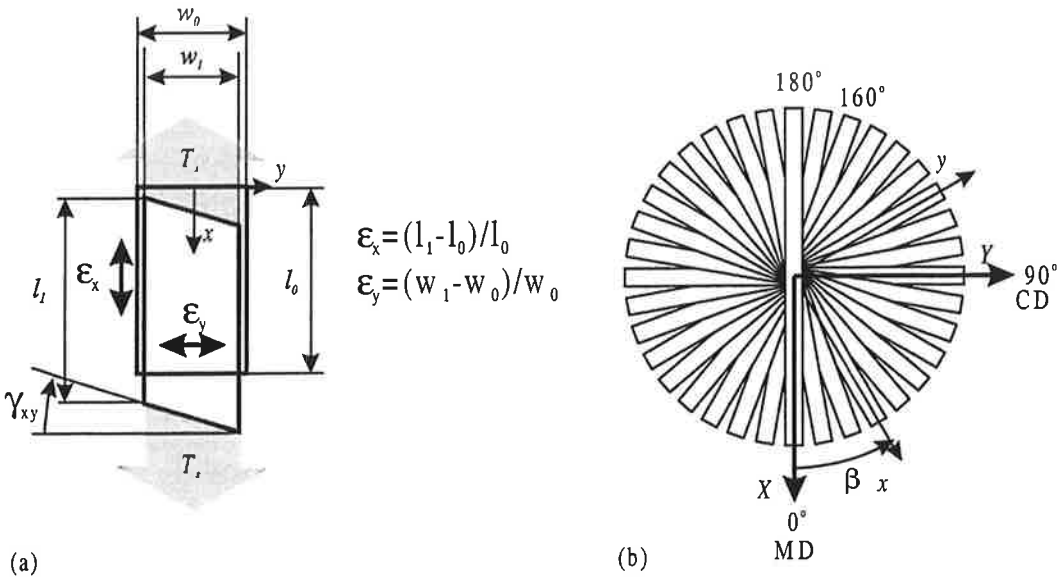

Figure 1. Uniaxial tensile test. (a) Measurements of plane strains ε_x, ε_y and γ_{xy}. (b) Sample stripe-cutting directions. MD=machine direction, CD = cross machine direction

In the case of paper material, the reference tension T_0 can not be zero, because the thin paper is not necessarily straight, and the measurement of dimensions is unreliable. In this test we have used low initial tension as a reference and forced the tension-strain curves to go trough origin by curve fitting.

The measurement arrangement is shown in figure 2. To minimize the end effects caused by end clamps, quite long test stripes have been used. Also, the clamps have been pivoted from the middle of the grip line of the clamps. We have tested the effect of the clamps to the shear strains by cutting the ends of the test pieces to narrow (2mm) stripes. Within the measurement accuracy, the results of striped samples can not be differentiated from the ordinary ones.

Especially the measurement of the shear strain is rather sensitive to errors in clamping. To minimize this effect, and to eliminate unsymmetries in the measurement device, every stripe has been measured twice using both sides. When we turn the sample around the longitudinal axis, we

should get the same shear strain with opposite sign. The shear strain values have been calculated from the average of the absolute values of these measurements. The strains have been measured in a small area in the middle of the stripe by image analysis described in chapter 5.

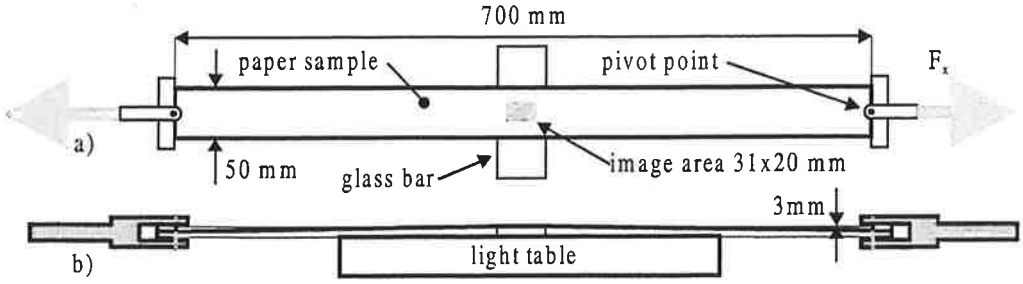

Figure 2. The measurement device and the arrangement. a) Front view b) Side view

The sample has been forced flat in the image area by bending it slightly over a glass bar as shown in figure 2b. If we assume the coefficient of friction to be 0.3, the friction force should be only 0.5 % of the tensile force, with this geometry. Of course, some forces caused by static electricity between the glass material and paper, and adhesive forces, can decrease the accuracy of the device. In future, we should develop air lubrication between the support plate and the sample, so that we can force the samples flat even at low-tension levels, without having disturbing frictions.

4. THE MATERIAL COMPLIANCE MATRIX AND THE ENGINEERING PARAMETERS

According to the generalized Hooke's law, the linear elastic relationship between stresses and strains can be given in a form of compliance matrix $[D]$ or material stiffness matrix $[C]$ according to equations (2) and (3). The compliance matrix is the inverse of the stiffness matrix $[D] = [C]^{-1}$.

$$\{\varepsilon\} = [D]\{T\} \tag{2}$$

$$\{T\} = [C]\{\varepsilon\} \tag{3}$$

If the material is isotropic or the material has elastic potential function, the matrix $[D]$ and $[C]$ are symmetric (Malvern 1977). Because the paper material is anisotropic and not perfectly elastic, the measured values of the compliance matrix do not have to be symmetric. In this measurement, however, we approximate the material as elastic and measure the *elastic* parameters. The equation (2) in detail, not including the assumption of symmetry, at local coordinate system rotated at angle β is written

$$\begin{Bmatrix} \varepsilon_x \\ \varepsilon_y \\ \gamma_{xy} \end{Bmatrix}_\beta = \begin{bmatrix} D_{11} & D_{12} & D_{13} \\ D_{21} & D_{22} & D_{23} \\ D_{31} & D_{32} & D_{33} \end{bmatrix}_\beta \begin{Bmatrix} T_x \\ T_y \\ T_{xy} \end{Bmatrix}_\beta \tag{4}$$

If we know the material parameters [D] or [C] in some coordinate system, we can rotate the matrix by using rotation matrix [R]. Derivation of the material stiffness rotation in matrix formulation is lucidly detailed in the book of Cook et al. (1989). In plane problems we need the rotation matrix [R] and the inverse of the matrix. The inverse of the rotation matrix can be achieved from the rotation matrix by replacing the rotation angle β by $-\beta$.

$$[R]_\beta = \begin{bmatrix} c^2 & s^2 & cs \\ s^2 & c^2 & -cs \\ -2cs & 2cs & c^2-s^2 \end{bmatrix} \quad and \quad [R]_\beta^{-1} = \begin{bmatrix} c^2 & s^2 & -cs \\ s^2 & c^2 & cs \\ 2cs & -2cs & c^2-s^2 \end{bmatrix} \tag{5}$$

$$where \quad c = \cos(\beta) \ , \ s = \sin(\beta)$$

The rotation of the stiffness matrix from global coordinate system to the local coordinate system, which is rotated by angle β, as in figure 1, can be carried out by using equation (6a). The inverse rotation is defined by (6b).

$$\begin{aligned} [C]_\beta &= [R]_\beta^{-T}[C][R]_\beta^{-1} \\ [C] &= [R]_\beta^{T}[C]_\beta[R]_\beta \end{aligned} \tag{6a,b}$$

Because the compliance matrix $[D]_\beta$ is the inverse of the stiffness matrix $[C]_\beta$ at any coordinate system, we can derive the rotations of the compliance matrix by taking matrix inverses of the equations (6a,b).

$$\begin{aligned} [D]_\beta &= [R]_\beta[D][R]_\beta^{T} \\ [D] &= [R]_\beta^{-1}[D]_\beta[R]_\beta^{-T} \end{aligned} \tag{7a,b}$$

In the uniaxial tensile test at certain angle β, the tension vector is $\{T\}_\beta=\{T_x,0,0\}_\beta^T$. Multiplying this vector with the rotated compliance matrix (7a), we can get three equations of the strains at that angle.

$$\begin{Bmatrix} \varepsilon_x \\ \varepsilon_y \\ \gamma_{xy} \end{Bmatrix}_\beta = T_x^\beta [A]_\beta \{D\} \tag{8}$$

Where $\{D\}$ is a vector of nine material parameters in the global coordinate system, T_x^β is the uniaxial tension in the test. The coefficient matrix $[A]_\beta$ depends only on the rotation angle (sample angle) β.

$$\{D\} = \{D_{11} \quad D_{12} \quad D_{13} \quad D_{21} \quad D_{22} \quad D_{23} \quad D_{31} \quad D_{32} \quad D_{33}\}^T$$

$$[A]_\beta = \begin{bmatrix} c^4 & c^2s^2 & c^3s & c^2s^2 & s^4 & cs^3 & c^3s & cs^3 & c^2s^2 \\ c^2s^2 & s^4 & cs^3 & c^4 & c^2s^2 & c^3s & -c^3s & -cs^3 & -c^2s^2 \\ -2c^3s & -2cs^3 & -2c^2s^2 & 2c^3s & 2cs^3 & 2c^2s^2 & c^4-c^2s^2 & c^2s^2-s^4 & c^3s-cs^3 \end{bmatrix}_\beta$$

$s = \sin(\beta), \quad c = \cos(\beta)$

If we assume symmetry of the compliance matrix, we have six independent material parameters.

$$\{D\} = \{D_{11}, D_{12}, D_{13}, D_{22}, D_{23}, D_{33}\}^T$$

$$[A]_\beta = \begin{bmatrix} c^4 & 2c^2s^2 & 2c^3s & s^4 & 2cs^3 & c^2s^2 \\ c^2s^2 & c^4+s^4 & cs^3-c^3s & c^2s^2 & c^3s-cs^3 & -c^2s^2 \\ -2c^3s & 2c^3s-2cs^3 & c^4-3c^2s^2 & 2cs^3 & 3c^2s^2-s^4 & c^3s-cs^3 \end{bmatrix}_\beta$$

Here, the strains are measured at angle β and the uniaxial stress acts at the same angle. The material parameter vector $\{D\}$ is a vector of independent components of $[D]$. In the symmetric case, we have six unknown material parameters to solve. Measuring at two different directions gives us six equations, but they are not linearly independent. Measuring at three different directions gives enough information to determine the six independent parameters. To increase accuracy of the measurement we can measure stripes at different angles (see fig. 1b), and solve the parameters from the overdetermined system by least squares method.

A. L. Rabinovich has proposed a system of "technical constants" for the general case of anisotropy (Lekhnitskii 1963). By modifyind the system and notation[2] of the general anisotropic case to the 2-dimensional plane stress case, we can express the compliance matrix in the terms of the engineering parameters.

$$\begin{bmatrix} \varepsilon_x \\ \varepsilon_y \\ \gamma_{xy} \end{bmatrix}_\beta = \begin{bmatrix} \frac{1}{S_x} & -\frac{\nu_{yx}}{S_y} & \frac{\eta_{xy}}{S_{xy}} \\ -\frac{\nu_{xy}}{S_x} & \frac{1}{S_y} & \frac{\eta_{yx}}{S_{xy}} \\ \frac{\eta_x}{S_x} & \frac{\eta_y}{S_y} & \frac{1}{S_{xy}} \end{bmatrix}_\beta \begin{bmatrix} T_x \\ T_y \\ T_{xy} \end{bmatrix}_\beta \tag{9}$$

Here the coordinates x,y refer to the local coordinate system defined by angle β. S_x is the tensile stiffness defined by uniaxial tensile test $S_x = T_x/\varepsilon_x$. The tensile stiffness S_y can be defined by rotating the coordinate system 90 degrees eg. $S_y^\beta = S_x^{\beta+\pi/2}$. S_{xy} is the shear stiffness of the material.

[2] Tensile stiffness and the shear stiffness are the Young's modulus and shear modulus integrated over the thickness of the material. Web tension is the stress integrated over the thickness. The notation of the shear couplings has been simplified for the 2-dimensional case, because we do not have to indicate the plane to which the parameter is connected to:
$\eta_x := \eta_{xy,x}$, $\eta_y := \eta_{xy,y}$, $\eta_{xy} := \eta_{x,xy}$, $\eta_{yx} := \eta_{y,xy}$.

Poisson ratio ν_{xy} defines the transverse strain in y-direction when uniaxial tension is applied in x-direction $\nu_{xy}=-\varepsilon_y/\varepsilon_x$. The shear coupling coefficients η_x and η_y define the couplings between shear strain and normal tensions. Shear coupling coefficients η_{xy} and η_{yx} define the couplings between the shear tension and normal strains. If the material is orthotropic, the shear couplings disappear in the coordinate systems where the directions of axes x and y coincide with the principal directions of elasticity. By using the symmetry of the *elastic* compliance matrix, we can express the matrix in terms of the six free engineering parameters.

$$\begin{bmatrix} D_{11} & D_{12} & D_{13} \\ D_{12} & D_{22} & D_{23} \\ D_{13} & D_{23} & D_{33} \end{bmatrix}_\beta = \begin{bmatrix} \frac{1}{S_x} & -\frac{\nu_{xy}}{S_x} & \frac{\eta_x}{S_x} \\ -\frac{\nu_{xy}}{S_x} & \frac{1}{S_y} & \frac{\eta_y}{S_y} \\ \frac{\eta_x}{S_x} & \frac{\eta_y}{S_y} & \frac{1}{S_{xy}} \end{bmatrix}_\beta \tag{10}$$

5. MEASUREMENT OF DEFORMATION BY IMAGE ANALYSIS

The measurement of the deformations of a thin paper web is best to do with visual methods, without disturbing the material. Several researchers like Kujala and Kajanto (1995), Korteoja (1997), Lif and Fellers (1995) have used image correlation analysis of paper deformations. The method used in this research is based on the methods used in these papers, and only the outlines of the algorithm is described here.

A digital intensity image is a matrix $[I_{ij}]$, whose values represent intensities within some range. In this test, we have used color camera with resolution of 3008x1960 pixels. The color image has been converted to intensity image by summing the three 8-bit (0...255) color RGB intensities to a grayscale image (0...765). The fiber structure of the transilluminated paper sample usually gives us the necessary random pattern for displacement detection.

The basic idea of correlation methods is to move small sub-images of the reference image (fig 3b) over an image of deformed material (fig 3c), and to find the best match between the images. The method is basically a simple search method. Gradient methods are not powerful for this kind of problems, because the error surface is too complicated having a lot of local minimum (local maximum of the cross-correlation function, see figure 3d). Usually we have some à priori information of the possible displacements for determining the search area in the deformed image, so that we do not have to search the whole image area for every control point. The measure of the similarity is the two-dimensional normalized cross-correlation between image pixel values. The values of the correlation as a function of displacement are called the cross-correlation function (fig 3d).

For computational efficiency, the cross correlation function is calculated in frequency domain using discrete Fourier transform as suggested by Matlab Image Processing Toolbox (2001). The basic maximum accuracy of strain measurement of this arrangement is ~1/3000 (1 pixel per 3008 pixels in horizontal direction). We can increase accuracy to the subpixel level by fitting a two-dimensional 2nd order polynomial to the pixel intensities surrounding the maximum peak of the

correlation function (fig 3e). By using subpixel method, we have tested the practical sensitivity to strain to be better than 1/10000.

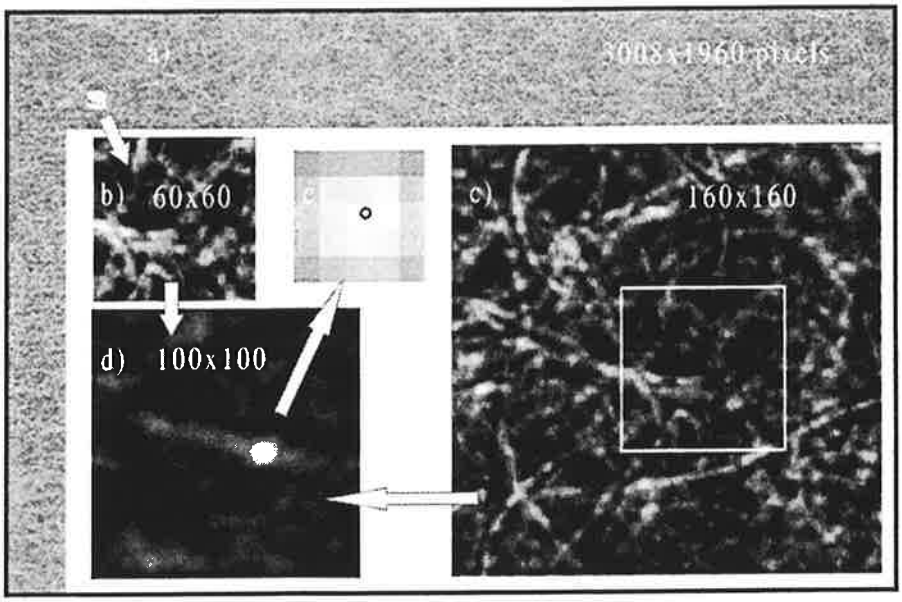

Figure 3. Principle of the image deformation analysis. Reference image (a), sub image of the reference image (b), search area of the deformed image (c), normalized cross correlation function between reference and deformed image (d), highest peak of the cross correlation function and the maximum value of the bicubic polynomial fitted to the peak (e)

When we have some area of homogenous material in an uniform tension field, the deformation is *affine,* including normal strains, shear strain, translation and rotation. Affine transformation of points from reference state (X,Y) to deformed state (x,y) is defined with six parameters as

$$\begin{aligned} x &= a_{11}X + a_{12}Y + a_{13} \\ y &= a_{21}X + a_{22}Y + a_{23} \end{aligned} \tag{11}$$

If we measure the displacements of three points (the center points of sub images); we have six equations to solve the six parameters. Because the values of x and y have some measurement error included, we have used a grid of control points and solved the parameters with least squares method. We are interested only of the strains, and ignore the rigid body translation and rotation. Using the definition of displacement components, $u=X-x$ and $v=Y-y$, we can get the (small) strains by partial derivatives of equations (11)

$$\begin{aligned} \varepsilon_x &= \partial u/\partial X = a_{11} - 1 \\ \varepsilon_y &= \partial v/\partial Y = a_{22} - 1 \\ \gamma_{xy} &= \partial u/\partial Y + \partial v/\partial X = a_{12} + a_{21} \end{aligned} \tag{12}$$

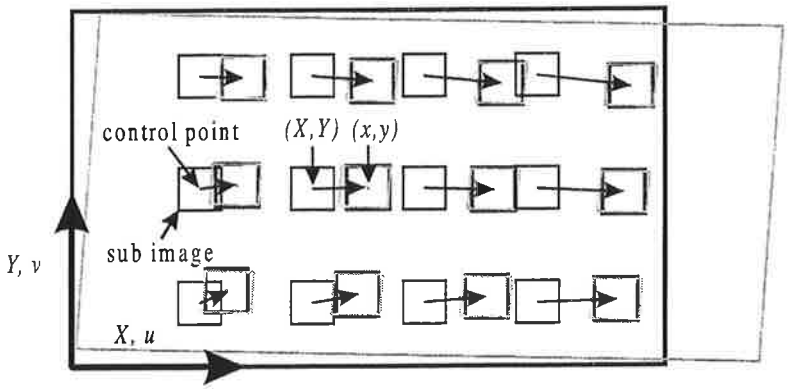

Figure 4. Displacement field between reference- and deformed image[3]

6. MEASUREMENT RESULTS

The results of measurements of one paper material at test tension T_x^{β}=1000 N/m is shown in figure 5. The material is sizer coated wood-free paper having basis weight of 115g/m² and coat weight of 2x7 g/m². The measurements show slight anisotropy, because the directions where the shear strain is zero are -6° and 86° (difference 92°), see figure 5c. Also, the directions of the maximum and minimum tensile stiffness are the same (see figure 6a).

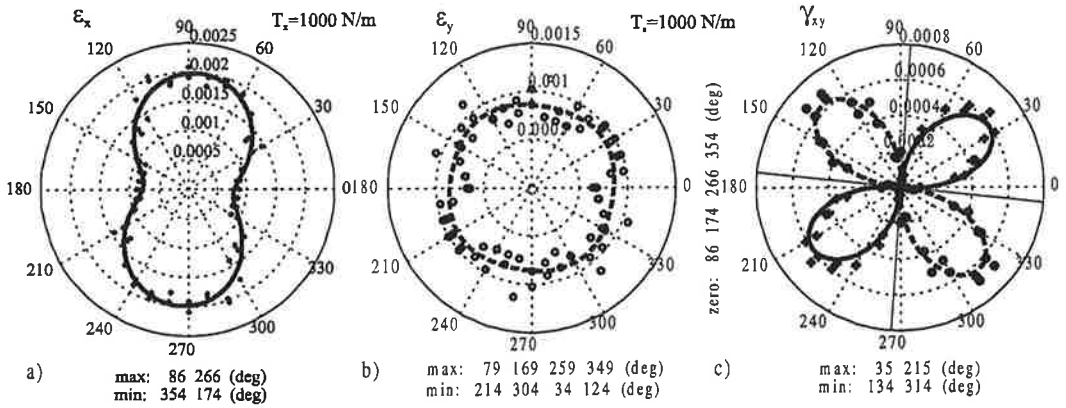

Figure 5. Strains measured by the uniaxial tensile test. Measured strains (points) and the fitted material model (lines). a) Strain in the direction of uniaxial tension ε_x. b) Strain perpendicular to uniaxial tension ε_y. c) Shear strain γ_{xy}. Positive values are indicated with symbol (+) and solid line (-), negative values with symbol (o) and dashed line (- -).

The fibers of the machine made paper is usually more oriented in the machine direction than in cross-machine direction. Also, the tensile stiffness is usually much higher in the MD. In this tests we have tried to find out, if we can estimate the direction of the elastic orientation from the fiber orientation. The fiber orientation has been measured by image analysis using the method described by Xu, Parker and Filonenko (1999).

[3] The d*eformed image* means an image of a deformed material. The pixels of a digital image do not move. They are new samples of the continuous intensity values of the material surface.

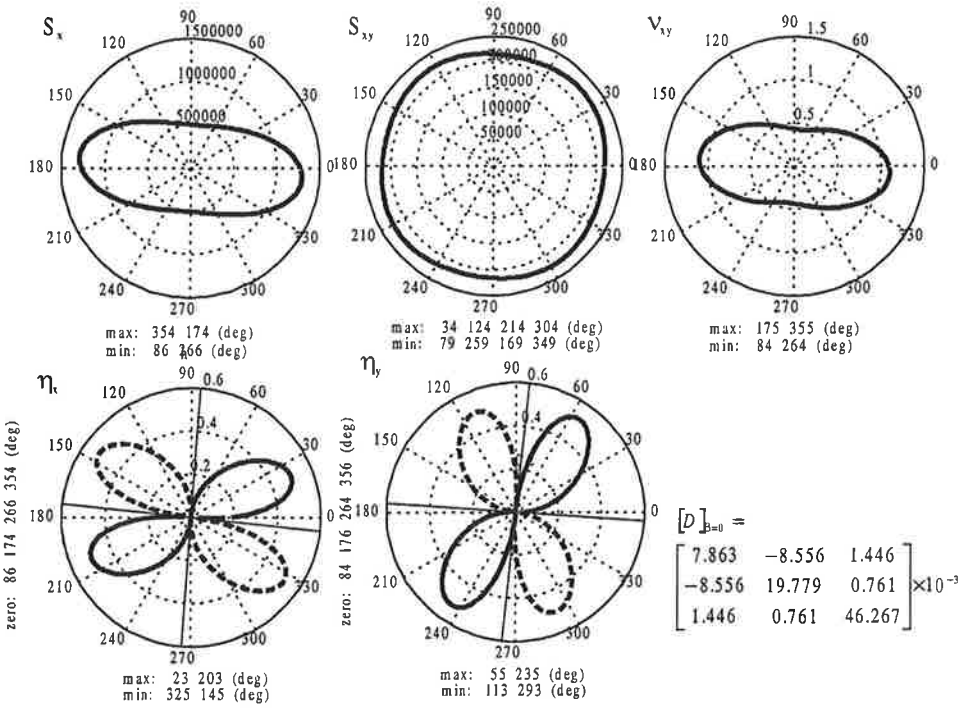

Figure 6. Engineering parameters as a function of direction angle β. The symmetric compliance matrix [*D*] is given in the global MD/CD coordinate system. Positive values (-) , negative values (- -).

The paper sample has been split in 11 layers using adhesive tape, and the fiber orientation of every layer has been determined (fig 7a). Because the top and bottom layers consist mainly of coating color, showing very low orientation, we have calculated the average orientation without those layers. The average fiber orientation is directed very close to machine direction (fig. 7b). The elastic orientation, however, has 6 degrees shift from the MD. In this tests we have not found good correlation between the fiber orientation and the elastic orientation, they have to be measured separately.

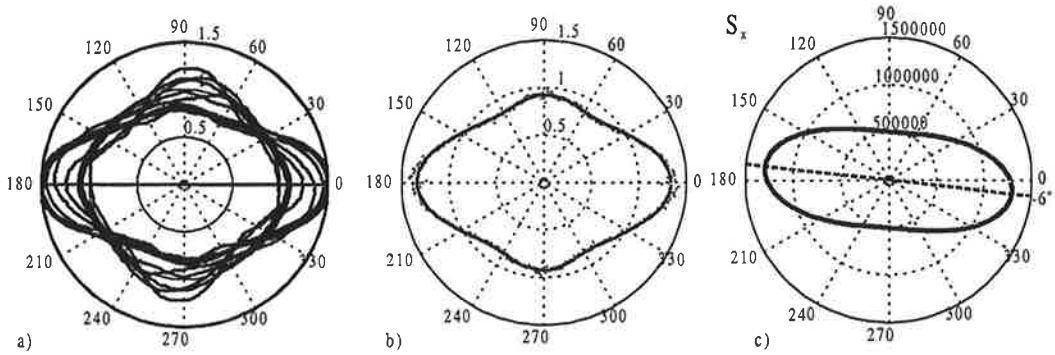

Figure 7. Fiber orientation and elastic orientation. a) Fiber orientations of 11 different layers of the paper b) Average of the fiber orientations of layers 2...10 c) Elastic orientation of the tensile stiffness.

REFERENCES

Salonen, E-M., 1999, *Determination of elastic material parameters experimentally in plane stress case*. Unpublished report, Helsinki University of Technology.

Seo, Y.B., 1999, *Determination of In-Plane Shear Properties by an Off-Axis Tension Method and Laser Speckle Photography,* Journal of Pulp and Paper Science, Vol. 25 No 9. Sept. 1999.

Malvern, L. E., 1977, *Introduction to the Mechanics of a Continuous Medium*, Prentice Hall

Lekhnitskii, S. G., 1963, *Theory of Elasticity of an Anisotropic Elastic Body*, Holden-Day, Inc., San Francisco.

Lekhnitskii, S. G., 1968, *Anisotropic Plates*, Gordon and Breach, Science Publishers, Inc., New York.

Cook, R. D., Malkus, D. S., Plesha, M. E., 1989, *Concepts and Applications of Finite Element Analysis*, 3^{rd} *ed.*,John Wiley & Sons Inc., New York.

Kujala, M., Kajanto, I., 1995, *Paperin poissonin vakioitten määrittäminen kuva-analyysillä*, PSC Communications 84, Oy Keskuslaboratorio -Centrallaboratorium Ab, Espoo.

Korteoja, M. J., 1997, *Damage and Fracture in Fibrous Compounds: The Effect of Structural Disorder,* PhD Dissertation, Helsinki University of Technology, Espoo.

Lif, J. O., Fellers, C.,1995, *Characterizing the In-Plane Deformations of Paper by Electronic Speckle Photography,* PFT-report no. 14, Skogsindistrins Tekniska Forskingsinstitut, Stockholm.

MATLAB, (2001), Image Processing Toolbox Users's Guide, MathWorks Inc

Xu, L., Parker, I., Filonenko, Y., 1999, *A New Technique for determining Fibre Orientation Distribution Trough Paper,* Proceedings of TAPPI International Paper Physics Conference 1999.

CHANNEL COMPOSITE MATERIAL PROPERTIES DETERMINATION

T-P. VUORINEN, M. KEMPPINEN, M. TANTTU, P. PYKÄLÄINEN
Mikkeli Polytechnic Research Centre YTI
P.O. Box 181, FIN-50101 Mikkeli
e-mail: tomi-pekka.vuorinen@mikkeliamk.fi

ABSTRACT

Channel composite is a special sandwich structure, in which v-shaped diagonal webs are added to a conventional foam core. In this study, the channel composite panel component elastic properties are measured separately, and the behavior of the complete channel composite panel is determined with the help of FEM-models. Different modeling techniques are introduced and discussed, and their results are compared with physical tests of beams and T-joints. Computational and empirical results have a good correlation, which proves the method to be reasonable. Surprisingly, a simple laminate element model gave more realistic results than a complicated solid model, being the right tool for practical vehicle engineering.

1. INTRODUCTION

Company Fibrocom Oy has patented a special sandwich structure, in which v-shaped diagonal webs are added to a conventional foam core, see Figure 1. The advantages of this special structure are increased stiffness, redundancy, increased crash energy absorption capacity and with special manufacturing techniques, lower production costs.

Currently, the most promising application for the material is a double-deck commuter train coach, which would have a self-supporting channel composite chassis structure. Companies Fibrocom Oy and Talgo Oy have performed intensive R&D work to develop the concept. Since no self-supporting composite train coaches exist in operative use, Mikkeli Polytechnic Research Centre YTI generated a research project to determine channel composite material properties to support the structural design, authority evaluation and positive client attitude towards the novel technology. VTT Technical Research Centre of Finland and University of Oulu also participated the project as research subcontractors.

Previously, Fibrocom Oy has tried to determinate the elastic and strength properties with channel composite panel specimens, but with remarkable results deviation. Hence, a new approach was suggested, in which the channel composite panel component–mould face plate, bagging face plate, diagonals and foam–elastic properties and strength are measured separately, and the behavior of the complete channel composite panel is determined with the help of a FEM-model. This paper introduces the process: the channel composite component material tests, the formulation of different FEM models and complete channel composite panel elastic properties determination with FEM, as well as the verification of the FEM results with physical tests. No material property values are listed, as they are proprietary to the client companies.

2. ELASTIC PROPERTIES OF CHANNEL COMPOSITE COMPONENTS

Figure 1 illustrates the structure of a complete channel composite panel consisting of glassfibre face plates, glassfibre diagonals and core foam.

To get sufficient data of the component elastic properties, we made the following tests for all the components:

- Tensile tests for glassfibre laminates
- Compression tests for glassfibre laminates
- Shear tests for fiber glassfibre laminates.

Due to the diagonal web structure, all the face laminate fibres are not continuous in y-direction. To be able to study the effect of the discontinuity, specimens were cut from various laminate locations. Figure 1 shows the labeling, location and orientation of the specimens tested.

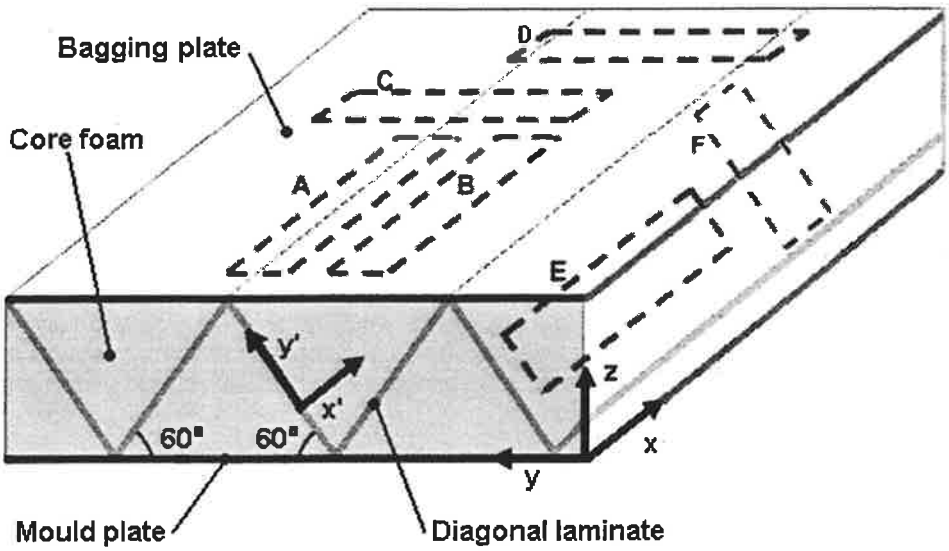

Figure 1. The labeling, location and orientation of the test specimens A-F.

The specimens were cut out from a complete channel composite panel with a circular saw. Excessive foam was removed with a abrasivebelt grinder, resulting in a neat laminate sheet, out of which the specimen were cut. Diagonal laminate specimens F were not cut out of channel composite structure, but laminated on table, since cut-out specimens would have been too short for reliable testing. The resulting error can be estimated by comparing the results of specimen E batches that have been manufactured both as cut-outs and laminated on table.

We did not extend the abrasivebelt grinding to the very surface of fiber glass layer, but left about 0.5 mm residual foam layer to prevent unintended fibre cutting. This excessive specimen thickness naturally decreases the elastic property and strength values. This effect is cancelled out when FEM-modeling the complete channel composite panel, as the input laminate thicknesses include the residual foam thickness. So, the excessive laminate thickness plays no role when considering complete channel composite panel elastic properties.

2.1 Tensile tests for glassfibre laminates

Most tensile tests were carried out at Mikkeli Polytechnic Machine Laboratory, employing Shimadzu Autograph AG-100kN universal testing machine that has been calibrated to the Accuracy Class 1. Elongation was measured with the extensometer MTS Model 632.31F-24, typically engaged with rubber bands. Materials were loaded to break.

The laminates were tested conforming ISO/DIS 527.1-2 standards [1, 2], testing speed was 2mm/min. Specimen shape was straight rectangular 25x250 mm ISO/DIS 527 type 2, with epoxy clued end tabs. Work drawing of test specimen is shown in Figure 2.

To find out the effect of specimen shape to the results and respective standard deviation, some tensile test series were also carried out with two different dog bone -shaped specimens that are depicted in Figure 3.

Young's Modulus was calculated by definition in ISO/DIS 527-1 part 4.6 and 10.3. Strain values 0,005% and 0,025 % were employed in the Young's Modulus calculation.

The ultimate tensile stresses and strains were also calculated.

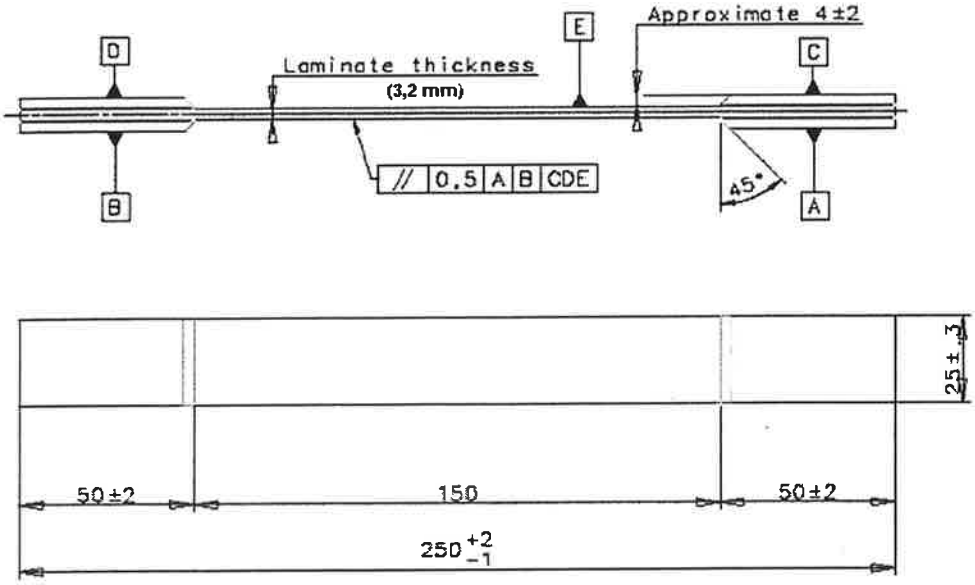

Figure 2. Work drawing of tensile test specimen with clued end tabs.

Tensile tests with different specimens shape batches indicated the standard deviations to be 2-10 % regardless the specimen batch shape. So, the specimen shape was not an issue, but the manufacturing tolerance had to be tight to yield small standard deviations. Circular sawing was found a good method for rectangular specimens and CNC-milling or water jet cutting for dog bone and shear specimens, starting from a mechanically drilled initial hole.

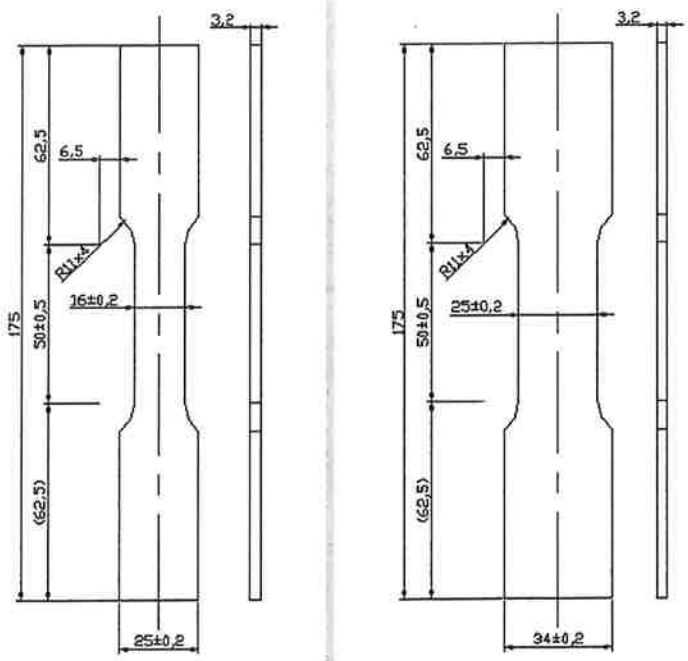

Figure 3. Dimension drawings of the two tested dog bone -shaped tensile test specimens.

2.2 Compression tests for fibre glass laminates

Most compression tests were carried out at Mikkeli Polytechnic Machine Laboratory, employing Shimadzu Autograph AG-100kN universal testing machine. Since no compression clamping jaws were available, a special fixture was used to convert the tensile motion to compression. Reduction was measured with the extensometer MTS Model 632.31F-24, typically engaged with rubber bands. Materials were loaded to break.

The laminates were tested conforming Standards DIN 53454 [3] mod. and ISO/DIS 527-1, [1], testing speed was 2mm/min. Compression specimen was modified from ISO/DIS 527 Type 1 to the 16 mm wide dog bone shape depicted in Figure 3.

The compression tests indicated considerable results standard deviation, varying between 12%-22%, and should therefore be addressed for advisory use only.

2.3 Shear test for fibre glass laminates

All shear tests were carried out at Mikkeli Polytechnic Machine Laboratory, employing Shimadzu Autograph AG-100kN universal testing machine. The shear properties were determined conforming Standard ASTM D4255 [4]. Load was introduced to the specimen by a three-rail testing fixture that was built after ASTM D4255 standard. The load magnitude was varied from 0 N to 5 kN in 250 N steps, and the microstrains were manually written down at each load step. For strains measurements, four strain gauge rosettes per specimen were attached. Figure 4 illustrates the test set-up and shows the strain gauge locations.

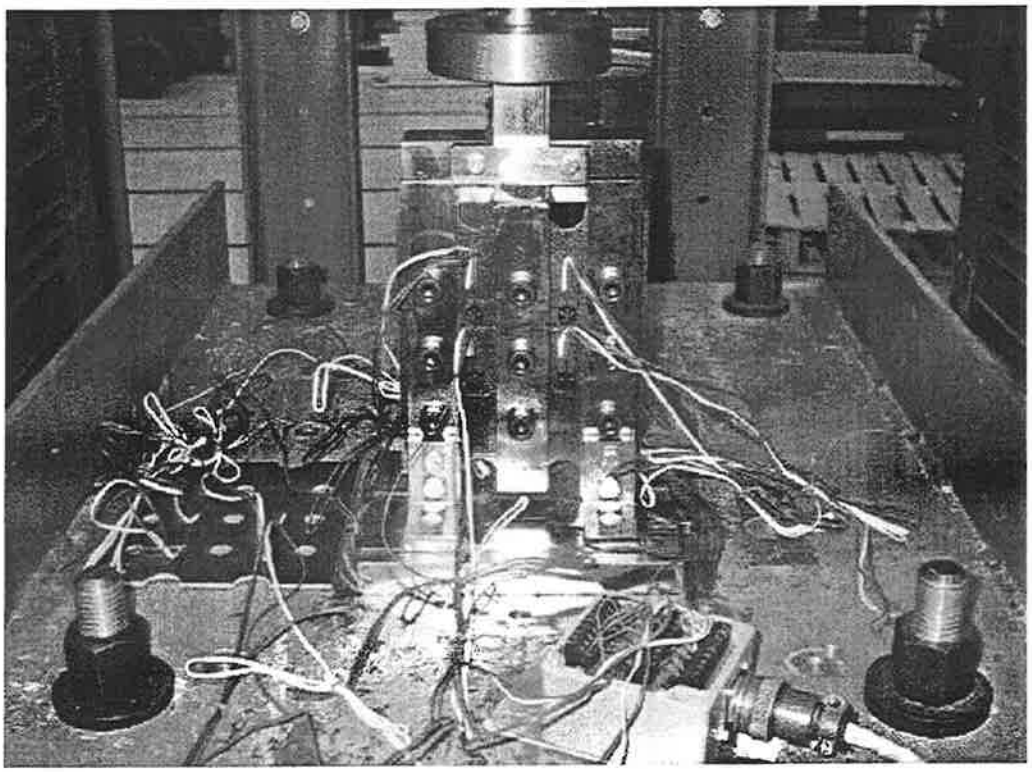

Figure 4. Shear Modulus test set-up.

Figure 5 shows the work drawing of the specimen. Due to the roughness of the channel composite bagging face plates, it was practical to test the mould face laminates only. The orientation of the specimen is along channel (direction x is vertical in Figure 5).

Shear Modulus G_{xy} is calculated after Standard ASTM D4255. Six specimens were tested, as required by the Standard. For Shear Modulus calculation, data points F=2 kN and F=5 kN lying in the linear region were chosen.

Prior to the fibre glass testing, we performed tests with polycarbonate plates to determine a correction coefficient to compensate for test fixture friction.

The standard deviation of measured G_{xy} values is relatively low, 8,8%, which indicates the test procedure to be pretty reliable. In addition to typical material and test system error sources it should be noted that the laminate is asymmetric and it tends to bend even when loaded in plane, thus generating more unknown friction forces and unknown strains to the stress gauges.

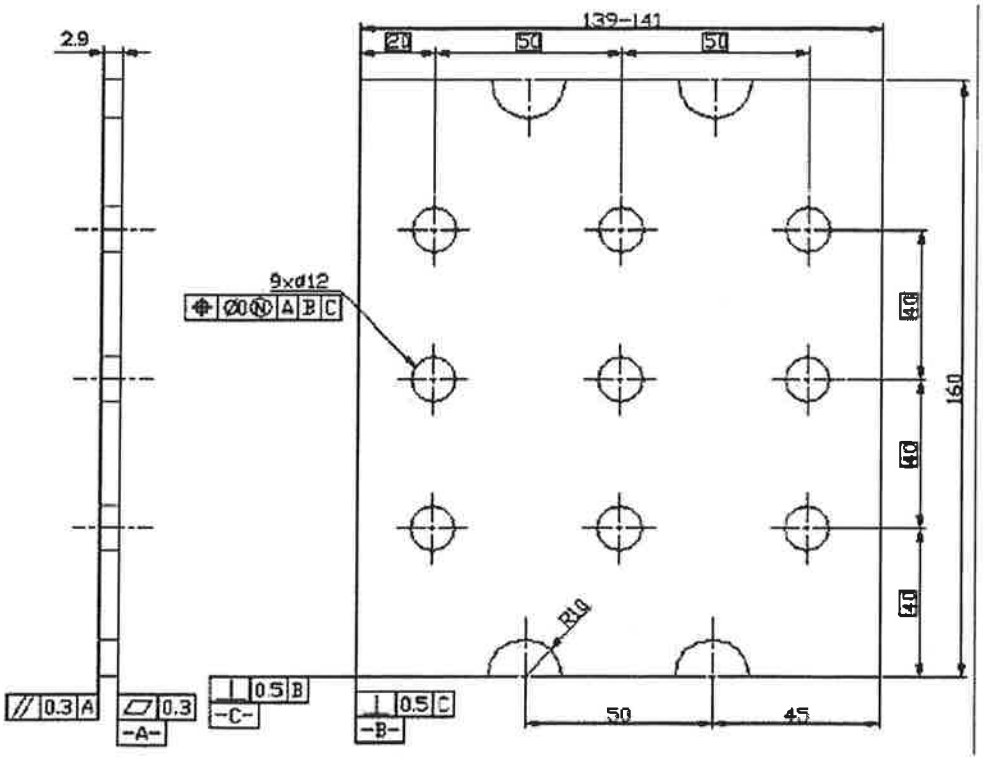

Figure 5. Shear Modulus test specimen work drawing.

3. COMPOSING THE CHANNEL COMPOSITE PANEL PROPERTIES WITH FEM

After the channel composite component elastic properties were determined by testing, we proceed to compose the elastic properties of a complete channel composite panel with the help of FEM. Since our aim is to simulate large structures with both a) shell elements and b) laminate elements for their performance comparison, we need to compose the combined elastic properties for both a) a complete channel composite panel and b) to a "virtual core" that represents the combined elastic properties of the foam and the diagonal laminates as a single orthotropic material.

The FEM analyses were performed employing I-DEAS 9.0 software. To find out the most productive modeling technique for future engineering applications, we tested two different modeling approaches and executed a number of test runs with different mesh sizes, element types, numbers of elements and element order (linear/quadrilateral):

1. Solid models, in which face plates, diagonals and foam are all modeled with solid elements.
2. Hybrid models, in which face plates and diagonals are modeled with shell elements and foam is modeled with solid elements.

Figure 6 shows a typical FEM model used in the analysis and Table 1 gives the boundary conditions used in the analysis.

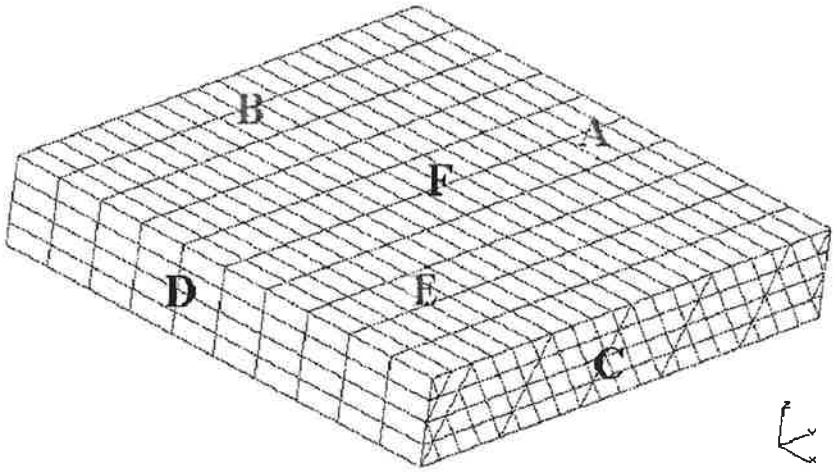

Figure 6. A typical FEM model used in the analysis. Black letters indicate the visible surfaces referred in Table 1, and grey letters indicate the hidden surfaces referred in Table 1, respectively.

Table 1. Loads, restraints and constraints definition for FEM analysis.

Case	Force face /direction	Restraints, face /Components	Additional restraints, face/ components	Constraints added to a face / direction
E_X	C/X	B/UX	One node on B/ UY, UZ	C/X, A/Y, D/Y, E/Z, F/Z
E_Y	A/Y	D/UY	One node on D/ UX, UZ	A/Y, B/X, C/X, E/Z, F/Z
E_Z	F/Z	E/UZ	One node on E/ UX, UY	F/Z, A/Y, D/Y, B/X, C/X
G_{XY}	A/X, C/Y	B/UX, D/UY	Node at origin/ UX, UY, UZ	A/X, C/Y, E/Z
G_{YZ}	F/Y	E/All		F/XYZ, B/X, C/X
G_{XZ}	F/X	E/All		F/XYZ, A/Y, D/Y

UX = Displacement, X-direction
UY = Displacement, Y-direction
UZ = Displacement, Z-direction

RX = Rotation around X-axis
RY = Rotation around Y-axis
RZ = Rotation around Z-axis

Elastic properties for both complete channel composite block and the core layer were calculated by defining the strains and shear values using displacement results of FEM-analysis, defining the stress values and by computing stiffness values E=s /e and G=t /? for the block.

In addition to the FEM models, we also created an analytical computing model for the composition of the elastic properties of a complete channel composite panel. The analytical model is fundamentally based on mixing formulas of the glassfibre sheets and the foam. For brevity, the analytical model is not discussed here, but since its results were pretty close to the FEM results, we consider the analytical solution to be a reliable and the most economical way to determine the complete channel composite panel elastic properties, see Table 3.

Table 2 shows the properties of a few FEM models we compared, and Table 3 shows different "virtual core" models results deviation from the analytical solution. The differences are small, the solid element model yields smallest overall deviation, but of course, with the largest modeling effort and cost. Surprisingly, the higher order models B and C have slightly larger differences than the linear models. The reason obviously is that the simple analytical model and "linear" problem setting favors the use of simple linear elements.

Table 2. Characterization of a few executed FEM-models.

	Model type	Element size	Element type	Model size [mm]
Model A	Shell + solid	Small	Linear	320 x 320 x 55
Model B	Shell + solid	Small	Parabolic	320 x 320 x 55
Model C	Shell + solid	Big	Parabolic	320 x 320 x 55
Model D	Solid	Small	Linear	640 x 640 x 55

Table 3. Result differences between the analytical solution and the FEM models of Table 2.

Quantity	Model A Difference %	Model B Difference %	Model C Difference %	Model D Difference %
E_X	0.4	0.4	0.4	0.4
E_Y	0.0	1.9	3.8	0.0
E_Z	0.0	0.0	-0.4	0.0
G_{XY}	-1.9	-3.7	3.7	0.0
G_{YZ}	1.9	1.9	1.9	1.9
G_{XZ}	-3.3	-4.1	-3.3	-0.8
$?_{XY}$	0.0	0.0	0.0	0.0

4. EMPIRICAL TESTS AND THE COMPARISON TO FEM RESULTS

To verify the validity of the elastic property values composed with FEM, the following test cases were computed with different FEM models and the respective physical comparison tests were carried out:

1. Three- and four-point bending tests for channel composite beams.
2. T-joint bending tests.
3. Natural frequency and damping tests for channel composite beams.

4.1 Three- and four-point bending tests for channel composite beams

The tests were performed at Mikkeli Polytechnic Machine Laboratory, employing Matertest 225kN universal testing machine that has been calibrated to the Accuracy Class 1. Displacement was measured with a Hottinger HBM Type WSF/50 telltale.

Beams were tested conforming Standard ASTM C 393-00 [5]. The specimens were loaded to break with the testing speed of 11 mm/min. Specimen dimensions were 900x210x55mm and the test span was 720 mm. Six along-channel oriented specimens and six across-channel oriented specimens were tested both in three- and four-point bending, yielding the total amount of 24 specimens. Figure 7 illustrates the three-point bending test set-up and Figure 8 illustrates the four-point bending test set-up.

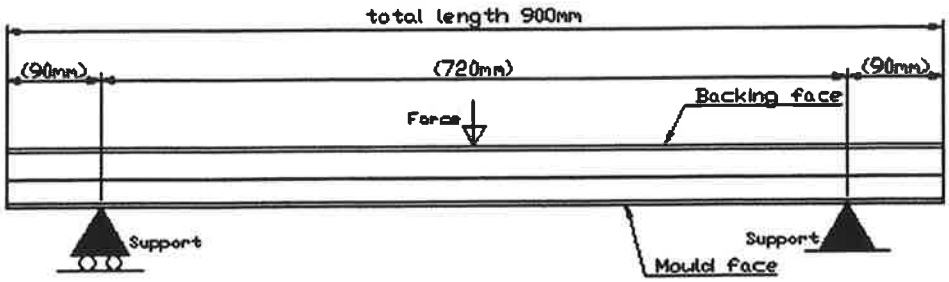

Figure 7. Three-point bending test set-up, along-channel orientation.

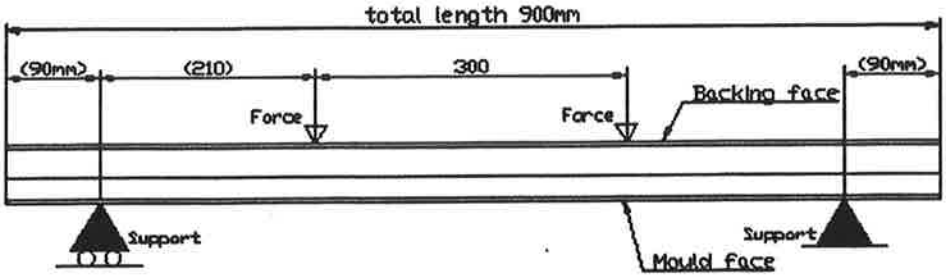

Figure 8. Four-point bending test set-up, along-channel orientation.

The tests were simulated with three different I-DEAS 9.0 FEM-models:

Model A: Face plates and diagonals are modeled using quadratic, rectangular orthotropic shell elements. Foam is modeled with isotropic solid elements.

Model B: All components are modeled with solid elements.

Model C: Face plates are modeled with orthotropic rectangular solids elements. The "virtual core" (diagonals+foam) is modeled with orthotropic rectangular solid elements.

Models were solved with linear analysis and load 5 kN, which lies well in the linear behaviour area of the physical tests. Table 4 gives the average bending at 5kN load in the physical test as well as the FEM model results difference percentage from the measured displacement

Table 4. Beam bending test average results and the difference percentage of FEM models A-C.

Test type	Orientation	Measured bending [mm]	FEM Model A %	FEM Model B %	FEM Model C %
3-point bending	Along channel	3.10	6.77	8.71	5.48
4-point bending	Along channel	2.30	8.26	10.43	7.39
3-point bending	Across channel	2.90	-3.45	1.38	-2.41
4-point bending	Across channel	2.30	-8.26	-3.48	-7.83
	Average difference	**N/A**	**6.69**	**6.00**	**5.78**

All the three different FEM models have a very good correlation with the measured results, especially, when taking the 2-10 % standard deviation of the initial material values into account. Since the solid model B requires most effort, but the "virtual core" model C requires least effort and cost, the virtual core method is recommended for engineering applications. Most probably, the use of simple laminate element model would have yielded as good results with lowest effort, but unfortunately, this alternative was not included in the study.

4.2 T-joint bending tests and the comparison to FEM results

T-joint bending test were carried out at Mikkeli Polytechnic Machine Laboratory with the same equipment as the beam bending tests. Two test specimens were employed in these static tests, while six more specimens were reserved for fatigue tests. The two static specimens were loaded to break with the testing speed of 17 mm/min. Figure 9 shows the test specimen geometry and the test set-up.

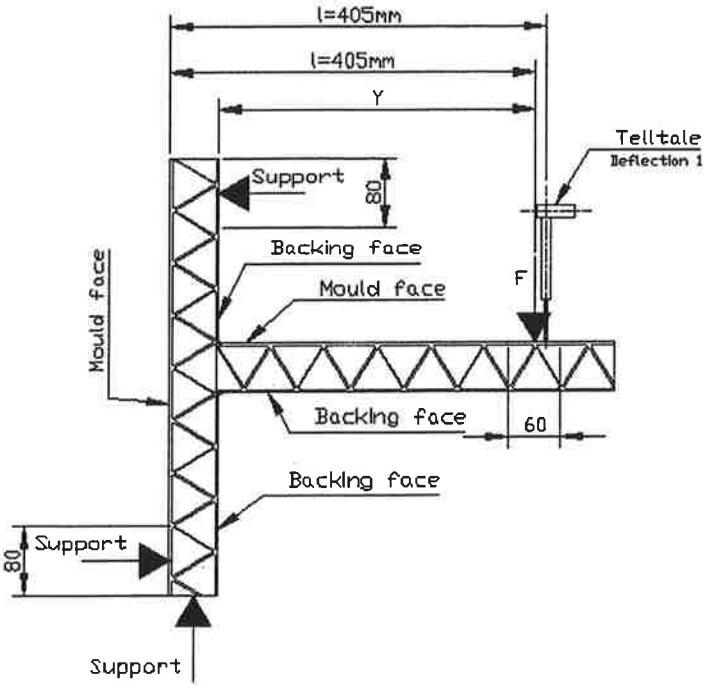

Figure 9. T-joint specimen geometry and the test set-up.

The tests were simulated with five different I-DEAS 9.0 FEM-models:

Model A: Face plates and diagonals are modeled using quadratic, rectangular orthotropic shell elements. Foam is modeled with isotropic solid elements. Diagonal joints are idealized to R=0mm. T-joint roundings R=10 mm are modeled as in reality.

Model B: As Model A, but diagonal joints have a realistic rounding of R=3mm.

Model C: As Model B, but T-joint backing face rounding is R=20mm.

Model D: Modeled with laminate shell elements.

Model E: Modeled with solid elements only.

Models were solved with linear analysis and load 800 N, which lies well in the linear behaviour area of the physical tests. Table 5 gives the average bending at 800N load in the physical test as well as the FEM model results, and the difference percentage from the measured displacement.

Table 5. T-joint bending test results, FEM Models A-E results and their difference percentage.

Quantity	Measured	Model A	Model B	Model C	Model D	Model E
Displacement [mm]	1,37	2,08	3,18	1,97	1,24	1,98
Difference from the measurement [%]	N/A	54%	136%	46%	-8%	47%

Only the laminate shell element model D gave proper results, being somewhat stiffer than the reality, as expected. Models A, C and E have a good mutual correlation, but the deflection is some 50% larger than in reality. Model B results are very far from reality. We have carefully cross-checked the models and the physical tests to find a trivial error source that would explain the results, but found nothing. Moreover, since models A, B, C and E assume all the fibers to be continuous between all the plates, but only some 50% of the fibers really are continuous, these models should yield smaller displacement than in reality.

So, we can't explain the result, but we are happy to note that the cost-effective and simple, laminate shell element model yields good correlation with reality, as this is the method we would like to use for modeling large structures.

4.3 Natural frequency tests and their comparison to FEM results

In addition to the static behaviour, we wanted to find out how well different FEM models simulate the dynamic behaviour of complete channel composite panels.

The empirical tests were carried out at the University of Oulu by hanging a test specimen with a rope, excitating the specimen with a hammer and measuring the specimen natural frequencies with two acceleration sensors. One along-channel oriented specimen and one across-channel oriented specimen were measured. Specimen dimensions were originally 800x150x57 mm, but the specimen length was cut in 60 mm steps down to 500 mm, and the specimen natural frequencies were re-measured after each cut to get more comparison data with ease.

The tests were simulated with three different I-DEAS 9.0 FEM-models:

Model 1. Face plates and diagonals are modeled using quadratic, rectangular orthotropic shell elements. Foam is modeled with isotropic solid elements.

Model 2. Face plates are modeled with orthotropic rectangular solids elements. The "virtual core" (diagonals+foam) is modeled with orthotropic rectangular solid elements.

Model 3. Modeled with laminate shell elements.

The FEM model dimensions were equal to the tested specimen. For resource reasons, only along-channel beam was modeled and executed with FEM. Table 6 summarizes results comparison.

Table 6. First natural frequency measurement and FEM Model 1-3 values for a beam.

L	$f_{1measurem.}$	$f_{1model1}$	$f_{1model1}$	$f_{1model2}$	$f_{1model2}$	$f_{1model3}$	$f_{1model3}$
[mm]	[Hz]	[Hz]	Diff. %	[Hz]	Diff. %	[Hz]	Diff. %
800	335	337	0.6	339	1.2	341	1.8
740	384	389	1.3	391	1.8	395	2.9
680	444	453	2.0	457	2.9	462	4.1
620	520	534	2.7	540	3.8	548	5.4
560	615	638	3.7	647	5.2	659	7.2
500	738	773	4.7	788	6.8	807	9.3

As Table 6 indicates, all three FEM models have a very good correlation with the experimental data. Not surprisingly, the correlation becomes worse as the beam becomes shorter, and no longer represents a proper beam, but rather a long brick with a complex internal structure. For the very same reason, Model 1, which has the most realistic internal structure, gives the most accurate results for a short beam, and the simplest Model 3 gives worst, but fair results for a short beam.

5. CONCLUSION

Channel composite panel component elastic properties can be detected employing standard material testing procedures with good accuracy and moderate standard deviation. In tensile tests, specimen shape has little influence on test results and deviation.

Complete channel composite panel elastic properties composition is most cost-effectively done with our analytical computing that is based on mixing formulas. Results comparison show that differently built FEM models produce pretty similar results. Should it be necessary to cross-check analytical results with FEM computation, simple hybrid models are recommended.

Comparison of empirical and FEM results had a good agreement with beam static and especially natural frequency results, but for a more complex T-joint, only simple laminate element FEM-model yielded good correlation with experimental data. We found no reason for the poor correlation of experimental data and more complex FEM model results.

Overall, the proposed process was proven a sound tool for channel composite structures simulation.

6. REFERENCES

1. ISO/DIS 527.1. Plastics -- Determination of tensile properties -- Part 1: General principles. International Organization for Standardization. 6. 5. 1996, Madrid, Spain.

2. ISO/DIS 527.2. 1996. Plastics -- Determination of tensile properties -- Part 2: Test conditions for moulding and extrusion plastics. International Organization for Standardization. 26. 8. 1996, Madrid, Spain.

3. DIN 53454. Testing of plastics; compression test. Deutsches Institut Für Normung E.V. 1. 6. 1988, Berlin, Germany.

4. ASTM D4255/D4255M-01. Test Method for In-Plane Shear Properties of Polymer Matrix Composite Materials by the Rail Shear Method. ASTM International. 1. 3. 2001, West Conshohocken, USA.

5. ASTM C393-00. Standard Test Method for Flexural Properties of Sandwich Constructions. ASTM International. 1. 3. 2001, West Conshohocken, USA.

RAJAKERROKSEN VAIKUTUS AKSIAALISESTI LIIKKUVAN NAUHAN OMINAISTAAJUUKSIIN

T. FRONDELIUS, J. LAUKKANEN, A. PRAMILA

Oulun yliopisto, Konetekniikan osasto,
Teknillisen mekaniikan laboratorio
PL 4200, 90014 Oulun yliopisto

TIIVISTELMÄ

Tarkasteltaessa aksiaalisessa liikkeessä olevaan, fluidin ympäröimää, nauhaa syntyy viskositeetin vaikutuksesta nauhan ja fluidin rajapintaan alue, jossa nopeusgradientin arvo on suuri. Tätä aluetta kutsutaan rajakerrokseksi. Aksiaalisesti liikkuvan nauhan ja sitä ympäröivän fluidin oletetaan tässä esityksessä muodostavan kerroksellisen systeemin. Lisäksi oletetaan kerroksien liikkuvan niin, että siirtymä poikittaissuunnassa on jokaisessa kerroksessa sama, eikä fluidissa ole vetoa. Kerrosten summan raja-arvona saadaan määrätty integraali systeemin paksuuden yli. Integroimalla edelleen tämän alueen yli kolmessa palassa saadaan liikeyhtälöön liikemäärä- ja siirtymäpaksuuteen verrannolliset lisätyn massan termit, jotka lasketaan rajakerrosteorian avulla.

Työn tuloksista mainittakoon, että laminaarisesta rajakerroksesta lasketuilla massoilla ei ole käytännössä vaikutusta systeemin ominaistaajuuksiin, kun taas turbulenttisen rajakerroksen kyseessä ollessa lisättyjen massojen merkitys ominaistaajuuksiin on huomattava. Suurimmillaan ero tässä työssä lasketun kriittisen nopeuden ja lähteessä [1] lasketun välillä on jopa 15 %.

1 JOHDANTO

Paperikoneiden tuottavuutta rajoittaa nykyisellään niiden ajonopeuksien ylärajat, sillä tuottavuutta ei enää kannata kasvattaa rakentamalla yhä leveämpiä koneita. Käyttönopeutta rajoittavat monet seikat. Yksi tärkeimmistä syistä on rainan lepatus, joka aiheuttaa laatuongelmia ja lisää tuotantokatkoksien todennäköisyyttä [2]. Myös rainan tasoa vastaan kohtisuorien värähtelyiden esiintyminen ja voimakkuus on kasvanut. Nämä seikat johtavat laatuongelmiin ja kasvattavat katkosten todennäköisyyttä paperin valmistuksessa. Rainan katkeamisen katsotaan yleensä johtuvan paperin paikallisesta heikkoudesta, mutta ainakin osa katkoista johtunee myös paperin värähtelyistä [3].

Mekaniikan näkökulmasta lepatus on tyypillinen aksiaalisesti liikkuvan materiaalin värähtelyilmiö [2]. Muista aksiaalisesti liikkuvan materiaalin värähtelyongelmista esimerkkeinä mainittakoon vannesahanterät, magneettinauhat, voimansiirtoketjut ja nestettä kuljettavat putket [4]. Aihetta on tutkittu aikaisemmin olettaen rainaa ympäröivä fluidi ideaaliseksi, ja esimerkiksi lähteessä [1] on aihetta käsitelty analyyttisesti.

Tässä esityksessä tarkastellaan aksiaalisesti liikkuvan nauhan ominaisvärähtelyjä ottamalla huomioon ympäröivä ilma rajakerrosteorian avulla. Nauhan ja sitä ympäröivän fluidin ajatellaan muodostavan kerroksellisen systeemin, jolla kuvataan nauhan ja virtauksen

vuorovaikutusta.

2 AKSIAALISESTI LIIKKUVA NAUHA

Aksiaalisesti liikkuvan materiaalin analyyseillä tarkoitetaan pituussuuntaisessa liikkeessä olevan rakenteen värähtely- ja stabiilisuustarkasteluja kulkusuuntaa vastaan kohtisuorassa suunnassa. Tarkastellaan kuvan 1 mukaista taipuisaa lankaa tai kapeaa nauhaa, jonka massa pituusyksikköä kohti on m, kireys P ja joka liikkuu tukien välillä pitkin x-akselia vakionopeudella v. Kohdassa x hetkellisesti olevan materiaalipisteen kohtisuora siirtymä, joka kuvaa nauhan muodon ajan funktiona, on muotoa $w(x,t)$ [4].

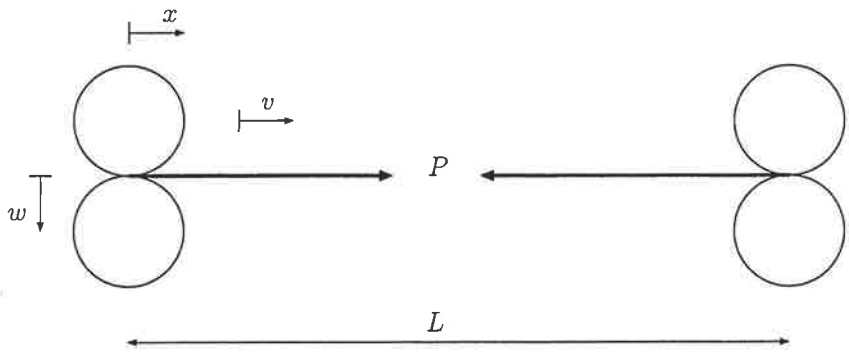

Kuva 1: Kapea nauha tai lanka

Nauhan liikeyhtälö on [4]

$$mw_{,tt} + 2mvw_{,xt} + mv^2w_{,xx} - Pw_{,xx} = 0. \tag{1}$$

Liikeyhtälön ensimmäistä termiä kutsutaan perinteiseksi inertiatermiksi, toista gyroskooppiseksi inertiatermiksi ja kolmatta keskeiskiihtyvyystermiksi. Jälkimmäiset termit johtuvat nauhan aksiaalisesta nopeudesta. Yhtälöstä (1) saadaan ratkaistua alin ominaistaajuus [1]

$$f_1 = \frac{(1 - \frac{mv^2}{P})}{2L}\sqrt{\frac{P}{m}}. \tag{2}$$

Lähteessä [1] ympäröivä ilma on otettu huomioon mm. lisäämällä massaan m ilman osuus termillä m_a, jolloin alimmaksi ominaistaajuudeksi saadaan

$$f_1 = \frac{(1 - \frac{(m+m_a)v^2}{P})}{2L}\sqrt{\frac{P}{(m+m_a)}}. \tag{3}$$

Lähteen [1] mukaan ympäröivän ilman voidaan ajatella myös liittyvän pelkästään perinteiseen inertiatermiin. Kun yhtälö (1) kirjoitetaan muodossa

$$(m + m_a)w_{,tt} + 2mvw_{,xt} + mv^2w_{,xx} - Pw_{,xx} = 0, \tag{4}$$

saadaan alimmaksi ominaistaajuudeksi [1]

$$f_1 = \frac{(1 - \frac{mv^2}{P})}{\sqrt{(1 + \frac{m_a}{m}) - \frac{m_a v^2}{P}}}\frac{1}{2L}\sqrt{\frac{P}{m}}. \tag{5}$$

3 YMPÄRÖIVÄN ILMAN VAIKUTUS

Kun tarkastellaan kevyttä nauhaa, on ympäröivällä ilmalla huomattava vaikutus systeemin dynaamiseen käyttäytymiseen. Perinteisesti tämän tyyppisen systeemin ympäröivää fluidia on tarkasteltu ideaalisena, jolloin nauhan aksiaalisella nopeudella ei ole vaikutusta fluidin virtaukseen. Todellinen tilanne ei kuitenkaan ole näin yksinkertainen, koska käytännössä kaikkien fluidien viskositeetti on suurempi kuin nolla.

3.1 KIINTEÄN MATERIAALIN JA YMPÄRÖIVÄN FLUIDIN MUODOSTAMA KERROSSYSTEEMI

Tarkastellaan kuvan 2(b) systeemiä seuraavin oletuksin:

1. Nauhan ja sitä ympäröivän ilman ajatellaan muodostavan kerrossysteemin
2. Oletetaan että kerrokset liikkuvat niin, että siirtymä w on jokaissa kerroksessa sama (toisin sanoen oletetaan, että kalvossa ja ilmassa on sama w)
3. Fluidissa ei ole vetoa ($P = 0$ ilmassa)
4. Kiinteän aineen tiheys on ρ_s
5. Fluidin tiheys on ρ_f
6. Nauhan leveys on b
7. Massa pituusyksikköä kohti on $b\int_{z_1}^{z_2} \rho \, dz$

Soveltamalla edellä mainittuja oletuksia liikeyhtälöön (1) saadaan

$$b\int_{-\infty}^{\infty} \rho w_{,tt}\,dz + b\int_{-\infty}^{\infty} 2\rho v(z) w_{,xt}\,dz + b\int_{-\infty}^{\infty} \rho v(z)^2 w_{,xx}\,dz - b\int_{-\infty}^{\infty} \frac{P}{h} w_{,xx}\,dz = 0 \qquad (6)$$

Jakamalla integraali osiin kiinteän aineen ja fluidin rajapinnoissa, sekä integroimalla paloittain saadaan

$$\begin{aligned}
&b\int_{-\frac{h}{2}}^{\frac{h}{2}} \rho_s w_{,tt}\,dz + b\int_{-\frac{h}{2}}^{\frac{h}{2}} \rho_s v w_{,xt}\,dz + b\int_{-\frac{h}{2}}^{\frac{h}{2}} \rho_s v^2 w_{,xx}\,dz - b\int_{-\frac{h}{2}}^{\frac{h}{2}} \frac{P}{h} w_{,xx}\,dz \\
&+b\int_{-\infty}^{-\frac{h}{2}} \rho_f w_{,tt}\,dz + b\int_{-\infty}^{-\frac{h}{2}} \rho_f u_f(z) w_{,xt}\,dz + b\int_{-\infty}^{-\frac{h}{2}} \rho_f u_f(z)^2 w_{,xx}\,dz \\
&+b\int_{\frac{h}{2}}^{\infty} \rho_f w_{,tt}\,dz + b\int_{\frac{h}{2}}^{\infty} \rho_f u_f(z) w_{,xt}\,dz + b\int_{\frac{h}{2}}^{\infty} \rho_f u_f(z)^2 w_{,xx}\,dz = 0, \qquad (7)
\end{aligned}$$

missä u_f on fluidin nopeus. Olettamalla lisäksi, että taipuma w on kaikissa termeissä sama, saadaan se ulos integraaleista. Laventamalla (7) vakionopeudella v

$$
\begin{aligned}
&b\int_{-\frac{h}{2}}^{\frac{h}{2}} \rho_s \,\mathrm{d}z\; w_{,tt} + b\int_{-\frac{h}{2}}^{\frac{h}{2}} \rho_s \,\mathrm{d}z\; v w_{,xt} + b\int_{-\frac{h}{2}}^{\frac{h}{2}} \rho_s \,\mathrm{d}z\; v^2 w_{,xx} - b\int_{-\frac{h}{2}}^{\frac{h}{2}} \mathrm{d}z\; \frac{P}{h} w_{,xx} \\
&+b\int_{-\infty}^{-\frac{h}{2}} \rho_f \,\mathrm{d}z\; w_{,tt} + b\int_{-\infty}^{-\frac{h}{2}} \rho_f \frac{u_f}{v} \,\mathrm{d}z\; v w_{,xt} + b\int_{-\infty}^{-\frac{h}{2}} \rho_f \frac{u_f^2}{v^2} \,\mathrm{d}z\; v^2 w_{,xx} \\
&+b\int_{\frac{h}{2}}^{\infty} \rho_f \,\mathrm{d}z\; w_{,tt} + b\int_{\frac{h}{2}}^{\infty} \rho_f \frac{u_f}{v} \,\mathrm{d}z\; v w_{,xt} + b\int_{\frac{h}{2}}^{\infty} \rho_f \frac{u_f^2}{v^2} \,\mathrm{d}z\; v^2 w_{,xx} = 0
\end{aligned}
\tag{8}
$$

Yhdistämällä termit saadaan liikeyhtälö edelleen muotoon

$$
\begin{aligned}
&b\left(\int_{-\frac{h}{2}}^{\frac{h}{2}} \rho_s \,\mathrm{d}z + \int_{-\infty}^{-\frac{h}{2}} \rho_f \,\mathrm{d}z + \int_{\frac{h}{2}}^{\infty} \rho_f \,\mathrm{d}z\right) w_{,tt} \\
&+b\left(\int_{-\frac{h}{2}}^{\frac{h}{2}} \rho_s \,\mathrm{d}z + \int_{-\infty}^{-\frac{h}{2}} \rho_f \frac{u_f}{v} \,\mathrm{d}z + \int_{\frac{h}{2}}^{\infty} \rho_f \frac{u_f}{v} \,\mathrm{d}z\right) v w_{,xt} \\
&+b\left(\int_{-\frac{h}{2}}^{\frac{h}{2}} \rho_s \,\mathrm{d}z + \int_{-\infty}^{-\frac{h}{2}} \rho_f \frac{u_f^2}{v^2} \,\mathrm{d}z + \int_{\frac{h}{2}}^{\infty} \rho_f \frac{u_f^2}{v^2} \,\mathrm{d}z\right) v^2 w_{,xx} - b\int_{-\frac{h}{2}}^{\frac{h}{2}} \mathrm{d}z\; \frac{P}{h} w_{,xx} = 0
\end{aligned}
\tag{9}
$$

Integroimalla kiinteän materiaalin yli saadaan nauhan massa pituusyksikköä kohti

$$m = \rho_s b h, \tag{10}$$

gyroskooppiseen termiin lisättävä massa pituusyksikköä kohti

$$m_{aG} = b\int_{-\infty}^{-\frac{h}{2}} \rho_f \frac{u_f}{v} \,\mathrm{d}z + b\int_{\frac{h}{2}}^{\infty} \rho_f \frac{u_f}{v} \,\mathrm{d}z, \tag{11}$$

keskeiskiihtyvyystermiin lisättävä massa pituusyksikköä kohti

$$m_{aK} = b\int_{-\infty}^{-\frac{h}{2}} \rho_f \left(\frac{u_f}{v}\right)^2 \mathrm{d}z + b\int_{\frac{h}{2}}^{\infty} \rho_f \left(\frac{u_f}{v}\right)^2 \mathrm{d}z, \tag{12}$$

ja perinteiseen inertiatermiin lisättävä massa pituusyksikköä kohti

$$m_a = b\int_{-\infty}^{-\frac{h}{2}} \rho_f \,\mathrm{d}z + b\int_{\frac{h}{2}}^{\infty} \rho_f \,\mathrm{d}z. \tag{13}$$

Yhtälöiden (10) - (13) avulla voidaan liikeyhtälö kirjoittaa muotoon

$$(m + m_a)w_{,tt} + 2(m + m_{aG})vw_{,xt} + (m + m_{aK})v^2 w_{,xx} - Pw_{,xx} = 0. \tag{14}$$

Liikeyhtälön gyroskooppitermistä havaitaan analogia siirtymäpaksuuden määritelmään ja keskeiskiihtyvyystermistä analogia liikemääräpaksuuden määritelmään. Lisätty massa gyroskooppiseen ja jäykkyystermiin voidaan siis laskea rajakerrosteorian avulla. Tulos on looginen, koska verrattaessa sitä kuvan 2(a) nopeusjakaumaan, oletettavaa on, että lisätty massa gyroskooppiseen- ja keskeiskiihtyvyystermiin ovat verrannollisia aksiaalisesti materiaalin mukana liikkuvan ilman massaan.

Perinteiseen inertiatermiin liittyvää lisättyä massaa ei voida laskea rajakerrosteorian avulla, sillä perinteiseen inertiatermiin liittyvä massa on verrannollinen materiaalin poikittaisen värähtelyn siirtämän ilman massaan. Edellisessä tarkastelussa tehtiin oletus, ettei taipuma ole z:n funktio (oletettiin taipumat pieniksi suhteessa rajakerroksen paksuuteen) ja siksi perinteiseen inertiatermiin lisättävä massa lasketaankin ottamatta huomioon nauhan aksiaalista nopeutta.

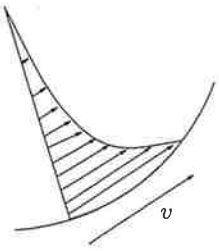

(a) Kaareva aksiaalisesti nopeudella v liikkuva materiaali ja sitä ympäröivän fluidin nopeusjakauma

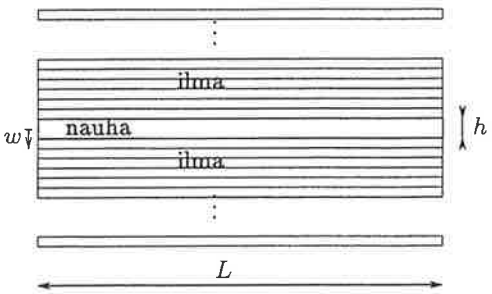

(b) Kiinteän materiaalin ja ympäröivän fluidin muodostama kerrossysteemi

Kuva 2: Kerrossysteemi ja nopeusjakauma

3.2 LISÄTTY MASSA INERTIATERMEILLE

Lisätty massa on hoikille rakenteille perinteisesti laskettu yhtälöstä

$$m_a = \frac{\pi \rho b^2}{4}. \tag{15}$$

Toisaalta lähteessä [5] lisättyä massaa kuvataan yhtälöillä, missä α ja β ovat vakioita, joille on esitetty arvoja parametrien b/L ja L/b funktioina taulukossa 1

$$m_a = \alpha \frac{\pi \rho b^2}{4} \tag{16}$$

$$m_a = \beta \rho L b, \tag{17}$$

Jäykkyys- ja gyroskooppiseen matriisiin liittyvät lisätyt massat pituusyksikköä kohti lasketaan siten, että elementtiä kohti kohdistuvan ilman tilavuus kerrotaan tiheydellä ja jaetaan elementin pituudella. Elementin ylä- ja alapuolelta kohdistuvat massat lasketaan yhteen. Kuvassa 3 varjostettu alue kerrottuna leveydellä b kuvaa yhteen elementtiin kohdistuvan

ilman tilavuutta. Kun tämä tilavuus kerrotaan ilman tiheydellä ρ, saadaan elementin lisätyiksi massoiksi pituusyksikköä kohti

$$m_{a_G} = \frac{\rho b}{L_e} \int_0^{L_e} \delta_a^* \, \mathrm{d}x + \frac{\rho b}{L_e} \int_0^{L_e} \delta_y^* \, \mathrm{d}x \tag{18}$$

ja

$$m_{a_K} = \frac{\rho b}{L_e} \int_0^{L_e} \theta_a \, \mathrm{d}x + \frac{\rho b}{L_e} \int_0^{L_e} \theta_y \, \mathrm{d}x, \tag{19}$$

missä δ:n ja θ:n alaindeksit a ja y viittaavat elementin ala- ja yläpuoleen.

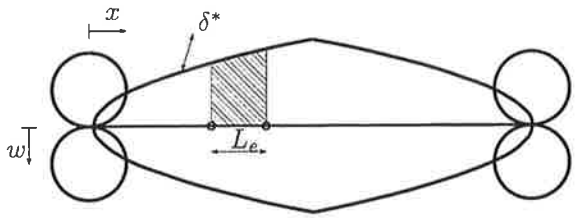

Kuva 3: Virtauskentän symmetrinen jakauma

Taulukko 1: Vakiot α ja β kaavoihin (16) ja (17) [5]

b/L	α	L/b	β
0	1,0	0,1	2,43
0,1	0,95	0,2	1,70
0,2	0,90	0,3	1,56
0,315	0,84	0,4	1,32
0,4	0,80	0,5	1,17
0,5	0,76	0,6	1,05
0,63	0,70	0,7	0,97
0,8	0,64	0,8	0,93
1,0	0,58	0,9	0,86
		1,0	0,81
		5,0	0,34

3.3 TURBULENTTINEN RAJAKERROSPAKSUUS

Lähteen [6] mukaan ainoa tyydyttävä menetelmä turbulenttisen rajakerroksen paksuuden määrittämiseksi annetulle pinnalle perustuu rajakerroksen liikemäärän differentiaaliyhtälöön. Tämä yhtälö on käypä sekä laminaariselle, että turbulenttiselle rajakerrokselle [6]. Liikemäärän differentiaaliyhtälö rajakerrokselle on [6]

$$\frac{\mathrm{d}}{\mathrm{d}x}(v^2\theta) = \frac{g_c \tau_f}{\rho}. \tag{20}$$

Nopeusjakaumaa arvioidaan yhtälöllä [6]

$$\frac{u_f}{v} = 1 - \hat{\eta}^{1/7}, \tag{21}$$

joka on analoginen putkivirtauksen turbulenttisen nopeusprofiilin kanssa. Arvio soveltuu määrätyn mittaiselle liikkuvalle tasaiselle levylle kohtuullisilla Reynoldsin luvuilla. Turbulenttinen nopeusjakauma saatiin, siis valitsemalla vastaava jakauma kuin äärellisen mittaiselle levylle. Tekemällä lisäksi oletuksen, että leikkausjännitys kiinteällä pinnalla noudattaa yhtälöä [6]

$$\frac{g_c \tau_f}{\rho v^2} = 0,0225\Big(\frac{\nu}{v\delta}\Big)^{1/4}, \tag{22}$$

saadaan liikemääräpaksuudeksi [6]

$$\theta = \frac{1}{v^2}\int_0^\infty u_f^2 \,\mathrm{d}y = \int_0^1 [1 - \hat{\eta}^{1/7}]^2 \delta \,\mathrm{d}\hat{\eta} = \frac{1}{36}\delta. \tag{23}$$

Sijoittamalla leikkausjännitys (22) ja liikemääräpaksuus (23) liikemäärän differentiaaliyhtälöön (20) sekä järjestelemällä termit uudelleen ja integroimalla lähtöpisteestä $\delta = 0$ kun $x = 0$, saadaan rajakerroksen paksuudeksi [6]

$$\begin{aligned} \frac{\mathrm{d}}{\mathrm{d}x}(v^2\theta) = \frac{g_c\tau_f}{\rho} \quad &\Longleftrightarrow \quad \frac{\mathrm{d}}{\mathrm{d}x}(v^2\frac{1}{36}\delta) = \frac{g_c}{\rho}\cdot\frac{\rho v^2}{g_c}\cdot 0,0225\Big(\frac{\nu}{v\delta}\Big)^{\frac{1}{4}} \\ &\Longleftrightarrow \quad \delta = 1,01\cdot x(\frac{vx}{\nu})^{-1/5}. \end{aligned} \tag{24}$$

Siirtymäpaksuus määritellään lähteessä [6]

$$\delta^* = \frac{1}{v}\int_0^\infty u_f \,\mathrm{d}y = \int_0^1 [1 - \hat{\eta}^{1/7}]\delta \,\mathrm{d}\hat{\eta} = \frac{1}{8}\delta = 0,126\cdot x(\frac{\nu}{vx})^{1/5}. \tag{25}$$

Liikemääräpaksuus saadaan edelleen sijoittamalla yhtälö (24) yhtälöön (23)

$$\theta = 0,028\cdot x(\frac{\nu}{vx})^{1/5}. \tag{26}$$

4 ELEMENTTIMALLI

Elementtimenetelmän yhtälö on johdettu liikeyhtälöstä käyttäen Hamiltonin periaatetta $\delta\int_{t_1}^{t_2}(T-V) = 0$ [7] ja se on ratkaistu Matlab ohjelmalla [7]. Diskretoitu liikeyhtälö voidaan kirjoittaa matriisimuodossa

$$\mathbf{M}\ddot{\mathbf{w}} + \mathbf{G}\dot{\mathbf{w}} + \mathbf{K}\mathbf{w} = 0, \tag{27}$$

missä M on massamatriisi, G gyroskooppinenmatriisi ja K jäykkyysmatriisi. Matriisit saadaan vastaavista elemementtien matriiseista sijoittelusummaamalla. Elementin matriisit saadaan kaavoista [7]: massamatriisi

$$\mathbf{M}^{\mathrm{e}} = (m + m_a)\int_0^{L_e} \mathbf{N}^{\mathrm{T}}\mathbf{N} \,\mathrm{d}x = \frac{(m+m_a)L_e}{6}\begin{bmatrix} 2 & 1 \\ 1 & 2 \end{bmatrix}, \tag{28}$$

gyroskooppimatriisi

$$\mathbf{G}^{\mathrm{e}} = (m + m_{aG})v \int_0^{L_e} (\mathbf{N}^{\mathrm{T}}\mathbf{N}_{,\mathrm{x}} - \mathbf{N}_{,\mathrm{x}}{}^{\mathrm{T}}\mathbf{N})\,\mathrm{d}x = (m + m_{aG})vL_e \begin{bmatrix} 0 & -1 \\ 1 & 0 \end{bmatrix}, \tag{29}$$

sekä jäykyysmatriisi

$$\mathbf{K}^{\mathrm{e}} = (P - (m + m_{aK})v^2) \int_0^{L_e} \mathbf{N}_{,\mathrm{x}}{}^{\mathrm{T}}\mathbf{N}_{,\mathrm{x}}\,\mathrm{d}x = \frac{P - (m + m_{aK})v^2}{L_e} \begin{bmatrix} 1 & -1 \\ -1 & 1 \end{bmatrix}. \tag{30}$$

4.1 LIIKEYHTÄLÖN RATKAISEMINEN

Sijoittamalla liikeyhtälöön (27) yrite $w = \mathrm{e}^{\lambda t}$ saadaan ominaisarvotehtävä

$$(\mathbf{K} + \lambda\mathbf{G} + \lambda^2\mathbf{M})\mathbf{X} = 0. \tag{31}$$

Ominaiskulmataajuus ω saadaan ominaisarvon λ imaginääriosan positiivisena neliöjuurena

$$\omega = \sqrt{\mathrm{Im}\lambda}, \tag{32}$$

ja edelleen ominaistaajuus saadaan tunnetusti

$$f = \frac{\omega}{2\pi}. \tag{33}$$

Otetaan käyttöön dimensioton nopeus ja dimensioton (ensimmäinen) ominaistaajuus [1]

$$V = v\sqrt{\frac{m}{P}} \tag{34}$$

$$F = f_1 \cdot 2L\sqrt{\frac{m}{P}}. \tag{35}$$

Koska ominaistaajuudet f riippuvat aksiaalisesta nopeudesta v, voidaan ne esittää graafisesti esimerkiksi vastaavien dimensiottomien suureiden avulla, eli dimensioton taajuus F dimensiottoman nopeuden V funktiona. Laskennassa käytetään adaptiivista dimensiottoman nopeuden askelta, koska F:n riippuvuus V:stä ei ole lineaarinen ja kuvaaja piirretään VF-koordinaatistoon pistepareina, joiden kautta piirretään murtoviiva. Askeleen laskemiseen hyödynnetään edellisiä tuloksia siten, että arvioidaan käyrän derivaattaa differenssiarviolla

$$F'_{i+1} = \frac{F_i - F_{i-1}}{V_i - V_{i-1}}. \tag{36}$$

Nyt lasketaan dimensioton nopeus lisäämällä edelliseen nopeuteen vakio kertaa derivaatan käänteisarvon vastaluku. Kaava (37) pienentää askelta kun käyrän jyrkkyys kasvaa. Pisteet lasketaan kaavalla

$$V_1 = 0, V_2 = 0,2 \quad \text{ja} \quad V_{i+1} = V_i + \frac{1}{400} \cdot \frac{V_{i-1} - V_i}{F_{i-1} - F_i} \quad \text{, kun} \quad i = 2, 3, 4, \ldots \tag{37}$$

missä V_i on edellisen kierroksen dimensioton nopeus ja vastaavasti dimensioton taajuus F_i vakiokerroin $\frac{1}{400}$ on empiirisesti määritetty kahden laskentakierroksen avulla. Ohjelmasilmukan lopetusehtona käytetään dimensiottoman taajuuden F absoluuttista arvoa $0,001$.

Toisin sanoen, kun dimensioton taajuus on pienempi kuin $0,001$, laskenta lopetetaan. Lisäksi tarkastellaan VF-käyrän numeerista derivaattaa. Jos derivaatta F'_{i+1} saa positiivisen arvon, lasketaan piste uudelleen puolitetulla askeleella.

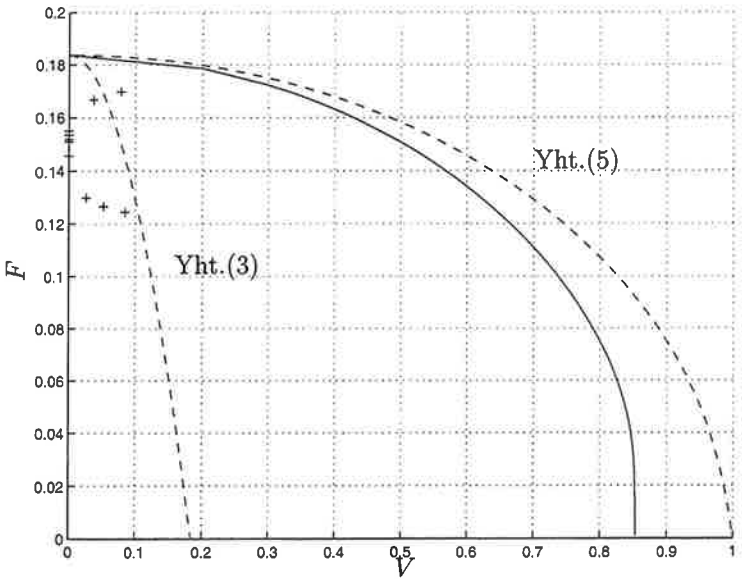

Kuva 4: Dimensioton taajuus F dimensiottoman nopeuden V funktiona. Katkoviivalla on esitetty tarkan ratkaisun tulokset [1] ja + merkillä lähteen [5] mittauspisteet. Solmupisteiden lukumäärä on 62. Jakauman tyyppi on turbulenttinen kasvava ja paperin massa pituusyksikköä kohti $m = 0,017\,\mathrm{kg/m}$. Perinteiseen inertiatermiin on lisätty massa kaavalla (17).

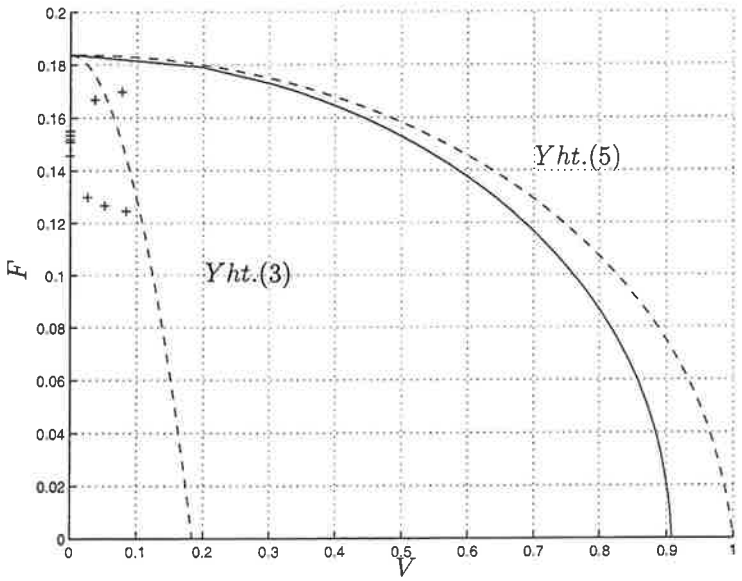

Kuva 5: Dimensioton taajuus F dimensiottoman nopeuden V funktiona. Katkoviivalla on esitetty tarkan ratkaisun tulokset [1] ja + merkillä lähteen [5] mittauspisteet. Solmupisteiden lukumäärä on 62. Jakauman tyyppi on turbulenttinen epäsymmetrinen ja paperin massa pituusyksikköä kohti $m = 0,017\,\mathrm{kg/m}$. Perinteiseen inertiatermiin on lisätty massa kaavalla (17).

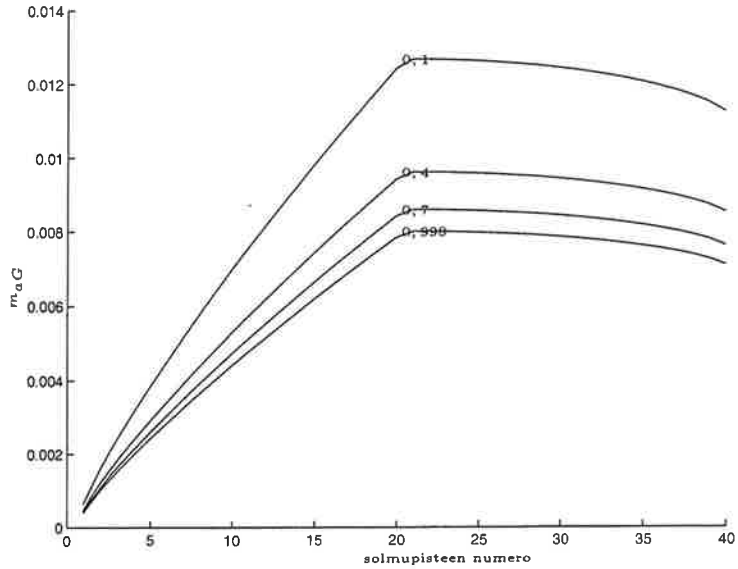

Kuva 6: Lisätyn massan turbulenttiset jakaumat pituuskoordinaatin x funktiona eri dimensiottoman nopeuden arvoilla, kun jakauma m_{aG} on epäsymmetrinen.

5 YHTEENVETO

Tässä esityksessä tarkasteltiin aksiaalisesti liikkuvan nauhan ominaisvärähtelyitä kitkallisessa fluidissa. Nauhan ja sitä ympäröivän ilman oletettiin muodostavan kerrossysteemin, ja näin ollen päädyttiin liikeyhtälössä muotoon, josta oli havaittavissa vastaavat termit kuin rajakerrosteorian avulla voidaan laskea, eli siirtymäpaksuus ja liikemääräpaksuus. Termit huomioitiin lisättynä massana, joka ei ole saman suuruinen joka termissä. Perinteiseen inertiatermiin lisätty massa m_a laskettiin vastaavasti kuin ilman aksiaalista nopeutta v laskettaisiin.

Koska lisätyt massat eivät ole vakioita nauhan aksiaalisuunnassa, ongelma ratkaistiin elementtimenetelmällä. Laskennassa käytettiin kaksivapausasteisia elementtejä ja ominaisarvotehtävä ratkaistiin numeerisella laskentaohjelmalla.

Vertaamalla saatuja tuloksia lähteessä [5] esitettyihin kokeellisiin havaitaan, että nauhaa ympäröivällä fluidilla on hyvin suuri merkitys nauhan ominaistaajuuksiin. Suurin vaikutus on perinteiseen inertiatermiin lisättävällä massalla m_a. Tässä esityksessä keskityttiin tarkastelemaan lisätyn massan vaikutusta gyroskooppiseen- ja jäykkyystermiin. Tuloksien mukaan lisätyllä massalla on vaikutusta — varsinkin suurilla dimensiottoman nopeuden arvoilla maksimissaan noin 15%, kun kyseessä on kasvava turbulenttinen jakauma ja paperi on kevyttä. Tulokset osoittavat, että kiinteää materiaalia ympäröivällä fluidilla ja fluidialueen muodolla on suuri merkitys rakenteen värähtelyihin.

Jatkossa kiinnostavaa olisi tietää fluidin aiheuttaman vaimennuksen suuruus ja toisaalta lisättyä massaa voisi yrittää laskea, jollain virtauslaskentaohjelmalla. Kytketyn ongelman (rakenteen värähtely ja virtaava fluidi) ALE-formulointi saattaisi olla mielenkiintoista ja haastavaa. Mahdollisesti mittauslaitteiston kehittäminen ja mittaaminen varsinkin suurilla dimensiottoman nopeuden V arvoilla saattaisi tarjota haasteita ja olisi merkittävää verrattaessa laskettuja tuloksia mitattuihin.

LÄHTEET

[1] Antti Pramila. Natural frequencies of a submerged axially moving band. *Journal of Sound and Vibration*, pages 198–203, 1987.

[2] Hannu Koivurova. *Aksiaalisesti liikkuvan kalvon ja sitä ohjaavan rakenteen kontaktin dynaaminen analysointi elementtimenetelmällä.* Oulu : [H. Koivurova], 1995. Lisensiaattityö.

[3] B. C. Young and P. M. Moretti. Interaction of fluttering webs with surrounding air. *Tappi*, pages 231–236, 1991.

[4] Antti Pramila. Peculiar features of axially moving materials. *VII Suomen mekaniikkapäivät Tampereella 25.-26.5.2000*, pages 31–42, 2000.

[5] Antti Pramila. Sheet flutter the interaction between sheet and air. *Tappi Journal*, pages 70–74, 1986.

[6] B. C. Sakiadis. Boundary-layer behavior on continuous solid surfaces: II. the boundary layer on a continuous flat surface. *A.I.Ch.E. Journal*, pages 222–225, 1961.

[7] Tero Frondelius. *Rajakerroksen vaikutus aksiaalisesti liikkuvan nauhan ominaistaajuuksiin.* Oulu: [T. Frondelius], 2003. Diplomityö.

NUMERICAL ANALYSES OF A WATER POOL UNDER LOADING CAUSED BY LARGE AIR AND STEAM BUBBLES

K.CALONIUS[1)], T.PÄTTIKANGAS[2)], A.SAARENHEIMO[3)]

1) VTT Industrial Systems, Espoo, kim.calonius@vtt.fi
2) VTT Processes, Espoo, timo.pattikangas@vtt.fi
3) VTT Industrial Systems, Espoo, arja.saarenheimo@vtt.fi

ABSTRACT

The experiments done at Lappeenranta University of Technology, where large air bubbles were injected in a water pool, were simulated by using the commercial computational fluid dynamics code Fluent. The CFD simulations were found to produce correctly the main features observed in the experiments. The pressure loads on the inner walls of the pool were determined and transferred to the structural analysis code ABAQUS using a transfer tool written for this study. The response of the structure to the transferred pressure loads was analysed.

1. INTRODUCTION

Behaviour of suppression pool during a loss-of-coolant accident (LOCA) is an important safety issue in boiling water reactors. During LOCA, a large amount of air and steam is injected into the suppression pool by the pressure difference of the drywell and the wetwell. Extensive experimental effort has been done on this topic during the past decades. In Marviken, small-scale experiments were performed with the Testa facility /1/ followed by full-scale containment experiments/2/. An example of recent experimental work is the thesis of Meyer /3/ which contains short reviews of different aspects of this field.

Behaviour of air bubbles injected in water pools has also been investigated by using computational fluid dynamics (CFD) during the past decades. The Volume Of Fluid (VOF) method introduced by Hirt and Nichols /4/ made possible simulations of large air bubbles with a reasonable computational cost. The early simulations were two-dimensional because of the limited computer resources /4,5,6/. Even the recent work of Meyer /3/ and Meyer and Yadigarogly /7/ contains only two-dimensional CFD simulations.

In the TOKE project of the Finnish Research Programme on Nuclear Power Plant Safety (FINNUS), injection of air and steam into a water pool is investigated experimentally at Lappeenranta University of Technology. In the first experimental series, air has been injected into the pool through a vertical pipe submerged in water. In the second series, experiments with steam are planned. In the planned steam experiments, possible occurrence of condensation water hammers may cause problems. The high loads due to water hammers may damage the pipe and the pool structures. Therefore, obtaining estimates for the loads and transferring them to structural analysis codes is of importance.

In the present work, the behaviour of large air bubbles in a water pool is investigated with three-dimensional CFD calculations. A method for transferring pressure loads from the computational fluid dynamics code Fluent to the structural analysis code ABAQUS is developed and tested. In the test case presented here, the loads on the pool structures are caused by sloshing of water during injection of air into the pool. The structural behaviour of the pool under the loads is numerically solved with a three-dimensional finite element model. The main aim is to solve numerically the three-dimensional loads caused by rapid water movements in a pool and to verify the transfer tool that interpolates the pressure from the CFD mesh to the structural analysis mesh. Another goal is to ensure that the future experiments with injected steam at Lappeenranta University of Technology are safe and in the right order before they are carried out.

2. EXPERIMENTAL SET-UP

In the TOKE project of the Finnish Research Programme on Nuclear Power Plant Safety (FINNUS), injection of air and steam into a water pool is investigated experimentally at Lappeenranta University of Technology. The pool constructed for the experiments is illustrated in Fig. 1. The pool is supported by beams to the floor and to the nearby concrete walls.

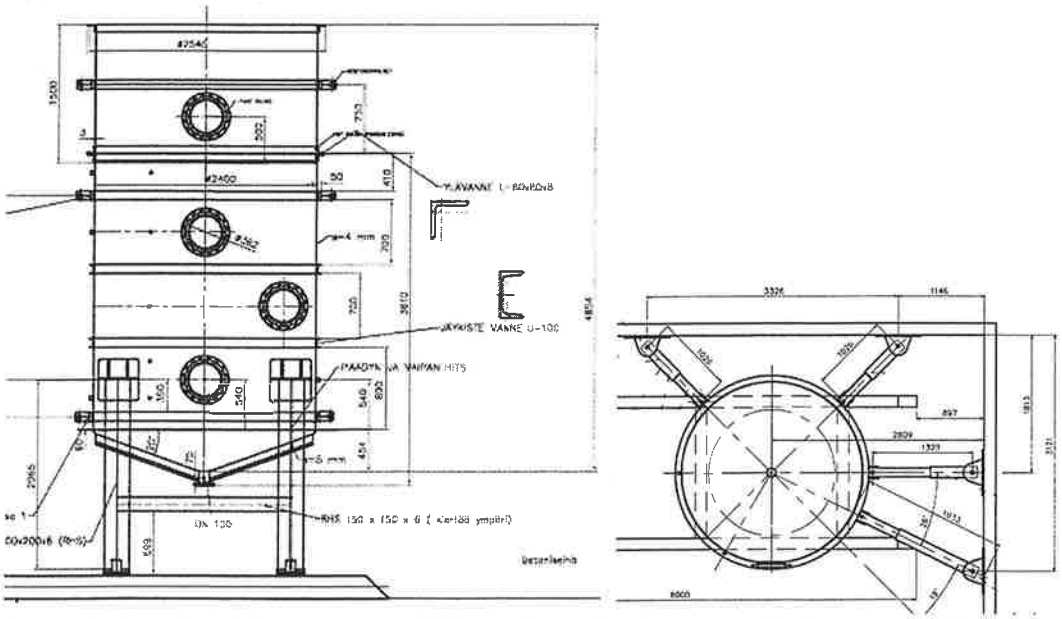

Figure 1. Experimental set-up in the TOKE-project at the Lappeenranta University of Technology /8/. The height is approximately 5 m and the diameter 2.4 m.

3. CFD MODEL

Injection of air into the pool shown in Fig. 1 was modelled with flow simulation. The height of the pool was 5.1 m and the pool diameter was 2.4 m. Initially, the pool contained water up to the level 2.87 m from the bottom. The axis of the vertical pipe was located 0.3 m from the pool axis. The diameter of the pipe was 300 mm and its submergence depth was 1.63 m.

Part of the surface mesh of the pool is shown in Fig. 2, where the bottom and part of the inner wall of the pool are shown. A fairly coarse mesh was used in the simulations: the number of grid cells was only about 80 000.

Pressure boundary conditions were applied at the pipe inlet and at the pool outlet. At the pipe inlet, air was injected into the pool and the relative total pressure was 20 kPa. The chosen value was somewhat larger than the hydrostatic pressure at the submergence depth of the pipe, which was 16.0 kPa. At the pool outlet, the relative total pressure was zero.

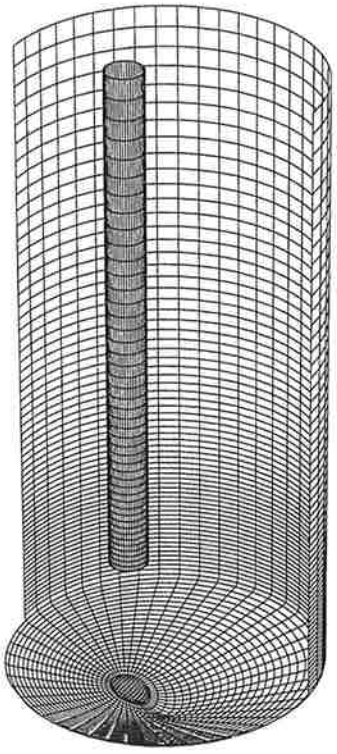

Figure 2. Surface mesh of the inner wall of the pool.

The flow equations were solved with the commercial Fluent 5.5.14 CFD program. The injection of air into water was described by using the Volume Of Fluid (VOF) model, where the surface between air and water is tracked during the simulation. The grid size used in the simulations sets a lower limit for the size of the bubbles that can be formed in the numerical model. Therefore, the break-up and the coalescence of the bubbles cannot be described accurately. Another limitation is that in Fluent 5.5 both water and air must be assumed incompressible. The compressibility of air would be an important effect especially inside the pipe, where pressure oscillations can occur.

4. CFD RESULTS

When air is injected into the water pool, pressure loads on the pool walls are caused by the sloshing motion of water in the pool. In addition, formation of large bubbles at the pipe outlet also pushes water further away from the pipe. When the large bubbles are detached from the pipe outlet, water hits strongly back against the pipe.

In Fig. 3, the vertical flow velocity is shown on the bubble surface at different instants of time. The iso-surface of volume fraction of air has been coloured with the vertical velocity of the surface, where blue and red stand for motion downwards and upwards, respectively. Initially at time $t = 0$, the water surface in the pool is at rest (cyan colour) but the surface starts rising when air is injected into the pool.

At time $t = 0$, the pressure at the inlet of the pipe rises by 20 kPa. The water column in the pipe starts moving downwards with increasing velocity. At time $t = 0.6$ s, a bubble starts forming at the pipe outlet, and it hits the bottom of the pool approximately at time $t = 0.8$ s. A ring-shaped bubble is formed in the bottom. The radius of this ring-shaped bubble increases and it moves towards the wall of the pool. At time $t = 1.0$ s, water hits back to the outlet of the pipe and a jet of water shoots into the pipe.

The first bubble is detached from the pipe outlet at time $t = 1.2$ s. The bubble starts rising towards the water surface. Formation of the second bubble starts at $t = 1.3$ s, and the first and second bubble reach the water surface almost simultaneously approximately at time $t = 1.56$ s. Formation of the third bubble at the pipe outlet starts at time $t = 1.6$ s, and it reaches the water surface at time $t = 2.0$ s.

When the bubbles break the water surface, water starts sloshing strongly in the pool. In the time intervals $t = 2...3$ s and $t = 4.5...5.0$ s, some water splashes over the edge of the pool. In Fig. 3, this splashing can be seen to occur on the left-hand side of the pool where the distance of the pipe from the wall is small. The weight of water moves from one side of the pool to the other side during the sloshing motion, which induces stresses in the supporting structures of the pool. The velocity of the water surface in this sloshing motion is typically between –3 and 3 m/s.

An air channel is formed from the pipe outlet to the water surface at time $t = 1.56$ s. The channel is rapidly closed by water hitting against the pipe. Such sudden opening and closing down of air channels causes rapid pressure variations in the pipe and in the pool.

In the early phase of the simulation, the time interval between the detaching bubbles is about $\Delta t = 0.4$ s. Later, the interval becomes somewhat shorter and the successive bubbles can not be distinguished so clearly. In the time interval $t = 2.73...5.33$ s, an increasing amount of small air bubbles are flowing around in the pool. Since the flow in the vicinity of the pipe is upwards, a return flow downwards is formed further away from the pipe. The smallest bubbles can be carried downwards by this return flow.

In Fig. 4, the relative static pressure on the pool wall is shown at eight different instants of time. At time $t = 0$, an overpressure of $\Delta p = 20$ kPa is applied at the pipe inlet and maintained until the end of the simulation. The effect of this overpressure propagates immediately to the pipe outlet and it also has some effect on the pool wall. At time $t = 0.20$ s, mainly the effect of the hydrostatic pressure can be seen in Fig. 4, where the pressure at the lowest point of the pool bottom is about 28 kPa.

At time $t = 0.70$ s, the water plug has been expelled from the pipe, where the flow velocity of air is 21 m/s. The pressure at the pool bottom is increased by 12 kPa due to the water plug hitting at the pool bottom with a velocity of about 5 m/s. The overpressure caused by the expulsion of the water plug from the pipe is followed by lower pressure at time $t = 1.00$ s. The first bubble breaks the water surface approximately at $t = 1.56$ s, and the sloshing of water leads to an increased load on the bottom of the pool.

The CFD simulations and the experiments performed in the TOKE project are discussed more closely by Pättikangas and Pokela /9/ and Laine /8/.

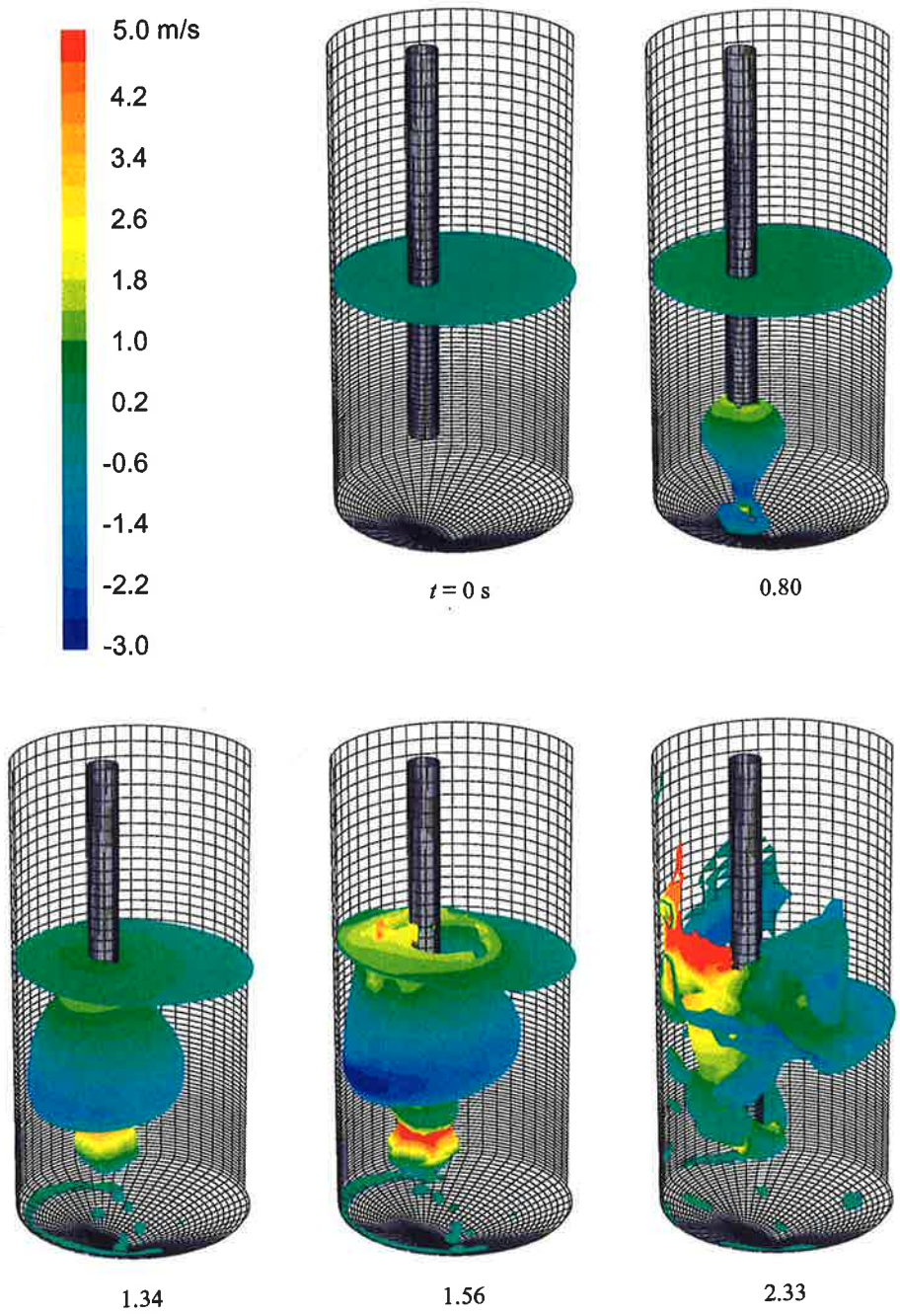

Figure 3. Axial flow velocity on the bubble surface. Iso-surface of volume fraction of air ($\alpha = 0.1$) coloured with axial velocity. All the velocities larger than 5 m/s and smaller than –3 m/s are shown as red and blue, respectively.

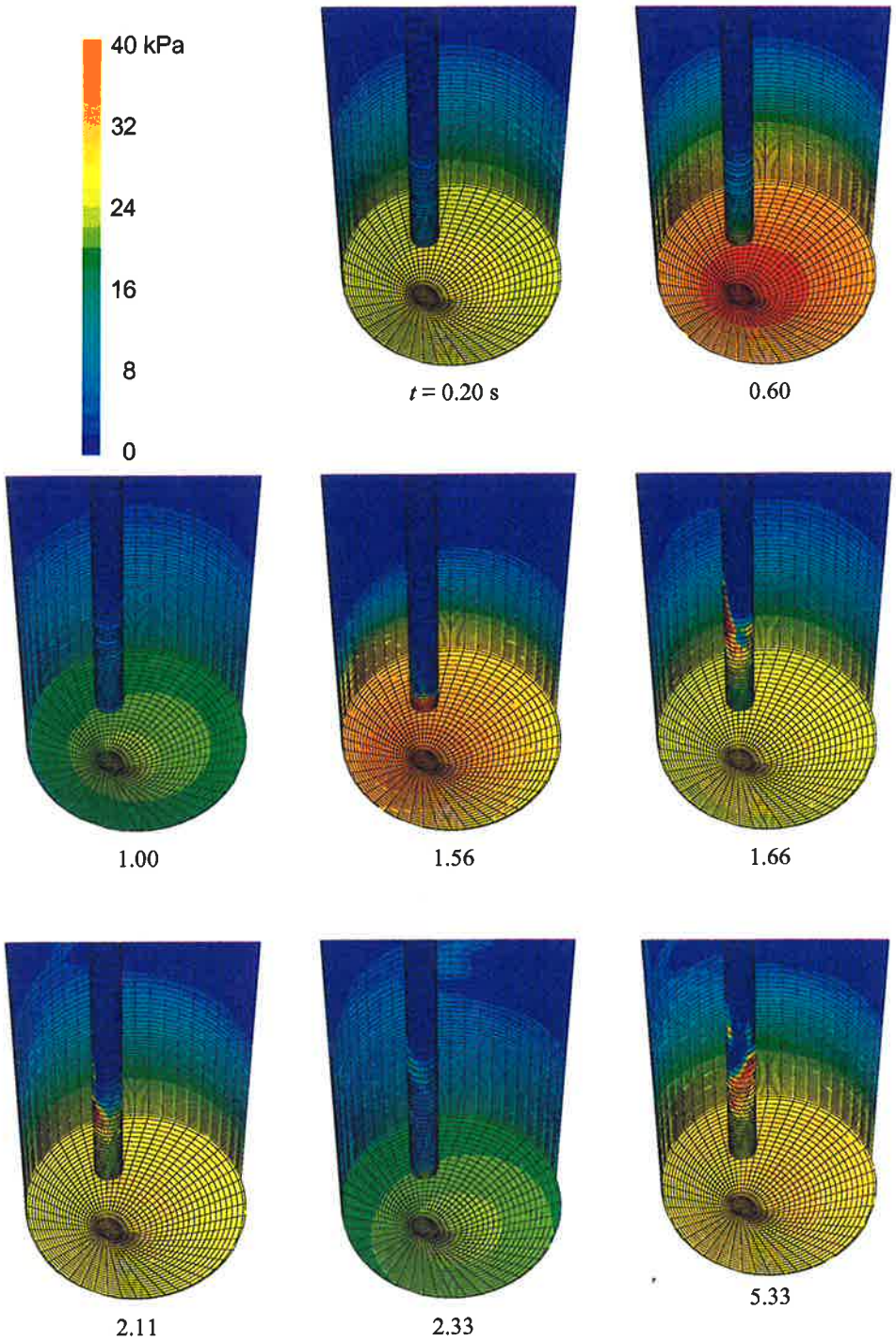

Figure 4. Relative static pressure on the inner wall and bottom of the pool at different instants of time.

5. TRANSFERING DATA

The transient inner wall pressure described above was transferred from the CFD calculation to the ABAQUS structural analysis code. In structural analysis, the numerical mesh was different compared to the CFD analysis. Therefore, interpolation of the pressure from the CFD mesh to the structural analysis mesh at the inner wall had to be performed. The interpolation was done by using the D2A v. 1.02 interpolation programme, which was written in collaboration with Ari Silde for this purpose /10/.

The D2A interpolation programme is based on the MpCCI library (Mesh-based parallel Code Coupling Interface) which has been written in the Fraunhofer Institute for Algorithms and Scientific Computing /11,12/. The MpCCI library enables coupling of two mesh based codes, such as CFD and structural analysis codes. The codes exchange coupling data, such as pressure, velocity and temperature on a meshed coupling surface. MpCCI provides tools for interpolation of the coupling data from the mesh of the sending code to the mesh of the receiving code. Bi-directional coupling of the codes via a moving coupling surface is also supported.

In the D2A interpolation programme that was implemented in this work, the basic features of MpCCI were used to obtain a simple one-directional coupling of Fluent and ABAQUS. The motion of the pool wall was not taken into account in the CFD calculation. The mesh on the coupling surface did not move during the simulation. In the present work, interpolation was tested only from quad to quad elements but the programme has been written to support all seven element types known by MpCCI. The bi-directional coupling is currently being tested.

6. FEM MODEL

The pool is simulated with an axisymmetric and a three-dimensional model. Some preliminary analyses not discussed here are conducted with the axisymmetric model. Boundary conditions and loads are altered in the three-dimensional model, but mainly one case is described in this article. Pressure loads onto the inner wall of the pool are transferred from the CFD analysis. The simulation results are verified against analytical calculations.

The pool stands in the corner of the large testing room and is supported from beneath by four bearers (200 mm x 200 mm x 6 mm) and from the side by five side stays (150 mm x 150 mm x 6 mm). Two horizontal beams (150 mm x 150 mm x 6 mm) are welded between the bearers. The bearers have springs under them, but they are not modelled until the second experimental series with injected steam. All beams are rectangular hollow sections.

A complex model with different element types is created for three-dimensional structural analyses. It corresponds relatively accurately to the real pool and its supporting structures. The mesh can be seen in Fig. 5. The pool is meshed with 4-node doubly curved general-purpose shell elements with finite membrane strains. Reduced integration with hourglass control is used. The length of the shell element edge is on the average 50 mm. The beams are meshed with 2-node linear beam elements. The elements are 100 mm long. Every node has six active degrees of freedom. Number of elements in the whole model is 6581, number of nodes is 7328 and total number of variables in the model is 39828.

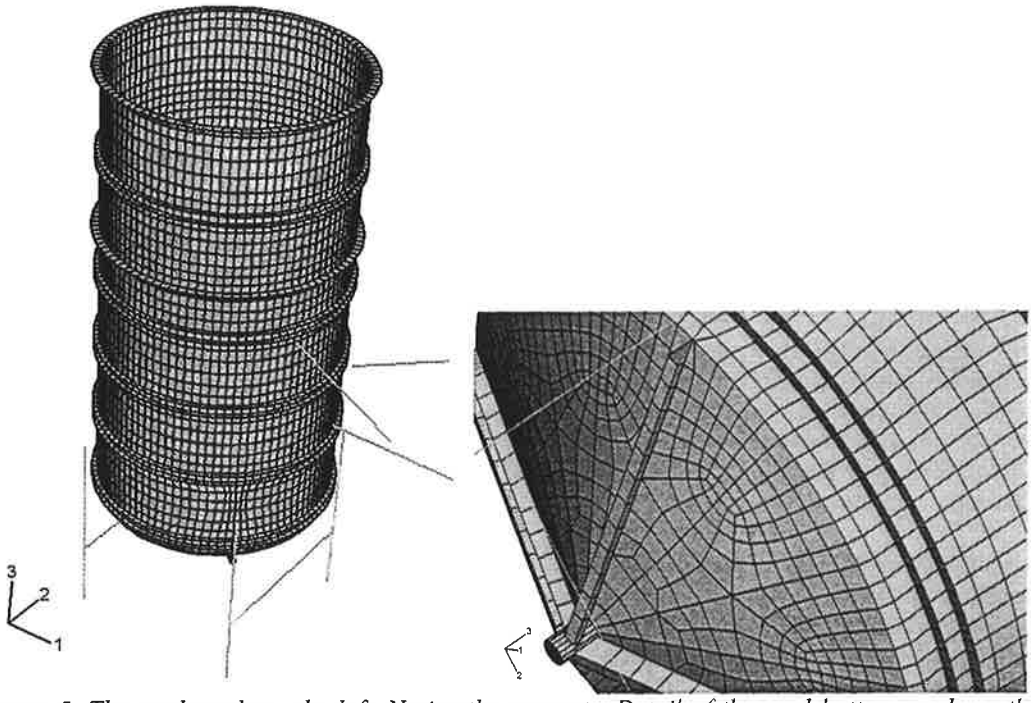

Figure 5. The pool mesh on the left. Notice the supports. Detail of the pool bottom mesh on the right. Notice the stiffening bracings.

Three different materials are used in the pool. The pool itself and the L-pipe around it are stainless steel SS2333, the U-pipe bracings around it are normal steel S235JRG2 and the rectangular beams are S355J2H. An elastic-plastic material model with von Mises yield function and isotropic yield hardening is adopted. The material properties are listed in Tables 1 and 2.

Table 1. Elastic material properties at room temperature. Young's Modulus [MPa], Poisson's ratio and density [kg/m^3]. /13/

	SS2333			S355J2H			S235JRG2		
T	*E*	*ν*	*ρ*	*E*	*ν*	*ρ*	*E*	*ν*	*ρ*
25	200000	0.3	7900	206000	0.3	7850	206000	0.3	7850

Table 2. Plastic material properties. Stress [MPa] and corresponding plastic strain. /13/

	SS2333		S355J2H		S235JRG2	
T	*σ*	*ε*	*σ*	*ε*	*σ*	*ε*
25	200	0	315	0	195	0
25	210	0.002	325	0.002	205	0.002
25	240	0.01	355	0.01	235	0.01

7. FEM RESULTS

The FE analyses were carried out using ABAQUS/Standard code version 6.3.1 /14/. A static analysis is conducted with the same air blow data than the dynamic analysis. The material does not reach the yield point at any moment in any area. The model behaves logically, like it should behave with the concerned data. This partly verifies the data and its transfer.

The eigenvalue extraction is done for two three-dimensional models. In the first one the water mass is not included in the dynamic equations of motion, but in the second one the mass is

included in the steel walls of the pool, where an equivalent density is used. In the first case, the total mass of the model is 2455 kg and the lowest eigenfrequency is approximately 20 Hz. In the second case, the total mass is 14352 kg and the lowest eigenfrequency is approximately 8 Hz.

Nonlinear dynamic analysis uses implicit time integration to calculate the transient dynamic response of the system. The pool is swaying back and forth and the supporting beams are bending. Fig. 6 shows the vertical displacement of the pool bottom of both cases mentioned above. The maximum displacement is approximately 0.87 mm downwards. The displacement magnitudes of both cases are close to each other, but the peaks are higher without the mass of water. The peaks coincide with the pressure peaks. The first lower pressure occurred after approximately 1 seconds and a clear overpressure occurred after 1.5 seconds, for example. From here on, only the results of the model without the mass of water are introduced.

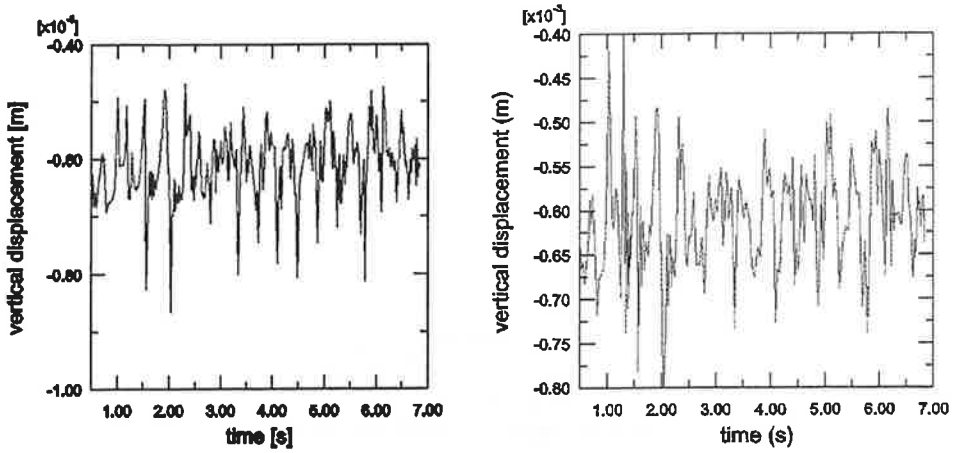

Figure 6. Vertical displacement of the pool bottom. Case without the mass of water on the left, case with it on the right.

The horizontal displacements of the top of the pool are surprisingly low. The maximum displacement is approximately 1.5 mm. The horizontal displacement magnitudes of the side stay and bearer leg ends from which they are joined to the pool stay below 0.6 mm.

The vertical reaction forces in the location where the legs are fixed into the floor are calculated. The mean value is approximately 27 kN and the magnitudes stay below 50 kN, which corresponds to analytical calculations that have been performed. The reaction forces alter by approximately 50 % during the analysis.

The maximum stress value during the whole analysis is approximately 97 MPa (at 1.567 s) and it is located in the rounding, i.e., the joint of pool cylinder wall and pool bottom wall. Outer wall has lower stresses in the pool rounding, but higher stresses where the supports are joined to the pool. Fig. 7 shows the hoop and axial stresses in the bottom of the pool, close to the rounding. Hoop stresses are compressive and they are higher by magnitude in the outer wall (46 MPa). In the axial direction there is approximately 30 MPa tension in the inner wall and 20 MPa compression in the outer wall. Fig. 8 shows a von Mises stress contour plot of the pool bottom. Notice the supporting beams and their effect on the stresses in the pool wall. The stresses correspond to analytical calculations.

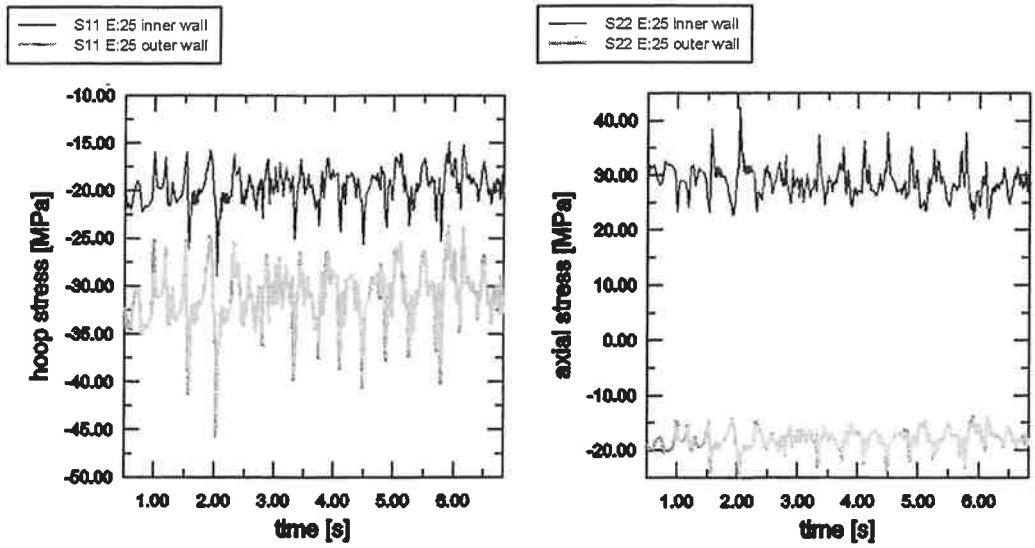

Figure 7. Hoop stresses on the left and axial (meridian) stresses on the right near the pool bottom rounding. The upper curves represent inner wall values.

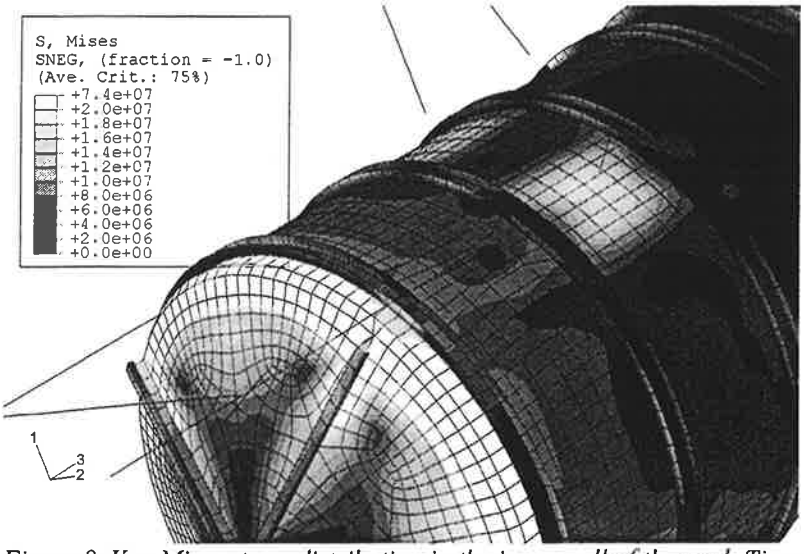

Figure 8. Von Mises stress distribution in the inner wall of the pool. Time instant is 1.999 seconds. The white colour represents stress magnitudes over 20 MPa.

8. SUMMARY AND CONCLUSIONS

Three-dimensional simulations of large air bubbles injected in a water pool have been performed by using the commercial computational fluid dynamics (CFD) code Fluent. The experiments performed at Lappeenranta University of Technology were modelled by using the volume of fluid (VOF) model for large bubbles. The CFD simulations were found to produce correctly the main features observed in the experiments. The pressure loads on the wall and the bottom of the pool were determined and transferred to the structural analysis code ABAQUS.

Pressure loads on the pool wall and bottom were caused by sloshing motion of the water. Rapid movements of water occur when large bubbles were detached from the pipe and when air channels

from the pipe outlet to the surface were suddenly closed. Then, water was found to hit strongly against the pipe causing rapid increases of pressure. Strong oscillation in the load occurs when the first bubble breaks the water surface. The variations of the pressure loads on the wall are about ±15 kPa. The loads on the pipe are somewhat larger.

Investigations of fluid-structure interactions are made possible by the tool written for transferring the pressure loads from Fluent to the structural analysis code ABAQUS. The transfer tool D2A is based on the MpCCI subroutine library. D2A interpolates the pressure load on the inner wall of the pool from the CFD mesh to the ABAQUS mesh. In D2A, only one-directional coupling of the codes has been implemented, i.e., the motion of the pool wall was not taken into account in the CFD simulation.

The structural effects caused by rapid water movements were examined. The stresses stayed below the yield point and no plastic deformations took place. The maximum stresses were expectedly located in the rounding between the pool cylinder wall and the end plate. The rapid water movements had no significant structural effect. The stress variations in the pool wall corresponded to the pressure load variations. The reaction forces in supports naturally varied more.

The motion of the pool was surprisingly minor. The largest displacements were only approximately 2 mm. According to the visual inspections in the experimental tests, the vibration amplitude was at least 10 mm. Otherwise, the model responded realistically to the transferred pressure loads. The addition of mass of water to the model had no significant effect on the structural response in these analyses. It probably would be more significant with higher pressure loads, when the pool clearly starts vibrating.

Preliminary analyses for water hammer loading caused by a steam bubble condensation were carried out using an axisymmetric FE model. The springs below the columns were modelled as an equivalent spring. A hydrodynamic material model was used for water. According to these analyses, the allowed stress level would clearly be exceeded in supporting columns.

An important application of the method used in this project is the load transients caused by water hammers. A condensation water hammer may occur in the future experiments, where steam is injected into the pool. In that case, material yielding is expected to take place. The springs under the supporting legs will be modelled also in the three-dimensional model.

ACKNOWLEDGEMENTS

This study is a part of SAFIR, a new research programme on nuclear power plants (Safety of nuclear power plants – Finnish national research programme). This study is funded by STUK, by the Ministry of Trade and Industry (KTM) and by VTT. The authors thank Mr. Rauli Keskinen (STUK) for his interest in this work. The authors are grateful to the members of the TOKE project at the Lappeenranta University of Technology, Mr. Jani Laine, Mr. Markku Puustinen and Mr. Heikki Purhonen, for invaluable discussions on their experimental results.

REFERENCES

/1/ Anon., 1977a. Summary report, Theoretical efforts on containment pressure oscillation, Joint theoretical and experimental study performed at Marviken, Sweden, Report TECPO-401.
/2/ Anon., 1977b. Description of the test facility. The Marviken full scale containment experiments, second series, Marviken, Sweden, Report MXB-101.
/3/ Meyer, M., 1999. Numerical and experimental study of large steam-air bubbles injected in a water pool. Dissertation ETH no 13091, ETH, Zürich, Switzerland.
/4/ Hirt, C. W. and Nichols, B. D., 1979. Eulerian methods with free boundaries. First international seminar on fluid-structure interaction in LWR systems, Berlin, Germany, August 20–21, 1979, p. 29.
/5/ Nichols, B D. and Hirt, C. W., 1979. Hydroelastic phenomena in boiling water reactor suppression pools. Transactions of the 5th international conference on structural mechanics in reactor technology, Berlin, Germany, 13 – 17 August, 1979, North-Holland, p. B 7/2.
/6/ McMaster, W. H., Gong, E. Y. and Landram, C. S., 1981. Improved fluid-structure coupling. Transactions of the 6th international conference on structural mechanics in reactor technology, vol. B, Paris, France, 17–21, North-Holland, p. B 1/4.
/7/ Meyer, M. and Yadigaroglu, G., 2000. Numerical and experimental study of large steam-air bubbles injected in a water pool. Nuclear Science and Engineering 136, p. 363.
/8/ Laine, J., 2002. Condensation pool experiments with non-condensable gas, Lappeenranta University of Technology, Research Report TOKE-2/2002, 46 p. + app. 14 p.
/9/ Pättikangas, T. and Pokela H., 2003. Wall-loadings caused by large air bubbles injected in a water pool, VTT Processes, Project Report PRO4/T7534/02, Espoo, Finland, 28 p.
/10/ Silde, A. and Pättikangas, T. D2A version 1.0, 2001. Interface between the DET3D and Abaqus codes, VTT Energy, Report ENE4-PD-3/01, 5 p. + app. 27 p.
/11/ MpCCI Team, 2002a. Mesh-based parallel Code Coupling Interface, User's guide of MpCCI version 1.3, Fraunhofer Institute for Algorithms and Scientific Computing, Sankt Augustin, Germany, 27 p.
/12/ MpCCI Team, 2002b. Mesh-based parallel Code Coupling Interface, Specification of MpCCI version 1.3, Fraunhofer Institute for Algorithms and Scientific Computing, Sankt Augustin, Germany, 125 p.
/13/ Rautaruukki. Rautaruukin paineastiakäsikirja 1999, ISBN 952-5010-27-9
/14/ ABAQUS Theory Manual. 2002.Version 6.3. Hibbit, Karlsson & Sorensen Inc. RI.

COMPUTATIONALLY ECONOMICAL COUPLED SIMULATIONS OF A GAS DAMPED MICROMECHANICAL RESONATOR

A. PURSULA and P. RÅBACK

CSC – Scientific Computing Ltd.
P.O. Box 405, FIN-02101 Espoo
e-mail: Antti.Pursula@csc.fi

ABSTRACT

A coupled model for gas damped micromechanical resonators is presented. The model includes 3D elasticity and gas flow in a narrow gap, which both are modeled by computationally economical methods. The displacement of a rigid block is expressed by the translational and rotational degrees of freedom of the center of mass. The gas damping is modeled by the Reynolds equation, which solves the pressure distribution in narrow channels. The reduced elasticity model is verified in a modal analysis. The effect of different design parameters on the behavior of the resonator is studied in transient simulations.

1 INTRODUCTION

In micromechanical systems, the gas restricted in narrow gaps between moving structures causes considerable forces on the structures. The gas may either be compressed or forced to flow out of the gap. The isothermal compression of gas is a reversible process and it results in a spring-like force on the resonating structure. The forced gas flow, on the other hand, results in damping of the oscillations, since kinetic energy of the resonator is used to overcome viscous resistance of the flow. In micromechanical dimensions these both phenomena are notable. The gas damping is often called the squeezed-film-damping, and it is most influential in planar resonators such as accelerometers or torsional micro mirrors.

In this paper we present a method for simulating micromechanical resonators under squeezed-film-damping and apply it to a simple accelerometer. We have previously described a similar model for a thin resonating membrane including perforation holes [1]. The current model is fully coupled, it is not restricted to small pressure deviations or small amplitudes, and it can manage the true three-dimensional geometry of the problem. The mathematical model is based on the linear elasticity equation and on the Reynolds equation describing the gas flow in narrow gaps. In addition, the deformations of the proof mass are assumed to be negligible compared to those of the elastic springs. A linear elasticity solver may be used since the displacements are small compared to the dimensions of the structure. The displacements, however, need not be small compared to the air gap height, because the Reynolds equation is not linearized. The Reynolds equation has been used in modeling of micromechanical systems in literature, *e.g.* in [2] and references therein.

A perfectly three-dimensional model of the gas damped resonator would require solving the elasticity and Navier-Stokes equations in a coupled manner. This is not feasible in finite

element simulations for several reasons. The large aspect ratios of the geometry results to a huge number of elements as the size of the elements is defined by the height of the channel. The number of mesh points may easily total in hundreds of thousands, and the problem would have more than a million degrees of freedom as the velocity field and the pressure should be solved on each node. The fluid-structure interaction problem present in squeezed-film-damping requires usually several iterations between the elasticity and fluidics, thus the Navier-Stokes equations have to be solved repeatedly. In transient problems, the number of solution steps is again greatly increased. Therefore the use of the full Navier-Stokes equations in realistic geometries is not possible in practice.

A computational difficulty is encountered also in solving the elasticity equation. Micromechanical structures have often regions which are very different in stiffness. A large part of the structure may be almost non-deforming and another, usually the smaller part, deformes significantly. An example of such a structure is an accelerometer for which we present results in Section 3. The stiffness matrix for such geometries is ill-conditioned, and consequently, the resulting matrix equation is difficult to solve. Often an iterative linear equation solver fails in this instance. However, the size and complexity of the matrix equation of elasticity is greatly decreased by replacing the nodal degrees of freedom in the non-deforming block by the degrees of freedom of a single point which represents the whole rigid domain. This scheme we have called reduced-order elasticity.

2 MATHEMATICAL MODELS

2.1 Linear elasticity

Elastic deformations can be computed from the well known linear elasticity equation

$$\rho \frac{\partial^2 v}{\partial t^2} - \nabla \cdot \tau = h, \tag{1}$$

where v is the displacement field, h is an external volume force, and τ is the stress tensor. The stress tensor for isotropic material is

$$\tau = 2\mu\varepsilon + \lambda \nabla \cdot dI, \tag{2}$$

where μ and λ are the first and second Lame parameters, respectively, I is the unit tensor, and ε is the linearized strain tensor

$$\varepsilon = \frac{1}{2}\left(\nabla v + (\nabla v)^T\right). \tag{3}$$

The Lame parameters may be expressed in terms of Youngs modulus Y and Poisson ratio κ by

$$\mu = \frac{Y\kappa}{(1-\kappa)(1-2\kappa)} \quad \text{and} \quad \lambda = \frac{Y}{2(1+\kappa)}. \tag{4}$$

The boundary conditions for the linear elasticity equation are either a Dirichlet condition $v = v_0$ implying a fixed value v_0 on the boundary or the Neumann boundary condition

$$\tau \cdot n = g, \tag{5}$$

which defines a force g acting on the boundary with outward unit normal vector n.

The modal analysis is performed with a Fourier transformed equation

$$\rho\omega^2 v_e = \nabla \cdot \tau(v_e), \tag{6}$$

where ω is the angular frequency. This equation is a generalized eigenproblem and may be solved to find the eigen frequencies and eigen vectors v_e.

2.2 Reduced-order elasticity

The elastic analysis may be reduced by assuming a part of the geometry to form a rigid body. The displacements of all points in the rigid block can be stated using the translations of and rotations about a single point, the mass center of the rigid block. For writing out the reduction scheme we need to work out two separate steps: transforming the distributed forces acting on the rigid block on the mass center point and expressing the displacements of an arbitrary point in terms of the degrees of freedom of the mass center point.

Let us first go through the relation of the displacement of an arbitrary point and the degrees of freedom of the mass center point. The rotation has remarkably simpler expressions in two dimensions and generalizing them into three dimensions is straigthforward. The details are thus gone through in 2D and briefly stated for 3D.

Assume we wish to rotate a point w over an angle φ about the mass center point w_c. The vector from the rotation axis we shall call $r = w - w_c$ and the rotated vector r'. The rotation can written as a matrix

$$r' = \begin{pmatrix} \cos\varphi & -\sin\varphi \\ \sin\varphi & \cos\varphi \end{pmatrix} r = Rr, \tag{7}$$

which gives for the displacement due to rotation

$$\mathrm{d}r' = r' - r = Rr - r = (R - I)r = Mr. \tag{8}$$

Using the summation formulae for the sines and cosines and assuming small rotations the linear matrix reads

$$M = \begin{pmatrix} 0 & -\varphi \\ \varphi & 0 \end{pmatrix}. \tag{9}$$

Finally, together with the translation the displacement vector v is

$$v = Mr + v_c, \tag{10}$$

where v_c is the translation of the rigid body mass center point. Now, inserting $r = w - w_c$ we finally get an expression for the displacements of a single node related to the displacement and rotation of the whole rigid block

$$\begin{aligned} v &= \begin{pmatrix} v_x \\ v_y \end{pmatrix} = \begin{pmatrix} -\varphi(y - y_c) \\ \varphi(x - x_c) \end{pmatrix} + \begin{pmatrix} v_{c,x} \\ v_{c,y} \end{pmatrix} \\ &= \begin{pmatrix} 1 & 0 & y_c - y \\ 0 & 1 & x - x_c \end{pmatrix} \begin{pmatrix} v_{c,x} \\ v_{c,y} \\ \varphi \end{pmatrix}, \end{aligned} \tag{11}$$

where x and y are the components of the vector w and x_c and y_c the components of the vector w_c.

In three dimensions the rotation is somewhat more cumbersome but the basic principle remains the same. We have used the Euler angles to represent the rotation with the order xyz, *i.e.* the first rotation being about the x-axis in cartesian coordinates, and so on. As with the two-dimensional case, the displacements due to rotation can be expressed by a linearized matrix

$$M = (R - I) = \begin{pmatrix} 0 & -\gamma & \beta \\ \gamma & 0 & -\alpha \\ -\beta & \alpha & 0 \end{pmatrix}, \tag{12}$$

into which the effect of translation may be incorporated as shown in the two-dimensional case.

Let us now consider the transformation of a distributed force on the mass center point. The forces acting on each nodal point, f_i, may be summed to form a resultant force on the mass center point. However, the torques about the mass center point have to be taken also into account. We may define a vector f_R which corresponds to the distributed force f_i on the nodal points w_i but acts on a single point as

$$f_R = \begin{pmatrix} \sum_i f_{i,x} \\ \sum_i f_{i,y} \\ \sum_i f_{i,z} \\ \sum_i [(w_i - w_c) \times f_i]_x \\ \sum_i [(w_i - w_c) \times f_i]_y \\ \sum_i [(w_i - w_c) \times f_i]_z \end{pmatrix}. \tag{13}$$

Now we are in a position to consider combining the pointwise transformations as a matrix reduction scheme. The starting point for the reduction is a system of linear equatios for the unknown displacements x, $Ax = b$, which is constructed by the finite element method just as usual. Instead of solving this matrix equation we aim to reduce its number of unknowns. Assume that in the geometry there are n nodes belonging to the elastic domain and m nodes belonging in the rigid domain. Then the $3(n+m) \times 3(n+m)$ matrix A will be reduced into a $3n+6 \times 3n+6$ matrix B. Corresponding reductions are made also for the vectors and the matrix equation takes the form $Bu = f$.

For the unknowns x the reduction can be represented by matrix multiplication: $x = Pu$, where the $3(n+m) \times 3n+6$ matrix P consists of a unit matrix block of size 3×3 for each node in the elastic domain and of m times the combined rotation-translation matrix block that was defined for 2D case in Equation (11). The vector u has the first n elements identical to those elements of vector x, which correspond to the elastic nodes of the mesh. After that there are six elements that correspond to the degrees of freedom of the rigid body.

In the same fashion, for the right hand sides, we can write define a matrix Q such as $f = Qb$. The $3n+6 \times 3(n+m)$ matrix Q has a unit matrix block of size 3×3 for the degrees of freedom of the elastic domain and m times the force transformation matrix, which may be derived from Equation (13). The reduced right-hand side vector f has as last six elements the resultant force vector f_R.

Writing out the matrices P and Q one notices that they are equal apart of a transpose operation. It is rather appealing that the matrix that is used to transform a distributed force to act on a single point is identical to the matrix, which is used to express the distributed displacements based on the displacement of the single point. The similarity of the matrices seems natural and brings confidence on the reduction method. This observation allows us to rename the matrices as follows

$$C \equiv Q = P^T. \tag{14}$$

It is now possible to write the original matrix equation as $AC^T u = b$ and the reduced-order matrix equation as $Bu = Cb$. Combining these gives for the reduced matrix

$$B = CAC^T. \tag{15}$$

The reduced matrix equation $Bu = f$ can be solved with standard numerical techniques. The solution vector u can be mapped back to the original group of nodes by multiplication, $x = C^T u$.

The advantage gained by the matrix reduction scheme is dependent on the relative amount of node points that belong to the rigid body. However, the reduction is usually beneficial even if a small part of the geometry can be assumed to be rigid. Also, the number of computer operations required in constructing the reduced matrix equation grows only linearly as the degrees of freedom increase.

2.3 Reynolds Equation

In narrow channels the computational mesh required for the solution of Navier-Stokes equations is not economic. In order to reduce the computational effort, the full Navier-Stokes equations may be replaced with the Reynolds equation for pressure p. The Reynolds equation is derived from the Navier-Stokes equations under the assumptions that the air gap height is far smaller that the side length of the gap, that the Reynolds number of the problem is small, which means that the mass of the gas can be neglected, and that the gas follows the ideal gas law for isothermal processes.

Under these assumptions, it is found that the pressure is not changing in the direction of the gap. Additionally, no-slip boundary conditions for the gas velocity are used and the plates are assumed not to move in lateral direction. With these boundary conditions, the gas flow follows a parabolic velocity profile with a time-dependent gap height. It then suffices to solve an equation for pressure in a plane. This equation is the Reynolds equation

$$\nabla \cdot \left(\frac{pd^3}{12\eta} \nabla p \right) = \frac{\partial (pd)}{\partial t}, \tag{16}$$

where d is the gap height and η is the viscosity of the gas [3]. The wake for the equation is thus the rate of change of the gap height $\dot{d}$, which equals the velocity of the elastic resonator. A possible boundary condition for the equation is

$$\frac{\partial p}{\partial n} = 0, \tag{17}$$

where n is the unit normal vector of the boundary. This condition implies symmetry or a closed wall. A boundary condition for an open wall is

$$p = p_0, \tag{18}$$

where p_0 is the ambient pressure.

The Reynolds equation is nonlinear with respect to the pressure. In the discretization of the equation this nonlinearity is preserved. The discretized iterative scheme is written by dividing the pressure into two components $p = p_0 + q$, where p_0 is the constant ambient pressure and q is the deviation from the ambient pressure. Using the derivation rule of summation and changing the order of the terms gives an equation for q

$$d\frac{\partial q}{\partial t} + \frac{\partial d}{\partial t} q - \nabla \cdot \left(\frac{(p_0 + q)d^3}{12\eta} \nabla q \right) = -p_0 \frac{\partial d}{\partial t}. \tag{19}$$

Accordingly, the nonlinear solution is found using the following iteration scheme

$$d\frac{\partial q^{(m)}}{\partial t} + \frac{\partial d}{\partial t} q^{(m)} - \nabla \cdot \left(\frac{(p_0 + q^{(m-1)})d^3}{12\eta} \nabla q^{(m)} \right) = -p_0 \frac{\partial d}{\partial t}, \tag{20}$$

where the superscripts correspond to the number of iteration. Thus, the nonlinear term is discretized by taking advantage of the iterative solution of the previous round. The iterations are continued until a defined convergence tolerance is achieved.

2.4 Coupling of equations

In the coupled model, the air gap needs not to be meshed but the Reynolds equation is solved utilizing the surface of the meshed three-dimensional elastic structure. A relevant surface of the elastic structure forms one side of the air gap, whereas the other side is defined by an equation for a plane

$$c_x x + c_y y + c_z z = c_0. \tag{21}$$

This approach allows the reference plane to be oriented freely as long as the assumption of a narrow gap is everywhere sustained.

The coupling of the elasticity equation and the Reynolds equation needs an itermediate step in which the gap height and gap height velocity are computed. This is done for each relevant nodal point on the surface of the elastic structure based on the reference plane defined above and on the current elasticity solution. For example, if the reference plane is defined by $z = -D$ then the gap height is $d = D + v_{S,z}$, and the rate of change of the gap height is $\dot{d} = \dot{v}_{S,z}$, where $v_{S,z}$ refers to the displacements of the relevant surface of the elastic structure.

The Reynolds equation is thus coupled with the elasticity, since the displacement of the elastic structure affects the pressure in the air gap. On the other hand, the gas pressure deviation q in the air gap causes a net force acting on the elastic body as a boundary condition according to Equation (5)

$$\tau \cdot n = q. \tag{22}$$

This fully coupled fluid-structure interaction problem is solved using a method of sequential iterations, where the coupled equations are iterated on every time step until convergence criteria for each equation are satisfied.

3 RESULTS

The mathematical models were used to simulate the behavior of an accelerometer structure shown in Figure 1. The dimensions of the accelerometer proof mass were 2.0mm× 1.5mm×0.45mm. The elastic springs were 1.0mm in length with a cross section of 50μm× 100μm. Elastic material parameters of Silicon were used (density $\rho = 2330\frac{kg}{m^3}$, Youngs modulus $Y = 130.0$GPa, Poisson ratio $\kappa = 0.27$). The accelerometer proof mass contained three square holes with sides measuring 200μm. The end surfaces of the elastic springs are attached to the wall. The models were implemented in and the simulations performed on Elmer finite-element software [4].

A linear tetrahedral meshing of the geometry was used. The mesh contained 72064 bulk elements and 14970 nodes. On the surface, where the Reynolds equation was solved, there were 1568 triangular surface elements. Altogether 83% of all nodes belonged to the rigid block. Netgen software was used in creating and meshing the geometry [5]. The simulations were performed on a Compaq AlphaServer ES45 system with a 1 GHz Alpha EV68 central processor.

3.1 Eigen mode computations

The eight smallest eigen frequencies and eigen modes of the structure were calculated. The calculations were used to compare the results and time consumption of the reduced-order elastic simulation and the full elastic simulation. The matrix equation from FEM discretization was solved using an iterative conjugate gradient method and a direct method. The results from different linear system solver types were identical at least up to sixth digit.

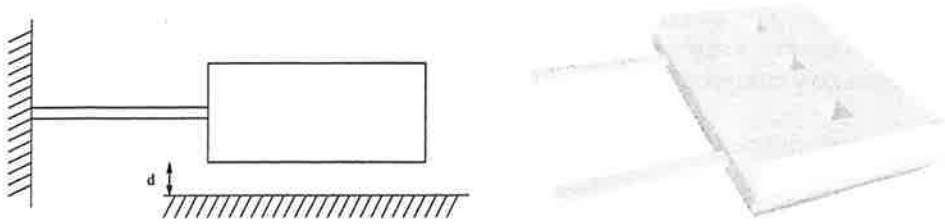

Figure 1: An accelerometer containing two elastic springs and a rigid proof mass; left, schematic picture not in scale; right, the geometry used in simulations.

Computing the first eight eigen modes with the reduced-order elasticity took 265 cpu seconds on an iterative solver and 394 cpu seconds on a direct solver. The time-consumption of the full elasticity was 4660 cpu seconds on a iterative solver and 1656 cpu seconds on a direct solver. Comparing the faster solvers the computer time consumption in reduced-order scheme is about one sixth of the full elasticity. However, the direct solver uses large amounts of computer memory, in this case with *ca.* 45000 degrees of freedom more than one gigabyte. Thus, the direct solution method is not often feasible due to memory limitations and an iterative solver has to be used also for the full elasticity. Then, in this test case, the time used to compute the full elasticity solution is almost twenty times longer than the one of the reduced-order scheme.

Usually, the iterative solvers are faster than direct solvers. However, the direct solver is here faster for the full elasticity, since iterative solvers are in trouble with ill-conditioned stiffness matrices. The direct solution of the reduced-order elasticity is relatively slow. The reason for this is that the structure of reduced matrix is not optimised for the direct solution method but the full matrix is optimised.

The eigen frequencies had some differences when calculating with the different schemes. The relative error of the reduced-order scheme results compared to the standard elasticity ranged from 0.4% in the first eigen mode up to 3.6% in the seventh mode. The eigen mode results are summarised in the Table 1. As the Table shows, the accuracy of the reduced-order elastic model is reasonably good, and together with its economical use of computer resources, the utilization of reduced-order elasticity in coupled simulations seems justified.

The eigen frequency computed by the reduced-order scheme was consistently higher than the value calculated by the full model. In words, this means that the reduced-order scheme makes the structure appear stiffer than in reality. This is quite natural, since some

Table 1: *Eigen frequencies (in Hz) computed with the reduced-order elasticity and with the full elasticity, and their difference (in %).*

Mode nbr	reduced-order	standard	rel. difference
1	$1.5409 \cdot 10^3$	$1.5351 \cdot 10^3$	0.38
2	$7.9590 \cdot 10^3$	$7.8130 \cdot 10^3$	1.9
3	$1.1207 \cdot 10^4$	$1.0890 \cdot 10^4$	2.9
4	$1.9756 \cdot 10^4$	$1.9215 \cdot 10^4$	2.8
5	$9.3159 \cdot 10^4$	$9.0872 \cdot 10^4$	2.5
6	$1.0777 \cdot 10^5$	$1.0528 \cdot 10^5$	2.4
7	$5.0048 \cdot 10^5$	$4.8321 \cdot 10^5$	3.6
8	$5.3287 \cdot 10^5$	$5.1531 \cdot 10^5$	3.4

small deformations may be removed by the assumption. The computation might be more accurate if the elastic domain extended a small distance into the proof mass, whereas the elastic domain now comprises just the thin springs.

3.2 Transient simulations

Transient simulations of the accelerometer structure were performed with the reduced-order elastic scheme coupled with the reduced-dimensional fluidics model, *i.e.* the Reynolds equation. The proof mass of the accelerometer was first statically loaded during a long time period with a constant external force so that the gas pressure had time to settle. When the mass is released it starts to oscillate around the equilibrium state. The open wall boundary condition defined in Equation (18) was used on all boundaries thus allowing the gas to flow in and out of the gap.

The transient simulations were used to study the effect of the ambient pressure and air gap height on the time evolution of the system. Other factors determining the damping behavior include the gas viscosity, the initial displacement, and the overall geometry of the system. The ambient pressure levels of 1atm, 0.1atm and 0.01atm were studied. Air gap heights of 5μm, 10μm and 20μm were used. The initial displacement was achieved with an external force with a magnitude of 150 Pascals for the simulation with the air gap height of 10μm. The external force for the other air gaps was chosen such that the relative displacement of the initial state in each simulation was identical. In this initial state, the mass center point of the rigid body was displaced a distance of 12% of the original air gap height. The gas was assumed to be air (viscosity $1.67{\cdot}10^{-5}\ \frac{Ns}{m^2}$) and the time step size of 15μs was used.

First, the effect of the air gap height was studied. Naturally one would expect a resonator with a larger air gap height to experience less gas damping than a resonator with a smaller air gap, since in a smaller gap the gas flow encounters stronger viscous resistance. Consequently, the pressure in the air gap reaches higher level in the smaller air gap. These dependencies are also present in our results. With the smallest studied air gap the damping of the system is over-critical, *i.e.* the resonator returns to the undisplaced state following an exponential curve without any oscillations. With the two larger air gap heights, the damping is weaker and the equilibrium state is reached via oscillations. The time behavior of the results is illustrated in Figure 2 and snapshots of the displaced accelerometer with pressure distribution in Figure 3.

The change in the ambient pressure level had more unexpected response. At first, it seems that the higher the ambient pressure the stronger the gas flow resistance should be. But in fact, the relation is not that simple. If the gas tends only to flow out of the gap and not significantly to compress, it turns out that the gas damping is not depending on the ambient pressure. This condition is compactly stated using a nondimensional parameter called the squeeze number

$$\sigma = \frac{12\eta\omega L^2}{p_0 D^2}, \tag{23}$$

where ω is the angular frequency of the oscillations, L is the effective side length of the resonator, and D is the air gap height at rest.

A small value of the squeeze number means that the gas flow is dominant and a large value that the gas compression dominates. Furthermore, $\sigma < 1$ implies roughly that the gas damping is not depending on the ambient pressure. The squeeze number, however, does depend on the ambient pressure, and in the current case the transition from $\sigma < 1$ to $\sigma > 1$ occurs when ambient pressure is reduced below 0.1atm. In accordance, the simulations with ambient pressures of 1.0atm and 0.1atm show almost identical behavior, but the simulation

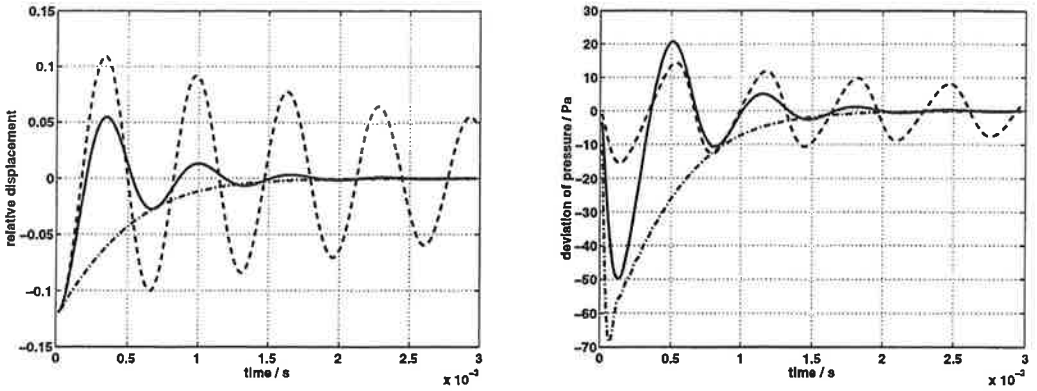

Figure 2: Left, the displacement of the mass center point of the rigid proof mass relative to the initial gap height, right, the mean pressure deviation from the ambient pressure in the air gap. Curves with different air gap heights; 5.0μm (dash-dot line), 10.0μm (solid line) and 20.0μm.

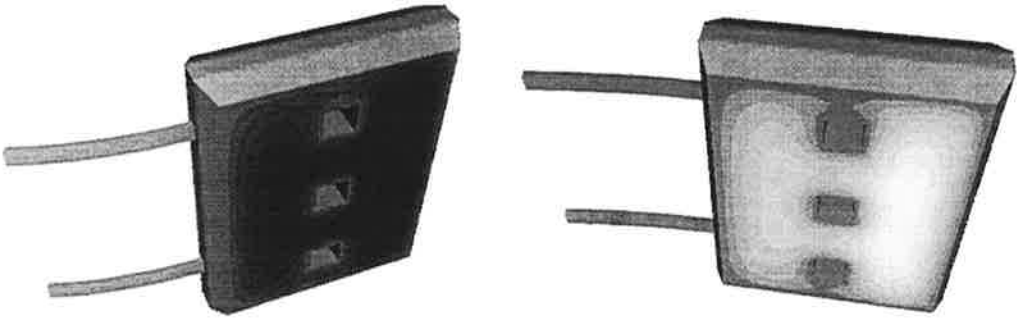

Figure 3: The pressure distribution under the accelerometer; left, time step 0.3ms (mass traveling up), right, time step 0.6ms (mass traveling down). The initial air gap height was 10μm and ambient pressure 1.0atm. Black and white colors mark the lowest and highest values of pressure, respectively. The displacement of the accelerometer is greatly exaggerated.

with ambient pressure 0.01atm results in considerably weaker gas damping. The results of these simulations are shown in Figure 4.

Figure 4 shows also that the frequency of the oscillations change when ambient pressure is low enough. This is further evidence on the above speculation that the behavior of the gas changes when the squeeze number is no longer small. The pure damping mode does not change the frequency of the oscillations, which in all other simulations were very close to the first eigen frequency and is thus determined by the elastic properties of resonator. In low pressures, however, when the gas compression is more notable, a fluidic spring-like force appears and changes the frequency of the oscillations. The effect of compression can be seen also in Figure 5, in which the mean pressure deviation in the air gap and the displacement of the rigid proof mass are plotted. As is seen in the figure, the phase shift between the pressure and the displacement is not 90 degrees in low ambient pressure, which indicates the presence of a fluidic spring force.

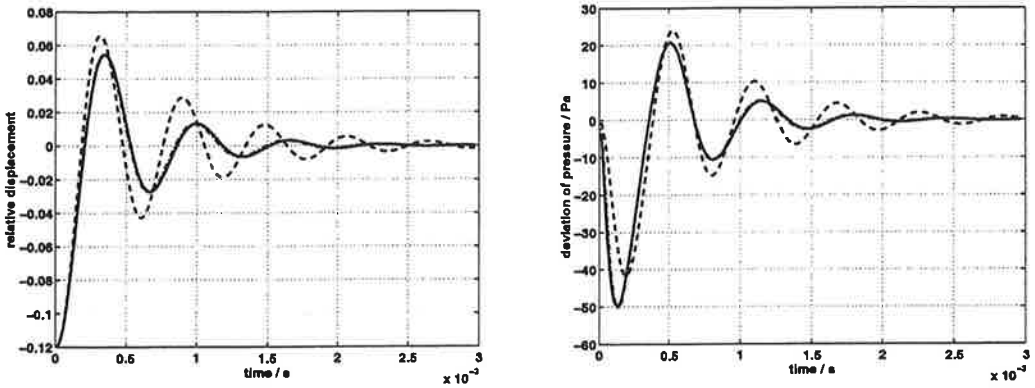

Figure 4: Left, the displacement of the mass center point of the rigid proof mass relative to the initial gap height, right, the mean pressure deviation from the ambient pressure in the air gap. Curves with different ambient pressures; 1.0atm (solid line), 0.1atm (dash-dot line practically coinciding with the solid line) and 0.01atm.

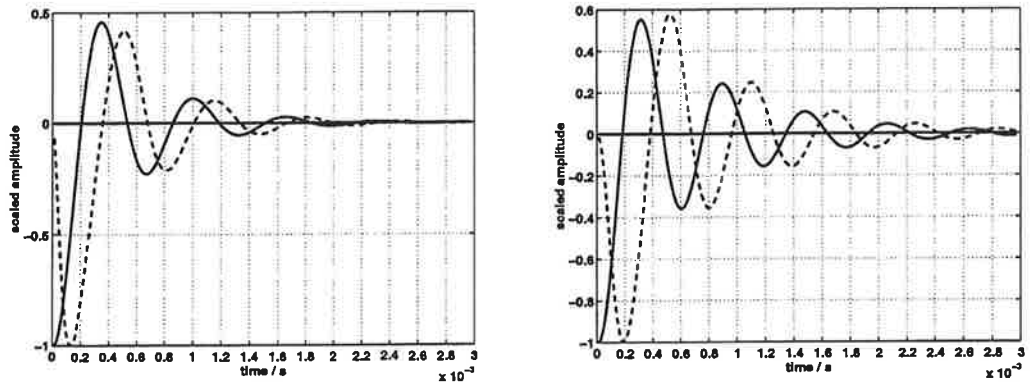

Figure 5: The displacement of the mass center point of the rigid body (solid line) and the mean pressure deviation from the ambient pressure in the air gap; left, ambient pressure 1.0atm, right, ambient pressure 0.01atm. The variables are plotted relative to their corresponding maximum amplitudes.

4 CONCLUSIONS

An economical modeling scheme for gas damped micromechnical resonators was proposed. The scheme enables a comparatively fast solution of the otherwise intractable fluid-structure interaction problem. The modeling method takes also into account the true 3D geometry without any assumption on the symmetry of the resonator. A clear benefit is also that only the resonator needs to be meshed, since the gas domain is taken into account by a fictitious reference plane. Thus, the method is well applicable to transient simulations of micromechanical devices under squeezed-film-damping.

The gas damping model could be further refined by taking into account the gas rarefication effects. The continuum theory of fluid flow is no longer accurate for gases when the problem dimensions are comparable to the mean free path of gas particles, which might be

the case in micro systems. In such a case, an effective viscosity could be used to compensate for the rarefied gas. A suitable effective viscosity is available for the parameter range encountered in micro devices [2].

The results of the modal analysis show that the proposed reduced-order elasticity model is sufficiently accurate to gain insight in the behavior of the resonator, although the reduced-order scheme appeared somewhat to stiffen the structure. A further refinement here would be to extend the elastic structure a small distance into the proof mass in order to better account for bending at the junction of the springs. The demands for computer resources, however, were greatly decreased compared to the full elasticity model.

The transient results show that the air gap height could be used to control the amount of damping in the system if other parameters are suitably chosen to make the squeeze number small. However, a small air gap is usually preferable in capacitive micromechanical components. Therefore the air gap may not be freely chosen and the squeezed-film-damping is controlled by creating holes in the resonating structure. Alternatively, the ambient pressure may be used to change the damping behavior. The amount of damping, however, does not depend linearly on the ambient pressure and it may also affect the frequency of the damped oscillations.

The problem of designing a micromechanical resonator with desired amount damping and desired frequency is complicated, as reflected also by the results in this paper. The differences in the system behavior that a change in parameters influence are often difficult to foresee. Thus, there is a definite need for accurate models for micro systems.

REFERENCES

[1] P. Råback, A. Pursula, V. Junttila and T. Veijola, *Hierarchial finite element simulation of perforated plates with arbitrary hole geometries*, Proceedings of MSM 2003, San Francisco, 23-27.2.2003.

[2] T. Veijola, *"Equivalent circuit models for micromechanical inertial sensors", doctoral thesis*, Circuit Theory Laboratory Report Series, Helsinki University of Technology, 1999.

[3] G. E. Karniadakis and A. Beskok, *"Micro flows, fundamentals and simulation"*, Springer-Verlag, New York, 2002.

[4] *ELMER finite element software homepage*, http://www.csc.fi/elmer

[5] *NETGEN mesh generator software homepage*, http://www.sfb013.uni-linz.ac.at/~joachim/netgen

A NUMERICAL CALCULATION METHOD FOR THE INVESTIGATION OF SHEAR DRIVEN FLOW BETWEEN THE HULL SURFACE OF A VESSEL AND ICE FLOES IN THE ICE SLIDING PHASE

Jorma Kämäräinen
c/o Laboratory of Physics
Helsinki University of Technology
P.O.Box 1100
FIN-02015 HUT
Jorma.Kamarainen@hut.fi

ABSTRACT

The purpose of this study is to present a numerical calculation method for the investigation of the flow between the hull of a vessel and a fully submerged ice floe, which is sliding along the hull, when the vessel is moving with constant speed in a level ice field. The analysis of the flow indicates that the calculation method has to be able to model time dependent laminar and turbulent flow with inertia effects. For this purpose, the constant density, constant viscosity incompressible RANS-equations for Newtonian fluid flow are simplified using shear layer approximations. The momentum equations are then integrated over the thickness of the fluid layer, in order to arrive at a two-dimensional formulation, assuming that the shape of the velocity profiles is not strongly affected by the presence of the inertia forces. A two-dimensional formulation greatly simplifies the grid generation and the numerical solution process. The turbulent lubrication model of Constantinescu based on the Prandtl mixing length model is used to model turbulent flow in the gap between the hull and the ice floe. A numerical solution of the resulting equations is presented using the finite-difference method. The computer program ICEFLO is verified comparing the results of the numerical solution with the analytical solution of Constantinescu and Galetuse.

1 INTRODUCTION

When an icebreaking vessel is moving in level ice, four different phases in the icebreaking process can be separated in time domain following the time history of the ice floes (Puntigliano, 1995): the breaking phase, the rotating phase, the sliding phase and the final phase.

The breaking phase starts when the ship makes contact with the intact ice sheet and ends when a crack occurs, the intact ice sheet breaks and a new ice floe is generated. During the rotating phase the bent ice floes are rotated until they are parallel to the hull surface. During the sliding phase the ice floes will then be pushed further downwards along the ship hull by other floes breaking later to a certain depth until they leave the hull. In the ice sliding phase the ice floes form a kind of "ice mat" below the forebody of the vessel consisting of irregular shaped ice floes as can be observed in figure 1-1.

The purpose of this study is to present a numerical model to investigate theoretically the pressure and viscous forces due to flow in the gap between the hull of a vessel and a fully submerged ice floe, which is sliding along the hull, when the vessel is moving with constant speed in a level ice field.

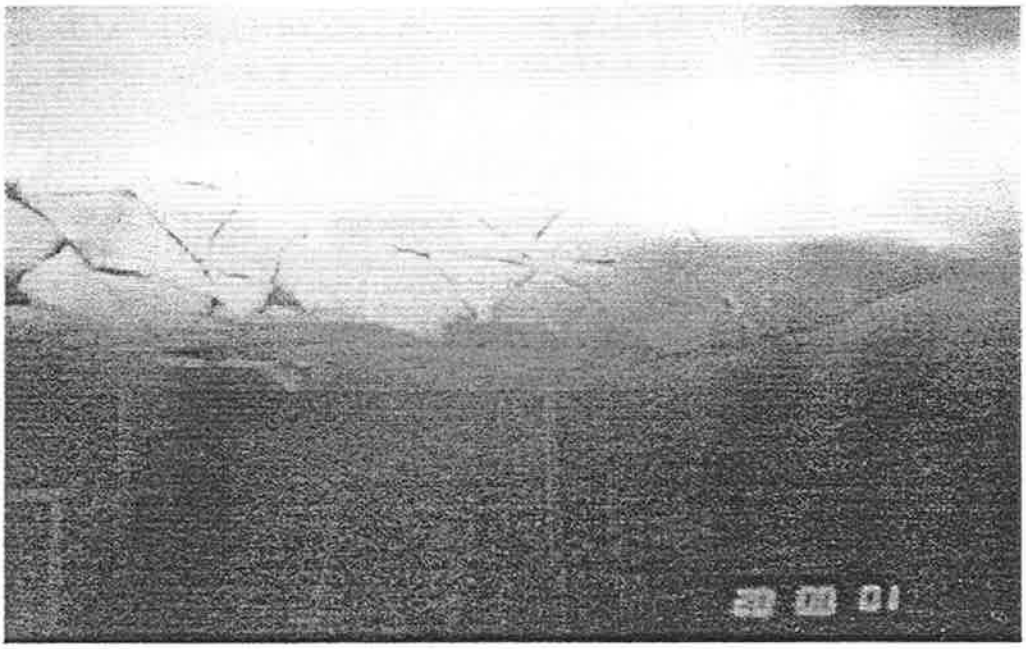

Figure 1-1. An underwater picture of a ship model advancing in thick level ice in the Wärtsilä Arctic Research Center's (WARC) ice tank. The underwater hull is fully covered by ice floes (Valanto, 2001, figure 4).

2 THE CALCULATION PROBLEM

The aim is to develop a numerical calculation method for calculation of the steady or unsteady shear driven flow and pressure in a converging-diverging gap shown in figure 2-1. The upper drawing in figure 2-1 depicts the gap between a rectangular ice floe and a convex hull form. The origin is placed in the middle of the contact area of the hull surface and the ice floe. The gap has a length l, a breadth b, and a height h which is a function of x and y. The hull surface has a radius of curvature R_x in the x-direction and R_y in the y-direction. The hull surface moves with speed U in the positive direction of the x-axis and the speed of the ice floe is assumed to be zero in the direction of the x-axis. The hull surface as well as the surface of the ice floe are assumed to be perfectly smooth. The fluid in the gap is assumed to be water in constant temperature with constant density and viscosity.

The lower drawing in figure 2-1 depicts a section A-A of the gap between the ice floe and the hull surface. A flow is generated in the gap due to motion of the hull surface. Assuming no-slip condition on the surfaces, on the surface of the ice floe the flow has zero speed and on the hull surface the flow speed equals the speed of the hull surface. The flow field and the pressure in the gap strongly depends on the boundary conditions on the edges of the ice floe.

The nature of the flow in the gap can be characterized by two dimensionless numbers, the Couette Reynolds number and the reduced Reynolds number. The Couette Reynolds number, Re_C, is defined as

$$\mathrm{Re}_C = \frac{Uh}{2\nu}, \tag{2.1}$$

where ν is the kinematic viscosity of the fluid, $\nu = \mu / \rho$, where μ is the molecular viscosity, and ρ is the density of the fluid. According to experiments, a Couette flow, i.e. flow between two parallel plates in relative motion is turbulent, if $\mathrm{Re}_C > 1300$ (Schlichting and Gersten, 2000).

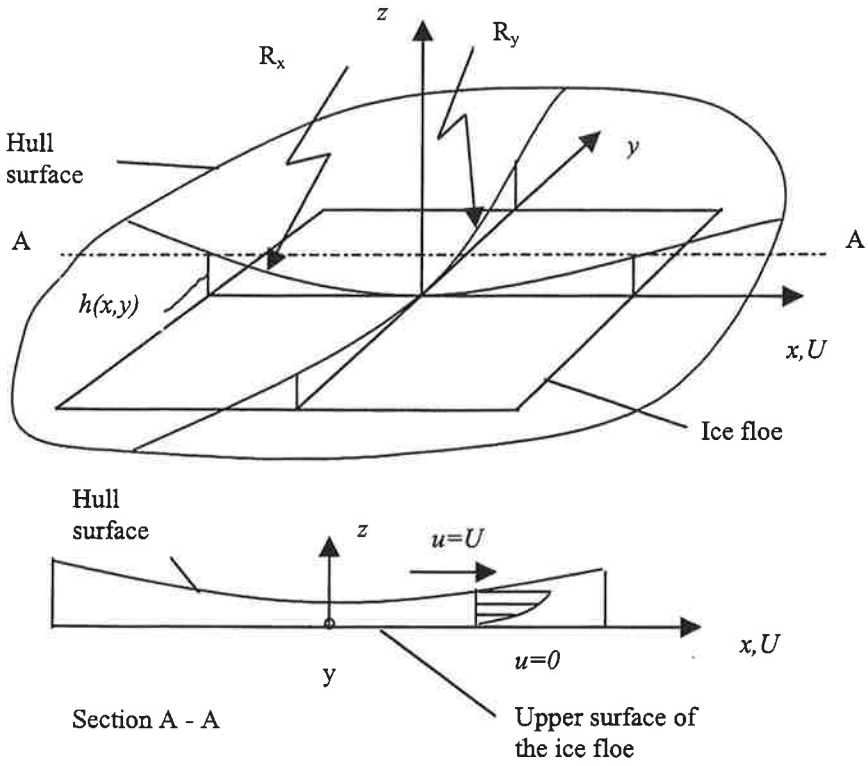

Figure 2-1. The geometry considered in the study.

The reduced Reynolds number, Re*, is defined as the ratio of viscous forces to inertia forces

$$\mathrm{Re}^* = \frac{Ul}{\nu}\left(\frac{h}{l}\right)^2 = \mathrm{Re}_C\left(\frac{2h}{l}\right), \tag{2.2}$$

where l is the length of the ice floe. The inertia forces can be neglected with respect to the viscous forces, if the reduced Reynolds number $\mathrm{Re}^* \ll 1$.

The analysis for the flow in the gap for a typical hull form, based on calculation of the Couette Reynolds number and the reduced Reynolds number, indicated that the calculation method has to be able to model time dependent laminar and turbulent flow with inertia effects.

3 THE EQUATIONS

The Reynolds averaged Navier-Stokes (RANS) equations with constant density and viscosity are

$$\frac{\partial}{\partial t}\left(\rho\overline{u_i}\right)+\frac{\partial}{\partial x_j}\left(\rho\overline{u_j u_i}\right)=-\frac{\partial\overline{p_d}}{\partial x_i}+\mu\frac{\partial^2\overline{u_i}}{\partial x_j\partial x_j}-\frac{\partial}{\partial x_j}\left(\rho\overline{u_j'u_i'}\right) \tag{3.1}$$

$$\frac{\partial\overline{u_i}}{\partial x_i}=0\,, \tag{3.2}$$

where $\overline{u_i}$ are the mean velocity components, $\overline{p_d}$ is the mean dynamic pressure, $\rho\overline{u_j'u_i'}$ are the Reynolds stresses, and t is time. Equations (3.1) and (3.2) can be simplified by making the boundary layer approximations, assuming that $h \ll l$ and $h \ll b$, and that the pressure in the boundary layer is constant in the vertical direction along the z-axis. Taking these assumptions into account, the RANS-equations (3.1) and (3.2) can be written in Cartesian coordinates as follows, known also as *Prandtl's turbulent boundary-layer equations*

$$\rho\frac{\partial\overline{u}}{\partial t}+\rho\frac{\partial}{\partial x}\left(\overline{uu}\right)+\rho\frac{\partial}{\partial y}\left(\overline{vu}\right)+\rho\frac{\partial}{\partial z}\left(\overline{wu}\right)=-\frac{\partial\overline{p_d}}{\partial x}+\mu\frac{\partial^2\overline{u}}{\partial z^2}-\rho\frac{\partial}{\partial z}\left(\overline{w'u'}\right) \tag{3.3}$$

$$\rho\frac{\partial\overline{v}}{\partial t}+\rho\frac{\partial}{\partial x}\left(\overline{uv}\right)+\rho\frac{\partial}{\partial y}\left(\overline{vv}\right)+\rho\frac{\partial}{\partial z}\left(\overline{wv}\right)=-\frac{\partial\overline{p_d}}{\partial y}+\mu\frac{\partial^2\overline{v}}{\partial z^2}-\rho\frac{\partial}{\partial z}\left(\overline{w'v'}\right) \tag{3.4}$$

$$0=-\frac{\partial\overline{p_d}}{\partial z} \tag{3.5}$$

$$\frac{\partial\overline{u}}{\partial x}+\frac{\partial\overline{v}}{\partial y}+\frac{\partial\overline{w}}{\partial z}=0\,, \tag{3.6}$$

where $\overline{u}, \overline{v}$ and $\overline{w}$ is the mean speed in the x-, y- and z-direction, respectively. Equation (3.5) indicates that

$$\overline{p_d}=\overline{p_d}(x,y)\,. \tag{3.7}$$

Equations can be further simplified by integrating them across the gap height, h. In this way we can reduce the dimensions of the calculation problem from three to two dimensions, which greatly simplifies the numerical calculation procedure. We now consider the momentum equations in the directions of the x- and y-axis. Integrating equations (3.3) and (3.4) gives, taking into into account equation (3.7)

$$\rho\int_0^h\frac{\partial\bar{u}}{\partial t}dz+\rho\int_0^h\frac{\partial}{\partial x}\left(\overline{uu}\right)dz+\rho\int_0^h\frac{\partial}{\partial y}\left(\overline{vu}\right)dz+\rho\overline{w_2u_2}-\rho\overline{w_1u_1}=$$
$$-h\frac{\partial\bar{p}_d}{\partial x}+\mu\left(\frac{\partial\bar{u}}{\partial z}\right)_2-\mu\left(\frac{\partial\bar{u}}{\partial z}\right)_1-\rho\overline{w_2'u_2'}+\rho\overline{w_1'u_1'} \tag{3.8}$$

and

$$\rho\int_0^h\frac{\partial\bar{v}}{\partial t}dz+\rho\int_0^h\frac{\partial}{\partial x}\left(\overline{uv}\right)dz+\rho\int_0^h\frac{\partial}{\partial y}\left(\overline{vv}\right)dz+\rho\overline{w_2v_2}-\rho\overline{w_1v_1}=$$
$$-h\frac{\partial\bar{p}_d}{\partial y}+\mu\left(\frac{\partial\bar{v}}{\partial z}\right)_2-\mu\left(\frac{\partial\bar{v}}{\partial z}\right)_1-\rho\overline{w_2'v_2'}+\rho\overline{w_1'v_1'}, \tag{3.9}$$

where the subscripts *1* and *2* denote the lower and upper surfaces, respectively. Using the Leibnitz-rule, assuming no-slip condition at the walls, and taking into account that the turbulent fluctuations vanish at $z=0$ and $z=h$, equations (3.8) and (3.9) can be written as follows, which are in fact the equivalent of the *von Karman's momentum integral equations for boundary layers* (Schlichting, 1960).

$$\rho\frac{\partial}{\partial t}\left(hu_m\right)+\rho\frac{\partial I_{xx}}{\partial x}+\rho\frac{\partial I_{xy}}{\partial y}=-h\frac{\partial\bar{p}_d}{\partial x}+\mu\left(\frac{\partial\bar{u}}{\partial z}\right)_2-\mu\left(\frac{\partial\bar{u}}{\partial z}\right)_1 \tag{3.10}$$

and

$$\rho\frac{\partial}{\partial t}\left(hv_m\right)+\rho\frac{\partial I_{yy}}{\partial y}+\rho\frac{\partial I_{yx}}{\partial x}=-h\frac{\partial\bar{p}_d}{\partial y}+\mu\left(\frac{\partial\bar{v}}{\partial z}\right)_2-\mu\left(\frac{\partial\bar{v}}{\partial z}\right)_1, \tag{3.11}$$

where we have defined the mean speed of the flow in the x-direction

$$u_m=\frac{1}{h}\int_0^h\bar{u}dz \tag{3.12}$$

and the mean speed of the flow in the y-direction

$$v_m=\frac{1}{h}\int_0^h\bar{v}dz, \tag{3.13}$$

and denoted

$$I_{xx}=\int_0^h\overline{uu}dz,\ I_{xy}=I_{yx}=\int_0^h\overline{uv}dz \text{ and } I_{yy}=\int_0^h\overline{vv}dz\ . \tag{3.14}$$

To proceed further assumptions must be made about the distribution of velocity within the fluid film in the gap. Constantinescu, 1970, and Constantinescu and Galetuse, 1974, assume that the shape of the mean velocity distribution in the film is unaffected by inertia. We now follow the method given in Leschziner, 1976, to determine the velocity profiles $\bar{u}(x)$ and $\bar{v}(x)$. Neglecting the inertia terms, and assuming the flow to be steady, equations (3.10) and (3.11) were integrated twice with respect to z, and after eliminating the pressure gradient we get

$$\bar{u}(z)=\left(\frac{z^2}{h^2}-\frac{z}{h}\right)(3U-6u_m)+\frac{z}{h}U \tag{3.15}$$

and

$$\bar{v}(z)=\frac{6v_m z}{h}\left(1-\frac{z}{h}\right). \tag{3.16}$$

Now I_{xx}, $I_{xy}=I_{yx}$ and I_{yy} can be calculated by inserting (3.15) and (3.16) into equations (3.14). We get finally

$$I_{xx}=h\left(\frac{6}{5}u_m^2-\frac{1}{5}Uu_m+\frac{2}{15}U^2\right), I_{xy}=I_{yx}=h\left(\frac{6}{5}u_m v_m-\frac{1}{10}Uv_m\right), I_{yy}=\frac{6}{5}hv_m^2. \tag{3.17}$$

Now we get, by inserting equations (3.17) into equations (3.10) and (3.11), and inserting equations (3.15) and (3.16) into the last two terms in equations (3.10) and (3.11), the following equations, which describe laminar two-dimensional flow with inertia effects in a gap between the hull surface and an ice floe:

$$\rho\frac{\partial(u_m h)}{\partial t}+\rho\frac{\partial}{\partial x}\left(\alpha u_m^2 h+\beta U^2 h-\gamma u_m Uh\right)+\rho\frac{\partial}{\partial y}\left(\alpha u_m v_m h-\delta Uv_m h\right)+$$
$$+h\frac{\partial\bar{p}_d}{\partial x}+\frac{\mu k_x}{h}\left(u_m-\frac{U}{2}\right)=0 \tag{3.18}$$

$$\rho\frac{\partial(v_m h)}{\partial t}+\rho\frac{\partial}{\partial x}\left(\alpha u_m v_m h-\delta Uu_m h\right)+\rho\frac{\partial}{\partial y}\left(\alpha v_m^2 h\right)+h\frac{\partial\bar{p}_d}{\partial y}+\frac{\mu k_y}{h}v_m=0 \tag{3.19}$$

where

$$\alpha=1.2,\ \beta=0.133,\ \gamma=0.2 \text{ and } \delta=0.1 \tag{3.20}$$

for laminar flow. These equations were originally given by Constantinescu and Galetuse, 1974, for steady flow. Leschziner, 1976, also presented the derivation of the equations for steady laminar flow. According to Constantinescu and Galetuse, 1974, the equations can be used for calculation of turbulent flow if we set

$$\alpha=1,\ \beta\cong 0.885\left[2\cdot \mathrm{Re}_C(x,y)\right]^{-0.367},\ \gamma=0 \text{ and } \delta=0. \tag{3.21}$$

In a similar way the continuity equation (3.6) can be integrated over the gap height, when we get

$$\frac{\partial(u_m h)}{\partial x}+\frac{\partial(v_m h)}{\partial y}+\frac{\partial h}{\partial t}=0. \tag{3.22}$$

Analytical solution of equations (3.18), (3.19) and (3.22) is not possible, except in special cases, but a numerical solution method has to be used.

4 NUMERICAL SOLUTION OF THE EQUATIONS

A computer program ICEFLO was written to solve equations (3.18), (3.19) and (3.22). The numerical solution method presented is based on the finite difference method given in Griebel *et al.*, 1998. The program can be used to calculate the velocity of the flow and the pressure in the gap between the hull surface and a rectangular ice floe.

4.1 Solution of the momentum equations

We first consider the time dependent terms of equations (3.18) and (3.19):

$$\rho\frac{\partial(u_m h)}{\partial t} = \rho h\frac{\partial u_m}{\partial t} + \rho u_m\frac{\partial h}{\partial t} \tag{4.1}$$

$$\rho\frac{\partial(v_m h)}{\partial t} = \rho h\frac{\partial v_m}{\partial t} + \rho u_m\frac{\partial h}{\partial t} \tag{4.2}$$

The time derivatives of u_m and v_m on the right hand side of equations (4.1) and (4.2) can be discretized by using Euler's method:

$$\left[\frac{\partial u_m}{\partial t}\right]^{(n+1)} := \frac{u_m^{(n+1)} - u_m^{(n)}}{\Delta t} \tag{4.3}$$

$$\left[\frac{\partial v_m}{\partial t}\right]^{(n+1)} := \frac{v_m^{(n+1)} - v_m^{(n)}}{\Delta t} \tag{4.4}$$

where the subscript n denotes the value of the variable at time t_n and (n+1) denotes the value of the variable at the next time step t_{n+1}, after time Δt has passed. Using equations (4.3) and (4.4), equations (3.18) and (3.19) can now be written in the following form:

$$u_m^{(n+1)} = F - \frac{\Delta t}{\rho}\frac{\partial \bar{p}_d}{\partial x} \tag{4.5}$$

$$v_m^{(n+1)} = G - \frac{\Delta t}{\rho}\frac{\partial \bar{p}_d}{\partial y} \tag{4.6}$$

where

$$F := u_m^{(n)} - \frac{\Delta t}{\rho h}\left[\rho\frac{\partial}{\partial x}\left(\alpha u_m^2 h + \beta U^2 h - \gamma u_m U h\right) + \rho\frac{\partial}{\partial y}\left(\alpha u_m v_m h - \delta U v_m h\right) + \right.$$
$$\left. + \frac{\mu k_x}{h}\left(u_m - \frac{U}{2}\right) + \rho u_m\frac{\partial h}{\partial t}\right] \tag{4.7}$$

and

$$G := v_m^{(n)} - \frac{\Delta t}{\rho h}\left[\rho\frac{\partial}{\partial x}\left(\alpha u_m v_m h - \delta U v_m h\right) + \rho\frac{\partial}{\partial y}\left(\alpha v_m^2 h\right) + \frac{\mu k_y}{h} v_m + \rho v_m\frac{\partial h}{\partial t}\right] \tag{4.8}$$

The spatial derivatives in F and G were calculated by replacing the first derivatives by centered differences and the second derivatives by the donor-cell discretization. If F and G are calculated at time t_n, and $\partial \bar{p}_d / \partial x$ and $\partial \bar{p}_d / \partial y$ at time t_{n+1}, we get the following time discretized equations of momentum

$$u_m^{(n+1)} = F^{(n)} - \frac{\Delta t}{\rho} \frac{\partial \bar{p}_d^{(n+1)}}{\partial x} \tag{4.9}$$

$$v_m^{(n+1)} = G^{(n)} - \frac{\Delta t}{\rho} \frac{\partial \bar{p}_d^{(n+1)}}{\partial y}. \tag{4.10}$$

A staggered rectangular grid is used to discretize equations (4.9) and (4.10) with respect to position (see figure 4-1).

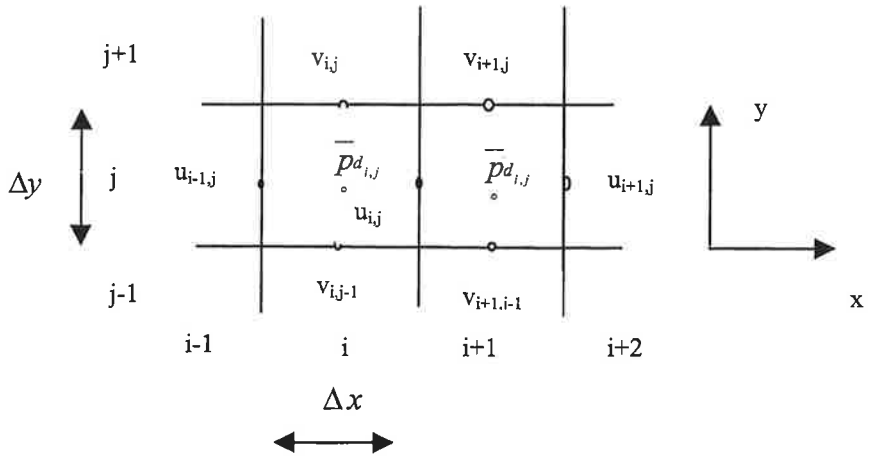

Figure 4-1. Staggered grid.

jmax+2							
jmax+1							
jmax							
5							
4							
3							
2							
i=1,j=1	2	3	4	5	imax	imax+1	imax+2

Figure 4-2. A calculation domain surrounded by one row of ghost cells (imax=6, jmax=6).

The velocities in the x-direction, $u_{i,j}$, in the cells of the calculation domain, are calculated on the right hand edges of the cells, the velocities in the y-direction, $v_{i,j}$, are calculated on the upper edges of the cells, and the pressure, $\overline{p}_{d_{i,j}}$, is calculated in the middle of the cells, in order to avoid pressure fluctuations during the iteration process.

A calculation domain surrounded by one row of ghost cells is depicted in figure 4-2. The ghost cells are used to define boundary conditions at the edges of the calculation domain. Equations (4.9) and (4.10) can now be discretized with respect to position

$$u_{m_{i,j}}^{(n+1)} = F_{i,j}^{(n)} - \frac{\Delta t}{\rho}\frac{\left(\overline{p}_{d_{i+1,j}}^{(n+1)} - \overline{p}_{d_{i,j}}^{(n+1)}\right)}{\Delta x}, i = 2,...,i\max+1, j = 2,...,j\max+1 \qquad (4.11)$$

$$v_{m_{i,j}}^{(n+1)} = G_{i,j}^{(n)} - \frac{\Delta t}{\rho}\frac{\left(\overline{p}_{d_{i+1,j}}^{(n+1)} - \overline{p}_{d_{i,j}}^{(n+1)}\right)}{\Delta y}, i = 2,...,i\max+1, j = 2,...,j\max+1 \qquad (4.12)$$

where F and G are discretized at the right and upper edges of the cells respectively.

4.2 The solution of the Poisson-type equation

In order to solve pressure at the new time step, the continuity equation (3.22) is first written as follows

$$h\frac{\partial u_m}{\partial x} + u_m\frac{\partial h}{\partial x} + h\frac{\partial v_m}{\partial y} + v_m\frac{\partial h}{\partial y} + \frac{\partial h}{\partial t} = 0. \qquad (4.13)$$

We now insert the velocity field $\left(u_m^{(n+1)}, v_m^{(n+1)}\right)^T$ from equations (4.11) and (4.12) into equation (4.13) and get the following Poisson-type equation

$$h\frac{\partial^2 \overline{p}_d^{(n+1)}}{\partial x^2} + h\frac{\partial^2 \overline{p}_d^{(n+1)}}{\partial y^2} + \frac{\partial h}{\partial x}\frac{\partial \overline{p}_d^{(n+1)}}{\partial x} + \frac{\partial h}{\partial y}\frac{\partial \overline{p}_d^{(n+1)}}{\partial y} =$$

$$\frac{\rho}{\Delta t}\left(h\frac{\partial F^{(n)}}{\partial x} + h\frac{\partial G^{(n)}}{\partial y} + \frac{\partial h}{\partial x}F^{(n)} + \frac{\partial h}{\partial y}G^{(n)} + \frac{\partial h}{\partial t}\right). \qquad (4.14)$$

The Poisson-type equation can now be discretized after which we get a set of linear equations, which has $imax \cdot jmax$ unknown values of $\overline{p}_{d_{i,j}}$, $i=1,...,imax$, $j=2,...,jmax$, which have to be solved by using a suitable algorithm, like the Gauss-Seidel method

$$A_{W_{i,j}}\overline{p}_{d_{i-1,j}} + A_{P_{i,j}}\overline{p}_{d_{i,j}} + A_{E_{i,j}}\overline{p}_{d_{i+1,j}} + A_{N_{i,j}}\overline{p}_{d_{i,j+1}} + A_{S_{i,j}}\overline{p}_{d_{i,j-1}} = B_{i,j} \qquad (4.15)$$

where

$$A_{W_{i,j}} = \frac{h_{c_{i,j}}}{\Delta x^2} - \frac{h_{u_{i,j}} - h_{u_{i-1,j}}}{2\Delta x^2},\ A_{P_{i,j}} = -\frac{2h_{c_{i,j}}}{\Delta x^2} - \frac{2h_{c_{i,j}}}{\Delta y^2},\ A_{E_{i,j}} = \frac{h_{c_{i,j}}}{\Delta x^2} + \frac{h_{u_{i,j}} - h_{u_{i-1,j}}}{2\Delta x^2}$$

$$A_{N_{i,j}} = \frac{h_{c_{i,j}}}{\Delta y^2} + \frac{h_{v_{i,j}} - h_{v_{i,j-1}}}{2\Delta y^2},\ A_{S_{i,j}} = \frac{h_{c_{i,j}}}{\Delta y^2} - \frac{h_{v_{i,j}} - h_{v_{i,j-1}}}{2\Delta y^2} \text{ and}$$

$$B_{i,j} = \frac{\rho}{\Delta t}\left(h_{c_{i,j}} \frac{F_{i,j} - F_{i-1,j}}{\Delta x} + h_{c_{i,j}} \frac{G_{i,j} - G_{i,j-1}}{\Delta y} \right) +$$

$$\frac{\rho}{\Delta t}\left(\frac{h_{u_{i,j}} - h_{u_{i-1,j}}}{\Delta x} \frac{F_{i,j} - F_{i-1,j}}{2} + \frac{h_{v_{i,j}} - h_{v_{i-1,j}}}{\Delta y} \frac{G_{i,j} - G_{i,j-1}}{2} + \frac{h_{c_{i,j}}^{(n+1)} - h_{c_{i,j}}^{(n)}}{\Delta t} \right),$$

where the subscripts in h_c, h_u and h_v mean that the height of the gap is calculated at the center of the cell, at the right edge of the cell, and at the upper edge of the cell, respectively. After the pressure in the cells of the calculation domain has been calculated at the new time step t_{n+1}, the new values for the speed components $u_{m_{i,j}}^{(n+1)}$ and $v_{m_{i,j}}^{(n+1)}$ can be calculated by using the discretized equations of motion (4.11) and (4.12). The iteration continues now until a preset value for the *L2*-norm of the change of speed between iteration cycles has been achieved. The *L2*-norm is defined as

$$\left\| r^{it} \right\|_2 := \left(\frac{1}{i_{\max} j_{\max}} \sum_{i=1}^{i_{\max}} \sum_{j=1}^{j_{\max}} \left(r_{i,j}^{it} \right)^2 \right)^{1/2} \tag{4.16}$$

where $r_{i,j}^{it}$ is the change of speed, $u_{i,j}^{n} - u_{i,j}^{n-1}$, between the successive iteration cycles.

4.3 The boundary conditions

The symmetric and periodic boundary conditions were used in this study.

Symmetric boundary

The symmetry boundary condition can be assigned e.g. for the lower edge of the calculation domain shown in figure 3-2 by setting:

$$\begin{aligned} u_{m_{i,1}} &= u_{m_{i,2}} \\ v_{m_{i,1}} &= 0 \\ \overline{p}_{d_{i,1}} &= \overline{p}_{d_{i,2}} \end{aligned} \tag{4.17}$$

Periodic boundary

The periodic boundary condition can be assigned e.g. for the left and right edges of the calculation domain shown in figure 3-2 by setting:

$$
\begin{aligned}
u_{m_{1,j}} &= u_{m_{i\max+1,j}}, \; u_{m_{i\max+2,j}} = u_{m_{2,j}} \\
v_{m_{1,j}} &= v_{m_{i\max+1,j}}, \; v_{m_{i\max+2,j}} = v_{m_{2,j}} \\
\overline{p}_{d_{1,j}} &= \overline{p}_{d_{i\max+1,j}}, \; \overline{p}_{d_{i\max+2,j}} = \overline{p}_{d_{2,j}}
\end{aligned}
\tag{4.18}
$$

4.4 The stability conditions

In order to ensure stability of the numerical algorithm and to avoid generating oscillations, stability conditions must be imposed on the step sizes Δx, Δy and Δt. In the program the *Courant-Friedrichs-Levy (CFL)* conditions were used, which state that no fluid particle may travel a distance greater than the mesh spacing Δx or Δy in time Δt:

$$
\Delta t < \frac{\Delta x}{|u_{\max}|}, \quad \Delta t < \frac{\Delta y}{|v_{\max}|}, \tag{4.19}
$$

where $|u_{\max}|$ and $|v_{\max}|$ are the maximal absolute values of the velocities occurring on the grid.

4.5 The turbulence model

The turbulence model of Constantinescu (see Constantinescu and Galetuse, 1974) based on the mixing length approach was used.

$$
\begin{aligned}
k_x &= 12 + 0.0136\left(2 \cdot \mathrm{Re}_C\right)^{0.9} \\
k_y &= 12 + 0.0043\left(2 \cdot \mathrm{Re}_C\right)^{0.96}
\end{aligned}
\tag{4.20}
$$

5 VERIFICATION OF THE COMPUTER PROGRAM ICEFLO

The computer program ICEFLO was verified for a one-dimensional flow against the results obtained by using the analytical solution given in Constantinescu and Galetuse, 1974. We consider now a steady one-dimensional flow in the gap between a curved wall at $z = h(x)$, moving with speed U in the x-direction, and a flat stationary wall at $y=0$, as depicted in figure 5-1. The length of the lower wall is l and the minimum distance between the walls is h_0 in the middle of the gap at $x = 0$.

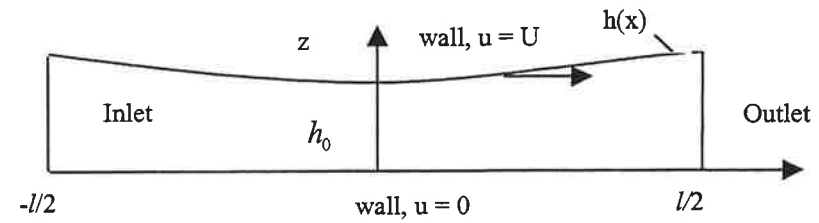

Figure 5-1. The geometry of the gap between a moving curved wall and a stationary flat wall.

We assume that the upper surface in figure 5-1 is an arc of a circle with radius R_x. The height of the gap between the walls can now be written as:

$$h(x) = h_0 + R_x - \sqrt{R_x^2 - x^2} \ . \tag{5.1}$$

The results of ICEFLO, when R_x = 75 m, l = 1 m and h_0 = 0.001 m, are compared in figure 5-2 with the results for turbulent flow obtained by using the analytical solution of Constantinescu and Galetuse. The fluid in the gap was water at 0°C, $\rho = 1000$ kg/m^3 and μ=0.001792 Pa·s. The velocity of the upper wall was 5 m/s in the x-direction. Periodic boundary conditions with zero dynamic pressure at the ends of the gap were used. The numerical solution seems to correlate very well with the analytical solution.

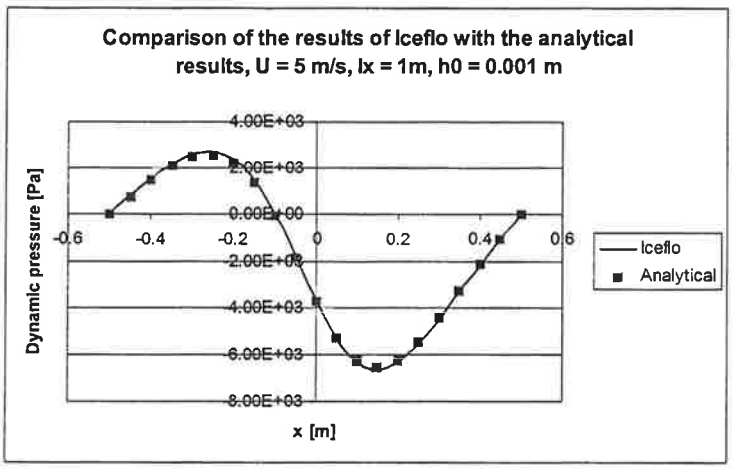

Figure 5-2. Comparison of the results of ICEFLO with the analytical solution of Constantinescu and Galetuse. Turbulent flow, U = 5 m/s, l = 1m, h_0 = 0.001 m.

6 A SAMPLE CALCULATION

A rectangular ice floe with dimensions 1 m x 1 m and a ball-shaped hull form with R_x = 75 m and R_y = 75 m was the chosen geometry for the sample run. The ice floe is assumed to be located symmetrically on the moving hull surface. The ball-shaped hull form was approximated by the following equation:

$$h \approx h_0 + \frac{x^2}{2R_x} + \frac{y^2}{2R_y}, \tag{6.1}$$

where h_0 is the distance of the hull and the ice floe at the origin. The origin was placed in the middle of the ice floe. Due to symmetry, half of the ice floe ($y \geq 0$) was chosen to be the calculation domain. For stability reasons h_0 was given a value of 0.0001 m. Six cells around the origin were marked as obstacle cells where the flow speed was zero. The symmetric boundary condition was set at the edge y = 0. It was assumed that the neighbouring ice floes are of the same size as the floe in question, and thus periodic boundary conditions given in equations (4.18) were set at the inlet (x = -0.5 m) and at the outlet (x = 0.5 m). At the edge y = 0.5 m a symmetric boundary condition was set. The velocity of the hull was 5 m/s in the x-direction. The fluid in the gap was water at 0°C, $\rho = 1000$ kg/m^3 and μ=0.001792 Pa·s. The flow in the gap is thus

predominantly turbulent, the maximum local Couette Reynolds number being about 4700, and the minimum about 140. The turbulence model of Constantinescu was used in the calculations. An equidistant grid with *imax* x *jmax* = 50 x 25 was used, giving a grid spacing of 0.02 m.

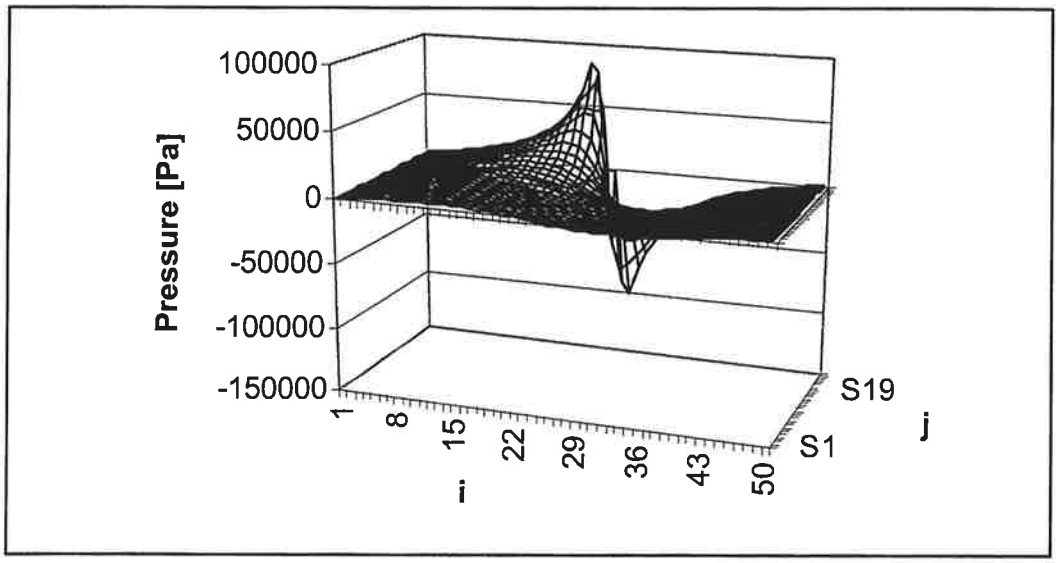

Figure 6-1. The pressure distribution in the gap between a ball-shaped hull form and a rectangular ice floe. The inlet is on the left-hand side, outlet on the right-hand side, and the centerline of the ice floe is at the back of the figure. The cell numbers, i and j, are shown on the x- and y-axis, respectively.

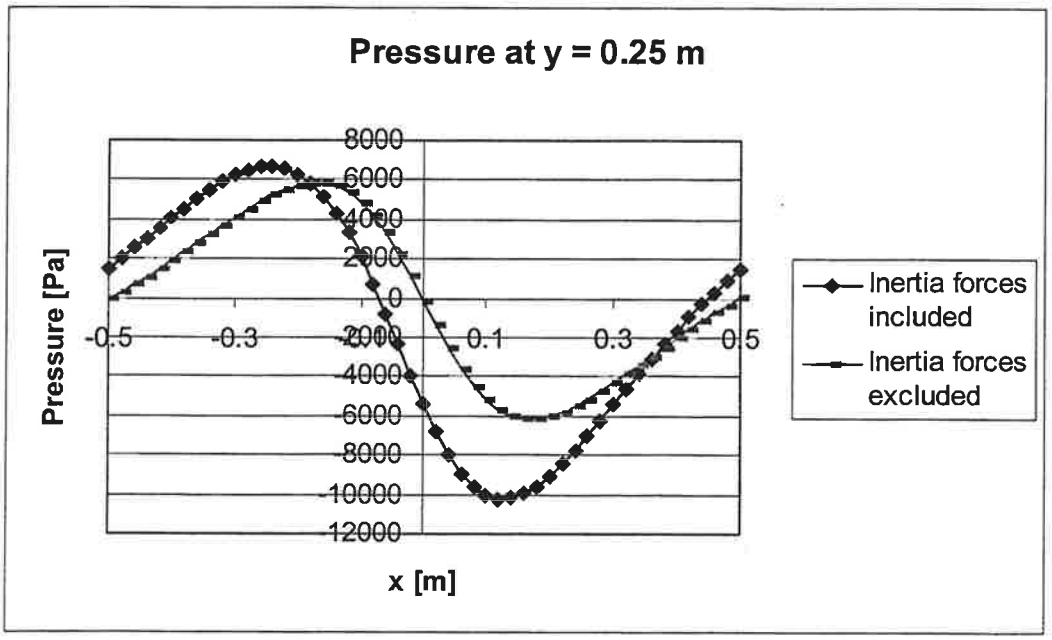

Figure 6-2. The pressure distribution at section y = 0.25 m shown with and without inertia forces.

The results of the calculation are shown in figures 6-1 and 6-2. In figure 6-2 the pressure distribution is given for a calculation with and without inertia forces. The case without the inertia forces is the same as the solution of the Reynolds equation. Figure 6-2 also indicates that the net dynamic pressure in the gap is negative. The effect of the inertia forces can be clearly seen.

7 SUMMARY

A computer program ICEFLO has been written to calculate the flow in a converging-diverging gap between the hull surface of a moving vessel and a stationary ice floe. The computer program can calculate both laminar and turbulent flow with inertia effects. The program was verified in 1d against the results calculated by using the analytical solution of Constantinescu and Galetuse. The preliminary calculations indicate that the inertia effects have an important role when calculating the pressure distribution in the gap between the hull surface of a vessel and ice floes.

REFERENCES

Constantinescu, V.N., 1970.
On the Influence of Inertia Forces in Turbulent and Laminar Self-Acting Films. Journal of Lubrication Technology, July 1970, pp. 473 - 481.

Constantinescu, V.N., and Galetuse S., 1974.
On the Possibilities of Improving the Accuracy of the Evaluation of Inertia Forces in Laminar and Turbulent Films. Journal of Lubrication Technology, July 1974, pp. 69 - 79.

Griebel, M., Dornseifer, Th., and Neunheffer, T., 1998.
Numerical Simulation in Fluid Dynamics. A Practical Introduction. The Society for Industrial and Applied Mathematics, 1998.

Leschziner, M.A., 1976.
Turbulent flow in finite width bearing films including turbulent transport and inertia effects. Thesis submitted for degree of Doctor of Philosophy in the Faculty of Engineering, University of London, August 1976.

Puntigliano F.M., 1995.
On the resistance components below the waterline in the continuous mode of icebreaking - model tests. HSVA Report No. E253/95.

Schlichting, H., 1960.
Boundary-Layer Theory. MacGraw-Hill Book Company, 1960.

Schlichting, H., and Gersten K., 2000.
Boundary-Layer Theory, 8th Revised and Enlarged Edition, Springer, 2000.

Valanto, P.U., 2001.
The Resistance of Ships in Level Ice. SNAME, 2001.

A COUPLED DISPLACEMENT-CRACK GROWTH ANALYSIS WITHOUT REMESHING FOR 2D PROBLEMS OF LEFM

S. FORTINO[1], A. BILOTTA[2]

[1] Laboratory for Mechanics of Materials
Helsinki University of Technology
P.O.Box 4100
FIN-02015 HUT, FINLAND
e-mail: stefania.fortino@hut.fi

[2]Dipartimento di Strutture
Università della Calabria
Cubo 39/C
87030 Rende (CS), ITALY
e-mail: antoniobilotta@labmec.unical.it

ABSTRACT

This work proposes a coupled displacement-crack growth analysis for two-dimensional problems of linear elastic fracture mechanics (LEFM). The main scope of the analysis is to evaluate the amount of crack propagation during a process of stable crack growth. The analysis is based on the coupled displacement-crack propagation problem defined by Q. S. Nguyen *et al.* in 1990. To avoid the remeshing usually needed for modelling crack growth, the analysis is implemented in a code where a PUFEM model is utilized. The proposed algorithm is valid for rectilinear crack growth in LEFM but it can be extended to evaluate curvilinear crack growth in materials showing dissipative deformations.

1 INTRODUCTION

At present the computer codes for simulation of crack growth (e.g. BEASY, FRANC2D, FRANC3D, ZENCRACK) do not calculate the amount of crack propagation on the basis of theoretical formulations. In fact the crack increments due to given loads are: (*a*) assigned after the determination of the direction of crack extension or (*b*) determined trough laws describing fatigue crack growth models (e.g. the empirical Paris law [1]). In this context, the direction of crack growth is computed by well known criteria defined in terms of the stress intensity factors (see the citations in [3]). The same kind of approach to crack growth simulation can be found in the recent finite element methods without remeshing [3] and in the meshless methods for crack propagation [4].

The codes and methods cited above, when no fatigue analysis is performed, are considered to be quasi-automatic, because the user needs to assign a crack length increment at the beginning of each simulation. As pointed out in [2], excessive increment sizes in such situations may lead to cumulative distortion in the crack propagation path. Furthermore the Paris law, used for fatigue crack growth problems only, is too basic for the accurate

prediction of crack growth in many practical situations.

In 1990 Q. S. Nguyen *et al.* [5] proposed a coupled displacement-crack length rate analysis for problems of stable rectilinear elastic crack growth characterized by crack opening mode. The analysis was based on the well known Griffith criterion of crack growth [1] and on a mathematical separation of the cracked body. The present work introduces a finite increment formulation of the Nguyen displacement-crack propagation rate analysis. For the sake of simplicity, only one rectilinear crack is considered. The proposed strategy allows the increments of displacement and crack propagation relative to assigned load increments in the case of stable rectilinear crack growth to be determined. The analysis is promising because it can be extended for evaluating curvilinear crack propagation in elastic and elastoplastic materials.

The analysis was implemented by the authors into a 2D FEM code. In order to avoid the remeshing required by the traditional FEM discretizations, a PUFEM model for crack growth [3] was also implemented.

2 FORMULATION OF THE COUPLED DISPLACEMENT-CRACK PROPAGATION PROBLEM IN 2D ELASTIC DOMAINS

The problem of stable rectilinear crack growth in linear elastic bodies under crack opening mode is studied. Let us consider a two-dimensional body Ω of unit thickness characterized by an initial rectilinear crack of length a_0 and surface $\Sigma = \Sigma_1 + \Sigma_2 + \Sigma_3$ in the direction of the x_1-axis (see Figure 1). No traction is applied along the surface of the crack. The body is subjected to a proportional load $\mathbf{T}(\lambda) = \lambda\hat{\mathbf{T}}$ applied on the boundary S_T. The material is assumed to be homogeneous and the body forces are neglected.

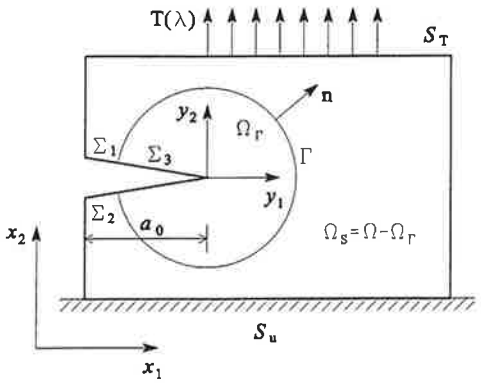

Figure 1: Fixed and moving coordinate systems in a cracked 2D domain.

The aim of this study is to determine the curve $(a(t), \lambda(t))$ (crack length–load multiplier) starting from the initial configuration $(a(0) = a_0, \lambda(0))$, where t represents the time.

Let us write the potential energy of the system which depends on the displacement field $\mathbf{u}(t) = \{u(x, y, t), v(x, y, t)\}$, on the crack length a and on the load multiplier λ:

$$\Pi(\mathbf{u}, a, \lambda) = \int_\Omega w(\varepsilon(\mathbf{u}, a))\, d\Omega - \int_{S_T} \mathbf{T}(\lambda) \cdot \mathbf{u}\, dS \tag{1}$$

where $\varepsilon(\mathbf{u}, a)$ represents the strain field and $w(\varepsilon(\mathbf{u}, a))$ is the strain energy density. The displacement field $\mathbf{u}$ belongs to the set of kinematically admissible displacements

$$\mathcal{U}(a, \lambda) = \{\mathbf{u} : \mathbf{u} \text{ regular in } \Omega;\ \ \mathbf{u} = \mathbf{u}_d \ \text{ on } S_u;\ \ [\![\mathbf{u}]\!] \geq 0 \text{ on } \Sigma\} \tag{2}$$

where S_u is the boundary with assigned displacements and $[\![\mathbf{u}]\!]$ is the difference in displacements across Σ.

In this work we refer to materials that exhibit flat R-curves, where R is the crack growth resistance (see [1]). The constant value of R is denoted by G_f which represents the fracture energy. We use the Griffith criterion for crack growth in the form given by Irwin [1] who defined the energy release rate G as $-\partial\Pi/\partial a$ when $\mathbf{u} = const.$ As pointed out in [5], during the evaluation of the energy release rate G in the presence of crack growth ($\dot{a} \neq 0$), the domain integrals containing the strain tensor diverge (see also [9] for the details). In order to avoid this divergence, in [5] the fracture zone containing the singularity was isolated into a subdomain Ω_Γ surrounding the crack tip and delimited by a closed curve Γ. In this way, the domain Ω is mathematically separated into two subdomains, Ω_Γ and $\Omega_S = \Omega - \Omega_\Gamma$. As proposed in [5], the moving coordinate system (y_1, y_2) is used to express the physical quantities within the domain Ω_Γ, while in Ω_S the fixed coordinate system (x_1, x_2) is utilized. For example, the displacement field $\mathbf{u}$ is described as

$$\mathbf{u} = \begin{cases} \mathbf{u}^{(1)}(x_1, x_2, t) & \text{in } \Omega_S \\ \mathbf{u}^{(2)}(y_1, y_2, t) & \text{in } \Omega_\Gamma \end{cases} \tag{3}$$

If the separation of the body described above is used, the Griffith criterion can be written in the following form:

$$\begin{cases} \dot{a} \geq 0 & \text{if } J = G_f \text{ and } \dot{J} = 0 \\ \dot{a} = 0 & \text{otherwise} \end{cases} \tag{4}$$

where J is the well known J integral of Rice which is path-independent when the material is elastic (linear or not) and homogeneous. In particular, when the material behaviour is linear elastic, the well known equality $J = G$ holds. Furthermore, as shown in detail in [5] and [9], $\dot{J}$ is given by the following path-independent integral

$$\dot{J} = \int_\Gamma (\mathbf{n} \cdot \boldsymbol{\sigma}_{,1} \cdot \overset{*}{\mathbf{u}} - \mathbf{n} \cdot \overset{*}{\boldsymbol{\sigma}} \cdot \mathbf{u}_{,1}) \, d\Gamma \tag{5}$$

where the subscript $(_{,1})$ indicates the partial derivative in the direction of crack propagation.

The analysis proposed in this work is based on the coupled displacement-crack propagation problem defined by Nguyen *et al.* in [5]. The coupled problem was expressed in terms of rates fields $\overset{\diamond}{\mathbf{u}}, \overset{\diamond}{\boldsymbol{\varepsilon}}, \overset{\diamond}{\boldsymbol{\sigma}}, \ldots$ defined as

$$\overset{\diamond}{\mathbf{u}}, \overset{\diamond}{\boldsymbol{\varepsilon}}, \overset{\diamond}{\boldsymbol{\sigma}}, \ldots = \begin{cases} \dot{\mathbf{u}}, \dot{\boldsymbol{\varepsilon}}, \dot{\boldsymbol{\sigma}}, \ldots & \text{in } \Omega_S \\ \overset{*}{\mathbf{u}}, \overset{*}{\boldsymbol{\varepsilon}}, \overset{*}{\boldsymbol{\sigma}}, \ldots & \text{in } \Omega_\Gamma \end{cases} \tag{6}$$

where $\dot{\mathbf{u}} = d\mathbf{u}^{(1)}(x_1, x_2, t)/dt$ represents the total time displacement derivative and $\overset{*}{\mathbf{u}} = \partial\mathbf{u}^{(2)}(y_1, y_2, t)/\partial t$ is the partial time displacement derivative. The following displacement jump condition holds:

$$[\![\overset{\diamond}{\mathbf{u}}]\!] + \dot{a}\mathbf{u}_{,1} = 0 \text{ on } \Gamma \tag{7}$$

where $[\![\overset{\diamond}{\mathbf{u}}]\!] = \dot{\mathbf{u}} - \overset{*}{\mathbf{u}}$ is the difference in displacement rates across Γ, while the traction rate $\overset{\diamond}{\boldsymbol{\sigma}} \cdot \mathbf{n}$ is subjected to the jump condition

$$[\![\overset{\diamond}{\boldsymbol{\sigma}} \cdot \mathbf{n}]\!] + \dot{a}\,\boldsymbol{\sigma}_{,1} \cdot \mathbf{n} = 0 \text{ on } \Gamma \tag{8}$$

where $[\![\overset{\diamond}{\boldsymbol{\sigma}} \cdot \mathbf{n}]\!] = (\dot{\boldsymbol{\sigma}} - \overset{*}{\boldsymbol{\sigma}}) \cdot \mathbf{n}$ and $\mathbf{n}$ is the outside normal to the curve Γ.

In order to describe the crack growth process, conditions (7) and (8), criterion (4) and some additional conditions must be added to the rate form of the usual equations

of linear elasticity (see [5] and [9]). The integral formulation of the obtained boundary value problem furnishes the following coupled displacement-crack propagation system valid $\forall\, \delta\mathbf{u},\ \mathbf{u} \in \mathcal{U},\ \delta a \geq 0$:

$$\begin{cases} \int_\Omega \dot{\boldsymbol{\sigma}} : \nabla \delta\mathbf{u}\, d\Omega - \int_{S_T} \dot{\mathbf{T}} \cdot \delta\mathbf{u}\, dS - \int_\Gamma \dot{a}\, \boldsymbol{\sigma}_{,1} \cdot \mathbf{n} \cdot \delta\mathbf{u}\, d\Gamma = 0 \\ - \int_\Gamma (\mathbf{n} \cdot \boldsymbol{\sigma}_{,1} \cdot \overset{*}{\mathbf{u}})\, \delta a\, d\Gamma + \int_\Gamma (\boldsymbol{\sigma}_{,1} \cdot \mathbf{n} \cdot \mathbf{u}_{,1})\, \dot{a}\, \delta a\, d\Gamma = 0 \end{cases} \tag{9}$$

Starting from the coupled problem (9) the following quadratic functional is obtained:

$$\begin{aligned} F(\overset{\circ}{\mathbf{u}}, \dot{a}) \;=\; & \frac{1}{2} \int_\Omega \overset{\circ}{\varepsilon} : \mathbf{E} : \overset{\circ}{\varepsilon}\, d\Omega - \dot{\lambda} \int_{S_T} \hat{\mathbf{T}} \cdot \overset{\circ}{\mathbf{u}}\, dS \\ & - \dot{a} \int_\Gamma \boldsymbol{\sigma}_{,1} \cdot \mathbf{n} \cdot \overset{*}{\mathbf{u}}\, d\Gamma + \frac{\dot{a}^2}{2} \int_\Gamma \boldsymbol{\sigma}_{,1} \cdot \mathbf{n} \cdot \mathbf{u}_{,1}\, d\Gamma \end{aligned} \tag{10}$$

defined on the convex domain

$$I = \{(\overset{\circ}{\mathbf{u}}, \dot{a}) \;\mid\; \overset{\circ}{\mathbf{u}} = \dot{\mathbf{u}}_d \text{ on } S_u;\ [\![\overset{\circ}{\mathbf{u}}]\!] \geq \mathbf{0} \text{ on } \Sigma \text{ if } [\![\mathbf{u}]\!] = \mathbf{0};\ \dot{a} \geq 0;\ [\![\overset{\circ}{\mathbf{u}}]\!] + \dot{a}\mathbf{u}_{,1} = \mathbf{0} \text{ on } \Gamma\}$$

3 ANALYSIS OF CRACK PROPAGATION WITHOUT REMESHING

The finite increment formulation of the coupled displacement-crack propagation problem allows to define a curve in the space $(\mathbf{u}, a, \lambda)$. Applying the explicit-forward Euler scheme to the equations describing the boundary value coupled problem, the unknowns can be expressed in terms of the increments

$$d\boldsymbol{\sigma} = \boldsymbol{\sigma}^{(k+1)} - \boldsymbol{\sigma}^{(k)},\quad d\mathbf{u} = \mathbf{u}^{(k+1)} - \mathbf{u}^{(k)}\quad da = a^{(k+1)} - a^{(k)} \tag{11}$$

where k indicates the generic initial step and $k+1$ the generic end-step. Then, using a discretization procedure like the finite element method, the incremental form of functional (10) becomes:

$$F(d\mathbf{u}, da) \;=\; \frac{1}{2} d\mathbf{u}^{\mathrm{T}} \mathbf{K}_u d\mathbf{u} - d\lambda \hat{\mathbf{T}}^{\mathrm{T}} d\mathbf{u} - d\mathbf{u}^{\mathrm{T}} \mathbf{K}_{ua} da + \frac{1}{2} da\, K_a\, da$$

where $\hat{\mathbf{T}}$ represents the assigned loads, $\mathbf{K}_u$ is the usual stiffness matrix of the body, K_a the matrix relative to the unknown crack growth increment and $\mathbf{K}_{ua}$ the mixed matrix related to both displacement and crack growth increments.

The algorithm adopted to follow the mechanical response in terms of the rectilinear growth of the initial crack can be summarized as follows:

1. Evaluation of the load multiplier λ_f connected with the reaching of G_f, i.e. the critical value of the J integral, and determination of the first point of the equilibrium curve $(\mathbf{u}, \lambda)$:

$$J[\mathbf{u}[\lambda]] = G_f \qquad \Rightarrow \qquad \lambda_f \tag{12}$$

where $\mathbf{u}[\lambda]$ is the elastic solution and assumes the following simple expression:

$$\mathbf{u}[\lambda] = \lambda \mathbf{u}_e, \qquad \mathbf{u}_e = \mathbf{K}_u^{-1} \hat{\mathbf{T}} \tag{13}$$

As a consequence equation (12) gives:

$$J[\mathbf{u}[\lambda]] = \lambda^2 J[\mathbf{u}_e] = J_f \qquad \Rightarrow \qquad \lambda_f = \sqrt{\frac{G_f}{J[\mathbf{u}_e]}} \tag{14}$$

2. Solution of the incremental displacement–crack propagation problem

$$\begin{bmatrix} \mathbf{K}_{\mathrm{u}} & -\mathbf{K}_{\mathrm{ua}} \\ -\mathbf{K}_{\mathrm{ua}} & K_{\mathrm{a}} \end{bmatrix} \begin{Bmatrix} d\mathbf{u} \\ da \end{Bmatrix} = \begin{Bmatrix} d\lambda \hat{\mathbf{T}} \\ 0 \end{Bmatrix} \tag{15}$$

on the basis of the scheme:

2.1 evaluation of the crack increment

$$da = -d\lambda\, \mathbf{K}_{\mathrm{ua}}^T \mathbf{u}_{\mathrm{e}} \left(\mathbf{K}_{\mathrm{ua}}^T \mathbf{u}_{\mathrm{f}} - K_{\mathrm{a}} \right)^{-1} \tag{16}$$

under the condition

$$da \geq 0 \tag{17}$$

2.2 evaluation of the displacement increment

$$d\mathbf{u} = d\lambda\ \mathbf{u}_{\mathrm{e}} + da\ \mathbf{u}_{\mathrm{f}} \tag{18}$$

where

$$\mathbf{u}_{\mathrm{f}} = \mathbf{K}_{\mathrm{u}}^{-1} \mathbf{K}_{\mathrm{ua}} \tag{19}$$

Inequality (17) implies that the sign of the assigned load increment $d\lambda$ must eventually be changed in equation (16).

3. Repeat step 2 until a suitable condition is reached, e.g. a maximum value of the displacement and/or a minimum value for the load are reached.

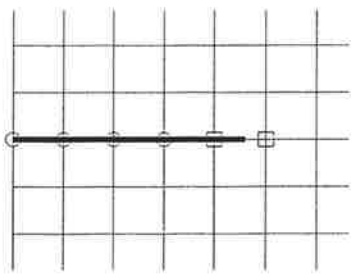

Figure 2: Nodal enrichment along a crack: the circled nodes are enriched with a discontinuous function and the boxed nodes are enriched with the asymptotic crack tip functions.

The proposed algorithm was implemented starting from the finite element code *"FEM-Object"* (for 2D and 3D linear elastic problems), distributed by *ZACE SERVICES Ltd Software engineering, Lausanne, Switzerland.* The program is based on a C++ object-oriented architecture. PUFEM (Partition of Unity Finite Element Model) elements were implemented by the authors to avoid the continuous remeshing of the domain. The partition of unity can be generated by using different methods related to data fitting techniques [6]. Within the PUFEM approach the partition of unity is built by using coarse patches of quadrilateral or triangular elements and the bilinear shape functions associated with these elements [7]. A PUFEM model suitable for describing one or more cracks in a 2D domain can be formulated as proposed in [3]. In order to carefully model the crack two items are required: (i) the description of the discontinuity of the displacement field along the crack;

(*ii*) the description of the solution near the tip of the crack. Then, the aforementioned requirements can be met by a suitable enrichment of the nodes placed on the crack.

The first requirement is satisfied by adopting the jump function

$$H(x,y) = \begin{cases} 1 & \text{for } y > 0 \\ -1 & \text{for } y < 0 \end{cases} \tag{20}$$

for the nodes placed on the crack but not near the crack tip (circled nodes of Figure 2). The following local approximation space is obtained:

$$\Psi_i = \{1, H(x,y)\} \tag{21}$$

The second requirement is satisfied by enriching the nodes which fork the crack tip through the asymptotic crack tip functions. In this case (boxed nodes of Figure 2), the local approximation space is given by

$$\Psi_i = \{1, \sqrt{r}\sin(\frac{\theta}{2}), \sqrt{r}\cos(\frac{\theta}{2}), \sqrt{r}\sin(\frac{\theta}{2})\sin(\theta), \sqrt{r}\cos(\frac{\theta}{2})\sin(\theta)\} \tag{22}$$

where the local approximations are defined with respect to a polar coordinate system with its center at the crack tip.

4 NUMERICAL EXAMPLE: CENTER CRACKED PLATE IN TENSION

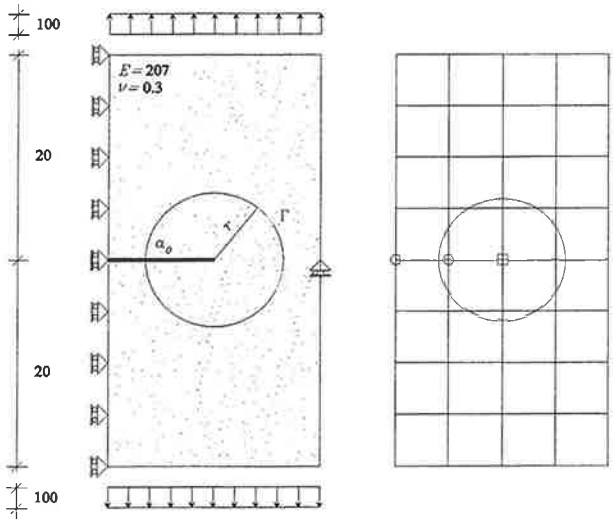

Figure 3: Center cracked plate in tension: description of the problem (a_0 = initial crack length, SI units) and example mesh. The mesh also shows the enriched nodes required by the PUFEM approach.

The crack growth analysis of a symmetric rectangular plate subjected to an initial uniform tensile stress $\mathbf{T}(\lambda_0) = 100$ (SI units) normal to a central horizontal crack is performed. Figure 3 shows the half plate considered for the analysis with the PUFEM model and the typical mesh adopted in the case of quadrangular elements. In particular, the half plate is

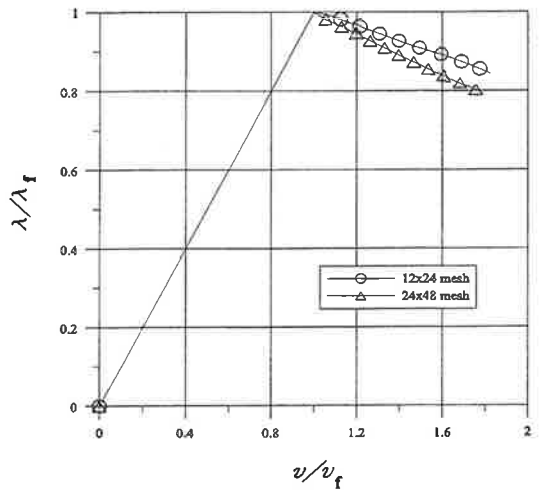

Figure 4: Center cracked plate in tension: plotting of the load multiplier λ with respect to the vertical displacement v of the left corner of the plate. The curves are normalized with respect to the values λ_f and v_f relative to the activation of crack growth, i.e. the peak of the curve.

modeled through PUFEM quadrilateral elements on the basis of a 12×24 mesh and of a 24×48 mesh. The crack growth analysis is performed by using load increments $d\lambda = 0.01$. The obtained load vs displacement curves and load vs crack length curves are reported respectively in Figure 4 and Figure 5.

5 CONCLUSIONS

The results obtained showed that the proposed algorithm permits the amount of crack growth in case of rectilinear elastic crack propagation to be calculated. This main feature, together with the typical advantages of the recent strategies based on unremeshing approaches (see [3]), makes the method very competitive with respect to the existing techniques for simulating crack growth in LEFM.

The present method can also be extended for describing curvilinear crack growth in linear elastic fracture mechanics. Starting from the basic algorithm and using suitable criteria for determining the crack growth direction, both the amount of crack growth and the direction of crack propagation can be determined.

The proposed method is interesting particularly because it can be extended to materials showing dissipative behaviour. In this case, a suitable criterion of crack propagation must be selected. In particular, crack growth criteria obtained by using thermomechanics approaches seem promising ([8]).

Acknowledgements

The present research was funded by the Academy of Finland in the context of the project No. 80926 "A thermomechanics based fracture assessment method for structural components".

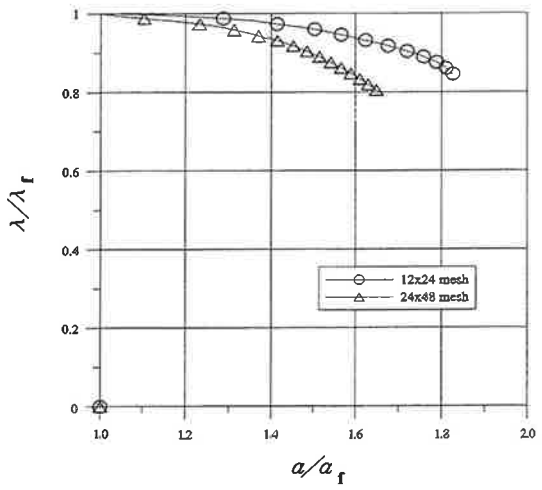

Figure 5: Center cracked plate in tension: plotting of the load multiplier λ with respect to the crack length a. The curves are normalized with respect to the values λ_f and a_f relative to the activation of crack growth, i.e. the peak of the curve.

REFERENCES

[1] Bazant ZP, Planas J. Fracture and size effect in Concrete and Other Quasibrittle Materials. CRC Press, 1998.

[2] Bittencourt TN, Wawrzynek PA, Ingraffea AR, Sousa JL. Quasi-automatic simulation of crack propagation for 2D LEFM problems, Engng Fract Mech 1996;55(2):321–334.

[3] Moës N, Dolbow J, Belytschko T. A finite element method for crack growth without remeshing. Int J Numer Meth Engng 1999;46:131–150.

[4] Rao BN, Rahman S. An efficient meshless method for fracture analysis of cracks. Comp Mech 2000;26:398–408.

[5] Nguyen QS, Stolz C and Debruyne G. Energy methods in fracture mechanics: stability, bifurcation and second variations. Eur J Mech, A/Solids 1990;9(2):157–173.

[6] Belytschko T, Krongauz Y, Organ D, Fleming M, Krysl P. Meshless methods: An overview and recent developments. Comput Methods Appl Mech Engng 1996;139:3–48.

[7] Stroubulis T, Babuska I, Copps K. The design and analysis of the Generalized Finite Element Method. Comput Methods Appl Mech Engng 2000;181:43–69.

[8] Santaoja K. J-vector theory for simulation of rectilinear crack growth. Technical Research Centre of Finland, VTT Publications 360, Espoo, Finland, 1998.

[9] Fortino S, Bilotta A. A J integral-based algorithm for the coupled displacement-crack propagation problem in linear elastic fracture mechanics. Research Report No. 35, Helsinki University of Technology, Laboratory for Mechanics of Materials, Espoo, Finland, 2002.

ASPECTS OF CRACK PROPAGATION OF SMALL CRACKS DURING VARIABLE AMPLITUDE FATIGUE

G. Marquis
Laboratory of Steel Structures
Lappeenranta University of Technology
P.O. Box 20, FIN-53851 Lappeenranta, FINLAND

ABSTRACT

This paper provides a summary of proposed life prediction methods for crack propagation during variable amplitude fatigue. Much of the published work relates to overload effect in thin sheet materials where plane stress dominates and retardation effects can be very large. Less attention is given to cracks propagating from nominally defect free components in the high cycle regime where a significant portion of the fatigue damage can be attributed to cycles with amplitude less that the fatigue limit observed under constant amplitude loading. This type of load spectrum is relevant for a number of mechanical engineering companies. Of special concern are those load spectra that produce crack growth acceleration and the traditional "Miner's Rule" becomes very non-conservative. An effective stress method for variable amplitude loaded is proposed and used on a high strength nodular iron.

1. INTRODUCTION

Variable Amplitude Life Prediction Methods

Because of its significance in both the aircraft and ground vehicle industries, variable amplitude fatigue has been extensively studied for several decades and numerous predictive models have been developed. Numerous overviews of variable amplitude life prediction methods have been published [1-5]. Figure 1 shows the relationships between several classes of models used for predicting fatigue crack propagation under variable amplitude loading. The non-interaction models on the left side of this figure are examples of models that were developed primarily for predicting the effect of R-ratio on the growth of fatigue cracks. These models can be applied to variable amplitude loading, but they predict that crack growth from any cycle is a function only of the magnitude and stress ratio of the cycle itself without regard for previous events. Forman [6] and Walker [7] proposed models of this type for the "Paris law" region of the crack growth rate curve while Barsom [8] and Lal [9] have proposed relationships for the near threshold region.

Models that consider the interaction between the current fatigue cycle and preceding cycles can generally be classified into closure based models and crack tip stress models. The yield zone models of Wheeler [10] and Willenborg [11] are based on the concept of residual stresses in the plastic zone. Wheeler used the ratio of the current and previous plastic zone sizes to compute crack retardation while Willenborg computed effective values of ΔK and R as a function of the overload plastic zone size. These models have historic significance in that they were attempts to use fracture mechanics concepts to explain changes in the crack growth rates observed during variable amplitude loading. However, following the observations of crack closure by Elber [12,13], these

models are rarely used in the scientific literature. Recent observations have led Sadananda et al. [14] to reject the significance of closure and propose the "Unified Approach" variable amplitude model based the stress state ahead of the crack tip. Sehitoglu and Sun [15] noted especially the significance of residual stresses ahead of the crack tip during plane strain and variable amplitude loading or for crack growth from micro notches.

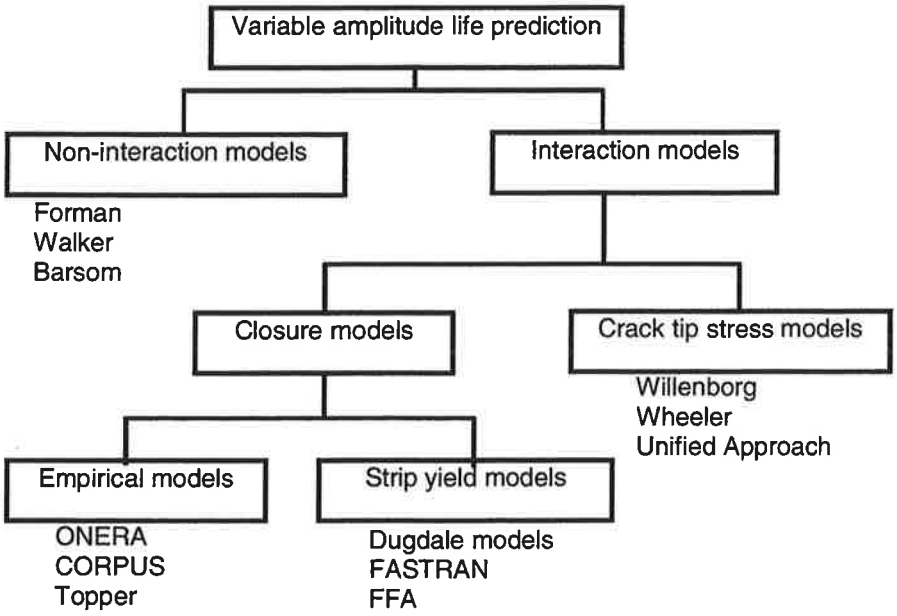

FIG. 1 - Classes of variable amplitude fatigue life prediction models.

The empirical closure models are intended to account especially for the effect of plasticity induced crack closure on fatigue crack propagation [16-18]. They model the effective stress intensity factor defined by Elber, $\Delta K_{eff} = (S_{max} - S_{op}) F (\pi a)^{0.5}$, where S_{max} is the maximum stress, S_{op} is the stress at which a crack is open and F is the geometry factor. Most empirical models have been developed with aircraft fatigue problems in mind. The ductile materials, load spectra with large mean stress shifts and thin sections found in these applications result in relatively large plastic zone sizes and frequently high degrees of closure. Various empirical relationships for computing S_{op} have been proposed and the models show significant improvements in life prediction capability as compared to non-interaction models [1]. The suitability for these models for other materials and other classes of load spectra is not fully confirmed.

Yield strip type models attempt to physically model the growing crack tip area and the plastic wake generated [19-21]. Modifications of the Dugdale-type plastic zone [22] concept are made so as to leave deformed material in the wake of an advancing crack. The crack closure contribution of this deformed plastic wake as function of crack advance is computed. These models are usually computationally demanding but they are successful in modeling a variety of transient events including multiple overloads and delayed retardation.

Small Cycle Damage

Machine components and structures are frequently subjected to variable amplitude loading in which significant portions of the fatigue cycles have amplitudes less than fatigue limit observed

under constant amplitude loading. Small amplitude cycles are normally associated with normal operation of rotating equipment, but maintenance operations, thermal events, or other transients may induce some cycles with amplitudes exceeding the fatigue limit. Numerous experimental studies have shown that small amplitude cycles that are part of a load spectrum are more damaging than the same size cycle applied using constant amplitude loading [23-49].

Topper and co-workers have performed numerous series of tests on both smooth and notched specimens of SAE 1045 steel, 2024-T231 aluminum and 319 cast aluminum alloy [23-31]. Intermittent over- or understraining was applied to specimens followed by blocks of low amplitude cycling. These authors found that cycles below the fatigue limit became damaging and that cycles slightly above the fatigue limit showed increased damage in the presence of either over- or understresses. The increase in damage for the small cycles was a maximum immediately following the over- or understress and then returned toward a steady state value as cycling progressed.

The number of experimental programs directed toward the problem of near-threshold fatigue under variable amplitude loading is limited, so some observations for spectrum load testing of nominally smooth components are also relevant. Conle and Topper [25,26] studied the question of small cycle fatigue damage with the goal of accelerating test times while retaining a sufficient portion of the fatigue damage. Small smooth specimens were tested under axial strain control loading. By successively editing out smaller and smaller fatigue cycles, the actual damage caused by cycles with different strain ranges could be determined. The actual damage produced by cycles with strain ranges below the endurance limit far exceeded what was predicted by constant amplitude test data. Three small cycle omission criteria were tested, but it was consistently observed that the actual damage omitted was greater than what was predicted, i.e., the small cycles were always more damaging in practice than what would be predicted based on constant amplitude tests.

In a similar set of experiments, constant amplitude fatigue life results and the bi-linear damage accumulation line as proposed by Haibach [32] were used to predict the fatigue life of simple notched steel components subject to random fatigue loads. The predicted lives were non-conservative by a factor of six at $N_f = 1 \times 10^6$ and by a factor of 12 at $N_f = 1 \times 10^7$[33]. In another large set of tests on five different automotive suspension components subject to constant amplitude and service loads, Schütz and Heuler [34] found that fatigue life was consistently over predicted when life estimations were based on linear damage accumulation rules and constant amplitude testing. Four damage accumulation hypotheses, including the three most common versions of Miner's rule, were used. It was argued that the complex process of crack initiation and propagation is oversimplified by linear damage accumulation rules. In general, the Zenner-Liu rule [35], which attributes an artificially large damage contribution to cycles with $\Delta S > \Delta S_o/2$, best fits the service load data.

Tokaji and Ando [36] conducted two level tests where the secondary stress was below ΔS_o. They found that the smaller stress cycles had little influence on the initiation of surface cracks up to about 80 μm in length. Scatter in these results, however, was very large with some tests showing a large damage contribution due to the small cycles and others showing a negative contribution, i.e., small cycles delayed crack initiation. Small cycles contributed significantly to crack growth in the range of 80 μm to 200 μm, but periods of both slow and fast propagation were observed. For cracks longer than 200 μm, even the lower stress cycles produced stress intensity ranges exceeding ΔK_{th}.

Yan et al. [37] have suggested an alternate curve-fitting algorithm for long-life specimen fatigue data. This method essentially recognizes that the constant amplitude fatigue process will have three regions depending on stress level: 1) the low cycle regime, 2) the high cycle regime, and 3) the endurance regime. When computing the proposed elastic strain amplitude vs. reversals to failure regression line, i.e., $\Delta e_{elastic}/2$ vs. $2N_f$, only data in the high cycle regime should be included and this line should be

extrapolated below the endurance regime when estimating the damage contribution of small cycles as part of a spectrum. The proposed $\Delta e_{elastic}/2$ vs. $2N_f$ curve has a steeper slope and, therefore, attributes more damage to small amplitude cycles than would be observed during constant amplitude loading. This method was shown to give better life predictions for spectrum loaded specimens as compared to the more conventional approach in which all elastic strain range data is used to compute the $\Delta e_{elastic}/2$ vs. $2N_f$ regression line.

Stanzl-Tschegg et al. [38] investigated the high cycle fatigue behavior of cast aluminum alloys under both constant amplitude and service load conditions with a cumulative frequency distribution considered representative of car wheel loading. The number of cycles to failure ranged from 10^6 to more than 10^9. Experimental lives were found to be seven to 23 times shorter than the fatigue life predicted using the original Palmgren-Miner damage accumulation rule.

Crack closure arguments are frequently used to explain the differences between constant and variable amplitude fatigue damage accumulation. Vormvald and Seeger [39] found that larger strain cycles caused an instantaneous change in the crack closure strain of the smaller cycles. The crack closure strain of the large cycle was approximately the same under both constant amplitude and variable amplitude loading. During a small strain cycle, the crack, which was closed for a considerable portion of the cycle under constant amplitude loading, was always open under variable amplitude loading. The effective strain range during which the crack was open was greater during variable amplitude loading and more crack growth per cycle occurred.

Variable amplitude load where a significant portion of the fatigue cycles are smaller than the fatigue limit brings up significant questions with regard to damage accumulation. It is clear that in such cases the linear damage rule proposed by Palmgren [50] and Miner [51] cannot be used because this simple rule attributes no damage to cycles less than the fatigue limit. This problem has led researchers to a variety of more complex damage accumulation rules. Fatemi and Yang [52] survey and categorize many of this many of these rules and report more than 50 modifications of Palmgren-Miner rule. Many of these were developed to account for the effect of cycles below the fatigue limit.

The Model

The life prediction model used in this paper is based on several fundamental assumptions:

1. The fatigue process is governed by the propagation/nonprogagation of fatigue cracks in which growth rate per cycle is related to the effective stress intensity factor range by a Paris-type equation.
2. The effective crack driving stress is affected by both maximum and minimum stresses in a history.
3. The material has an intrinsic threshold below which cracks will not propagate if the effective stress range is less than the threshold.
4. High cycle fatigue behavior of this material is controlled by the presence of shrinkage pores that behave as initial cracks.
5. Over- or underload events alter the crack driving force and, if a crack is not arrested, the driving force returns to the steady state value as an exponential function similar to that in the Topper model.

The most difficult aspect in developing the model is determining the intrinsic threshold, i.e., defining the effective driving force at the limit where crack propagation is not observed, $\Delta K_{th,int}$. During the variable amplitude underload tests at high mean stresses, it was observed that cycles with amplitudes equivalent to 60% of the constant amplitude fatigue limit produced failure at

about 100 million cycles in about half the test specimens. This value is therefore used as a practical engineering value.

If it is assumed that the effective stress is related to the intrinsic threshold at the fatigue limit, a relationship between effective driving force and applied stress can be established. Effective driving force can be defined in terms of S_{max} and S_{min}. This is illustrated in Fig. 2. This figure indicates that under completely reversed loading only a small portion of the applied stress cycle is effective in propagating a crack.

In the experiments reported here, no attempts were made to specifically measure the crack opening loads of the small cracks during the fatigue process. Such measurments have been reported by DuQuesnay et al. [27] Varvani-Farahani and Topper [28], Vormwald and Seeger [39], and McClung and Sehitoglu [53]. In the current experiments, the difference between applied stress range and effective stress range may be attributable to crack closure but some researchers have suggested that stresses ahead of the crack tip are more significant that closure stresses [2,14,15]. Stresses ahead of the crack tip become more significant in the case of plane strain or cracks propagating from micro notches as is the case with nodular cast iron.

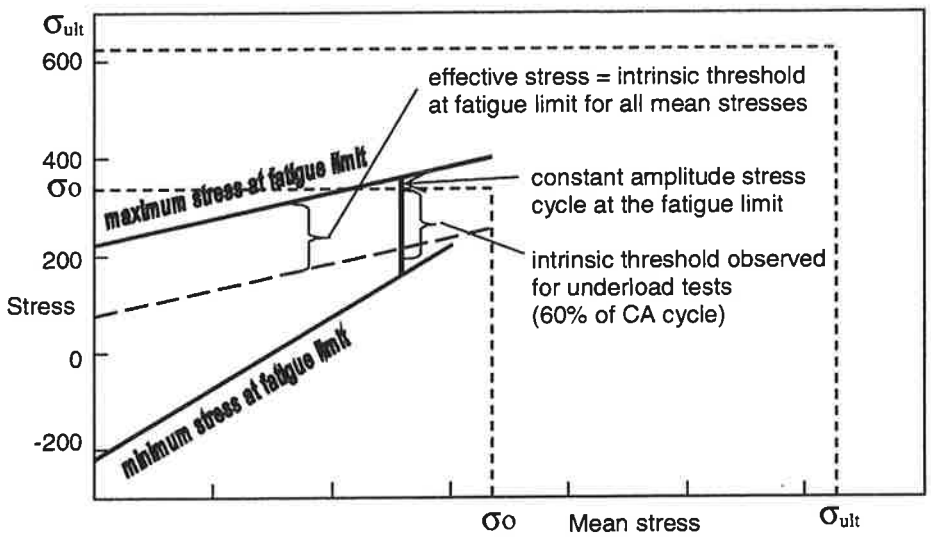

FIG. 2 – Smith diagram: relationship between maximum and effective stress.

Most types of defects for thick-section castings can be avoided using high quality foundry practices, however, shrinkage pores cannot be completely avoided. The role of micro shrinkage pores on the high cycle fatigue behavior of this nodular cast iron has been well documented [54-58]. SEM investigations have shown that long life fatigue failures in test specimen can normally be attributed to crack initiation and growth from individual defects. The statistical size distribution of shrinkage pores has also been determined. Throughout his paper, a maximum defect size corresponding to 50% probability of occurrence is used. Using a crack propagation based model it is also possible to compute other probability of failure curves based on the statistical distribution of defects.

After the issues of initial crack size and intrinsic threshold stress intensity are established, the crack growth constants C and m used in a modified Paris-type relationship are relatively easy to establish based on either finite life test data or direct observations of small crack propagation.

$$\frac{da}{dN} = C\left[\left(K_{max} - K_{op}\right)^m - \Delta K_{th,int}{}^m\right] \quad (1)$$

The variable amplitude interaction model chosen is based on that used by Topper and colleagues [18, 22, 23]. This model assumes that the interactive damage for a given cycle decreased as an exponential function of the number of small cycles following an overload or underload. It is assumed that, under constant amplitude loading, a small crack will have a certain driving force based on the maximum stress, stress ratio and crack size. In the case of underloads, the driving force is assumed to increase immediately after the underload and then gradually decay back toward the original constant amplitude state.

EXPERIMENTS

Test Material

Nodular cast iron is used extensively in the production of ground vehicle components and large machinery. When compared to gray iron, nodular cast irons have significantly higher fatigue strengths that can be used to advantage in the design of fatigue-loaded components. Rigid quality control during the casting operation can eliminate the relatively large defects often associated with complex castings, but small microstructural irregularities can never be completely eliminated for large thick-section castings. These shrinkage pores, inclusions, and other types of naturally occurring defects have a controlling effect on the endurance limit strength. Interest in this material for fatigue-loaded components is reflected in the large number of recent scientific publications devoted to this material [54-68]. Test bars were cut from either 100 x 100 x 300 mm ingots or from the cylinder head of a Wärtsilä 64 diesel engine. Material from both the ingots and cylinder head were nominally identical, GRP 500/ISO 1083 nodular cast iron, but were received from two different foundries.

Material taken from the cylinder head had average tensile properties of $R_{p0.2}$ =307 MPa and R_m = 517 MPa while material taken from the ingots was slightly stronger with $R_{p0.2}$ =340 MPa and R_m = 620 MPa. Both showed approximately the same distribution of nodular graphites and a dual ferritic-pearlitic matrix. Material from the cylinder head was approximately 50% pearlite, 40% ferrite and 10% graphite and material from the ingots is 77% pearlite, 10% ferrite and 13% graphite.

Fatigue Testing

Fatigue testing was accomplished using a computer controlled resonant type test machine. Test frequency was nominally 160 Hz. Axial test specimens were ϕ12 mm with a 30 mm gage section and 50 mm transition radius. Axial testing was performed using several stress ratios or mean stress levels. The staircase strategy was used to determine the constant amplitude fatigue limit at several different R ratios. Tests exceeding $1x10^7$ cycles were considered run-outs. Material from both foundries was used in the constant amplitude fatigue limit testing.

The variable amplitude history is illustrated generally in Fig. 3 with details of the spectra given in Table 1. In all cases the variable amplitude spectrum consisted of a large number of small amplitude cycles at a high mean stress followed by a single unloading event to near zero stress. Only the material taken from the ingots was used in the variable amplitude testing. Due to the natural scatter in result found in fatigue of cast iron, most variable amplitude histories were repeated. The number of specimens used for a single load history is also given in Table 1.

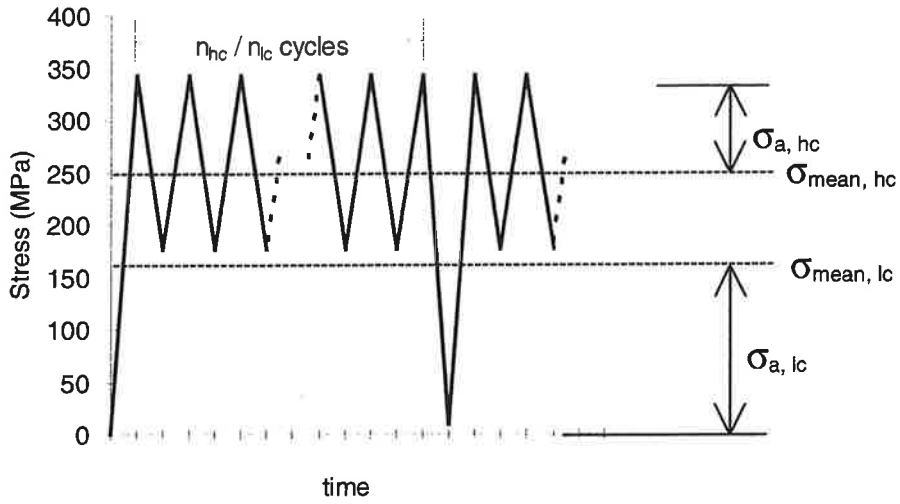

FIG. - 3 Aspects of the variable amplitude spectrum (see also Table 1).

Table 1 – Details of variable amplitude test matrix

$\sigma_{mean,\ lc}$	$\sigma_{a,\ lc}$	$\sigma_{mean,\ hc}$	$\sigma_{a,\ hc}$	mean cycles to failure, N_f	n_{hc} / n_{lc}	# of specimens
190	180.5	260	111	543 900	3 300	10
177.5	167	260	83,5	4 636 200	20 000	10
167.5	157.5	260	65	80 000 000+	300 000	10
180.4	170.4	260	90,7	3 274 000	10 000	3
180.4	170.4	260	90,7	47 800 000	100 000	1
177.5	167	260	83,5	27 026 000	220 000	6
177.5	167	260	83,5	3 986 000	5 000	1

+ six of ten specimens resulted in run-outs, $N_f > 150x10^6$

RESULTS AND DISCUSSION

Crack Growth Parameters

Since the work of Elber on crack closure, many studies have been devoted to quantifying the effect of closure under a variety of load situations. Several empirical or semi-empirical relationships have been proposed to compute the crack opening stress based on a combination of loading and material parameters. Models by Newman [69], Sehitoglu [70] and Duquesny et al. [27] are similar in the respect that opening load is computed to be a function of S_{max}, S_{min} (or R ratio) and material strength, i.e., yield strength, cyclic yield strength, or flow strength.

If it is assumed that the small cracks reported here grow in plane strain, the Newman model applied to near threshold crack growth predicts that small cracks are fully open for stress ratios above approximately 0.2. Similarly the Duquesny et al. model for positive stress ratios assumes that there is a minimum stress above which the stress range at the fatigue limit becomes constant. As seen from Fig. 4, the nodular iron reported here shows no such constant stress range even for stress ratios approaching 0.5.

Based on the Smith diagram of Fig. 2, it is assumed that, at the fatigue limit, the effective crack driving stress is independent of mean stress. This allows the crack opening stress to be formulated as a linear function of either the maximum or minimum stress. The variable amplitude spectra of interest consisted only of underload histories, so it was chosen to use a linear function of minimum stress.

$$S_{op} = 170 + 0.36 \cdot S_{min} \tag{3}$$

For other types of load histories it would be necessary to formulate opening stress in terms of S_{max} and S_{min}.

For material taken from ingots, a 50% probability of occurrence defect size was about 180μm [57], i.e. half-circular defect with radius 180μm. As previously presented, the intrinsic threshold stress range was about 60% of the applied stress range in the longest variable amplitude tests. This correlates to an intrinsic threshold stress intensity factor of 2.2 MPa $m^{1/2}$ for da/dN < $1x10^{-9}$ mm/cy. It should be remember that the value of 60% was found for stress cycles with relatively high R ratios, R ≈ 0.4. For completely reversed strain cycles, Bonnen and Topper [30] found no effect from the small cycles only when the amplitude was 1/3 the fatigue limit. The current data would be very close to this value for R = -1 cycling. On a microstructural level it has been observed that cycles as small as $\Delta S_o/2$ still cause changes in the materials dislocation structure [71].

Based on the constant amplitude finite life data, crack growth parameters for the Paris equation are found to be m = 4 and C = $4x10^{-9}$ (units: mm/cycle, MPa $m^{1/2}$). Constant amplitude fatigue life from experiment and analysis are show in Fig. 5. At high stress amplitudes for the high mean stress data the analytical predictions give slightly longer fatigue lives. This is partially explained in that the maximum stress for these cases is approaching the flow strength of the material so significant plastic deformation is present and linear elastic assumptions are violated. Scatter in the experiment results is due largely to the significant scatter observed in the initial defect sizes.

Variable Amplitude Life Predictions

Table 1 gives the number of specimens tested for each of the seven variable amplitude histories and the mean fatigue life. It can be noted from this table that the number of repetitions of the underload stress was always very small. The damage contribution of the larger stress cycles was always less than 1%. In a typical case the large cycle was repeated 300 times in a variable amplitude tests where a cycle of that size in constant amplitude loads would required 2 x 10^5 repetitions for failure, i.e., large cycle damage contribution = 300 / $2x10^5$ = 0.15%.

Based on a comparison of variable amplitude tests with similar $\sigma_{a,lc}$, $\sigma_{m,lc}$, $\sigma_{a,hc}$, and $\sigma_{m,hc}$, but with different N_{hc}/N_{lc}, it was possible to compute the rate at which the crack growth rate returned to a steady state value. A best fit was obtained for κ = -0.0008 where

$$\Delta S_{eff,N_{UL}} = \Delta S_{eff,CA} + \left(\Delta S_{eff,ul} - \Delta S_{eff,CA}\right) e^{\kappa N_{UL}} \tag{4}$$

In this equation $\Delta S_{eff,N_{UL}}$ is the effective stress range for cycle N_{UL} after the under load, $\Delta S_{eff,CA}$ is the effective crack driving stress range of the small amplitude cycle under constant amplitude loading, and $\Delta S_{eff,ul}$ is the effective driving force of the underload cycle during constant amplitude loading. The value κ = -0.0008 means that 6000 load cycles following an underload, the crack driving stress range has returned to within 1% of the constant amplitude stress value. Linking the change in crack driving stress range to the number of cycles following an

underload event is a matter of convenience. Physically it would be more appropriate to link this to the crack advance.

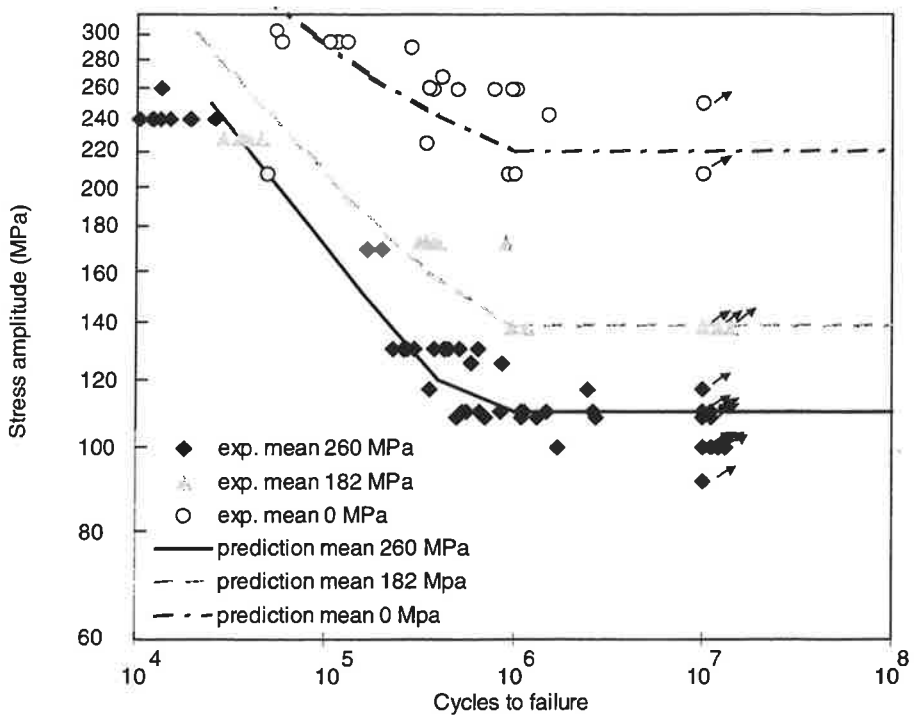

FIG 5. – Experimental constant amplitude data and crack growth predictions

Crack growth for a typical variable amplitude test, $\sigma_{a,lc} = 83.5$, $N_{hc}/N_{lc} = 20\,000$, is shown in Fig. 7. The prediction in this figure is made based on previous computed values of C, m, $\Delta K_{th,int}$, and κ.

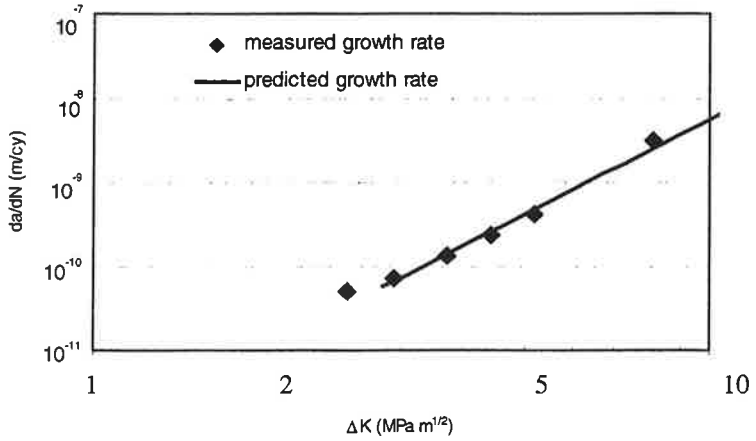

FIG. 7 – Observed and predicted crack growth for one test, $\sigma_{a,lc} = 83.5$, $N_{hc}/N_{lc} = 20\,000$.

Figure 8 shows the predicted S-N curves in comparison to the experimental data for the long-life variable amplitude tests. These curves tend to follow the mean of the experiment data. Using this

type of fracture mechanics approach, however, it is relatively easy to compute curves representing other failure probabilities based on knowledge of the shrinkage pore distributions.

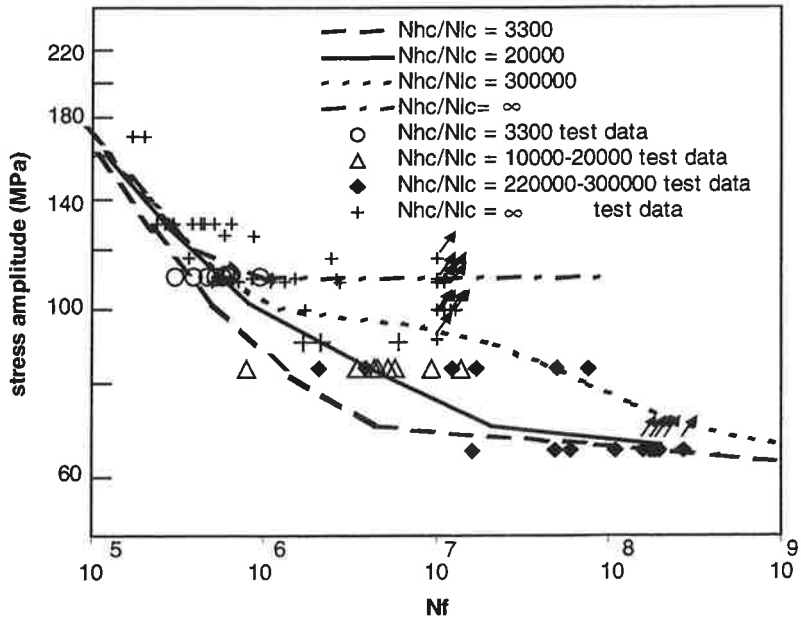

FIG. 8 – Measured fatigue lives and predicted SN curves for several variable amplitude histories.

CONCLUSIONS

This paper has reviewed numerous life prediction methods for variable amplitude fatigue. Special attention was given to cracks propagating from nominally defect free components in the high cycle regime where a significant portion of the fatigue damage can be attributed to cycles with amplitude less that the constant amplitude fatigue limit. An effective stress method for variable amplitude loaded similar to the Topper model is presented for long-life fatigue of a nodular cast iron. Model parameters are derived from a constant amplitude S-N curve and the Haigh diagram. Two sets of long- life variable amplitude tests were used to derive the underload interaction parameters.

Previously measured shrinkage pore distributions for the iron were used to determine the 50% probability of occurrence initial defect size. This size defect was chosen to illustrate the model, but in design a much lower probability of occurrence initial defect size would need to be chosen.

Current experiments were limited to constant amplitude loading and variable amplitude loading containing underloads so the crack driving stress was formulated only in terms of the minimum stress in a cycle of block of cycles. Good agreement is found between the experiments and the model prediction. However, a relationship between the maximum load and the effective crack driving stress would also need to be established for more general loading situations that also include overloads.

REFERENCES

[1] Schjive, J. *Fatigue of Structures and Materials*, Kluwer Acad. Publ., Dordrecht, 2001.

[2] Sehitoglu, H., Gall, K., and Garcia, A. M., *Int. J. Frac.*, **80,** 1996, pp. 165-192.
[3] Lawson, L., Chen, E. Y., and Meshii, M., *Int. J. Fatigue*, **21**, 1999, pp. 15-34.
[4] Geary, W., *Int. J. Fatigue*, **14**, 1992, pp. 377 - 386.
[5] Kumar, R., *Eng. Frac. Mech.*, **42**, 1992, pp. 151-158.
[6] Forman, R., Kearny, V., and Engle, R., *Trans. ASME J Basic Eng.*, **D89**, 1967, pp. 458-464.
[7] Walker, K., *Effects of Environment and Complex Load History on Fatigue Life, ASTM STP 462*, ASTM, Philadelphia, PA, 1970.
[8] Barsom, J. and Rolfe, S., *Fracture Control in Structures*, Prentice-Hall, Englewood Cliffs, 1977.
[9] Lal, D. N., *Fatigue Frac. Eng. Mat. Struc.*, **15**, 1992, pp.1199 - 1212.
[10] Wheeler, O. E., *J. Basic Eng.*, **94,** 1972, pp. 181-186.
[11] Willenborg, J., Engle, R. M., and Wood, H. A., *AFFDL-TR71-1*, Wright-Patterson AFB, 1971.
[12] Elber, W., *Eng. Frac. Mech*, Vol. 2, 1970, pp. 37 - 45.
[13] Elber, W., *Damage Tolerant Aircraft Structures, ASTM STP 486*, ASTM, Philadelphia, PA, 1971, pp. 230 - 242.
[14] Sadananda, K, Vasudevan, A., Holtz, R., and Lee, E., *Int. J Fatigue*, **21**, 1999, pp.S233-S246.
[15] Sehitoglu, H., and Sun, W., *ASME J Eng. Mat. Tech.*, **113,** 1990, pp. 31-40.
[16] Baudin, G. and Robert, M., *ECF5*, Lisbon, 1984, pp. 779-792.
[17] de Koning, A. U., *Fracture Mechanics, ASTM STP 743*, R. Roberts (ed.) ASTM, Philadelphia, PA, 1981, pp. 63-85.
[18] Topper, T. H. and Yu, M. T., *Int. J Fatigue*, **7**, 1985, pp. 159 - 164.
[19] Führing, H., and Seeger, T., *Fracture Mechanics, ASTM STP 677*, C. W. Smith (ed.), ASTM, Philadelphia, PA, 1979, pp. 144-167.
[20] Newman Jr., J. C., *Methods and models for predicting fatigue crack growth under random loading, ASTM STP 748*, J. Chang and C. Hudson (eds.), ASTM, Phil., PA, 1981, pp. 53-84.
[21] Wang, G. S., and Blom, A. F., *Eng. Frac. Mech.*, **40** , 1991, pp.507-533.
[22] Dugdale, D. S., *J. Mech. Phys. Solids*, **8**, 1960, pp. 100-104.
[23] Pompetzki, M. A., Topper, T. H. and DuQuesnay, D. L., *Int. J Fatigue*, **12**, 1990, pp. 207 - 213.
[24] Jurcevic, R., Duquesnay, D., Topper, T. & Pompetzki, M., *Int. J Fatigue*, **12**, 1990, pp. 259 - 266.
[25] Conle, A., and Topper, T. H., *Int. J Fatigue*, **1**, 1979, pp. 23 - 28.
[26] Conle, A., and Topper, T. H., *Int. J Fatigue*, **2**, 1980, pp. 130 - 136.
[27] DuQuesnay, D. L., Topper, T. , Yu M., and Pompetzki, M. A., *Int. J Fatigue*, **14**, 1992, pp. 45-50.
[28] Varvani-Farahani, A., and Topper, T. H., *Fatigue crack growth thresholds, endurance limits, and design, ASTM STP 1372*, J.C. Newman, Jr. and R.S. Piascik (eds.), ASTM, West Conshohocken, PA, 2000, pp. 192-206.
[29] MacDougall, C., and Topper, T. H., *Int. J Fatigue*, **19**, 1997, pp. 389-400.
[30] Bonnen, J. J. F., and Topper, T. H., *Int. J Fatigue*, **21**, 1999, pp. 23-33.
[31] Lam, T. S., Topper, T. H., and Conle, F. A., *Int. J Fatigue*, **20**, 1998, pp. 703-710.
[32] Haibach, E., *Proceedings of the Conference on Fatigue of Welded Structures*, Vol. 2. Abington, Cambridge: The Welding Institute. 1971, pp. 328 - 339.
[33] Gassner, E., and Lipp, W., *Service Fatigue Loads Monitoring, Simulation and Analysis, ASTM STP 671*, P.R. Abelkis. and J. M. Potter (eds.), ASTM, Philadelphia, PA, 1979, pp. 222 - 239.
[34] Schütz, W. & Heuler, P., "Miner's Rule Revisited," 77. AGARD-SMP Meeting, Bordeaux, 27 September - 1 October 1993. Ottobrunn: Industrieanlagen-Betriebsgesellshaft GmbH.
[35] Zenner, H. and Liu, J., *Konstruction*, **1**, 1992, pp. 9 - 17.
[36] Tokaji, K. and Ando, Z., *Fatigue Frac. Eng. Mat. Struc*, **7**, 1984, pp. 109 - 119.
[37] Yan, X., Cordes, T. S., Vogel, J. H. and Dindinger, P. M., *SAE Transactions, J. Mat. And Manufac.*, **101**, 1992, pp. 544-553.
[38] Stanzl-Tschegg, S.E., Mayer, H.R., Beste, A., Kroll, S., *Int. J Fatigue*, **17**, 1995, pp.149-155.
[39] Vormwald, M. and Seeger, T., *Fatigue Frac. Eng. Mat. Struc*, **14**, 1991, pp. 205 - 225.
[40] Zhou, Z. and Zwerneman, F. J., *Advances in Fatigue Lifetime Predictive Techniques: 2nd Vol., ASTM STP 1211*, M. Mitchell and R. Landgraf (eds), ASTM, Philadelphia, 1993, pp. 45 - 53.
[41] Hénaff, G., Petit, J. & Journet, B., *Fatigue Frac. Eng. Mat. Struc.*, **15**, 1992, pp. 1155 - 1170.

[42] Kikukawa, M., Jono, M. and Kondo, Y., *Advances in Fracture* Research (Fracture '81), Pergamon Press, Oxford, 1982, pp. 1799 - 1806.
[43] Koterazawa, R., *Int. J Frac.*, **12**, 1976, pp. 169 - 170.
[44] Koterazawa, R., Mudjijana, Y., Qinsheng, W., Tian-Jian, W., and Nosho, T., *Fatigue Frac. Eng. Mat. Struc.*, **17**, 1994, pp. 1033 - 1041.
[45] Sunder, R., *Advances in Fatigue Lifetime Predictive Techniques: Second Volume, ASTM STP 1211*, M. R. Mitchell and R. W. Landgraf (eds), ASTM, Philadelphia, 1993, pp. 19 - 29.
[46] Sunder, R., Prakash, R. V. and Mitchenko, E. I., *Advances in Fatigue Lifetime Predictive Techniques: 2nd Vol., ASTM STP 1211*, M. R. Mitchell and R. W. Landgraf (eds), ASTM, Philadelphia, 1993, pp. 30 - 44.
[47] Sunder, R., *Advances in Fatigue Lifetime Predictive Techniques: Second Volume, ASTM STP 1122*, M. R. Mitchell and R. W. Landgraf (eds), ASTM, Philadelphia, 1992. Pp. 161 - 175.
[48] Marquis G. *High cycle spectrum fatigue of welded components*, VTT Publications 240, Technical Research Centre of Finland, Espoo, 1995.
[49] Ohta, A., Maeda, Y., Machida, S.,and Yoshinari, H., *Trans. Jpn Weld. Soc.*, **19**, 1988, pp.69-73.
[50] Palmgren, A, *Verfahrenstechinik*, Berlin, 1924, **68**, 339-341.
[51] Miner, M. A., *ASME J of App. Mech.*, **12**, 1945, pp. A159 - 164.
[52] Fatemi, A., and Yang, L., *Int J Fatigue*, **20**, 1998, pp. 9-34.
[53] McClung, R.C., and Sehitoglu, H., *Mechanics of fatigue crack closure, ASTM STP 982*, 1988, pp. 279-299.
[54] Marquis, G. and Karjalainen-Roikonen, P., *Proc. 6th Int. Conf. Biaxial/Multiaxial Fatigue and Fracture*, M. M. de Freitas (ed.), 2001, pp. 151-159.
[55] Marquis, G., *Proceeding of ECF 13*, San Sebastian, Spain Paper 3m.314, 2000.
[56] Marquis, G. and Solin, J. *Long-life fatigue design of GRP 500 nodular cast iron components*, VTT Research Notes 2043, Espoo, 2000, 70 p.
[57] Marquis, G. and Murakami, Y., *Materials Science Research International, Special Technical Publication*, T. Hoshide (ed.), Kyoto, 2001, pp. 92-96.
[58] Marquis, G., Rabb, R., and Siivonen, L., *ASTM STP 1372*, J. C. Newman and R. S. Piascik, Eds., ASTM, West Conshohocken, 1999, pp 411-426.
[59] Clement, P, Angeli, J. P., and Pineau, A. *Fatigue Frac. Eng. Mat. Struc.*, **7**, 1984, pp. 251 - 265.
[60] Tokaji, K., Ogawa, T., and Shamoto, K., *Int. J Fatigue*, **16**, 1994, pp. 344-350.
[61] Yaacoub Agha, H., Béranger, A.-S., Billardon, R., and Hild, F., *Fatigue Frac. Eng. Mat. Struc.*, **21**, 1998, pp. 287 - 296.
[62] Nadot, Y., Ranganathan, N., Mendez, J., and Béranger, A.-S.,*Scrip.Mat.*, **37**,1997,pp. 549-553.
[63] Palin-Luc, T., Lasserre, S., Froustey, C. and Bérard, J.Y., "Experimental approach of damage cumulation in high cycle fatigue with random loadings in blocks," In*: Mechanisms and Mechanics of Damage and Failure: ECF11,* J. Petit (ed.), EMAS, UK, 1996, pp. 1337-1342.
[64] Nadot, Y., Ranganathan, N., Mendez, J., and Béranger, A.-S., *Mechanisms and Mechanics of Damage and Failure: ECF11,* J. Petit (ed.), EMAS, UK, 1996, pp. 1155-1160.
[65] Schleicher, M., Bomas, H., and Mayr, P., *Fracture from Defects: ECF 12,*M.W. Brown, E.R. de los Rios and K.J. Miller (eds.), EMAS, UK, 1998, pp. 91-96.
[66] Nadot, Y., Ranganathan, N., Mendez, J., and Béranger, A.-S, *Fracture from Defects: ECF 12,* M.W. Brown, E.R. de los Rios and K.J. Miller (eds.), EMAS, UK, 1998, pp. 85-90.
[67] Greno, G. L., Otegui, J. L., and Boeri, R. E., *Int. J Fatigue*, **21**, 1999, pp. 35-43.
[68] Lin, C.-K., and Lee, W.-J., *Int. J Fatigue*, **20**, 1998, pp. 301-307.
[69] Newman, J.C., Jr. *Int. J Frac.*, **24**, 1984, R131-R135.
[70] Sehitoglu, H., *Eng. Frac. Mech.*, **21**, 1985, pp. 329-339.
[71] Fukuoka, C., and Nakagawa, Y. G., *Scrip. Mat.*, **34**, 1996, pp. 1497-1502.

FAILURE STRAIN DETERMINATION USING RUPTURE TESTS WITH REACTOR PRESSURE VESSEL HEAD MODELS

H. TALJA, H. KEINÄNEN, E. HOSIO, P. PANKAKOSKI & K. RAHKA
VTT Industrial Systems
P.O.Box 1704
FIN-02044 VTT, FINLAND

ABSTRACT

In the LISSAC project (LImit Strains in Severe ACcidents), partly funded by the EC Nuclear Fission and Safety Programme within the 5th Framework programme, an extensive experimental and computational research programme was conducted to study the stress state and size dependence of ultimate failure strains. The results are aimed especially to make the assessment of severe accident cases more realistic.

For the project a block of material of the German Biblis C reactor pressure vessel (RPV) was available. As part of the project, RPV head models from this material (22 NiMoCr 3 7) were tested under quasistatic pressure load at room temperature up to rupture at VTT. Half of the specimens contained holes describing the control rod penetrations of an actual RPV head. In this paper, the experimental results are presented and compared with numerical predictions.

1. SPECIMENS AND EXPERIMENTAL SETUP

At VTT totally eight pressure vessel head models were tested. The specimens were delivered by FzK and they were loaded up to rupture under quasistatic pressure load at room temperature. Six first specimens were of the smaller size (diameter $\phi = 90$ mm, wall thickness $t = 5$ mm) and for the other two, all dimensions were scaled by a factor of 5. Half of the specimens contained 73 equiaxial holes, describing the control rod penetrations in an actual reactor pressure vessel head.

One of the main challenges in planning the test arrangements was to obtain failure at the test specimens without losing the tightness of the support structures. A 3 mm thick aluminium liner was designed for the tests with the small specimens with holes. In order to estimate the stiffening effect of the liner, also one of the small specimens without holes was tested using a liner. The testing counterparts were not allowed to undergo significant plastic deformations as they had to be used several times. Rather stiff support structures, shown schematically in Figure 1, were thus necessary.

For testing, the specimens were bolted to a rigid base plate using a fixture ring. The geometry of the specimen and the principle of the experimental setup are shown in Figure 1. The main dimensions of the smaller specimens are given in Table 1.

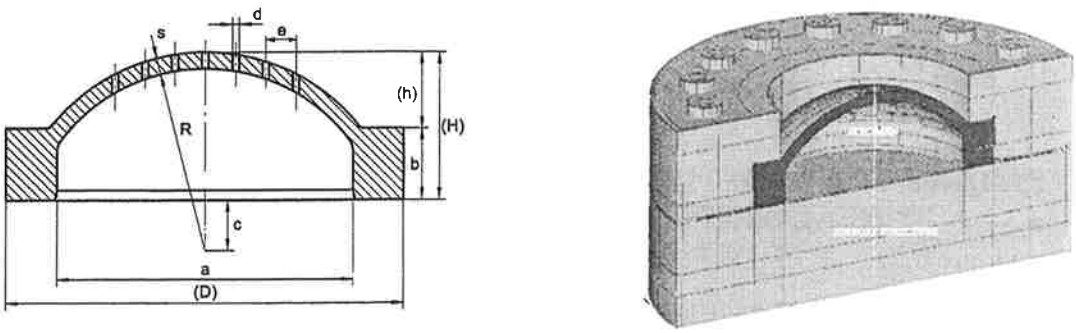

Fig. 1. Geometry of the small pressure vessel models with holes (left) and a schematic presentation the experimental setup (right).

Table 1. Main dimensions of the smaller pressure vessel models.

a [mm]	R [mm]	s [mm]	h [mm]	b [mm]	d [mm]	e [mm]
90.6	55.6	5	23.2	22	2	4.6

2. FE ANALYSES FOR PLANNING THE EXPERIMENTS

The experimental setup was carefully designed to withstand the failure pressure of the specimen, which was estimated to be around 1150 bar. The fixture system had to be very rigid, in order to ensure that no tightness problems would occur during the tests. Besides, no essential plastic deformations were allowed as the same fixture system had to be used in all tests with the same specimen size. Axisymmetric and three-dimensional finite element analyses were conducted to assess the behaviour of the experimental setup (see Fig. 2). Actually, only the smaller specimens without holes were modelled. An important goal of the analyses was to help in assuring the reliability of the support structures and other facilities during the tests. Also, the specimen behaviour during the test was estimated. The analyses have been reported in [2].

As the dimensions of the fixture ring set limitations for the size and number of bolts, one of the main concerns in planning the test arrangements was the endurance of the bolts. On the other hand, due to the high expected failure pressure it was of paramount importance that no failure of test arrangements would occur during the tests. To ensure the proper functioning, both axisymmetric and three-dimensional finite element (FE) models were used in the computations. The 3D model enabled a more accurate estimation of the bolt behaviour.

The elasto-plastic analyses were performed using Abaqus 5.8-14 finite element code [3]. Large strains and deformations were taken into account. In the analyses, mechanical properties documented by the LISSAC theoretical task group [4] were applied for the specimen.

The main result of the analyses was that the maximum pressure would be about 1140 bar. So the bolts had to be able to carry a total load of 735 kN in the smaller size and 18 500 kN in the larger size. The results also indicated that no problems concerning to deformations and loss of integrity were to be expected.

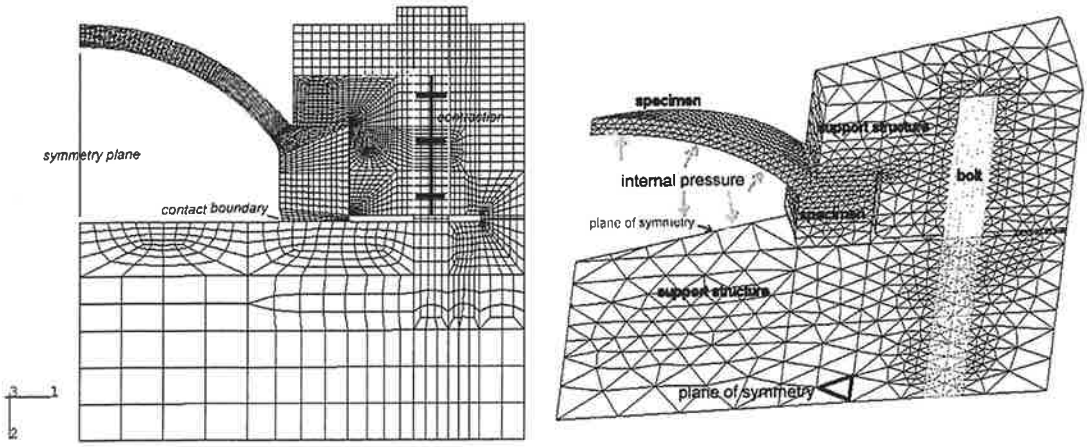

Fig. 2. Axisymmetric and three-dimensional finite element models used in the analyses [2]. The 3D model describes 1/32 of the whole geometry, corresponding to 32 bolts.

3. EXPERIMENTAL RESULTS

Seven from the eight tests were completed totally successfully. In the test with the large specimen with holes, the properties of the aluminium liner material proved to differ from those of the smaller ones. As a consequence the experiment ended at the failure of the liner. All other tests yielded very consistent results which also agreed well with the numerical predictions.

3.1 Global results

During all tests the internal pressure and the dome displacement were recorded up to failure. For small specimens also some strain measurements were performed. After the test, the minimum thickness values of the specimens without holes were measured.

For none of the eight performed tests, any interruptions or repetitions were necessary [1]. Seven tests were an immediate success. Although pressure loading is to be considered as a load controlled type loading, the test specimens strained in full control far beyond the strains at maximum pressure, as it was not possible to maintain the pressure level when the specimen started to yield rapidly. This was because the low displacement pump provided no accumulator to feed more water to compensate for the volume increase of the test piece. For the test with the large specimen with holes, however, the test ended prematurely before reaching failure of the specimen.

Table 2 compares the maximum pressure and related displacement values. It shows that the tests were very well reproducible. All tests with specimens without holes which were tested without liner, i.e. specimens EU1, ET1 and EW, gave maximum pressure values deviating only by ± 0.2 % from the mean value of 115 MPa, which agrees well with the estimated ultimate load of 114 MPa. The scatter of the scaled maximum dome displacement values was 4.2 % from the mean value 69.9 % and, quite surprisingly, it was largest for the large specimen.

The three tests with small specimens with holes, EZ1, EY1 and FA1, also showed quite modest variation in the measured maximum pressures (0.7 % of the mean value 110 MPa). The failure occurred at a scaled displacement of 28.2 % with a fairly small scatter of ± 1.1 %. According to Figure 6 this seems to correspond roughly to the ultimate load. In the test with the large specimen a pressure of 115 MPa, which seems to be smaller than the ultimate load, was reached. This

different behaviour is most probably due to the lesser ductility of the liner material, compared to that of the small liners, although they were assumed to be identical and chosen with such expectations.

Table 2. Summary of main results from the pressure vessel head model tests.

Specimen	Diameter a [mm]	Holes	Liner	Max. pressure [MPa]	Max. displ. [% of dome height]
EU1	90.6			116	69.1
ET1	90.6			115	66.9
EV1	90.6		x	126	34.8
EZ1	90.6	x	x	111	27.9
EY1	90.6	x	x	109	28.3
FA1	90.6	x	x	109	28.4
EW	453			115	73.6
FB	453	x	x	117	17.3

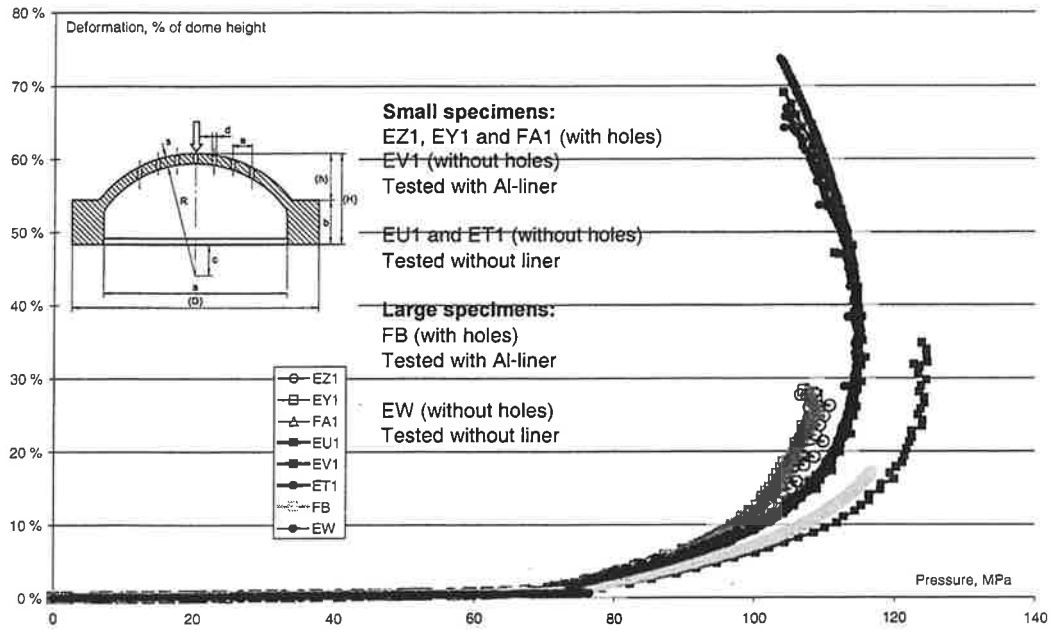

Fig. 3. Scaled dome displacement as a function of internal pressure.

Figure 3 shows the measured scaled dome displacement of each test as a function of pressure. The results seem to fall in four groups:

1) the tests with the specimens EU1, ET1 and EW without holes;
2) the test with the small specimen EV1 without holes which was tested with liner for comparison;
3) the three test results with small specimens EZ1, EY1 and FA1 with holes and

4) the test with the large specimen FB with holes.

Groups 2 and 4 contain both only one tests. Only in group 1 the tests continued beyond the strain at maximum pressure whereas this happened in none of the tests with a liner. Comparison of test groups 1 and 2 indicates that the liner increases the maximum pressure by about 10 MPa. The increase of maximum pressure appears to be an artefact due to the observed liner displacement during the test such that the strength of the lower ring of the liner increases the strength of the assembly.

Lowest maximum pressure values were obtained in the tests of group 3. The three tests in this group show very similar behaviour. The test with specimen FB (group 4) shows abnormal behaviour. The measured pressure values exceed clearly those in the corresponding tests with small specimens (group 3) while no difference was observed in the case of different specimen sizes without holes. Obviously the difference is thus connected to the behaviour of the liner.

Normalisation for the effect of the holes and the liner

Pressure-displacement records were normalised using global membrane stress and shape criteria and relative strength values for the steel specimens and the aluminium liners (Fig. 4). The test pressures were converted into steel net section membrane stress by adopting the usual sphere stress formula and factors for the liner thickness and strengths and the hole configuration.
The normalisation factors are:
for sphere stress $\sigma = p*R/2s * hf * lf$, where

p = the internal pressure,
R = dome inside radius and
s = dome thickness = sst below
yielding R/2s = 5.56.

Further, hf = hole factor (hf = 1 for tests without holes and as given below for tests with holes) and lf = liner factor (lf = 1 for tests without liner and as given below for the liner effect).

Here the hole factor is hf = 1 / (1-d/2e), where d/2e = 2/9.2 = 10/46 = 0.217391 for small and large specimen sizes. Thus hf = 1.28 .

The liner factor is lf = 1 / (1+ k*YSal/YSst * sal/sst), in which k is a fitting parameter and YSal/YSst the ratio of flow strengths aluminium/steel. Here YSal/YSst = 234/500 = 0.47 and sal/sst = thickness ratio liner/specimen.

It was found that a value for k = 0.32 for the smaller liner and k = 0.72 for the larger produced consolidation of the different test records (taking aluminium yield stresses as 234 MPa for both small and large liners). A ratio of 1.13 is found for the "strengthening" effect of the holes using these net section membrane stress criteria, or a factor of 1.13/1.28 = 0.884 for the weakening effect of the holes on the global behaviour disregarding holes in the stress calculation. The consolidated curves are shown in Figure 4.

The factor 1.13 on the net section strength is interesting because it is close to the ratio of fully plastic principal stress components for plane strain and equibiaxial strain thus proposing that the specimen ligaments between holes adopt a plane strain deformation mode whereas the dome without holes remains in the equibiaxial mode. This interpretation may be fortuitious, because the stress-strain concentration effect of the holes is neglected and the net section factor 1.28 is related to the less densely spaced 90 degree configuration prevailing in the dome centre.

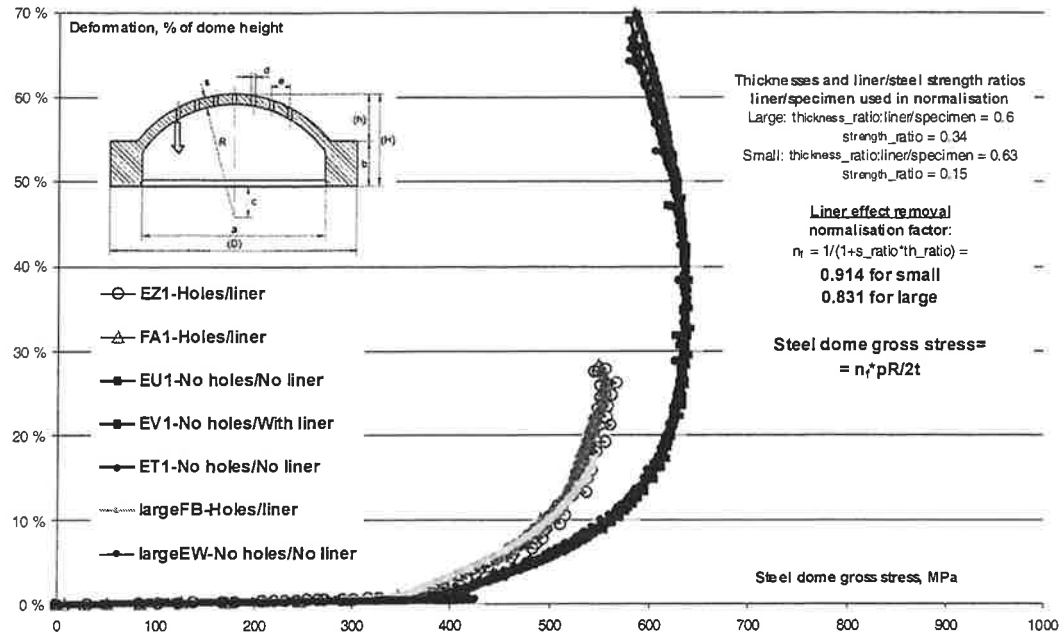

Fig. 4. Normalised membrane net stress for steel dome versus deformation of specimen.

The factors k for small and large liners differ by a factor slightly larger than 2 for several tentative reasons. The factor 2 can be deduced back to the retaining effect of the larger lower flange of the larger liner (relatively the 0-ring groove is much smaller than in the small liner) preventing the larger liner to slip into the test specimen during pressurisation and causing the large liner into equibiaxial tension. The smaller liner was observed to slip into the steel dome during its deformation indicating that the small liner was forced into a "deep drawing" or pure shear deformation mode, which occurs at half the value of principal stress compared to equibiaxial tension. Hence the ratio around 2 between the aluminium flow stress factors k in the normalisation for the effect of small and large liners.

3.2 Failure modes

Some specimens after the tests are shown in Figures 5 to 8. From the photos the failure modes of each specimen can be recognised.

Figure 5 shows a typical example of a tested small specimen without holes. The failure occurred as a leak at the uppermost part of the dome where the tensile strains are the highest. The effect of the liner reduced the failure strain and changed the mode of failure is demonstrated in Figure 6. As shown in Figure 7, the failure of the large specimen without holes (EW) was quite dramatic. A part of a size of about 20x15 cm^2 fragmented from the specimen. The related damage around the test set up was contained due to the precaution of testing upside down. Accordingly the loose part hit against a rigid floor and no serious damage was caused to the surroundings.

Figures 8 and 9 show tested specimens with holes. Figure 8 is a typical example of a tested specimen with holes. Also the liner is shown. In this case the specimen broke along the first row of densely spaced holes, counting from the dome top. The test with the large specimen FB (Figure 9) ended somewhat prematurely due to the failure of the liner. However, a similar yield pattern can already be recognised to develop which has caused the failure of the specimen EZ1.

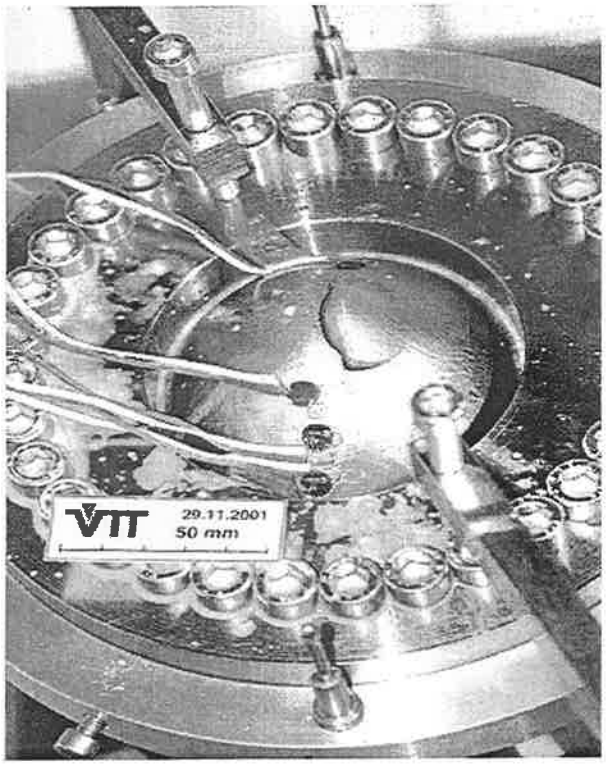

Fig. 5. Specimen EU1 after testing. The specimen failed along the uppermost part of the dome.

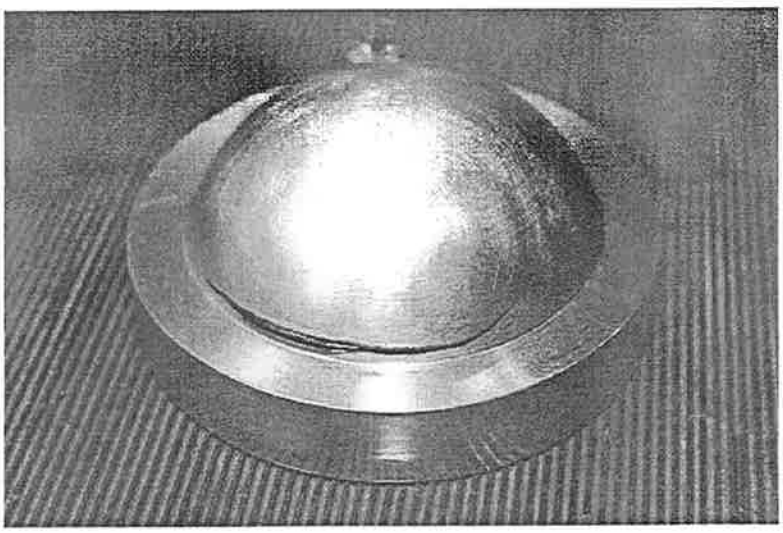

Fig. 6. Specimen EV1 after testing. This specimen was tested using a liner, which caused a premature failure by a failure mode deviating from those tested without liner.

Fig. 7. Specimen EW (large size) after testing.

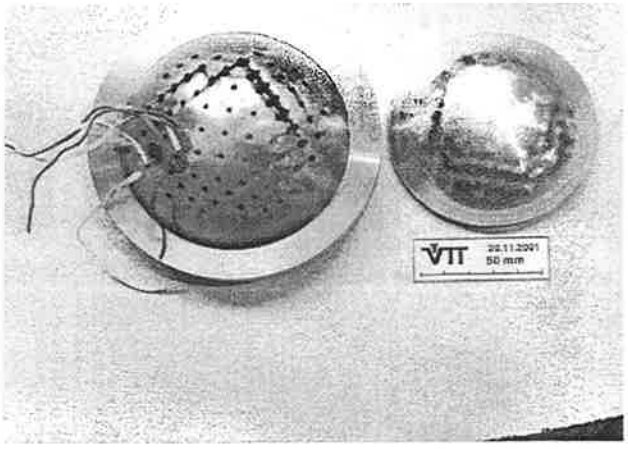

Fig. 8. Specimen EZ1 (small size) after testing, shown with the liner.

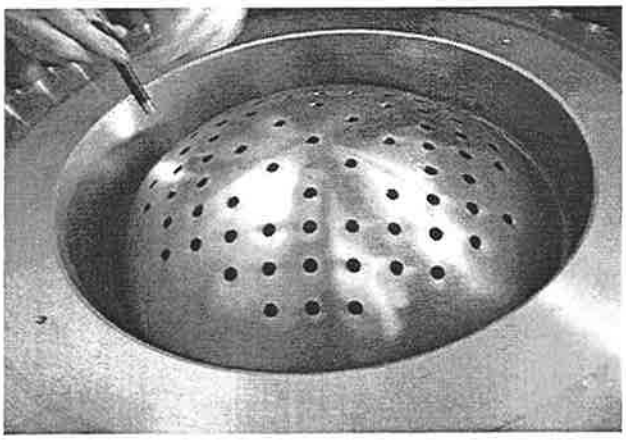

Fig. 9. Specimen FB after testing. The test ended due to the failure of the liner.

3.3 Local results

Thickness values were measured after the tests for the specimens without holes. The specimens with holes were sent for measurements to FzK. One of the small specimens without holes (ET1) had already been delivered to FzK. The measurements were actually performed for only two specimens.

The measured smallest thickness s_f of specimen EU1 was 2.0 mm and that of specimen EW was 10.4 mm. According to the method presented by Krieg and Dolensky [5], knowing the linear strain in the thickness direction, $\varepsilon_s = -(s - s_f)/s$, the linear in-plane strain is first calculated assuming zero volume change. Based on reference strain calculated from the linear strains in thickness and in-plane directions, Krieg and Dolensky [5] end up to define the true equivalent strain $\varepsilon_{e,true}$ at failure as

$$\varepsilon_{e,true} = \ln\left(1 + \frac{2}{3}\left|\sqrt{\frac{1}{1+\varepsilon_s}} - (1+\varepsilon_s)\right|\right). \qquad (1)$$

According to Eq. 1, the values of failure strains are 56.3 % and 58.1 % for the larger and smaller specimens, respectively. These values are practically identical. Other reasons why no conclusions concerning the size effect can be drawn based on these results are the small number of measurements and the rather limited accuracy of thickness measurement.

Failure strain calculation for tests with holes would require a method considering the strain concentration due to the holes.

4. COMPARISON OF NUMERICAL AND EXPERIMENTAL RESULTS

Figure 10 shows a comparison of the results of the computations, which were aimed for planning of the experimental setup, to the measured ones for the specimens without holes. As the computed results were produced using a classical elastic-plastic material model without considering the softening effect due to damage, they reproduce only the ascending part of the load path. For this part the experimental results are predicted very well with both computations and the estimated maximum pressure is within 1% agreement with the experimental result.

The results of the pressure vessel head models have been used as a benchmark in the work package "Sample calculations for selected severe accident loads" of LISSAC. The tests using specimens without holes have been simulated by NRG, MPA and VTT. NRG has performed analyses with a non-local Gurson model and MPA with the Rousselier model. The results of the benchmark will be published later.

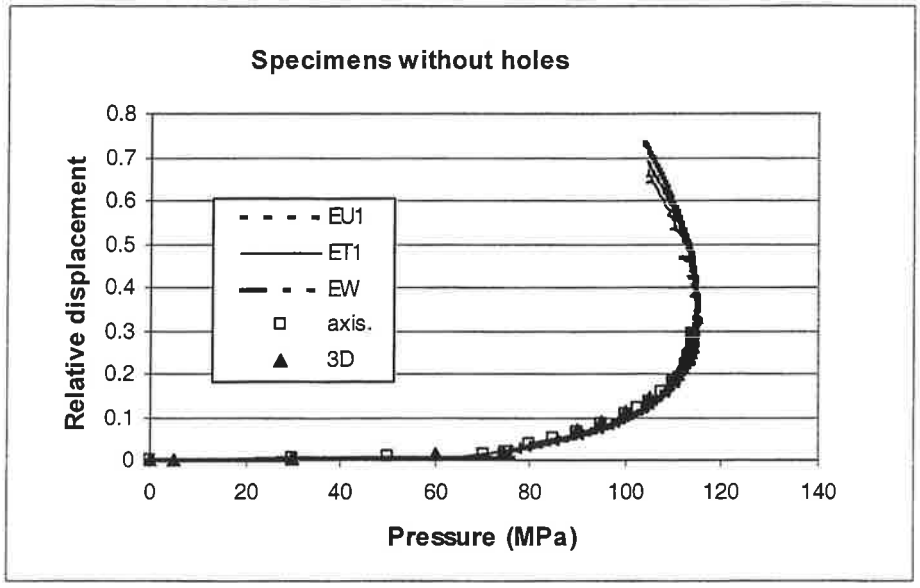

Fig. 10. Comparison of axisymmetric and three-dimensional FE results with the experimental ones for the specimens without holes.

5. COMPARISON WITH OTHER TEST RESULTS

The whole test matrix of the LISSAC project comprised tests with

- flat specimens with central holes of two sizes,
- flat specimens with slots,
- flat specimens with notches,
- circular specimens with notches,
- bending specimens with notches (wide and narrow),
- biaxial tests with shell models (RPV head models) and
- biaxial tests with flat specimens [6].

In Figure 11 all failure strain values, obtained from static tests at room temperature using the methodology presented in [6], are compared to each other. Values of local failure strain are presented as a function of the radius of the hole or notch. VTT's results are marked as biaxial tests. Similar plots were produced also for dynamic tests and tests at elevated temperatures.

The results showed a size dependence of failure strains as a function of notch radius. As the final result of the project it was proposed that up to temperatures of 400°C a failure strain value of 20% can be applied [6].

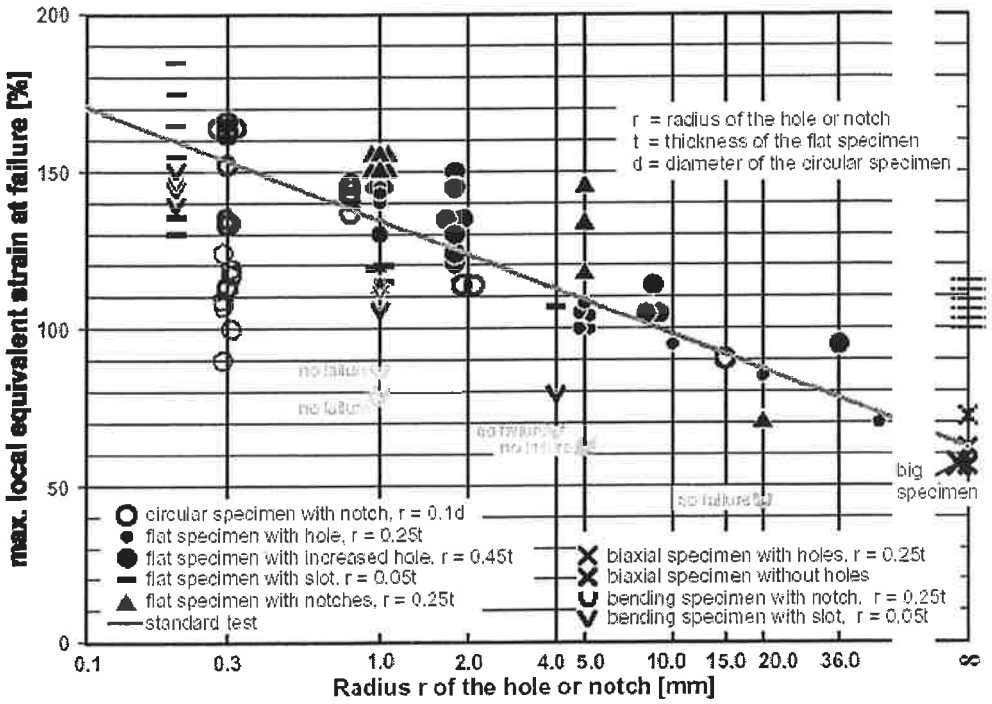

Fig. 11. Compilation of main LISSAC results, static tests at room temperature [6].

SUMMARY AND CONCLUSIONS

In the auspices of the LISSAC project reactor pressure vessel head models from actual reactor pressure vessel material were tested up to rupture using internal pressure loading. The tests form a part of an extensive experimental programme where the stress state and size dependence of ultimate failure strains is studied.

At VTT specimens of two sizes were tested. The small specimens had an inside diameter of about 90 mm. The dimensions of the large specimens were scaled by a factor of 5. Half of the specimens contained a pattern of equiaxial holes describing the control rod penetrations. They were tested using an aluminium liner for tightening.

For the eight performed tests, interruptions or repetitions were unnecessary. Seven tests succeeded completely as planned. The maximum pressures varied between 1080 and 1250 bar. Although pressure loading is to be considered as a load controlled type loading, the tests ended only markedly after the maximum pressure, as it was not possible to maintain the pressure level when the specimen started to yield rapidly. The test with the large specimen with holes, however, ended prematurely before reaching the maximum pressure due to the failure of the liner. All other tests succeeded as planned and the test results were very well reproducible. Consolidation of test data was successful assuming different behaviours of large and small liners of the tests with holes. These differences were traced back mainly to geometrical differences of the two different liner sizes associated with the 0-ring seal grooves used.

Compared to the results of other project partners, obtained using different specimen types, the experimental results presented here are in good agreement. Our results have also been used as a benchmark in the work package "Sample calculations for selected severe accident loads" of LISSAC. The tests using specimens without holes have been simulated by NRG, MPA. Framamtome and VTT. The results of the benchmark will be published later.

REFERENCES

1. Talja, H., Pankakoski, P., Hosio, E., Rahka, K. and Keinänen, H., Results of the LISSAC pressure vessel head model specimen tests. Research report TUO72-021094. VTT Industrial Systems, Espoo, 2003.

2. Keinänen, H. and Talja, H., Estimation of the limit load and strength of the LISSAC pressure test specimen. Research report VAL64-023620. VTT Industrial Systems, Espoo, 2002.

3. Abaqus 5.8. Hibbitt, Karlsson & Sorensen, Inc. 1998. Pawtucket, RI, USA.

4. LISSAC theoretical task group. Definition of stress strain law. Document: L_MPA_M01a.doc

5. Krieg, R. & Dolensky, B. 2002. Methods to determine the local failure strains for the broken LISSAC specimens. LISSAC project report SAM-LISSAC-D025.

6. Krieg, R. 2003. Limit Strains for Severe Accident Conditions (LISSAC). Contract N° FIKS-CT1999-00012 Draft of final report 7.4.2003. 199 p.

RISK AND LIFETIME ANALYSIS METHODS FOR STRUCTURAL SYSTEMS AND COMPONENTS OF POWER PLANTS

OTSO CRONVALL
VTT Industrial Systems
Espoo, P.O.Box 1704, FIN-02044 VTT, Finland

ABSTRACT

Lifetime analyses of structural systems and components of power plants necessitate a thorough knowledge of structural properties, loads, the relevant ageing mechanisms and prevailing environmental conditions. Due to distributed nature of many of these properties or phenomena, probabilistic modelling methods are deemed suitable for the lifetime analyses. System or component failure probabilities combined with knowledge of failure consequences make it possible to perform a risk analysis. This presentation is based on a public VTT research report "Risk and lifetime analysis methods for structural systems and components of power plants" /1/ the making of which was financed by VTT Industrial Systems.

1. INTRODUCTION TO PROBABILISTIC AND RISK ANALYSIS METHODS

There exists a number of methods to determine the probabilities of the variable(s) of interest of a system. Monte Carlo simulation (MCS) is a simple and most accurate procedure to analyse probability distributions. Due to MCS being often rather costly and laborious to perform, approximation methods for the calculation of variable probabilities are of great interest. Examples of these methods are:

- First Order Second Moment (FORM) – first order approximation of the failure surface at the most probable point (MPP),
- Second Order Reliability Method (SORM) – second order approximation of the failure surface,
- Fast Probability Integration (FPI) method – a numerically enhanced SORM,
- Mean Value method (MV) – first order Taylor expansion of the response function at the mean values,
- Advanced Mean Value method (AMV) – a numerically enhanced MV.

Examples of refined and less laborious MCS methods are:

- Importance sampling – modifying the sampling density function to 'important regions' of the failure space, e.g. response surface methods,
- Stratified sampling – sampling space is divided into subspaces from which the sampling is performed, e.g. Latin hypercube sampling (LHS),
- Directional sampling – sampling along random vectors,

- Adaptive sampling – successive updating of the sampling density function,
- Axis orthogonal simulation – a semi-analytic technique.

Risk analysis is a technique for identifying, characterising, quantifying and evaluating hazards. It is widely used by private and government agencies to support regulatory and resource allocation decisions /2/.

The engineering definition of risk is now accepted as being the product of the likelihood and the consequence of an event /3/. In mathematical terms this simply becomes:

$$\text{Risk} = \text{Probability of failure} \cdot \text{Consequence} \tag{1}$$

Risk analysis, or rather risk assessment, consists of two distinct phases /2/:

- A qualitative step of identifying, characterising and ranking hazards.
- A qualitative step of risk evaluation, which includes estimating the likelihood and consequences of hazard occurrence.

The risk analysis approaches can be divided to the following two categories /4/:

- Qualitative
- Quantitative

Qualitative risk analysis is based primarily on engineering judgements. The likelihood and consequences of failure are expressed descriptively and in relative terms. Risks within a qualitative approach are usually presented within in a risk matrix as combinations of the likelihood and consequences. In a quantitative risk analysis, the likelihood and consequences of equipment failure are determined for each accident scenario from the underlying distributions of the variables using reliability analysis methods. The consequences of each accident scenario are analysed in detail, and probabilistic risk assessments are used to determine the probabilities of various consequences on a global scale /4/.

In the following is a list of the risk analysis methods that are commonly applied in the structural reliability/ safety examinations:

- Failure Mode and Effect Analysis (FMEA) – prediction, consequence determination and occurrence minimisation of failure events,
- Fault tree analysis – represents with a vertical tree diagram the relationships in a system between a fault and the possible events from which it results,
- Event tree analysis – represents with a horizontal tree diagram the relationships in a system between a fault and the possible consequential events,
- Expert opinion – the motivation for the use of multiple experts is to obtain as much information as possible of the system or component in question.

2. EVALUATION OF THE LIFETIME OF STRUCTURAL SYSTEMS AND COMPONENTS

Ageing in power plants should be managed so as to ensure that the design functions remain available throughout the service life of the plant. From the safety perspective, this implies that ageing degradation of systems, structures and components important to safety remain within acceptable limits, and that procedures

and personnel training remain adapted. Unchecked, ageing degradation has the potential to reduce the safety of operating power plants. Many ageing mechanisms are plant specific.

The objective of component ageing analyses is to identify the degradation mechanisms and the increase in failure occurrences, to assess the remaining lifetime and to find suitable means to prevent or mitigate the effects of ageing. The ageing analyses should be focused on those components that are the most significant from the safety point of view /5/.

Ageing degradation can be observed in a variety of changes in physical properties of metals, concrete and other materials in a power plant. These materials may undergo changes in their dimensions, ductility, fatigue capacity and mechanical or dielectric strength. Ageing degradation results from a variety of ageing mechanisms and physical or chemical processes. Ageing mechanisms act on power plant components due to a challenging environment with high heat and pressure, radiation, reactive chemicals and synergistic effects /6/.

Main degradation mechanisms of components in power plant environments are /7/:

- Fatigue: high cycle, low cycle, thermal
- Corrosion: uniform, local, stress corrosion cracking (intergranular, transgranular, primary water, irradiation assisted), flow accelerated corrosion
- Irradiation embrittlement
- Thermal ageing
- Creep
- Wear
- Environmental effects: freeze-thaw cycling, chemical attack, wetting and drying

Fatigue of materials refers to the changes in properties resulting from the application of cyclic loads. Characteristic of fatigue in metals is strain hardening under reversed loading conditions /8/ as well as nucleation, coalescence and stable growth of crack(s) that ultimately can lead to net section yielding or brittle fracture /9/. One of the most successful applications of the theory of fracture mechanics is in the characterisation of fatigue crack propagation /8/. The procedures for analysing constant amplitude fatigue under small scale yielding conditions are fairly well established, although a number of uncertainties remain. Variable amplitude loading, large scale plasticity and short cracks introduce additional complications that are not yet fully understood /10/. As the effects of thermal loading are in most cases similar to those of mechanical loading, most models for mechanical fatigue are applicable also for the modelling of thermal fatigue.

Probably the most well known fatigue crack growth model is the Paris-Erdogan equation. It is an empirical equation that relates the crack growth rate (per cycle) to the intermediate stress intensity factor range. This equation has the form /11/:

$$\frac{da}{dN} = C \cdot (\Delta K)^m \tag{2}$$

where a is the crack size, N is the number of loading cycles, ΔK is the stress intensity factor range, i.e. K_{max} - K_{min} and C and m are material constants.

Other fatigue models include:

- $S-N$ curves: a method that is used to predict the number of cycles to failure at a single stress level.
- The Palmgren-Miner rule (or Miner's rule): a linear damage accumulation rule used to predict the cycles to failure under variable amplitude loading.
- Several multiaxial fatigue criteria exist also, and they may be categorised into three groups: stress-based, strain-based and energy-based methods.

Stress corrosion cracking (SCC) is a localised non-ductile failure which occurs only under the combination of three factors: tensile stress, aggressive environment and susceptible material. Crack propagation is the favoured action once the stress intensity factor exceeds a critical value, that is mainly determined by the surface energy on the plane crack propagation, and the energy dissipated in the plastic zone ahead of the crack /12/. The following often used equation for SCC in the intermediate ΔK region is mathematically similar to the Paris-Erdogan fatigue crack growth model /13/:

$$\frac{da}{dt} = C \cdot K_I^n \tag{3}$$

where t is time, K_I is the type I stress intensity factor at the crack tip, C is a constant and n is an exponent characterising the material, environment, temperature, etc.

Also for SCC several other models exist. Some of them contain many variables, and some are as simple as equation (3). A drawback of most SCC models is that they are material and conditions specific, due to which they have a narrow range of applicability. The physical mechanism of SCC is not yet fully understood, so the research and consequent model developing continues.

The material changes in metals caused by neutron irradiation are connected to the fracture resistance of materials. As a rule, irradiation reduces the fracture toughness of the materials and therefore it is important to know the rate of reduction as a function of irradiation dose. The drop in fracture toughness values can be calculated with equations in Appendix A of ASME XI /14/. These equations are a function of the drop in nil-ductility temperature RT_{NDT} of the material, which can be calculated according to a commonly used model by U.S. Nuclear Regulatory Commission (NRC), which is given in reference /15/.

Flow accelerated corrosion (FAC), also called corrosion/ erosion mechanism, refers to the combined action of erosion (i.e. the mechanical action of a fluid on a metal surface) and corrosion. The severity of erosion vary with the material type, the fluid temperature, the fluid velocity, the oxygen content in the fluid and the component geometry. Carbon and low-alloy steels are susceptible to FAC /7/. The three most used FAC models are KWU-KR model /16,17/, EPRI-CH model /18/ and the model in the BRT-Cicero code (by Electricité de France).

Thermal ageing refers to gradual and progressive changes in the microstructure and properties of a material exposed at an elevated temperature for an extended period of time. Cast austenitic-ferritic stainless steels (duplex structures) and martensitic stainless steels are susceptible to thermal ageing in the normal operating temperatures near 300 °C /7/.

During the growth of a macroscopic crack at high temperatures, all types of creep response can occur simultaneously in the most general case. When the crack grows with time, the behaviour of the structure depends on the crack growth rate relative to the creep rate. In brittle materials, the crack growth rate is so fast

that it overtakes the creep zone, and the crack growth can be characterised by K_I because the creep zone at the tip of the growing crack remains small. At the other extreme, if the crack growth is sufficiently slow for the creep zone to spread throughout the structure, C^* integral is the appropriate characterising parameter. The C^* integral is defined by replacing strains with strain rates, and displacements with displacement rates in the J contour integral /10/.

Some models have been proposed to account for the joint action of several ageing mechanisms. This is a relatively new approach, and so still in a developing state. Two widely known approaches to model the combined action of fatigue and SCC crack growth under constant amplitude loading are the superposition and the process competition models. Although mechanistically too simple, these models can be useful for interpolative estimates of crack growth, thereby overcoming to some extent the limitations of the test data. The superposition model proposes that the overall crack growth rate is the sum of a component of the fatigue crack growth and a component due to SCC. On the other hand, the process competition model assumes that fatigue and SCC are mutually competitive and that the crack will grow at the fastest available rate, whether that is the fatigue crack growth rate or the crack growth per cycle owing to stress corrosion /19/.

Time dependent probabilistic models can be used to identify possible trends and to predict the future behaviour of a component. Different probabilistic approaches to model ageing phenomena are used depending on the rate of the functional degradation of a component.

The time dependence in failure occurrence can be expressed with the failure rate $\lambda(t)$, defined as the probability of failure given the component has been in operation for a certain time /12,20/:

$$\lambda(t) = \frac{f(t)}{R(t)} \tag{4}$$

where $f(t)$ is the probability density function of component failure. The failure rate is also called the hazard rate /12/. The reliability of the component at time t can be defined in the following way /12,20/:

$$R(t) = \exp\left[-\int_0^t \lambda(\tau) d\tau \right] \tag{5}$$

If the probability of a failure within a short time interval $(t,\ t + \Delta t)$ is independent of the age of the component, t, the failure times are exponentially distributed and the failure occurrence is independent of time. In this case the failure rate is constant. When the failure rate is increasing, it is said that component is ageing. Several distributions commonly used in reliability engineering are suitable to describe events with an increasing failure rate. These include Weibull, gamma and log-normal distributions. There exists several probabilistic component ageing models for both time independent and time dependent ageing.

3. PROBABILISTIC FRACTURE MECHANICS (PFM)

PFM is strongly based on deterministic fracture mechanics (DFM) procedures, but considers one or more of the input variables to be random instead of having deterministic values /21/. The advantages of PFM include the removal of unrealistic and conservative assmuptions included in deterministic analyses, as well as the

possibility of modelling clearly the uncertainties related to the material degradation process, and thus being able to perform sensitivity analyses of the factors affecting this process.

A typical PFM analysis is described in the following. First, one or more parameters or variables are randomised, depending on the characteristics of the employed analysis model. Next, crack growth simulations are performed. Fracture mechanics models employed are based on linear elastic fracture mechanics (LEFM), e.g. Newman-Raju solutions, influence functions and others or on elastic plastic fracture mechanics (EPFM) or on a combination of LEFM and EPFM. Besides, creep crack growth can be simulated based on the non-linear fracture mechanics. During the crack growth simulation, pre- and in-service inspection are considered and failure judgements of failure states, e.g. leak or rupture, are performed. Cumulative failure probabilities are calculated as functions of operation time /22/.

Numerical techniques for generation of failure probabilities from PFM models are generally required for more complex problems. Application of these techniques does not necessarily lead to a large amount of computations or complicating factors, as workable techniques are readily available. Numerical results from the construction of PFM models are produced in a variety of ways. Techniques include: K_I / K_{Ic} (where K_{Ic} is fracture toughness) overlap, variance/ covariance, convolution and MCS.

Most of the applications of PFM to nuclear power plant (NPP) components lead to very low failure probabilities, which have to be determined with sophisticated numerical procedures from rather scarce and incomplete input data. Another problem with PFM procedures is that they are not standardised, due to which any comparison between components that have been analysed with different methods will be questionable /23/.

4. RISK AND AGEING ANALYSIS SOFTWARE

There are many analysis software tools that can be used for system and component risk and ageing analyses. A brief overview of these analysis tools is presented here. A more thorough presentation of various system and component risk and ageing analysis software is given in reference /1/.

In the general analysis applications any failure mode, fracture or other, can be addressed using the appropriate limit states. Validation of such software is usually carried out by benchmark exercises between different programs since it is not feasible to compare results with real failure statistics. The probabilistic analysis approaches of the analysis software vary from FORM and SORM to MCS. Some analysis software are commercially available and some are proprietary, being thus difficult or impossible to purchase.

Component risk and ageing analysis software that are based on PFM include PRAISE, PIFRAP, SRRA, VISA II and OCA-P. Some component analysis software apply a failure assessment diagram (FAD) together with MCS, SORM, etc. Examples of these are ProSINTAP and CALREL. Also general component reliability analysis software exists. Examples of these are STRUREL, NESSUS and RR-PRODIGAL.

System risk and ageing analysis software are usually based on a more general probabilistic analysis approach. Some analysis tools are probabilistic risk/ safety assessment (PRA/ PSA) applications. Examples of these are

SAPHIRE, WinNUPRA, Faultree+ and PSA Professional. Many analysis tools are more general reliability and risk analysis applications. Examples of these are CAFTA, Avsim+, LOGAN Fault and Event Tree Analysis, LOGAN Monte Carlo Simulation, Relex 7.5, Weibull++ 6, CARA - FaultTree and ITEM ToolKit.

It appears that most of the available component analysis tools consider only one or two degradation mechanisms, e.g. PIFRAP considers only SCC and vibration fatigue, and PC-PRAISE considers only fatigue and SCC. This is a drawback, as the number of relevant failure mechanisms is much greater. The author of this study did not find or learn of any such analysis code, that would cover all or most of the relevant degradation mechanisms. This is quite understandable, as a code the scope of which would cover several degradation mechanisms and various different components would be quite large and probably computationally uneconomical.

Probabilistic models that predict rare events cannot be validated by comparing the results to observed failure and degradation data. One way to verify these models to some extent is to benchmark the independently developed models describing the same phenomena against each other /24/. Thus the main sources of difference can be identified, based on which the models can be developed further. Such comparisons have resulted in identification of errors and model improvements.

5. RISK INFORMED IN-SERVICE INSPECTION

Risk informed in-service inspection (RI-ISI) involves the planning of an inspection on the basis of the information obtained from a risk analysis of the equipment. The purpose of the risk analysis is to identify the potential degradation mechanisms and threats to the integrity of the equipment and to assess the consequences and risks of failure. The inspection plan can then target the high risk equipment and be designed to detect potential degradation before fitness-for-service could be threatened /4/.

The number of locations included in the inspection program is often considerably smaller in new RI-ISI programs than in older and more conservative inspection programs. Thus remarkable financial savings can be achieved. Another benefit, which concerns NPPs, is the shorter times which NDT personnel have to work under radiation exposure.

An impending failure and its consequences are not prevented or changed by RI-ISI unless additional mitigating actions are taken. Inspection is an initiator for actions such as the repair or replacement of deteriorating equipment, or a change to the operating conditions. By identifying potential problems, RI-ISI increases the chances that mitigating actions will be taken, and thereby reduces the frequency of failure /4/.

The three main RI-ISI methodologies used in the nuclear industry are the Westinghouse Owners Group (WOG) methodology, the Electric Power Research Institute (EPRI) methodology, and the Optimisation de la Maintenance par la Fiabilité (OMF)-Structures process by Electricité de France (EDF) /25/.

6. APPLICATION OF PROBABILISTIC FAILURE ANALYSIS TO A NPP PIPING SYSTEM

A description of the probabilistic failure analyses performed with program PIFRAP (PIpe FRActure Probability) to an unidentified NPP piping system is presented in the following. PIFRAP is based on PFM

and is developed by DNV (former SAQ Kontroll). The implementation of PFM in PIFRAP code is based on the model described by Nilsson et al. /26/. The analyses were performed with program version 1.0 rev. 10, which was published in 1997.

The values of the material and loading parameters were chosen so that they correspond the conditions that the piping system in question is exposed to for most of the time, which are operational conditions.
The analysed piping system consists of hundreds of circular piping components having various section dimensions. The components are joined by welding in the circumferential direction, and the total number of weldments in the piping system is approximately 500. The total length of the piping system is approximately 400 m. Most piping components run in horizontal or vertical directions, and a minor portion of the piping components runs in oblique directions. The maximum length of a horizontal span, where span means the straight distance between the midpoints of two adjacent supports, is approximately 8.5 m, and the maximum length of a vertical span is approximately 6 m. The average length of a horizontal span is approximately 2.5 m, and the average length of a vertical span is approximately 2.3 m. The pipe diameter and wall thickness varied approximately between 60 - 320 mm and 4 - 18 mm, respectively.

The components of the piping system are made of various metallic materials. The most common material of straight piping components is austenitic stainless steel 376 TP 304, and the most common material of pipe bends is austenitic steel 403 WP 304 W. Material property values for various materials were taken from Section II of the ASME code /27/. In the operational temperature, which is 286 °C, the yield and tensile stresses of both materials are approximately 110 MPa and 400 MPa, respectively.

The loads considered in the analyses are mechanical and thermal. The locations of the piping components examined in the analyses are weldings and heat affected zones (HAZs), as they are more susceptible to various degradation phenomena than the base materials. Due to the choice of examined locations, also the residual stress distribution caused by the welding process must be considered. The mechanical loads are: dead weight of the pipe and of the fluid inside the pipe, which is assumed to be water, internal pressure and residual stress distribution in the weldment. Thermal loading is caused by the fluid inside the pipe.
Under operational conditions the values of internal pressure and temperature of the fluid are 7.0 MPa and 286 °C, respectively. The bending stresses caused by the dead weight of the pipe and fluid were calculated with beam theory. The values of the axial residual stress distribution in the weld centerline and HAZ were taken from the recommendations by Brickstad and Josefson /28/. To some extent conservative value of 55 MPa was used in the analyses for thermal stress.

PIFRAP calculates the yearly probability of fracture for a loaded pipe with circumferential cracks that may propagate due to intergranular stress corrosion cracking (IGSCC) or IGSCC in combination with high cycle fatigue, water hammer loads, seismic loads, etc. With fracture is meant a complete break due to *J*-controlled fracture or plastic collapse. The value of the *J*-integral is calculated according to R6 procedure. Account is taken to the probability that the crack remains undetected during successive inspections. If the crack penetrates the pipe wall, account is taken to the probability that the leaking crack will be undetected by leak rate detection. The theory and procedure behind PIFRAP are given in reference /29/. The parameters assumed to be random in the PIFRAP procedure are the following:

- the initial length of the crack (the distribution parameters of which are estimated from the Swedish experience),
- leak rate (when calculating the probability of leak detection)

Other parameters in the PIFRAP procedure, such as the crack growth law and its parameters, are assumed to be deterministic.

In the performed PIFRAP analyses the only considered load case was operational conditions, and the only considered degradation mechanism was IGSCC.

The crack growth law used in PIFRAP is the following:

$$\frac{da}{dt} = C_0 \cdot (K_I - C_1)^n \tag{6}$$

where parameter C_1 [MPa·√m] is a treshold value for IGSCC to occur.

In order to be on the safe side, the fracture toughness properties used in the analyses were that of the weld material, and the rest of the material properties used were that of the base material. The authors of the program use the same approach in reference /28/.

The number and locations of the analysed piping sections were chosen so, that they cover the whole of the piping system. To see the range of variation in the failure probabilities, the analysed piping sections cover also the whole range of loading conditions, from the most loaded to the least loaded sections. The total number of examined piping sections was 57.

To observe the effect of changing some parameter values in the model response, the quality of NDT team performance and inspection interval were varied in the analyses. The quality categories of NDT in PIFRAP are Poor, Good and Advanced. The analysis results of the case where there is no inspection are presented for the first time here, other results are taken from reference /1/. In the following is a presentation of the analysis results, together with a short discussion.

The results from PIFRAP analyses show that the pipe sections having the highest stresses have also the biggest failure probabilities, which was expected. The resulting failure probabilities are not very dependent of the pipe diameter but are, on the other hand, quite dependent of the wall thickness. The stress component causing the highest stresses for the examined weld sections is the axial residual weld stresses, which were here taken from /28/. The magnitude of these stresses is generally such, that the bigger the wall thickness, the lower the residual stresses. This also shows in the analysis results, as the weld sections with bigger wall thickness have generally smaller failure probabilities than the sections with smaller wall thickness. The stress component causing the second highest stresses is the bending stresses due to restricted thermal expansion.

The values of the resulting pipe failure probabilities vary from 0.5E-23 to 0.3E-4. The weld section having the smallest failure probability values, has also the biggest wall thickness of the whole piping system. The weld section having the highest failure probability values, has also the smallest wall thickness of the whole piping system, and thereby the highest weld residual stresses. However, these two weld sections are quite exceptional in the piping system, as the failure probability values of all other weld sections vary between 1.0E-16 - 1.0E-6. The mean value of all failure probabilities of all examined weld sections is 1.6E-7. All weld sections but one fulfill the requirements for yearly failure probabilities defined by The Finnish Radiation and Nuclear Safety Authority (STUK) in reference /30/ .

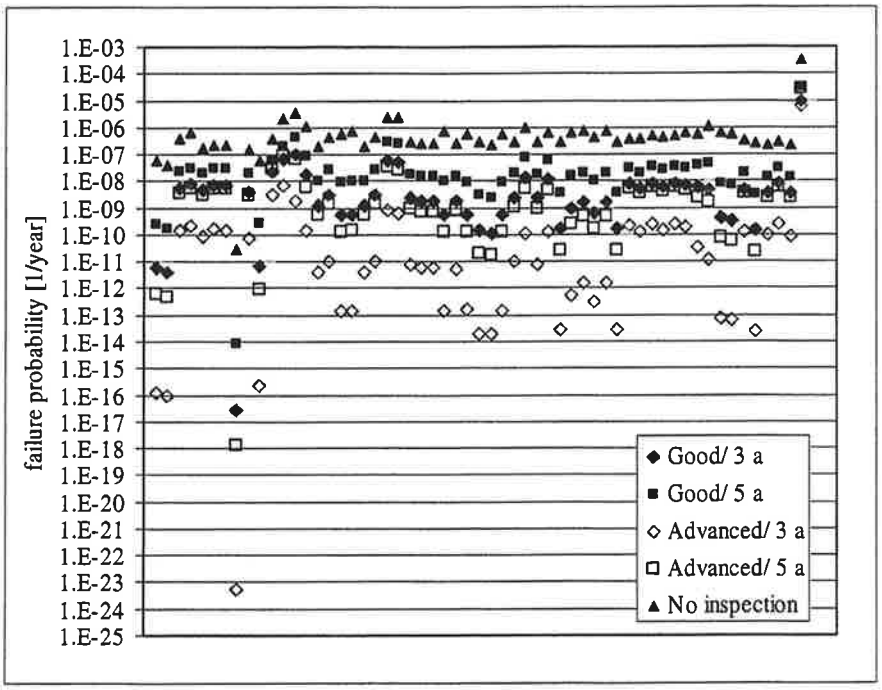

Figure 1 The failure probability values from PIFRAP analyses performed to all examined piping weld sections.

Table 1 Some characteristic failure probability values from PIFRAP analyses performed to all piping weld sections.

Inspection quality	Inspection interval [years]	Failure probability [1/year]			
		Mean value	Standard deviation	Maximum value	Minimum value
Good	3	1.730E-07	1.242E-06	9.383E-06	2.912E-17
Good	5	6.036E-07	4.251E-06	3.213E-05	9.053E-15
Advanced	3	1.047E-07	7.885E-07	5.953E-06	5.377E-24
Advanced	5	4.588E-07	3.417E-06	2.580E-05	1.379E-18
No inspection		6.654E-06	4.576E-05	3.460E-04	2.914E-11
All cases		1.599E-06	2.063E-05	3.460E-04	5.377E-24

The effect of varying the values of inspection quality and inspection interval parameters also shows in the analysis results. The mean value of the relative differences in the failure probabilities per weld varies between 1.9E+01 - 2.6E+5. However, when exluding the maximum value, which differed considerably from the rest of the values, the relative differences varied between 1.9E+1 - 5.0E+3. The differences in the scatter

of the failure probability results per weld are caused by a number factors. The lower the stresses and/ or the bigger the pipe dimensions, the slower the crack grows. For such cracks it takes a longer time to propagate through the pipe wall, and thus more inspections are made during that time span, which naturally results in smaller failure probabilities. The longer the crack stays small, the more inspections are probably needed before the crack is detected, however, which extends the scatter of the failure probabilities per weld.

The presented results from PIFRAP analyses are supposed to be conservative, due to the assumptions made concerning input data. As or more significant than looking at single pipe failure probability values, is to compare these values to each other. This viewpoint also serves the needs of RI-ISI. The formation of component groups according to risk level in RI-ISI is preceded by formation of component groups according to failure probability and failure consequences.

Due to assumptions concerning the analysis procedure and input data, the PIFRAP analysis results presented here are to some extent suggestive.

7. SUMMARY

Risk and lifetime analyses of structural systems and components of power plants are discussed in this presentation. Various relevant component degradation mechanisms together with their common modelling approaches are presented. Then, a selection of system and component risk and lifetime analysis tools is presented. Also, brief overviews of PFM and RI-ISI are given. Finally a description is given of the failure probability analyses performed to an unidentified NPP piping system with analysis program PIFRAP, which is based on PFM. All analysed weld sections but one fulfill the requirements for yearly failure probabilities defined by STUK.

References

1 Cronvall, O. Risk and lifetime analysis methods for structural systems and components of power plants. Technical Research Centre of Finland (VTT), Research Group Structural Integrity, Research Report TUO72-032000. 246 p.

2 Modarres, M. What Every Engineer Should Know about Reliability and Risk Analysis. Marcel Dekker Inc. New York, 1993. 351 p.

3 Chapman, O., J., V. Risk-informed approaches. Integrity of Pressurised Components of Nuclear Power Plants, EUROCOURSE 2001. 17 to 21 September 2001, MPA-Stuttgart. 19 p.

4 HSE Health & Safety Executive. Best practice for risk based inspection as a part of plant integrity management. Prepared by TWI and Royal & SunAlliance Engineering for the Health and Safety Executive. CONTRACT RESEARCH REPORT 363/2001. 122+57 p.

5 Methodology for the Management of Ageing of Nuclear Power Plant Components Important to Safety. International Atomic Energy Agency (IAEA), Technical Reports Series No. 338. Vienna, 1992. 62 p.

6 U.S. Congress, Office of Technology Assessment, Aging Nuclear Power Plants: Managing Plant Life and Decommissioning, OTA-E-575 (Washington, DC: U.S. Government Printing Office, September 1993).

7 European Commission. Nuclear Safety and Environment. Safe Management of NPP Ageing in the European Union, Final Report, 2001. 363 p.
8 Suresh, S. Fatigue of materials. Cambridge University Press, England, 1991. 586 p.
9 Socie, D., Marquis, G. Multiaxial Fatigue. Society of Automotive Engineers (SAE), Inc. Warrendale, U.S.A., 1998.
10 Anderson, T., L. Fracture Mechanics, Fundamentals and Applications. CRC Press, January 1994. 688 p.
11 Paris, P., C., Erdogan, F. A Critical Analysis of Crack Propagation Laws. Journal of Basic Engineering, Vol. 85, 1960, pp. 528-534.
12 Sanzo, D. et al. Survey and Evaluation of Aging Risk Assessment Methods and Applications, NUREG/CR-6157. U.S. Nuclear Regulatory Commission, Washington D.C., 1994. 159 p.
13 Congleton, J., Craig, I., H. "Corrosion Fatigue" in Corrosion Processes, Parkins, R., N., Ed., Applied Science Publishers, 1982.
14 Section XI, ASME Boiler and Pressure Vessel Code. American Society of Mechanical Engineers, New York, 2001.
15 Regulatory Guide 1.99, Radiation Embrittlement of Reactor Vessel Materials, Revision 2. U.S. Nuclear Regulatory Commission, Washington, 1988.
16 Kastner, W., Riedle, E.. Empirical Model for Calculation of Material Losses Due to Corrosion Erosion. VGB Kraftwerkstechnik 66, No. 12, 1986. pp. 1023-1029.
17 Kastner, W. Erosion-Corrosion Experiments and Calculation Model. EPRI Workshop on Erosion-Corrosion of Carbon Steel Piping: Nuclear and Fossil Plants, April 14-15, 1987.
18 Chexal, B., J. S. Horowitz, R. Jones, B. Dooley, C. Wood. Flow-Accelerated Corrosion in Power Plants. EPRI TR-106611, Electric Power Research Institute. Palo Alto, 1996.
19 Wanhill, R., J., H. Fracture Control Guidelines for Stress Corrosion Cracking of High Strength Alloys. NRL Technical Publication, TP 91006 L, 1991. 80 p.
20 Simola, K. Probabilistic methods in nuclear power plant component ageing analysis. VTT Publications 94, VTT Technical Research Centre of Finland, Finland, 1992. 82 p.
21 Besuner, P., M., Probabilistic fracture mechanics. In: Provan, J.W. (ed.). Probabilistic Fracture Mechanics and Reliability. 1987, Martinus Hijhoff Publishers. pp. 387-436.
22 Yagawa, G., Yoshimura, S. A study on probabilistic fracture mechanics for nuclear pressure vessels and piping. International Journal of Pressure Vessels & Piping, Vol. 73(1997), pp. 97-107.
23 Nilsson, F. et al. Probabilistic Safety Analysis versus Probabilistic Fracture Mechanics -Relation and Necessary Merging. Seminar Proceedings, SKI report 97:26. Swedish Nuclear Power Inspectorate (SKI), Sweden, 1997.
24 Simola, K., Sarkimo, M. Review of models for quantification of pipe degradation probabilities for RI-ISI applications. VTT Report TAU A013, VTT Technological Research Centre of Finland, Finland, 2001. 28 p.
25 Codron, P. - RIBA PROJECT - Risk-Informed Approach for In-Service Inspection of Nuclear Power Plant Components. Task 1: Final report. European Commission, DG TREN - Energy and Transport, 2001. 53 p.
26 Nilsson, F. et al. Failure probability of nuclear piping due to IGSCC. International Journal of Pressure Vessels and Piping, 43(1990)205-219.
27 ASME Boiler and Pressure Vessel Code, Section II. 2001.
28 Brickstad, B., Josefson, B. A parametric study of residual stresses in multi-pass butt-weld stainless steel pipes. International journal of Pressure Vessels and Piping, 75(1998)11-25.
29 Bergman, M. et al. A procedure for estimation of pipe break probabilities due to IGSCC. SAQ/FoU-Report 97/06, SAQ Kontroll AB, Stockholm, Sweden, 1997.
30 Probabilistic Safety Analyses. YVL Guide 2.8. Radiation and Nuclear Safety Authority (STUK), 1996. The document was obtained at 28.4.2003 from http://www.stuk.fi/saannosto/YVL2-8e.html.

FROM STRAIGHT ARCHES TO SEGMENTAL BEAMS

A. MIETTINEN, H. PARLAND
Laboratory of Structural Mechanics
Tampere University of Technology
P.O. Box 600
33101 TAMPERE FINLAND

ABSTRACT

Since the middle ages straight arches of inclined voussoirs were frequently used over apertures of masonry walls. The stability of the structure was then determined by a statical analysis of a rigid body assemblage of voussoirs. The development of the theory of bending and compression of beams in the 1820:th introduced the elasticity into the structural design. Based on these two approaches, including a contact mechanical analysis of the joints between the blocks, a unified theory of mechanics of segmental beams is developed. Assuming that the joints of the beam don't transfer tensile stresses the state of deformation of the segmental beam can be separated into two components: a) that of the monolithic elastic beam (without joints) and b) that of a sequence of rigid blocks, which at the joints experience mutual translations, rotations and partial interpenetrations. An elastic analysis of the strains of the monolithic beam and the discontinuities between adjacent blocks provides then their linear dependences on the governing quantities: the normal stress $N(x)$, the moment $M(x)$, the shear force $Q(x)$ and their values at the joints, respectively. The theory provides a rational base for the dimensioning of structures composed of segments, from voussoir arches to prestressed columns and bridge systems of prefabricated units.

INTRODUCTION

The paper presents an extension of the classical theory of bending and compression of beams developed in the 1820th by Navier. This extension goes back to an earlier development of structural mechanics, the mechanics of rigid body assemblages. Starting from the 17th century (Derand 1643; La Hire 1679) this theory, applied to arches and vaults, was further developed during the 18th century (Poleni 1748; Coulomb 1713) and brought to its perfection in the 19th century (Culmann 1866; Cremona 1872). The theory of voussoir arches and corresponding domes was purely geometric and its development was closely connected with that of the projective geometry (Desargue 1669; La Hire 1727) . A late intermediate link provided the elastic nontension theory of reinforced concrete beams about 1860-70 and, finally, the mechanics of elastic contact initiated by Hertz (1881).

The purpose of this paper is to present a case study how the two directions, the geometrical one of rigid body assemblages and that of classical elasticity are united into a synthesis.

THE NONMONOLITHIC ELASTIC BEAM

We consider an elastic cylindrical beam divided by cross-sectional joints into segments. The dimensions of the beam are: length L, cross section A with centroid axis x, symmetry axis z and corresponding second moment I_z , respectively. The external load p* acting in the xz-plane induce normal forces N(x), shear forces and moments $M_y(x)$ defined by the cross sectional stresses σ_x, τ_{xy}, τ_{xz}, respectively (Fig. 1)

$$N(x) = \int_{A(x)} \sigma_x dA\,; \quad Q_z(x) = \int_{A(x)} \tau_{xz} dA; \quad M_y(x) = \int_{A(x)} \sigma_x z dA \tag{1}$$

At the cross sections $A_v(x_v)$ of the dry joints, the stress vectors $\mathbf{p}_{v-1,v}(y,z) = \sigma_x\,\mathbf{i} + \tau_{xy}\,\mathbf{j} + \tau_{xz}\,\mathbf{k} = -\mathbf{p}_{v,v-1}(y,z)$ are subjected to the constraint

$$\sigma_X \le 0; \sqrt{\tau_{xz}^2 + \tau_{xy}^2} \le f|\sigma_x| \qquad \text{(f coefficient of friction)} \tag{2}$$

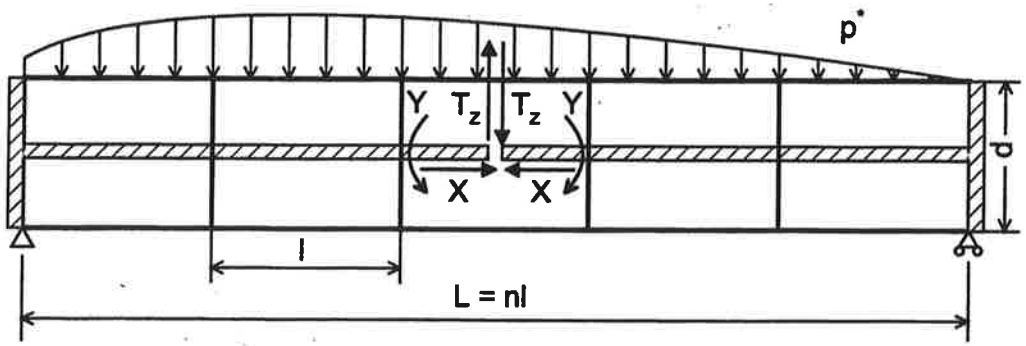

Figure 1. Segmental beam, loading and redundants.

The cross sections $A_v(x_v)$ divide the beam into segments (1)...(ν).... Within each segment (ν) there applies for the displacements $\{u_i\}$, the strains $\{\varepsilon_{ij}\}$ and the stresses $\{\sigma_{ij}\}$ the rules of linear elasticity

$$\varepsilon_{ik} = \frac{1}{2}\left(\frac{\partial u_i}{\partial x_k} + \frac{\partial u_k}{\partial x_i}\right); \quad \varepsilon_{ik}(\sigma) = \frac{1+\nu}{E}\left(\sigma_{ik} - \frac{\nu}{1+\nu}\sigma_a \delta_{ik}\right); \quad \frac{\partial \sigma_{ij}}{\partial x_i} = -p_j \tag{3a,b,c}$$

where $\delta_{ij} = 1$ if $i = j$; $\delta_{ij} = 0$ if $i \neq j$, and $\sigma_a = \sigma_x + \sigma_y + \sigma_z$. To these conditions must be added the equilibrium condition on the external surface Γ_e

$$p_i(x,s) = \sigma_{ij}\cos(n,j);\ i,j = x,y,z \tag{4}$$

At the joint A_v between segments (v-1) and (v) there occurs a discontinuity $[\mathbf{u}(x_v,y,z)]$ of the displacements across A_v that defines the gap vector $\boldsymbol{\gamma}$ (Fig. 4a)

$$[\mathbf{u}(x_v,y,z)] = \mathbf{u}_v(x_v,y,z) - \mathbf{u}_{v-1}(x_v,y,z) = \boldsymbol{\gamma}_{v,v-1}(y,z) \tag{5}$$

where $\boldsymbol{\gamma} = \gamma_x \mathbf{i} + \gamma_y \mathbf{j} + \gamma_z \mathbf{k}$. Here γ_x defines the dilatation of the gap. This is subjected to the impenetrability condition if in the initial unloaded state $\boldsymbol{\gamma} = 0$:

$$\gamma_x(y,z) \geq 0 \tag{6}$$

If $\{u', \varepsilon', \gamma'\}$ is a kinematic state of the cracked beam induced by load p* and $\{p_e'', \sigma_e''\}$ is a solution to a loading $\mathbf{p}_e''$ $\mathbf{p}^*$ of the uncracked beam there applies, because of (4a,b,c) and Green's theorem, the equation of virtual stresses :

$$\int_{\Gamma_e} \mathbf{p}''_e \cdot \mathbf{u}' d\Gamma = \int_V \sigma''_{ij} \varepsilon'_{ij} dV + \sum \int_{A_v} \mathbf{p}'' \cdot \gamma' dA \tag{7}$$

The work of virtual load $\mathbf{p}''_e$ on the displacements $\mathbf{u}'$ of the uncracked solution of the beam equals the sum of the work of the virtual stresses σ''_e on the strains ε' and the corresponding work of virtual stresses $\mathbf{p}''$ on gap deformation $\boldsymbol{\gamma}'$ induced by load $\mathbf{p}^*$.

In order to extract out of the displacement field {u} the effect of the discontinuities caused by the cracks and joints we subject the cracked beam at the endfaces A(-L/2), A(+L/2) to unit force couples N', M_y'', $\{M_y''', Q_z'''\}$. These induce in the uncracked beam the elastic stress fields according to (9) with G = E/(2(1+ν))

$$\begin{aligned} &N'=1 \quad \text{induces} \quad \sigma'_x = \frac{1}{A};\ \varepsilon'_x = \frac{1}{EA};\ \varepsilon'_y = \frac{-\nu}{EA};\ \varepsilon'_z = \frac{-\nu}{EA} \\ &M''_y = 1 \ \text{induces} \quad \sigma''_x = \frac{z}{I_y};\ \varepsilon''_x = \frac{z}{EI_y};\ \varepsilon''_y = \frac{-\nu z}{EI_y};\ \varepsilon''_z = \frac{-\nu z}{EI_y} \end{aligned} \tag{8a}$$

$$\begin{Bmatrix} Q'''_z = 1 \\ M'''_y = Q'''_z L/2 \end{Bmatrix} \quad \text{induces} \quad \begin{Bmatrix} \tau'''_{xz} = \frac{S_y(z)}{b_y I_y};\ \tau'''_{xy} = \frac{2y}{b_y}\frac{\partial b_y}{\partial y}\tau'''_{xz};\ \gamma'''_{xz} = \frac{\tau'''_{xz}}{G};\ \gamma'''_{xy} = \frac{\tau'''_{xy}}{G} \\ \sigma'''_x = \frac{xz}{I_y};\ \varepsilon'''_x = \frac{xz}{EI_y};\ \varepsilon'''_y = \frac{-\nu xz}{EI_y};\ \varepsilon'''_z = \frac{-\nu xz}{EI_y} \end{Bmatrix} \tag{8b}$$

These stresses and strains correspond to a loading by forces N', M_y'', Q_z''' acting at x = 0 on lever arms connected to the endfaces A(-L/2) and A(L/2). The works performed by the unit forces N', M_y'' at x = 0 on the displacements {u} at A(-L/2) and A(L/2) induced by the load p* are according to (7) and (8) and (1)

$$\begin{Bmatrix} 1 \cdot v_x \\ 1 \cdot \omega_y \end{Bmatrix} = \begin{Bmatrix} \int \frac{1}{A}\left(u_x(L/2) - u_x(-L/2)\right) dA \\ \int \frac{z}{I_y}\left(u_x(L/2) - u_x(-L/2)\right) dA \end{Bmatrix} = \begin{Bmatrix} \int_V \sigma'_x \varepsilon_x dV \\ \int_V \sigma''_x \varepsilon_x dV \end{Bmatrix} + \sum_{v+1}^{n} \begin{Bmatrix} \int_A \sigma'_x \gamma_x dA \\ \int_A \sigma''_x \gamma_x dA \end{Bmatrix} \tag{9}$$

According to (1), (8a) and $\varepsilon_x = \frac{1}{E}(\sigma_x - \nu(\sigma_y + \sigma_z))$ we obtain

$$v_x \cong \int_{-L/2}^{+L/2} \frac{N}{EA} dx + \sum \int_A \frac{\gamma_x}{A} dA$$

$$\omega_y \cong \int_{-L/2}^{+L/2} \frac{zM}{EI_y} dx + \sum \int_A \frac{z\gamma}{EI_y} dA$$

where the effect of the Poisson's ratio ν has been neglected ($\nu < 02$). Observing further that the integrals of the second terms of (9) can be expressed by the gap volumes V_{hv} of the gaps at A_v and their centroid coordinates y_{hv} , z_{hv}

$$\int_{A_v} \gamma_x dA = V_{hv} \; ; \; \int_{A_v} y\gamma_x dA = y_{hv} V_{hv} \; ; \; \int_{A_v} z\gamma_x dA = z_{hv} V_{hv} \tag{10}$$

the equation (9) can be written

$$v_x = \int_{-L/2}^{L/2} \frac{N}{EA} dx + \sum_v \frac{V_{hv}}{A_v} \tag{11a}$$

$$\omega_y = \int_{-L/2}^{L/2} \frac{M_y}{EI_y} dx + \sum_v \frac{z_{hv} V_{hv}}{I_{yv}} \tag{11b}$$

Applying the unit forces $Q_z''''=T_z$ we obtain the generalized shear deformations v_z of the beam

$$v_z = \int_{-L/2}^{L/2} \left(\frac{M_y x}{EI_y} + \frac{Q_z}{GA}\xi_z\right) dx + \sum_v \left(\frac{x\, z_h V_h}{I_y} + \bar{\gamma}_z\right)_v \tag{11c}$$

where

$$\bar{\gamma}_z = \int_{z_{min}}^{z_{max}} \frac{S_y}{I_y} \gamma_z \left(1 + \frac{2y}{b} \frac{\partial b_y}{\partial z}\right) dz \tag{11d}$$

and $S_y(z) = \int_z^{zmax} \zeta b(\zeta) d\zeta$ where $b_y(\zeta)$ is the width of the cross-section at ζ

The integrals in (11a, b, c) represent the deformations v_{xe}, v_{ze}, ω_e of the elastic uncracked beam whereas the sums represent the discontinuities of the displacement field of an assemblage of rigid bodies

$$v_{xh} = \int_{A_v} \frac{\gamma \, dA}{A} = \frac{V_h}{A}$$

$$\omega_{yh} = \int_{A_v} \frac{\gamma \, z dA}{I_y} = \frac{z_h V_h}{I_y}$$

$$v_{zh} = \int_{A_v} (\gamma_y \tau'''_{xy} + \gamma_z \tau'''_{xz}) \, dA$$

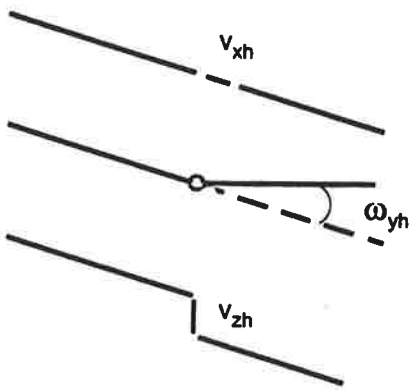

Figure 2. Discontinuities of the displacements of the beam axis.

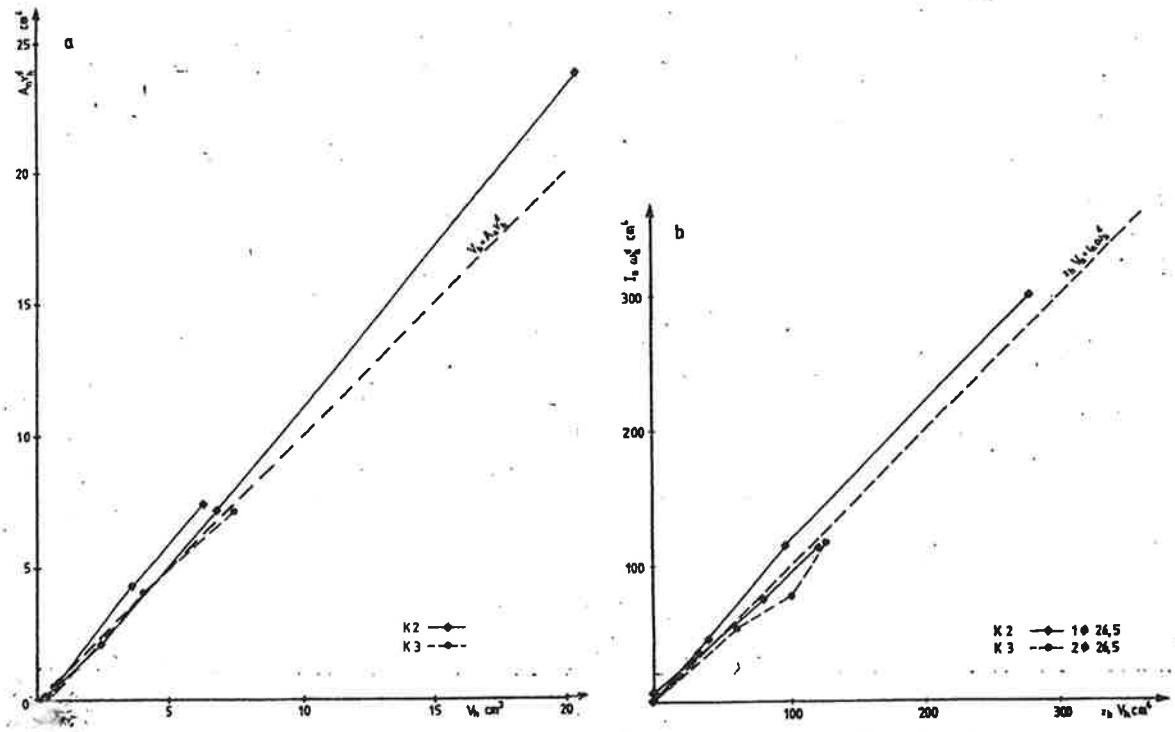

Figure 3. Test of prestressed granite beam with unbonded tendons, net area of section A_n.
a) Measured extension v_h^d of centroid axis versus gap volume V_h.
b) Measured mutual rotation ω_h^d versus gap moment $z_h V_h$.

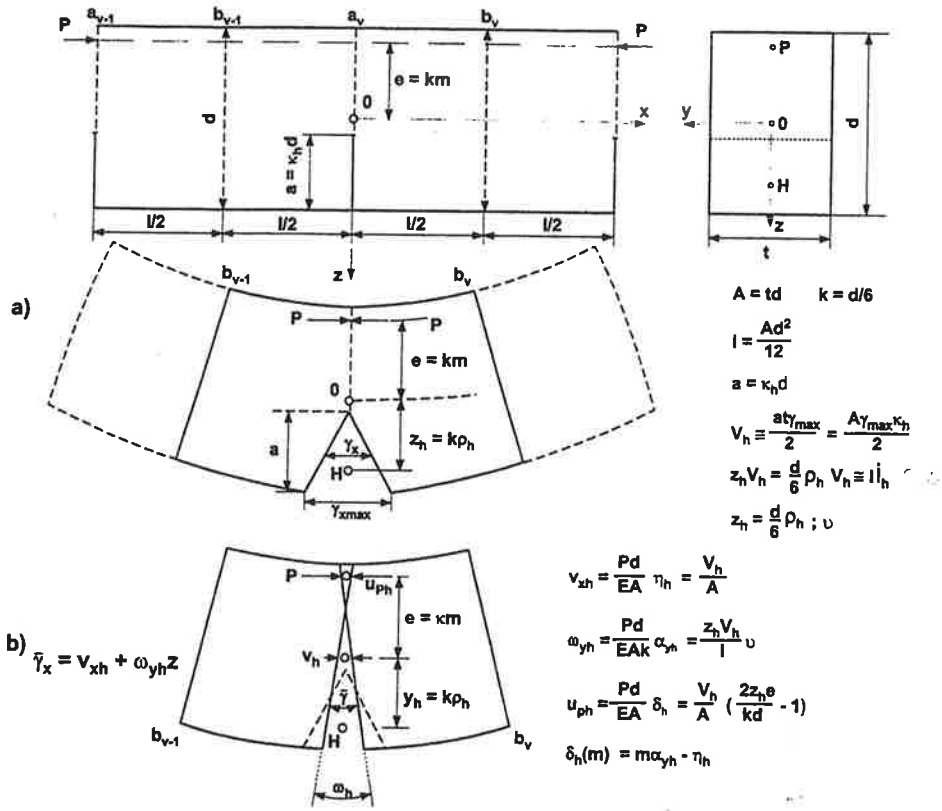

Figure 4. Deformation at dry joint of segmental beam at symmetric loads. a) Actual state of deformation. b) Linearized state of deformation.

elastic monolithic beam	assemblage of rigid bodies	
$v_{xe} = \int_L \frac{N}{EA} dx$	$v_{xh} = \sum_v \left(\frac{V_h}{A} \right)_v \geq 0$	(12a, b)
$\omega_{ye} = \int_L \frac{M_z}{EI_z} dx$	$\omega_{yh} = -\sum_v \left(\frac{y_h V_h}{I_z} \right)_v$	(13a, b)
$v_{ze} = \int_L \left(\frac{M_y x}{EI_y} + \frac{Q_z \xi_z}{GA} \right) dx$	$v_{zh} = \sum_v \left(\frac{x z_h V_h}{I_y} + \bar{\gamma}_z \right)_v$	(14a, b)

The equations (12, 13, 14) express that the generalized mutual longitudinal displacements of the endfaces of the monolithic beam Δu_e as well as those of the corresponding rigid body assemblage Δu_h are linear functions of the cross sectional coordinates (Fig. 4b):

$$\Delta u_{xe} = v_{xe} + \omega_{ye} z \; ; \qquad \Delta u_{ze} = \text{constant} \tag{15a}$$

$$\Delta u_{xh} = v_{xh} + \omega_{yh} z; \qquad \Delta u_{zh} = \text{constant} \tag{15b}$$

At frictional sliding it is generally not possible to achieve a unique solution of stress-displacement problems. But if the joint can be considered as a plane of symmetry then the edge effect of the joint $\{\sigma_h, u_h\}$ can be split into a symmetric part $\{\sigma^s, u^s\}$ and an antisymmetic part $\{\sigma^a, u^a\}$ and these can unambiquously be seperately determined.

We consider an assemblage (Fig. 4b) of two equal half segments $(\nu\text{-}1)$ and (ν) of the beam separated by a joint (ν) that represents a plane of symmetry of the assemblage. The assemblage is at its middle section (a) loaded only by an axial compressive force P with eccentricity $z_p = -\bar{k}_z m_z$. Here $\bar{k}_z$ denotes an average core point distance and m_z denotes the relative eccentricity of P, respectively. The symmetric load P induces then in the assemblage a symmetric field of stress and strain $\{\sigma^s, \varepsilon^s\}$ to which, according to (15-19), correspond the symmetric generalized deformations v_i^s, ω_i^s.

In the uncut segment	In the joint (ν)	
$v_{xe} = -\dfrac{Pl}{EA}$	$v_{xh}^{\nu} = \dfrac{P^{\nu} d}{EA}\eta_h (m_y)^{\nu} = \dfrac{V_h^{\nu}}{A}$	(16a, b)
$\omega_{ye} = \dfrac{M_y l}{EI_y}$	$\omega_{yh}^{\nu} = -\dfrac{P^{\nu} d}{EA\bar{k}_z}\alpha_{zh} (m_y)^{\nu} = \dfrac{z_h^{\nu} V_h^{\nu}}{I_y}$	(17a, b)

whereas v^{ν}_{ze}, v^{ν}_{zh} remain zero because of symmetry of loading.

Equations (17b - 18b) determine the linearized gap deformation (Fig. 1b)

$$\bar{\gamma}_x(z) = v_{xh} + \omega_{yh} z = \frac{Pd}{EA}\left(\eta_h + \alpha_{yh}\frac{z}{k_z}\right) \tag{18}$$

as function of load P. The parameters η_h , α_h determine the interpenetration u_{ph} at z_p where, because of (18)

$$u_{ph} = \frac{Pd}{EA}\delta_h; \qquad \delta_h = \alpha_{yh} m_z - \eta_h \; ; \qquad \frac{\partial \delta_h}{\partial m_z} = 2\alpha_{yh} \tag{19}$$

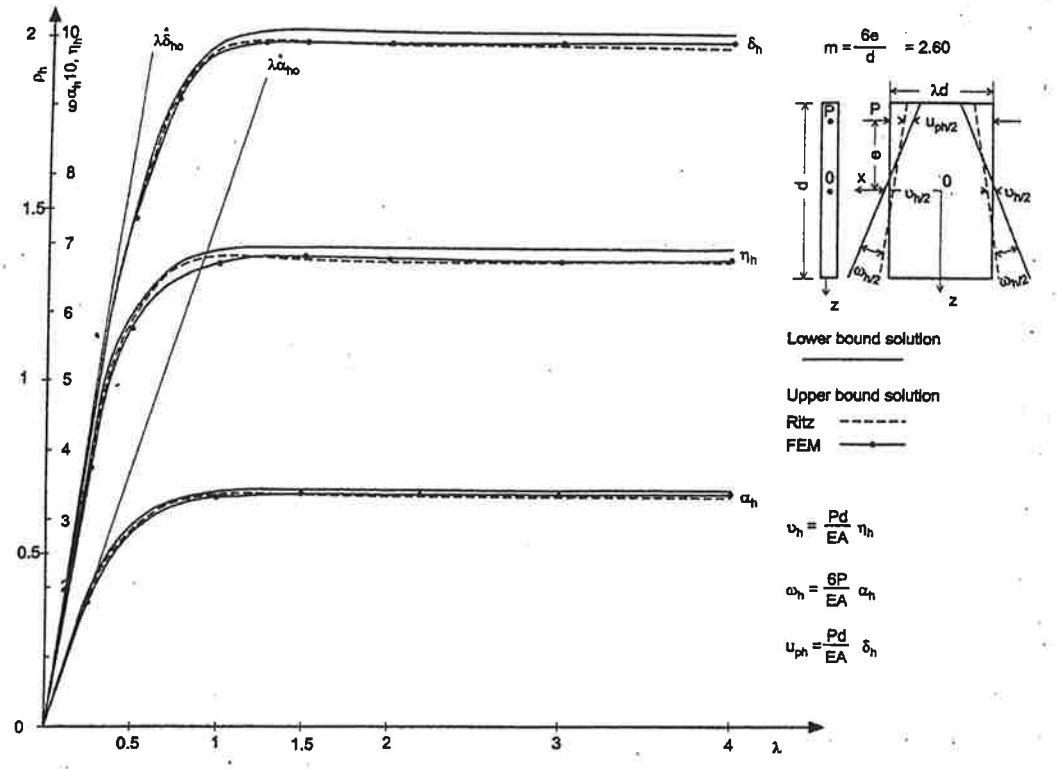

Figure 5. Deformation parameters η_h , α_h , δ_h of segment with rectangular coross-section versus slenderness $\lambda = \frac{l}{d}$

The crack volume V_h and the coordinates y_h , z_h of its centroid are, accordingly

$$V_h = Pd\eta_h/E; \quad z_h = \bar{k}_z \rho_{zh} = \frac{i_y^2}{\bar{k}_z} \frac{\alpha_{yh}}{\eta_h} \tag{20}$$

Closed expressions for the parameters η_h , α_h , δ_h cannot generally be obtained. Their determination is rather complicated with one exception where the compressive stress distribution in the cross section is bilinear. This materializes in a beam with very dense crack spacing $\lambda \to 0$ in accordance with the classical theory of bending of reinforced concrete beams. In this exceptional case the contact problem may be solved by elementary means because the parameters α_{ho} , η_{ho} , δ_{ho} are proportional to the slenderness of the segments

$$\alpha_{yho} = \lambda \dot{\alpha}_{yh}(m_y, m_z); \quad \eta_{ho} = \lambda \dot{\eta}_h(m_y, m_z) \quad ; \quad \delta_{ho} = \lambda \dot{\delta}_h(m_y, m_z) \tag{21a}$$

For a rectangular section the quantities $\dot{\eta}_h, \ldots, \dot{\delta}_h$ are with $m_y = 0$, $m_z = m = -6z_p/d$

$$\dot{\eta}_h = (|m|-1)^2/(3-|m|)^2$$
$$\dot{\alpha}_h = \text{sign}(m)(4-|m|)(|m|-1)^2/(3(3-|m|)^2) \qquad (21b)$$
$$\dot{\delta}_h = (|m|-1)^3/(3(3-|m|))$$

Lower bound solutions for the stiffness of the structure, with upper bounds for δ_h'' , are obtained by Castigliano's minimum principle using Kantorovich's-type stress function expansions for plates. Upper bound solutions, with lower bounds for δ_h' , are obtained by FEM and by Ritz method using the minimum principle of the potential energy (Parland, Heinisuo, Koivula 1982).

The dependence of the parameters η_h , α_h , δ_h on λ appear on Fig. 5. After a linear phase at small λ, according to (21a), there follows a nonlinear phase for intermediate values of λ , and if $\lambda > 1$ the parameters approach asymptotically limit values $\eta_h(m,\infty)$, $\alpha_h(m,\infty)$ and $\delta_h(m,\infty)$. For a segment with rectangular cross section the functions $\eta_h(m,\lambda)$, $\alpha_h(m,\lambda)$ and $\delta_h(m,\lambda)$ have been determined using upper bound and lower bound solutions $\{u',\sigma'\}$, $\{u'',\sigma''\}$, respectively. It appears (Fig. 5) that not only stiffness parameters δ_h are subjected to the rule $\delta_h''(m,\lambda) \geq \delta_h'(m,\lambda)$ but also $\eta_h''(m,\lambda) \geq \eta_h'(m,\lambda)$ and $\alpha_h''(m,\lambda) \geq \alpha_h'(m,\lambda)$.

From the upper and lower bound solutions the following average approximations have been determined for $\lambda \to 1$

$$\delta_h(m,\infty) \cong a(1-(|m|-2)^2)^r \dot{\delta}_h$$
$$\eta_h(m,\infty) \cong (3+r(2-|m|)|m|)\delta_h(m,\infty)/(1-(2-|m|)^2) \qquad (22)$$
$$\alpha_h(m,\infty) \cong (4-|m|+r(2-|m|)\delta_h(m,\infty)/(1-(2-|m|)^2)$$
$$\rho_h(m,\infty) \cong 3(4-|m|+r(2-|m|))/(3+r(2-|m|)|m|)$$

with $a \cong 0.74$ and $r \cong 0.55$.

The relations between the symmetric and corresponding antisymmetric state and their dependence on the coefficent of friction f is expressed by the lemma:

Lemma: If the friction f is purely dissipative and a dry joint with area A° constitutes a plane of symmetry of its neighbourhood, a symmetric load P^s will induce a symmetric stress strain field $\{\sigma^s_{ij}, \varepsilon^s_{iu}, u^s_j, \gamma^s_x\}$ and at joint a contact area $A^s_c \subset A^\circ$, where $\sigma^s_x < 0$; $\gamma^s = 0$ and a dilatational area A^s_d where $\sigma^s_x = 0$; $\gamma^s_x \geq 0$ and zero tangential stresses τ and slips γ_t, independently of the friction f.

Then any on P^s superimposed antimetric load P^a will induce an additional antisymmetric state $\{\sigma^a_{ij}, \varepsilon^a_{ij}, u^a, \gamma^a\}$ with unchanged area of contact A^s_c, where $\sigma^a_x, \gamma^a_x = 0$ and $|\tau^a| \leq f|\sigma^s_x|$ with non zero slip $\gamma^a_t \neq 0$. The relations between the governing quantities P^s, P^a and the generalized slip $\bar{\gamma}_t$ depends on f and the ratio $q = \dfrac{P^a(f)}{fP^s} = \dfrac{P^a(1)}{P^s}$ as follows:

a) If load $P^a(1)$ at friction $f(1) = 1$ induces contact slip $\gamma_t(1)$ on $A_g(1) \subset A^s_c$ and gross-slip $\bar{\gamma}_t(1)$ on A° then $P^a(f) = fP^a(1)$ at friction f induces contact slip $\gamma_t(f) = f\gamma_t(1)$ on unchanged $A_g(1)$ and gross-slip $\bar{\gamma}_t(1) = f\bar{\gamma}_t(1)$ on A°.

b) If load $P^a(f, q)$ at friction f induces $A_g(q)$ and gross-slip $\bar{\gamma}_t(f,q)$, then load $P^a(f,q_1)$ at same friction f induces $A_g(q_1) \cong \frac{q_1}{q} A_g(q)$ and gross-slip $\bar{\gamma}_t(f,q_1) > \frac{q_1}{q}\bar{\gamma}_t(f,q)$ if $q_1 > q$. (Fig. 6)

a) and b) can be expressed according to (19) as

$$P^a(f,q) = fqP^s; \qquad \bar{\gamma}_t = \frac{P^a d}{GA^o}\psi(m,q) = \frac{fqP^s}{GA^o}\psi(m,q) \tag{23, 24}$$

where $\psi(m^s, q)$ increases monotonously with q and $A_g(q) < qA^s_c$ where m depends on the σ^s_x - distribution (Fig. 6).

Proof: The theorem follows from the linear dependence of u^a, γ^a at proportional loading on f, at constant q and their nondecreasing dependence of ψ on q at contant f.

a) Indeed if $P^a(f) = fP^a(1)$ then $\gamma^t(f) = f\gamma_t(1)$ and $A_g(f) = A_g(1)$ and therefore $\bar{\gamma}_t(f) = f\bar{\gamma}_t(1)$, because all u^a, γ_t are proportional to $P^a(f)$ and their zero borders remain unchanged.

b) If again f is fixed, an increase of q and hence also of P^a must, because of the friction limit $\tau(t) \le f|\sigma_x|$, also increase the area A_g of contact sliding where $\tau^a(t) = f|\sigma^s|$ and therefore also the generalized slip $\bar{\gamma}_t$.

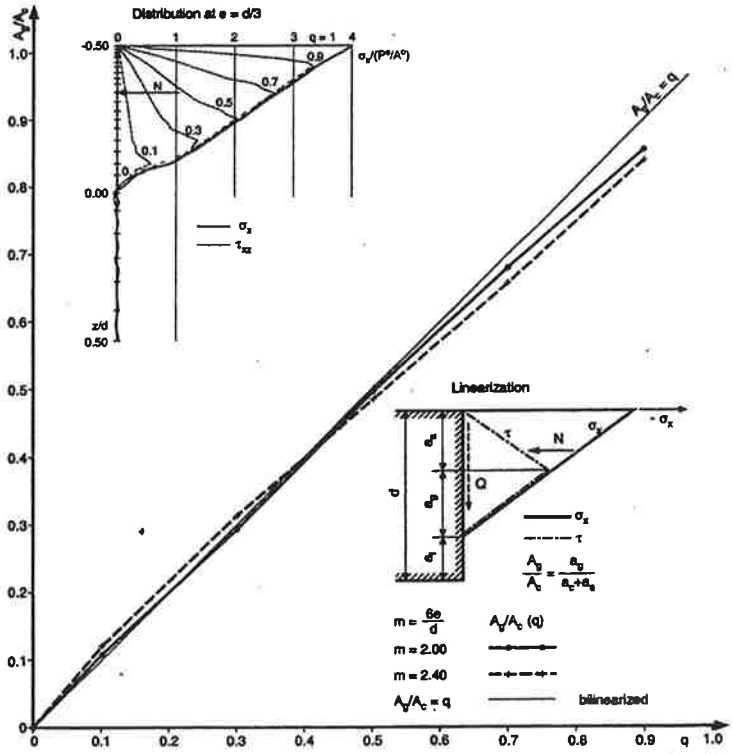

Figure 6. Relative area of contact sliding $\frac{A_g}{A_c}$ versus relative shear force $q^a = \frac{Q^a}{|N|}$ of dry joint with rectangular cross-section of segmental beam determined by FEM at λ=2.

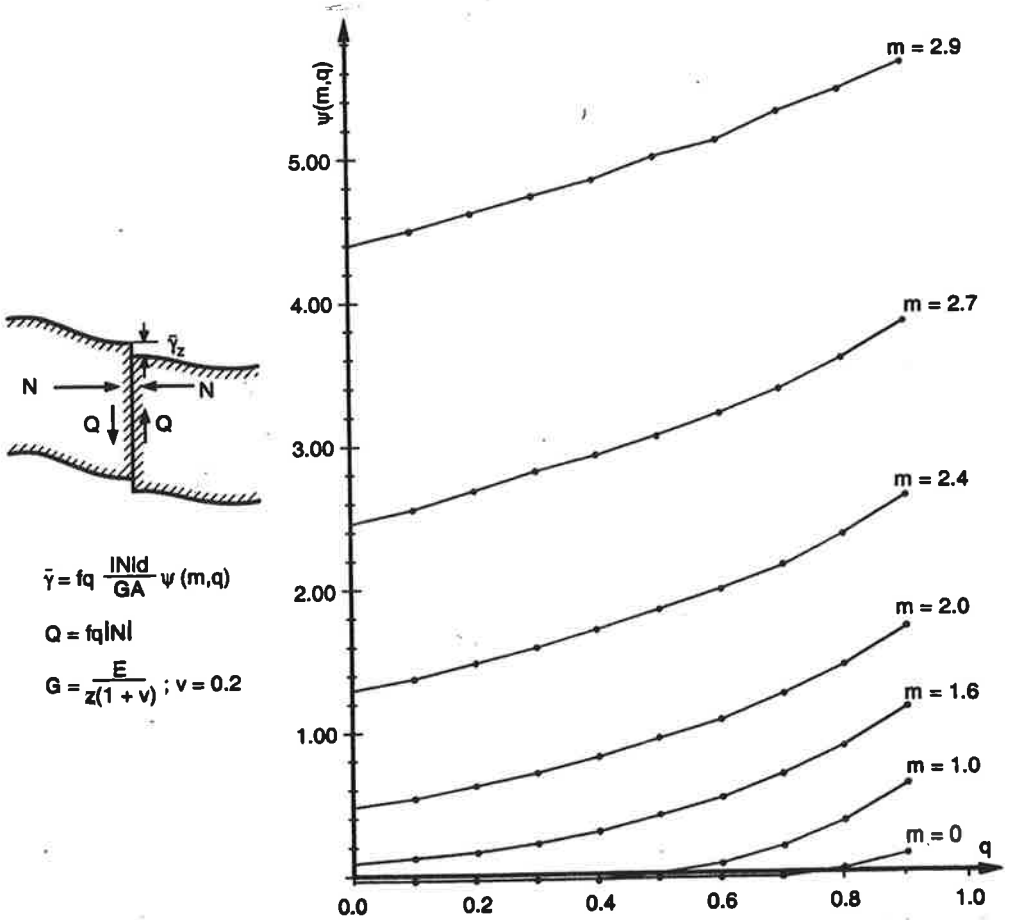

Figure 7. Dependence of slip parameter ψ on relative eccentricty m_z and relative shearforce $q = \frac{Q_z}{fP_x^s}$ of dry joint with retangular cross-section.

If the cross-section A° is rectangular and $P^a = Q_z = fqP^s$. The generalized slip $\bar{\gamma}_z$ in direction z is

$$\bar{\gamma}_z = \frac{Q_z d\psi(m_z, q)}{GA^\circ} \tag{25}$$

where $\psi(m_z, q)$ at given m is a non decreasing function of q (Fig. 7).

Inserting the values $\bar{\gamma}_x$, ω_{yh} , $\bar{\gamma}_z$ into equations (12b - 14b) we obtain the generalized deformations of the endfaces

$$\begin{aligned} v_{xh} &= \sum\nolimits_v v_{xh}^v = \sum\nolimits_v \left(\frac{|N|d}{EA} \eta_h(m_z) \right)_v \\ \omega_{yh} &= \sum\nolimits_v \omega_{yh}^v = \sum\nolimits_v \left(\frac{|N|d}{EAk_z} \alpha_{yh}(m_z) \right)_v \end{aligned} \tag{26}$$

$$v_{zh} = \sum_v \left(\frac{x \mid N \mid d}{EAk_z} \alpha_{yh}(m_z) + \frac{Q_z d}{GA} \psi_z(m_z, q) \right)_v \qquad (27)$$

where $v_{xh}{}^v$, $\omega_{yh}{}^v$ at given m_y are proportional to N^v at any loading and the $v_{zh}{}^v$ at given m_z are proportional to N^v only at proportionally increasing Q_z .

The equilibrium of segmental beams are determined by 5 redundants, the horizontal thrust X, the bending moments Y and Z and the shear force T_z which act as opposite couples on the ends of rigid lever arms fixed to the end faces A(L/2), A(-L/2). The normal force N(x), the bending moments $M_y(x)$, $M_z(x)$ and the shear forces $Q_y(x)$, $Q_z(x)$ are thus (Fig. 1)

$$N(x) = N^o(x) - X \qquad M_y(x) = M_y^o(x) - T_z x - Y \qquad Q_z(x) = Q_z^o(x) - T_z \qquad (28\text{-}30)$$

Inserting these values into (14) and (22-24, 28, 29) we obtain the equations for the determination of redundant quantities X, Y, T_z

$$\begin{aligned} X \int \frac{dx}{EA} &= \int_L \left(\frac{N^o}{EA} \right) dx - v_x + \sum_v \left(\frac{|N|d}{EA} \eta_h(m_z) \right)_v \\ Y \int \frac{dx}{EI_y} &= \int_L \left(\frac{M_y^o}{EI_y} \right) dx - \omega_y + \sum_v \left(\frac{|N|d}{EAk} \alpha_{yh}(m_z) \right)_v \end{aligned} \qquad (31a)$$

$$\begin{aligned} T_z \int \left(\frac{x^2}{EI_y} + \frac{\xi_z}{GA} \right) dx &= \\ = \int_L \left(\frac{M_y^o x}{EI_y} + \frac{Q_z^o d}{GA} \xi_z \right) dx - v_z + \sum_v \left(\frac{x \mid N \mid d}{EAk_z} \alpha_{yh}(m_z) + \frac{Q_z^o d}{GA} \psi_z(m_z) \right)_v \end{aligned} \qquad (31b)$$

Every integral on the right hand side expresses the share of the monolithic structure whereas the corresponding sum expresses the share of the cracks in the redundants in question.

REFERENCE LIST

C. Culmann. Die graphische Statik. Zürich 1866.

H. Hertz. Über du Berührung fester elastischer Körper. Journal f. Mathematik, Vol. 92, 1882.

P. de la Hire. "Traité de mechanique" Memoires de l'Academie Royale des Sciences depuis 1666 jusqu'à 1699 Vol. 9 1730.

J. Kalker. Three-dimensional elastic bodies in rolling contact. Kluwer Academic Publishers, Dordrech 1990.

A. Miettinen, H. Parland. On the stiffness characteristics of nonmonolithic elastic structures. Part II. Int. Journal Solids and Structures 39(2002) p. 1701-1728.

H. Parland, M. Heinisuo, R. Koivula. On the Problem of Bending and Compression of Masonry Structures. Sixth International Brick Masonry Conference. Rome 1982.

NEW EIGENVALUE FORMULATION FOR STABILITY ANALYSIS USING SECOND ORDER GENERALISED BEAM THEORY

T. HALME
Lappeenranta University of Technology
Department of Mechanical Engineering
Box 20, FIN-53851 Lappeenranta
e-mail: tapani.halme@lut.fi

ABSTRACT

The second order Generalised Beam Theory (GBT) offers the possibility to evaluate the local and distortional buckling capacities when these important failure modes of thin-walled structures are solved. In GBT the total deformation, e.g., due to buckling, is separated into transverse and longitudinal deformation modes, which are then combined for the final analysis. Transverse deformation modes, i.e. bending about principal axes, torsion and distortional modes, are calculated in the first stage as part of the basic cross-sectional properties. Individual buckling modes based on these transverse deformation modes can then be easily separated and calculated for pin-ended compressed structural members using a half-sine wave as the assumed longitudinal buckling deformation mode. The matrix eigenvalue formulation required in the interaction of multi-mode buckling is also straightforward if the boundary conditions are such that the assumption of half-sine wave can be justified for all the modes required in the calculation. In this paper the interaction of the basic modes is taken into account by formulating an eigenvalue problem that allows for the use of different longitudinal buckling deformation modes. The proposed method is verified by comparing the results obtained from finite element analysis using thin shell elements.

1. INTRODUCTION

Cold-formed structural members have become more and more attractive as basic structural elements for designers and end users of buildings and machines for a number of reasons. Thin-walled sections can be produced from steel sheet less than 1 mm thick, producing very lightweight structures with almost unlimited scope of cross-sectional geometries. The introduction of high strength steels has increased the efficiency of these structures considerably. These improvements in manufacturing and metallurgical processes has generated a need for predictive and reliable design with regard to the various behaviour and failure modes inherent in these structures, e.g. different buckling phenomena, vibrations, and non-linear material and geometrical behaviour.

The stability of thin-walled structural members has been an active research area in the scientific community. Early work in the first half of the 20th century concentrated on the Euler-Bernoulli-Vlasov beam theory, which developed the procedures and formulas used in analysing centrally loaded columns. Buckling modes were flexural, pure torsional or flexural-torsional (also called lateral-torsional) buckling when cross–section deformations were not included in the analysis. The formulas developed during this time are now integral part of different national codes dealing with thin-walled structures (Eurocode 1993, AISI 1996, AS/NZS 1996). However, the research during this time also revealed that short elastic thin-walled columns are prone to periodic

buckling with significant cross-section deformation over a certain buckling length. This phenomenon was called local buckling or local plate buckling, e.g. Lundquist&Stowell (1939), Kimm (1941). Perhaps the latest form of instability mode discovered in the latter part of 20th century is the so-called distortional buckling, see e.g. Hancock (1985), Lau&Hancock (1987). A more accurate expression is, perhaps, local distortional buckling, since the form of the buckled column is periodical in a fashion similar to the local plate buckling. However, the buckling length for the distortional mode is typically much longer. In general, the interaction between all these basic instability modes must be taken into account in a rigorous physical analysis of the buckling phenomenon. The buckling phenomenon can thus be described as general spatial buckling, when axially loaded column loses its stability by simultaneous translation of the column axis, rotation and arbitrary deformation (distortion) of the cross-section. Design engineers have met this challenge for a more advanced calculation by using powerful and efficient finite element method (FEM), e.g. Zienkiewicz (1977), Bathe (1982) or more restricted finite strip method (FSM), Cheung (1978), and powerful cost-effective computers. However, the research for a theoretical basis of the structural behaviour of different thin-walled structures has continued.

Generalised Beam Theory (GBT), developed by Prof. Schardt and his associates in Darmstadt, Schardt (1989), Schardt&Heinz (1990) is a fairly new tool to be used in this general spatial buckling analysis of prismatic thin-walled structures. GBT handles the different degrees of freedom, i.e. extension, bending about the principal axes, torsion and the distortional degrees of freedom as deformation modes. In first order theory these are orthogonal, which means that they are uncoupled and can be analysed separately before their effects are combined with the simple procedure of superposition, as in the basic beam bending analysis. In the second order theory the modes are coupled which allows for the previously mentioned general spatial buckling analysis be performed. However, previously this has been restricted to structural members with simple supports at the ends. In this paper the interaction of the individual buckling modes is taken into account by formulating a generalised stability analysis in GBT that also allows for the use of different boundary conditions for longitudinal buckling deformation modes.

2. THEORETICAL BACKGROUND OF GBT

The generalised displacement along the length of prismatic beam, i.e. $V(x)$, can be solved from the basic equation of GBT, which is written in a form

$$E \cdot {}^{k}C \cdot {}^{k}V'''' - G \cdot {}^{k}D \cdot {}^{k}V'' + {}^{k}B \cdot {}^{k}V = {}^{k}q \,. \tag{1}$$

The index k refers to the deformation modes or eigenmodes of a prismatic cross-section which are orthogonal, i.e. independent of each other. The modes are hierarchically numbered, e.g. torsion mode is $k = 4$. When deriving the basic equation, the following cross-sectional properties for a folded plate structure with coordinate s along the length of the wall of a plate, are defined as

$${}^{k}C = \int_{A} {}^{k}\tilde{u}(s)^2 \,\mathrm{d}A + \frac{K}{E} \int_{s} {}^{k}\tilde{f}(s)^2 \,\mathrm{d}s \,, \tag{2a}$$

$${}^{k}D = \frac{t^3}{3} \int_{s} {}^{l}\dot{\tilde{f}}(s)^2 \,\mathrm{d}s - \frac{2 \cdot \nu \cdot K}{G} \int_{s} {}^{k}\ddot{\tilde{f}}(s) \cdot {}^{k}\tilde{f}(s) \,\mathrm{d}s \,, \tag{2b}$$

$${}^{k}B = K \int_{s} {}^{k}\ddot{\tilde{f}}(s)^2 \,\mathrm{d}s \qquad K = \frac{E t^3}{12(1-\nu^2)} \,, \tag{2c}$$

where ~ denotes normalised quantity, $u(s)$ is the warping function of the cross-section, $f(s)$ is the out-of-plane deformation function and $f_s(s)$ is the in-plane deformation function. The first two

cross-sectional properties above are analogous the well known section properties of engineering beam theory. The warping constant ${}^{k}C$ is analogous to the flexural moment of inertia or sectorial moment of inertia in torsion and ${}^{k}D$ is the torsion constant. The third property, ${}^{k}B$, is the transverse bending stiffness, which defines the stiffness of the cross-section in distortion. The cross-section deformation modes can be divided into two basic modes. The first comprises rigid section modes, which are extension, bending about principal axes, and torsion. The flexible section modes are the distortional modes starting from mode $k = 5$, i.e. the first distortional mode.

Second order GBT in stability analysis

The virtual work done by the deviating forces due to axial stresses caused by stress resultant ${}^{i}W$, (axial force at the ends or end moment), can be directly added to the basic equation of GBT. The deviating forces require the solution of the cross-sectional property ${}^{ijk}\kappa_{\sigma}$, which is the interaction coefficient coupling two different deformation modes j and k when load is connected to deformation mode i. When the axial stresses are caused only by the stress resultant ${}^{i}W$, e.g. ${}^{1}W \equiv$ normal force N, imposed at the ends of the structure, the basic equation of second order GBT is based on the equilibrium between restoring and deviating forces, Schardt (1994):

$$E \cdot {}^{k}C \cdot {}^{k}V'''' - G \cdot {}^{k}D \cdot {}^{k}V'' + {}^{k}B \cdot {}^{k}V \;\; + {}^{i}W \sum_{j=1}^{n} {}^{ijk}\kappa_{\sigma} \cdot {}^{j}V'' = 0 \,. \tag{3}$$

Single mode buckling as a bifurcation problem

The deformed mode of a buckled member is assumed to take form (simply supported ends)

$${}^{k}V(x) = {}^{k}V_{m} \cdot \sin\frac{\pi x}{L}, \quad {}^{k}V_{m} = \text{amplitude}, \; L = \text{buckling length}..$$

When only one mode governs the buckled shape, i.e. single mode buckling, only one second order term ${}^{ikk}\kappa$ appears in the basic second order equation of GBT resulting

$${}^{ik}W = \frac{1}{{}^{ikk}\kappa_{\sigma}}\left[E \cdot {}^{k}C \cdot \left(\frac{\pi}{L}\right)^{2} + G \cdot {}^{k}D + {}^{k}B \cdot \left(\frac{L}{\pi}\right)^{2} \right]. \tag{4}$$

This is the explicit equation for the critical buckling load of a beam with end loads producing constant axial stress. It is valid for buckling of any individual mode k when interaction between modes is not taken into account. The critical or minimum wavelength can be obtained from Eq. 4 resulting

$${}^{ik}L_{crit} = \pi \cdot \sqrt[4]{\frac{E \cdot {}^{k}C}{{}^{k}B}} \,. \tag{5}$$

When inserting the critical wavelength into Eq. 4, the minimum or critical axial force component ${}^{ik}W_{cr}$ can be calculated as

$${}^{ik}W_{cr} = \frac{1}{{}^{ikk}\kappa_{\sigma}}\left[2 \cdot \sqrt{E \cdot {}^{k}C \cdot {}^{k}B} \; + G \cdot {}^{k}D \right] . \tag{6}$$

Multimode buckling as a bifurcation problem

The individual modes in general case of multi-mode interaction between modes are coupled and, consequently, a system of differential equations must be solved. When sinusoidal deformation is assumed for all modes in the analysis, the multi-mode buckling formulation for beams with simple supports is given as

$$\left[\begin{bmatrix} {}^{2}P(L) & & & 0 \\ & {}^{3}P(L) & & \\ & & \ddots & \\ 0 & & & {}^{n}P(L) \end{bmatrix} - \lambda \sum_{i=1}^{m} {}^{i}W_0 \cdot \begin{bmatrix} {}^{i22}K_\sigma & {}^{i32}K_\sigma & \cdots & {}^{in2}K_\sigma \\ {}^{i23}K_\sigma & {}^{i33}K_\sigma & \cdots & {}^{in3}K_\sigma \\ \vdots & \vdots & \ddots & \vdots \\ {}^{i2n}K_\sigma & {}^{i3n}K_\sigma & \cdots & {}^{inn}K_\sigma \end{bmatrix}\right] \cdot \begin{Bmatrix} a_2 \\ a_3 \\ \vdots \\ a_n \end{Bmatrix} = 0 \tag{7}$$

where modal stiffness of mode k is defined as

$${}^{k}P(L) = E \cdot {}^{k}C \cdot \left(\frac{\pi}{L}\right)^2 + G \cdot {}^{k}D + {}^{k}B \cdot \left(\frac{L}{\pi}\right)^2. \tag{8}$$

Using matrix symbols the formulation can be written as

$$\left([P] - \lambda \cdot [K_\kappa]\right) \cdot A = 0\,, \tag{9}$$

in which $[P]$ is the diagonal matrix representing the modal stiffnesses of individual buckling deformations and $[K_\kappa]$ is the kappa-matrix factored by the stress resultant (seed load) ${}^{i}W_0$ and the common load factor λ. The buckling load is then ${}^{i}W_{cr} = \lambda\, {}^{i}W_0$ which is obtained by some numerical iteration method when the generalised eigenvalue problem is solved. The corresponding eigenvector A refers to the relative amplitudes of different deformation modes in interaction.

New formulation for eigenvalue problem

In this section a new formulation for the previous eigenvalue problem is derived, which allows for the use of different boundary conditions at the ends of the compressed member. The 'classical' formulation does not take into account the number of periodic deformations in the longitudinal direction of a buckled structural member. To correct this shortcoming, an interaction correction is proposed, which properly describes the interaction of modes when longitudinal deformations are different, i.e. ${}^{k}V(x) \neq {}^{j}V(x)$. In the first phase the basic second order equation is divided with corresponding interaction term producing

$$\frac{E \cdot {}^{k}C \cdot {}^{k}V'''' - G \cdot {}^{k}D \cdot {}^{k}V'' + {}^{k}B \cdot {}^{k}V}{{}^{ikk}K_\sigma \cdot {}^{k}V''} = \frac{-{}^{i}W \cdot \sum_{j} {}^{ijk}K_\sigma \cdot {}^{j}V''}{{}^{ikk}K_\sigma \cdot {}^{k}V''}. \tag{10}$$

Taking into account the general expression for single mode buckling obtained from Eq. 3, which is

$${}^{ik}W_\sigma = \frac{E \cdot {}^{k}C \cdot {}^{k}V'''' - G \cdot {}^{k}D \cdot {}^{k}V'' + {}^{k}B \cdot {}^{k}V}{{}^{ikk}K_\sigma \cdot {}^{k}V''}, \tag{11}$$

produces the following matrix expression for multimode buckling with arbitrary boundary conditions:

$$\begin{bmatrix} {}^{ik}W_\sigma \cdot {}^{ikk}\kappa_\sigma & & 0 \\ & \ddots & \\ 0 & & {}^{il}W_\sigma \cdot {}^{ill}\kappa_\sigma \end{bmatrix} \cdot \begin{Bmatrix} {}^{k}V'' \\ {}^{k+2}V'' \\ \vdots \\ {}^{l}V'' \end{Bmatrix} = -\lambda \cdot {}^{i}W_0 \cdot \begin{bmatrix} {}^{ikk}\kappa_\sigma & \cdots & \cdots & {}^{ilk}\kappa_\sigma \\ \vdots & \ddots & \cdots & \vdots \\ \vdots & \vdots & \ddots & \vdots \\ {}^{ikl}\kappa_\sigma & \cdots & \cdots & {}^{ill}\kappa_\sigma \end{bmatrix} \cdot \begin{Bmatrix} {}^{k}V'' \\ {}^{k+2}V'' \\ \vdots \\ {}^{l}V'' \end{Bmatrix}. \quad (12)$$

Note, that $l = k + n - 2$, $k = 2,4,6...n$ or $k = 3,5,7...n - 1$, i.e. either symmetric or antisymmetric modes are in interaction, see chapter presenting numerical example. This formulation relaxes the assumption of simple supports at the ends since the matrices used in the generalised eigenvalue problem include terms, which are either cross-sectional properties or critical loads of independent deformation modes. These critical loads are solved for the boundary conditions used in the problem. In this formulation the eigenvectors present the relative proportions of second derivatives of the displacement functions of different modes. These vectors can be substituted back to Eq. 12 producing the modal ratio

$${}^{k}r = \frac{{}^{i}W_\sigma}{{}^{ik}W_\sigma} = \frac{{}^{ikk}\kappa_\sigma \cdot {}^{k}V''}{\sum_j {}^{ijk}\kappa_\sigma \cdot {}^{j}V''} \le 1. \quad (13)$$

This ratio provides the relative extent of mode effect or the weight coefficients of a single mode k in the interaction of the multi-mode buckling load. The sum of all the ratios must be equal to one.

Interaction correction

The presented basic interaction formulation must be modified when interacting modes have different deformation functions, which is the normal situation in multimode buckling when local modes are included in the analysis. This modification takes into account the fact that the ratio between design length L_d and the critical length of local modes is $r = L_d / L_\sigma$. This ratio can be used to reduce the off-diagonal interaction coefficients ${}^{ijk}\kappa$, $j \neq k$, which otherwise would excessively emphasize the interaction between modes. In the following numerical verification with example profile, the correction function is defined as

$${}^{jk}c = \frac{1}{r} = \frac{{}^{j}L_\sigma}{{}^{k}L_d}, \; {}^{k}L_d \ge {}^{j}L_\sigma \quad (14)$$

$${}^{k}L_d = \text{analysis length of mode } k$$

and the off-diagonal interaction coefficients in the kappa-matrix are then

$${}^{jk}c \cdot {}^{ijk}\kappa_\sigma, \; j \neq k. \quad (15)$$

The new formulation based on these two modifications is called the generalised stability analysis in GBT.

3. SOLVING THE GENERALISED STABILITY ANALYSIS IN GBT USING BEAM ON ELASTIC FOUNDATION (BEF) ANALOGY

The reason for using solution methods of BEF in the first order generalised beam theory is the analogy between the differential equation of the beam on elastic foundation under compressive axial force

$$EI \cdot w'''' + N \cdot w'' + k \cdot w = 0 \tag{16}$$

and the equation of second order GBT, Eq. 2. The following substitutions must be made when the BEF analogy is used in the context of GBT:

Second moment of inertia $I = {}^{k}C$

Compressive axial force $N = {}^{i}W \sum {}^{ijk}\kappa_{\sigma} - G \cdot {}^{k}D$

Foundation modulus $k = {}^{k}B$.

The differential equation of the elastic line of BEF can be solved by substituting $w = e^{mx}$, which leads to a characteristic equation , Hetenyi (1946):

$$EI\, m^4 + Nm^2 + k = 0\,. \tag{17}$$

The four roots of Eq. 17 can be written in a form

$$m_{1,2,3,4} = \pm\sqrt{-\frac{N}{2EI} \pm i\sqrt{\frac{k}{EI} - \left(\frac{N}{2EI}\right)^2}}\,. \tag{18}$$

The general solution of Eq. 16 is obtained then as

$$w = \left(C_1 e^{\beta x} + C_2 e^{-\beta x}\right)\cos\alpha x + \left(C_3 e^{\beta x} + C_4 e^{-\beta x}\right)\sin\alpha x\,, \tag{19}$$

where

$$\alpha = \sqrt{\sqrt{\frac{k}{4EI}} + \frac{N}{4EI}}$$

$$\beta = \sqrt{\sqrt{\frac{k}{4EI}} - \frac{N}{4EI}}.$$

The four unknowns in Eq. 19 can be solved using the boundary conditions at the ends of the beam. In this paper the results for two boundary conditions, i.e. clamped-clamped and clamped-simply supported are presented. The pin-ended boundary condition is solved in Eq. 4.

Clamped–clamped boundary conditions at the ends

The boundary conditions for clamped-clamped beam with finite length L lead to equation

$$a^2\left(\cos 2\bar{\beta}L-1\right)=2\beta^2\sin^2\alpha L\,. \tag{20}$$

The critical buckling load ${}^{ik}W_{cr}$ for single mode buckling for clamped end supports, using iterative procedure in finding the roots of Eq. 20, can be found when the substitutions for GBT are made, which give

$$\alpha=\sqrt{\sqrt{\frac{{}^{k}B}{4\cdot E\cdot {}^{k}C}}+\frac{{}^{ik}W\cdot {}^{ikk}\kappa_{\sigma}-G\cdot {}^{k}D}{4\cdot E\cdot {}^{k}C}}$$

$$\beta=\sqrt{\sqrt{\frac{{}^{k}B}{4\cdot E\cdot {}^{k}C}}-\frac{{}^{ik}W\cdot {}^{ikk}\kappa_{\sigma}-G\cdot {}^{k}D}{4\cdot E\cdot {}^{k}C}} \tag{21}$$

$$\bar{\beta}=\sqrt{\frac{{}^{ik}W\cdot {}^{ikk}\kappa_{\sigma}-G\cdot {}^{k}D}{4\cdot E\cdot {}^{k}C}-\sqrt{\frac{{}^{k}B}{4\cdot E\cdot {}^{k}C}}}\,.$$

The numerical solution for Eq. 20 can be found either using trial and error procedure or by using some numerical method in finding the roots of the equation.

Simply supported – clamped boundary conditions at the ends

The boundary conditions for simply supported-clamped beam with finite length L lead to

$$\beta^2\sin 2\alpha L=-\alpha\,\bar{\beta}\sin 2\bar{\beta}L\,. \tag{22}$$

The same substitutions as before must be made when solving the critical buckling load from the roots of Eq. 22.

Analysis procedure

The analysis procedure in multi-mode buckling analysis in GBT, when the cross-sectional properties are obtained based on given cross-section geometry, is as follows:

- Choose the number of modes n used in the analysis
- Solve the critical loads for global modes
- Solve the critical loads for local modes $k = 5\ldots n$ from Eqs. 4, 20 or 22 depending on the boundary conditions at the end of the column
- Solve the critical lengths ${}^{ik}L_{cr}$ for local modes $k = 5\ldots n$ from Eq. 5
- Calculate the interaction correction coefficients from Eq. 14
- Formulate and solve the eigenvalue problem in Eq. 12
- Calculate the mode effect ${}^{k}r$ from Eq. 13 for all the modes used in the analysis

4. NUMERICAL EXAMPLE

A buckling analysis was performed for a lipped channel profile as a case study. The profile had the dimensions: web height H = 100 mm, flange width B = 60 mm, lip length C = 15 mm and thickness t = 2.7 mm. The first eight deformation modes are given in Fig. 1.

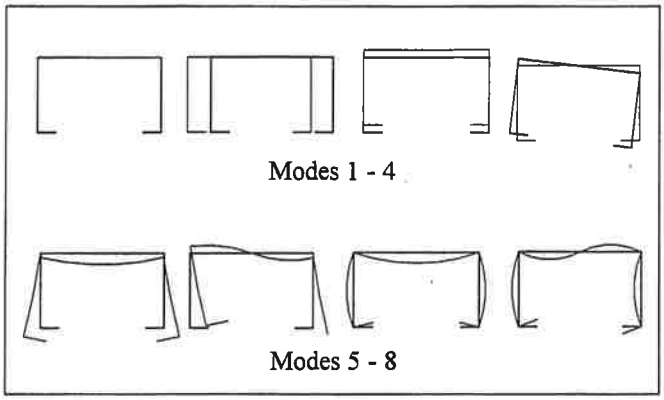

Figure 1: Deformation modes k = 1...8

The proposed generalised stability analysis formulation was used in the parametric study of the test profile. The basic cross-sectional properties for the analysis in GBT are given in Table 1 and the interaction coefficients in Table 2.

Table 1. The basic cross-sectional properties of the example profile

	$k=1$	$k=2$	$k=3$	$k=4$	$k=5$	$k=6$	$k=7$	$k=8$
${}^{k}C$	675.0	473.2	248.01	104.9	30.36	35.42	0.9455	1.435
${}^{k}D$	0	0	0	$2.045\text{x}10^{-4}$	$2.434\text{x}10^{-3}$	$2.994\text{x}10^{-3}$	$6.157\text{x}10^{-3}$	$2.748\text{x}10^{-2}$
${}^{k}B$	0	0	0	0	$2.213\text{x}10^{-2}$	$6.476\text{x}10^{-2}$	0.4191	2.653

Table 2. The ${}^{1/k}\kappa$ -values of the example profile $\text{x}10^{-3}$

	$k=2$	$k=3$	$k=4$	$k=5$	$k=6$	$k=7$	$k=8$
$j=2$	-0.400	0	-0.3679	0	-0.5487	0	0.6041
$j=3$	0	-0.6782	0	-0.3584	0	-0.5979	0
$j=4$	-0.3679	0	-0.6244	0	-0.6400	0	0.6228
$j=5$	0	-0.3584	0	-2.235	0	-0.9506	0
$j=6$	-0.5487	0	-0.6400	0	-2.232	0	1.087
$j=7$	0	-0.5979	0	-0.9506	0	-2.098	0
$j=8$	0.6041	0	0.6228	0	1.087	0	-3.184

The ${}^{1/k}\kappa$ -values are used in the kappa-matrix of Eq. 12 with the interaction correction coefficients when required. Axial normal force ${}^{1}W_0$ = 1 kN as a seed load was imposed at the ends of the structure. Analysis lengths were L_d = 300,400...1400 mm. At the ends of the beam the combination clamped – simply supported boundary condition was chosen. Finite element program ANSYS Ver. 5.7 was used for comparison purposes. Quadrilateral four-node thin shell elements (SHELL63) were used in modelling the structure.

Typical mesh as well as the buckled form obtained from the FE -analysis for L_d = 700 mm can be seen in Fig. 2:

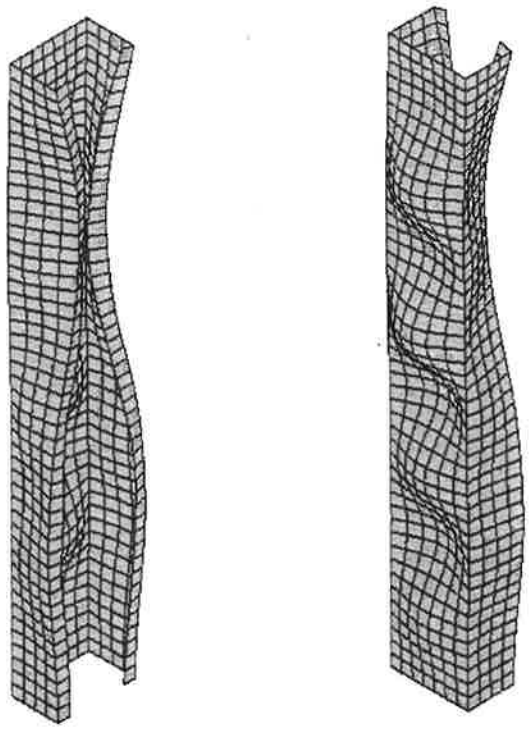

Figure 2: ANSYS results: local and distortional buckling modes in interaction, L_d = 700 mm.

Comparison of buckling loads between FEA and GBT with eight modes in the analysis is presented in Fig. 3. The results show the difference between methods being below 6 %.

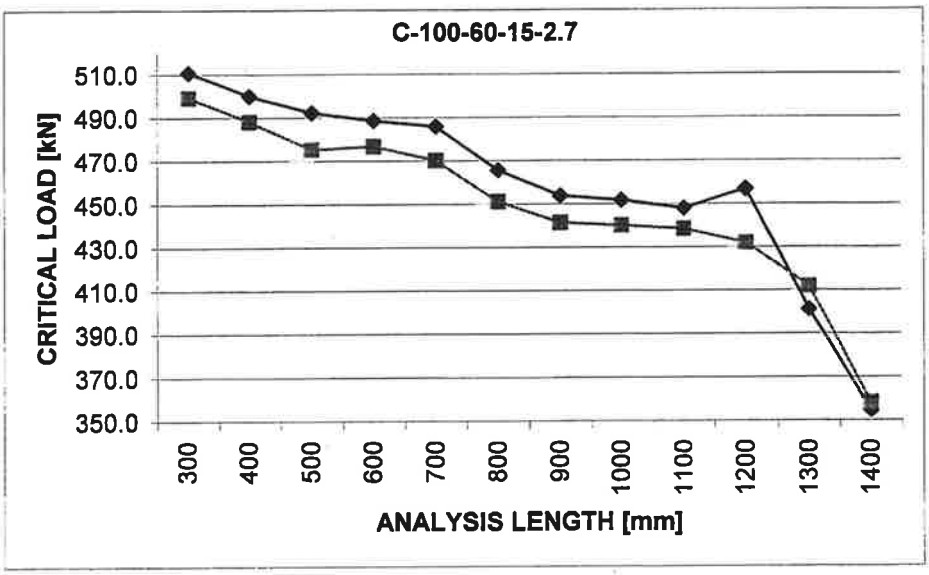

Figure 3: Buckling load comparison between FEA (upper curve) and GBT using eight modes.

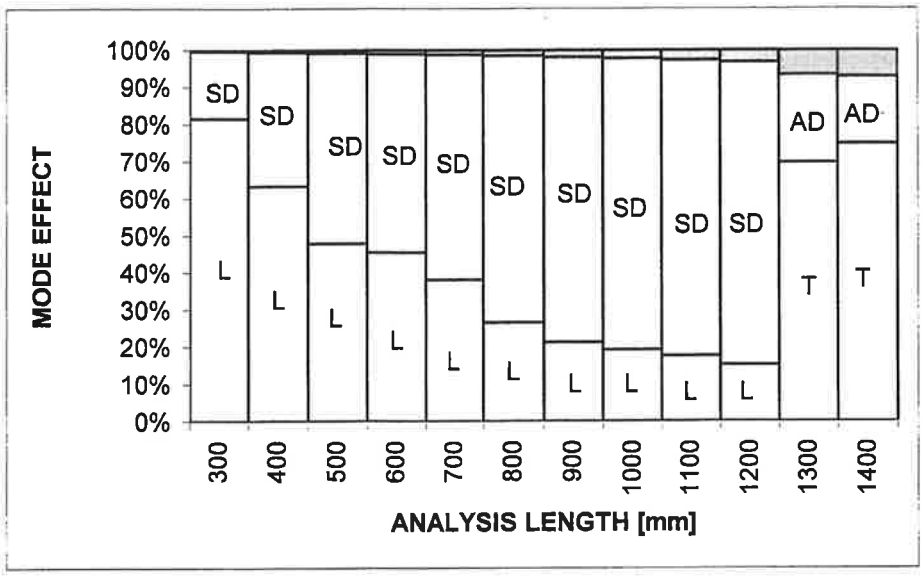

Figure 4: Mode effect based on Eq. 13. L = symmetric local plate buckling, SD = symmetric distortional buckling, AD = antisymmetrical buckling, T = torsional buckling. Shaded area presents global buckling.

The mode effect in different analysis lengths is presented in Fig. 4. The local plate buckling, i.e. mode $k = 7$, clearly dominates in the short analysis lengths. This rapidly changes into dominance of symmetric distortion, i.e mode $k = 5$. The effect of global buckling, i.e. mode $k = 3$ is negligible. The results from FEA analysis can be visually compared to GBT in Fig. 3, which clearly shows the strong interaction between modes. The local-distortional buckling modes changes in analysis length $L_d = 1300$ mm into torsional-flexural-distortional buckling.

5. CONCLUSIONS

Thin-walled compressed structural members have often failure modes relating to local buckling modes, i.e. local or distortional buckling. The normal assumption of simply supported ends in local, distortional and global buckling leads to simple expressions for the single mode buckling phenomenon when Generalised Beam Theory is utilised. However, when the effect of differing boundary conditions from simply supported ends for beams is taken into account, closed form solutions cannot be obtained for the local and distortional modes due to the nature of underlying physical phenomenon, i.e. the beam on elastic foundation. The interaction of different modes must also be taken into account when buckling loads are calculated. The classical multimode buckling eigenvalue formulation in GBT is based on half-sinus function, which does not take into account the number of periodic modes in the longitudinal direction of the compressed structural member. In this paper a new formulation leading to generalised stability analysis in GBT is presented, which takes into account the differing boundary conditions as well as the number of periodic buckling modes for local modes, i.e. for modes relating to local plate buckling and distortional buckling. Case study was examined using a channel profile, which was analysed in GBT using the new formulation and the results were compared to finite element analysis results using thin shell elements. The buckling load as well as the corresponding buckling mode were in excellent agreement with the results obtained from the proposed formulation, although no numerical information concerning the interaction of modes can be extracted from FE –analysis since the modes are unseparated.

REFERENCES

AISI (1996), *Specification for the design of cold-formed steel structural members*. American Iron and Steel Institute.

AS/NZS (1996). *Cold-formed steel structures*. Australian/New Zealand Standard.

Bathe, K-J, *Finite Element Procedures in Engineering Analysis*, Prentice-Hall Inc., 1982, ISBN 0-13-317305-4.

Cheung, Y.K., 1976, *Finite Strip Method in Structural Analysis*, Pergamon Press, New York. ISBN 0-08-018308-5.

Eurocode 3: ENV1993-1-3: Supplementary rules for cold formed thin gauge members and sheeting : February 1996.

Hetenyi, M. 1947, *Beams on Elastic Foundation*, University of Michigan Press, Ann Arbor, MI, USA.

Kimm, G. 1941. Beitrag zur Stabilität dunnwandiger U-profile mit konstantem Wandstärke im elastischen Bereich. *Luftfart-Forschung* 14(9):444-57.

Lundquist, E. & Stowell, E. *Local instability of columns with I-, Z-, channel and rectangular tube sections*. Technical Notes TN 743, Washington, USA: Nat. Adv. Com for Aeron (NACA).

Schardt, R. 1989, *Verallgemeinerte Technische Biegetheorie*. Springer-Verlag, Berlin. ISBN 3-540-51339-6.

Schardt, R. & Heinz, D. 1990, *Vibrations of Thin-walled Prismatic Structures Under Simultaneous Static Load Using Generalized Beam Theory*, In: Krätzig et al. (eds.), Structural Dynamics 1990 Balkema, Rotterdam. ISBN 90-6191-168-0.

Schardt, R. 1994, Generalized Beam Theory - An Adequate Method for Coupled Stability Problems, *Thin-Walled Structures* 19: p.161-180.

Vlasov, V.Z. 1961, *Thin-walled Elastic Beams*. Israel program for scientific calculations. Translation of: Tonkostennye uprugie sterzhni, Jerusalem.

Zienkiewicz, O.C., *The Finite element method*, McGraw-Hill, 1977, ISBN 0-07-084072-5.

IMPROVED SPR METHOD FOR PLANE ARCH PROBLEM

M. PERÄLÄ

Helsinki University of Technology
Laboratory of Structural Mechanics
P.O. Box 2100, 02015 HUT
e-mail: Martti.Perala@hut.fi

ABSTRACT

Calculation of smoothed stress resultants and a posteriori error estimation for a plane arch in connection with the displacement based finite element method is introduced. Two patch recovery methods are used to smoothen the consistent stress resultants. The first one is the well known SPR method [1]. The second one is an improved version of SPR method which uses information from the equilibrium equations of the problem. By using the recovered solutions in connection with the Zienkiewich-Zhu type error estimate [2] an efficient a posteriori error estimates are established. The two patch recovery methods are applied in connection with two types of curved finite elements. In the numerical part a semicircular arch is used as a test problem.

1 INTRODUCTION

Patch recovery methods [1], [3] - [6] combined with the Zienkiewich-Zhu error estimate [2] have proved out to be efficient tools for a posteriori error analysis of finite element results. The consistent derivative quantities are first improved using a suitable smoothing procedure, e.g. SPR method [1]. In plane arch problem those derivative quantities are normal force and bending moment (and shear force). The difference between the smoothed and consistent derivatives is regarded to represents the error [2].

Wiberg and Abdulwahab [5] and independently Blacker and Belytchko [6] were the first to use information from the equilibrium equations to improve the accurary of a patch recovery procedure. In presented method the information from the equilibrium equations is also used. The method differs, however, those of refs. [5], [6]. In the SPR method the smoothing is done separately for each stress resultant. In the proposed method stress resultants smoothing are coupled due to the use of equilibrium equations.

The patch recovery methods of refs. [3] and [4] are based on displacement (basic unknown) formulation of equilibrium (field) equations. In the present method stress resultant formulation of equilibrium equations is used. Local polynomial representations for the stress resultants which contain unknown parameters is first formed. By using the information from the equilibrium equations constraint equations between the unknown parameters are formed. With the help of the constraint equations the number of parameters can be effectively reduced. Finally, we have local polynomial representation for stress resultants, which contain information from the equilibrium equations "built-in". Comparing the proposed method to that of ref. [5], it is noted that the proposed method does not contain any adjustable parameters.

2 GOVERNING EQUATIONS

Equilibrium equations in axial and tranverse directions for a plane arch are

$$N_{,s} + \frac{M_{,s}}{R} + n + \frac{m}{R} = 0, \tag{1}$$

$$M_{,ss} - \frac{N}{R} + q + m_{,s} = 0, \tag{2}$$

where coordinate s follows the arch midline. In equations (1) and (2) N is normal force, M is bending moment and R is a radius of the arch. n, q and m are distributed axial, transverse and moment loads. Equation for shear force is: $Q = M_{,s} + m$.

Constitutive equations are: $N = EA\varepsilon$ and $M = EI\kappa$, where ε is (membrane) strain and κ is curvature change. EA and EI are axial and bending stiffnesses of the arch, where E is a modulus of elasticity, A is a cross-sectional area and I is a moment of inertia. Using assumption of the Bernoulli-Euler beam theory we get for rotation: $\theta = v_{,s} - \frac{u}{R}$. Strain and curvature change $\kappa = -\theta_{,s}$ can be written in terms of axial and tranverse displacements u and v as

$$\varepsilon = u_{,s} + \frac{v}{R}, \tag{3}$$

$$\kappa = -v_{,ss} + (\frac{u}{R})_{,s}. \tag{4}$$

3 FEM ANALYSIS

Finite element equations are derived from the virtual work equation: $\delta W = \delta W^i + \delta W^e$, where internal virtual work for the plane arch is

$$\delta W^i = -\int_s (N\delta\varepsilon + M\delta\kappa)\ ds \tag{5}$$

and external virtual work is

$$\delta W^e = \left[N\delta u + Q\delta v - M\delta\theta\right]_{s_1}^{s_2} + \int_s (n\delta u + q\delta v - m\delta\theta)\ ds, \tag{6}$$

where $\delta(\cdot)$ are corresponding virtual quantities.

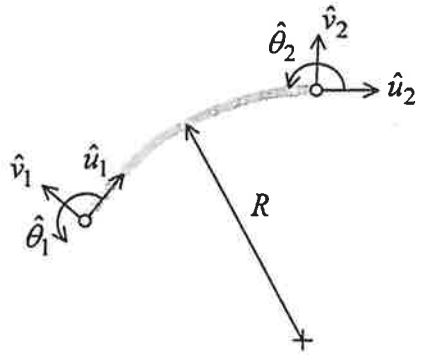

Figure 1: Curved arch element.

A simple curved arch element is a two-noded element where the degrees of freedom (d.o.f.) are nodal values of u, v and θ [7], [8] (Fig. 1.). This element allows linear variation for axial displacement and cubic variation for tranverse displacement. The problem of this element, is membrane locking which occurs when the arch becomes very thin and ratio A/I becomes large. Membrane locking can be avoided by using selective integration in evaluating the stiffness matrix [8]. Let us designate this element as CL (Cubic-Linear) element in the numerical study.

Raveendranath et al. [9] proposed a curved arch element in which the displacement approximations are coupled. In this procedure, cubic polynomial field is first assumed for tranverse displacement. Axial displacement field is then derived from the homogeneous axial equilibrium equation (1) (written in terms of the displacements). This leads to fourth-order polynomial field for the axial displacement. This element is free of locking and full integration can be used in evaluating the stiffness matrix [9]. This element has also six d.o.f. per element. Let us designate it here as CQ (Cubic-Quartic) element.

4 SPR METHOD AND ITS IMPROVEMENT

Let us look how the SPR method [1] can be applied for the plane arch problem. At first, normal force and bending moment are represented locally (within the patch) as complete polynomials of degrees q_n and q_m

$$\tilde{N}(\lambda) = \sum_{i=0}^{q_n} \lambda^i N_i, \qquad \tilde{M}(\lambda) = \sum_{i=0}^{q_m} \lambda^i M_i, \tag{7}$$

where N_i ($i = 0, \cdots, q_n$) and M_i ($i = 0, \cdots, q_m$) are unknown parameters and $\lambda = (s - s_0)/h$ is a dimensionless patch coordinate, where s_0 is a s-coordinate of the patch assembly point and h is a size of the patch (Fig. 2).

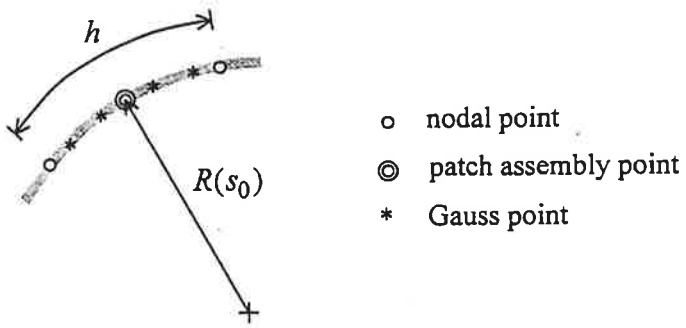

Figure 2: Curved patch.

The unknown parameters N_i and M_i are determined by least squares fitting of the polynomial representations $\tilde{N}$ and $\tilde{M}$ to the corresponding finite element solutions $\hat{N}_j$ and $\hat{M}_j$ at the Gauss points of the patch (Fig. 2). The least squares fitting procedures are made separately for N and M. The least squares function, for example, in case of the normal force is

$$\Pi(N_i) = \sum_{j=1}^{n_s} [\tilde{N}(s_j) - \hat{N}_j]^2, \tag{8}$$

where n_s is the number of Gauss (sampling) points. Minimization of function (8) with respect to parameters N_i results to system of linear equation from which the parameters N_i can be solved.

We can modify the SPR method by taking into account the information from the equilibrium equations (1) and (2). This improved SPR method is called here as SPRI method. We use now equal order approximations both normal force and bending moment, thus $q_n = q_m = q$ in eqs. (7). We write the residuals of equilibrium equations as complete polynomials

$$\tilde{R}_u(\lambda) = \sum_{i=0}^{q-1} \lambda^i R_{ui}, \qquad \tilde{R}_v(\lambda) = \sum_{i=0}^{q-2} \lambda^i R_{vi}. \tag{9}$$

Based on one dimensional Taylor series of residuals $R_u(s)$ and $R_v(s)$, the corresponding coefficients have expression

$$R_{ui} = \frac{h^i}{i!}\frac{d^i R_u}{ds^i}(s_0), \qquad R_{vi} = \frac{h^i}{i!}\frac{d^i R_v}{ds^i}(s_0). \tag{10}$$

The number of unknown parameters in representations of N and M is then $q+1$. Demanding that polynomial representations (9) of the residuals should vanish with all values of λ results to two set of equations:

$$R_{ui} \equiv (N_{,s})_i + (\frac{M_{,s}}{R})_i + n_i + (\frac{m}{R})_i = 0; \qquad i = 0, \cdots, q-1, \tag{11}$$

$$R_{vi} \equiv (M_{,ss})_i - (\frac{N}{R})_i + q_i + (m_{,s})_i = 0; \qquad i = 0, \cdots, q-2. \tag{12}$$

Equations (11) and (12) are valid for variable R. If we assume R as constant, we get equations

$$R_{ui} \equiv \frac{1}{h}\frac{(i+1)!}{i!}N_{i+1} + \frac{1}{hR}\frac{(i+1)!}{i!}M_{i+1} + n_i + \frac{m_i}{R} = 0, \tag{13}$$

$$R_{vi} \equiv \frac{1}{h^2}\frac{(i+2)!}{i!}M_{i+2} - \frac{N_i}{R} + q_i + \frac{1}{h}\frac{(i+1)!}{i!}m_{i+1} = 0. \tag{14}$$

Equations (13) and (14) are constraint equations between the parameters N_i and M_i. Details of writing constraint equations in terms of the unknown parameters is found from ref. [3] (App. A). The number of constraint equations is $2q-1$. With the help of the constraint equations a part of the original parameters N_i and M_i can be expressed in terms of the $2(q+1)-(2q-1) = 3$ remaining ones (a_1, a_2 and a_3), which can be considered as independent parameters. We can, for example, choose $a_1 = N_0, a_2 = M_0$ and $a_3 = M_1$. The new polynomial representations for N and M in terms of independent parameters a_i can then be written as

$$\tilde{N}(\lambda) = \sum_{i=1}^{3} P_{ni}(\lambda)a_i + \bar{n}_0(\lambda), \tag{15}$$

$$\tilde{M}(\lambda) = \sum_{i=1}^{3} P_{mi}(\lambda)a_i + \bar{m}_0(\lambda), \tag{16}$$

where polynomial representations (15) and (16) contain "built-in" information from the equilibrium equations.

The unknown parameters a_i are determined by least squares fitting procedure where the least squares function is now

$$\Pi^*(a_i) = \sum_{j=1}^{n_s} \Big\{ h^2 \big[\tilde{N}(s_j) - \hat{N}_j\big]^2 + \big[\tilde{M}(s_j) - \hat{M}_j\big]^2 \Big\}. \tag{17}$$

Normal force and bending moment fittings are now coupled due to the use of equilibrium equations.

Final nodal values of normal force and bending moment are calculated by using the patchwise representations (15) and (16) for them and averaging at the system nodes. The final, C^0-continuous fields are then interpolated by using Lagrange shape functions for both N and M.

Constraint equations when R is variable

We now show the expressions for constraint equations ((13) and (14)) in terms of unknown parameters when the radius is variable. The curvature $\frac{1}{R}$ of the arch is represented as complete polynomial of order $q-1$ as $\frac{1}{R}(\lambda) = \sum_{i=0}^{q-1} \lambda^i (\frac{1}{R})_i$, where $(\frac{1}{R})_i = \frac{h^i}{i!} \frac{d^i(1/R)}{ds^i}(s_0)$. Constraint equations are then

$$R_{ui} \equiv \frac{1}{h} \frac{(i+1)!}{i!} N_{i+1} + \sum_{j=0}^{i} \Big[\frac{1}{h} \frac{(j+1)!}{j!} (\frac{1}{R})_{i-j} M_{j+1} \Big] + n_i + \sum_{j=0}^{i} (\frac{1}{R})_{i-j} m_j = 0, \tag{18}$$

$$R_{vi} \equiv \frac{1}{h^2} \frac{(i+2)!}{i!} M_{i+2} - \sum_{j=0}^{i} \Big[(\frac{1}{R})_{i-j} N_j \Big] + q_i + \frac{1}{h} \frac{(i+1)!}{i!} m_{i+1} = 0. \tag{19}$$

5 NUMERICAL EXAMPLE

A semicircular arch with clamped ends and concentrated center load P was used as a test problem [8] (Fig. 3). Radius of the arch is R and cross-section is rectangular with thickness t and width b. In the finite element analysis half of the arch was modelled by CL and CQ elements described in section 3. Following numerical values were used: $P = 20\text{kN}$, $E = 210\text{GPa}$, $t = 0.1\text{m}$, $b = 0.05\text{m}$ and $R = 10\text{m}$.

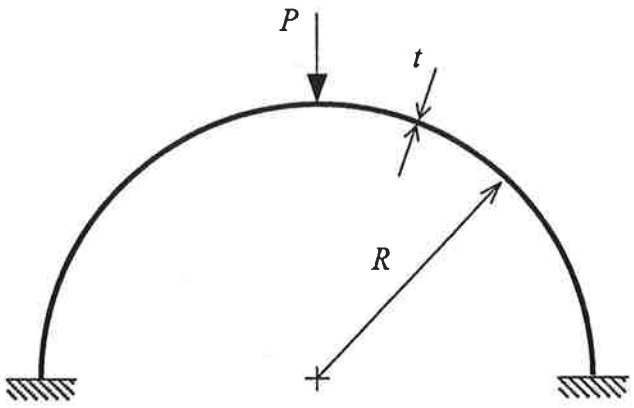

Figure 3: Semicircular arch.

Figures 4 and 5 show exact and finite element (using three CQ elements) normal force and bending moment distributions. Smoothed nodal values of SPRI method are plotted by stars. Values of finite element (using CL elements in FEM) normal force show excellent agreement with the exact values at element mid-points. Thus normal force fitting was done at element mid-points in connection with the CL elements. Due to similar reasons two Gauss points per element were used in bending moment fitting for both CL and CQ elements and in normal force fitting for CQ elements (see Figs. 4 and 5).

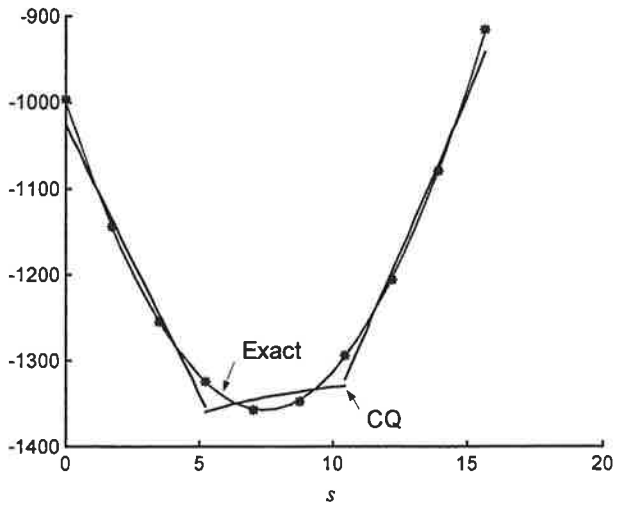

Figure 4: Normal force ([N]).

Polynomial degree $q = 1$ was used for normal force and $q = 2$ for bending moment in SPR method (and in final interpolation) in connection with CL elements. Degree $q = 3$ was used both N and M in SPR method (with CQ elements) and in SPRI method (with the CL and CQ elements). Correspondingly, cubic Lagrange shape functions were used in the final interpolation.

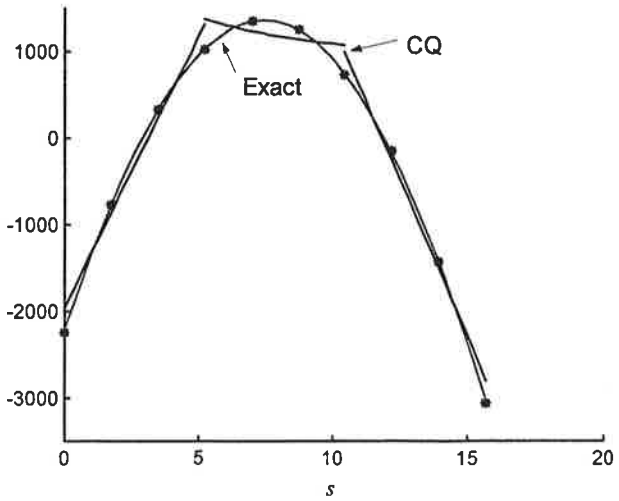

Figure 5: Bending moment ([Nm]).

The relative errors in L_2-norm for normal force and bending moment were used as error measures. These for the consistent normal force $\hat{N}$ and the smoothed one $\tilde{N}$ are

$$\eta_{2,N}^{\text{cons}} = \frac{\|\hat{N} - N\|_2}{\|N\|_2}, \qquad \eta_{2,N}^{\text{smoo}} = \frac{\|\tilde{N} - N\|_2}{\|N\|_2}. \tag{20}$$

Corresponding Zienkiewich-Zhu error estimate [2] is

$$\eta_{2,N}^{\text{esti}} = \frac{\|\hat{N} - \tilde{N}\|_2}{\|\tilde{N}\|_2}, \tag{21}$$

where

$$\|\hat{N} - \tilde{N}\|_2 = \sqrt{\int_s (\hat{N} - \tilde{N})^2 \, ds}, \qquad \|N\|_2 = \sqrt{\int_s N^2 \, ds}. \tag{22}$$

Similar expressions are used for the bending moment. Effectivity index θ, which is a measure of the quality of a posteriori error estimation is

$$\theta = \frac{\eta_2^{\text{esti}}}{\eta_2^{\text{cons}}}. \tag{23}$$

Figures 6 and 7 present results of experimental convergence study of the relative error (η_2) in L_2-norm of the normal force and the bending moment. h is element size and L is length of the arch.

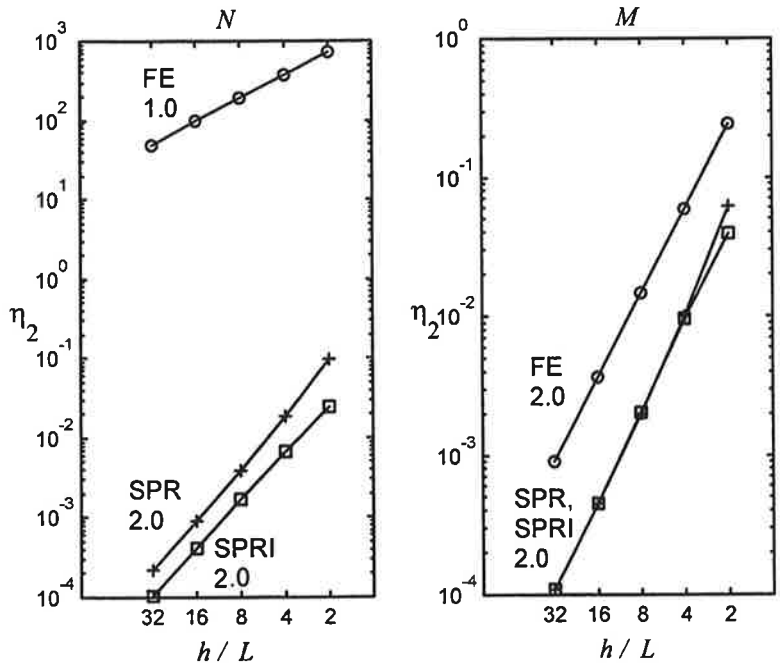

Figure 6: Relative error (η_2) in case of CL elements for N and M.

Figure 6 shows that both SPR and SPRI methods work well in case of normal force smoothing. Relative errors of the smoothed solutions are much smaller than those of the consistent (FE) ones. Convergence rates of SPR and SPRI are also superconvergent. In case of bending moment, the convergence rates of the smoothed solutions are equal to those of the consistent ones. Relative errors are, however, smaller.

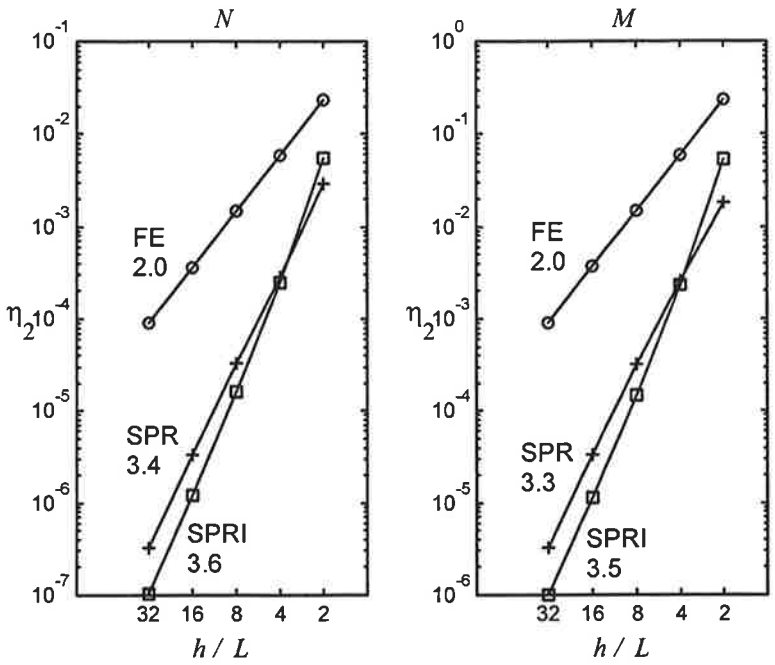

Figure 7: Relative error (η_2) in case of CQ elements for N and M.

In case of CQ elements, both SPR and SPRI methods give convergence rates which are superconvergent both for normal force and bending moment. Relative errors are also smaller than those of the consistent ones.

Figure 8 shows effectivity indices for normal force and bending moment. Figures a) and b) show effectivity indices in connection with the CL elements and figures c) and d) show them in connection with the CQ elements.

6 CONCLUSIONS

SPR and SPRI methods were applied for plane arch problem. Improved version of SPR method, SPRI method, used information from the equilibrium equations. Both methods were tested in connection with two curved arch finite elements: older Cubic-Linear element and newer Cubic-Quartic element. It seems that both SPR and SPRI methods work well in smoothing of stress resultants of the plane arch. In the future, it would be interesting to see whether the conjoint interpolation technique [6] gives even better results. The possibility to applying the idea of SPRI method to axisymmetric shells could be also studied.

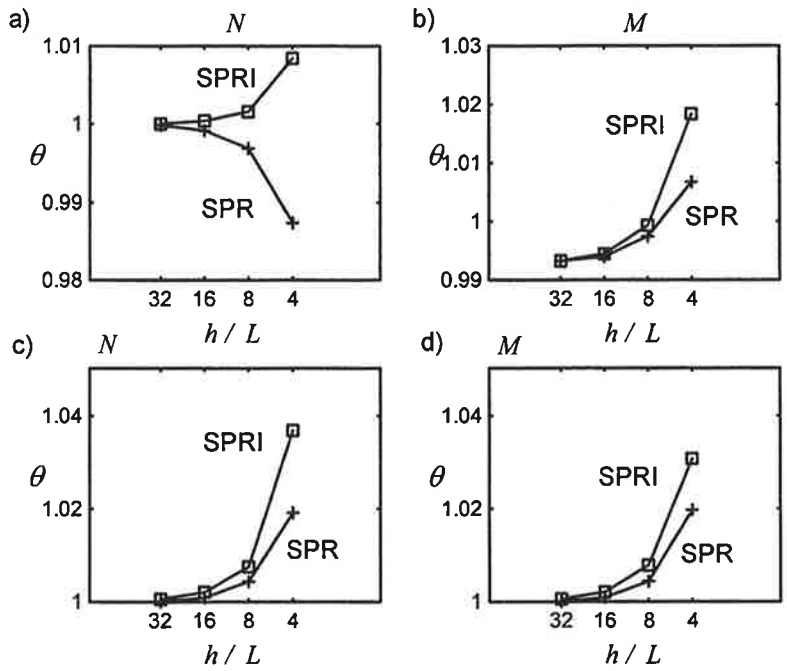

Figure 8: Effectivity indices for normal force (N) and bending moment (M).

Aknowlegments

Thanks to Professor Jukka Aalto, from the structural mechanics laboratory of HUT, for discussions of the subject.

REFERENCES

[1] O.C. Zienkiewich, J.Z. Zhu, *The superconvergent patch recovery and a posteriori error estimates. Part 1: The recovery technique*, Int. J. Num. Eng., 33, (1992), 1331-1364.

[2] O.C. Zienkiewich, J.Z. Zhu, *A simple error estimator and adaptive procedures for practical engineering analysis*, Int. J. Num. Eng., 24, (1987), 337-357.

[3] J. Aalto, M. Perälä, *Two robust patch recovery methods with built-in field equations and boundary conditions*, Finite Element Methods: Superconvergence, Post-Processing and A Posteriori Estimates, Eds. M. Krizek, P. Neittaanmäki and R. Stenberg, Lecture Notes in Pure and Applied Mathematics 196, Marcell Dekker, Inc., (1998), 1-17.

[4] J. Aalto, M. Åman, *Polynomial representations for patch recovery procedures*, Computers and Structures 73, (1999), 91-118.

[5] N.E. Wiberg, F. Abdulwahab, F. Ziukas, *Enhanced superconvergent patch recovery incorporating equilibrium and boundary conditions*, Int. J. Num. Meth. Engng. 37, (1994), 3417-3440.

[6] T. Blacker, T. Belytchko, *Superconvergent patch recovery with equilibrium and conjoint interpolant enhancements*, Int. J. Num. Meth. Engng. 37, (1994), 1517-1536.

[7] D.G. Ashwell, A.B. Sabir, T.M. Roberts, *Further studies in the application of curved finite elements to circular arches*, Int. J. mech. Sci. 13, (1971), 507-517.

[8] R.D. Cook, D.S. Malkus, M.E. Plesha, *Concepts and applications of finite element analysis*, 3rd Edition. John Wiley & Sons. 1989, p. 604.

[9] P. Raveendranath, G. Singh, B. Pradhan, *Free vibration of arches using a curved beam element based on a coupled polynomial displacement field*, Computers and Structures 78, (2000), 583-590.

DERIVATION OF THE KOLLBRUNNER-HAJDIN THEORY OF THE THIN-WALLED RECTANGULAR BOX BEAM UNDER TORSION BY DIVIDING THE BEAM INTO GUIDED VLASOV BEAMS WITH OPEN CROSS-SECTION.

Risto Koivula, MSc
Muroleenkatu 6 A 1, 33720, Tampere

ABSTRACT

Due to the double symmetry of the box beam, the fields of normal stress given rise by the axial force or the bending moments are orthogonal with those given rise by the torsion (and distortion). Thus the former can be independently superposed on the latter. Then for the antisymmetrical warpings like torsion and distortion the intersectional axes of the planes of symmetry with the box sides can be regarded as continuous non-compressible axial supports, along which the beam can be cut to guided Vlasov beams with open cross-section, which can be analysed using the formal methods of the theory of guided beams.

However, the main aim of this study is not to create an "exact" solution of the problem in terms of the theory of guided beams, in this case, but to interpret the standard Kollbrunner-Hajdin solution in terms of this theory.

THE SYSTEMS OF AXES AND SPECIAL POINTS FOR THE HALF PROFILE

The displacement and force quantities are in a right-handed system *uvw,* but the coordinates *xyz* with the cross-sectional integrals in a left-handed system. This makes some important matrices in the theory symmetrical, and all signs plus in the formulae of normal stresses.

First the beam is devided into two guided Vlasov beams with a U cross-section along one of the two planes of symmetry of the beam. The part beams are U profiles which are guided by non-compressible axes along the edges of the "flanges", in other words along the mid-lines of the box sides. These edges of "flanges" are guided by lateral restraints to keep the distance from the original box centre (C), around which the half box is guided to rotate. These guidings result from the symmetry properties of the entire box beam.

In the beginning two independent degrees of freedom must be regarded for the U profile with the non-compressible axes along the edges, but *without* the lateral support: First, caused by the normal stresses given rise by the bimoment warping, the cross-section tends to rotate around a sectorial pole, around which it is possible to draw a sectorial area with zero value at the non-compressible axes. This guided sectorial pole (D) is placed on the symmetry axis of the U cross-section at the "flange" length distant from the web to the opposite direction with the "flanges".

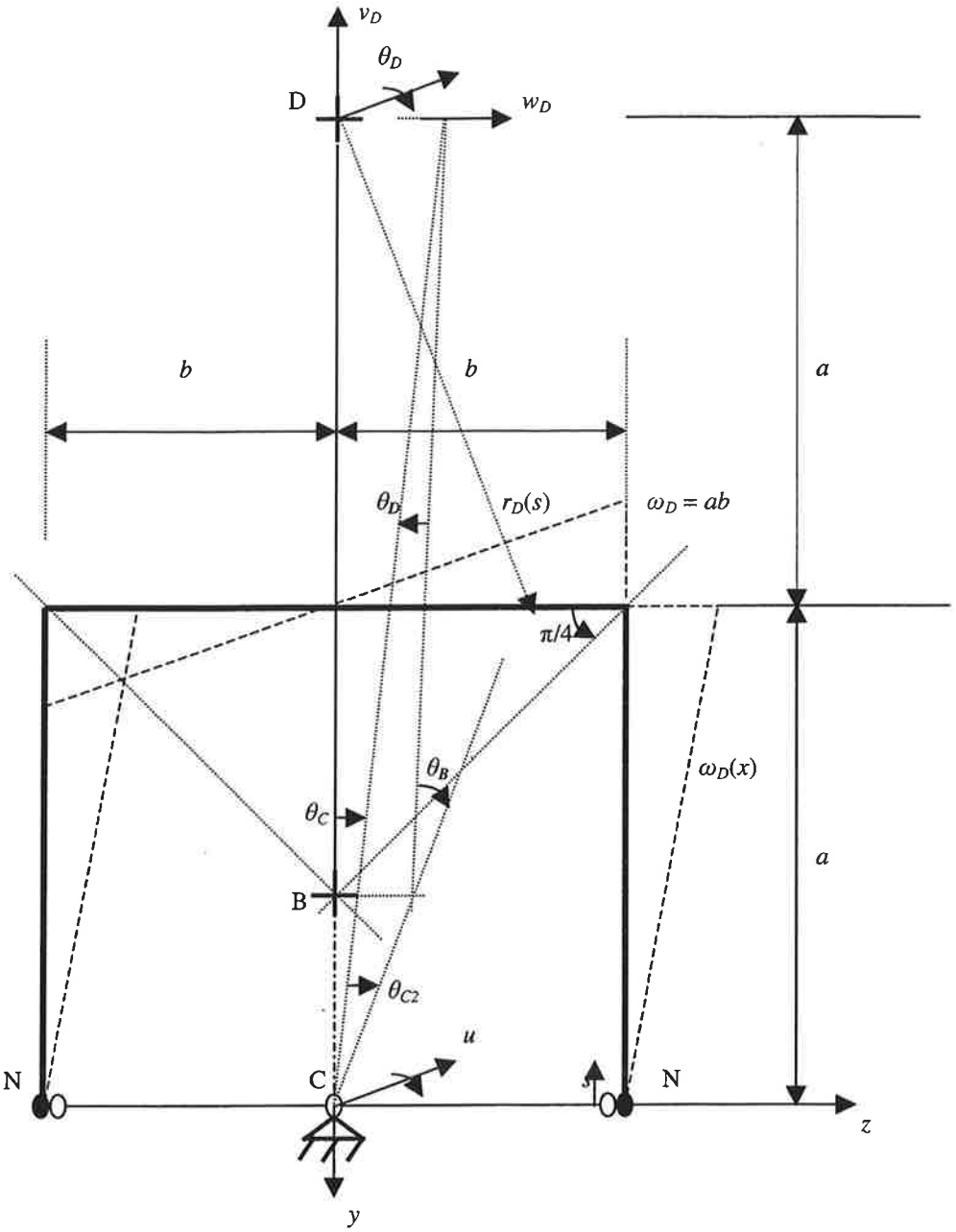

D = distortional centre, or the guided sectorial pole of the half box

B = the centre of twist for the StVenant torsion of the half box

C = the centre of torsion of the entire box and of the laterally guided half box, the guided origin

N = the non compressible edges

$\omega_D(x)$ = the sectorial area around the distortional centre D.

Figure 1. The half-box as a guided beam.

Second, for a case on guided beams with two non-compressible axes, the shear deformation from the constant shear flow between these axes must be taken into consideration as an independent degree of freedom. Caused by the constant shear flow deformation, the axially guided along the flange edges, but laterally non-guided U cross section tends to rotate around a St Venant torsional centre, which is placed at the intersectional point of the bisectors of the angles, at equal perpendicular distant from all three sides of the cross-section, if the wall thickness is constant.

The lateral guiding constitutes a coupling between these for a laterally non-guided U profile independent degrees of freedom, the warping and the St.Venant torsion.

THE KOLLBRUNNER-HAJDIN THEORY

Like in the theory of guided beams, the idea of the Kollbrunner-Hajdin theory of box beams is to separate the shear deformation given rise by the constant shear stress flow around the tube, and the axial deformation from normal stresses caused by the deplanation of the cross-section. Shear deformations from the shear stresses given rise by this warping degree on freedom are neglected as small compared with the former. The shear deformation of the wall midline (profile line) is then:

$$\gamma_{xs}(x,s) = \frac{\partial u_x(x,s)}{\partial s} + \frac{\partial \upsilon_s(x,s)}{\partial x} - \gamma^*_{xs}(x) \tag{1}$$

In torsion the translation field in the profile line direction s is

$$\upsilon_s(x,s) = \theta_u(x) h_C(s), \tag{2}$$

where $h_C(s)$ is the perpendicular distance of the pole C from the profile line tangent drawn at point s. Then the axial translation field, in other words the deplanation at the profile line is:

$$u_x(x,s) = \int_{s_0}^{s} \left[\theta'_u(x) h_C(s) - \gamma^*_{xs}\right] ds = \theta'_u(x)\hat{\omega}(s) \text{ , from which is obtained} \tag{3}$$

$$\gamma^*_{xs} = \frac{\omega_C(4a+4b)}{4(a+b)}\theta'_u(x) \text{. Then:} \tag{4}$$

$$\hat{\omega}(s) = \omega_C(s) - \frac{s\omega_C(4a+4b)}{4(a+b)} = \int_0^s h_C(s)ds - \frac{s}{4(a+b)}\oint_S h_C(s)ds = \omega_C(s) - \frac{2ab}{a+b}s \tag{5}$$

$$\hat{\omega}_0 = \omega(b) - \frac{2ab}{a+b}b = ab - \frac{2b}{a+b}ab = \frac{a-b}{a+b}ab \tag{6}$$

Using the methods of the variational calculus, the following differential equation was obtained (3/, eq. III.32):

$$\rho E I_{\hat{\omega}} \theta_u^{(4)}(x) - G I_t \theta''_u(x) = m_C(x) \tag{7}$$

One more presupposition is that the moment load $m_c(x)$ is linear: in most general form in this formula is included an extra term including $m_c''(x)$ and first derivative of bimoment load, $b_c'(x)$.

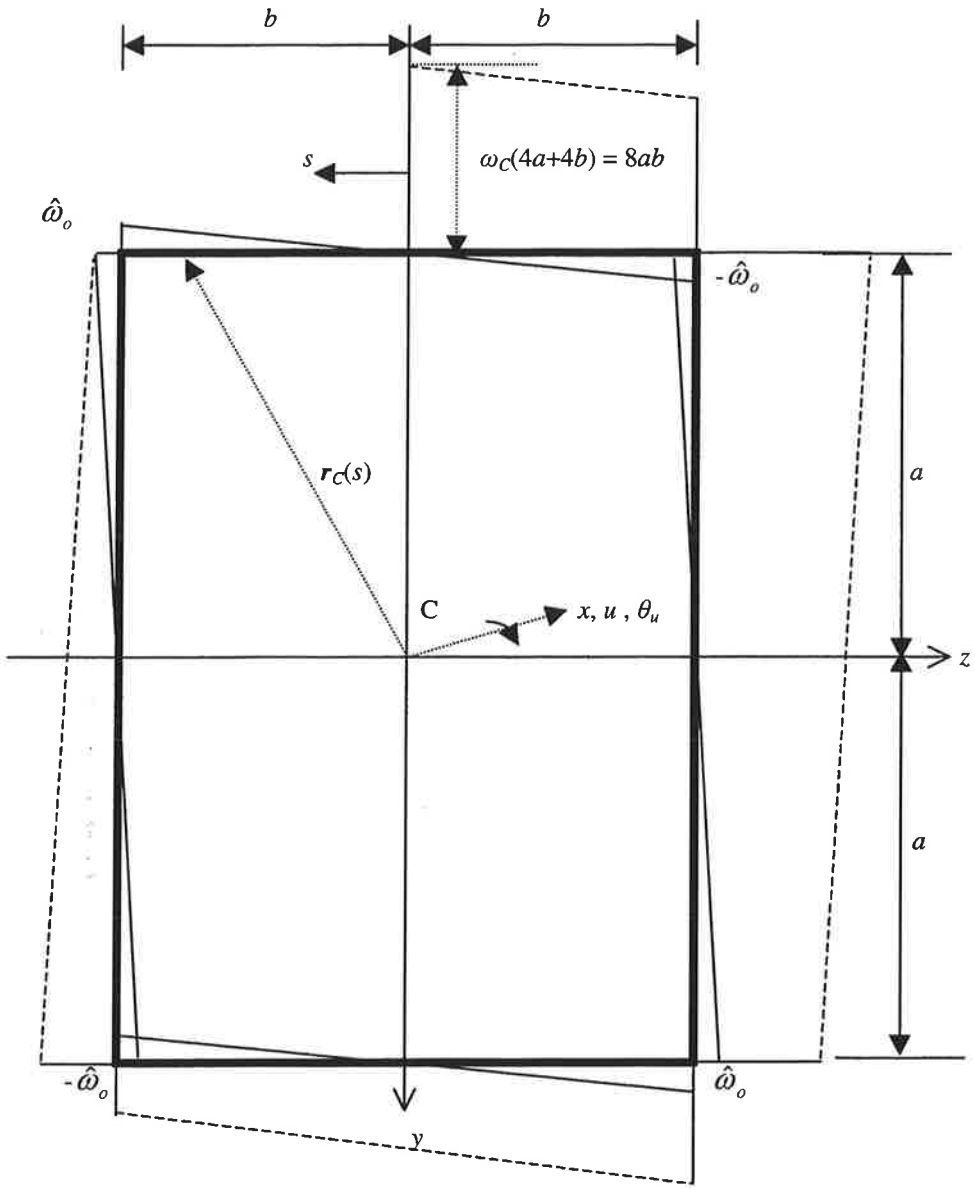

Figure 2. The deplanation form of the rectangle box cross-section according to the Kollbrunner-Hajdin theory

The sectorial quadratic moment

$$I_{\hat{\omega}} = \int_A \hat{\omega}^2(s)dA = \frac{4}{3}ta^2b^2\frac{(a-b)^2}{a+b} \tag{8}$$

The torsional moment of inertia of a closed cross-section

$$I_t = \frac{4t\Omega^2}{S} = \frac{4t16a^2b^2}{4(a+b)} = \frac{16ta^2b^2}{a+b} \tag{9}$$

The radial quadratic moment

$$I_h = \int_A {h_C}^2(s)dA = 4tab(a+b) \tag{10}$$

The coefficient in the differential equation (7)

$$\rho = \frac{I_h}{I_h - I_t} = \frac{4t(a+b)ab}{4t(a+b)ab - \frac{16ta^2b^2}{a+b}} = \left(\frac{a+b}{a-b}\right)^2 \tag{11}$$

So, for a rectangular box profile with constant wall-thickness t equation (7) takes the form

$$\frac{4}{3}Eta^2b^2(a+b)\theta_u^{(4)}(x) - \frac{16ta^2b^2}{a+b}\theta_u''(x) = m_{uC1}(x) \tag{12}$$

The bimoment is now obtained from equation (3/, III.39, the sign is different due to different systems of axes):

$$\hat{B}_C(x) = \rho EI_{\hat{\omega}}\theta''(x) \tag{13}$$

The normal stresses according to this theory are (3/,II.42):

$$\sigma_x(x,s) = \frac{\hat{B}_C(x)\hat{\omega}_C(x)}{I_{\hat{\omega}}} \tag{14}$$

There are some problems in the Kollbrunner-Hajdin theory. For instance, because both the shear flow stresses and the normal stresses give rise to angle of twist around the box centre C, so which of the angles of Figure 1. is θ_u(x) of the Kollbrunner-Hajdin theory? How to measure θ_u(x)? How does the model behave, when $a \to b$?

THE MECHANICAL MEANING OF THE TERMS OF THE KOLLBRUNNER-HAJDIN THEORY IN TERMS OF THE THEORY OF GUIDED BEAMS

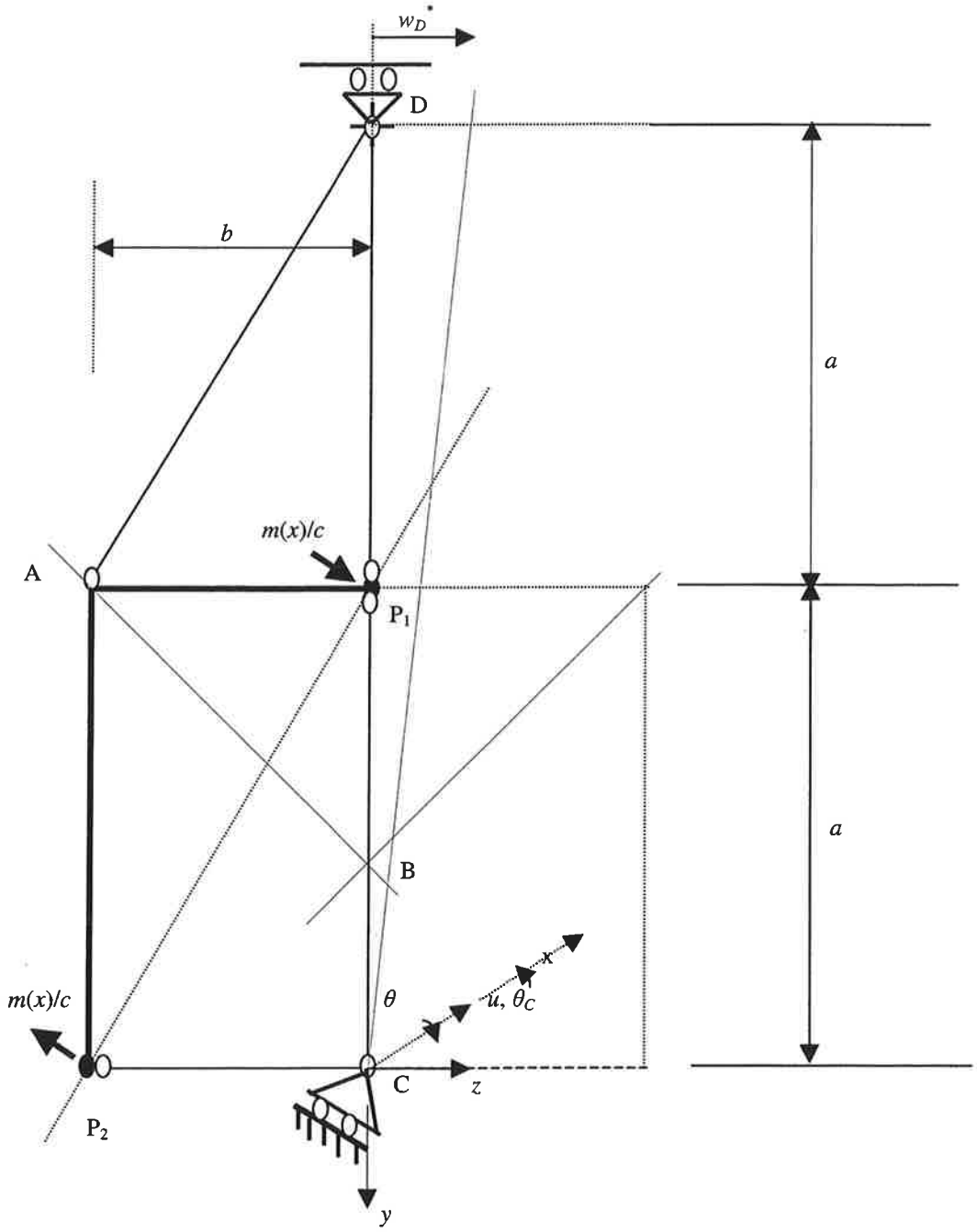

Figure 3. The quadrant of the box beam as a guided beam

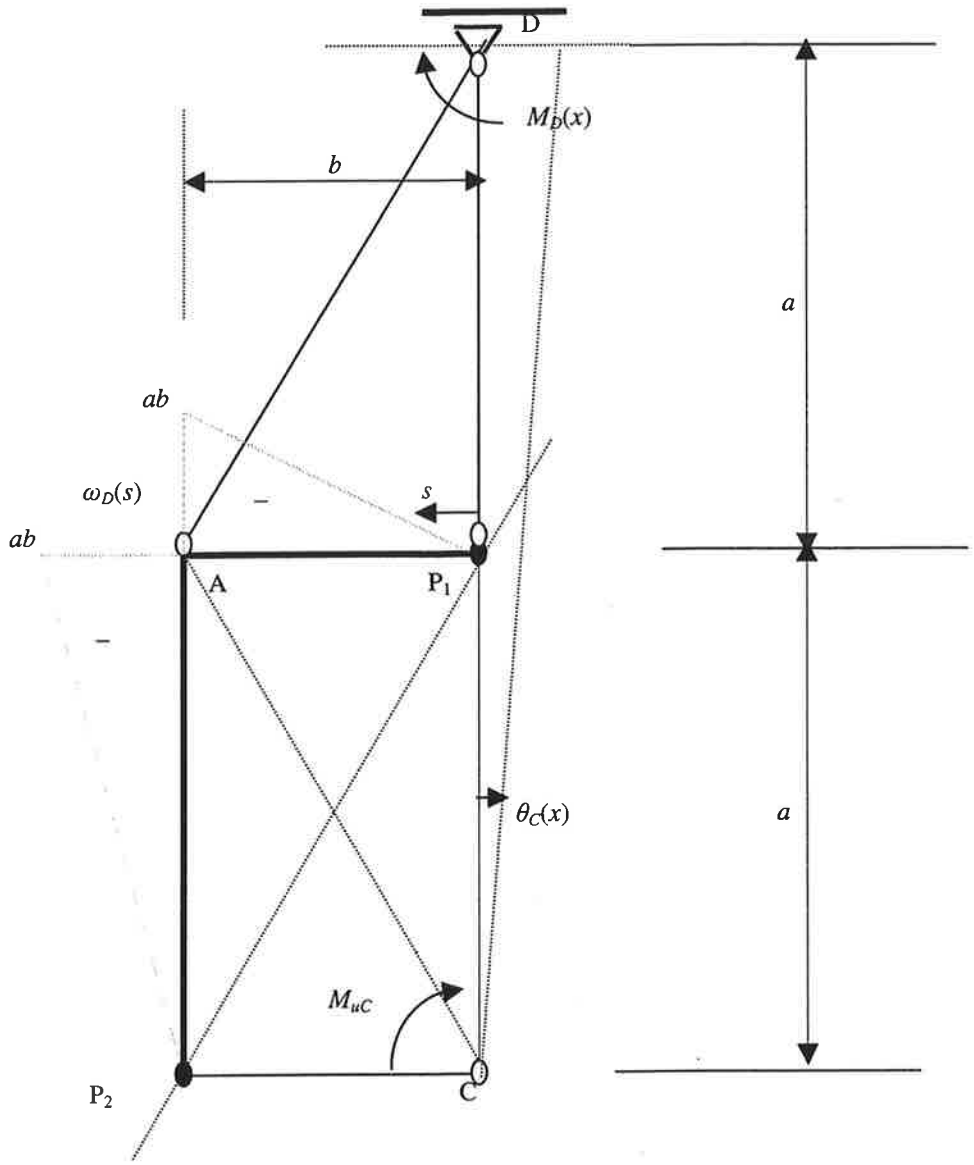

Figure 4. The sectorial areas, moments and the angle of twist $\theta_C(x)$.

We devide the half box from figure 1 further to two quadrants of the box profile, applying the information of the special points of the half pipe.

And we see still a little further: For the case of laterally non-guided angle cross-section the corner A is both the sectorial and StVenant torsional centre. Then it is the flexural axis along which the laterally non-guided deflection is measured, and it is also the axis of shear translation when the angle beam is loaded through this axis in parallel direction with the line P_1P_2. The deflection is perpendicular to this guided neutral axis of the cross-section. To match the deformations from warping around the guided sectorial pole D and twisting around the guided StVenant centre of twist C, we must match the translations of point (axis) A from these two degrees freedom of the cross-section.

Now, according to the rules of the theory of Guided Vlasov beams, for a case two axial non-compressible axes P_1 and P_2 a lateral pendulum support, the sectorial pole is situated at the intersectional point of the pendulum line and a line which is parallel to the line P_1P_2 and goes through the sectorial pole of the laterally non-guided cross-section (A). This intersectional point is D.

For D is allowed a perpendicular to the pendulum line shear translation, but not any deflection from normal stresses.

Such point at the pendulum line, around which the cross-section rotates without any tendency to deplanation and normal stresses, is the point B. But, we are not now constructing any best of all models of the problem in terms the theory guided beams, but seeking the mechanical interpretation of the Kollbrunner-Hajdin model in this new theory. This part of the model is allowable, although its evident that it is not exact. It is another, still more interesting task to find the best possible "exact" model. (A StVenant torsion around any other poin than B , for instance around C, means a model where there is a non-compressible axis also along the corner line A.)

The moments and bimoments are calculated in the usual terms of guided beams:

The bimoment:

$$B_D(x) = \iint_A \omega_D(s)\sigma_x(x,s)dA = EI_{\omega D}\theta''_{uD}(x) = EI_{\omega D}\theta''_{uC}(x) \tag{15}$$

The moment of the shear stresses from the bimoment warping, around D:

$$M_{uD}(x) = -B'_D(x) = -EI_{\omega D}\theta'''_{uC}(x) \tag{16}$$

The sectorial quadratic moment around D:

$$I_{\omega D} = \frac{1}{3}a^2b^2(a+b) \tag{17}$$

The StVenant torsional stiffness moment around C:

$$I_{t2} = \frac{[\omega_C(s_2) - \omega_C(s_1)]^2}{S} = \frac{4a^2b^2}{a+b} = \frac{I_{t1}}{4} \tag{18}$$

The moment of the shear flow stresses around C:

$$M_{uC}(x) = GI_{t2}\theta'_{uC}(x) \tag{19}$$

The total moment ist the sum the two moments:

$$M_u(x) = M_{uC}(x) + M_{uD}(x) \tag{20}$$

The equilibrium of torsional loads and moments:

$$M_u'(x) = M_{uC}'(x) + M_{uD}'(x) = -m_{u2}(x) \tag{21}$$

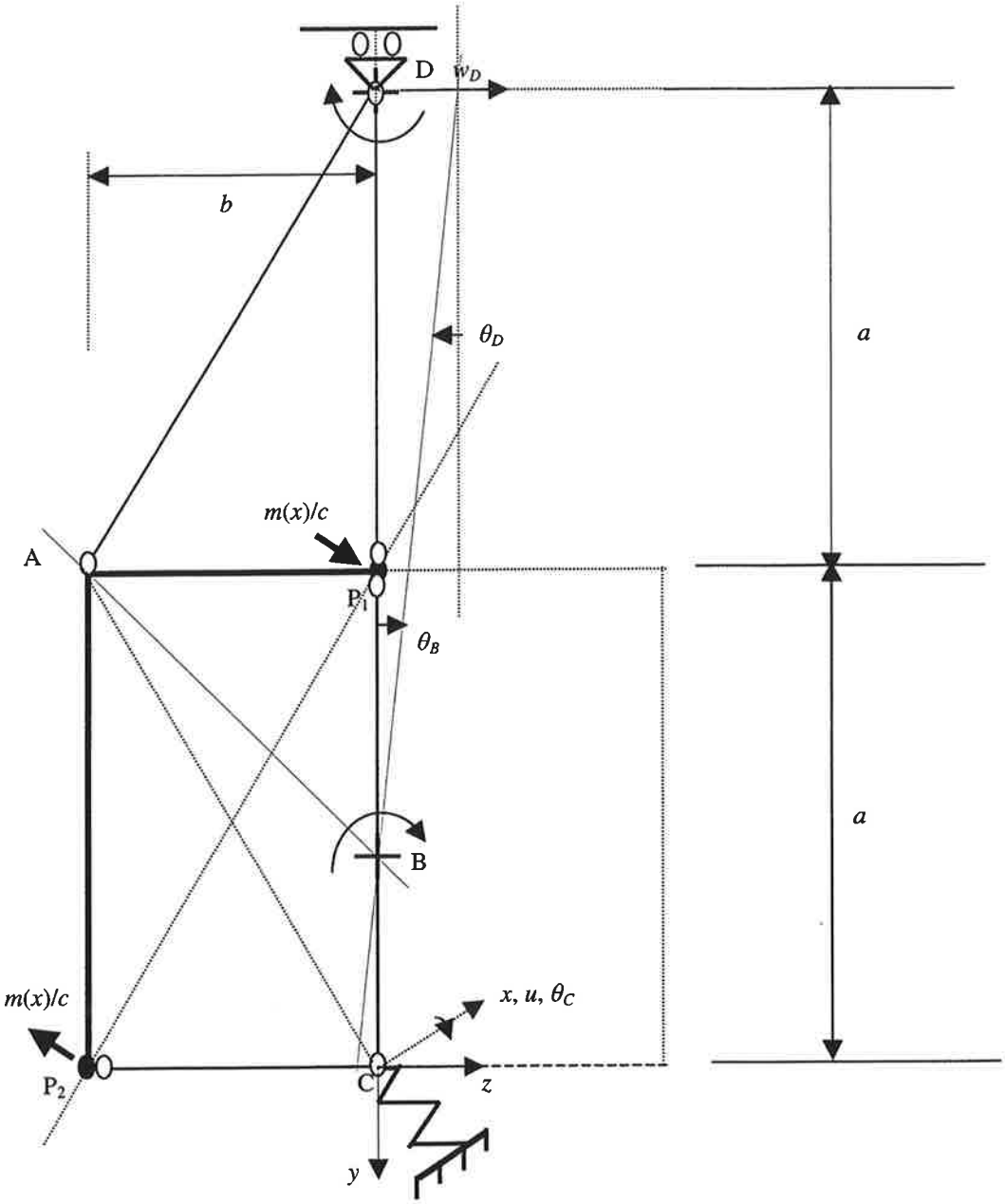

Figure 5. An advanced guided beam theory model of the torsional and distortional degrees of freedom for a rectangular box profile quadrant with flexible cross-section. The spring is due to the plate bending of the walls like in reference 2/. This is not the Kollbrunner-Hajdin model.

And finally from (16), (19) and (21) the equilibrium equation:

$$-EI_{\omega D}\theta_u^{(4)}(x)+GI_{t2}\theta_u'(x)=-m_u(x) \tag{22}$$

In terms of (17) and (18):

$$\frac{Et}{3}a^2b^2(a+b)\theta_u^{(4)}(x)-\frac{4Gta^2b^2}{a+b}\theta_u''(x)=-m_u(x)=-m_{C1}(x)/4 \tag{23}$$

Equation (24) is equal to equation (12), only multiplied by 4.

The normal stresses are now given from equation

$$\sigma_x(x,s)=\frac{B_D(x)\omega_D(x)}{I_{\omega D}} \tag{24}$$

Compared with the Kollbrunner-Hajdin solution the sectorial area and the bimoment are multiplied with $-(a+b)/(a-b)$, and the quadratic sectorial moment with $(a+b)^2/(a-b)^2$, so the stresses are the same.

DISCUSSION

The Kollbrunner-Hajdin model of torsion of rectangular box profiles, created using the variational method in order to model the influence of the normal stresses on the torsional stiffness properties of a box profile, is a model of torsion of a box beam with rigid cross-section. Accordig to this interpretation the two warpings, the bimoment and StVenant torsion act like two separate beams taking each one´s part on the total capacity.

Better models can be constructed based on the theory of guided beams, like in Figure 5. Another, allowable, but not "exact" model, is found in reference 2/

The notion *distortional centre* for the point D in this article is introduced y professor Erkki Niemi independent of the theory of Guided beam, as a point loaded through which symmetrically in torsion the beam does not distort.

REFERENCES

1/ Koivula, Risto: "Transformations of Force and Displacement Quantities between Different Systems of Axes and Special Points", Proceedings of the 2nd International Conference of Thin Walled Structures, Singapore 1998

2/ Koivula, Risto: "Analysis of Distortion of a Thin-Walled rectangle Beam Using the Theory of Guided Vlasov Beams" , Proceedings of the VII Finnish Mechanical Days, Tampere 2000

3/ Kollbrunner, Curt F. , Hajdin, Nikola: Dünnwandige Stäbe, Band 1, Zürich/Belgrad 1972

TELESKOOPPIPUOMIN MALLINTAMINEN ELEMENTTIMENETELMÄLLÄ

H. MARJAMÄKI*, J. MÄKINEN

*VTT, Tuotteet ja tuotanto
TTY, Teknillinen mekaniikka ja optimointi
s-posti: heikki.marjamaki@vtt.fi

TIIVISTELMÄ

Tässä työssä on esitetty, miten teleskooppipuomi voidaan mallintaa epälineaarista elementtimenetelmää käyttäen. Mallinnus on tehty siten, että syntyvä laskentamalli ei sisällä algebrallisia sidosehtoja. Puomi kootaan Reissnerin kinemaattiseen malliin perustuvista palkkielementeistä. Toisiinsa liittyvät liukuvat puomin osat on liitetty erityiselementeillä, joissa palkki-elementtiin liittyy liuku-jousielementti, joka on kytketty orjuutustekniikkaa käyttäen palkkielementin neutraaliakselille. Teleskooppiliike on toteutettu hydraulisylinteriä kuvaavilla pituuttaan muuttavilla sauvaelementeillä. Teleskooppisylinteri liikuttaa vain ensimmäistä jatkopuomia ja seuraava liukuva puomijäsen on kytketty edelliseen sisään- ja ulosvetoketjuja kuvaavalla kytkentäelementillä. Puomiston mallinnuksessa tarvittavat nivelet on toteutettu käyttäen palkkielementtejä, jotka sisältävät nivelen tarvitseman kinemaattisen kytkennän ja tarvittavat lisävapausasteet.

1 JOHDANTO

Monet työkoneet, joiden tehtävänä on nostaa tavaraa tai ihmisiä, on varustettu teleskooppipuomilla. Teleskooppipuomilla tarkoitetaan palkkirakennetta, jossa on tietty määrä sisäkkäin asetettuja palkkeja eli teleskooppijaksoja, jotka liukuvat toisiinsa nähden. Teleskooppiliike saadaan aikaiseksi tavallisesti hydraulisylinterillä, joka on kytketty ensimmäisen ja toisen jakson välille. Mikäli jaksoja on enemmän kuin kaksi, niin muita jaksoja liikutetaan yleensä sisään- ja ulosvetoketjujen välityksellä.

Tällaisen puomiston mallinnus FEM -valmisohjelmalla on hankalaa jo tasotapauksessa [3]. Mallinnus kolmiulotteisena tuo lisävaikeutta nivelten kuvauksen sekä suurten kiertymien muodossa. Mallinnus edellyttää sidosehtojen antamista toisiinsa nähden liukuvien teleskooppijaksojen välillä sekä rotaationivelten osalta. Myöskään hydraulisylintereiden kuvaamiseen ei ole valmiita elementtejä. Seuraavassa esityksessä on esitetty vaihtoehtoinen tapa mallintaa teleskooppipuomi käyttäen välitysketjua, hydraulisylintereitä, nivelpalkkia sekä liukumista kuvaavia erityiselementtejä.

Mekaanisen järjestelmän laskentamalli on ohjelmoitu käyttäen suurten siirtymien ja äärellisten rotaatioiden kinematiikkaa. Edelleen mekaanisen järjestelmän ainemalli on oletettu lineaariseksi. Liikettä toteuttavat hydraulisylinterit on mallinnettu käyttäen pituuttaan muuttavia sauvaelementtejä.

2 VIRTUAALISEN TYÖN PERIAATE

Mekaniikan tehtävissä ratkaistavana on tavallisesti ulkoisten kuormitusten vaikutuksesta muotoaan muuttava kappalesysteemi. Perustuntemattomana on tällöin yleensä kappalesysteemin siirtymäkenttä. Tällöin usein käytetty menetelmä tehtävän formuloinnissa on virtuaalisen työn periaate.Virtuaalisen työn lausekkeen

$$\delta W = \delta W_{\text{ext}} - \delta W_{\text{int}} - \delta W_{\text{acc}} = 0 \tag{1}$$

termit koostuvat ulkoisten voimien tekemästä virtuaalisesta työstä δW_{ext}, sisäisten voimien virtuaalisesta työstä δW_{int} ja hitausvoimien δW_{acc} virtuaalisesta työstä, missä miinus merkki on valittu siten, että sisäisten voimien ja hitausvoimien tekemä työ on vastakkaismerkkinen ulkoisten voimien tekemään virtuaaliseen työhön nähden.

Kun elementtimenetelmän mukainen diskretointi, interpolointi ja linearisointi on tehty, saadaan virtuaalisen työn periaatetta soveltamalla johdettua elementtien sisäiset solmuvoimat sekä tangenttioperaattorit, kuten jäykkyys- ja massamatriisit. Kinemaattiset sidokset voidaan upottaa malliin, erityisesti, mikäli ne ovat holonomisia eli yhtälötyyppisiä siirtymärajoituksia.

2.1 Vapausastemittausjärjestelmän muuttaminen

Kinemaattiset sidokset ja vapausastemittausjärjestelmän muuttaminen voidaan hoitaa seuraavaksi esitettävää orjuutustekniikkaa ("isäntä-orja") käyttäen. Perusajatus orjuutustekniikassa on esittää orjasiirtymät, jotka edustavat orjaelementin siirtymämuuttujia isäntäsiirtymien avulla [1]. Isäntäsiirtymät ovat vapausasteita, jotka syntyvät mallinnettaessa erilaisia kinemaattisia kytkentöjä, kuten joustava translaatioliitos, jonka vapausaste kuvaa liitettyjen elementtien asemaa toisiinsa nähden mitattuna elementin keskiviivaa pitkin.

Olkoon $\mathbf{f}$ derivoituva kuvaus kahden kytketyn siirtymämittausjärjestelmän $\mathbf{u}$ ja $\mathbf{v}$ välillä:

$$\mathbf{u} = \mathbf{f}(\mathbf{v}) \tag{2}$$

missä $\mathbf{u}$ on orjasiirtymävektori ja $\mathbf{v}$ vastaava isäntäsiirtymävektori. Tällöin orjasiirtymän $\mathbf{u}$ ja isäntäsiirtymän $\mathbf{v}$ välinen linearisoitu yhteys saadaan

$$\delta\mathbf{u} = D_{\mathbf{v}}\mathbf{f}(\mathbf{v}) \bullet \delta\mathbf{v} = \mathbf{B}(\mathbf{v}) \bullet \delta\mathbf{v} \tag{3}$$

missä $D_{\mathbf{v}}$ viittaa derivointiin isäntäsiirtymien $\mathbf{v}$ suhteen. Yhtälö (3) määrittelee kinemaattisen matriisin $\mathbf{B}(\mathbf{v})$, jonka avulla voidaan määrittää orjasiirtymien variaatiot $\delta\mathbf{u}$ kun isäntäsiirtymien variaatiot $\delta\mathbf{v}$ tunnetaan. Oletetaan vielä, että kinemaattisen matriisin $\mathbf{B}$ ranki on täysi.

Koska molemmissa mittausjärjestelmissä tehty virtuaalinen työ tulee olla yhtä suuri, on vastaavien voimamittausten välillä on yhteys

$$\delta W = \delta\mathbf{u} \bullet \mathbf{F}_{\mathbf{u}} = \delta\mathbf{v} \bullet \mathbf{F}_{\mathbf{v}} \tag{4}$$

ja vastaavien voimamittausten $\mathbf{F}_{\mathbf{v}}$ ja $\mathbf{F}_{\mathbf{u}}$ välinen yhteys saadaan sijoittamalla yhteys (3) yhtälöön (4)

$$\mathbf{F}_{\mathbf{v}} = \mathbf{B}^{\mathrm{T}}\mathbf{F}_{\mathbf{u}} \tag{5}$$

Edellä oleva yhtälö on erityisen tärkeä yhteys orjuutustekniikkaa käytettäessä. Jäykkyysmatriisi mittausjärjestelmässä $\mathbf{v}$ saadaan linearisoimalla voimamittausten välinen yhteys (5) pisteessä $\mathbf{v}_0$ tai vastaavassa orja-pisteessä $\mathbf{u}_0 = \mathbf{f}(\mathbf{v}_0)$ suuntaan $\Delta\mathbf{v}$ käyttäen mittausjärjestelmään $\mathbf{u}$ kuuluvia voimia:

$$\begin{aligned} \mathscr{I}(\mathbf{F}_{\mathbf{v}}; \Delta\mathbf{v}) &= \mathbf{B}^{\mathrm{T}}\mathbf{F}_{\mathbf{u}_0} + \mathbf{B}^{\mathrm{T}} D_{\mathbf{v}}(\mathbf{F}_{\mathbf{u}}) \bullet \Delta\mathbf{v} + D_{\mathbf{v}}(\mathbf{B}^{\mathrm{T}}\overline{\mathbf{F}}_{\mathbf{u}}) \bullet \Delta\mathbf{v} \\ &= \mathbf{F}_{\mathbf{v}_0} + \mathbf{B}^{\mathrm{T}}\mathbf{K}_{\mathbf{u}}\mathbf{B} \bullet \Delta\mathbf{v} + \mathbf{K}_{\mathbf{g}} \bullet \Delta\mathbf{v} \end{aligned} \tag{6}$$

Viiva orjamittauksen $\mathbf{F}_u$ päällä tarkoittaa, että voimaa pidetään vakiona derivoitaessa jälkimmäistä termiä, eli derivointi kohdistuu kinemaattiseen kytkentään. Yhtälö (6) määrittelee materiaalisen jäykkyysmatriisin, jonka lauseke nähdään toisesta termistä sekä geometrisen jäykkyysmatriisin $\mathbf{K}_g$, jonka lauseke saadaan jälkimmäisestä termistä. Massamatriisin $\mathbf{M}$ ja hitausvoimien vektorin $\mathbf{F}_{cent}$ määritykseen tarvitaan hitausvoimien tekemää virtuaalista työtä

$$\delta W_{acc} = \delta \mathbf{u} \cdot (\mathbf{M}_u \ddot{\mathbf{u}}) \tag{7}$$

Derivoimalla yhtälö (2) ajan suhteen, saadaan yhteys mittausjärjestelmien nopeuksien ja kiihtyvyyksien välille

$$\begin{aligned} \dot{\mathbf{u}} &= D_v \mathbf{f}(\mathbf{v}) \bullet \dot{\mathbf{v}} = \mathbf{B}\,\dot{\mathbf{v}} \\ \ddot{\mathbf{u}} &= \mathbf{B}\,\ddot{\mathbf{v}} + \dot{\mathbf{B}}\,\dot{\mathbf{v}} \end{aligned} \tag{8}$$

Sijoittamalla (8) yhtälöön (7) saadaan hitausvoimien virtuaalinen työ mittausjärjestelmässä $\mathbf{v}$

$$\begin{aligned} \delta W_{acc} &= \delta \mathbf{v} \bullet \mathbf{B}^T \mathbf{M}_u (\mathbf{B}\,\ddot{\mathbf{v}} + \dot{\mathbf{B}}\,\dot{\mathbf{v}}) \\ &= \delta \mathbf{v} \bullet \left(\mathbf{B}^T \mathbf{M}_u \mathbf{B}\,\ddot{\mathbf{v}} + \mathbf{B}^T \mathbf{M}_u \dot{\mathbf{B}}\,\dot{\mathbf{v}} \right) \end{aligned} \tag{9}$$

Massamatriisi ja nopeudesta riippuvien hitausvoimien aiheuttama solmuvoimavektori mittausjärjestelmässä $\mathbf{v}$ saadaan mittausjärjestelmän $\mathbf{u}$ vastaavien suureiden avulla

$$\begin{aligned} \mathbf{M}_v &= \mathbf{B}^T \mathbf{M}_u \mathbf{B} \\ \mathbf{F}_{cent} &= \mathbf{B}^T \mathbf{M}_u \dot{\mathbf{B}}\,\dot{\mathbf{v}} \end{aligned} \tag{10}$$

3 KIERTYMISLIIKKEEN KUVAUS KIERTYMÄVEKTORI AVULLA

Kiertymisliike voidaan esittää kiertymisoperaattoreiden avulla, joiden muodostama joukko määritellä kaavalla

$$SO(3) := \left\{ \mathbf{R} : \mathbb{E}^3 \to \mathbb{E}^3 \ \text{ lineaarinen } \middle| \mathbf{R}^T\mathbf{R} = \mathbf{I},\ \det \mathbf{R} = +1 \right\}. \tag{11}$$

Kiertymisoperaattori $\mathbf{R}$ on siis ortogonaalinen operaattori, joka säilyttää kuvauksessa alkuperäisen kätisyyden. Ortogonaalisuusehto asettaa kuusi toisistaan riippumatonta sidosehtoa kiertymisoperaattorille, jolloin kiertymisoperaattoreiden joukko $SO(3)$ muodostaa 3-uloitteisen pinnan, tai oikeammin moniston, 9-uloitteiseen – toisen kertaluvun tensoreiden muodostamaan – avaruuteen. Vastaavasti mikä tahansa kiertymisoperaattori voidaan esittää kiertymävektorin $\boldsymbol{\Psi}$ avulla, joka määritellään

$$\boldsymbol{\Psi} := \psi \mathbf{n}, \quad \mathbf{n} \in \mathbb{E}^3, \psi \in \mathbb{R}_+, \tag{12}$$

missä $\mathbf{n}$ on kiertymisakselin ykkösvektori $\|\mathbf{n}\| = 1$ ja ψ on positiivinen kiertymiskulma. Kiertymävektorin ja kiertymisoperaattorin välinen yhteys nähdään kuvasta 1, jolloin kiertyneeksi vektoriksi $\mathbf{p}_1$ saadaan

$$\begin{aligned} \mathbf{p}_1 &= \mathbf{p}_0 - \mathbf{r}_0 + \mathbf{r}_1 \\ &= \mathbf{p}_0 + (1 - \cos\psi)\mathbf{n} \times (\mathbf{n} \times \mathbf{p}_0) + \mathbf{n} \times \mathbf{p}_0 \sin\psi \\ &= \mathbf{R}\,\mathbf{p}_0. \end{aligned} \tag{13}$$

Näin saatu kiertymisoperaattori $\mathbf{R}$ voidaan myös kirjoittaa kiertymävektorin $\boldsymbol{\Psi}$ avulla muotoon

$$\mathbf{R} := \mathbf{I} + \frac{\sin\psi}{\psi}\tilde{\boldsymbol{\Psi}} + \frac{1 - \cos\psi}{\psi^2}\tilde{\boldsymbol{\Psi}}^2 = \exp\left(\tilde{\boldsymbol{\Psi}}\right), \quad \psi = \|\boldsymbol{\Psi}\|, \tag{14}$$

missä vinosymmetrinen tensori $\tilde{\boldsymbol{\Psi}}$ määritellään kaavalla

$$\tilde{\boldsymbol{\Psi}}\mathbf{h} = \boldsymbol{\Psi} \times \mathbf{h}, \qquad \forall \mathbf{h} \in \mathbb{E}^3. \tag{15}$$

Toisin sanoen $\tilde{\Psi}$ on akselivektoria Ψ vastaava vinosymmetrinen tensori. Vinosymmetristen tensoreiden avaruudelle käytetään tavallisesti $so(3)$ -merkintää.

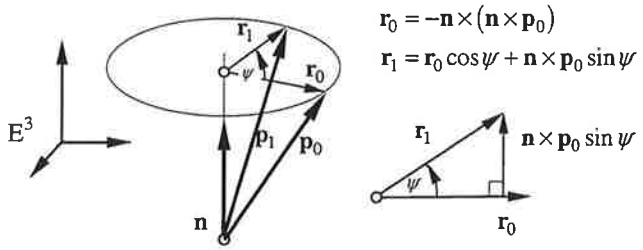

Kuva 1. *Kiertymisliike, jossa alkuperäinen vektori* $\mathbf{p}_0$ *kierretään akselin* $\mathbf{n}$ *ympäri vastapäivään kulman* ψ *verran vektoriksi* $\mathbf{p}_1$

Yhdistetyn kiertymän, siis kahden peräkkäisen kiertymisliikkeen, aineellinen esitysmuoto on

$$\mathbf{R}_{\text{uusi}} = \mathbf{R}\,\mathbf{R}_{\text{lisäys}} = \mathbf{R}\exp\left(\tilde{\Theta}_{\mathbf{R}}\right), \tag{16}$$

missä $\Theta_{\mathbf{R}}$ on aineellinen kiertymälisäysvektori pisteessä $\mathbf{R}\in SO(3)$. Uusi kiertymisoperaattori $\mathbf{R}_{\text{uusi}}$ saadaan siis kertomalla oikealta kiertymisoperaattorin lisäyksellä $\mathbf{R}_{\text{lisäys}}$, mikä vastaa kiertymälisäystä kiinteiden koordinaatistojen suhteen.

Derivoimalla yhteys $\mathbf{R}\exp(t\tilde{\Theta}_{\mathbf{R}})$ parametrin t suhteen ja asettamalla $t=0$ saadaan aineellinen tangenttiavaruus mielivaltaisessa kantapisteessä $\mathbf{R}\in SO(3)$

$${}_{\text{aine}}T_{\mathbf{R}}SO(3) := \left\{\tilde{\Theta}_{\mathbf{R}} := \left(\mathbf{R},\tilde{\Theta}\right)\middle|\ \mathbf{R}\tilde{\Theta},\ \mathbf{R}\in SO(3),\ \tilde{\Theta}\in so(3)\right\} \tag{17}$$

Merkintä $(\mathbf{R},\tilde{\Theta})$ edustaa vinosymmetristä tensoriavaruutta $\tilde{\Theta}\in so(3)$ kantapisteessä $\mathbf{R}\in SO(3)$. On huomattava, ettei tensoreita $\tilde{\Theta}_{\mathbf{R}}\in {}_{\text{aine}}T_{\mathbf{R}}SO(3)$ ja $\tilde{\Psi}_{\mathbf{I}}\in {}_{\text{aine}}T_{\mathbf{I}}SO(3)$ saa laskea yhteen vektoreiden suunnikassäännöllä, sillä ne eivät kuulu samaan tangenttiavaruuteen, ks. kuva 2

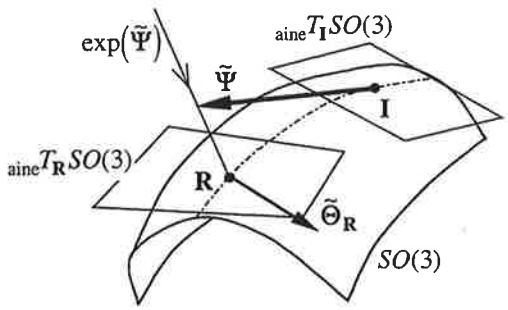

Kuva 2. *Aineellisten kiertymien ja niiden lisäysten geometrinen tulkinta*

Haetaan seuraavaksi kiertymävektorin lisäyksen ja kokonaiskiertymävektorin muutoksen välinen yhteys. Derivoidaan lauseke

$$\exp\left(\tilde{\Psi}+t\cdot\delta\tilde{\Psi}\right) = \exp\left(\tilde{\Psi}\right)\exp\left(t\cdot\delta\tilde{\Theta}_{\mathbf{R}}\right), \tag{18}$$

parametrin t suhteen ja asettamalla $t=0$, jolloin saadaan yhteys

$$\delta\Theta_R = \mathbf{T}\cdot\delta\Psi$$
$$\mathbf{T} := \frac{\sin\psi}{\psi}\mathbf{I} - \frac{1-\cos\psi}{\psi^2}\tilde{\Psi} + \frac{\psi-\sin\psi}{\psi^3}\Psi\otimes\Psi, \tag{19}$$
$$\psi := \|\Psi\|, \qquad \mathbf{R} = \exp(\tilde{\Psi}), \qquad \lim_{\Psi\to 0}\mathbf{T}(\Psi) = \mathbf{I},$$

missä $\delta\Psi$ on kokonaiskiertymävektorin variaatio, $\delta\Theta_R$ on kiertymälisäyksen variaatio ja $\mathbf{T}$ on tangenttimuunnos avaruuksien ${}_{\text{aine}}T_I SO(3) \rightarrow {}_{\text{aine}}T_R SO(3)$ välillä. Tangenttimuunnoksella $\mathbf{T}$ voidaan siis kuvata eri tangenttiavaruuksissa olevat kiertymävektorin variaatiot samaan tangenttiavaruuteen [5]. Määritellään tensoriavaruudelle (17) vastaava (aineellinen) vektoriavaruus

$${}_{\text{aine}}T_R := \left\{\Theta_R := \Psi + \Theta \;\middle|\; \mathbf{R} = \exp\left(\tilde{\Psi}\right) \in SO(3),\ \Theta \in \mathbb{E}^3\right\}, \tag{20}$$

jolloin tangenttimuunnos on kuvaus $\mathbf{T} : {}_{\text{aine}}T_I \rightarrow {}_{\text{aine}}T_R$. Merkintä (20) mahdollistaa kirjanpidon kiertymävektoreiden välillä, jotka sijaitsevat kiertymismoniston $SO(3)$ tangenttiavaruuksissa.

Kulmanopeudet ja kulmakiihtyvyydet – samoin kuin kaarevuudet – voidaan myös lausua kokonaiskiertymävektorin ja sen aikaderivaattojen sekä tangenttimuunnoksen $\mathbf{T}$ avulla

$$\begin{aligned}
&\Omega_R = \mathbf{T}(\Psi)\cdot\dot{\Psi}, && \Omega_R \in {}_{\text{aine}}T_R,\ \dot{\Psi},\Psi \in {}_{\text{aine}}T_I,\\
&\mathbf{A}_R = \mathbf{T}(\Psi)\cdot\ddot{\Psi} + \dot{\mathbf{T}}(\Psi,\dot{\Psi})\cdot\dot{\Psi}, && \mathbf{A}_R \in {}_{\text{aine}}T_R,\ \Psi,\dot{\Psi},\ddot{\Psi} \in {}_{\text{aine}}T_I,\\
&\mathbf{K}_R = \mathbf{T}(\Psi)\cdot\Psi', && \mathbf{K}_R \in {}_{\text{aine}}T_R,\ \Psi',\Psi \in {}_{\text{aine}}T_I,
\end{aligned} \tag{21}$$

missä $\Omega_R, \mathbf{A}_R, \mathbf{K}_R$ ovat aineelliset kulmanopeus- ja kulmakiihtyvyys- sekä kaarevuusvektori, ja $\dot{\Psi}$ on kokonaiskiertymävektorin aikaderivaatta, ja Ψ' on kokonaiskiertymävektorin paikkaderivaatta palkin pituusparametrin suhteen. Jäykän kappaleen liikkeen kuvausta on tarkemmin käsitelty lähteessä [7]

4 RAKENNEOSIEN MALLINNUS

Yksinkertaisuuden vuoksi tässä esityksessä ei kuvata eri elementtien massamatriisien lausekkeita. Kiinnostunut lukija löytää niitä alan kirjallisuuden lisäksi lähteistä [4] ja [6].

4.1 Pituuttaan muuttava sauvaelementti

Kuvassa 1 on esitetty pituuttaan muuttava sauvaelementti, joka on mahdollisimman yksinkertainen elementti hydraulisylinterin toiminnan mallintamiseen. Elementin kinematiikka perustuu insinöörivenymän käyttöön. Edelleen sauvan jännitysten ja venymien välisen yhteyden oletetaan noudattavan Hooken lakia. Sauvan kuormittamaton pituus L_c muuttuu ajan funktiona. Sauvan vastaava deformoitunut pituus on L_n.

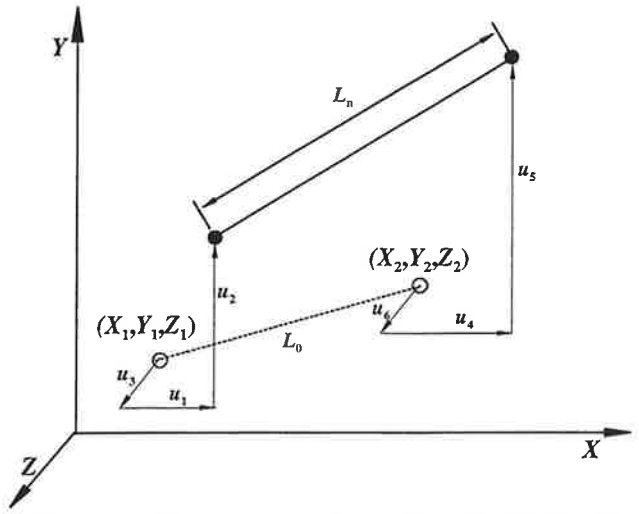

Kuva 3. *Pituuttaan muuttavan sauvaelementin alkutila (katkoviiva) ja deformoitunut tila (yhtenäinen viiva)*

Sauvan alkutilan deformoitumatonta tilaa mitataan asemavektorilla $\mathbf{X} = \{X_1\, Y_1\, Z_1\, X_2\, Y_2\, Z_2\}$. Elementtiä kuormitettaessa se siirtyy uuteen asemaan $\mathbf{x} = \mathbf{X} + \mathbf{u}$ ja syntynyttä deformaatiota mitataan solmusiirtymävektorilla $\mathbf{u} = \{u_1\, u_2\, u_3\, u_4\, u_5\, u_6\}$ kuvan 3 mukaisesti. Sauvan jännityksetön pituus ajan hetkellä t saadaan yhteydestä

$$L_c = L_0 + L(t) \tag{22}$$

missä L_0 sauvan pituus alkutilassa ja $L(t)$ pituuden muutos, joka siis on ajan funktio. Sauvan jäykän kappaleen liikkeestä riippumaton insinöörivenymä määritellään elementille

$$\varepsilon = \frac{L_n}{L_c} - 1 \tag{23}$$

Sauvan sisäisten solmuvoimien vektorin johtamiseksi tarvitaan sauvan venymän ensimmäinen variaatio

$$\delta\varepsilon = \frac{\delta L_n}{L_c} = \frac{1}{L_c L_n}\mathbf{x}^{\mathrm{T}}\mathbf{A}\,\delta\mathbf{u} = \mathbf{B}\,\delta\mathbf{u} \tag{24}$$

missä $\mathbf{B}$ on kinemaattinen matriisi (vaakavektori) virtuaalisten siirtymien $\delta\mathbf{u}$ ja virtuaalisten venymien $\delta\varepsilon$ välillä ja

$$\mathbf{A} = \begin{bmatrix} 1 & 0 & 0 & -1 & 0 & 0 \\ & 1 & 0 & 0 & -1 & 0 \\ & & 1 & 0 & 0 & -1 \\ & & & 1 & 0 & 0 \\ & & & & 1 & 0 \\ sym & & & & & 1 \end{bmatrix} \tag{25}$$

Summaamalla sauvan normaalijännitysten σ_E tekemä virtuaalinen työ elementin tilavuuden V_c yli saadaan sauvaelementin sisäisten solmuvoimien vektori

$$\mathbf{q}_{int} = \int_{V_c} \mathbf{B}^{\mathrm{T}}\sigma_E\, dV_c = \frac{A_0\sigma_E}{L_n}\mathbf{A}(\mathbf{X}+\mathbf{u}) = \frac{A_0 E\varepsilon}{L_n}\mathbf{A}\,\mathbf{x} \tag{26}$$

missä A_0 on sauvan alkuperäinen poikkileikkauksen pinta-ala, E on kimmomoduuli. Sauvan tangentiaalisen jäykkyysmatriisin lauseketta varten tulee sisäisten voimien lauseke linearisoida suuntaan $\Delta\mathbf{u}$ ja Δt

$$\mathscr{I}(\mathbf{q}_{\text{int}};\Delta\mathbf{u},\Delta t) = \mathbf{q}_{\text{int}0} + \left(\frac{A_0\sigma_E}{L_n}\mathbf{A} + \left(\frac{EA_0}{L_n^2 L_c} - \frac{A_0\sigma_E}{L_n^3}\right)\mathbf{A}\,\mathbf{x}\,\mathbf{x}^T\mathbf{A}\right)\bullet\Delta\mathbf{u} - \frac{EA_0\dot{L}}{L_c^2}\mathbf{A}\,\mathbf{x}\bullet\Delta t \qquad (27)$$

$$= \mathbf{q}_{\text{int}0} + \mathbf{k}_t\bullet\Delta\mathbf{u} + \dot{\mathbf{q}}_{\text{int}}\bullet\Delta t$$

missä $\mathbf{k}_t$ on tangentiaalinen jäykkyysmatriisi.

4.2 Kytkentäelementti

Kuvattaessa erilaisia kinemaattisia kytkentöjä, voidaan käyttää elementtiä, joka vetosuunnassa vastaa köyttä. Elementti ottaa kuitenkin köydestä poiketen vastaan myös puristuspuolen kuormitukset. Tämä käyttäytyminen on puhtaasti tarkoituksenmukaisuuskysymys ja tarvittaessa elementti voitaisiin korvata kahdella vain vetokuormituksen vastaanottavalla elementillä. Kytkentäelementti on esitetty kuvassa 4.

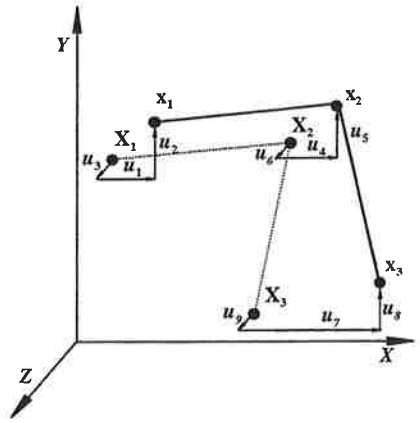

Kuva 4. *Kytkentäelementti alkutilassa (katkoviiva)ja deformoituneessa tilassa (yhtenäinen viiva)*

Kytkentäelementin siirtymättömässä tilassa sen kolmen solmun asema mitataan alkutilan yleistetyllä paikkavektorilla

$$\mathbf{X} = \{X_1\,Y_1\,Z_1\,X_2\,Y_2\,Z_2\,X_3\,Y_3\,Z_3\} = \{\mathbf{X}_1^T\,\mathbf{X}_2^T\,\mathbf{X}_3^T\} \qquad (28)$$

Elementtiä kuormitettaessa se siirtyy uuteen asemaan $\mathbf{x} = \mathbf{X} + \mathbf{u}$ ja syntynyttä siirtymää mitataan elementin solmusiirtymävektorilla

$$\mathbf{u} = \{u_1\,u_2\,u_3\,u_4\,u_5\,u_6\,u_7\,u_8\,u_9\} \qquad (29)$$

Elementin insinöörivenymä on

$$\varepsilon = \frac{L_n}{L_0} - 1 \qquad (30)$$

Sisäisten solmuvoimien vektorin johtamiseksi varioidaan venymän lauseke

$$\delta\varepsilon = \frac{\delta L_n}{L_0} = \frac{1}{L_0}\mathbf{x}^T\left(\frac{\mathbf{A}_1}{L_1} + \frac{\mathbf{A}_2}{L_2}\right)\delta\mathbf{u} = \mathbf{B}\,\delta\mathbf{u} \qquad (31)$$

missä matriisit $\mathbf{A}_1$ ja $\mathbf{A}_2$ ovat

$$\mathbf{A}_1 = \begin{bmatrix} 1 & 0 & 0 & -1 & 0 & 0 & 0 & 0 & 0 \\ & 1 & 0 & 0 & -1 & 0 & 0 & 0 & 0 \\ & & 1 & 0 & 0 & -1 & 0 & 0 & 0 \\ & & & 1 & 0 & 0 & 0 & 0 & 0 \\ & & & & 1 & 0 & 0 & 0 & 0 \\ & & & & & 1 & 0 & 0 & 0 \\ & & & & & & 0 & 0 & 0 \\ & & & & & & & 0 & 0 \\ sym & & & & & & & & 0 \end{bmatrix} \quad \mathbf{A}_2 = \begin{bmatrix} 0 & 0 & 0 & 0 & 0 & 0 & 0 & 0 & 0 \\ & 0 & 0 & 0 & 0 & 0 & 0 & 0 & 0 \\ & & 0 & 0 & 0 & 0 & 0 & 0 & 0 \\ & & & 1 & 0 & 0 & -1 & 0 & 0 \\ & & & & 1 & 0 & 0 & -1 & 0 \\ & & & & & 1 & 0 & 0 & -1 \\ & & & & & & 1 & 0 & 0 \\ & & & & & & & 1 & 0 \\ sym & & & & & & & & 1 \end{bmatrix} \tag{32}$$

Sisäisten solmuvoimien vektori saadaan sisäisten voimien virtuaalisen työn lauseketta soveltamalla muotoon

$$\mathbf{q}_{\text{int}} = \int_{V_0} \mathbf{B}^{\mathrm{T}} \sigma_{\mathrm{E}} \, dV_0 = A_0 \sigma_{\mathrm{E}} \left(\frac{\mathbf{A}_1}{L_1} + \frac{\mathbf{A}_2}{L_2} \right) \mathbf{x} \tag{33}$$

Tangentiaalinen jäykkyysmatriisi saadaan linearisoimalla sisäisten solmuvoimien vektori

$$\begin{aligned} \mathscr{L}(\mathbf{q}_{\text{int}}; \Delta\mathbf{u}) &= \mathbf{q}_{\text{int}\,0} + \left[A_0 \sigma_{\mathrm{E}} \mathbf{A} + \frac{E A_0}{L_0} \mathbf{A}\,\mathbf{x}\,\mathbf{x}^T \mathbf{A} - A_0 \sigma_{\mathrm{E}} \left(\frac{\mathbf{A}_1}{L_1^3} \mathbf{x}\mathbf{x}^T \mathbf{A}_1 + \frac{\mathbf{A}_2}{L_2^3} \mathbf{x}\mathbf{x}^T \mathbf{A}_2 \right) \right] \cdot \Delta\mathbf{u} \\ &= \mathbf{q}_{\text{int}\,0} + \mathbf{k}_{\mathrm{t}} \cdot \Delta\mathbf{u} \end{aligned} \tag{34}$$

missä on käytetty lyhennettä

$$\mathbf{A} = \frac{\mathbf{A}_1}{L_1} + \frac{\mathbf{A}_2}{L_2} \tag{35}$$

4.3 Epälineaarinen avaruuspalkkielementti

Seuraavassa esiteltävä lähteen [2] mukainen epälineaarinen avaruuspalkkielementti perustuu Reissnerin kinemaattisesti tarkkaan palkkiteoriaan, missä siirtymäkenttä mitataan kiinteään koordinaatistoon nähden. Rajoittaudutaan taas vain palkkielementtiin, jolla on kaksi solmua ja lineaariset muotofunktiot. Elementillä on kuusi solmuvapausastetta, kolme siirtymävapausastetta sekä kolme kiertymävapausastetta.

Palkin sisäinen solmuvoimavektori saadaan virtuaalisen työn periaatetta soveltamalla yhtälöstä

$$\mathbf{q}_{\text{int}} = \int_{L_0} \mathbf{B}^{\mathrm{T}} \mathbf{S} \, dL_0 \tag{36}$$

Kolmiulotteiselle palkkielementille kinemaattinen matriisi **B** on [2]

$$\begin{aligned} \mathbf{B} &= \begin{bmatrix} \mathbf{R}^{\mathrm{T}} & \mathbf{0} & \widetilde{\mathbf{R}^{\mathrm{T}} \mathbf{x}_0'} \mathbf{T} \\ \mathbf{0} & \mathbf{T} & \widetilde{\mathbf{K}} \mathbf{T} + \mathbf{T}' \end{bmatrix} \mathbf{Q} \\ \mathbf{Q} &= \begin{bmatrix} N_1' \mathbf{I} & \mathbf{0} & N_2' \mathbf{I} & \mathbf{0} \\ \mathbf{0} & N_1' \mathbf{I} & \mathbf{0} & N_2' \mathbf{I} \\ \mathbf{0} & N_1 \mathbf{I} & \mathbf{0} & N_2 \mathbf{I} \end{bmatrix} \end{aligned} \tag{37}$$

ja jännitysresultanttivektori $\mathbf{S} = \mathbf{D}_2\,\boldsymbol{\varepsilon}$, missä jännitysvektori $\mathbf{S}$ sisältää normaali- ja leikkausvoimakomponentit sekä vääntö- ja taivutusmomenttikomponentit. Palkin poikkileikkauksen jäykkyysmatriisi

$$\mathbf{D}_2 = diag\left[EA, GA_{sy}, GA_{sz}, GI_v, EI_y, EI_z\right] \tag{38}$$

koostuu aksiaalijäykkyydestä EA, leikkausjäykkyyksistä GA_{sy} sekä GA_{sz}, vääntöjäykkyydestä GI_v ja taivutusjäykkyyksistä EI_y ja EI_z. Yleistetty venymävektori $\boldsymbol{\varepsilon}$ määritellään

$$\boldsymbol{\varepsilon} = \begin{bmatrix} \boldsymbol{\Gamma} \\ \mathbf{K} \end{bmatrix} = \begin{bmatrix} \varepsilon_1 \\ \varepsilon_2 \\ \varepsilon_3 \\ \kappa_1 \\ \kappa_2 \\ \kappa_3 \end{bmatrix} = \begin{bmatrix} \mathbf{R}^{\mathrm{T}}\left(\mathbf{x}_0' - \mathbf{e}_1\right) \\ \mathbf{T}(\boldsymbol{\Psi})\boldsymbol{\Psi}' \end{bmatrix} \tag{39}$$

missä venymät ε viittaavat aksiaaliseen venymään ja leikkaumuodonmuutoksiin sekä κ kiertymään ja kaarevuuksiin. Palkkielementin tangentiaalinen jäykkyysmatriisi saadaan yhtälöstä

$$\mathbf{k}_t = \int_{L_0} \mathbf{B}^{\mathrm{T}}\mathbf{D}_2\,\mathbf{B}\,dL_0 + \int_{L_0} D_u(\mathbf{B}^{\mathrm{T}}\bar{\mathbf{S}})\,dL_0 \tag{40}$$

4.4 Epälineaarinen nivelellinen avaruuspalkkielementti

Tarkastellaan kuvan 5 mukaista avaruuspalkkielementtiä, jonka loppusolmussa on nivel, joka sallii kiertymisen akselin $\mathbf{n}_j$ ympäri. Elementti mallinnetaan käyttämällä orjuutustekniikkaa siten, että sen loppusolmun kohdalla oletaan lisäksi olevan orjasolmu, joka kuvaa nivelen kiertymistä.

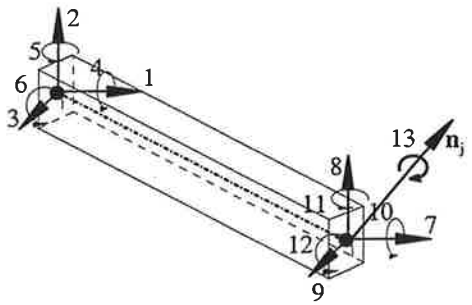

Kuva 5. Epälineaarinen nivelellinen avaruuspalkkielementti ja sen vapausastenumerointi

Kiertymisnivelelle on voimassa yhdistetyn kiertymisliikkeen esitysmuoto (16)

$$\mathbf{R}_s = \mathbf{R}_m\mathbf{R}_j, \tag{41}$$

missä $\mathbf{R}_s = \exp(\boldsymbol{\Psi}_s)$ orjasolmun s kiertymisoperaattori, ja $\mathbf{R}_m = \exp(\boldsymbol{\Psi}_m)$ on isäntäsolmun m kiertymisoperaattori. $\mathbf{R}_j = \exp(\varphi\mathbf{n}_j)$ on nivelen kiertymisoperaattori, missä φ nivelkiertymiskulma, ja $\mathbf{n}_j$ on nivelen kiertymisakseli. Varioimalla kaavaa (41) saadaan kinemaattinen yhteys

$$\delta\boldsymbol{\Theta}_s = \mathbf{R}_j^{\mathrm{T}}\delta\boldsymbol{\Theta}_m + \mathbf{n}_j\delta\varphi \tag{42}$$

missä $\delta\Theta_m \in {}_{mat}T_{R_m}$ and $\delta\Theta_s \in {}_{mat}T_{R_s}$ ovat isäntä- ja orjakiertymävektoreiden variaatioita. Nivelkiertymän variaatio $\mathbf{n}_j\delta\varphi$ kuuluu vastaavasti tangenttiavaruuteen ${}_{mat}T_{R_mRj} = {}_{mat}T_{R_s}$.

Sijoittamalla kaavaan (42) yhteydet $\delta\Theta_{s/m} = \mathbf{T}(\Psi_{s/m})\delta\Psi_{s/m}$, vertaa (19), saadaan haluttu relaatio kokonaiskiertymävektorin variaatiolle

$$\delta\Psi_s = \mathbf{B}_s\begin{pmatrix}\delta\Psi_m\\ \delta\varphi\end{pmatrix},$$
$$\mathbf{B}_s := \left(\mathbf{T}^{-1}(\Psi_s)\mathbf{R}_j^T\mathbf{T}(\Psi_m) \quad \mathbf{T}^{-1}(\Psi_s)\mathbf{n}_j\right), \tag{43}$$

missä $\mathbf{B}_s$ on kinemaattinen matriisi orja- ja isäntäkiertymävektorin sekä nivelen kiertymiskulman välillä. Elementin sisäisten solmuvoimien vektori saadaan nyt suoraan yhteydestä (5) ja tangentiaalinen jäykkyysmatriisi yhteydestä (6).

4.5 Offset-jousi-liukupalkkielementti

Kuvassa 6 on esitetty offset-jousi-liukupalkkielementin periaatekuva ja sen vapausasteet. Elementti koostuu palkkielementistä, jonka solmut on siirretty pois neutraaliakselilta ja johon on liitetty liuku-jousi. Jousi pääsee liukumaan vapaasti palkin neutraaliakselia pitkin. Tätä liikettä kuvaa vapausaste 19. Elementillä pyritään mallintamaan joustavaa johdeliitosta. Liitoksen joustavuus määräytyy jousielementin joustavuuden perusteella.

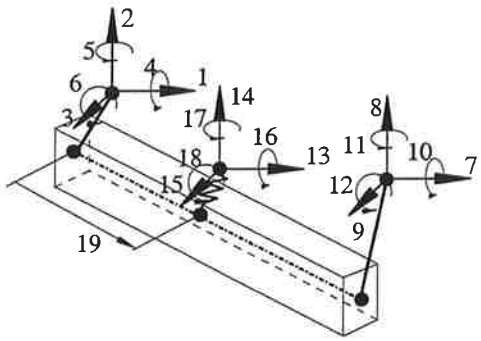

Kuva 6. Offset-jousi-liukupalkkielementti ja sen vapausasteet

Elementin sisäisten solmuvoimien vektorin ja tangentiaalinen jäykkyysmatriisin lausekkeet voidaan johtaa vastaavasti, kuin lähteessä [4] on esitetty.

5 LASKENTAESIMERKKI

5.1 Laskentamalli

Laskentamenetelmän testaamiseksi laadittiin elementtimetelmäohjelmisto, johon mallinnettiin kuvan 7 mukainen teleskooppipuomi. Puomissa on kaksi teleskooppijatketta ja sitä voidaan nostaa nostosylinteriä kuvaavalla pituuttaan muuttavalla sauvaelementillä numero 9 avulla. Teleskooppiliike toteutetaan teleskooppisylinteriä kuvaavalla elementillä numero 10 sekä katkoviivalla esitetyllä ketjua kuvaavalla kytkentäelementillä. Kuvassa olevat teleskooppiliikkeeseen liittyvät elementit on piirretty selvyyden vuoksi eri korkeuksille. Laskentamallissa ne sijaitsevat samalla suo-

ralla. Puomiston liike *Y*-akselin ympäri saadaan aikaan pituuttaan muuttavalla sauvaelementillä numero 17.

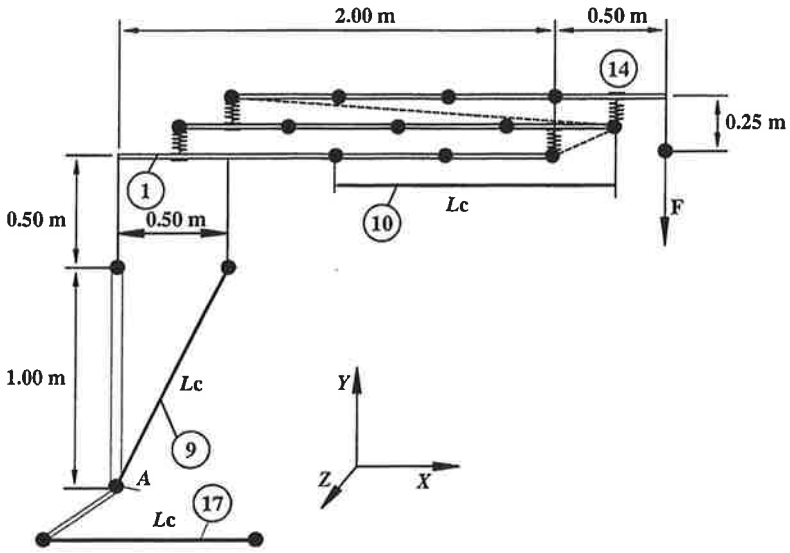

Kuva 7. Telekooppipuomin laskentamallin periaatekuva

Laskentamallin ratkaisemista sekä statiikan, että dynamiikan tehtävänä on käsitelty lähteessä [4].

5.2 Laskentatulokset

Kuvassa 8 on esitetty teleskooppipuomin jännityksettömät tilat laskennan alkaessa (vasen kuva) ja laskentajakson lopussa (oikea kuva).

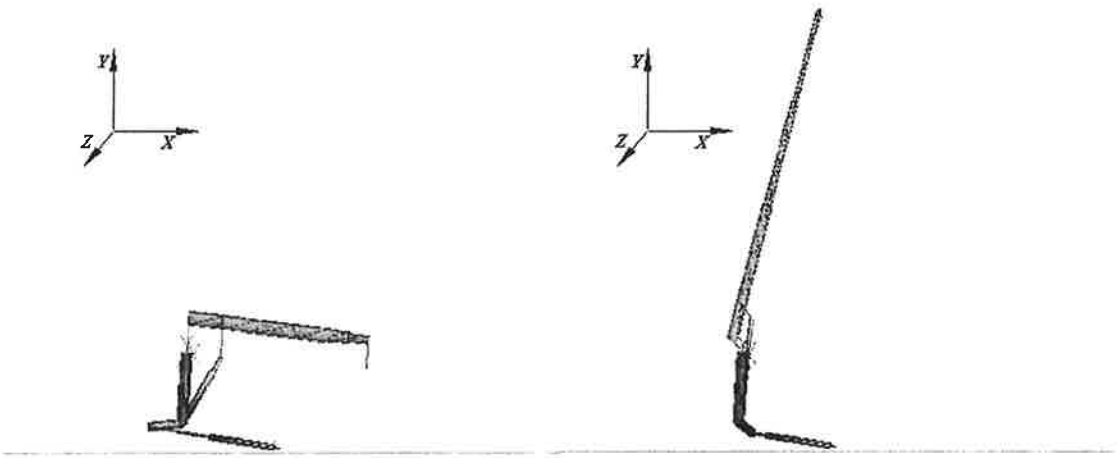

Kuva 8. Laskentamallin alkuasema (vasen kuva) ja siirtynyt tila (oikea kuva)

6 JOHTOPÄÄTÖKSET

Työssä on kuvattu lyhyesti eräs tapa mallintaa kolmiulotteinen joustava teleskooppipuomisto epälineaarista elementtimenetelmää käyttäen. Teleskooppiliikkeisiin sekä nivelten kiertymiin liittyvät liikkeiden sidosehdot on upotettu erilaisten erikoiselementtien kinemaattisiin kuvauksiin. Käytetty orjuutustekniikka johtaa minimimäärään vapausasteita ilman algebrallisia sidosehtoja. Tästä syystä edellä kuvatun kaltaisten avaruusmekanismien staattisten ja dynaamisten vasteiden laskennassa voidaan käyttää suuria askeleita.

Jatkotutkimuksena aihealuetta voisi laajentaa konemekanismien optimointiin, työkoneiden kaatumisvakavuuden määrittämiseen sekä erilaisten onnettomuustilanteiden analysointiin.

LÄHTEET

[1] Crisfield, M.A. (1997), Non-linear Finite Element Analysis of Solids and Structures, Vol. 2: Advanced Topics, J. Wiley & Sons, New York, 494 s.

[2] Géradin, M., Cardona, A. (2001), Flexible Multibody Dynamics: A Finite Element Approach, J. Wiley & Sons, New York, 327 s.

[3] Marjamäki H. (2000), Teleskooppipuomin mallintaminen tasossa, VII Suomen mekaniikkapäivät. Tampere, nide 1 sivut 177 – 185.

[4] Marjamäki H., Mäkinen J., (2003), Modelling Telescopic Boom – The Plane Case: Part I, hyväksytty julkaistavaksi Computers and Structures -lehdessä.

[5] Mäkinen, J., (2001), "Critical Study of Newmark-Scheme on Manifold of Finite Rotations", Computer Methods in Applied Mechanics and Engineering, 191(8-10), s. 817-828.

[6] Mäkinen, J., (2003), "Total Lagrangian Reissner's Geometrically Exact Beam Element without Singularities", lähetetty arvioitavaksi Computer Methods in Applied Mechanics and Engineering -lehteen.

[7] Mäkinen, J., (2003), "Eulerin differentiaaliyhtälön kuvaus kiertymismonistolta lineaariseen avaruuteen", VIII Suomen mekaniikkapäivät, Helsinki, 12-13.6.2003.

NEW CHALLENGES IN ICE SHEET SIMULATION

T. ZWINGER, P.-L. FORSSTRÖM

CSC – Scientific Computing Ltd.
Box 405, FIN-02101 Espoo
e-mail: Thomas.Zwinger@csc.fi

ABSTRACT

Model approaches for ice sheet simulations are presented. Basic concepts in computational glaciology are discussed. Special attention is turned on polythermal codes based on the widely used Shallow Ice Approximation (SIA), for which results obtained on the past glaciation of Eurasia with special focus on the Fennoscandian ice sheet will be discussed. Furthermore, an outlook on ongoing trends towards improved implementation of ice rheology as well as fully three-dimensional resolving ice sheet codes will be given.

1 INTRODUCTION

Earth's cryosphere, mainly consisting of ice sheets (land-based ice masses of continental size) and ice shelves (floating ice nourished from adjacent ice sheets) is a good indicator for global long-term temperature and thus climate changes (e.g., greenhouse effect). On the other hand, simulation of past time glaciation can help to understand the distribution of geologic features such as end moraines and thus also play an important role in reconstruction of geologic events during glaciation. This makes ice sheet simulations a valuable tool to understand past climate dynamics as well as to develop an understanding of future climatic trends.

The high sensitivity of ice sheets with respect to the thermal (temperature, heat-flux) as well as mechanical (mass accumulation/ablation, calving, transition into floating ice) boundary conditions makes external forcing a key issue in an ice sheet simulation. The embedding of an ice sheet in its surrounding environment is depicted in Fig. 1. The mathematical formulation of these boundary conditions will be discussed later in this article.

2 ICE SHEET EQUATIONS

Ice sheet models are currently extensively used in order to simulate the dynamics of ice sheets in the past, present and also to plot future scenarios. The field equations, many of these models are based on, have been formulated by Fowler and Larson [1] as well as Hutter [2]. The issue of more recent trends on introducing anisotropic behavior of the material will be raised later in this article.

2.1 Ice rheology

The material properties of ice are very much dependent on its temperature. Hence, a tight thermo-mechanical coupling is a key feature of ice flow models. This fact is also reflected in the theoretical flow laws of ice.

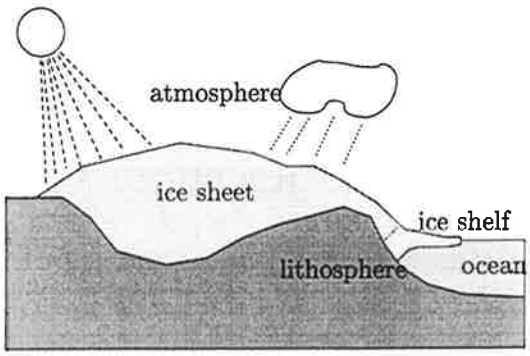

Figure 1: Interaction of an ice sheet with the surrounding environment. Processes in the atmosphere, ocean and lithosphere contribute to the mass balance as well as the energy balance of the ice sheet

The homologous temperature,

$$T' = T - T_{\mathrm{M}} \tag{1}$$

is defined as the difference between the local temperature, T, and the pressure melting point,

$$T_{\mathrm{M}} = T_0 - \beta^* p. \tag{2}$$

Here $T_0 = 0\,^{\circ}\mathrm{C}$ stands for the melting temperature at normal conditions, p is the pressure field and β^* the Clausius-Clapeyron constant [3].

Depending on the homologous temperature, two principal types of ice can be distinguished:

- **Cold ice** is frozen water showing a temperature below the pressure melting point, $T' < 0$. It has the property of a highly viscous, incompressible single phase fluid.
- **Temperate ice** is ice exactly at the pressure melting point, $T' \equiv 0$. Up to 5% of its volume may exist in form of liquid water. Hence, compared to cold ice temperate ice is softer and in principle a two component mixture.

Most modern ice sheet simulation codes utilize an isotropic stress-strain relation for cold as well as temperate ice in form of a power law [4],

$$\mathbf{D} = E\,A\,\sigma^{n-1}\mathbf{T}^{\mathrm{R}}. \tag{3}$$

This law relates the strain rate tensor, $\mathbf{D}$, to the stress deviator, $\mathbf{T}^{\mathrm{R}}$, introducing a **rate factor**, A, and a creep response function that is proportional to the power $(n-1)$ of the effective shear stress, $\sigma = \sqrt{1/2\,\mathrm{tr}(\mathbf{T}^{\mathrm{R}2})}$. An additional **enhancement factor**, E, is commonly used to model ice fluidity changes due to embedded sediment and/or polycrystal effects [3]. In cold ice, the rate factor is depending on the homologous temperature, whereas in temperate ice the water mass fraction, w, takes the role as main thermodynamic quantity.

2.2 Field equations

The mass balance for the cold ice as well as for the ice water mixture in the temperate regions is the one written for an incompressible fluid,

$$\operatorname{div} \mathbf{v} = 0. \tag{4}$$

Here $\mathbf{v}$ is the ice particle velocity for cold ice or the baricentric mixture velocity for temperate ice, respectively.

Splitting the stress tensor into an isotropic part (i.e., pressure) and the deviatoric stress,

$$\mathbf{T} = -p\,\mathbf{1} + \mathbf{T}^{\mathrm{R}}, \tag{5}$$

we obtain the formulation for the momentum balance,

$$-\mathbf{grad}\, p + \operatorname{div} \mathbf{T}^{\mathrm{R}} + \rho\,\mathbf{g} = \rho\,\dot{\mathbf{v}}. \tag{6}$$

The acceleration due to gravity, $\mathbf{g}$, is taken to be aligned with the z-direction of the applied coordinates. The density, ρ, is taken to be constant. Dealing with highly viscous flow, the acceleration on the right-hand side of (6) (the dot above the variable indicates the total time derivative) usually can be set to zero, i.e., pure Stokes flow prevails [4]. Taking (3) as the the stress-strain rate relation in the second term on the right-hand side of (6), the rate factor is expressed using an Arrhenius law,

$$A(T') = A_0\, e^{-Q/R(T_0+T')}. \tag{7}$$

Whereas $R = 8.314\,\mathrm{J\,mol^{-1}\,K^{-1}}$ is a constant (universal gas constant), the activation energy, Q, and A_0 are set according to the temperature regime [3],

$$\begin{array}{ll} T' \leq -10^\circ\,\mathrm{C}: & 60\,\mathrm{kJ\,mol^{-1}}, \\ T' \geq -10^\circ\,\mathrm{C}: & 139\,\mathrm{kJ\,mol^{-1}}, \\ T' \equiv -10^\circ\,\mathrm{C}: & A = 5.2 \cdot 10^{-25}\,\mathrm{s^{-1}\,Pa^{-3}}. \end{array} \tag{8}$$

Mind that values in the transitional range (i.e., $-10^\circ\,\mathrm{C} < T' < 0^\circ\,\mathrm{C}$) are fitted rather than experimentally determined.

Thermodynamics plays an essential role in ice sheet models. Consequently, an energy balance has to be defined for the cold ice region,

$$\rho\,\dot{\epsilon} = -\operatorname{div} \mathbf{q} + \operatorname{tr}\left(\mathbf{T}^{\mathrm{R}}\,\mathbf{D}\right). \tag{9}$$

The total temporal change (local and convective) of internal energy consists of the conductive heat transport plus viscous heat production on the right-hand side of (9). Additional constitutive relations in order to express the heat flux and the internal energy, ϵ, as a function of temperature, T, are to be introduced into (9). Whereas the first of this constitutive relations is expressed in form of a Fourier type heat conduction law,

$$\mathbf{q} = -\kappa(T)\operatorname{div} T, \tag{10}$$

the latter is given by the caloric equation of state,

$$\dot{\epsilon} = c(T)\,\dot{T}. \tag{11}$$

Both, the heat conductivity for cold ice, $\kappa(T)$, as well as the specific heat, $c(T)$, are taken to be functions of the temperature.

In temperate ice the temperature by definition is equal to the pressure melting point, $T \equiv T_{\mathrm{M}}$, and hence immediately follows from the the pressure field, c.f. equation (2). Consequently, the water mass fraction, w, takes the role of the dominant thermodynamic field variable. The balance equation for this variable takes the following form

$$\rho \dot{w} = -\mathrm{div}\,\mathbf{j} + M. \tag{12}$$

The diffusive mass flux – i.e., the water motion, $\mathbf{v}_{\mathrm{w}}$, relative to the baricentric velocity of the mixture – may be expressed by a Fickian law,

$$\mathbf{j} = \rho w \cdot (\mathbf{v}_{\mathrm{w}} - \mathbf{v}) = -\nu\, \mathbf{grad}\, w. \tag{13}$$

The diffusivity, ν, is taken to be constant. In comparison to (9), the energy balance in the temperate ice region,

$$\rho \dot{\epsilon} = \rho \cdot \left(L \dot{w} + c \dot{T}_{\mathrm{M}} \right) = -\mathrm{div}\,(\mathbf{q} + L\mathbf{j}) + \mathrm{tr}\left(\mathbf{T}^{\mathrm{R}}\,\mathbf{D}\right), \tag{14}$$

additionally accounts for the contribution of latent heat, L, to the internal energy as well as the heat flux . The conductive heat flux, $\mathbf{q}$, takes the same form as (10). Comparison between (12) and (14) implies that the net melting rate is of the following form [4]

$$M = \frac{1}{L} \cdot \left[\mathrm{tr}\left(\mathbf{T}^{\mathrm{R}}\,\mathbf{D}\right) - \mathrm{div}\,\mathbf{q} - \rho c \dot{T}_{\mathrm{M}} \right]. \tag{15}$$

Summing up, the mass balance (4) as well as the momentum balance (6) have to be solved with the according flow law inserted in the cold as well as in the temperate ice region. The balance equation describing the thermodynamic condition in the cold ice region is given by (9) the one for the temperate region by (12).

Models that account for a temperate ice layer are called **polythermal models**. Temperate layers normally are very shallow and narrow areas situated at the bedrock. Hence, it is commonly sufficient to account for these layers by imposing different kinematic and dynamic boundary conditions at the bed rock and treating the whole ice core to consist of cold ice. This strategy is reflected by the name **cold ice models**.

2.3 Boundary- and transition conditions

Mass exchange at the boundary between the atmosphere and the ice sheet is reflected by the **accumulation-ablation function**, $a_{\perp}^{(\mathrm{s})}$, appearing on the right hand side of the evolution equation of the implicit free surface function, $F_{\mathrm{s}} = z - h(x, z, t)$, i.e., the kinematic boundary condition,

$$\frac{\partial F_{\mathrm{s}}}{\partial t} + \mathbf{v}^{-} \cdot \mathbf{grad}\, F_{\mathrm{s}} = -\|\mathbf{grad}\, F_{\mathrm{s}}\| \cdot a_{\perp}^{(\mathrm{s})}(\mathbf{x}, t). \tag{16}$$

The symbol h stands for the vertical coordinate of the free surface. The dynamic and thermodynamic boundary condition are given in form of a stress free surface, $\mathbf{T}^{\mathrm{R}} \cdot \mathbf{grad}\, F_{\mathrm{s}} = \mathbf{0}$, and a prescribed surface temperature, $T = T_{\mathrm{s}}(\mathbf{x}, t)$, respectively. It is important to stress the fact that the properties $T_{\mathrm{s}}(\mathbf{x}, t)$ and $a_{\perp}^{(\mathrm{s})}(\mathbf{x}, t)$ have to be provided by external forcing. Their influence on the ice sheet dynamics is essential and hence the quality of the results of the ice sheet simulation very much depend on the quality of this input data. In principle there are two ways to evaluate the surface temperature and the accumulation-ablation function:

- As analytical expressions obtained from statistical climate data
- As boundary values of computed properties from a Global Climate Model (GCM) in combination with statistical data

In the past the previous of these two methods preferably was utilized in ice sheet simulations. This was mainly due to the fact that in comparison with ice sheet simulations, GCM's show a very much higher demand on computational resources. Recently attempts to embed ice sheet simulations in a GCM have increased (e.g., [5]). The results, nevertheless, still show the need of improvement of this type of external forcing.

Depending on the homologous temperature, different types of boundaries can be identified at the bottom (i.e., the bedrock):

- A **cold ice base** is given if a cold ice core is solid frozen to the bedrock
- A **temperate ice base** is given if temperate conditions appear at the boundary with the cold ice core
- A **temperate layer base** occurs in polythermal ice sheet models if a temperate ice layer is adjacent to the bedrock (water drainage may occur in this layer)

The bedrock underneath the ice sheet is displaced by its overburden. In technical terms, this is equal to a Fluid Structure Interaction (FSI) problem. Commonly, quite simple concepts of delayed isostatic displacement (i.e., the lithosphere dipping into the underlying asthenosphere – the liquid part of Earth's crust) in response to a change of the ice load are sufficient to account for bedrock displacement [6]. As a result of such a model the bedrock elevation, $b(x,y,t)$, and, consequently, the implicit function describing the bedrock, $F_\mathrm{b}(\mathbf{x},t) = b(x,y,t) - z$, are obtained. In analogy to (16), this function appears in the kinematic boundary condition at the bedrock,

$$\frac{\partial F_\mathrm{b}}{\partial t} + \mathbf{v}^- \cdot \mathbf{grad}\, F_\mathrm{s} = -\|\mathbf{grad}\, F_\mathrm{b}\| \cdot a_\perp^{(\mathrm{b})}. \tag{17}$$

The melting rate at the bedrock (i.e., water volume flux through the bedrock), $a_\perp^{(\mathrm{b})}$, is – due to the lack of water and the fact that ice cannot penetrate the bedrock – not existing at the cold ice base. Nevertheless, it has to be modeled for a temperate layer base (e.g., [4]).

The dynamic boundary condition is given in form of a friction law,

$$\mathbf{v}_\parallel = C_\mathrm{slip}\mathbf{t}_\parallel, \tag{18}$$

with the tangential velocity, $\mathbf{v}_\parallel = \mathbf{v} - \mathbf{n}\,(\mathbf{v}\cdot\mathbf{n})$, and the basal shear stress, $\mathbf{t}_\parallel = \mathbf{T}^\mathrm{R}\cdot\mathbf{n} - \mathbf{n}\,[(\mathbf{T}^\mathrm{R}\cdot\mathbf{n})\cdot\mathbf{n}]$. The surface normal is defined as

$$\mathbf{n} = \frac{\mathbf{grad}\, F_\mathrm{b}}{\|\mathbf{grad}\, F_\mathrm{b}\|}. \tag{19}$$

For cold ice base a no-slip condition is imposed, which is expressed by vanishing slip-coefficient, $C_\mathrm{slip}|_{T'<0} = 0$. In the case of a temperate base, a model relating this coefficient to the field variables, $C_\mathrm{slip}|_{T'=0} = C_\mathrm{slip}(\mathbf{T}^\mathrm{R}\cdot\mathbf{n},\dots)$, has to be provided (e.g., [7]). In the case of floating ice (i.e., ice shelves) no condition on the tangential component of the velocity is imposed. This is equivalent to a vanishing shear stress.

The thermodynamic boundary condition at the bedrock is given by the energy jump relation. This is expressed by

$$\mathbf{q} - \mathbf{q}_{\perp} = -\mathbf{v}_{\parallel} \cdot \mathbf{T}^{\mathrm{R}} \cdot \mathbf{n}, \tag{20}$$

with $\mathbf{q}_{\perp}$ standing for the heat flux from the lithosphere entering the ice core perpendicular to the bedrock surface. In last consequence, $\mathbf{q}_{\perp}$ is obtained from the solution of the heat conduction equation inside the lithosphere with the geothermal heatflux as boundary condition at the interface with the asthenosphere [4]. If slip occurs at the bedrock, the viscous heating at the right-hand side in (20) also contributes to the jump condition for internal energy.

In polythermal ice sheet models the so called Cold-temperate Transition Surface (CTS) is situated at the interface between cold and temperate ice layer. Additional transition conditions in form of jump relations for mass, momentum and energy have to be provided. These jump relations have to account for the fact that phase transition occurs at the CTS [4].

2.4 Shallow Ice Approximation

The previously derived equations for the (polythermal) ice sheet until recently have been of too high complexity for a direct numerical implementation for an ice sheet of continental size. This is basically caused by the fact that in a truly three-dimensional model approach horizontal, ΔL, have to be of the same order of magnitude as vertical spatial resolutions, ΔH. Taking the total present ice volume of Antarctica of about $3 \cdot 10^7\,\mathrm{km}^3$ [8], a grid spacing in the range of 1 km would result in a total amount of up to 10^8 computational cells. Even for fairly smaller problem sizes only modern supercomputer are capable of dealing with problems of such dimensions. For the resolution of internal ice sheet features (such as enclosed ice lakes) even finer resolutions may be needed.

As a consequence of this discrepancy caused by the large scales of ice sheets, most ice sheet models utilize a scaling technique known as the Shallow Ice Approximation (SIA) [9] in order to reduce the size, not of the physical but of the computational problem. The basic idea behind this procedure is to make the governing equations dimensionless. A complete discussion on the basis of Dimensional Analysis would go beyond the scope of this article. Essentially for the understanding of the SIA is the fact that, out of in total 17 obtained dimensionless products [4], the aspect ratio, $\varepsilon = H/L = V_{\mathrm{H}}/V_{\mathrm{L}}$, and the Froude number, $\mathrm{Fr} = V_{\mathrm{L}}^2/g \cdot L$, take on very small values. The aspect ratio is defined as the ratio of the characteristic vertical, H, to horizontal, L, extent of the ice sheet. Due to (4), the ratio between vertical, V_{H}, and horizontal, V_{L}, velocity shows the same order of magnitude. The Froude number is defined with respect to the horizontal spatial and velocity scales as well as the absolute value of the acceleration due to gravity, g. The SIA then is obtained by the double limit,

$$\varepsilon \to 0, \quad \frac{\mathrm{Fr}}{\varepsilon} \to 0, \tag{21}$$

if terms of order $\mathcal{O}(\varepsilon^m)$, with $m \geq 1$, are neglected in the governing equations [4]. The cells of the computational discretization applying SIA have to show the same ratio,

$$\Delta H/\Delta L = \mathcal{O}(\varepsilon). \tag{22}$$

Compared to the truly three-dimensional approach the amount of needed computational cells for the same vertical resolution is reduced by a factor of ε^2 – indeed a significant reduction.

The basic drawback of the SIA is given by the fact, that this asymptotic theory breaks down, if – to what reason ever – (21) is violated. This certainly is the case at strongly inclined ice margins and at very high ice domes. From the scientific point of view, nevertheless, these regions are of particular interest.

Ice shelves also obey the equations obtained by SIA [10], but the characteristic scales differ from these used in ice sheets. Consequently, matching a SIA ice shelf model to an ice sheet model is a multi-scale problem and hence a mathematically very difficult task.

3 SIMULATION OF THE EURASIAN GLACIATION

In order to reconstruct the glaciation of Eurasia during the late Weichselian ice age phase, simulation runs with the thermodynamic mechanic ice sheet simulation code SICOPOLIS (Simulation Code for Polythermal Ice Sheets) have been carried out. Special attention has been directed to study fast flow features in the Fennoscandian area around the Last Glaciation Maximum (LGM) [11].

3.1 Ice sheet siulation code SICOPOLIS

SICOPOLIS numerically integrates the previously discussed polythermal ice sheet equations utilizing SIA [4]. It is based on a Finite Difference approach. The structured hexagonal grid consists of equidistant points in horizontal directions, x and y, perpendicular to the direction of gravity. The vertical coordinate, z, is mapped on the interval $[0,1]$ (σ-transformation, [12]).

The key issue in the numerical integration of the ice sheet equations is the solution of the free surface evolution equation (16). Applying the simplifications introduced by SIA this equation reduces to

$$\frac{\partial h}{\partial t} + v_x \frac{\partial h}{\partial x} + v_y \frac{\partial h}{\partial y} - v_z = a_\perp^{(\mathrm{s})}(x,y,z,t) + \mathcal{O}(\varepsilon), \tag{23}$$

where v_i $(i = x,y,z)$ are the components of the velocity vector, $\mathbf{v}$. The scaled evolution equation of the bedrock surface takes a similar form as (23),

$$\frac{\partial b}{\partial t} + v_x \frac{\partial b}{\partial x} + v_y \frac{\partial b}{\partial y} - v_z = a_\perp^{(\mathrm{b})}(x,y,z,t) + \mathcal{O}(\varepsilon). \tag{24}$$

We would like to stress the fact that relations (23) and (24) are written in dimensionless variables.

Integrating the mass balance (4) from the bedrock up to the free surface and inserting these relations, the thickness evolution equation in the SIA formulation is obtained,

$$\frac{\partial h}{\partial t} = -\frac{\partial q_x}{\partial x} - \frac{\partial q_y}{\partial y} + a_\perp^{(\mathrm{s})}(x,y,z,t) - a_\perp^{(\mathrm{b})}(x,y,z,t) - \frac{\partial b}{\partial t} + \mathcal{O}(\varepsilon). \tag{25}$$

The volume fluxes in horizontal directions are defined as follows

$$q_i = \int_b^h v_i \, dz, \quad (i = x,y). \tag{26}$$

Relation (25) is a diffusion type of equation. Greve and Calov [12] compared the implementation of explicit, alternating-direction implicit (ADI) as well as the over-implicit (OVI) numerical discretization schemes in combination with equation (25). In the computations

conducted for the Eurasian area, the unconditionally stable [13] OVI scheme has been applied in order to enable reasonably large timesteps and hence reduce the overall computation time.

In SIA the velocity field is obtained diagnostically from the stress-strain relation (3) in combination with the hydrostatic pressure distribution, $p(\mathbf{x},t) = \rho g \cdot (h(x,y,t) - z)$, occurring in the scaled momentum equations. The only three-dimensional partial differential equation remaining to be solved is given by the balance of the thermodynamic field variable, i.e., (9) in cold ice and (12) in temperate ice. In SICOPOLIS this advection-diffusion type of equation is solved applying an explicit upwind scheme in the horizontal directions and an implicit scheme in vertical directions using a staggered grid technique [14]. Usually, solution procedures for these equations run stable on a far longer timestep compared to the thickness evolution equation (25). Thus, the temperature/water mass fraction field is not updated every time, which additionally saves computational resources.

3.2 External forcing

Models for external forcing can be divided into two categories: diagnostic or prognostic. A diagnostic model describes a process (like parameterization of surface mass balance). On the other hand, a prognostic model predicts how a process or quantity evolves in time. Many diagnostic models are valid for present day values only. It is not clear if they can be applied to very different conditions like past climate. Sensitivity experiments with such models are needed in order to asses how small changes in the diagnostic equations affect the modeled ice sheet behavior.

In the simulations of Eurasian glaciation, we apply two types of forcing:

- anomaly from present conditions have been obtained from the results of a GCM-model [15]
- perturbations from present measured surface temperatures and precipitation obtained from proxy data (like ice core oxygen isotope measures defining temperature)

The accumulation is defined from current precipitation, corrected for surface temperature variations and changes in surface slope. For ablation, we use the Positive Degree-Day (PDD) method, which is based on empirical relation between melting rate and air temperature [16].

In our first studies, we computed the seasonal temperatures and precipitations linearly between their present values and values from GCM simulations at the LGM using a glaciation index $g(t)$. This index scales the GRIP δ^{18}O record [17] to represent LGM ($g = 1$) and present ($g = 0$) conditions. Here, we refine this approach by defining anomalies between LGM and modern by values obtained by GCM's,

$$f_{\text{anom}}(x,y) = f^{\text{GCM}}_{\text{LGM}}(x,y) - f^{\text{GCM}}_{\text{present}}(x,y), \tag{27}$$

where f represents either seasonal temperature or precipitation. The temperature and precipitation at an arbitrary time t are calculated based on the Legates and Wilmott (L&W) [18] data-sets for modern precipitation and temperature,

$$f(x,y,t) = f^{\text{L\&W}}_{\text{present}}(x,y) + g(t)\, f_{\text{anom}}(x,y), \tag{28}$$

where x and y are Cartesian coordinates which span the stereographic plane, t is the time, f is the surface temperature or precipitation and $f_{\text{present}}(x,y)$ and $f_{\text{LGM}}(x,y)$ are the spatially resolved data for the two time-slices, respectively.

3.3 Results

The geographical area in our simulations reaches from the Northern Atlantic to the Taymyr Peninsula, and covers an area of 6040 × 2840 km^2. The stereographic projection with a reference latitude of 71° is applied. The grid spacing for the simulations in horizontal directions is 40 km, leading to a total of 151×71 grid points. The vertical resolution is 21 grid points in the cold-ice region, 11 grid points in the temperate-ice region (if run in polythermal mode) and 11 grid points in the lithosphere. Simulation start-up was from 250 ka ago, with arbitrarily chosen ice-free conditions. The first approx. 50 ka are required for system spin-up. Our main focus is on the dynamical reconstruction of the Late Weichselian glaciation and deglaciation.

In several runs we studied the effect of different climate data sets, cold and polythermal mode and different PDD-factors. Representing simulation results for the ice sheet at LGM using either UKMO data [19] or datasets obtained by PMIP simulation runs [20] for computation of the temperature/precipitation anomaly in (27) are presented in Fig. 2.

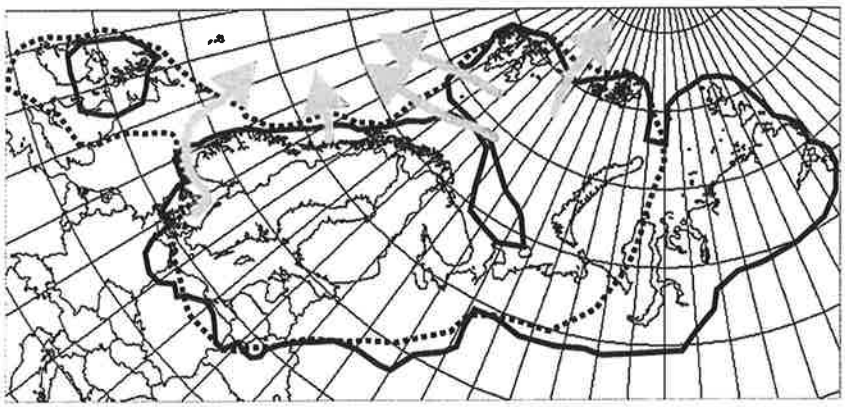

Figure 2: Simulated ice sheet extent at LGM (22 ka p.b.) obtained with UKMO data (solid line) or PMIP data (dashed line).

It is clear to be seen that different data sets produce quite different ice sheet extents. The fast flow features in the simulation output are marked with arrows. These fast flow areas are located at topographic troughs, and can be connected to paleo ice streams. These ice streams transport ice to the ice margin with velocities up to 1000 m/a [11].

4 CONCLUSIONS AND OUTLOOK

Models based on SIA are widely used to simulate scenarios on a continental scale. They are of sufficient accuracy to cope with such problems, but fail in certain situations. There have been attempts to account for higher order terms in ε (e.g., [21]), but in last consequence it is inevitable to deal with a truly three-dimensional model in order to cope with detailed glaciological problems. Additionally, most of modern ice sheet simulation codes apply isotropic flow models as dynamic closure relations. It is well known, that poly-crystalline

ice can show very different response towards shear, depending on the direction the shear is applied.

4.1 Three-dimensional solution of ice sheet equations

As already mentioned, a numerical implementation of the ice sheet equations that does not apply SIA scaling for a given vertical resolution increases the needed horizontal resolution by a factor of $1/\varepsilon^2$. Typical aspect ratios of continental ice sheets are in the range of 10^{-3}, leading to a increase factor of 10^6 in model sizes. Additionally, in SIA models the momentum equations reduce to a diagnostic relation for the velocity fields. Numerically, this is solved by a simple quadrature. The three-dimensional problem, on the other hand, demands the solution of a set of partial differential equation for the field variables p, v_x, v_y and v_z (i.e., the Stokes equations). Since a simple quadrature numerically is far less demanding compared to the solution of a partial differential equation, in principle a coupled system of 5 fully three-dimensional partial differential equations (mass balance, three components of momentum balance, energy/mass fraction balance) in contrast to only one (energy/mass fraction balance) for a SIA model have to be solved. Hence, not only the increase in the model size but also the addition of four three-dimensional degrees of freedom (DOF) contribute to the enormous increase in demand for computational resources of truly three-dimensional numerical implementations of the ice sheet equations.

Nevertheless, the advantages of such an approach are clear:

- no restrictions on the discretization by global aspect ratio
- information on all components of the stress field
- the same equations are valid for ice sheets, ice shelves as well as ice flow around enclosed sub-glacial ice lakes
- easy integration of anisotropic ice flow models

The list of these features accounts for future requirements in computational glaciology.

4.2 Anisotropic ice flow model

Anisotropic flow laws for ice have been integrated into SIA based ice sheet models (e.g., [22]). Nevertheless, a truly three-dimensional approach certainly is favorable, because in this formulation the momentum equation formally is not dependent on the type of constitutive relation. Hence, different model approaches for stress-strain rate relations easily can be implemented in such a code.

Isotropic flow laws in the general form of (3) introduce a linear relation between strain rate tensor and stress deviator,

$$\mathbf{D} = E\,A(T)\,\mathcal{F}(\sigma)\,\mathbf{T}^{\mathrm{R}}. \tag{29}$$

Mind, that in (3) the function $\mathcal{F}(\sigma)$ takes the form of a power-law. A generalized anisotropic flow law introduces a structure tensor, $\mathbf{M}$, that accounts for the properties of the crystal. The stress-strain rate relation then is a tensor-like function, $\mathbf{F}$, of the following general form [23]

$$\mathbf{T}^{\mathrm{R}} = \frac{\mathbf{F}(\mathbf{M},\mathbf{D})}{\tilde{\mathcal{F}}(\sigma,T)}. \tag{30}$$

The properties of the ice crystals change with the flow. Hence, additional n equations for a n-dimensional geometry describing the evolution of the parameters defining the structure tensor have to be solved. These equations describe the temporal change of the poly-crystal regarding the stress history a fluid particle has been exposed along its path. In order to obtain the linear law (3) in the limit of isotropic grain structure, the right-hand side of (30) has to show the limit $\mathbf{F}(\mathbf{M},\mathbf{D})/\tilde{\mathcal{F}}(\sigma, T) \rightarrow \mathbf{D}/(E\,A(T)\,\mathcal{F}(\sigma))$ [24].

4.3 Further developments

Inside CSC developments towards the implementation of the truly three dimensional ice sheet equations in ELMER, a multiphysics code based on the Finite Element Method (FEM) (see `http://www.csc.fi/elmer`) are under way. Additionally, the orthotropic ice flow law developed by Meysonier and Gagliardini [24] has been implemented in ELMER. Efforts are now taken in order to obtain a stable numerical scheme for the hyperbolic evolution equation of the free surface as well as the fabric parameters of the ice. In a longer perspective the coupling of an ice sheet model with a GCM would also be a desirable task to be performed within a high performance computing center, such as CSC.

Acknowledgments

The authors would like to thank Ralf Greve for supplying us with his ice sheet simulation code SICOPOLIS and for the fruitful cooperation over the past two years.

REFERENCES

[1] A. Fowler, D.A. Larson *On the flow of polythermal glaciers. I. Model and preliminary analysis*, Proc. R. Soc. Lond., A **363**, 217-242 (1978)

[2] K. Hutter *A mathematical model of polythermal glaciers and ice sheets*, J. Geophys. Astrophys. Fluid Dyn., **21**, 201-224 (1982)

[3] W.S.B. Paterson *The physics of glaciers*, third edition, Pergamon Press (1994)

[4] R. Greve *A continuum-mechanical formulation for shallow polythermal ice sheets*, Phil. Trans. R. Soc. Lond., A **355**, 921–974 (1997).

[5] S.-I. Shin, Z. Liu, B. Otto-Bliesner, E.C. Brady, J.E. Kutzbach, S.P. Harrison *A simulation of the Last Glacial Maximum Climate Using the NCAR-CCSM*, Clim. Dyn., **20**, 127-151 (2003)

[6] R. Greve *Glacial Isostacy: Models for the Response of the Earth to Varying ice Loads*, in *Continuum Mechanics and Applications in Geophysics and the Environment*, In: Straughan B., Greve R., Ehrentraut H., Wang Y. (editors), Springer, 307-325 (2001)

[7] R. Calov *Das thermomechanische Verhalten des Grönländischen Eisschildes unter Wirkung verschiedener Klimaszenarien. Antworten eines theoretisch-numerischen Modells*, PhD. thesis, Inst. f. Mechanik, Technische Hochschule Darmstadt (1994)

[8] M.J. Siegert *Ice Sheets and Late Quaternary Environmental Change*, John Wiley & Sons (2001)

[9] K. Hutter *Theoretical glaciology; material science of ice and the mechanics of glaciers and ice sheets*, D. Reidel Publishing Company (1983)

[10] M. Weis, R. Greve, K. Hutter *Theory of shallow ice shelves*, Cont. mech. Thermodyn, **11**, 15-50 (1999)

[11] P.-L. Forsström, O. Sallasmaa, R. Greve, T. Zwinger *Simulation of fast-flow features of the Fennoscandian ice sheet during the Last Glaciation Maximum*, Annals of Glaciology, **37**, in print (2003)

[12] R. Greve, R. Calov *Comparison of numerical schemes for the solution of the ice-thickness equation in a dynamic/thermodynamic ice-sheet model*, Journal of Computational Physics **179** (2), 649-664 (2002)

[13] R.C.A. Hindmarsh *Notes on basic glaciological computationak methods and algorithms* In: Straughan B., Greve R., Ehrentraut H., Wang Y. (editors), Springer, 222-249 (2001)

[14] R. Greve *Thermomechanisches Verhalten polythermer Eisschilde* PhD. thesis, Inst. f. Mechanik, Technische Hochschule Darmstadt, published in Verlag Shaker (1995)

[15] S. Charbit, C. Ritz, G. Ramstein *Simulations of Northern Hemisphere ice-sheet retreat: sensitivity of physical mechanisms involved during the Last Deglaciation*, Quatern. Sci. Rev., **21**, 243–265 (2002)

[16] N. Reeh *Parameterization of melt rate and surface temperature on the Greenland ice Sheet*, Polarforschung, **59**(3), 741-153 (1991)

[17] W. Dansgaard, S.J. Johnsen, H.B. Clausen, D. Dahl-Jensen, N.S. Gundestrup, C.U. Hammer, C.S. Hvidberg, J.P. Steffensen, A.E. Sveinbjörnsdottir, J. Jouzel and G. Bond *Evidence for general instability of past climate from a 250-kyr ice-core record*, Nature, **364**, 218–220 (1993)

[18] D.R. Legates, C.J. Wilmott *Mean seasonal and spatial variability in global surface air temperature*, Theor. Appl. Climatol., **41**, 11–21 (1990)

[19] C.D. Hewitt, J.F.B. Mitchell *Radiative forcing and response of a GCM to ice age boundary conditions: cloud feedback, and climate sensitivity*, Climate Dyn., **13** (11), 821–834.(1997)

[20] M. Kageyama, O. Peyron, S. Pinot, P. Tarasov, J. Guiot, S. Joussame, G. Ramstein *The Last Glacial Maximum climate over Europe and western Siberia: a PMIP comparison between models and data*, Clim. Dyn., **17**, 23–43 (2001)

[21] D.R. Baral *Asymptotic theories of large scale motion, temperature and moisture distributions in land based polythermal ice shields and in floating ice shelves. A critical review and new developments* PhD. thesis, Inst. f. Mechanik, Technische Universität Darmstadt (1999)

[22] A. Mangeney and F. Califano *The shallow ice approximation for anisotropic ice : formulation and limits* J. Geophys. Res., **103**(B1), 691-705 (1998)

[23] O. Gagliardini, J. Meysonnier *Simulation of anisotropic ice flow and fabric evolution along the GISP-GRIP2 flow line (Central Greenland)*, Ann. Glaciol., **30**, 217-223 (2000)

[24] J. Meysonnier, O. Gagliardini *Constitutive Modelling and Flow Simulation of Anisotropic Polar Ice*, In: Straughan B., Greve R., Ehrentraut H., Wang Y. (editors), Springer, 250-275 (2001)

ON FREEZING AND THAWING OF GROUND WITH IMPLICATIONS OF GLACIERS

J. HARTIKAINEN

Laboratory of Structural Mechanics, Helsinki University of Technology
P.O.Box 1100, FIN-02015 HUT, Finland
e-mail: juha.hartikainen@csc.fi

ABSTRACT

Freezing and thawing of ground are integral parts of a glaciation cycle which is presumed to occur on Northern hemisphere within the next hundred thousand years after the fashion of the past glaciation cycles. The thermal regime determines the creation of frozen ground such that during a cold and dry pre-glacial stage freezing can penetrate to depths of several hundreds meters appearing as permafrost while in humid climate an insulating snow cover reduces the freezing considerably and especially, during a glacial stage permafrost thaws beneath an up-building ice sheet due to geothermal heat. The creation of frozen ground involves coupled processes of heat and mass transfer changing the hydrogeological geometry of the ground. The pressure and the stress fields generated by these processes result in frost heaving of the frozen ground and consolidation of the unfrozen ground and in changes in the salinity concentration of groundwater. Besides having a major impact on thawing of permafrost glaciers are a significant groundwater recharge. A transient ice sheet generates a water pressure field with steep gradients and a stress field leading to movement of groundwater, hydrofracturing and deformations of the ground and to redistribution of groundwater salinity.

A study is undertaken of the effects of the glacial cycle on thermal conditions and development of permafrost, on groundwater pressure and flow, on stresses and deformations in the ground and on the transportation of solutes. It is related to the Bench Mark Test 3 (BMT3) of the international project DECOVALEX III dealing with impacts of glaciation cycle on the behaviour of the bedrock in which a hypothetical spent nuclear fuel repository is located [1]. Thermomechanical modelling of the problem is carried out by use of the approach for soil freezing [2]. A thermomechanical model based on the basic principles of continuum mechanics and macroscopic thermodynamics and on the theory of mixtures is proposed for saline water saturated rock mass which undergoes freezing and thawing processes during a glacial cycle. An ice sheet model is used to create thermal, hydraulic and mechanical boundary conditions for the rock mass at the Whiteshell site in Canada [3]. Significant effects, such as penetration of permafrost and local overpressuring to depths in excess of the repository level, are discussed with a special attention to the coupling between glaciers and permafrost.

REFERENCES

[1] T. Chan, R. Christiansson, J. Andersson, G.S. Boulton, F.W. Stanchell, and P. Vidstrand. *DECOVALEX III, Task 3, BMT 3 BENCHBAR Work-Package 4; Glaciation bench mark test*, Prepared by Atomic Energy of Canada Limited for Ontario Power Generation, Ontario Power Generation, Nuclear Waste Management Technical Memorandum Report 06819(UF)-03781-T10-R00, Toronto, Ontario (2001)

[2] M. Mikkola and J. Hartikainen. *Mathematical model of soil freezing and its numerical implementation*, Int. J. Num. Meth. Eng. **52**, 543–557 (2001)

[3] G.S. Boulton and A. Payne. *Mid-latitude ice sheets through the last glacial cycle: glaciological and geological reconstructions*, In Duplessy, J.-C. and Spyridakis, M.-T. (eds.): Long-term climatic variations, NATO ASI Series 1 **20**, 177–212 (1994).

KUORMITUSNOPEUDEN VAIKUTUS SAVEN PAINUMAPARAMETREIHIN

O. KORHONEN
Helsingin kaupunki

M. LOJANDER
Teknillinen korkeakoulu. Rakennus ja ympäristötekniikan osasto.

TIIVISTELMÄ

Saven jännitys- ja muodonmuutoskäyttäytymistä perinteellisen ödometrikokeessa vallitsevassa tilassa (sivusiirtymät estetty) simuloidaan mitattujen jännitysten ja niitä vastaavien muodonmuutosten relaatioiden perusteella empiirisellä muodonmuutosyhtälöllä, joka on kehitetty niin, että se on osana populaatiomekaniikassa yleisesti sovellettua lineaarista systeemiä. Tässä esitellään kriittisen tilan mallin laajennus jännityssuhteen q/p ja dilataatiokulman ψ ollessa vakio.

Saven jatkuvapuristeiset ödometrikokeet on tehty Teknillisen Korkeakoulun pohjarakennuslaboratoriossa.

1. TUTKIMUKSET

Teknillisen Korkeakoulun pohjarakennuslaboratoriossa on 1980-luvulta alkaen tutkittu koheesio- ja kitkamaalajien sekä murskeen ja kevytsoran muodonmuutos- ja lujuusominaisuuksia em. materiaalien mekaanista käyttäytymistä simuloivien matemaattisten mallien kehittämistä varten.

Tässä yhteydessä käsitellään jatkuvapuristeisella ödometrilaitteella (CRS) tutkitun Espoon Vantinlaaksontien saven koetuloksia koejärjestelyillä, joissa samaa savikerrosta on tutkittu eri suuruisilla koenopeuksilla. Nopeudet vaihtelivat rajoissa 0,0015 – 0,015 mm/min eli noin 0,45 – 4,5 %/tunti. Koesarjan savinäytteet olivat riittävän tarkasti "identtisiä", jolloin eri kokeissa ainoa muuttuja oli koenopeus. Vanttilan savi on erittäin häiriintymisherkkää.

2. MUODONMUUTOSYHTÄLÖT

Vantinlaaksontien savella tehtyjen kokeiden tulokset on esitetty tehokkaiden jännitysten ja vastaavien aksiaalisten muodonmuutosten avulla. Koetuloksia approksimoidaan yleisesti perinteisellä ns. tangenttimoduulimenetelmän empiirisellä yhtälöllä. Vantinlaaksontien saven ödometrikokeiden tuloksia on esitetty kuvassa 1. Kuvassa on esitetty myös koetuloksia approksimoiva empiirisen muodonmuutosyhtälön (3) kuvaaja. Yhtälö (1) perustuu kriittisen tilan malliin [CSM, Schofield & Wroth 1968; Wood 1990].

$$v_\lambda = v+\lambda \ln p = (\lambda-\kappa)(1- \eta/M) + \Gamma = \text{vakio} \qquad (1)$$

v on ominaistilavuus

M on kriittisen tilan jännityssuhde

λ, κ ja Γ ovat kriittisen tilan mallin parametreja

p_y on hydrostaattinen jännitys myötöhetkellä

Koskinen [2001] on esittänyt, että savea vakiojännityssuhteella kolmiakselilaitteistolla konsolidoimalla dilataatiokulma myödön jälkeen on vakio. Ödometrikokeen reunaehdot edellyttävät dilataatiokulman olevan yhtälön (2) mukaisesti vakio.

$$\Psi = d\varepsilon_v / d\varepsilon_s = 3/2 \qquad (2a)$$

Olettamalla myödön tapahtuvan assosioidusti, saadaan tällöin ödometrikokeessa vallitsevan jännityspolun yhtälöksi

$$q = \Psi^{-1} p = 2/3\ p \text{ eli } \eta = 2/3 \qquad (2b)$$

Tällöin yhtälö (1a) yksinkertaistuu muotoon

$$v = v_y - \lambda \ln (p/p_y) \quad (1b)$$

v_y on ominaistilavuus myötöhetkellä ja p_y on myötöjännitys

Nopeasti suoritetuissa ödometrikokeissa on usein osoittautunut, että yhtälö (1a) ei riittävällä tarkkuudella esitä koetuloksia, toisin sanoen koetulokset eivät asetu suoralle v – ln (p) – koordinaatistossa. Vastaavasti käyttämällä ns. tangenttimoduulimenetelmää saadaan tulokset helposti "sopimaan" spiraalin kaarelle, joka kuitenkaan ei edusta selkeää fysikaalista mallia.

Korhonen et al [2003].ovat esittäneet Porvoo- Koskenkylän (POKO) savella [Koskinen et al 2002] tehdyillä kolmiakselikokeilla yhtälön (1b) laajennuksen, jolloin koetuloksia voidaan tulkita logistisen yhtälön (3) avulla.

$$dp/dv = (a_1 v + b_1)p$$

$$\ln (p) = 0{,}5a_1 v^2 + b_1 v + \ln(p_y) = k\, dv/du \quad (3)$$

u on huokospaine ja a_1, b_1 ja k ovat parametrejä.

Koska useimmat kaupalliset jatkuvakuormitteiset ödometrilaitteet tulostavat koetulokset koordinaatistossa $\varepsilon_1 - \sigma_1$, muunnetaan yhtälö (3) muotoon

$$\ln (\sigma_1) = 0{,}5a\varepsilon_1^2 + b\varepsilon_1 + \ln(\sigma_y) \quad (3a)$$

Yhtälö (3a) linearisoituu derivoimalla yhtälöksi $(d\sigma_1/d\,\varepsilon_1)/\,\sigma_1 = a\varepsilon_1 + b$, jotka suureet standardi CRS-koe tulostaa suoraan.

Yhtälö (3) on Bernoullin differentiaaliyhtälö, jonka ratkaisu on logistinen käyrä (3b).

$$v(u) = 1/(1/v_f + (1/v_y - 1/v_f)\exp(-Au)) \quad (3b)$$

A on parametri ja v_f on ominaistilavuus konsolidaation lopussa.

3. MITTAUSTULOKSET

Kuvassa 1 on esimerkki yhtälön (3a) soveltuvuudesta Vantinlaaksontien saven ödometrikokeen havaintotuloksiin. Parametrit a ja b ovat ainakin koenopeudesta riippuvia. Parametri b on analoginen parametrin λ kanssa.

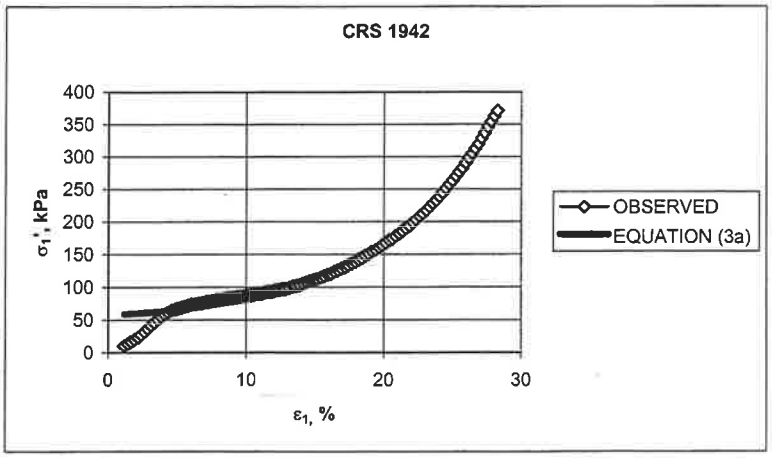

Kuva 1. Vantinlaaksontien savi, syvyys 6,6 m. CRS-koe. Koenopeus 0,015 mm/min. $\varepsilon_1 - \sigma_1$.

Taulukossa 1 esitetään Vantinlaaksontien saven ödometrikokeiden tulosten tulkinta soveltaen yhtälöä (3a).Taulukon konsolidaatiojännityksen arvot on määritetty lasketun kuvaajan ja ylikonsolidoituneen alueen mittaustulosten leikkauspisteestä. Samalla esitetään tangenttimoduulimenetelmällä määritetyt muodonmuutosparametrit vertailun vuoksi. Yhtälön (3a)

parametrien määritys esitetään kuvassa 2 sekä logistisen yhtälön (3b) soveltuvuus ominaistilavuuden ja huokospaineen kuvaajana kuvassa 3.

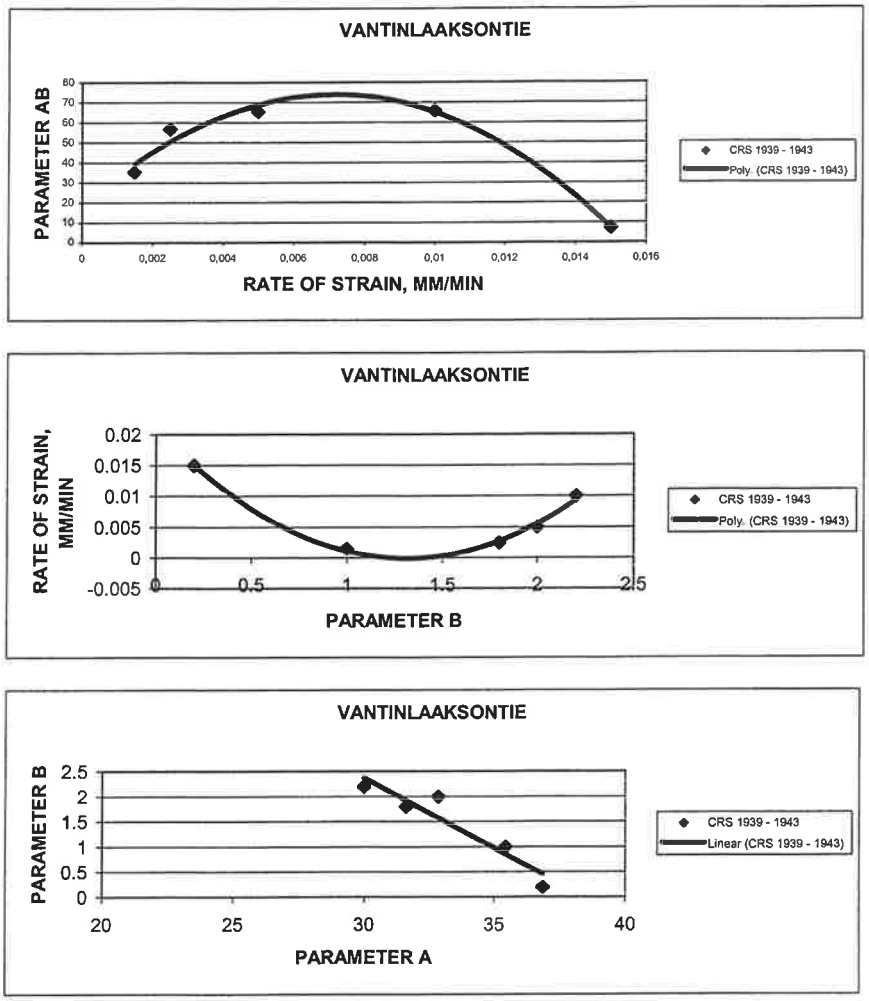

Kuva 2 Vantinlaaksontien savi. Yhtälön (3a) parametrien määritys.

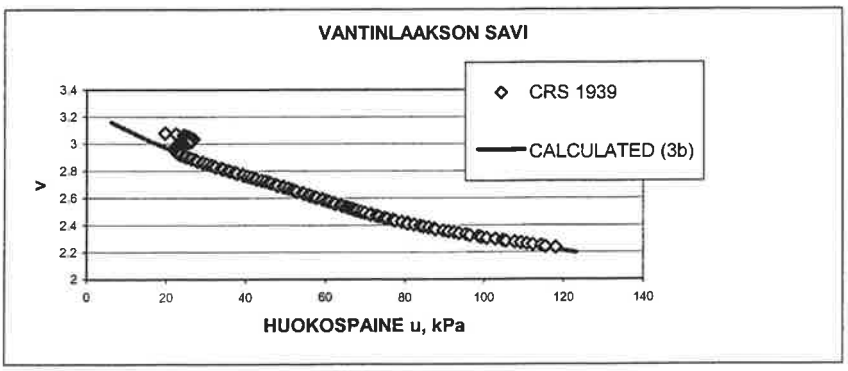

Kuva 3. Vantinlaaksontien savi. Ominaistilavuuden ja huokospaineen vuorosuhde sekä yhtä (3b) kuvaaja

Taulukko 1. Vantinlaaksontien savi. CRS-kokeiden tulokset.

koe	nopeus	a	b	kons jänn	w	m	β	kons jänn
	mm/min			kPa	%			kPa
crs 1940	0.0015	35.45	1.0	67	77.1	5.4	-0.928	70.4
crs 1941	0.0025	31.61	1.8	63	81	5.1	-0.812	69.1
crs 1942	0.005	32.86	2.0	65	76.5	5.5	-0.74	68.1
crs 1943	0.01	30.00	2.2	67	78.7	5.5	-0.687	68.6
crs 1939	0.015	36.88	0.2	75	79.5	4.7	-0.759	77.7

Yhtälöillä (3) ja (3a) on mahdollista simuloida ns. nollanopeuskokeen tuloksia. Laskelmien ja koetulosten välinen yhteys esitetään kuvassa 4. Kuvassa 4 esitetään myös kuormitusnopeutta 0 mm/min vastaava teoreettinen kuvaaja. Lasketuista kuvaajista (4 kpl) nähdään selvästi nopeuden vaikutus kuvaajan muotoon sekä konsolidaatiojännitykseen.

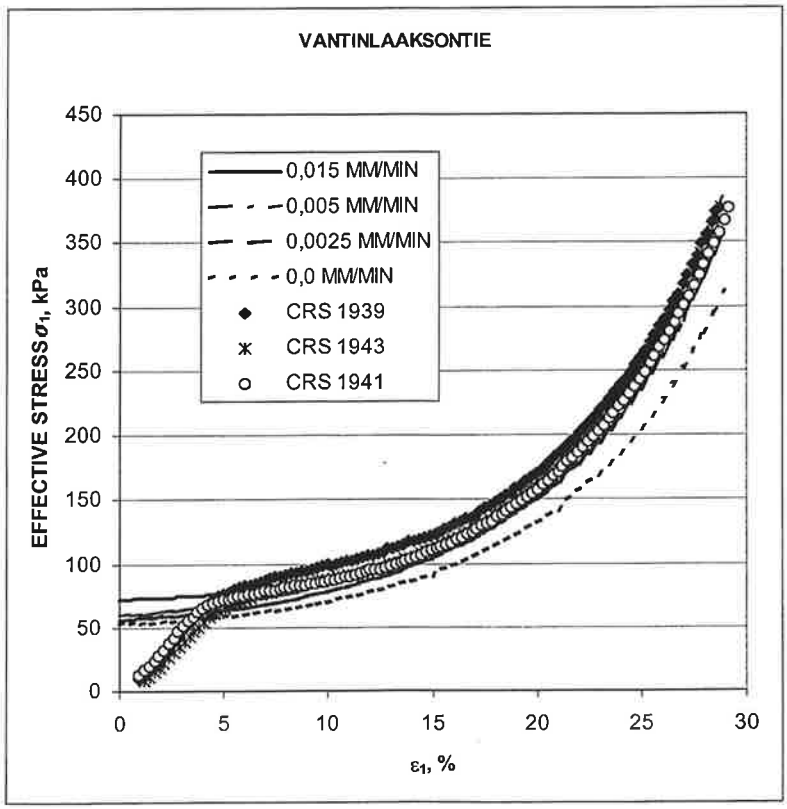

Kuva 4. Vantinlaaksontien savi. Esimerkki koetuloksista sekä yhtälön (3a) perusteella lasketut kuvaajat..

4. YHTEENVETO

Edellä on lyhyesti esitelty perinteisestä tangenttimoduulimenetelmästä poikkeava, kriittisen tilan malliin liittyvän muodonmuutosyhtälön periaatteet. Yhtälö (3) edustaa laajennettuna yleisesti ödometrikokeen ja kolmiakselikokeen tulkinnassa käytettyä muodonmuutosyhtälöä. Toisen asteen termi $a_1 v^2$ antaa mahdollisuuden tutkia myös koenopeuden vaikutusta koetuloksiin. Termi a_1 vastaa populaatiomekaniikassa kuolleisuutta (konsolidaatioprosessiin osallistuneet partikkelit) ja termi b_1 vastaavasti syntyvyyttä (jäljellä oleva konsolidaatio).

Tangenttimoduulimenetelmän huono puoli on se, ettei sen muodonmuutosyhtälön parametreillä ole selkeää fysikaalista merkitystä. Vaikka tässä yhteydessä (taulukko 1) esitetyt konsolidaatiojännityksen erot menetelmien välillä ovat pieniä, aiheuttaa itseisarvoltaan suuri jännitysexponentti β hankaluuksia käytännön painumalaskennassa ja lopputulos on usein epärealistisen korkea. Kirjallisuudessa [Länsivaara 2000] usein esitetyt empiiriset parametrien nopeuskorjaukset eivät takaa onnistunutta painumalaskentaa.

KIRJALLISUUSLUETTELO

Korhonen, O.,Korhonen, K-H.; Lojander, M.: The potential function of oft clay. XIIIth EuropeanConference on Soil Mechanics and Geotechnical Engineering. Praha 2003. (Painossa).

Koskinen, M.: Anisotropy and destructuration of soft clays. Masters thesis. Helsinki University of Technology 2001.

Koskinen, M: Zentar, R.; Karstunen, M.: Anisotropy of reconstituted Poko clay. Numerical Models in Geomechanics – NUMOG VIII, p. 99-105. Lisse 2002,

Länsivaara, T.: Painumalaskentamenetelmien käyttökelpoisuuden arviointi. Tielaitoksen selvityksiä 44/2000. Helsinki 2000.

Wood, D. M.: Soil behaviour and critical state soil mechanics. Cambridge University Press 1990.

Schofield, A.; Wroth, P.: Critical state soil mechanics. Mc Graw – Hill. London 1968.

MURRON SAVEN PAINUMAPARAMETRIT

Asko Aalto, Olli Ravaska, Matti Lojander
Teknillinen korkeakoulu. Rakennus ja ympäristötekniikan osasto.

TIIVISTELMÄ

Saven varaan tehtävien rakenteiden painumalaskenta on eräs geoteknisen suunnittelun rutiinitehtävistä. Perinteisesti arvioita painumista on helpoissa tapauksissa voitu tehdä jopa pelkän vesipitoisuuden perusteella. Laskelmien tarkkuusvaatimukset ovat kuitenkin kohonneet ja lisäksi entistä vaikeampia rakentamispaikkoja halutaan ottaa käyttöön. Kokeneillekin suunnittelijoille on tullut vaikeuksia ja tästä johtuen on tullut tarvetta kehittää eteenpäin käytännönläheisiä painumalaskentamenetelmiä rinnan elementtimenetelmää vaativien mallien kehittelyn kanssa.

Tässä artikkelissa tarkastellaan primääripainuman suuruuden laskemiseen tarvittavien parametrien määritystä.

1. JOHDANTO

Painuvien täyttöjen ja penkereiden hallittu suunnittelu edellyttää, että painumat osataan etukäteen laskea ajan funktiona riittävän tarkasti. Kokemuksesta tiedetään kuitenkin, että painumalaskujen tarkkuus ei ole kovin hyvä. Tarkkuuden arvioimiseksi Tielaitos järjesti v. 1997 Haarajoen savikolle rakennetun koepenkereen kansainvälisen painumalaskentakilpailun, jonka tulokset olivat yllättäviä (Pietikäinen & Smura, 2000, Lojander et al 2001). Vaikka kaikilla kilpailuun osallistujilla oli käytössään samat lähtötiedot, laskentatulosten hajonta oli valtava. Kun kahden vuoden jälkeen mitattu painuma kahdessa laskentapisteessä oli 320 ja 500 mm, etukäteislaskelmien tulokset vaihtelivat välillä 120...1800 mm. Tulokset osoittivat myös, että perinteisten laskentamenetelmien käyttö hallittiin paljon paremmin kuin uusien FEM-pohjaisten menetelmien. Kaiken kaikkiaan tulos oli masentava ja osoitti, että painumalaskelmien tarkkuudessa on paljon parantamista.

Koska TKK:n pohjarakennuksen ja maamekaniikan laboratorio oli painumalaskentakilpailun pohjatutkija ja asiantuntijaelin, tulosten suuri hajonta antoi aiheen tarkastella laskentamenetelmiä ja niissä käytettäviä parametreja tarkemmin. Alustavissa tutkimuksissa todettiin, että sekä kokonaispainuman että aika-painuman laskennassa laskentaparametreja vakioidaan surutta, vaikka niiden riippuvuuksista esim. jännityksestä on ollut ainakin epämääräistä tietoa. Laboratoriossa käynnistettiinkin v. 2002 Suomen Akatemian rahoittama projekti, jonka päämäärä on vanhan, huonoksi osoittautuneen painumasapluunan vääntäminen oikeammaksi painumaparametrien jännitysriippuvuuksien osalta. Tässä esityksessä tarkastellaan kokonaispainuman laskentaan käytettävää Ohde-Janbun jännitys-muodonmuutosmalliin perustuvaa tangenttimoduulimenetelmää ja mallin parametrien jännitysriippuvuutta.

2. AINEISTO

Valtatie 18 suunnittelun yhteydessä Tielaitoksen Vaasan tiepiiri rakensi Seinäjoelle, Murroon, v. 1993 koepenkereen (Selkämaa 1994). Koepenger on rakennettu n. 20m paksuisen savikerroksen varaan. Koepenger on hyvin instrumentoitu ja painuma-, siirtymä- ja huokosvedenpainemittauksia edelleen jatketaan. Koepenger on 2metrin korkuinen. Kahdeksan vuoden aikana koepenger on painunut jo n. 80cm ja ennustettu 30v painuma on n. 0,8 - 1m (Koskinen et al 2002, Koskinen et al 2002, Länsivaara 2001). Pohjasuhteet koepenkereen alla on esitetty kuvassa 1.

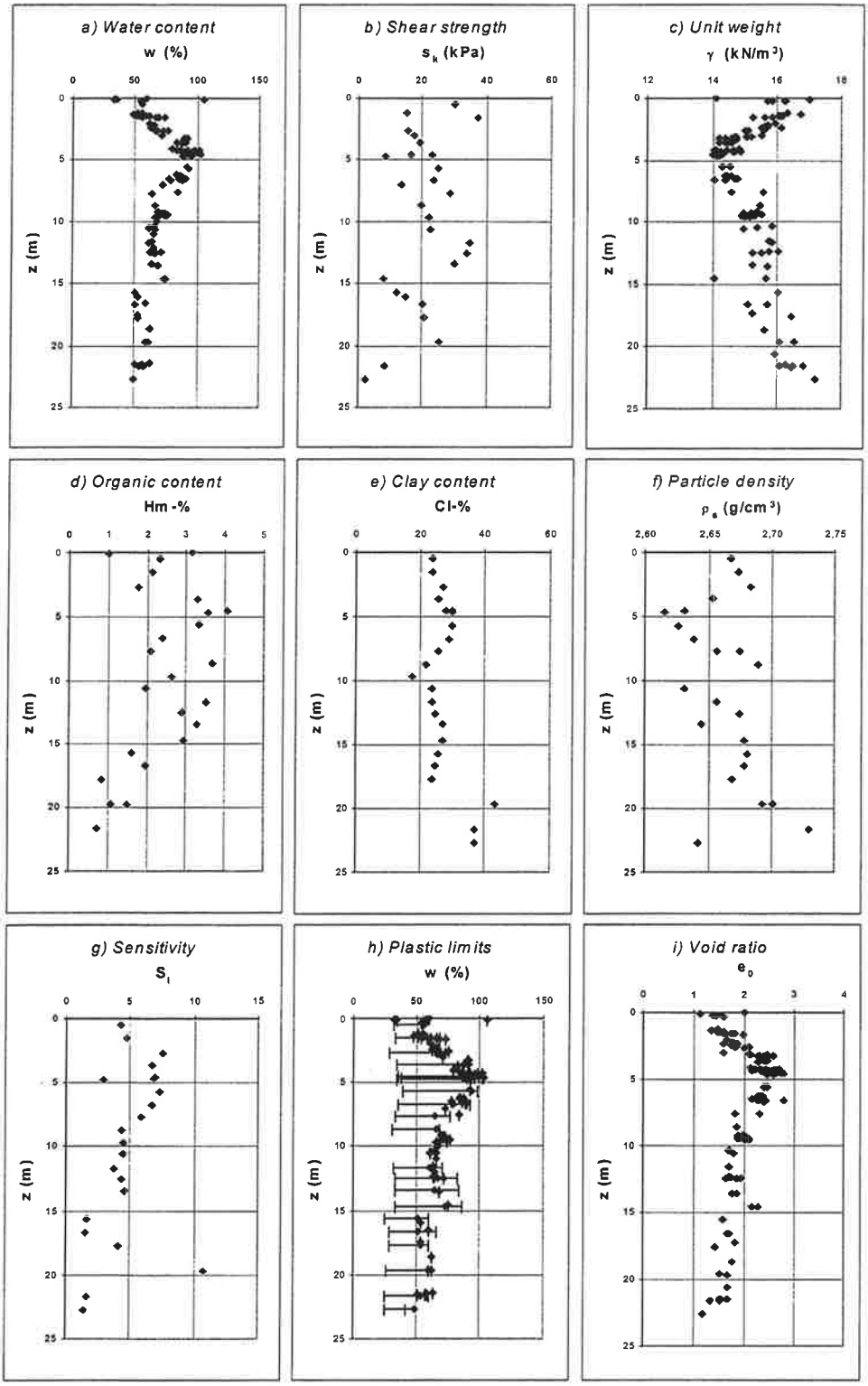

Kuva 1. Murron maa-aineksen luokitusominaisuudet 1993, ennen koepenkereen rakentamista. (Koskinen et al 2002)

Murron koepenkereestä on tehty poikkeuksellisen laajat tutkimukset ja hyvän seurantaohjelman ansiosta penger on mukana EU:n rahoittamassa kansainvälisessä yhteistyöprojektissa SCMEP (Soft Clay Modelling for Engineering Practice). SCMEP-projektissa kehitetään pehmeälle savelle mekaanista mallia, jossa otetaan huomioon myös saven anisotropia ja rakenne. Murron koepenkereen painuma-, sivusiirtymä- ja huokospainehavaintoja tullaan analysoimaan näillä uusilla kehittyneillä malleilla. Mallien arviointia varten on kuitenkin välttämätöntä pystyä tekemään luotettavia arvioita myös klassisilla ja käytännöllisillä laskentamenetelmillä. Tässä yhteydessä tarkastellaan ainoastaan primäärisen konsolidaatiopainuman (huokosveden poispurkautumisen aiheuttama) loppuarvon laskemiseen tarvittavia parametreja. Painumisnopeuden kannalta keskeisin parametri on konsolidaatiokerroin, jonka suuruus on suoraan verrannollinen vedenläpäisevyyteen. Tutkimusprojekti aloitettiin vedenläpäisevyyden ja painumaparametrien välisen riippuvaisuuden selvityksellä (Ravaska et al 2001, 2002, 2003). Varsinaiseen painumalskentaan tarvitaan vielä näiden lisäksi sekundaaripainuman (raerungon hiipumisen) laskentamenetelmä. Nykyisin käytettävät menetelmät perustuvat yleensä puolilogaritmiseen aika-painumamalliin ja niiden soveltaminen on ollut epämääräistä. Suomalaisen saven ominaisuudet poikkeavat mm. erilaisen mineralogian vuoksi muualla esiintyvistä savista ja tämä aiheuttaa tarpeen jatkuvasti tarkistaa muualta omaksuttavien menetelmien käyttökelpoisuutta Suomessa (Messerling et al 2003).

3. TANGENTTIMODUULI JA SEN PARAMETRIT

Suomessa käytetään savimaiden kokoonpuristumisen arviointiin Ohden (1939) ja Janbun (1967) kehittelemää tangenttimoduulikonseptia (kaava 1)

$$\varepsilon_1 = \frac{1}{m\beta}\left(\frac{\sigma_1}{\sigma_v}\right)^{\beta} + c \quad , \text{kun } \beta \neq 0 \tag{1a}$$

$$\varepsilon_1 = \frac{1}{m}\left(\frac{\sigma_1}{\sigma_p}\right)^{\beta} + c \quad , \text{kun } \beta = 0 \tag{1b}$$

$$M_t = \frac{d\sigma_1}{d\varepsilon_1} = m\sigma_v\left(\frac{\sigma_1}{\sigma_1}\right)^{1-\beta} \tag{1c}$$

ϵ_1 on suhteellinen kokoonpuristuma

σ_1 jännitys

σ_v vertailujännitys ($\sigma_v = 100$ kpa)

σ_p esijännitys

c paikantamisvakio

M_t tangenttimoduuli

Tangenttimoduulin (kaava 1c) sijasta käytetään laskelmissa useimmiten tangenttimoduulin parametreja m ja β ja tämä tarjoaa valitettavasti mahdollisuudet suuriinkin virheisiin, mikäli koetulosta käytetään väärällä jännitystasolla. Perinteinen kansainvälinen painumalaskentamenetelmä käyttää kokoonpuristuvuusindeksiä C_c. Tämä menetelmä vastaa tapausta, jossa jännityseksponentti β=0 (kaava 1b). Suomalaisilla savilla tämä puolilogaritminen malli soveltuu vain rajalliselle jännitysalueelle ja vuosikymmenien ja tuhansien ödometrikoeiden perusteella on havaittu savinäytteiden jännityseksponentin olevan pienempi kuin nolla. Länsivaara (2000) on erinomaisesti osoittanut minkälaisia tuloksia painumalaskennassa saadaan, mikäli

muodonmuutosparametreja sovelletaan redusoimattomina muussa jännitystilassa kuin siinä, missä koe on tehty.

Tässä artikkelissa on käsitelty tangenttimoduulin ja sen parametrien jännitystilariippuvaisuuksia. Murron kohde on tähän käyttöön erittäin sopiva, sillä painuvan maakerroksen paksuus on >20m ja esijännityksessä on suuria eroja.

Useimmiten painumalaskelmissa vaikein asia on konsolidaatiotilan selvitys. Konsolidaatiotilaa kuvataan ylikonsolidoitumisasteella , OCR (kaava 2).

$$OCR = \sigma_p / \sigma'_{v0} \qquad (2)$$

OCR on	ylikonsolidoitumisaste
σ_p	esijännitys
σ'_{v0}	vallitseva, tehokas pystysuuntainen jännitys

Vallitseva jännitys lasketaan päällä olevien maakerrosten tehokkaiden tilavuuspainojen ja kerrospaksuuksien summana. Tilavuuspaino pystytään yleensä luotettavasti määrittämään tai arvioimaan, mutta pohjaveden pinnan korkeudesta ja maassa olevan huokosvedenpaineen suuruudesta ei useinkaan ole riittävän pitkäaikaisia havaintoja. Vuoden kestäneen kuivan ajanjakson jälkeen monin paikoin on jo havaittu yli metrin suuruinen pohjaveden pinnan lasku.

Esijännityksen (esikuormitus, esikonsolidaatiojännitys, esikonsolidaatiopaine...) määrittämiseksi on kehitetty useita erilaisia menetelmiä (Kotzias 1963), mutta mitään niistä ei voida pitää yleispätevänä. Parametreja määritettäessä tapana onkin käyttää useampaa menetelmää ja lopulta itse arvioida paras arvo. Tässä artikkelissa esitetty menetelmä soveltuu erittäin hyvin portaittaisen ödometrikokeen tulosten käsittelyyn, varsinkin jos kokeessa on tehty myös toistokuormitus.

4. TULOKSET

Ödometrikokeiden havaintopisteisiin on sovitettu potenssifunktio (kaava 1), jolloin ensikuormituskäyrältä ($\sigma_1 > \sigma_p$) saadaan laskettua normaalistikonsolidoituneen alueen parametrit (m_1, β_1, C_1) ja toistokuormituskäyrältä ylikonsolidoituneen alueen parametrit (m_2, β_2, C_2).

Esijännityksen (σ_p) määrittämiseksi toistokuormituskuvaaja (parametrit: m_2, β_2, C_2) siirretään ylikonsolidoituneella puolella olevaan pisteeseen A, joka on lähellä esijännitystä, mutta varmasti pienempi kuin esijännitys. Tämän siirretyn kuvaajan ja normaalikonsolidoituneen alueen kuvaajan (parametrit: m_1, β_1, C_1) leikkauspisteestä saadaan esijännitys (σ_p). Menetelmä on sovellus Ohden (1939) ja Van Zelstin (1948) menetelmistä ja toistokuormituksen puuttuessa voidaan käyttää myös palautuskuvaajan parametrejä. Menetelmää on havainnollistettu kuvassa 2.

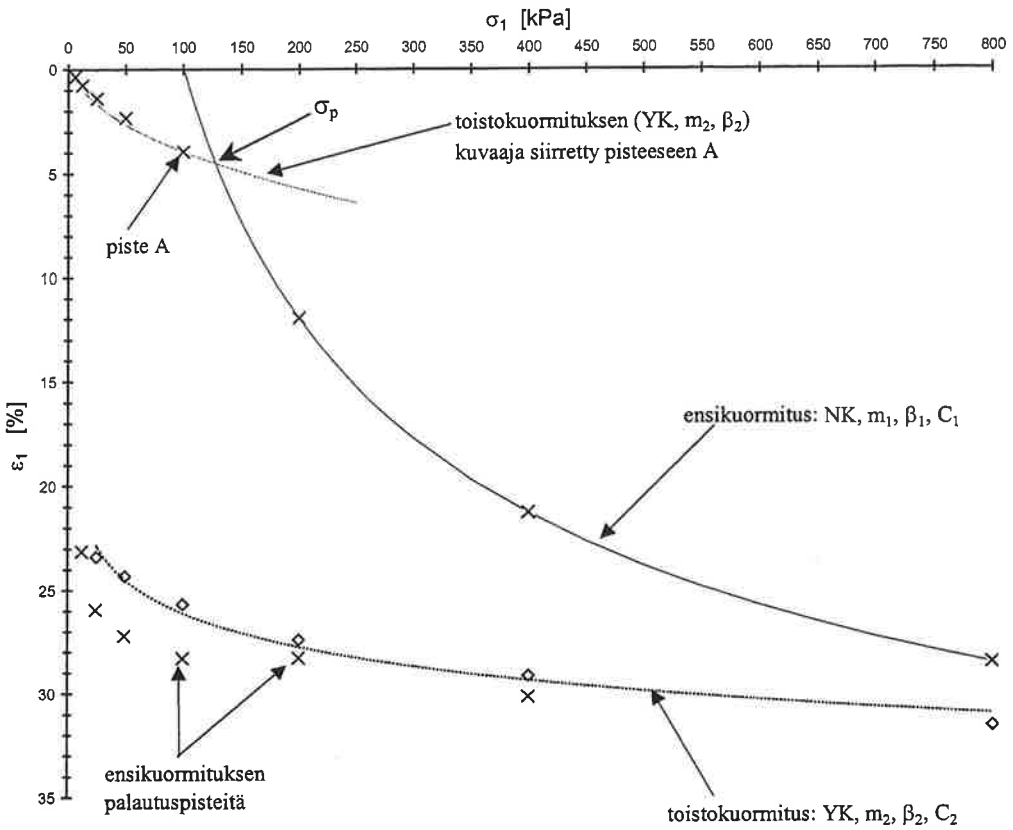

Kuva 2. Esijännityksen määrittäminen (koe 3404T).

Alustavissa tarkasteluissa ödometritulokset ($\sigma_1 - \varepsilon_1$) määritettiin 1 vuorokauden tuloksista (1d-tarkastelu), ja näiden tulosten perusteella maa-aines oli normaalikonsolidoitunutta koko syvyysprofiililtaan ($\sigma_p = \sigma'_{vo}$, OCR = 1). Myöhemmin tarkastelu tehtiin käyttäen Taylorin menetelmää (EOP), jossa primäärikonsolidaation kesto todettiin huomattavasti lyhyemmäksi, ts. primaaripainumat pienemmiksi kuin 1d-tarkastelussa; ylikonsolidoitumisaste (OCR) vaihteli tällöin syvyysprofiililla 1,15 – 1,57 (kuva 3). Näin menetelmän valinnalla on huomattava vaikutus.

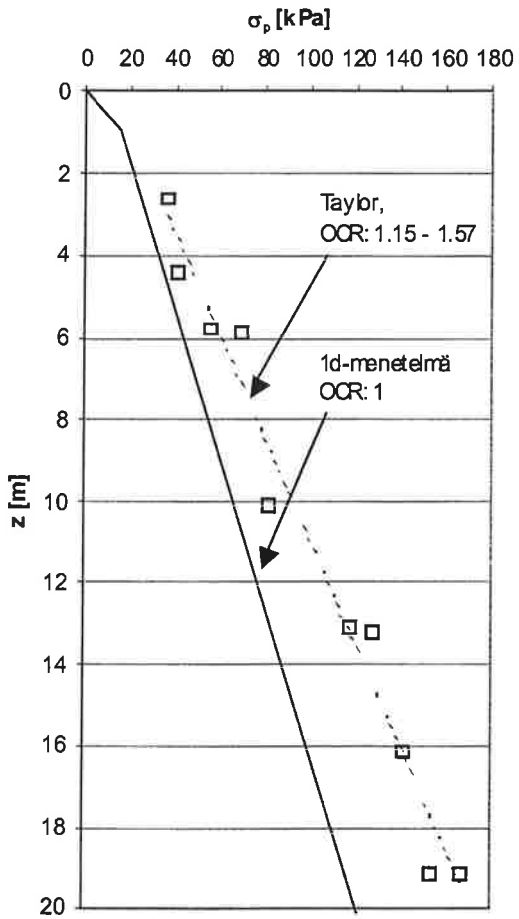

Kuva 3. Tarkastelumenetelmän vaikutus ylikonsolidoitumisasteeseen (OCR)

Kuvassa 4 on esitetty tangenttimoduuli (M_t) jännityksen funktiona. Ylikonsolidoituneella alueella ($\sigma'_{vo} < \sigma_1 < \sigma_p$) tangenttimoduuli (kaava 1c) on laskettu parametrien m_2 ja β_2 avulla. Esijännitystä suuremmilla jännityksen arvoilla ($\sigma_1 > \sigma_p$) tangenttimoduuli on laskettu parametrien m_1 ja β_1 avulla.

Kuvassa 5 on esitetty tangenttimoduulin laskennallinen arvo esijännityksen kohdalla sekä 20 kPa:n lisäjännityksen kohdalla. Kuvasta 5 voidaan havaita, että tangenttimoduuli (M_t) on myös riippuvainen esijännityksestä (σ_p).

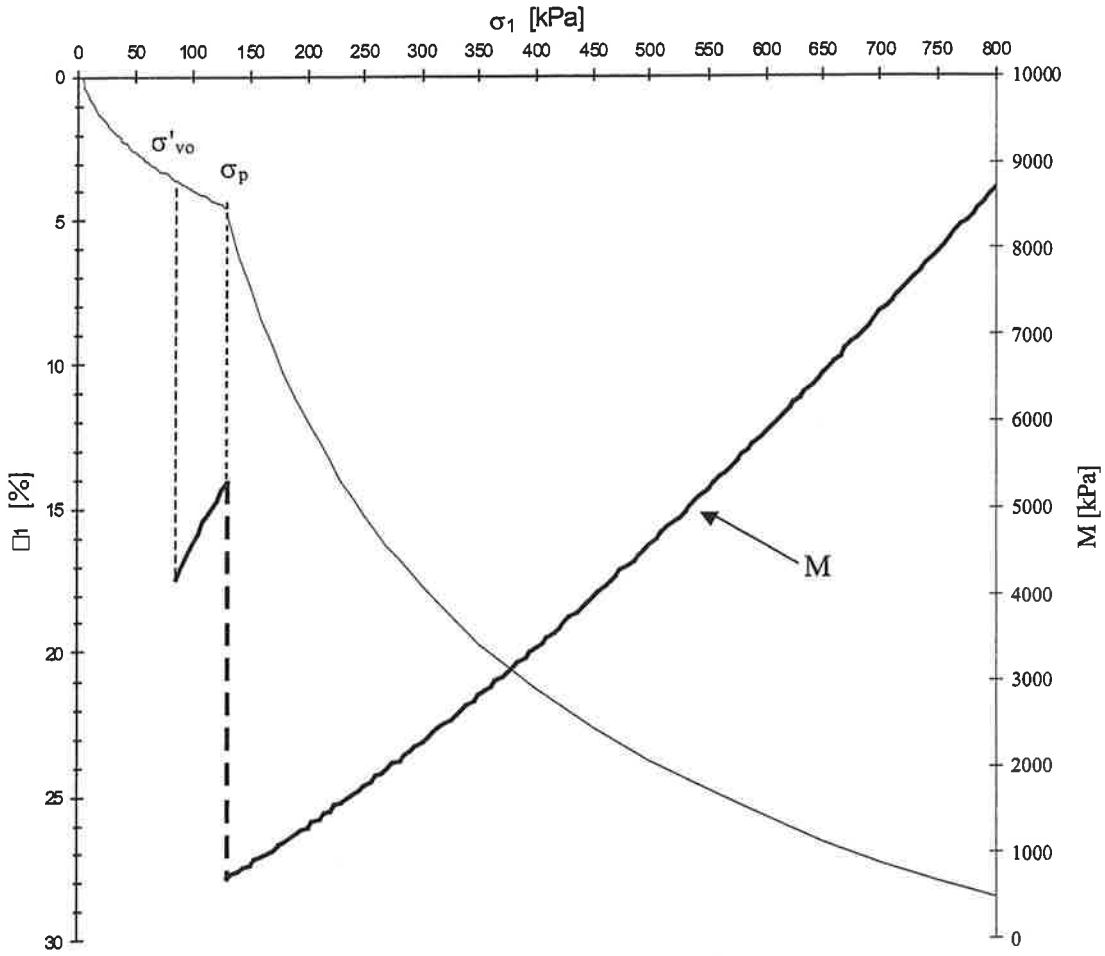

Kuva 4. Tangenttimoduuli (M_t) jännityksen funktiona (koe 3404T).

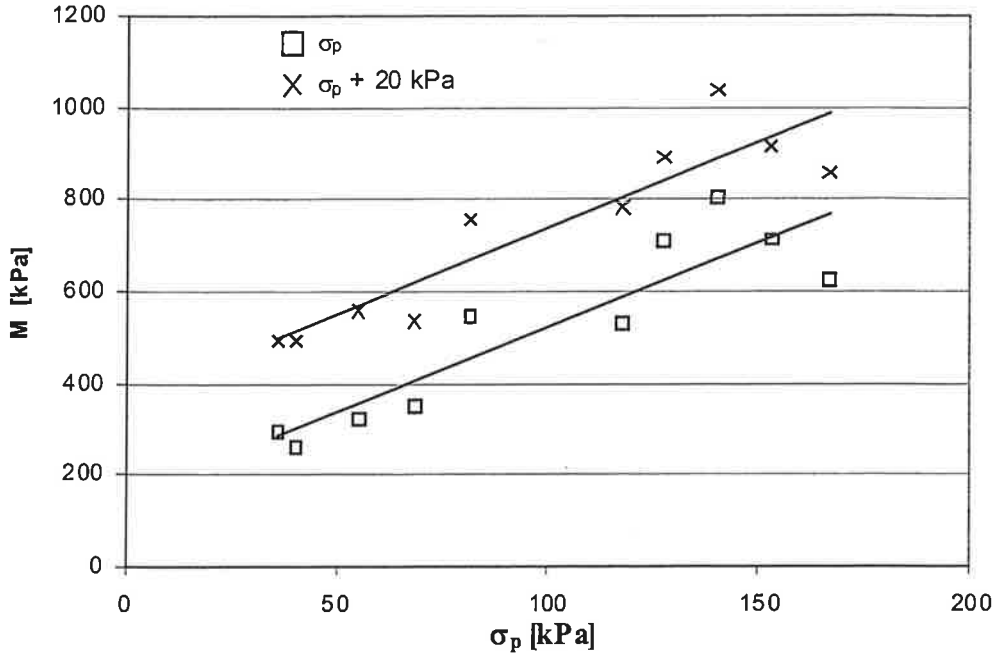

Kuva 5. Tangenttimoduuli (M_t) esijännityksen funktiona.

Kuvassa 6 on esitetty tangenttimoduulin parametrien m_l ja β_1 riippuvuus esijännityksestä (σ_p). Kuvassa 6a ja 6b on esitetty koetuloksiin parhaiten sopivat tulokset (taulukko 1). Kuvassa 6c on jännityseksponentin β_1 arvo kiinnitetty β_1 = -0.200, joka on vastaava arvo kuin 20 metrisen kerroksen puolivälistä otetusta näytteestä määritetty β_1 (koe 3535kT). Vaikka parhaassa sovituksessa β_1 arvo vaihtelee $-0{,}1 < \beta_1 < -0.9$ on pakotettu sovitus arvolla β_1 = -0.200 erittäin hyvä ja käytännön painumalaskennan tarpeisiin aivan riittävä.

Moduuliluvun (m_l) ja esijännityksen (σ_p) välistä riippuvuutta esittäviin kuviin on liitetty myös Länsivaaran (2000) esittämä moduuliluvun muuntaminen jännitystason avulla (kaava 3) / (Länsivaara 2000).

$$m_{laskenta} = m_{koe} \times \left(\frac{\sigma_{p\,koe}}{\sigma_{p\,laskenta}} \right)^{-\beta} \qquad (3)$$

$m_{laskenta}$ on laskennassa käytettävä moduuliluvun arvo

m_{koe} kokeesta määritetty moduuliluvun arvo

$\sigma_{p\,koe}$ kokeesta määritetty esijännitys [kPa]

$\sigma_{p\,laskenta}$ laskennassa käytettävä esijännitys [kPa]

Kuvaan 6c kaavalla 3 sovitetun kuvaajan koetuloksena on käytetty 10 metrin syvyydeltä otetun näytteen (koe 3535kT) koetulosta, jolloin jännityseksponentin paras sovitus on β_1 = -0,205. Menetelmä osoittautui tässä tapauksessa erittäin käyttökelpoiseksi.

Murron koepenger valittiin tutkimuskohteeksi, koska tutkittava maakerros on verrattain homogeeninen 2...20 m syvyydellä. Mikäli maapohja sisältää useita erilaisia geoteknisiä kerroksia ei tällaista menettelyä voida soveltaa kuin kerroskohtaisesti.

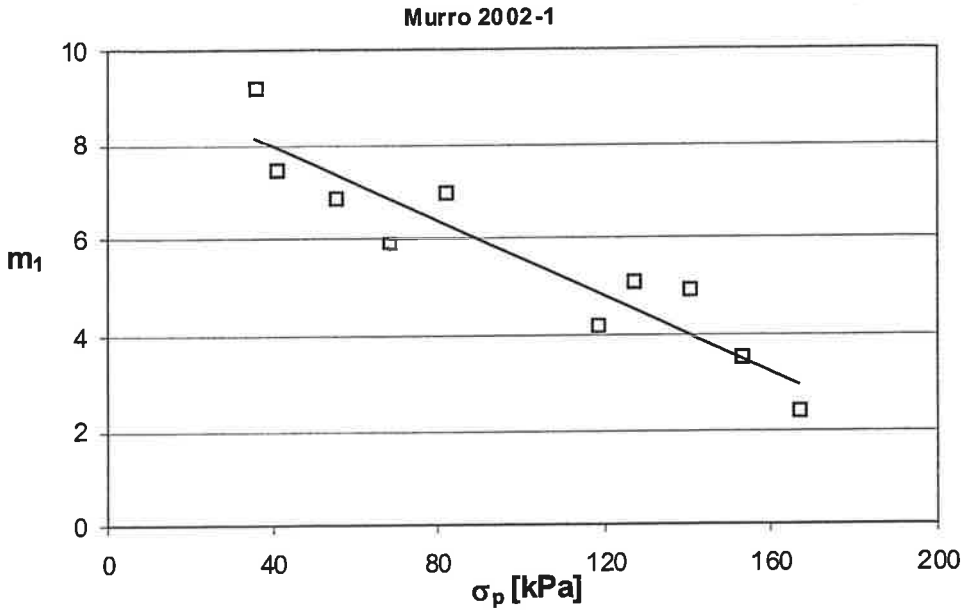

Kuva 6a. Moduuliluku (m_1) esijännityksen funktiona.

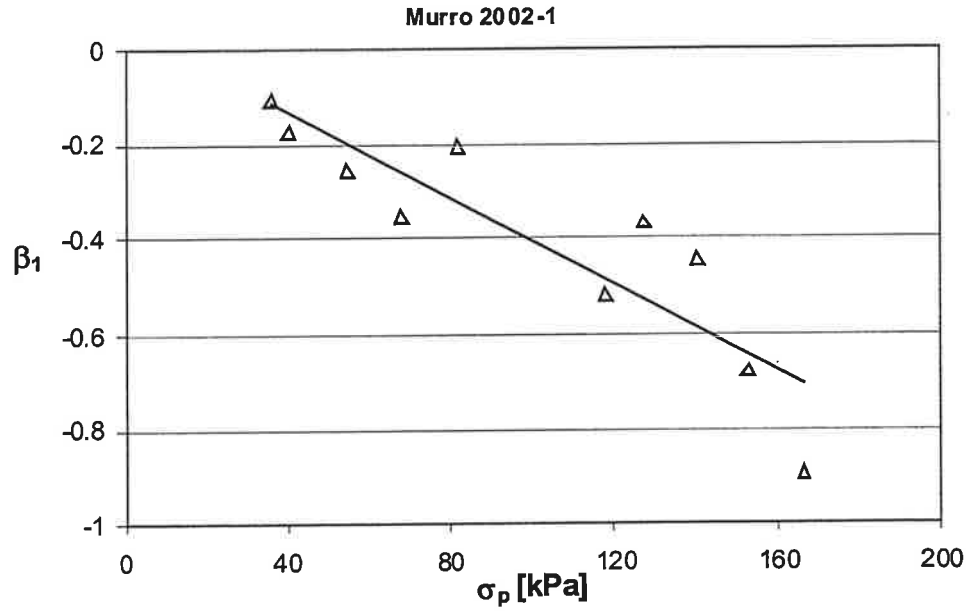

Kuva 6b. Jännityseksponentti (β_1) esijännityksen funktiona.

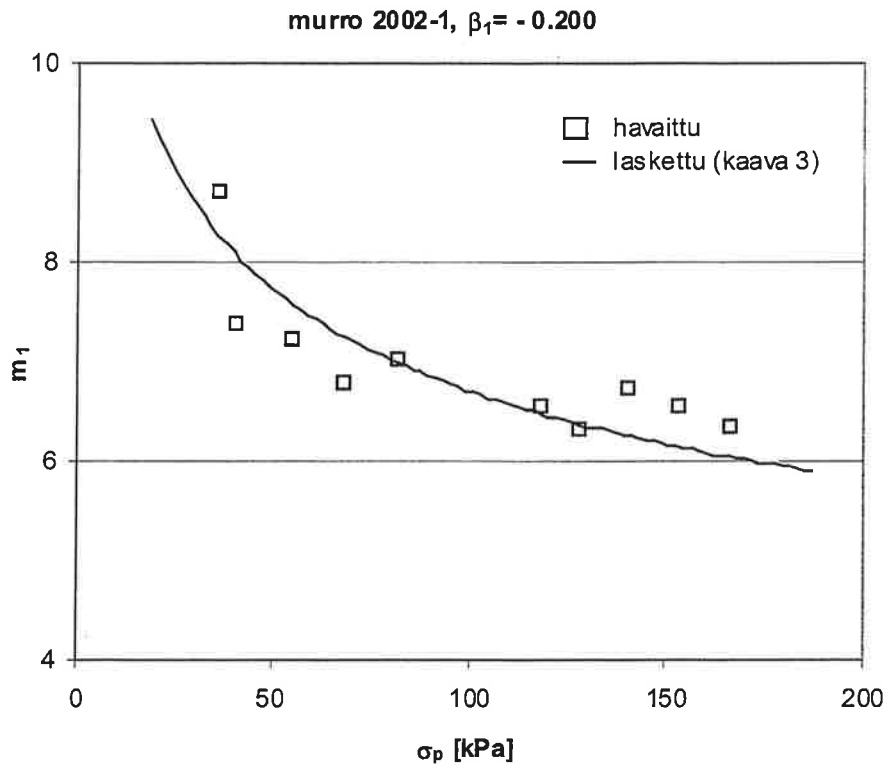

Kuva 6c. Moduuliluku (m_1) esijännityksen funktiona; β_1 = -0.200 pakotettu. Havaitut ja lasketut (kaava 3) (Länsivaara 2000) arvot.

koe	syvyys [m]	w [%]	γ kN/m^3	e_0	S_r [%]	σ'_{vo} [kPa]	σ_p [kPa]	m_1	β_1	m_2	β_2
3405T	2.635	68.5	15.35	1.875	98	26	36	9.22	-0.105	64.87	0.280
3426T	4.385	97.1	14.16	2.645	98	35	41	7.52	-0.170	77.88	0.435
3477kT	5.775	88.7	14.75	2.388	100	43	55	6.86	-0.255	165.93	0.505
3408T	5.885	87.9	14.51	2.392	98	43	68	5.92	-0.350	57.09	0.535
3535kT	10.125	69.3	15.52	1.849	100	67	82	6.99	-0.205	64.87	0.280
3424kT	13.065	67.2	15.45	1.865	97	83	118	4.16	-0.515	110.3	0.320
3403T	13.185	69.2	15.10	1.930	96	83	128	5.09	-0.365	45.86	0.430
3425T	16.145	55.9	16.10	1.534	97	100	141	4.92	-0.440	99.26	0.435
3416kT	19.155	60.9	15.99	1.664	99	116	167	2.38	-0.895	98.34	0.365
3404T	19.185	63.1	15.91	1.685	100	116	153	3.5	-0.680	63.48	0.440

Taulukko1. Murron savi. Ödometrikokeiden tulokset.

5. YHTEENVETO

Koepenkereiden tutkimusten yhteydessä on havaittu, että myös perinteiset ja yleisesti tunnetut ja käytetyt painumalaskentamenetelmät ja menetelmissä käytettävien parametrien määrittäminen vaatii terävöittämistä, mikäli laskelmilla odotetaan saatavan luotettavia painumaennusteita. Perinteinen hyväksi havaittu tangenttimoduulikonseptikin on aiheuttanut suuria eroja painumalaskentatuloksiin samoja tutkimustuloksia käytettäessä. Lisäpiirteenä on viime vuosina mukaan tulleet nopeasti tehtävät jatkuvapuristeiset ödometrikokeet, joita niitäkin tulkittu samoilla menetelmillä kuin portaittaisia kokeita, vaikka parametrien arvot ovat olleet yllättäviä.

Kokeissa käytettäviin kuormitusaikoihin tulee kiinnittää huomiota. Vallitsevaa jännitystä pienemmät kuormitusportaat saavat olla lyhyitä ja tuloksia laskettaessa tulisi joka tapauksessa käyttää havaintoja, jotka osuvat lähelle primääripainuman loppua. Normaalistikonsolidoituneella alueella aika-painumakuvaajista voidaan tarkalleen laskea primääripainuman loppuhetki ja määrittää parametrit EOP-käyrältä (End Of Primary). Perinteisesti portaittaisesta ödometrikokeesta on painumaparametrit laskettu 1 vrk arvoilla. Murron saven kohdalla muutos 1vrk arvoista EOP-käyrälle aiheuttaa niin suuren muutoksen esijännityksen arvoihin, että aikaisemmin normaalisti konsolidoituneeksi oletettu maapohja pitäisikin laskemissa tulkita niin ylikonsolidoituneeksi, että vain 2...10m syvyydellä 2m penkereen aiheuttama lisäjännitys ylittää maapohjan konsolidaatiojännityksen. Tämä muutos aiheuttaa myös sen, että painumisnopeuslaskelmiin on saatava mukaan myös sekundaaripainuman laskentaosuus. Ylikonsolidoituneiden maakerrosten primääripainuma tapahtuu niin nopeasti, että jo muutaman vuoden jälkeen sekundääripainuman osuus on merkittävä.

Tangenttimioduulin parametreja tarkasteltaessa on aina muistettava, että sekä moduuliluku että jännityseksponentti vaikuttavat painuman suuruuteen. Niitä ei voida tarkastella toisistaan irrallaan. Murron tapauksessa jännityseksponentti voidaan valita vakioksi ja tällöin voidaan moduuliluvun jännitysriippuvaisuutta tarkastella. Moduuliluvun ja jännityseksponentin väliselle riippuvaisuudelle näyttäisi löytyvän helposti yhteys. Mikäli jännityseksponenttia ei voida vakioida saadaan järkevä tarkastelu suoraan tangenttimoduulin avulla. Tangenttimoduulille voidaan kokemusperäisesti asettaa minimiarvo, jolloin vältytään huomaamatta käyttämästä nollaa lähestyviä moduulin arvoja, kuten pelkillä parametreillä operoitaessa saattaa sattua. Suurin osa käytössä olevista painumalaskntaohjelmista kuitenkin edelleen käyttää tangenttimoduulin sijasta tangenttimoduulin parametreja, joten tämän virheen välttämiseksi parametrien jännitysriippuvaisuuden tarkastelu on hyödyllistä.

Tämä artikkeli on tehty Suomen Akatemian rahoittaman tutkimusprojektin "Kokonaisvaltainen aika-painumamalli" tuella.

KIRJALLISUUSLUETTELO

Janbu, N.: Settlement calculations based on the tangent modulus concept. Soil mechanics and foundation engineering, the Technical university of Norway. Trondheim 1967.

Koskinen, M.; Lojander, M.; Tolla, P.; Vepsäläinen, P.: Numerical Analysis on Murro Test Embankment, 5th European Conference of Numerical Methods in Geotechnical Engineering, Paris, 4-6 September, 2002.. Paris 2002, LCPC, s. 397-402.

Koskinen, Mirva; Lojander, Matti; Vepsäläinen Pauli: Modelling of Anisotropic behaviour of clays, Test Embankment in Murro, Seinäjoki, Finland. Helsinki: Tiehallinto, 2002. 62 s (Tiehallinnon selvityksiä).

Kozias, P.: Zusammen Drückbarkeit von Schluff. Aachen 1963.

Lojander, M.; Vepsäläinen, P. Haarajoen Koepenkereen Painumalaskentakilpailu. Loppuraportti. Helsinki: Tiehallinto, 2001. 50 (Tiehallinnon selvityksiä 54/2001).

Länsivaara, T.: Painumalaskentamenetelmien käyttökelpoisuuden arviointi. Tielaitoksen selvityksiä 44/2000. helsinki 2000.

Länsivaara, T.: Painuman ennustaminen painumahavaintojen perusteella. Tiehallinnon selvityksiä 49/2001. Helsinki 2001.

Messerklinger S.; Kahr G., Plötze M.; Trausch Giudici J.; Springman S.; Lojander M.:Mineralogical and mechanical behaviour of soft Finnish and Swiss clays. Proc. Int. Workshop on Geotechnics of Soft Soils - Theory and Practice, 17-19 September 2003, Noordwijkerhout, Netherlands 2003. Vermeer, Schweiger, Karstunen & Cudny (eds.). (In Press)

Ohde, J.: Zur Theorie der Druckverteilung im Baugrund Bauingenieur 14 (1939):33/34, p. 451-458.

Pietikäinen, E., Smura, M. (2000). Competition to calculate settlements at Haarajoki test embankment. NGM-2000, XIII Nordiska Geoteknikermötet, Helsinki 5.-7. Juni 2000. Finnish Geotechnical Society r.y. Building Information Ltd. Helsinki 2000, pp. 475-478.

Ravaska, O.; Vepsäläinen, P.: On the stress dependence of consolidation parameters. Proc. Of the XV Int. Conf. Of Soil Mechanics and Geotechnical Engineering, Istanbul 27 - 31. August 2001. Vol. 1 A.A. Balkema Publishers Lisse/Abingdon/Exton (PA)/Tokyo 2001. ISBN 90 2651 839 0. P. 251-254.

Ravaska, O.; Aalto, A.: Modelling permeability in consolidation. Proc. Of the XIII Eur. Conf. Of Soil Mech. And Geotech. Eng., Praha 25.-28.8.2003 (Julkaisematta).

Ravaska, O.; Aalto, A.: Lojander, M.:Consolidation properties of natural and disturbed clay. Int. Workshop on Geotechnics of Soft Soils-Theory and Practice. Vermeer, Schweiger, Karstunen & Cudny (eds.) VGE 2003.

Selkämaa, E.: Koepenger Seinäjoki, Murro. Seinäjoen teknillinen oppilaitos. Insinöörityö 1994.

Van Zelst. 1948. An Investigation of the factors affecting Laboratory Consolidation of Clay. Proc.Of the 2nd ICSMFE. Vol. 7. s. 257-265.

Vepsäläinen, P.; Lojander, M.; Takala J. & Törnqvist, J. The pixel soil layer model: Theory,practical aspects and examples. NGM-2000. XIII Nordiska Geoteknikermötet, Helsinki 5. - 7.6.2000.. Helsinki 2000 , Finnish Geotechnical Society, p. 497 - 504.

FINITE ELEMENT MODELING OF STRESS WAVE PROPAGATION DUE TO CONTACT-IMPACT IN ROCK DRILLING

TIMO SAKSALA
Institute of Applied Mechanics and Optimization
Tampere University of Technology
P.O. Box 589 FIN-33101, TAMPERE FINLAND

ABSTRACT

In this paper we present a fast and explicit algorithm for modeling the stress wave propagation due to contact-impact in problems with a non-reflecting boundary. We deal only with a simple frictionless contact-impact problem, that is, a problem that can be modeled by using the node-to-node contact interface. We impose the contact constraints exactly with the forward increment Lagrange multiplier method, which is compatible with explicit time integrators. We use the explicit modified Euler time integration scheme for solving the finite element discretized equations of motion. As a non-reflecting boundary, we employ the viscous damper type quiet boundary scheme. We demonstrate the algorithm by solving a three dimensional numerical example.

1. INTRODUCTION

Numerical modeling of stress wave propagation is an important task in many fields of engineering. In this paper, we consider the stress wave propagation due to contact-impact phenomena. This problem arises especially in rock drilling. The purpose of this paper is to present a fast and explicit algorithm, which satisfies the contact constraints exactly, for solving the contact-impact problems occurring in the rock drilling. With this application in mind, we do the following assumptions:

1. Friction can be neglected during the contact.
2. Contacting surfaces are known prior to impact and they remain the same during contact.
3. Deformations of the contacting bodies are small, and the yield strength of the material is not exceeded.

The first assumption is justified because no sliding of contacting surfaces occurs in most of the rock drilling problems. The second assumption is clear, for only certain prescribed parts of the drill (e.g. the drill bit, the threads of the joints, and the head of the piston) can contact in the rock drilling. The second assumption implies that we can use the most simple contact model, namely the node-to-node contact interface model and we don't need the contact search algorithms. The third assumption is also clear because plastic deformation is not allowed in the drill parts. Moreover, as a consequence of the third assumption, we can use the linear theory of elasticity.

The outline of this paper is as follows. In sections 2 to 6, we present our problem and introduce the concepts needed for solving the problem, including the quiet, or non-reflecting, boundary scheme. Then, in section 7, we present the algorithm based on the forward increment Lagrange multiplier and the modified Euler methods. Finally, in section 8, we demonstrate the algorithm with a 3D-numerical example of longitudinal impact of cylindrical bars.

2. EQUATIONS OF MOTION AND CONTACT CONSTRAINTS

We consider the problem of two impacting bodies in Figure 1. We have denoted the current configurations of the bodies by Ω_A and Ω_B, unit normal vectors of the boundaries of the bodies by $\mathbf{n}_A$ and $\mathbf{n}_B$, the displacements of the two boundary points from current configuration by $\mathbf{u}_A$ and $\mathbf{u}_B$, and the material co-ordinates of two arbitrary boundary points by $\mathbf{X}_A$ and $\mathbf{X}_B$. In addition, the dotted line in Figure 1 represents the contact surfaces denoted by Γ_A and Γ_B.

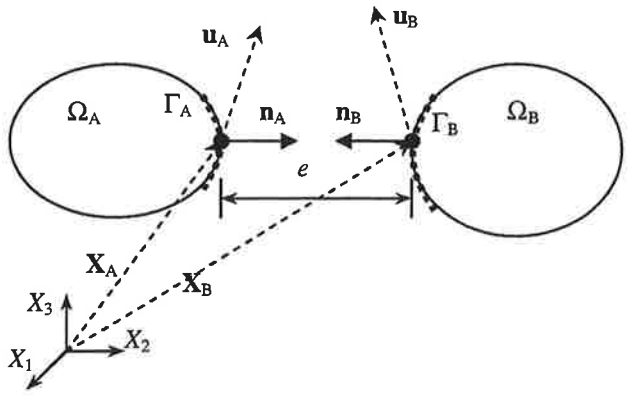

Figure 1 Illustration and nomenclature for the problem of two impacting bodies

We state the linear elasticity based equations of motion governing the wave propagation as [4]

$$\begin{aligned} &\sigma_{ij,j} + f_i = \rho \ddot{u}_i \,, \\ &\sigma_{ij} = C_{ijkl}\varepsilon_{kl} \,, \qquad \text{in } \Omega_A \cup \Omega_B \\ &\varepsilon_{kl} = \tfrac{1}{2}(u_{k,l} + u_{l,k}) \quad (i,j,k,l = 1,2,3) \end{aligned} \tag{1}$$

In equations (1) we have used following notations: σ_{ij} denotes the components of Cauchy stress tensor, u_i, $\ddot{u}_i$ and f_i denote the components of displacement, acceleration, and the body force, respectively, ε_{kl} denotes the components of the linear strain tensor, and C_{ijkl} denotes the components of the linear fourth-order elasticity tensor.

For our simple contact problem the impenetrability condition $\Omega_A \cap \Omega_B = \varnothing$ can be given in a displacement form as

$$\mathbf{n}_A \bullet \mathbf{u}_A + \mathbf{n}_B \bullet \mathbf{u}_B \le -b \qquad \text{in } \Gamma_A \cup \Gamma_B \tag{2}$$

where $b = \mathbf{n}_A \bullet \mathbf{X}_A + \mathbf{n}_B \bullet \mathbf{X}_B$. We have also assumed that $\mathbf{n}_B = -\mathbf{n}_A$.

We can write the kinetic contact constraint, which says that tractions over the contact surface must observe the conservation of momentum law, for normal tractions (the tangential ones vanish because we neglect the friction) as [2]

$$\mathbf{t}_n^A + \mathbf{t}_n^B = \mathbf{0} \tag{3}$$

where $t_n^A = -t_n^B = t_j^A n_j^A = \sigma_{ji}^A n_i^A n_j^A$. At last, we give the unitary contact constraint as

$$t_n e = 0 \tag{4}$$

where $t_n = t_n^A$ and e represents the smallest distance between the contact surfaces (see Fig.1). Equation (4) says that if $t_n > 0$, then $e = 0$, and vice versa.

3. DISCRETIZED PROBLEM

We discretize the equations of motion (1) by the finite element method. We don't go into the details but give the spatially discretized form of equations (1) as

$$\begin{aligned} &\mathbf{M}\ddot{\mathbf{u}} + \mathbf{K}\mathbf{u} = \mathbf{f}_{ext} \\ &\boldsymbol{\sigma} = \mathbf{E}\boldsymbol{\varepsilon} \qquad\qquad \text{in } \Omega_A \cup \Omega_B \\ &\boldsymbol{\varepsilon} = \mathbf{B}\mathbf{u} \end{aligned} \tag{5}$$

where **M** and **K** denote the mass and the stiffness matrices, respectively. Symbol $\mathbf{f}_{ext}$ represents the external forces, and **u** and $\ddot{\mathbf{u}}$ the nodal displacement and acceleration, respectively. Furthermore, $\boldsymbol{\sigma}$ and $\boldsymbol{\varepsilon}$ represent the nodal stress vector and nodal strain vector respectively, and finally, **B** and **E** are the kinematic matrix and elasticity matrix, respectively.

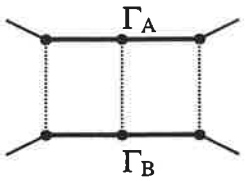

Figure 2 Node-to-node contact interface

When having a node-to-node contact interface (see Figure 2), in which the nodes of the discretized contact interface of the body Ω_A can contact only with their corresponding nodes of the discretized contact interface of the body Ω_B, we can write the equation (2) for both bodies as

$$\mathbf{G}(\mathbf{u}+\mathbf{X}) = \mathbf{G}\mathbf{u} + \mathbf{G}\mathbf{X} = \mathbf{G}\mathbf{u} - \mathbf{b} \geq \mathbf{0} \qquad \text{in } \Gamma_A \cup \Gamma_B \tag{6}$$

where the entries of matrix **G** consist of the components of the outward unit normal vectors of the element faces forming the contact surface.

4. LAGRANGE MULTIPLIER METHOD

The most common methods to enforce the contact constraints are the Lagrange multiplier method and the penalty function method. The major weaknesses of the latter are that the impenetrability condition is satisfied only approximately (penetration occurs) and there is no general guide to choose the penalty parameter for every problem. On the other hand, in the Lagrange multiplier method the impenetrability condition is satisfied exactly. In applying the Lagrange multiplier method, we arrive at following equation [9]

$$\begin{bmatrix} \mathbf{M} & \mathbf{0} \\ \mathbf{0} & \mathbf{0} \end{bmatrix} \begin{Bmatrix} \ddot{\mathbf{u}} \\ \mathbf{0} \end{Bmatrix} + \begin{bmatrix} \mathbf{K} & \mathbf{G}^T \\ \mathbf{G} & \mathbf{0} \end{bmatrix} \begin{Bmatrix} \mathbf{u} \\ \boldsymbol{\lambda} \end{Bmatrix} = \begin{Bmatrix} \mathbf{f}_{ext} \\ \mathbf{b} \end{Bmatrix} \tag{7}$$

From equation (7) we notice that the amount of unknowns has increased by the amount of Lagrange multipliers (denoted by $\boldsymbol{\lambda}$).

5. QUIET BOUNDARY SCHEME BASED ON VISCOUS DAMPING

We introduce a quiet boundary scheme that is based on viscous damping invented by Lysmer and Kuhlemayer [6]. The method is to attach viscous dampers on the boundary of the domain so that the wave arriving at the boundary is absorbed approximately. In three dimensional problems the dampers are attached as shown in Figure 3. The absorption depends on the incident angle φ (see Fig. 3).

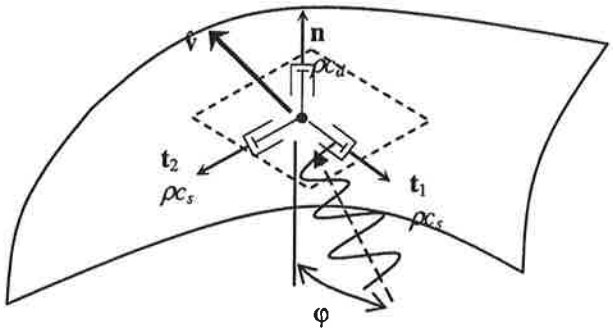

Figure 3 Viscous damper type quiet boundary concept

When the wave arrives at the boundary, the viscous dampers cause normal and tangential tractions

$$t_n = -\rho c_d v_n\,, \quad t_{s1} = -\rho c_s v_{t1}\,, \quad t_{s2} = -\rho c_s v_{t2} \tag{8}$$

In equation (8), c_d and c_s denote the velocities of a dilatation wave and a shear wave respectively, v_n denotes the normal component, and v_{t1}, v_{t2} denote the tangential components of the nodal velocity $\hat{\mathbf{v}}$, respectively. In the discretized model we calculate the equivalent nodal forces caused by tractions (8) as [7]

$$\begin{aligned} \mathbf{f}_{qp} &= -\iint_S \rho c_d \mathbf{N}^{\mathrm{T}}\mathbf{n}\mathbf{n}^{\mathrm{T}}\mathbf{N}dS\hat{\mathbf{v}} = \mathbf{C}^e_{qp}\hat{\mathbf{v}} \\ \mathbf{f}_{qs} &= -\iint_S \rho c_s \left(\mathbf{N}^{\mathrm{T}}\mathbf{t}_1\mathbf{t}_1^{\mathrm{T}}\mathbf{N} + \mathbf{N}^{\mathrm{T}}\mathbf{t}_2\mathbf{t}_2^{\mathrm{T}}\mathbf{N}\right)dS\hat{\mathbf{v}} = \mathbf{C}^e_{qs}\hat{\mathbf{v}} \end{aligned} \tag{9}$$

Here $\mathbf{n}$, $\mathbf{t}_1$ and $\mathbf{t}_2$ denote the normal and tangent unit vectors (see Fig. 3) respectively, and $\mathbf{N}$ is the interpolation matrix. First of the formulas (9) represents the equivalent nodal force at the quiet boundary due to the dilatational wave, and the second represents that of the shear wave. In addition, $\mathbf{C}^e_{qp}$ and $\mathbf{C}^e_{qs}$, whose definitions are clear from (9), denote the element damping matrices corresponding to the dilatation and shear waves, respectively.

7. MODIFIED EULER METHOD

We choose the explicit time integration because, although these methods are conditionally stable, the time step limitation is of less harm because in many problems the stress wave propagation is a physically fast phenomenon and thus requires small time steps in order to achieve sufficient accuracy. Furthermore, the small time step decreases trouble caused by discontinuities due to the contact-impact [7].

The modified Euler scheme is an explicit time integration method whose characteristic equations are [5]

$$\ddot{\mathbf{u}}^t = \mathbf{M}^{-1}\left(\mathbf{f}^t - \mathbf{K}\mathbf{u}^t\right), \quad \dot{\mathbf{u}}^{t+\Delta t} = \dot{\mathbf{u}}^t + \Delta t\ddot{\mathbf{u}}^t, \quad \mathbf{u}^{t+\Delta t} = \mathbf{u}^t + \Delta t\dot{\mathbf{u}}^{t+\Delta t}. \tag{10}$$

The stability criterion for this method is $\Delta t \le T_{\min}/\pi$ [5], which is the same as for the central difference method, for which the corresponding formulas are

$$\begin{aligned}
&\mathbf{u}^{t+\Delta t} = \Delta t^2 \mathbf{M}^{-1}\left(\mathbf{f}_{ext}^t - \mathbf{K}\mathbf{u}^t\right) + 2\mathbf{u}^t - \mathbf{u}^{t-\Delta t} \\
&\dot{\mathbf{u}}^t = \frac{1}{2\Delta t}\left(\mathbf{u}^{t+\Delta t} - \mathbf{u}^{t-\Delta t}\right),\ \ddot{\mathbf{u}}^t = \frac{1}{\Delta t^2}\left(\mathbf{u}^{t-\Delta t} - 2\mathbf{u}^t + \mathbf{u}^{t+\Delta t}\right)
\end{aligned} \tag{11}$$

The reason why we don't use the central difference method here is that if we want to use the quiet boundary scheme based on viscous damping we need to know the velocity $\mathbf{u}^t$ at the beginning of a time step for the calculation of the forces (9). However, the central difference method doesn't provide this velocity directly as we can see from equations (11).

8. FORWARD INCREMENT LAGRANGE MULTIPLIER METHOD

Carpenter and others did not only prove that equation (7) is incompatible with the explicit time integrators but also provided a compatible modification of it, which they called forward increment Lagrange multiplier method [3]. They applied it with the central difference method, but we, for the reason explained in the previous section, apply it with the modified Euler method. In this modification, the equations of motion are satisfied at time t as the explicit methods demand, but the kinematic contact constraints are satisfied at time $t+\Delta t$. Thus, the (time) incremental form of equation (7) is [3]

$$\begin{aligned}
&\mathbf{M}\ddot{\mathbf{u}}^t + \mathbf{K}\mathbf{u}^t = \mathbf{f}_{tot}^t - \mathbf{G}^{\mathrm{T}}\boldsymbol{\lambda}^t \\
&\mathbf{G}\mathbf{u}^{t+\Delta t} - \mathbf{b} = \mathbf{0}
\end{aligned} \tag{12}$$

After substituting from equations (10) to (12), we get the following formulas for computing the incremental response

$$\begin{aligned}
&\ddot{\mathbf{u}}^t = \tilde{\ddot{\mathbf{u}}}^t - \mathbf{M}^{-1}\mathbf{G}^{\mathrm{T}}\boldsymbol{\lambda}^t \\
&\dot{\mathbf{u}}^{t+\Delta t} = \dot{\mathbf{u}}^t + \Delta t\ddot{\mathbf{u}}^t \\
&\mathbf{u}^{t+\Delta t} = \mathbf{u}^t + \Delta t\dot{\mathbf{u}}^t + \Delta t^2\ddot{\mathbf{u}}^t
\end{aligned} \tag{13}$$

where

$$\begin{aligned}
&\tilde{\ddot{\mathbf{u}}}^t = \mathbf{M}^{-1}\left(\mathbf{f}_{ext}^t + \mathbf{f}_{qp}^t + \mathbf{f}_{qs}^t - \mathbf{K}\mathbf{u}^t\right) \\
&\tilde{\mathbf{u}}^{t+\Delta t} = \mathbf{u}^t + \Delta t\dot{\mathbf{u}}^t + \Delta t^2\tilde{\ddot{\mathbf{u}}}^t \\
&\boldsymbol{\lambda}^t = \left(\Delta t^2\mathbf{G}\mathbf{M}^{-1}\mathbf{G}^{\mathrm{T}}\right)^{-1}\left(\mathbf{G}\tilde{\mathbf{u}}^{t+\Delta t} - \mathbf{b}\right)
\end{aligned} \tag{14}$$

The solution process of these incremental equations is as follows. First we predict the acceleration $\tilde{\ddot{\mathbf{u}}}^t$ while neglecting the contact force, which is the physical interpretation of Lagrange multipliers $\boldsymbol{\lambda}^t$. Next we predict the displacement $\tilde{\mathbf{u}}^{t+\Delta t}$ also while neglecting the contact force. Then we calculate the Lagrange multipliers $\boldsymbol{\lambda}^t$ corresponding to the predicted displacement $\tilde{\mathbf{u}}^{t+\Delta t}$. Finally we correct the acceleration by the first of formulas (13) and calculate the velocity and the displacement for next time step by the second and the third of formulas (13).

This method seems very effective (*a priori*) in computational characteristics and in accuracy. Firstly, it is accurate in the sense that it satisfies the impenetrability constraint exactly. Secondly, it is fast, for when we use the node-to-node contact interface and the lumped (diagonal) mass matrix formulation, matrix $\mathbf{G}\mathbf{M}^{-1}\mathbf{G}^{\mathrm{T}}$ is diagonal because all the degrees of freedom are uncoupled. Thus,

the inverse $\left(\Delta t^2\mathbf{G}\mathbf{M}^{-1}\mathbf{G}^{\mathrm{T}}\right)^{-1}$ is easy to calculate even if the number of contact constraints would be large. Furthermore, if the assumption 2 in the introduction holds, we need to calculate $\left(\Delta t^2\mathbf{G}\mathbf{M}^{-1}\mathbf{G}^{\mathrm{T}}\right)^{-1}$ only once at the beginning of the solution process. So the computationally largest operation during a general time step is the calculation of the internal force $\mathbf{f}_{in}^t = \mathbf{K}\mathbf{u}^t$. Finally, it is simple: Because the degrees of freedom are uncoupled, we can, in order to satisfy the 'inequational part' of (6), update the contact force vector simply by setting its component $(f_{cont}^t)_i$, corresponding to the ith degree of freedom, to zero when this component is positive, i.e. $(f_{cont}^t)_i > 0$ (tensile tractions are not allowed).

Now we can write the algorithm for solving (12) as follows:

Algorithm Lag-MEM
Initialization:

1. Compute $\mathbf{M}^{-1}$, $\left(\Delta t^2\mathbf{G}\mathbf{M}^{-1}\mathbf{G}^{\mathrm{T}}\right)^{-1}$
2. From initial values $\mathbf{u}^0, \dot{\mathbf{u}}^0$, calculate $\ddot{\mathbf{u}}^0 = \mathbf{M}^{-1}(\mathbf{f}_{ext}^0 - \mathbf{K}\mathbf{u}^0)$

Computations during general time step:

1. Calculate forces: $\mathbf{f}_{in}^t = \mathbf{K}\mathbf{u}^t$, $\mathbf{f}_{ext}^t$, $\mathbf{f}_{qp}^t = \mathbf{C}_{qp}\dot{\mathbf{u}}^t$, $\mathbf{f}_{qs}^t = \mathbf{C}_{qs}\dot{\mathbf{u}}^t$
2. Predict acceleration: $\tilde{\ddot{\mathbf{u}}}^t = \mathbf{M}^{-1}\left(\mathbf{f}_{ext}^t + \mathbf{f}_{qp}^t + \mathbf{f}_{qs}^t - \mathbf{f}_{in}^t\right)$
3. Predict displacement without contact force: $\tilde{\mathbf{u}}^{t+\Delta t} = \mathbf{u}^t + \Delta t\dot{\mathbf{u}}^t + \Delta t^2\tilde{\ddot{\mathbf{u}}}^t$
4. Calculate contact force: $\mathbf{f}_{cont}^t = \left(\Delta t^2\mathbf{G}\mathbf{M}^{-1}\mathbf{G}^{\mathrm{T}}\right)^{-1}\left(\mathbf{G}\tilde{\mathbf{u}}^{t+\Delta t} - \mathbf{b}\right)$
5. Update the contact force vector $\mathbf{f}_{cont}^t$ by setting $(f_{cont}^t)_i = 0$, if $(f_{cont}^t)_i > 0$
6. Correct the acceleration: $\ddot{\mathbf{u}}^t = \tilde{\ddot{\mathbf{u}}}^t - \mathbf{M}^{-1}\mathbf{G}^{\mathrm{T}}\mathbf{f}_{cont}^t$
7. Calculate velocity and displacement for next time step: $\dot{\mathbf{u}}^{t+\Delta t} = \dot{\mathbf{u}}^t + \Delta t\ddot{\mathbf{u}}^t$, $\mathbf{u}^{t+\Delta t} = \mathbf{u}^t + \Delta t\dot{\mathbf{u}}^t + \Delta t^2\ddot{\mathbf{u}}^t$
7. Set $t = t + \Delta t$ and go to 1.

In the above algorithm we have denoted the Lagrange multipliers $\boldsymbol{\lambda}^t$ by the contact force $\mathbf{f}_{cont}^t$. Next we demonstrate the algorithm by solving a numerical example.

8. NUMERICAL EXAMPLE: LONGITUDINAL IMPACT OF CYLINDRICAL BARS

In this section we solve a crucial problem concerning our application area, namely, the problem of longitudinal impact of two cylindrical bars shown in Figure 4. Valeš et al. [8] have solved this problem analytically by using the exact three dimensional theory of elasticity. Because the analytical solutions for the responses in the bars are far from being trivial to evaluate numerically, we use the results calculated by Valeš et al.

The finite element model and other data needed are given in Figure 4. We use the eight node hexahedral trilinear element with the lumped mass matrix formulation in solving the problem.

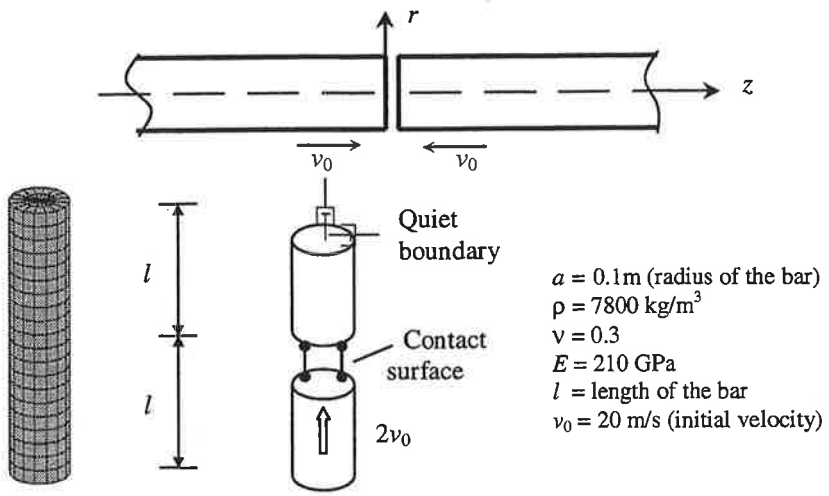

Figure 4 Problem of longitudinal impact of two thick semi-infinite bars (above) and finite element model (below), the element division of the mesh is denoted by $n_z \times n_r \times n_\theta$ where n_z, n_r, and n_θ are the number of elements in z, r, θ (circumferential) directions, respectively

We begin with demonstrating the quiet boundary (QB) scheme presented in section 5. We compute the axial stresses at the end of the bar with and without the quiet boundary condition. The results are shown in Figure 5.

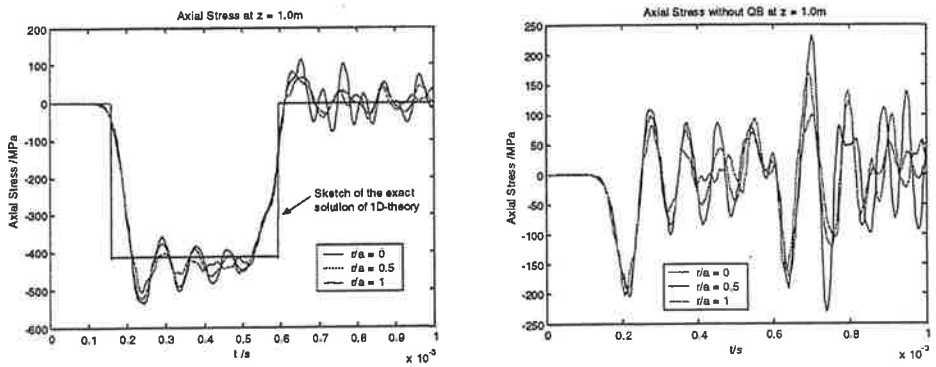

Figure 5 Axial stress vs. time at different locations of bars cross section with QB (left) and without QB (right), l = 1m, mesh division: 10×2×16 elements for each bar, Δt = 3 μs

From Figure 5 we see the effect of viscous quiet boundary: it absorbs the compression wave quite well when the incident angle φ is zero.

Next we compare the responses obtained by algorithm Lag-MEM with the analytical solutions. In order to get an overall picture of the performance of the algorithm, we compute the axial stress near the contact surface and the radial displacement far from the contact surface. We plot the results for dimensionless quantities defined as follows

$$t^* = \frac{c_d t}{a}, \quad u_r^* = \frac{c_s u_r}{v_0 a}, \quad \sigma_z^* = \frac{\sigma_z}{\lambda \frac{v_0}{c_d}} \tag{15}$$

where λ is Lamé constant. Computed responses and the numerical evaluations of analytical solutions are shown in Figure 6.

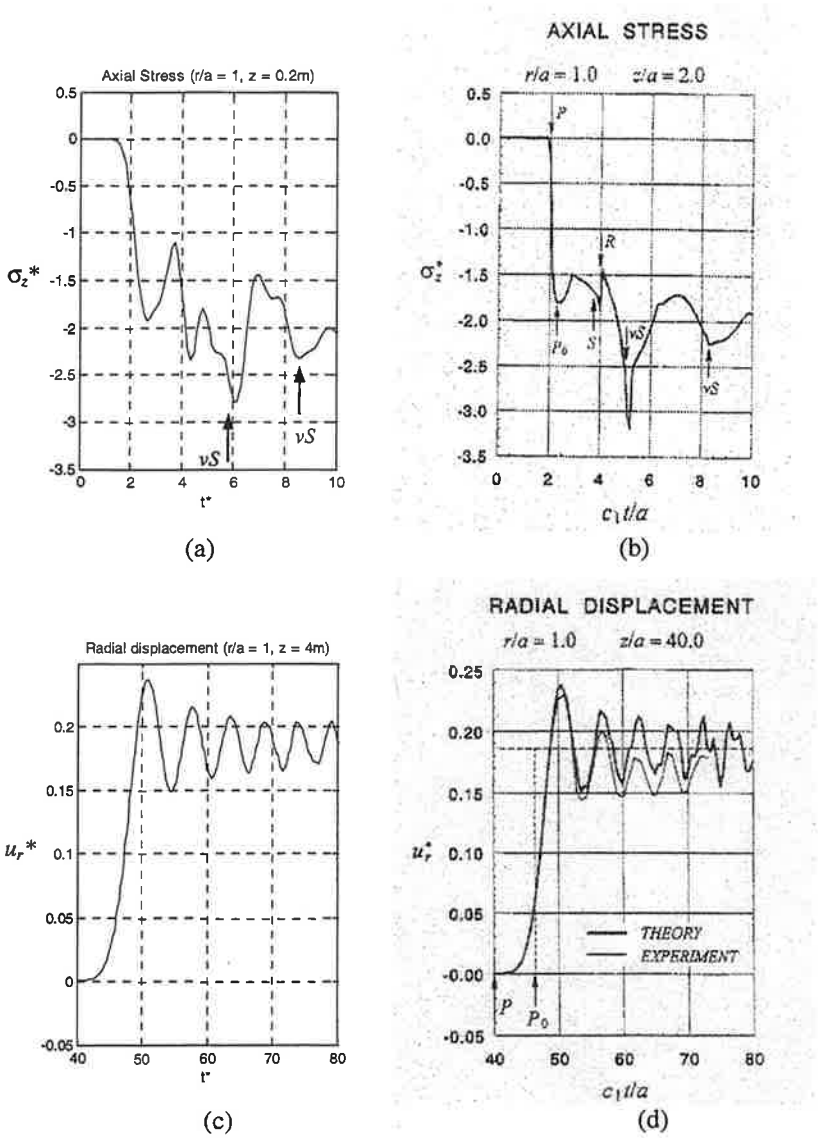

Figure 6 Axial stress vs. time (near-field): Lag-MEM (l = 1m, mesh division: 40×3×16 for each bar, Δt = 2 μs) (a) Analytical solution [8] (b), Radial displacement vs. time (far-field): Lag-MEM (l = 6m, mesh division: 120×3×16 for each bar, Δt = 2 μs) (c) Analytical solution [8] (d)

According to Valeš et al., the error of their numerical evaluations (in Figs. 6 (b), (d)), which consist of the first 50 longitudinal modes, is "only several percent". In Figure 6 (b) the symbols P, S, vS, R, and P_0 denote the arrival times of dilatational wave, shear wave, von Schmidt wave, Rayleigh wave and longitudinal thin-bar wave respectively. In addition, the experimental result due to Miklowitz is plotted in Figure 6 (d).

From Figure 6 (a) we see that the main features of the analytical solution for the axial stress can also be found in the FEM solution (Fig. 6 (b)). There are differences between them (e.g. the slight delay at the arrival of the first von Schmidt wave) but it is, however, natural because the stress, being computed via **EB** from **u**, is only secondary unknown in the displacement based FEM. On the other hand, the computed radial displacement (Fig. 6 (c)), being a component of the primary unknown **u**, is in good agreement with the analytical solution (Fig. 6 (d)).

Finally, we note that the solution time for the radial displacement analysis, for which there were 35574 degrees of freedom and 49 contact constraints in the FEM model, was about 500 seconds (analysis time was 1.5 ms with time step 2 μs). The computer used in the computations was a PC with AMD Athlon 1.53 GHz processor and 512 MB RAM.

9. CONCLUSION

We have developed an explicit algorithm for modeling the stress wave propagation in frictionless and simple (in the sense of satisfying the assumptions 1 to 3 in the introduction) contact-impact problems with non-reflecting boundaries. On the basis of the discussion made in this paper and the numerical results computed in the previous section, we can conclude that the present algorithm is fast and accurate. It at least meets the requirements of the rock drilling engineering community.

ACKNOWLEDGEMENT

The computations in section 8 were carried out with a MatLab based FEM-code FEFEC3D written by Dr. Markku Keskiniva, a research engineer of Sandvik-Tamrock Corp.

REFERENCES

[1] Belytschko T., and M. O. Neal. *Contact-Impact by the Pinball Algorithm with Penalty and Lagrangian Methods.* International Journal for Numerical Methods in Engineering. Vol. 31. 1991. 547 - 572.

[2] Belytschko T., et al. *Nonlinear Finite Elements for Continua and Structures.* New York: Wiley & Sons Ltd. 2000.

[3] Carpenter N. J., et al.. *Lagrange Constraints for Transient Finite Element Surface Contact.* International Journal for Numerical Methods in Engineering. Vol. 32, 1991. 103 - 128.

[4] Graff, K. F. *Wave motion in elastic solids.* Oxford. Clarendon Press. 1975.

[5] Hahn, G. D. *A Modified Euler Method for dynamical analyses.* International Journal for Numerical Methods in Engineering. Vol. 32. 1991. 943 - 955.

[6] Lysmer J., and R. L. Kuhlemeyer. *Finite dynamic model for infinite media.* Journal of Engineering Mechanics Division, ASCE, Vol. 95, 377-392. 1969.

[7] Saksala, T. "*Jännitysaallon simulointiin tarkoitetun FEM-ohjelman kehitys ja testaus*". MSc.Thesis (in Finnish), Department of Mechanical Engineering, Tampere University of Technology, Finland. 2002.

[8] Valeš, F., et al. *Wave Propagation in a Thick Cylindrical Bar Due to Longitudinal Impact.* JSME International Journal, Series A: Mechanics and Material Eng. Vol 39 (1). 1996. 60 - 70.

[9] Zhong. Zhi-Hua. *Finite Element Procedures for Contact-Impact Problems.* Oxford. Oxford Science Publications. 1993.

A SIMPLE NUMERICAL SOLUTION METHOD FOR PLANE CABLES

E.-M. SALONEN* and R. HOLOPAINEN**
*Laboratory of Structural Mechanics
Helsinki University of Technology
P.O. Box 2100
FIN-02015 HUT, FINLAND
**HVAC-laboratory
Helsinki University of Technology
P.O. Box 4100
FIN-02015 HUT, FINLAND

ABSTRACT

Programs such as Maple, Mathcad, Mathematica, MATLAB, etc. have made it possible to solve various smallish non-linear problems often with a relatively small effort. An example of this is given in connection with a flexible inextensible plane cable using the Mathcad and Mathematica programs. The method presented may have some value in teaching of basic structural mechanics.

INTRODUCTION

The well-known equilibrium equations for a string or flexible cable are in the plane case in intrinsic coordinates

$$\frac{\mathrm{d}T}{\mathrm{d}s} = -q_s\,, \tag{1}$$

$$T\frac{\mathrm{d}\theta}{\mathrm{d}s} = q_n\,. \tag{2}$$

T is the cable force or the so-called tension ($[T] = \mathrm{N}$), s the curve length coordinate ($[s] = \mathrm{m}$), θ the inclination angle of the curve tangent to the horizontal ($[\theta] = -$) (Figure 1(a)). The loading is assumed to consist here of smoothly varying distributed loading $\mathbf{q}$ per unit cable length ($[\mathbf{q}] = \mathrm{N/m}$) having components q_s and q_n in the cable tangent and normal directions, respectively. Their positive directions are shown in Figure 1(b). In more detail, positive q_s is in the growing direction of s and positive q_n is directed 90 degrees clockwise with respect to q_s. The differential geometry diagram in Figure 1(c) gives the relations

$$\cos\theta = \frac{\mathrm{d}x}{\mathrm{d}s}, \tag{3}$$

$$\sin\theta = \frac{\mathrm{d}y}{\mathrm{d}s}. \tag{4}$$

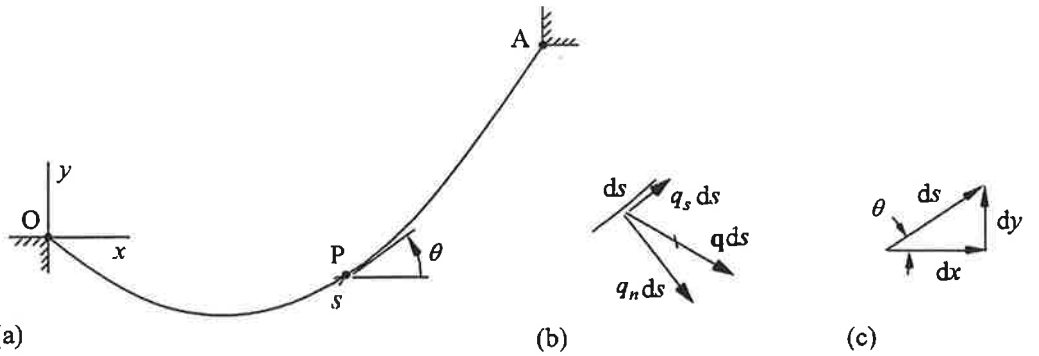

Figure 1(a) Some geometrical notations. **(b)** Distributed force component notations. **(c)** A differential geometry diagram.

If we put the origin of the xy- coordinate system at the beginning of the cable, from where s is measured (Figure 1(a)), integration of (3) and (4) gives the x- and y- coordinates of a generic cable point P by

$$x(s)=\int_0^s \cos\theta(s')\mathrm{d}s', \tag{5}$$

$$y(s)=\int_0^s \sin\theta(s')\mathrm{d}s'. \tag{6}$$

We assume here the cable to be inextensible with length L. Considering the other end of the cable suspended at point A (Figure 1(a)) with given coordinates x_A and y_A, we obtain from (5) and (6) two kinematical constraint equations

$$x_\mathrm{A}=\int_0^L \cos\theta(s)\mathrm{d}s, \tag{7}$$

$$y_\mathrm{A}=\int_0^L \sin\theta(s)\mathrm{d}s \tag{8}$$

as a kind of boundary conditions.

Equations (1), (2), (7), (8) describe the problem at hand. The unknowns to be determined are the functions $\theta=\theta(s)$ and $T=T(s)$. The problem is far from trivial, as the field equation (2) is strongly non-linear and as the components q_s and q_n can depend on the inclination of the cable. Further, the constraint equations (7) and (8) are also nonlinear in θ. The flexible cable may be considered as the simplest structural model: not capable to resist either the bending moment or the shearing force. This means that without loading the cable has no natural initial configuration. The equilibrium position it takes is determined solely by the loading. This makes the cable model quite unique compared, say, to models of bars or beams, where the equilibrium position is usually very near the initial configuration. These facts complicates the treatment of the cable model in teaching as realistic cases lead analytically to very involved calculations or are in practice not amenable to the analytical treatment at all. We suggest in the following a simple numerical method to solve the cable problem. We have applied in the following the Mathcad and the Mathematica programs.

SOLUTION METHOD

We employ the collocation method with trial solutions containing undetermined parameters and in addition Simpson's rule for numerical integration. The collocation method is the simplest of the four main criteria to determine the parameter values in connection with the method of weighted residuals described in Crandall (1956).

Instead of the independent variable s it is convenient to make use of the corresponding dimensionless variable

$$\xi = \frac{s}{L}, \tag{9}$$

which now varies between 0 and 1. We assume the trial solutions

$$\theta(\xi) \approx \tilde{\theta}(\xi) = \sum_{i=1}^{m} \alpha_i \varphi_i(\xi) = \alpha_1 \varphi_1(\xi) + \alpha_2 \varphi_2(\xi) + \alpha_3 \varphi_3(\xi) + \cdots + \alpha_m \varphi_m(\xi), \tag{10}$$

$$T(\xi) \approx \tilde{T}(\xi) = \sum_{i=1}^{m} \beta_i \varphi_i(\xi) = \beta_1 \varphi_1(\xi) + \beta_2 \varphi_2(\xi) + \beta_3 \varphi_3(\xi) + \cdots + \beta_m \varphi_m(\xi). \tag{11}$$

Thus, for simplicity, the basis functions are taken to be the same for the two unknowns. In the numerical applications to follow we have usually selected $m = 10$, so there are together twenty parameters α and β to be determined. As basis functions are taken

$$\varphi_1 = 1, \quad \varphi_2 = \xi, \quad \varphi_3 = \sin(\pi\xi), \quad \varphi_4 = \sin(2\pi\xi), \cdots, \quad \varphi_{10} = \sin(8\pi\xi). \tag{12}$$

These were arrived at by ad hoc reasoning. The first two allow an exact representation of the solution $T = \text{constant}$, $\mathrm{d}\theta/\mathrm{d}s = \text{constant}$ for a cable with pressure type loading ($q_s = 0$, $q_n = \text{constant}$, later the first application) which was considered beneficial. To continue simply with high order powers of ξ may give poorly behaving results for complicated loadings as the power functions are "far from orthogonal". Some numerical experiments also confirmed this. Therefore the sine functions starting with the first with one half-wavelength seemed a more promising simple alternative. Parameters α are seen to be dimensionless and parameters β have the dimension of force.

The field equations (1) and (2) are represented in a discrete form by substituting the approximations (10) and (11) into them and by applying point collocation:

$$\sum_{i=1}^{m} \beta_i \varphi_i'(\xi_k) = -L\, q_s(\xi_k), \quad k = 1, \cdots, r, \tag{13}$$

$$\left(\sum_{i=1}^{m} \beta_i \varphi_i(\xi_k) \right) \left(\sum_{i=1}^{m} \alpha_i \varphi_i'(\xi_k) \right) = L\, q_n(\xi_k), \quad k = 1, \cdots, r. \tag{14}$$

The factors L appear due to the relation $\mathrm{d}(\cdot)/\mathrm{d}s = 1/L \times \mathrm{d}(\cdot)/\mathrm{d}\xi \equiv 1/L \times (\cdot)'$. The notation ξ_k refers to the value of ξ at the collocation point k. We take here $r = 9$, which gives eighteen

equations. The collocation points are taken by dividing the domain $0 \le \xi \le 1$ into nine equal length subintervals and by placing the points at their middle. Thus, $\xi_1 = 1/18$, $\xi_2 = 3/18, \cdots$, $\xi_9 = 17/18$.

We consider next the discretization of (7) and (8). Using the non-dimensional formulation we obtain first ($\mathrm{d}s = L\mathrm{d}\xi$) the forms

$$x_A = L\int_0^1 \cos\theta(\xi)\mathrm{d}\xi, \tag{15}$$

$$y_A = L\int_0^1 \sin\theta(\xi)\mathrm{d}\xi. \tag{16}$$

To take the cosine and sine of $\tilde{\theta}(\xi)$ and then perform the integrations in (15) and (16) is not feasible. Instead, we employ numerical integration with the well-known Simpson's rule to get approximately

$$\begin{aligned} x_A = L\frac{h}{3}\big[&\cos\tilde{\theta}(\xi_0) + 4\cos\tilde{\theta}(\xi_1) + 2\cos\tilde{\theta}(\xi_2) + 4\cos\tilde{\theta}(\xi_3) \\ &+ \cdots + 2\cos\tilde{\theta}(\xi_{2n-2}) + 4\cos\tilde{\theta}(\xi_{2n-1}) + \cos\tilde{\theta}(\xi_{2n})\big], \end{aligned} \tag{17}$$

$$\begin{aligned} y_A = L\frac{h}{3}\big[&\sin\tilde{\theta}(\xi_0) + 4\sin\tilde{\theta}(\xi_1) + 2\sin\tilde{\theta}(\xi_2) + 4\sin\tilde{\theta}(\xi_3) \\ &+ \cdots + 2\sin\tilde{\theta}(\xi_{2n-2}) + 4\sin\tilde{\theta}(\xi_{2n-1}) + \sin\tilde{\theta}(\xi_{2n})\big]. \end{aligned} \tag{18}$$

Here $2n$ is the number of equal length ($= h = 1/2n$) subintervals used. The coordinates of the function evaluation points are thus $\xi_0 = 0$, $\xi_1 = h = 1/2n$, $\xi_2 = 2h = 2/2n$, $\cdots$, $\xi_{2n} = 1$. In the applications we have taken $2n = 10$. Of course, other possibilities exists to evaluate the integrals, however, Simpson's rule is convenient due to its simplicity and relative accuracy. Formulas (17) and (18) give directly two discrete equations containing the undetermined parameters buried inside the cosines and sines.

Altogether the discretized non-linear algebraic system consists of the twenty equations (13), (14), (17), (18). This system is solved by the Find command in Mathcad and by the FindRoot command in Mathematica.

APPLICATIONS

Some preliminaries

The numerical solution for the geometry gives initially only the function $\tilde{\theta}(\xi)$. If values are wanted for x and y, we have to use (5) and (6) now in the forms

$$\tilde{x}(\xi) = L\int_0^{\xi} \cos\tilde{\theta}(\xi')\mathrm{d}\xi', \tag{19}$$

$$\tilde{y}(\xi) = L\int_0^{\xi} \sin\tilde{\theta}(\xi')\mathrm{d}\xi'. \tag{20}$$

We are satisfied here to evaluate these numerically for certain discrete values of ξ. This is a straightforward post-processing procedure, where $\tilde{\theta}(\xi)$ with the solution obtained for the parameters α is substituted in (19) and (20) and calculated with numerical integration commands by Mathcad or Mathematica. Alternatively, continuous expressions can be obtained with some extra effort for instance by basing the treatment on closed form integrations of the piecewise parabolic approximations used in deriving Simpson's rule. We have not applied this alternative here.

Two example cases with known analytical solutions are treated in the following to get an idea about the accuracy attainable by the discrete formulation. These cases are the circular solution and the common catenary solution. For lack of space we do not present the corresponding detailed analytical formulas here but simply rely on graphics produced by the Mathematica program. Further, a kind of combination of the two cases is finally described. The geometry is selected so that $x_A = l$, $y_A = 3l/4$, $L = 5l/2$, where l is a given length equal to the horizontal distance between the suspension points. The Mathcad and the Mathematica programs gave practically identical results in the applications.

Circular solution

We consider the case, where the distributed loading p is perpendicular to the cable and of constant magnitude; we will call this as pressure loading. In equations (1) and (2) (p positive)

$$\begin{aligned} q_s &= 0, \\ q_n &= p. \end{aligned} \tag{21}$$

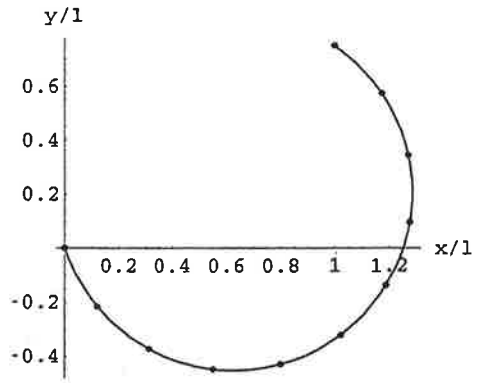

Figure 2 Shape: analytical solution (–) discrete solution points (•).

The shape the cable takes is from symmetry reasons naturally simply an arc of a circle of the form $\theta(\xi) = a + b\xi$, where a and b are certain constants. The tension has a constant value $T = pR$, where R is the radius of the circle. The discrete results coincide essentially with the analytical values. The very small errors found are associated with the use of Simpson's rule. The solution for the geometry is shown in Figure 2. Some rough initial parameter values must be given for the non-linear programs to proceed. Quite interestingly, the other theoretical unstable equilibrium configuration with compression (obtainable from the configuration of Figure 2 by reflection about

the line through the suspension points) was also produced by the program by just starting with certain alternative parameter values.

Catenary solution

The second example case concerns the common catenary. The shape a cable takes with constant loading q (with respect to magnitude and direction) per unit length is called common catenary, Synge and Griffith (1959). This case corresponds to the situation where the cable is homogeneous and under gravity. The loading intensities to be used in (1) and (2) are thus (positive q)

$$\begin{aligned} q_s &= -q\sin\theta, \\ q_n &= q\cos\theta. \end{aligned} \tag{22}$$

The results for the inclination angle θ and for the tension T are shown in Figures 3 and 4. It may be mentioned that in the determination of the analytical solution, a numerical procedure is in fact already needed to take into account the boundary conditions.

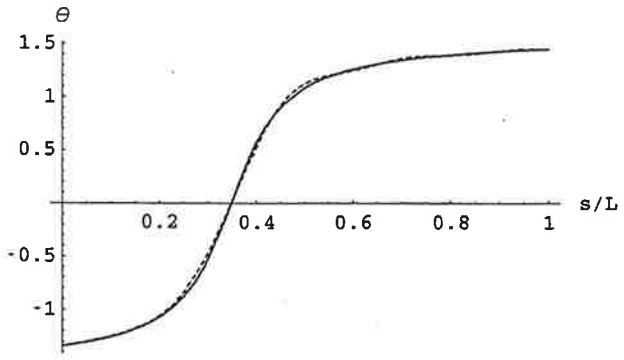

Figure 3 Inclination angle: analytical solution (solid line), discrete solution (dashed line).

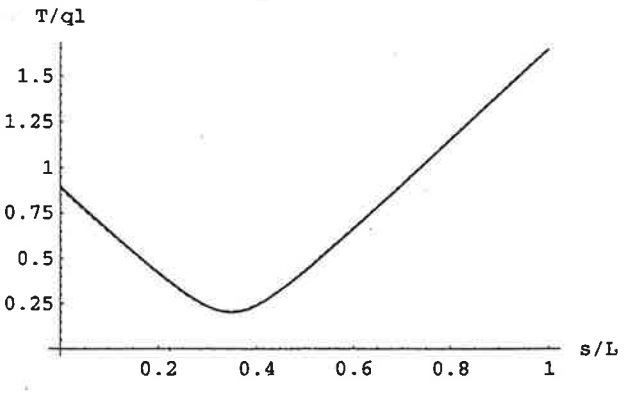

Figure 4 Tension: analytical solution (solid line), discrete solution (dashed line).

For the tension the two solutions are hardly distinguishable. The shape obtained is shown in Figure 5.

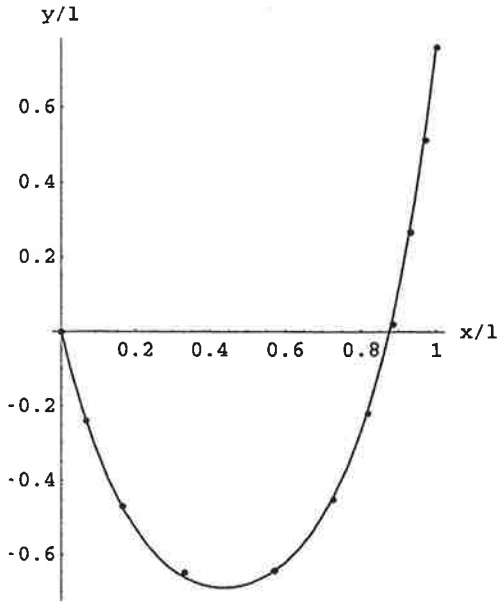

Figure 5 Shape: analytical solution (–), discrete solution points (•).

Combined constant pressure and gravity solution

Here we take the loading to consist of (positive constant q)

$$\begin{aligned} q_s &= -q\sin\theta, \\ q_n &= q\cos\theta + p \end{aligned} \tag{23}$$

with $p = -4q$. This is the case of an inflated tension structure type problem with the internal pressure four times the magnitude of the gravity loading. We are not aware of a possible exact solution for the problem. Figure 6 gives the shape obtained with a rather crude number of discrete solution points shown. For comparison, obvious solutions for pure gravity loading and for pure pressure loading are also indicated.

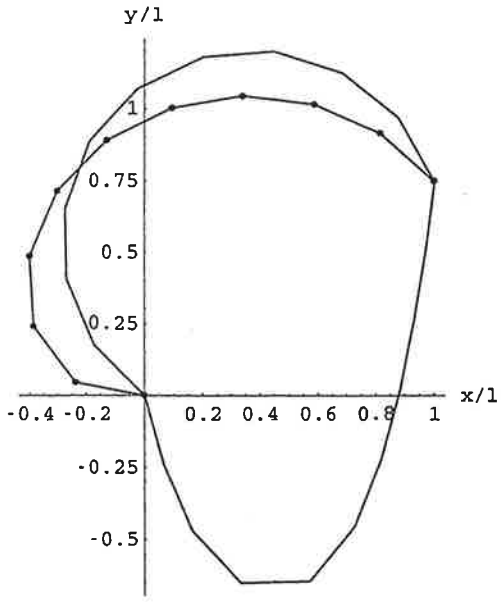

Figure 6 Solution (solid line with dots).

CONCLUDING REMARKS

The purpose of the presentation is mainly to demonstrate that programs like Maple, Mathcad, Mathematica, MATLAB, etc. make it nowadays possible to solve even non-linear problems often with a rather small effort. The obvious conclusion drawn is that more emphasis in teaching can be put on the basics as once a proper formulation of a problem is achieved, new efficient tools are available for obtaining the corresponding numerical solution. As samples, parts of the Mathcad and Mathematica codes used in connection with the circular solution case are given in Appendix 1 and 2, respectively. For simplicity of presentation, the number of undetermined parameters is only eight. No special effort to achieve elegance is attempted as in small problems it is convenient produce lines just with the "copy, paste and modify technique".

The straightforward numerical method, described above, is not to be applied if the loading of the cable is non-smooth; especially if there are point loads. Then it is appropriate to employ a "proper" finite element type weighted residual procedure. The derivatives on T and θ are removed by integration by parts manipulations and discontinuous approximations are used for T and θ. This kind of approach needs quite a lot of bookkeeping and is probably not suitable for demonstration purposes in basic teaching.

REFERENCES

S. H. Crandall, *Engineering Analysis, A Survey of Numerical Procedures*, McGraw-Hill, New York, 1956.

J. L. Synge and B. A. Griffith, *Principles of Mechanics*, 3rd ed., McGraw-Hill, New York, 1959.

APPENDIX 1

Cable problem, pressure loading, eight parameters, h=1/10

Data:

$$L := \frac{5}{2}, \quad p := 1, \quad h := \frac{1}{10}$$

Cable inclination angle approximation and its derivative

$$\theta(\alpha_1,\alpha_2,\alpha_3,\alpha_4,\xi) := \alpha_1 + \alpha_2\cdot\xi + \alpha_3\cdot\sin(\pi\cdot\xi) + \alpha_4\cdot\sin(2\cdot\pi\cdot\xi)$$

$$d\theta(\alpha_1,\alpha_2,\alpha_3,\alpha_4,\xi) := \frac{d}{d\xi}\theta(\alpha_1,\alpha_2,\alpha_3,\alpha_4,\xi)$$

Cable tension approximation and its derivative

$$T(\beta_1,\beta_2,\beta_3,\beta_4,\xi) := \beta_1 + \beta_2\cdot\xi + \beta_3\cdot\sin(\pi\cdot\xi) + \beta_4\cdot\sin(2\cdot\pi\cdot\xi)$$

$$dT(\beta_1,\beta_2,\beta_3,\beta_4,\xi) := \frac{d}{d\xi}T(\beta_1,\beta_2,\beta_3,\beta_4,\xi)$$

Left-hand sides of the equations

$$lhsT(\beta_1,\beta_2,\beta_3,\beta_4,\xi) := \frac{d}{d\xi}T(\beta_1,\beta_2,\beta_3,\beta_4,\xi)$$

$$lhs\theta(\beta_1,\beta_2,\beta_3,\beta_4,\alpha_1,\alpha_2,\alpha_3,\alpha_4,\xi) := T(\beta_1,\beta_2,\beta_3,\beta_4,\xi)\cdot d\theta(\alpha_1,\alpha_2,\alpha_3,\alpha_4,\xi)$$

$$lhs7(\alpha_1,\alpha_2,\alpha_3,\alpha_4) := L\cdot\frac{h}{3}\cdot\begin{pmatrix}\cos(\theta(\alpha_1,\alpha_2,\alpha_3,\alpha_4,0)) + 4\cdot\cos(\theta(\alpha_1,\alpha_2,\alpha_3,\alpha_4,h)) \dots \\ + 2\cdot\cos(\theta(\alpha_1,\alpha_2,\alpha_3,\alpha_4,2\cdot h)) + 4\cdot\cos(\theta(\alpha_1,\alpha_2,\alpha_3,\alpha_4,3\cdot h)) \dots \\ + 2\cdot\cos(\theta(\alpha_1,\alpha_2,\alpha_3,\alpha_4,4\cdot h)) + 4\cdot\cos(\theta(\alpha_1,\alpha_2,\alpha_3,\alpha_4,5\cdot h)) \dots \\ + 2\cdot\cos(\theta(\alpha_1,\alpha_2,\alpha_3,\alpha_4,6\cdot h)) + 4\cdot\cos(\theta(\alpha_1,\alpha_2,\alpha_3,\alpha_4,7\cdot h)) \dots \\ + 2\cdot\cos(\theta(\alpha_1,\alpha_2,\alpha_3,\alpha_4,8\cdot h)) + 4\cdot\cos(\theta(\alpha_1,\alpha_2,\alpha_3,\alpha_4,9\cdot h)) \dots \\ + \cos(\theta(\alpha_1,\alpha_2,\alpha_3,\alpha_4,10\cdot h))\end{pmatrix}$$

$$lhs8(\alpha_1,\alpha_2,\alpha_3,\alpha_4) := L\cdot\frac{h}{3}\cdot\begin{pmatrix}\sin(\theta(\alpha_1,\alpha_2,\alpha_3,\alpha_4,0)) + 4\cdot\sin(\theta(\alpha_1,\alpha_2,\alpha_3,\alpha_4,h)) \dots \\ + 2\cdot\sin(\theta(\alpha_1,\alpha_2,\alpha_3,\alpha_4,2\cdot h)) + 4\cdot\sin(\theta(\alpha_1,\alpha_2,\alpha_3,\alpha_4,3\cdot h)) \dots \\ + 2\cdot\sin(\theta(\alpha_1,\alpha_2,\alpha_3,\alpha_4,4\cdot h)) + 4\cdot\sin(\theta(\alpha_1,\alpha_2,\alpha_3,\alpha_4,5\cdot h)) \dots \\ + 2\cdot\sin(\theta(\alpha_1,\alpha_2,\alpha_3,\alpha_4,6\cdot h)) + 4\cdot\sin(\theta(\alpha_1,\alpha_2,\alpha_3,\alpha_4,7\cdot h)) \dots \\ + 2\cdot\sin(\theta(\alpha_1,\alpha_2,\alpha_3,\alpha_4,8\cdot h)) + 4\cdot\sin(\theta(\alpha_1,\alpha_2,\alpha_3,\alpha_4,9\cdot h)) \dots \\ + \sin(\theta(\alpha_1,\alpha_2,\alpha_3,\alpha_4,10\cdot h))\end{pmatrix}$$

Initial values

$\alpha_1 := -1 \quad \alpha_2 := 4 \quad \alpha_3 := 0 \quad \alpha_4 := 0 \quad \beta_1 := 1 \quad \beta_2 := 0 \quad \beta_3 := 0 \quad \beta_4 := 0$

Discrete equations by collocation with three collocation points and by Simpson's rule with ten subintervals

Given

$$\text{lhsT}\left(\beta_1, \beta_2, \beta_3, \beta_4, \frac{1}{6}\right) = 0$$

$$\text{lhsT}\left(\beta_1, \beta_2, \beta_3, \beta_4, \frac{3}{6}\right) = 0$$

$$\text{lhsT}\left(\beta_1, \beta_2, \beta_3, \beta_4, \frac{5}{6}\right) = 0$$

$$\text{lhs}\theta\left(\beta_1, \beta_2, \beta_3, \beta_4, \alpha_1, \alpha_2, \alpha_3, \alpha_4, \frac{1}{6}\right) = p \cdot L$$

$$\text{lhs}\theta\left(\beta_1, \beta_2, \beta_3, \beta_4, \alpha_1, \alpha_2, \alpha_3, \alpha_4, \frac{3}{6}\right) = p \cdot L$$

$$\text{lhs}\theta\left(\beta_1, \beta_2, \beta_3, \beta_4, \alpha_1, \alpha_2, \alpha_3, \alpha_4, \frac{5}{6}\right) = p \cdot L$$

$$\text{lhs7}\left(\alpha_1, \alpha_2, \alpha_3, \alpha_4\right) = 1$$

$$\text{lhs8}\left(\alpha_1, \alpha_2, \alpha_3, \alpha_4\right) = \frac{3}{4}$$

Solution

$$\begin{pmatrix} \alpha_1 \\ \alpha_2 \\ \alpha_3 \\ \alpha_4 \\ \beta_1 \\ \beta_2 \\ \beta_3 \\ \beta_4 \end{pmatrix} := \text{Find}\left(\alpha_1, \alpha_2, \alpha_3, \alpha_4, \beta_1, \beta_2, \beta_3, \beta_4\right)$$

$\alpha_1 = -1.25213 \quad \alpha_2 = 3.79126 \quad \alpha_3 = -0 \quad \alpha_4 = 0$

$\beta_1 = 0.65941 \quad \beta_2 = 0 \quad \beta_3 = 0 \quad \beta_4 = 0$

APPENDIX 2

Cable problem, pressure loading, eight parameters, h=1/10

Data

```
L = 5/2; p = 1; h = 1/10;
```

Cable inclination angle approximation and its derivative

```
θ = α1 + α2 ξ + α3 Sin[Pi ξ] + α4 Sin[2 Pi ξ];
dθ = D[θ, ξ];
```

Cable tension approximation and its derivative

```
aT = β1 + β2 ξ + β3 Sin[Pi ξ] + β4 Sin[2 Pi ξ];
daT = D[aT, ξ];
```

Governing continuum equations with approximations substituted

```
eqT = daT == 0;
eqθ = aT dθ == p L;
```

Discrete equations by collocation with three collocation points and by Simpson's rule with ten subintervals

```
eq1 = eqT /. ξ → 1/6;
eq2 = eqT /. ξ → 3/6;
eq3 = eqT /. ξ → 5/6;
eq4 = eqθ /. ξ → 1/6;
eq5 = eqθ /. ξ → 3/6;
eq6 = eqθ /. ξ → 5/6;
eq7 =
  L h/3 × ((Cos[θ] /. ξ → 0) + 4 (Cos[θ] /. ξ → 1/10) + 2 (Cos[θ] /. ξ → 2/10) +
     4 (Cos[θ] /. ξ → 3/10) + 2 (Cos[θ] /. ξ → 4/10) + 4 (Cos[θ] /. ξ → 5/10) +
     2 (Cos[θ] /. ξ → 6/10) + 4 (Cos[θ] /. ξ → 7/10) + 2 (Cos[θ] /. ξ → 8/10) +
     4 (Cos[θ] /. ξ → 9/10) + (Cos[θ] /. ξ → 1)) == 1;
eq8 =
  L h/3 × ((Sin[θ] /. ξ → 0) + 4 (Sin[θ] /. ξ → 1/10) + 2 (Sin[θ] /. ξ → 2/10) +
     4 (Sin[θ] /. ξ → 3/10) + 2 (Sin[θ] /. ξ → 4/10) + 4 (Sin[θ] /. ξ → 5/10) +
     2 (Sin[θ] /. ξ → 6/10) + 4 (Sin[θ] /. ξ → 7/10) + 2 (Sin[θ] /. ξ → 8/10) +
     4 (Sin[θ] /. ξ → 9/10) + (Sin[θ] /. ξ → 1)) == 3/4;
```

Solution with an initial guess

```
FindRoot[{eq1, eq2, eq3, eq4, eq5, eq6, eq7, eq8},
 {α1, -1}, {α2, 4}, {α3, 0}, {α4, 0}, {β1, 1}, {β2, 0},
 {β3, 0}, {β4, 0}]
```

$\{\alpha_1 \to -1.25213,\ \alpha_2 \to 3.79126,\ \alpha_3 \to 7.95877 \times 10^{-18},$
$\alpha_4 \to 4.15721 \times 10^{-18},\ \beta_1 \to 0.659412,\ \beta_2 \to 0.,\ \beta_3 \to 0.,\ \beta_4 \to 0.\}$

KULMANMUUTOSMENETELMÄSTÄ JA SEN IMPLEMENTOINNISTA

J. AALTO

Teknillinen korkeakoulu
Rakenteiden mekaniikka
PL 2100, 02015 TKK
e-mail: Jukka.Aalto@hut.fi

TIIVISTELMÄ

Artikkelissa käsitellään tasokehän ratkaisemista kulmanmuutosmenetelmällä elementtimenetelmän formalismia käyttäen. Erityisesti tarkastellaan (i) kuinka rakenteen siirtymätila ilmaistaan riippumattomien sauvakiertymien avulla, (ii) kuinka muodostetaan rakenteen siirtymäyhtälöt ja (iii) kuinka kehän aksiaalisesti jäykiksi otaksuttujen sauvojen normaalivoimajakaumat voidaan systemaattisesti määrittää. Tavanomaisen mekaanisen kuormituksen lisäksi tarkasteluun on sisällytetty alkumuodonmuutoksen vaikutus. Esitetyn pohjalta on kehitetty yksinkertainen ohjelma tasokehän analysoimiseksi kulmanmuutosmenetelmällä.

1. JOHDANTO

Kulmanmuutosmenetelmä [1], [2] on klassinen kehärakenteiden analysointimenetelmä, joka on ollut käytössä jo runsaan puolen vuosisadan ajan ja jota käytetään edelleen rakenteiden mekaniikan peruskurssien opetuksessa. Menetelmä on siirtymämenetelmä, jossa kehän sauvat noudattavat teknistä taivutusteoriaa ja ne otaksutaan aksiaalisesti jäykiksi ($EA = \infty$). Tuntemattomiksi ratkaistavaan yhtälöryhmään tulee pelkästään kiertymiä, nimittäin rakenteen nurkkien kiertymiä ja niinsanottuja riippumattomia sauvakiertymiä. Se, että tuntemattomien lukumäärä jää realististenkin tehtävien yhteydessä kohtuulliseksi, selittää menetelmän pitkän iän ja erinomaisen soveltuvuuden osaksi rakenteiden mekaniikan peruskoulutusta.

Tasokehän analysointi yleisellä siirtymämenetelmällä, jossa sauvat otaksutaan aksiaalisesti venyviksi ($EA \neq \infty$) ja jossa tuntemattomina ovat sekä nurkkien siirtymät että kiertymät, on varsin suoraviivainen prosessi, joka nojautuu tavanomaiseen elementtimenetelmän systematiikkaan. Tämän vuoksi yleiseen siirtymämenetelmään (elementtimenetelmään) perustuva kehäohjema on rakenteeltaan yksinkertainen. Tasokehän analysointi kulmanmuutosmenetelmällä on selvästi monimutkaisempi tehtävä. Koska menetelmää käytetään opetuksessa nimenomaan käsinlaskumenetelmänä, ei sen ratkaisuprosessia ole yleensä pyritty formuloimaan systemaattiseksi kokonaisuudeksi, joka käsittää joukon kaavoja. Tämän artikkelin tarkoituksena on esittää kulmanmuutosmenetelmän yhtälöt tällä tavoin käyttäen apuna elementtimenetelmän formalismia.

Siirtyvän kehän ratkaiseminen kulmanmuutosmenetelmällä on osoittautunut olevan ylivoimaisesti vaikein sauvarakenteita käsittelevän kurssin tenttitehtävätyyppi erityisesti silloin, kun kehässä on vinoja sauvoja. Myöskin mielekkäiden probleemien laatiminen käsipelillä on varsin työläs toimenpide. Tämän työn yhteydessä kehitetty yksinkertainen kulmanmuutosmenetelmäohjelma on tarkoitettu tukemaan sauvarakenteiden opetusta. Opettaja voi käyttää sitä apuna tentti- ja harjoitustehtävien laadinnassa ja tarkistamisessa. Opiskelija voi tarkistaa sillä käsin laskemiensa harjoitustehtävien tuloksia sekä ratkaista sellaisia realistisempia probleemia, joiden ratkaiseminen käsin ei enää ole mielekästä. Ohjelmointiympäristönä on MATLAB, johon sisällytetty mahdollisuus määritellä halutut matriisit harvoiksi [3], säästää muistitilaa ja helpottaa ohjelmointia merkittävästi.

2. RAKENTEEN SIIRTYMÄVAPAUSASTEIDEN JA SAUVAKIERTYMIEN ILMAISEMINEN RIIPPUMATTOMIEN SAUVAKIERTYMIEN AVULLA

Kuvassa 1 on esitetty sauvaelementti e ja sen solmusiirtymät sauva- ja rakennekoordinaatistoissa. Kulmanmuutosmenetelmässä otaksutaan, että elementit $e = 1, \cdots, E$ ovat aksiaalisesti jäykkiä ($EA = \infty$). Tässä otaksutaan lisäksi, että ne voivat saada vakiosuuruisen alkuvenymän ε_0^e. Tällöin elementin e pituuden muutokselle ΔL^e voidaan kirjoittaa

$$\Delta L^e = \varepsilon_0^e L^e \approx u_2^e - u_1^e . \tag{1}$$

Kulmanmuutosmenetelmälle ominainen suure on elementin e ns. ***sauvakiertymä*** ψ^e, joka määritellään sen päiden (solmujen) 1 ja 2 välisen janan kiertymänä. Sille saadaan kuvan 2 perusteella

$$\psi^e = \frac{v_2^e - v_1^e}{L^e} . \tag{2}$$

Kaavoista (1) ja (2) seuraa elementin sauvakoordinaatistossa ilmaistujen solmusiirtymien ja sauvakiertymän välille seuraavat yhtälöt

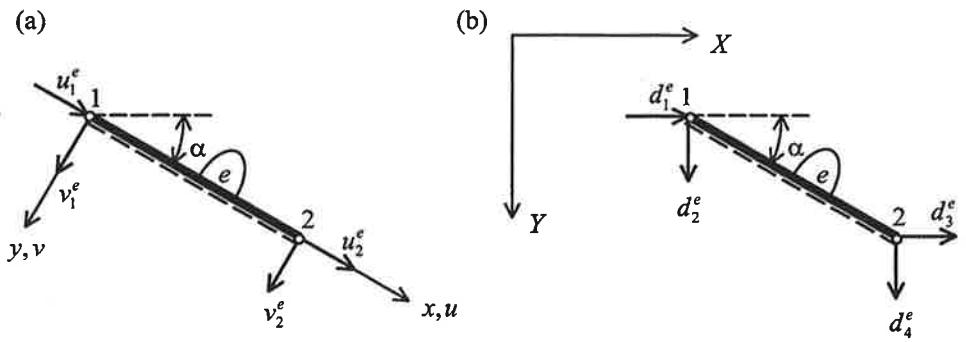

Kuva 1: Elementin solmusiirtymät (a) sauvakoordinaatistossa x,y ja (b) rakennekoordinaatistossa X,Y.

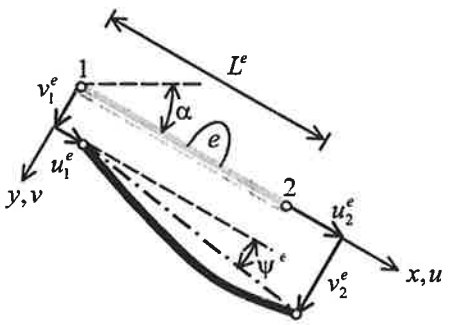

Kuva 2: Sauvaelementin e sauvakiertymä.

$$u_2^e - u_1^e = \varepsilon_0^e L^e,$$
$$v_2^e - v_1^e = \psi^e L^e. \tag{3}$$

Käyttäen hyväksi rakenne- ja sauvakoordinaatiston siirtymäkomponenttien välillä olevia yhteyksiä

$$\left.\begin{aligned} d_1^e &= cu_1^e - sv_1^e \\ d_2^e &= su_1^e + cv_1^e \end{aligned}\right\}, \quad \left.\begin{aligned} d_3^e &= cu_2^e - sv_2^e \\ d_4^e &= su_2^e + cv_2^e \end{aligned}\right\}, \tag{4}$$

missä $c = \cos\alpha$, $s = \sin\alpha$ ja α sauvan kaltevuuskulma, saadaan elementin e päiden rakenne-koordinaatistossa ilmaistujen siirtymien ja sauvakiertymän välille yhtälöpari

$$d_3^e - d_1^e + sL^e\psi^e = cL^e\varepsilon_0^e,$$
$$d_4^e - d_2^e - cL^e\psi^e = sL^e\varepsilon_0^e, \tag{5}$$

Nämä yhtälöt voidaan esittää matriisimuodossa seuraavasti

$$\mathbf{A}^e \begin{Bmatrix} \mathbf{d}^e \\ \psi^e \end{Bmatrix} = \mathbf{B}^e, \tag{6}$$

missä

$$\mathbf{d}^e = \begin{Bmatrix} d_1^e \\ d_2^e \\ d_3^e \\ d_4^e \end{Bmatrix} \tag{7}$$

on elementin siirtymävapausastevektori ja

$$\mathbf{A}^e = \begin{bmatrix} -1 & 0 & 1 & 0 & sL^e \\ 0 & -1 & 0 & 1 & -cL^e \end{bmatrix}, \quad \mathbf{B}^e = \begin{Bmatrix} cL^e\varepsilon_0^e \\ sL^e\varepsilon_0^e \end{Bmatrix}. \tag{8}$$

Muodostamalla yhtälöt (6) kaikille elementeille ja ottamalla samalla huomioon elementtien ja rakenteen siirtymävapausasteiden väliset yhteensopivuusehdot saadaan yhtälöryhmä

$$\mathbf{A} \begin{Bmatrix} \mathbf{d} \\ \psi \end{Bmatrix} = \mathbf{B}, \tag{9}$$

missä $\mathbf{d}$ on systeemin siirtymävapausastevektori (dimensiot $M \times 1$) ja

$$\underset{E\times 1}{\psi} = \begin{Bmatrix} \psi^1 \\ \vdots \\ \psi^E \end{Bmatrix}, \quad \underset{2E\times 1}{\mathbf{B}} = \begin{Bmatrix} \mathbf{B}^1 \\ \vdots \\ \mathbf{B}^E \end{Bmatrix}. \tag{10}$$

Kerroinmatriisin **A** dimensiot ovat $2E\times(M+E)$. Yhtälöryhmä (9) käsittää $2E$ rajoiteyhtälöä, jotka sitovat rakenteen siirtymätilaa kuvaavat siirtymävapausasteet **d** ja sauvakiertymät ψ toisiinsa. Siirtymävapausasteita ja sauvakiertymiä, jotka ovat probleemassa tuntemattomia, on yhteensä $M+E$ kappaletta ja niiden välisiä yhtälöitä siis $2E$ kappaletta. Yhtälöistä (9) voidaan $2E$ tuntematonta ratkaista muiden tuntemattomien avulla. Jälkimmäisiksi on tarkoituksenmukaista valita pelkästään sauvakiertymiä. Valittuja sauvakiertymiä kutsutaan ***riippumattomiksi sauvakiertymiksi*** ja niiden lukumäärä on $N=M-E$. Kirjoitetaan yhtälö (9) muotoon

$$\mathbf{A}_I\begin{Bmatrix}\mathbf{d}\\ \psi'\end{Bmatrix}+\mathbf{A}_{II}\Psi=\mathbf{B}, \tag{11}$$

missä vektori Ψ sisältää riippumattomat sauvakiertymät ja vektori ψ' rakenteen muut sauvakiertymät. Mikäli riippumattomat sauvakiertymät on valittu sopivasti, matriisi $\mathbf{A}_I$ on ei-singulaarinen ja yhtälöstä (11) seuraa

$$\begin{Bmatrix}\mathbf{d}\\ \psi'\end{Bmatrix}=-\mathbf{A}_I^{-1}\mathbf{A}_{II}\Psi+\mathbf{A}^{-1}\mathbf{B}. \tag{12}$$

Käyttäen hyväksi tulosta (12), rakenteen siirtymävapausasteet **d** ja muut sauvakiertymät ψ' voidaan ilmaista riippumattomien sauvakiertymien lineaarisina lausekkeina muodossa

$$\mathbf{d}=\mathbf{C}_d\Psi+\mathbf{D}_d, \tag{13}$$

$$\psi'=\mathbf{C}'_\psi\Psi+\mathbf{D}'_\psi, \tag{14}$$

missä matriisi $\mathbf{C}_d$ muodostuu matriisin $-\mathbf{A}_I^{-1}\mathbf{A}_{II}$ M ensimmäisestä vaakarivistä ja matriisi $\mathbf{C}'_\psi$ muodostuu sen $2E-M$ viimeisestä vaakarivistä. Vastaavasti pystyvektori $\mathbf{D}_d$ muodostuu vektorin $\mathbf{A}^{-1}\mathbf{B}$ M ensimmäisestä alkiosta ja pystyvektori $\mathbf{D}'_\psi$ muodostuu sen $2E-M$ viimeisestä alkiosta. Alkuperäisille sauvakiertymille ψ^e, $e=1,\cdots,E$ ja riippumattomille sauvakiertymille Ψ_i, $i=1,\cdots,N$ voidaan nyt kirjoittaa seuraavia yhteyksiä

$$\psi^e=\Psi_i, \tag{15}$$

kun ψ^e on i:s riippumaton sauvakiertymä ja

$$\psi^e=\sum_{i=1}^{N}C'_{\psi ij}\Psi_j+D'_{\psi i}, \tag{16}$$

kun ψ^e on muu sauvakiertymä, jonka järjestysnumero vektorissa ψ' on i. Näin alkuperäiset sauvakiertymät voidaan ilmaista riippumattomien sauvakiertymien lineaarisena lausekkeena muodossa

$$\psi=\mathbf{C}_\psi\Psi+\mathbf{D}_\psi. \tag{17}$$

2. KULMANMUUTOSMENETELMÄN YHTÄLÖT

2.1 Kulmanmuutosmenetelmän perusyhtälöt

Kulmanmuutosmenetelmässä sauvan (elementin) e sauvanpäämomentit M_i^e ilmaistaan sauvanpääkiertymien φ_i^e ja sauvakiertymän ψ^e avulla muodossa

$$\begin{aligned} M_1^e &= a_1^e\varphi_1^e + b^e\varphi_2^e - c_1^e\psi^e + MK_1^e, \\ M_2^e &= b^e\varphi_1^e + a_2^e\varphi_2^e - c_2^e\psi^e + MK_2^e, \end{aligned} \tag{18}$$

missä a_i^e, b^e ja $c_i^e = a_i^e + b^e$ ovat sauvavakiot ja MK_i^e kuormitustermit. Sauvavakiot a_i^e, b^e jäykkyydeltään muuttuville sauvoille esitetään usein muodossa

$$a_1^e = a_1^* \frac{EI_c}{L^e},\ a_2^e = a_2^* \frac{EI_c}{L^e},\ b^e = b^* \frac{EI_c}{L^e}, \tag{19}$$

missä EI_c on sauvan taivutusjäykkyyden arvo sen valitussa kohdassa ja a_i^* ja b^* ovat sauvavakioiden dimensiottomat kertoimet. Tasajäykän sauvan tapauksessa $a_1^* = 4$, $a_2^* = 4$ ja $b^* = 2$ sekä $EI_c = EI = \text{vakio}$. Sauvavakioita jäykkyydeltään muuttuville sauvoille on taulukoitu lähteissä [1] ja [2]. Myöskin kuormitustermejä sekä tasajäykille että jäykkyydeltään muuttuville sauvoille löytyy näistä samoista teoksista. Yhteydet (18) voidaan esittää matriisimuodossa seuraavasti

$$\mathbf{M}^e = \mathbf{K}_{\varphi\varphi}^e\boldsymbol{\varphi}^e + \mathbf{K}_{\varphi\psi}^e\psi^e + \mathbf{MK}_\varphi^e, \tag{20}$$

missä

$$\mathbf{M}^e = \begin{Bmatrix} M_1^e \\ M_2^e \end{Bmatrix},\ \mathbf{K}_{\varphi\varphi}^e = \begin{bmatrix} a_1^e & b^e \\ b^e & a_2^e \end{bmatrix},\ \boldsymbol{\varphi}^e = \begin{Bmatrix} \varphi_1^e \\ \varphi_2^e \end{Bmatrix},\ \mathbf{K}_{\varphi\psi}^e = -\begin{Bmatrix} c_1^e \\ c_2^e \end{Bmatrix},\ \mathbf{MK}_\varphi^e = \begin{Bmatrix} MK_1^e \\ MK_2^e \end{Bmatrix}. \tag{21}$$

2.2 Nurkkien momenttitasapainoyhtälöt

Rakenteen nurkan kiertymävapausasteeseen i liittyvällä vapausastemomentilla M_i ymmärretään ko. nurkkaan liittyvistä elementeistä tähän nurkkaan kohdistuvien sauvanpäämomenttien summaa. Käyttäen hyväksi lausekkeita (20) sekä elementtien ja rakenteen kiertymävapausasteiden välisiä yhteensopivuusehtoja, vapausastemomenteista M_i muodostettu pystyvektori $\mathbf{M}$ voidaan saattaa muotoon

$$\mathbf{M} = \mathbf{K}_{\varphi\varphi}\boldsymbol{\varphi} + \mathbf{K}_{\varphi\psi}\psi + \mathbf{MK}_\varphi, \tag{22}$$

missä systeemimatriisien $\mathbf{K}_{\varphi\varphi}$, $\mathbf{K}_{\varphi\psi}$ ja systeemivektorin $\mathbf{MK}_\varphi$ alkiot voidaan koota vastaavien elementtimatriisien $\mathbf{K}_{\varphi\varphi}^e$ $\mathbf{K}_{\varphi\psi}^e$ ja elementtivektorien $\mathbf{MK}_\varphi^e$ alkioista käyttäen elementtimenetelmän kokoamismenettelyä.

Rakenteen nurkkien kiertymävapausasteisiin liittyvät ***momenttitasapainoyhtälöt*** voidaan esittää muodossa

$$\mathbf{M} = \bar{\mathbf{M}}, \tag{23}$$

missä pystyvektori $\bar{\mathbf{M}}$ sisältää rakenteen kiertymävapausasteisiin liittyvät mahdolliset vapausaste-kuormat (pistemomentit). Sijoittamalla momenttivektori (22) momenttitasapainoyhtälöön (23) ja ilmaisemalla vielä sauvakiertymät ψ riippumattomien sauvakiertymien Ψ avulla kaavalla (17), saadaan nurkkien momenttitasapainoyhtälöt lopulliseen muotoonsa

$$\mathbf{K}_{\varphi\varphi}\varphi + \mathbf{K}_{\varphi\Psi}\Psi = \mathbf{R}_{\varphi}, \tag{24}$$

missä

$$\mathbf{K}_{\varphi\Psi} = \mathbf{K}_{\varphi\psi}\mathbf{C}_{\psi} \tag{25}$$

ja

$$\mathbf{R}_{\varphi} = \bar{\mathbf{M}} - \mathbf{M}\mathbf{K}_{\psi} - \mathbf{K}_{\varphi\psi}\mathbf{D}_{\psi}. \tag{26}$$

2.3 Siirtymäyhtälöt

Kulmanmuutosmenetelmässä muodostetaan lisää tasapainoyhtälöitä, ns. ***siirtymäyhtälöt***, käyttäen virtuaalisen työn periaatetta seuraavasti. Otetaan virtuaaliseksi siirtymätilaksi jäykistä nivelsauvoista koostuvaksi oletetun mekanismin virtuaalisia riippumattomia sauvakiertymiä $\delta\Psi$ vastaava siirtymätila. Olkoon nyt $\delta\psi^e$ näitä vastaavat virtuaaliset sauvakiertymät, jolloin niiden muodostamalle pystyvektorille pätee

$$\delta\psi = \mathbf{C}_{\psi}\delta\Psi. \tag{27}$$

Sauvan e saadessa virtuaalisen kietymän $\delta\psi^e$, sen sauvanpäämomentit M_1^e ja M_2^e tekevät virtuaalisen työn

$$\delta W_{\text{int}}^e = \delta\psi^e (M_1^e + M_2^e), \tag{28}$$

joka saa kaavojen (18) perusteella muodon

$$\delta W_{\text{int}}^e = \delta\psi^e (-\mathbf{K}_{\psi\varphi}^e \varphi^e - K_{\psi\psi}^e \psi^e + MK_{\psi}^e), \tag{29}$$

missä

$$\mathbf{K}_{\psi\varphi}^e = -[c_1^e,\ c_2^e] = (\mathbf{K}_{\varphi\psi}^e)^T,\quad K_{\psi\psi}^e = c_1^e + c_2^e,\quad MK_{\psi}^e = MK_1^e + MK_2^e. \tag{30}$$

Koko rakenteen sisäinen virtuaalinen työ saadaan summaamalla elementtien osuudet (30). Ottamalla samalla huomioon elementtien ja rakenteen kiertymävapausasteiden väliset yhteensopivuusehdot, voidaan rakenteen sisäisen virtuaalisen työn lauseke saattaa muotoon

$$\delta W_{\text{int}} = \delta \boldsymbol{\psi}^T (-\mathbf{K}_{\psi\varphi}\boldsymbol{\varphi} - \mathbf{K}_{\psi\psi}\boldsymbol{\psi} + \mathbf{MK}_{\psi}), \tag{31}$$

missä

$$\mathbf{K}_{\psi\varphi} = \mathbf{K}_{\varphi\psi}^T, \quad \mathbf{K}_{\psi\psi} = \begin{bmatrix} K_{\psi\psi}^1 & \cdots & 0 \\ \vdots & \ddots & \vdots \\ 0 & \cdots & K_{\psi\psi}^E \end{bmatrix}, \quad \mathbf{MK}_{\psi} = \begin{Bmatrix} MK_{\psi}^1 \\ \vdots \\ MK_{\psi}^E \end{Bmatrix}. \tag{32}$$

Ilmaisemalla vielä todelliset ja virtuaaliset sauvakiertymät vastaavien riippumattomien sauvakiertymien avulla kaavoilla (17) ja (27), saadaan rakenteen sisäisen virtuaalinen työ lauseke (31) muotoon

$$\delta W_{\text{int}} = \delta \boldsymbol{\Psi}^T \mathbf{C}_{\psi}{}^T (-\mathbf{K}_{\psi\varphi}\boldsymbol{\varphi} - \mathbf{K}_{\psi\psi}\mathbf{C}_{\psi}\boldsymbol{\Psi} - \mathbf{K}_{\psi\psi}\mathbf{D}_{\psi} + \mathbf{MK}_{\psi}). \tag{33}$$

Koska sauvan virtuaalisen siirtymän otaksutaan olevan jäykän kappaleen liikettä, voidaan elementtiin e vaikuttava kuormitus ajatella korvatuksi sen kanssa ekvivalenteilla vapausastekuormilla. Näiden kuormien komponentit sauvakoordinaatistossa, ts. sauvan akselin suuntaiset ja poikittaiset komponentit UK_i^e, $(i = 1,2)$ ja VK_i^e, $(i = 1,2)$, voidaan määrittää kuten vapaastituetun palkin tukireaktiot sauvan akselin suuntaisesta ja poikittaisesta kuormituksesta. Näiden vapausastekuormien komponentit FK_i^e, $(i = 1,\cdots,4)$ rakennekoordinaatistossa saadaan edellisistä kaavoilla

$$\left.\begin{aligned} FK_1^e &= cUK_1^e - sVK_1^e \\ FK_2^e &= sUK_1^e + cVK_1^e \end{aligned}\right\}, \quad \left.\begin{aligned} FK_3^e &= cUK_2^e - sVK_2^e \\ FK_4^e &= sUK_2^e + cVK_2^e \end{aligned}\right\}. \tag{34}$$

Näin elementtiin e vaikuttavan kuormituksen tekemä ulkoinen virtuaalinen työ voidaan esittää muodossa

$$\delta W_{\text{ext}}^e = \sum_{r=1}^{4} \delta d_r^e FK_r^e \equiv (\delta \mathbf{d}^e)^T \mathbf{FK}^e. \tag{35}$$

Kaikkien elementtien osuus rakenteen ulkoisesta virtuaalisesta työstä saadaan summaamalla elementtien osuudet. Ottamalla samalla huomioon elementtien ja rakenteen siirtymävapausasteiden väliset yhteensopivuusehdot, saadaan elementteihin vaikuttavan kuormituksen osuus rakenteen ulkoisesta virtuaalisesta työstä muotoon

$$\delta W_{\text{ext,elem}} = \sum_{i=1}^{M} \delta d_i FK_i = \delta \mathbf{d}^T \mathbf{FK}, \tag{36}$$

missä systeemivektori $\mathbf{FK}$ saadaan elementtivektoreista $\mathbf{FK}^e$ käyttäen elementtimenetelmän kokoamismenettelyä. Elementteihin vaikuttavan kuormituksen lisäksi myös siirtymävapausasteisiin liittyvät vapausastekuomat $\overline{F}_i$ tekevät ulkoista virtuaalista työtä. Näin rakenteen ulkoiselle virtuaaliselle työlle saadaan

$$\delta W_{\text{ext}} = \delta \mathbf{d}^T \mathbf{FK} + \delta \mathbf{d}^T \overline{\mathbf{F}} = \delta \mathbf{d}^T (\mathbf{FK} + \overline{\mathbf{F}}), \tag{37}$$

missä pystyvektori $\overline{\mathbf{F}}$ sisältää nollasta eroavat vapausastekuormat $\overline{F}_i$. Ottamalla lopuksi huomioon virtuaalisten siirtymien ja riippumattomien sauvakiertymien yhteys

$$\delta \mathbf{d} = \mathbf{C}_d \delta \Psi \,, \tag{38}$$

saadaan rakenteen ulkoinen virtuaalinen työ muotoon

$$\delta W_{\text{ext}} = \delta \Psi^T \mathbf{C}_d^T (\mathbf{F}\mathbf{K} + \overline{\mathbf{F}}) \,. \tag{39}$$

Virtuaalisen työn periaatteesta $\delta W_{\text{int}} + \delta W_{\text{ext}} = 0$ seuraa nyt lopulliset ***siirtymäyhtälöt***

$$\mathbf{K}_{\psi\varphi} \varphi + \mathbf{K}_{\psi\psi} \Psi = \mathbf{R}_\Psi \tag{40}$$

missä

$$\mathbf{K}_{\Psi\varphi} = \mathbf{C}_\psi{}^T \mathbf{K}_{\psi\varphi} = \mathbf{K}_{\varphi\Psi}^T \,, \tag{41}$$

$$\mathbf{K}_{\Psi\Psi} = \mathbf{C}_\psi{}^T \mathbf{K}_{\psi\psi} \mathbf{C}_\psi \,, \tag{42}$$

$$\mathbf{R}_\Psi = \mathbf{C}_\psi^T (\mathbf{M}\mathbf{K}_\psi - \mathbf{K}_{\psi\psi} \mathbf{D}_\psi) + \mathbf{C}_d^T (\mathbf{F}\mathbf{K} + \overline{\mathbf{F}}) \,. \tag{43}$$

2.4 Kulmanmuutosmenetelmän yhtälöryhmä

Lopullinen yhtälöryhmä kiertymien ja riippumattomien sauvakiertymien määrittämiseksi muodostuu nyt yhtälöistä (24) ja (40). Se voidaan esittää muodossa

$$\mathbf{K}\mathbf{a} = \mathbf{R} \,, \tag{44}$$

missä

$$\mathbf{K} = \begin{bmatrix} \mathbf{K}_{\varphi\varphi} & \mathbf{K}_{\varphi\Psi} \\ \mathbf{K}_{\Psi\varphi} & \mathbf{K}_{\psi\Psi} \end{bmatrix}, \quad \mathbf{a} = \begin{Bmatrix} \varphi \\ \Psi \end{Bmatrix}, \quad \mathbf{R} = \begin{Bmatrix} \mathbf{R}_\varphi \\ \mathbf{R}_\Psi \end{Bmatrix}. \tag{45}$$

3. JÄNNITYSRESULTANTTIEN MÄÄRITTÄMINEN ELEMENTIN ALUEELLA

3.1 Leikkausvoiman ja taivutusmomentin määrittäminen

Kun yhtälöryhmä (44) on ratkaistu ja vapausastekiertymät φ ja riippumattomat sauvakiertymät Ψ tunnetaan, saadaan sauvakiertymät ψ lasketuksi kaavoilla (17). Tarkasteltavan elementin e solmukiertymät φ_i^e saadaan nyt käyttäen rakenteen ja elementin kiertymävapausasteiden välisiä yhteensopivuusehtoja ja sauvakiertymä ψ^e on suoraan pystyvektorin ψ e:s alkio. Elementin sauvanpäämomentit M_1^e ja M_2^e saadaan tämän jälkeen käyttämällä kulmanmuutosmenetelmän

perusyhtälöitä (18). Leikkausvoiman arvo sauvan e päässä 1 saadaan muodostamalla momenttitasapainoyhtälö sauvan pään 2 suhteen. Sille saadaan näin $Q_1^e = VK_1^e - (M_1^e + M_2^e)/L^e$. Leikkausvoimalle ja taivutusmomentille elementin e alueella saadaan nyt lausekkeet

$$Q(x) = Q_1^e - \int_0^x q(x')dx', \tag{46}$$

$$M(x) = M_1^e + Q_1^e x + \int_0^x m(x')dx' - \int_0^x q(x')(x-x')dx', \tag{47}$$

missä x on elementin e sauvakoordinaatti ja x' on integrointimuuttuja. Näissä kaavoissa on otaksuttu, että mahdolliset elementin alueella vaikuttavat poikittaiset pistekuormat ja pistemomentit on sisällytetty jakautuneen poikittaisen kuorman $q(x)$ momenttikuorman $m(x)$ lausekkeisiin Dirac'in delta-funktioita käyttäen.

3.2 Normaalivoiman määrittäminen

Normaalivoimien määrittäminen kulmanmuutosmenetelmässä ei ole yhtä suoraviivaista. Kun sauvanpääleikkausvoimat ja -momentit tunnetaan, voidaan käsinlaskussa aina menetellä siten, että kirjoitetaan kehän kaikkien nurkkien (solmujen) ja sauvojen (elementtien) voimatasapainoyhtälöt ja ratkaistaan niistä sauvanpäänormaalivoimat. Tämän prosessin ohjelmointi ei kuitenkaan onnistu aivan helposti. Seuraavassa esitetään virtuaalisen työn periaatteeseen perustuva vaihtoehtoinen normaalivoimien määrityskeino, joka on systemaattinen ja helppo implementoida.

Tarkastellaan normaalivoiman määrittämistä sauvassa (elementissä) $\bar{e}$. (Tarkasteltavaan elementtiin viittaava symboli $\bar{e}$ varustetaan tässä yläviivalla, jotta se erottuisi yleiseen elementtiin viittaavasta symbolista e.) Ajatellaan kehän (jäykissä) sauvoissa vaikuttava jakautunut aksiaalinen kuorma $p(x)$ redusoiduksi rakenteen solmuihin. Tällöin kussakin sauvassa voidaan ajatella vaikuttavan pelkästään tuntematon, vakiosuuruinen rajoitevoima T^e, joka pakottaa sauvan pituuden muutoksen olevan suuruudeltaan $\Delta L^e = \varepsilon_0 L^e$. Otetaan virtuaaliseksi siirtymätilaksi sellaisen jäykistä nivelsauvoista koostuvan mekanismin siirtymätila, jonka tarkasteltava sauva $\bar{e}$ saa ykkösen suuruisen pituudenmuutoksen. Rakenteen sisäinen virtuaalinen työ voidaan nyt, käyttäen hyväksi tulosta (31), esittää muodossa

$$\delta W_{\text{int}} = -T^{\bar{e}} \cdot 1 + \delta \boldsymbol{\psi}^T \mathbf{M}_{\psi}, \tag{48}$$

missä on käytetty lyhennysmerkintää

$$\mathbf{M}_{\psi} = -\mathbf{K}_{\psi\varphi}\boldsymbol{\varphi} - \mathbf{K}_{\psi\psi}\boldsymbol{\psi} + \mathbf{M}\mathbf{K}_{\psi} \tag{49}$$

ja $\delta\boldsymbol{\psi}$ on tarkasteltavaa virtuaalista siirtymätilaa vastaavien sauvakiertymien muodostama pystyvektori. Rakenteen ulkoinen virtuaalinen työ on kaavan (37) mukainen, missä myös pystyvektori $\delta\mathbf{d}$ on tarkasteltavaa virtuaalista siirtymätilaa vastaava. Soveltamalla virtuaalisen työn periaatetta $\delta W_{\text{int}} + \delta W_{\text{ext}} = 0$ saadaan rajoitevoimalle $T^{\bar{e}}$ tulos

$$T^{\bar{e}} = \delta \boldsymbol{\psi}^T \mathbf{M}_{\psi} + \delta \mathbf{d}^T (\mathbf{F}\mathbf{K} + \bar{\mathbf{F}}). \tag{50}$$

Seuraavassa tarkastellaan lyhyesti, kuinka rajoitevoiman $T^{\bar{e}}$ määrittämiseksi tarvittava virtuaalinen siirtymätila ja sitä vastaavat vektorit $\delta\mathbf{d}$ ja $\delta\psi$ voidaan määrittää. Elementin e päiden virtuaalisten siirtymien δd_i^e ja sauvakiertymän $\delta\psi^e$ välille saadaan kaavoja (5) ja (6) vastaten

$$\left.\begin{aligned}\delta d_3^e - \delta d_1^e + sL^e\delta\psi^e = 0\\ \delta d_4^e - \delta d_2^e - cL^e\delta\psi^e = 0\end{aligned}\right\}\ \text{kun } e\neq\bar{e},\qquad \left.\begin{aligned}\delta d_3^e - \delta d_1^e + sL^e\delta\psi^e = c\\ \delta d_4^e - \delta d_2^e - cL^e\delta\psi^e = s\end{aligned}\right\}\ \text{kun } e=\bar{e}, \tag{51}$$

eli

$$\mathbf{A}^e\begin{Bmatrix}\delta\mathbf{d}^e\\ \delta\psi^e\end{Bmatrix} = \mathbf{B}^e, \tag{52}$$

missä $\mathbf{A}^e$ on kaavan (8) mukainen ja

$$\mathbf{B}^e = \begin{Bmatrix}0\\0\end{Bmatrix},\ \text{kun } e\neq\bar{e},\quad \mathbf{B}^e = \begin{Bmatrix}c\\s\end{Bmatrix},\ \text{kun } e=\bar{e}. \tag{53}$$

Tarkastelu palautuu siis kohdassa 1 esitettyyn vain sillä erolla, että nyt elementtivektorit $\mathbf{B}^e$ määritetään kaavalla (53). Näin vektoreille $\delta\mathbf{d}$ ja $\delta\psi$ voidaan kaavoja (14) ja (17) vastaten kirjoittaa

$$\delta\mathbf{d} = \mathbf{C}_d\delta\Psi + \mathbf{D}_d,\quad \delta\psi = \mathbf{C}_\psi\delta\Psi + \mathbf{D}_\psi. \tag{54}$$

Virtuaaliset riippumattomat sauvakiertymät voidaan tässä tapauksessa valita vapaasti, joten on luontevaa ottaa $\delta\psi = \mathbf{0}$. Näin vektoreille $\delta\mathbf{d}$ ja $\delta\psi$ saadaan

$$\delta\mathbf{d} = \mathbf{D}_d,\quad \delta\psi = \mathbf{D}_\psi, \tag{55}$$

ja elementin $\bar{e}$ rajoitevoiman $T^{\bar{e}}$ lopulliseksi kaavaksi tulee

$$T^{\bar{e}} = \mathbf{D}_\psi^T\mathbf{M}_\psi + \mathbf{D}_d^T(\mathbf{FK}+\bar{\mathbf{F}}), \tag{56}$$

missä vektorit $\mathbf{D}_d$ ja $\mathbf{D}_\psi$ on luonnollisesti määritetty kaavan (53) mukaisista elementtivektoreista $\mathbf{B}^e$ kootun systeemivektorin $\mathbf{B}$ avulla.

Normaalivoima elementin e päässä 1 saadaan kaavalla $N_1^e = UK_1^e + T^e$. Normaalivoimalle elementin e alueella saadaan tämän avulla lauseke

$$N(x) = N_1^e - \int_0^x p(x')dx'. \tag{57}$$

Tässä kaavassa on otaksuttu, että mahdolliset elementin alueella vaikuttavat aksiaaliset pistekuormat on sisällytetty jakautuneen aksiaalisen kuorman $p(x)$ lausekkeeseen Dirac'in delta-funktioita käyttäen.

4. IMPLEMENTOINNIN RAJAUSTA

Edellä esitettyjen yhtälöiden pohjalta voidaan laatia varsin monipuolinen tietokoneohjelma tasokehän analysoimiseksi kulmanmuutosmenetelmällä. Tässä työssä esitetty ohjelma on kuitenkin haluttu pitää kooltaan pienenä ja sen rakenne selkeänä. Tämän vuoksi implementointiin on tehty joitakin rajauksia: (i) Sauvat (elementit) on otaksuttu tasajäykiksi. Näin sauvavakioiden ja kuormitustermien ohjelmointi erilaisille, muuttuvan poikkileikkauksen omaaville sauvoille on rajattu pois. (ii) Elementillä vaikuttavan kuormituksen otaksutaan muodostuvan pelkästään aksiaalisesta ja poikittaisesta jakautuneesta kuormasta, joka on lineaarisesti jakautunut. (iii) Elementin alkuvenymä ja alkukäyristymä on myös otaksuttu vakioiksi. Tällä tavoin kuormitustermien määrittämiseen ja jännitysresultanttien jakautumien laskemiseen tarvittava ohjelmointityö on voitu rajata pelkästään yhteen tapaukseen. Sauvoihin vaikuttavat pistekuormat ja pistemomentit voidaan kuitenkin käsitellä ohjelmalla siten, että niiden vaikutuskohtiin sijoitetaan solmut, jolloin kuormitukset voidaan antaa näihin solmuihin liittyvinä vapausastekuormina. Siinä tapauksessa, että sauvan taivutusjäykkyydellä, jakautuneella kuormalla tai alkumuodonmuutoksella on sauvan alueella hyppäys, sijoitetaan hyppäyskohtaan solmu ja sauva jaetaan näin kahdeksi elementiksi. (iv) Ohjelmalle ei voida antaa nollasta eroavia pakkosiirtymiä ja pakkokiertymiä eikä myöskään vinoja reunaehtoja.

Lopuksi esitetään vielä joitakin ohjelmassa tarvittavia kaavoja, joiden lopullinen muoto määräytyy vasta yllä tehdyn elementtiin vaikuttavaa kuormitusta koskevan rajauksen jälkeen: Elementillä e vaikuttava lineaarisesti jakautunut aksiaalinen ja poikittainen kuorma esitetään muodossa $p(\xi) = p_1^e + (p_2^e - p_1^e)\xi$ ja $q(\xi) = q_1^e + (q_2^e - q_1^e)\xi$, missä $\xi = x/L^e$ ja p_1^e, p_2^e, q_1^e ja q_2^e ovat kuorman arvot elementin päissä. Tätä kuormitusta vastaaville ekvivalenteille vapausastevoimille ja kuormitustermeille saadaan lausekkeet

$$UK_1^e = \frac{L^e}{6}(2p_1^e + p_2^e),\ UK_2^e = \frac{L^e}{6}(p_1^e + 2p_2^e),\ VK_1^e = \frac{L^e}{6}(2q_1^e + q_2^e),\ VK_2^e = \frac{L^e}{6}(q_1^e + 2q_2^e),$$
$$MK_1^e = -\frac{(L^e)^2}{60}(3q_1^e + 2q_2^e) - EI\kappa_0,\ MK_2^e = \frac{(L^e)^2}{60}(2q_1^e + 3q_2^e) + EI\kappa_0 \qquad (58)$$

sekä elementin normaalivoiman, leikkausvoiman ja taivutusmomentin lausekkeet (57), (46) ja (47) saavat muodon

$$N(\xi) = N_1^e - p_1^e L^e \xi - \frac{(p_2^e - p_1^e)L^e}{2}\xi^2,\quad Q(\xi) = Q_1^e - q_1^e L^e \xi - \frac{(q_2^e - q_1^e)L^e}{2}\xi^2,$$
$$M(\xi) = M_1^e + Q_1^e L^e \xi - \frac{q_1^e (L^e)^2}{2}\xi^2 - \frac{(q_2^e - q_1^e)(L^e)^2}{6}\xi^3. \qquad (59)$$

5. OHJELMASTA JA SEN KÄYTÖSTÄ

Ohjelma muodostuu joukosta MATLAB makroja, jotka on sijoitettu samaan hakemistoon. Tiedosto `kulmu.m` sisältää pääohjelman. Tiedostot `kokab.m`, `kokb.m`, `kokfk.m` ja `kokkmk.m` sisältävät systeemimatriisien ja systeemivektoreiden kokoaja-aliohjelmat. Tiedostot `muoabe.m`, `muobe.m`, `muofke.m` ja `muokmke.m` sisältävät elementtimatriisien ja elementtivektoreiden muodostaja-aliohjelmat. Tiedosto `jaaa.m` sisältää aliohjelman, joka jakaa matriisin $\mathbf{A}$ osiin $\mathbf{A}_I$ ja $\mathbf{A}_{II}$, sekä tiedosto `lasres.m` aliohjelman, joka laskee taulukot, jotka sisältävät jännitysresultanttien arvoja tasavälisesti kunkin elementin alueella sijaitsevissa pisteissä. Tiedostot `dat1.m`, `dat2.m`, jne. sisältävät esimerkkiprobleemien datamakroja. Hakemistossa on

lisäksi tiedostot `esi.m` ja `jal.m`, jotka sisältävät esikäsittelijän ja jälkikäsittelijän. (Näitä ohjelmia ei ole dokumentoitu.) Hakemistossa on lisäksi WORD-dokumentti `ohje.doc`, joka sisältää lyhyen ohjelman käyttöohjeen.

Ohjelman käyttö tapahtuu seuraavasti: Käynnistetään MATLAB ja siirrytään hakemistoon, jossa ohjelmaan liittyvät tiedostot sijaitsevat. Käynnistetään datamakro (esimerkiksi `dat1.m`) komennolla `dat1`. Datamakron määrittelemät lähtötiedot siirtyvät MATLAB:in työtilaan. Käynnistetään esikäsittelijä komennolla `esi`. Se piirtää joukon lähtötietoja havainnollistavia kuvia. Käynnistetään varsinainen ohjelma komennolla `kulmu`. Ohjelma ratkaiseen tehtävän ja tulokset jäävät MATLAB:in työtilaan. Käynnistetään jälkikäsittelijä komennolla `jal`. Se piirtää joukon tuloksia havainnollistavia kuvia. Datamakron laatiminen tapahtuu editorilla. Tehtävään voi käyttää joko MATLAB:n omaa tai jotakin muuta editoria.

Kehitettyyn ohjelmaan liittyvät tiedostot voi kopioida itselleen Teknillisen korkeakoulun rakenteiden mekaniikan laboratorion verkkosivuilta.

6. YHTEENVETO

Työssä tarkasteltiin tasokehän ratkaisemista kulmanmuutosmenetelmällä elementtimenetelmän formalismia käyttäen. Esitetyn pohjalta kehitettiin yksinkertainen MATLAB-ohjelma tasokehän ratkaisemiseksi. Selkeyden vuoksi ja implementointityön vähentämiseksi ohjelmaan tehtiin mm. seuraavat rajaukset: Elementit otaksutiin tasajäykiksi, elementteihin vaikuttava kuormitus lineaarisesti jakautuneeksi sekä elementtien alkuvenymät ja alkukäyristymät vakioiksi. Ohjelman rakenne on kuitenkin pyritty laatimaan siten, että siihen voidaan helposti sisällyttää myös sauvoja, joiden poikkileikkaus on muuttuva sekä monimutkaisempia kuormitustapauksia (esim. elementin alueella vaikuttavat pistekuormat ja -momentit).

LÄHTEET

1. R. Guldan, Rahmentragwerke und durchlaufträger, Sechste Auflage, Springer-Verlag, Wien, 1959.
2. P. Loikkanen, Rakenteiden statiikka 2, Staattisesti epämääräiset sauvarakenteet, Otava, Helsinki, 1975.
3. MATLAB 5 Documentation, Using MATLAB, The Math Works, Inc., 1996.

A PARALLEL MULTI-BLOCK NAVIER-STOKES SOLVER FOR LARGE-EDDY SIMULATION IN COMPLEX FLOWS

P. MAJANDER AND T. SIIKONEN

Laboratory of Applied Thermodynamics, Helsinki University of Technology
P.O. Box 4400, FINLAND
e-mail: Petri.Majander@hut.fi

ABSTRACT

A parallel pressure-based Navier-Stokes solver. The spatial discretization is based on a co-located finite-volume tecnique and a body fitted co-ordinate system. The solution is based on the traditional SIMPLE method. Time-dependent problems are solved with an implicit three-level method. The parallelization is based on a division of a computational domain into separate blocks and assigning each block into a processor of its own. Several flow cases are studied to test the solver, a steady-state cavity flow, a partly turbulent cavity flow, a fully developed turbulent pipe flow and finally jet in cross flow that has been studied experimentally by Crabb et. al [3]. The results are compared with the measurements and the efficiency of the parallelization is shown.

1 INTRODUCTION

The time-dependent solution of turbulent flow is computationally extremely intensive. In a direct numerical simulation (DNS) essentially all scales present in the flow field are solved. Due to the need of huge computational resources, DNS is usually applied with a relatively low Reynolds number in basic flows such as a channel flow. Spectral methods are often utilized because they reduce the number of the grid points needed due to their accuracy. The application of spectral methods in complex domains is difficult which makes them less appealing as engineering tools.

In a large-eddy simulation (LES) the small-scale motion is not solved which reduces the computational cost. The effect of the small-scale motion is usually modelled with a subgrid-scale model (SGS -model). As the computational power has increased, the applications in engineering have become feasible. Therefore, low-order finite-difference solutions in LES have recently become popular as shown by publications [1] and [2] to name just two.

In this study a parallel multi-block solver for incompressible flow is described. A spatial discretization is based on a co-located and structured finite-volume method with Rhie and Chow pressure coupling. An iterative three-level imlicit time stepping is implemented. The parallelization is based on a division of a computational domain into separate blocks, which are assigned in separate processors. The Message-Passing Interface (MPI) is used for exchanging the boundary data.

In the next sections the numerical method is derived and the algorithm of the parallel solver is presented. In Section 4, test cases are described and results are shown. The efficiency of the parallelization is studied. Also, a high-Reynolds number large eddy simulation of a jet in crossflow (JICF) is performed and some preliminary results are shown. The JICF has been studied experimentally by Crabb et. al [3].

2 GOVERNING EQUATIONS

The Navier-Stokes equations for isothermal incompressible flows are written as

$$\begin{aligned} \frac{\partial u_i}{\partial x_i} &= 0 \\ \frac{\partial u_i}{\partial t} + \frac{\partial u_i u_j}{\partial x_j} &= -\frac{1}{\rho}\frac{\partial p}{\partial x_i} + \nu \frac{\partial^2 u_i}{\partial x_j \partial x_j}, \end{aligned} \tag{1}$$

where u_i is the velocity, p is the pressure and ν is the kinematic viscosity. The LES equations are formally derived by applying a filtering operation: a filtered variable is defined as

$$\bar{f}(\mathbf{r}, t) = \int_V G(|\mathbf{r} - \mathbf{r}'|) f(\mathbf{r}', t) d\mathbf{r}', \tag{2}$$

where V is the volume of filtering and G is the filter function. After filtering Eqs. (1) the LES equations take the following form

$$\frac{\partial \overline{u}_i}{\partial x_i} = 0 \tag{3}$$

$$\frac{\partial \overline{u}_i}{\partial t} + \frac{\partial \overline{u}_i \overline{u}_j}{\partial x_j} = -\frac{1}{\rho}\frac{\partial \overline{p}}{\partial x_i} - \frac{\partial \tau_{ij}}{\partial x_j} + \nu \frac{\partial^2 \overline{u}_i}{\partial x_j \partial x_j}, \tag{4}$$

where the SGS stresses are

$$\tau_{ij} = \overline{u_i u_j} - \overline{u}_i \overline{u}_j. \tag{5}$$

Boussinesq approximation

$$\tau_{ij} - \frac{\delta_{ij}}{3}\tau_{kk} = -2\nu_T \overline{S}_{ij} = -\nu_T \left(\frac{\partial \overline{u}_i}{\partial x_j} + \frac{\partial \overline{u}_j}{\partial x_i} \right) \tag{6}$$

relates subgrid-scale stresses τ_{ij} to the eddy viscosity ν_T the resolved-scale strain rate tensor $\overline{S}_{ij}$. The Smagorinsky model for the eddy viscosity is written as

$$\nu_T = (C_s \Delta)^2 |\overline{S}|, \tag{7}$$

where C_s is called a Smagorinsky constant, Δ is a length scale and $|\overline{S}| = \sqrt{2\overline{S}_{ij}\overline{S}_{ij}}$ [17]. The length scale represents the cell size and it is usually computed as $V^{1/3}$. A value 0.18 for C_s has been evaluated for the inertial range dynamics [10]. In the presence of shear flow a smaller value must be used, which was first discovered by Deardorff [4]. He studied a channel flow and found that a smaller value for $C_s = 0.1$ had to be used in the presence of a strong shear-driven turbulence. This observation has since been confirmed by many studies. Furthermore, in the vicinity of the walls, the eddy viscosity must be reduced. This is usually carried out with the van Driest damping function. Germano et al. [6] presented a dynamic SGS model, where the model coefficient is calculated during the simulation. This is based on the application of two different filters. In addition to the grid filter G, a test filter $\widehat{G}$ is applied. The test filter width $\widehat{\Delta}$ is larger than the grid filter width Δ, usually $\widehat{\Delta} = 2\Delta$. The term grid filter implies that usually discretization takes care of the filtering in numerical computations without any explicit procedure. The grid filter and the test filter are applied to the momentum equations (1) to obtain the following equation:

$$\frac{\partial \widehat{\overline{u}}_i}{\partial t} + \frac{\partial \widehat{\overline{u}}_i \widehat{\overline{u}}_j}{\partial x_j} = -\frac{1}{\rho}\frac{\partial \widehat{\overline{p}}}{\partial x_i} - \frac{\partial T_{ij}}{\partial x_i} + \nu \frac{\partial^2 \widehat{\overline{u}}_i}{\partial x_j \partial x_j}, \tag{8}$$

where subtest stresses are given by

$$T_{ij} = \widehat{\overline{u_i}\overline{u_j}} - \hat{\overline{u}}_i \hat{\overline{u}}_j. \tag{9}$$

The test filter is now applied to the grid-filtered equations (4) ;

$$\frac{\partial \widehat{\overline{u}}_i}{\partial t} + \frac{\partial \widehat{\overline{u}}_i \widehat{\overline{u}}_j}{\partial x_j} = -\frac{1}{\rho}\frac{\partial \widehat{\overline{p}}}{\partial x_i} - \frac{\partial \widehat{\tau}_{ij}}{\partial x_i} - \frac{\partial \mathcal{L}_{ij}}{\partial x_i} + \nu \frac{\partial^2 \widehat{\overline{u}}_i}{\partial x_j \partial x_j}, \tag{10}$$

$$\mathcal{L}_{ij} = \widehat{\overline{u}_i \overline{u}_j} - \hat{\overline{u}}_i \hat{\overline{u}}_j. \tag{11}$$

Using Eqs. (8) and (10), the expression for $\mathcal{L}_{ij}$ can be written as

$$\mathcal{L}_{ij} = T_{ij} - \hat{\tau}_{ij} \tag{12}$$

Eqs. (9) represent the subtest-scale stresses whose length scale is less than the subtest filter width $\hat{\Delta}$. Eqs. (12) represent then the resolved turbulent stresses by the scales between the grid filter width Δ and the subtest filter width $\hat{\Delta}$. Let us model both τ_{ij} and T_{ij} by the same functional form of the Smagorinsky model:

$$\tau_{ij} - \frac{\delta_{ij}}{3}\tau_{kk} = -2C\Delta^2 |\overline{S}| \overline{S}_{ij} = -2C\beta_{ij}, \tag{13}$$

$$T_{ij} - \frac{\delta_{ij}}{3} T_{kk} = -2C\hat{\Delta}^2 |\widehat{\overline{S}}| \widehat{\overline{S}}_{ij} = -2C\alpha_{ij}. \tag{14}$$

In order to solve C from Eqs. 13 and 14 Piomelli and Liu [13] developed the following localized dynamic model

$$\mathcal{L}_{ij} - \frac{\delta_{ij}}{3}\mathcal{L}_{kk} = -2C\alpha_{ij} + 2\widehat{C\beta_{ij}}, \tag{15}$$

where the coefficient C under the filter is replaced with an estimate C^*, which is assumed to be known. Eqs. (15) can be solved by the contraction :

$$C = -\frac{1}{2}\frac{\left(\mathcal{L}_{ij} - 2\widehat{C^*\beta_{ij}}\right)\alpha_{ij}}{\alpha_{mn}\alpha_{mn}} \tag{16}$$

For C^* one can use the value of the previous time step or iteration C^{n-1}. An important feature is that the coefficient calculation is based on the local information. However, the values for C must usually be limited in order to prevent destabilizing negative viscocity [13].

3 FLOW SOLVER

3.1 Conservation Form

The continuity equation in a conservation form becomes

$$\int_S \rho \mathbf{V} \cdot d\mathbf{S} = 0, \tag{17}$$

where ρ is the density and $\mathbf{V} = u\mathbf{i} + v\mathbf{j} + w\mathbf{j}$ is the velocity of the fluid. The integration is taken over the control volume faces. This constraint simply states that at every moment the mass flow out from the control volume equals the mass flow in. The momentum equation in the x-direction is written as

$$\frac{\partial}{\partial t}\int_V \rho u dV + \int_S \rho u \mathbf{V} \cdot \vec{n} dS + \int_S p n_x dS - \int_V \rho g_x dV - \mu \int_S \left(n_x \frac{\partial u}{\partial x} + n_y \frac{\partial u}{\partial y} + n_z \frac{\partial u}{\partial z} \right) dS = 0. \tag{18}$$

Above, p is the pressure, $\rho g_x$is the body force and $\mathbf{n} = n_x\mathbf{i} + n_y\mathbf{j} + n_z\mathbf{k}$ is a unit normal of the control volume face. The equations in the y- and z-directions are obtained by replacing the velocity component u with v and w and the wall-normal component n_x in the pressure term with n_y and n_z, respectively.

3.2 Momentum Equations

Cartesian equations are solved sequentially. Within each Cartesian directions, a contribution from all curvilinear grid directions is computed. A following time-stepping method is used in solving Eq. (18), which, after discretization for a node (ijk) becomes

$$V_{ijk}\left(\frac{(1+\gamma)\rho u^{n+1} - (1+2\gamma)\rho u^n + \gamma\rho u^{n-1}}{\Delta t}\right)_{ijk} = -\sum_{\phi=1}^{faces}(\hat{F}_\phi^{inv} - \hat{F}_\phi^{visc})^{n+1}S_\phi, \quad (19)$$

where the parameter γ defines a first-order accurate implicit Euler method with value 0 and a second-order accurate three-level imlicit method (3-LI) with value 0.5. The inviscid flux in the x-direction at the cell face ϕ is

$$F_\phi^{inv} = \hat{F}_\phi^{inv}S_\phi = S_\phi\rho u_\phi\mathbf{V}_\phi\cdot\mathbf{n}_\phi + (Sn_xp)_\phi = \dot{m}_\phi u_\phi + (Sn_xp)_\phi. \quad (20)$$

Here, $\dot{m}_\phi = S_\phi\rho\mathbf{V}_\phi\cdot\mathbf{n}_\phi$ is a mass flow through the face ϕ. In linearization of the viscous fluxes, a thin-shear-layer approximation is used in each co-ordinate direction instead of calculating the derivatives by using the generalized divergence theorem of Gauss. This approximation is done to avoid a large molecule in the matrix. In a Cartesian grid, both approximations are the same. At the face $(i+\frac{1}{2}, jk)$ (i.e. in the i-direction), the simplified viscous flux for the u-momentum equation becomes

$$F_{i+\frac{1}{2},jk}^{visc} = \frac{S\mu}{\Delta\xi}\left(u_{i+1,jk} - u_{ijk}\right), \quad (21)$$

where $\Delta\xi$ is the distance between the nodes (ijk) and $(i+1, jk)$. After linerization, a Poisson type equation is obtained for the velocity increment Δu

$$\sum_{nb}A_{nb}\Delta u_{nb} = -\sum_{\phi=1}^{faces}(Sn_x)_\phi\Delta p_\phi - \sum_{\phi=1}^{faces}(\hat{F}_\phi^{inv} - \hat{F}_\phi^{visc})^k - D_{ijk}^k, \quad (22)$$

where the sum on the left-hand side is over the neighbour nodes. In $\Delta u = u_{ijk}^{n+1} - u_{ijk}^k$ the state k lies between the solved state n and the state $n+1$ to be computed. The first term on the right hand side includes the pressure at the time level $n+1$ and in an iterative solution the term is ignored. Term D_{ijk}^k includes the time derivative as a source term. The coefficients and a more accurate derivation can be found in [11].

3.3 Pressure Coupling

The solution of the momentum equation must be coupled with pressure. The last two terms of Eq. (22) cancel when the iteration is converged. The linearized increments Δu and Δp are replaced in the following by iterative corrections u' and p':

$$\sum_{nb}A_{nb}u_{nb}' = -\sum_{\phi=1}^{faces}S_\phi n_{\phi x}p_\phi', \quad (23)$$

where the standard simplification utilized in a SIMPLE method is to drop the non-diagonal terms from Eq. (23) to derive a manageable equation. The continuity equation states that

$$\sum_{\phi=1}^{faces_{ij}} (\rho(\mathbf{V}^* + \mathbf{V}') \cdot \mathbf{S})_\phi = 0$$

$$\sum_{\phi=1}^{faces_{ij}} (u' n_x S)_\phi + (v' n_y S)_\phi + (w' n_z S)_\phi = - \sum_{\phi=1}^{faces_{ij}} (\rho \mathbf{V}^* \cdot \mathbf{S})_\phi, \tag{24}$$

where $\mathbf{V}^*$ is the velocity field that does not obey the mass balance and $\mathbf{V}'$ is the iterative correction.

After some assumptions and manipulations of the terms we finally obtain the Poisson equation for the pressure corrections

$$B_{P,ijk} p'_{ijk} + B_{W,ijk} p'_{i-1,jk} + B_{E,ijk} p'_{i+1,jk} + B_{S,ijk} p'_{i,j-1,k} + B_{N,ijk} p'_{i,j+1,k} + B_{B,ijk} p'_{ijk-1} + B_{T,ijk} p'_{ijk+1} = -\Delta \dot{m}_{ijk}, \tag{25}$$

where the coefficients can be found in [11].

3.4 Calculation of Cell-Face Velocities

In a co-located, orthogonal grid, the velocity does not depend on the pressure at the same node (ijk), which can lead to a non-physical converged solution, a phenomenom known as a checker-board solution. Therefore methods have been developed to couple the pressure and the velocity in the calculation of mass balance. Rhie and Chow [15] have presented a remedy for uncoupling, which is in wide use. In a calculation of mass balance, the cell-face velocities are computed as

$$\bar{u}_{i-\frac{1}{2},jk} = \frac{1}{2}(\bar{u}_{i-1,jk} + \bar{u}_{ijk}) + C \frac{S_{i-\frac{1}{2},jk}}{4 A_{P,i-\frac{1}{2},jk}} [p_{i-2,jk} - 3p_{i-1,jk} + 3p_{ijk} - p_{i+1,jk}]. \tag{26}$$

The pressure term in Eq. (26) adds numerical dissipation. In a smooth pressure field, the term will become negligible. The pressure term is multiplied by a constant C in the range $0.01 - 0.5$ to adjust an optimum coupling [12].

3.5 Block Structure and Parallelization

A computational grid may be difficult to define on complex geometries by utilizing a structured grid. A well-known cure for this is a multi-block structure, where the computational domain is divided between many structured blocks that are connected together [9], [16]. A layer of ghost cells are used to set the boundary condition. Two layers of cells are defined to ensure a second-order accuracy if upwind-biased discretizations are used and for the Rhie and Chow interpolation. The cell values at the two layers at the edge of the block are transferred to the ghost cells of the neighbouring block and vice versa. The neighbouring blocks may have a different orientation. The connective boundary condition applies an orientation matrix and an offset vector at each connective face. These relate the indeces in the boundary data transfer as illustrated in Fig. 1. In the current version of the solver, each face must connect completely to another face and the grid lines must be continuous. The parallelization is based on dividing the blocks among different processors although many blocks can be assigned in one processor. The parallelization is implemented with a standart called Message-Passing Interface (MPI) [8]. Each block reserves a memory space which is used to transmit the boundary data with MPI_SEND and MPI_RECV operations. These operations are blocking; that is, the control does not return to the user program until the message has been received. Therefore, the order of communication between the processes is solved before the computation is

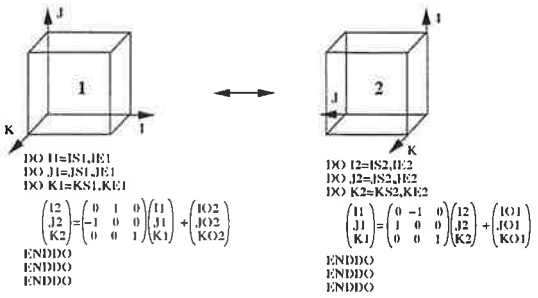

Figure 1: The connective boundary condition takes into account a different orientation between the blocks. An orientation matrix and an offset vector relates the indeces between the blocks.

started. Each sent message must be received in a proper order, otherwise the computation deadlocks. The grid should be divided as equally as possible to different processors in order to provide a good balancing. All processes compute equally the problem but only the master proces reads in an input file, a boundary data file and the grid. The master defines the boundary data needed and computes the order of the communication. The master transmits the data by MPI_BCAST command to all workers and the worker's part of the grid by MPI_SEND command. A flow chart of the solver is presented in Fig. (2). After reading the input data and the mesh each process computes the memory needed and allocates a one-dimensional table that contains all flow variables. No memory space is wasted even if the blocks would differ in size within one proces or between processes.

The computation is started with an initial guess, which is also copied at the previous time levels. The momentum equations (22) are solved in series with a multigrid solver. The mass balance is calculated with face velocities (26) that are coupled with the pressure. The mass flux error is used as a source in the pressure correction equation (25), which is solved with a multigrid (MG) solver. The MG algorithm solves the problem at the dense level first and moves the residual to the next coarsest level as a source. The coarse grid problem is approximated from the finer one. The process is called a Galerkin Coarse-Grid Approximation (GCA). After the coarsest grid level, the corrections are added to the unknown of each finer level, or the problem can be iterated also on the way up. The line Gauss Seidel (LGS) method is used at each level as a smoother. Reference [12] and Pensala (unpublished memorandum '3-D multigrid solver for Poisson-type equations' (in Finnish), HUT, 1996) give a detailed description of the MG solver. The pressure corrections p' and the velocity corrections are added to the pressures and the velocities multiplied by the underrelaxation coefficients α_p and α_u, respectively. Depending on the case, α_p usually varies from 0.1 to 0.8. In order for the velocities to satisfy the continuity equation, α_u should be 1 at this stage.

The Poisson equations for the momentum and pressure are solved independently in all blocks. During the iteration a Diriclet condition ($\Delta \mathbf{V}, p' = 0$) is set at the first ghost cell. After each subiteration cycle the boundary condition is updated for velocities and pressure ($\mathbf{V}, p$). The boundary value is lagging in time which is cured by iterating within a time step. In a similar vay to that of Bui [2], all the boundary values at the connecting boundary are copied in a single vector that is transmitted with a single message passing call. The criterion of convergence can be set in many different ways and it can depend on any primary variable or the balance of mass fluxes. Usually, an L_1- or L_2-norm of a residual of some variable must converge below a preset limit. As the convergence is reached, the solution of the new time level is started by updating the variables at the old and present time levels.

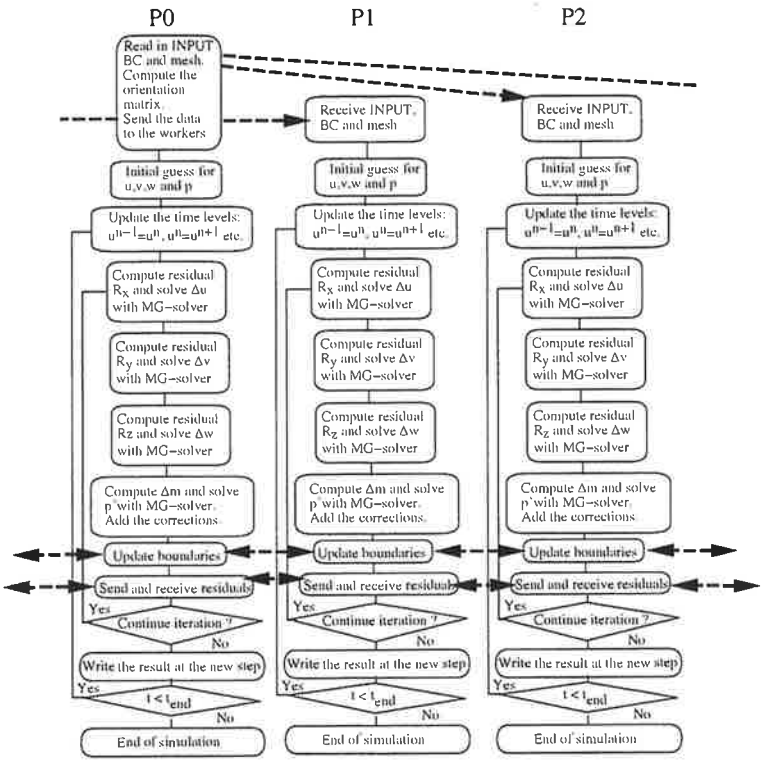

Figure 2: A flow diagram of the parallel code. The dashed arrows represent commmunication between the processors.

4 TEST CALCULATIONS

4.1 Steady State Cavity Flow

The first test case is a steady state cavity flow, where the Reynolds number $Re = \dfrac{U_w L}{\nu} = 400$, which means that the flow is stationary and two-dimensional. Here, U_w is the velocity of the upper lid of the cavity. A first-order Euler method is used to iterate a converged result and a second-order central discretization scheme is applied for the convective and diffusive terms. The grid points are equally distributed and the number of cells is $96 \times 96 \times 8$, where the cells in the k-direction are set for the MG solver. A no-slip condition is used at every solid wall and at the sliding wall. A zero-gradient condition is set for the pressure in the wall-normal direction. The domain is partitioned in equal sub-domains which are assigned in separate processors. The steady-state solution with the implicit Euler scheme was iterated until the L_2-norm of u-velocity was decresed below 10^{-10}. The computations were performed in an SGI-server equipped with eight 250 MHz R10000 processors. The u-velocity scaled by the wall velocity U_w along the vertical centerline in the cavity is shown in Fig. 3. With eight processors the number of iterations increased by 10 % compared to that needed by the single processor computation with a single domain. The CPU-time is decreased more than linearly as the number of processors is increased. Fig. 3 shows the speed-up of the computation per iteration number. The super-linear speed-up is probably due to the more efficient usage of a cache memory that the processor is capable of with the smaller domain assigned to it.

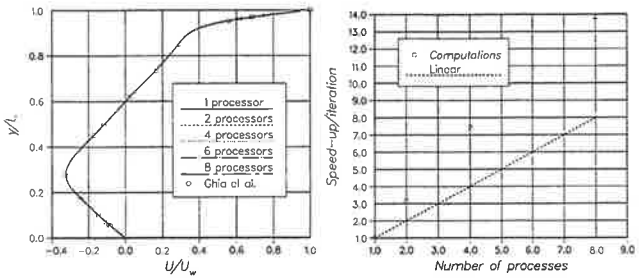

Figure 3: Cavity flow at Re=400. Converged u/U_w-velocity along the vertical centreline in the left and the speed-up per iteration. Reference result by Ghia et al. [7].

4.2 Turbulent Cavity Flow

The second test case is a cavity flow at a Reynolds number of 10000. The width of the cavity (W)is half of the length and the height (L) of the cavity. This flow has been studied experimentally by Prasad and Koseff [14].

The grid contains 64 × 64 × 32 grid cells and it is geometrically streched from the wall. The domain is partitioned in equal 1, 2, 4, and 8 sub-domains which are assigned in separate processors. Large eddy simulations were calculated with and without a subgrid-scale model. The $L1$-norm of the mass balance is iterated to be smaller than 10^{-8}. With four processors a non-modelled computation requires 9.6 iterations and a modelled one 5.8 iterations per time step for this criterium. Fig. 4 represent the results along the vertical and horizontal centerline. The computations overpredict the thickness and the maximum velocity on the downstream and especially on the upstream wall. The insufficient resolution of the interior coarse grid might cause the discrepancies between the computed and the measured data. The dynamic model does not affect the results much on the vertical and horizontal centerlines. The model computes the largest viscosity near the downstream eddy, where the flow is turbulent. The speed-up is again superlinear although not as strongly as in the steady-state case where the mesh is smaller.

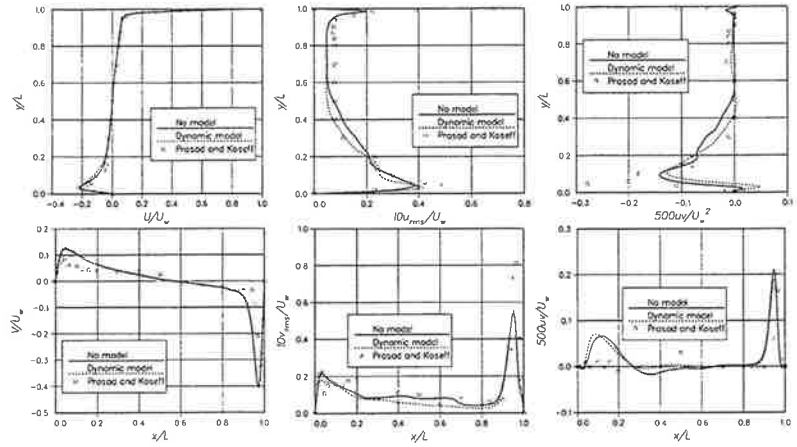

Figure 4: Cavity flow at Re=10000. Top : U/U_w-velocity, $10u_{rms}/U_w$ and $500uv/U_w^2$ along the vertical centreline. Bottom : V/U_w-velocity, $10v_{rms}/U_w$ and $500uv/U_w^2$ along the vertical centreline.

4.3 Fully Turbulent Pipe Flow

The third test case is a fully turbulent pipe flow at a friction velocity based Reynolds number $Re_\tau = \frac{u_\tau D}{\nu} = 621.4$, which was set by forcing the flow with a constant body force. This approximately equals $Re_b = \frac{U_b D}{\nu} \approx 10000$, where U_b is the bulk flow velocity and D is the diameter of the pipe. The shortest mesh is 1.2 D long and it consists of 5 blocks, each containing $32 \times 32 \times 32$ cells, altogether 163840 cells. The height of the two cells next to the wall is approximated to be around one in wall units ($r^+ = 1$) from the law of the wall. The streching ratio varies between 1.075-1.087 in the four outer blocks. The azimuthal mesh spacing $R\Delta\theta^+$ at the wall is 15 and the streamwise mesh-spacing Δz^+ is 24. This flow was first computed by using one Power4 -processor, after which all blocks were assigned to separate processors. The basic mesh was then multiplied and connected together, so that the computations were performed by using multiple pipe lenghts up to 30 processors. The pipe flow may be considered a simple flow physically, but computationally it possesses many complex features for the current Cartesian solver. Non-modelled large eddy simulations were calculated first. Within the time step of $0.05T$ ($T = D/U_b$) eight subiterations were taken which was considered to provide a sufficient convergence. The period during which the statistics was gathered varied between 200 T and 500 T depending on the mesh size. In the end the data was averaged also in the axial and radial directions. The velocity profile is slightly flatter than the measured one. The streamwise rms fluctuations are overpredicted whereas the radial rms fluctuations are underpredicted as seen in Fig. 5. The fluctuations obtained from the simulation using the shortest pipe lenght $1.2D$ deviate somewhat from the rest of the results. A localized SGS-model was

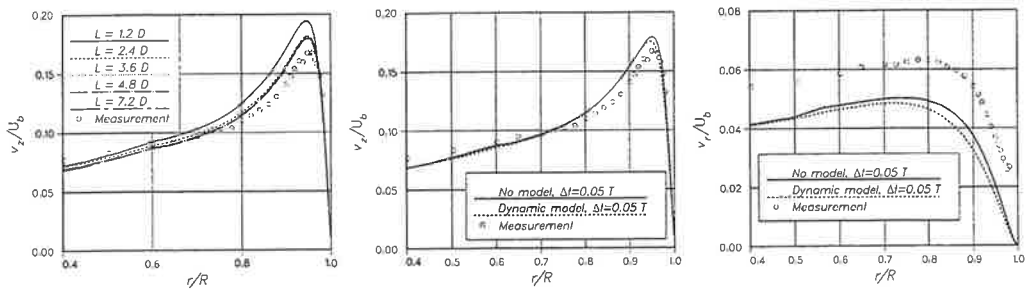

Figure 5: Results from the pipe flow at $Re_\tau = 621.4$. At left streamwise fluctuations with different mesh lengths. The effect of the SGS model on the streamwise and radial fluctuations at the centre and the right, respectively. The reference measurements by den Toonder and Nieuwstadt [5].

utilized with the pipe length of $3.6D$. The model dampens slightly the resolved turbulent intensities as shown in Fig. 5. Near the wall the model dampens itself excluding the need for the van Driest damping function, which requires a distance from the wall. In complex geometries the definition of the wall distance may be ambiguous. The parallelization was linear in these calculations.

4.4 Jet in crossflow

The setup of the jet in crossflow (JICF) is sketched in Fig. 6. The Reynolds number $Re_D = 46700$ referred to the pipe diameter is rather large for an LES of the whole jet. Therefore the computational domain has been reduced from that of the wind tunnel used by Crabb et al. [3], who have measured both average velocities and turbulent intensities in the case. In the LES a frictionless wall condition is applied at the lateral boundaries, and a no-slip condition at the lower wall. At the inlet a uniform velocity U_∞ is set and a zero-gradient condition is extrapolated at the outlet for all

variables. For the jet there is an inlet pipe one diameter D long. At the lower end, a fully developed average flow profile is applied. For the pressure the zero-gradient is set at all boundaries. The grid is geometrically streched in streamwise and jetwise directions. The smallest cell next to the wall is $0.002D$ high. The mesh is divided equally into 25 blocks consisting of 2 764 800 cells altogether. A constant Smagorinsky model was used in the computation because the dynamic model did not stabilize the computation. A rather large Smagorinsky constant $C_s = 0.17$ was used, and in the start of the calculation even higher value was needed. The flow was integrated during a time of 96 T, where $T = D/U_\infty$ and the statistics used to present the results here was gathered during the last 42 T. The recirculation zone seems to be located closer to the jet an closer to the wall than the experiment suggests (Figs. 7, 8). Turbulent fluctuations seem grow later in simulation, probably partly due to the Smagorinsky model and the steady inlet contitions. The jet profile peak right above the jet exit is higher than the measured one. The jet pipe profile might not be fully developed but flatter in the experiment. A closer examination of the results will be reported later elsewhere.

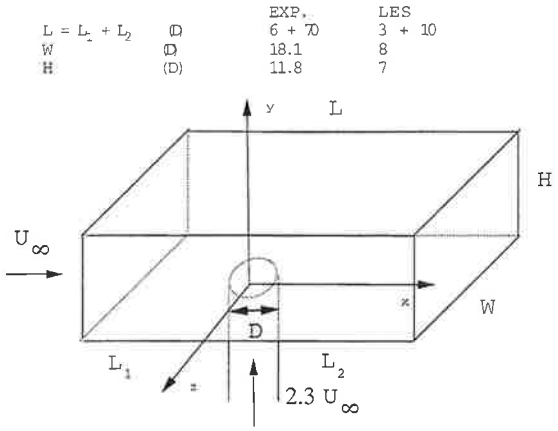

Figure 6: Schematics of the domain in the jet in crossflow. Experiment refers to the windtunnel used by Crabb et al. [3] whereas the LES refers to the computational domain size.

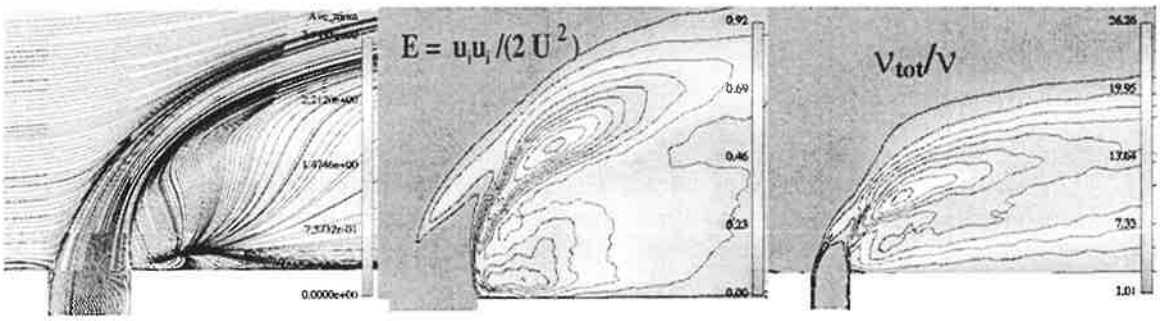

Figure 7: The averaged streamlines, the effective viscosity and the resolved turbulent energy shown from left to right, respectively.

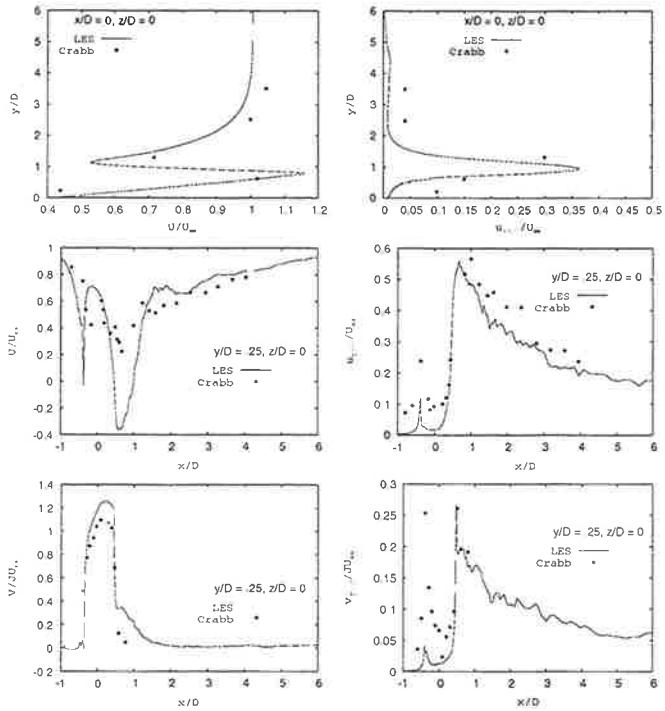

Figure 8: Top : The streamwise velocity and the rms velocity at x/D = 0 at the symmetry plane. Centre : The streamwise velocity and the rms velocity at y/D = 0.25 at the symmetry plane. Bottom : The vertical velocity and the rms velocity at y/D = 0.25 at the symmetry plane.

5 CONCLUSIONS

A parallel, finite-volume solver was developed for large-eddy simulation. The algorithm is based on a traditional SIMPLE technique and an implicit iterative time stepping is applied. The implicit part of the solution is solved independently in each block and proces and the boundary values are exchanged only after each outer iteration loop. This simplifies the code a lot without affecting much the convergence. Also, the amount of the message passing between the processes is reduced. The parallelization of the present solver shows good scaling in the present ideally balanced computations.

Several flows are simulated to test the solver. The dynamic model reduces the viscosity correctly in the vicinity of the wall without any ad hoc damping functions. Unfortunately, it does not always stabilize the computation. In the jet in crossflow a traditional Smagorinsky model was used.

ACKNOWLEDGEMENTS

This research project has been funded by the Graduate School of Computational Fluid Dynamics and IVO foundation, whose support is gratefully acknowledged. CSC, the Center of Scientific Computation, is acknowledged for providing us with the IBM cluster.

REFERENCES

[1] M. Breuer. Large eddy simulation of the subcritical flow past a circular cylinder: numerical and modeling aspects. *International Journal for Numerical Methods in Fluids*, 28:1281–1302,

1998.

[2] T.T. Bui. A parallel, finite-volume algorithm for large-eddy simulation of turbulent flows. *Computers & Fluids*, 29:877–915, 2000.

[3] D Crabb, D.F.G Durao, and J.H. Whitelaw. A round jet normal to a crossflow. *Transactions of the ASME: Journal of Fluids Engineering*, 103:568–580, 1981.

[4] J.W. Deardorff. A numerical study of three-dimensional turbulent channel flow at large Reynolds numbers. *Journal of Fluid Mechanics*, 41:453–480, 1970.

[5] J.M.J. den Toonder and F.T.M. Nieuwstadt. Reynolds number effects in a turbulent pipe flow for low to moderate Re. *Physics of Fluids*, 9:3398–3409, November 1997.

[6] M. Germano, U. Piomelli, P. Moin, and W.H. Cabot. A dynamic subgrid-scale eddy viscosity model. *Physics of Fluids A*, 7:1760–1765, 1991.

[7] U. Ghia, K. Ghia, and C. Shin. High-re solutions for incompressible flow using the navier-stokes equations and a multigrid method. *Journal of Computational Physics*, 48:387–411, 1982.

[8] W. Gropp, E. Lusk, and A. Skjellum. *Using MPI: Portable Parallel Programming with the Message-Passing Interface, Second Edition*. The MIT Press, Cambridge, Massachusetts, 1999. ISBN 0-262-57132-3.

[9] J. Hoffren. Time-accurate schemes for a multi-block Navier–Stokes solver. Report A-14, Helsinki University of Technology, Laboratory of Aerodynamics, 1992. ISBN 951–22–1350–8.

[10] M. Lesieur. *Turbulence in Fluids, Third Revised and Enlargened Version*. Kluwer Academic Publishers, Dordrecht, 1997. ISBN 0-7923-4416-2.

[11] P. Majander. Deveplopments in large eddy simulation. Report 128, Helsinki University of Technology, 2000. ISBN 951–22–4861–1.

[12] A. Miettinen. A study of the pressure correction approach in the colocated grid arrangement. Technical report no. 110, Helsinki University of Technology, Laboratory of Applied Thermodynamics, 1997. ISSN 1237–8372.

[13] U. Piomelli and J. Liu. Large-eddy simulation of rotating channel flows using a localized dynamic model. *Physics of Fluids*, 7(4):839–848, April 1995.

[14] A.K. Prasad and J.R. Koseff. Reynolds number and end-wall effects on a lid-driven cavity flow. *Physics of Fluids A*, 1(2):208–218, February 1989.

[15] C.M. Rhie and W.L. Chow. Numerical study of the turbulent flow past an airfoil with trailing edge separation. *AIAA Journal*, 21(11):1525–1532, November 1983.

[16] A. Rizzi, P. Eliasson, I. Lindblad, C. Hirsch, C. Lacor, and J. Haeuser. The engineering of multiblock/multigrid software for navier-stokes flows on structured meshes. *Computers & Fluids*, 22(2):341–367, 1993.

[17] J. Smagorinsky. General circulation experiments with the primitive equations, part I: The basic experiment. *Montly Weather Review*, 91:99–152, 1963.

USING MATHEMATICAL CONCEPTS IN SOFTWARE DESIGN OF COMPUTATIONAL MECHANICS

K. HILTUNEN, M. LAITINEN, A. NIEMISTÖ, P. TARVAINEN

Numerola Oy
Väinönkatu 11A, FIN-40100 Jyväskylä
e-mail: Mika.Laitinen@numerola.fi

ABSTRACT

The ideal software in computational mechanics is efficient, flexible and easy to use. The balance between these factors is difficult to achieve, especially, for a general purpose software where user can enter own models. In this paper, we present software design concepts which aim to increase the usability, still maintaining the flexibility and reasonable efficiency. Then, we illustrate a realization of these principles, Numerrin 2.0 software. Finally, we demonstrate the software by modeling the "die-swell" problem.

1 INTRODUCTION

The most popular software packages in computational mechanics are based on a fixed set of models. This allows an easy interface for solving problems. However, entering new models or material laws to these software packages is often difficult or impossible. Also, coupling different phenomena and optimization can pose difficulties. Therefore, there is a need for software in which the user can define his or her own set of variables and equations.

There are several extensive software packages on the market for this purpose, take for example Femlab [1], Elmer [5], Diffpack [2], deal.II [4], FlexPDE [3] and Freefem [6]. However, the balance between applicability, computational efficiency and usability is difficult to achieve and we feel that this area of software engineering is somewhat immature. There are obvious reasons for this immaturity. First, proper software tools and numerical methods to increase usability have been around only for about a decade. Secondly, the problems which these software packages are designed to solve, require a lot of computational resources and, therefore, the developers of these systems have put their best efforts on computational efficiency. Less attention has been focused on user efficiency: How easily the software can be learned? How fast the user can set up a problem? How much from the overall modeling time is spent on secondary tasks such as debugging?

In order to increase the user efficiency of the modeling software, we propose the following software design principles:

- The concepts of the software should follow closely the language of mathematics. This offers a general and multidisciplinary framework.
- The software engineering concepts that the user needs to know should be kept at minimum. This lowers the user threshold and keeps the focus on modeling.

- The low-level details of numerical methods should be hidden from the user. Nevertheless, the user should be able to control the key aspects of the numerical methods. Most of the details are merely mechanical and error-prone. The vast number of details also make the model definition difficult to read.

- The derivatives needed for linearizations should be computed automatically by the software, including also sensitivities needed for optimization. Computing derivatives by hand is often a mechanical, time-consuming and error-prone task. Also, maintaining a code with hand-coded derivatives is problematic, since modification of the model always implies modification of the derivatives.

- Defining a system of coupled models should be as natural as defining the models one at the time. Too often, linking the software components describing the separate models are difficult and time-consuming.

According to our knowledge, none of the above listed software packages [1]–[6] completely fulfills these design principles. For instance, many of them are still very software engineering oriented and need hand-coded derivatives. In this article, we illustrate the realization of these principles with Numerrin 2.0 software developed by Numerola Oy. This software is a general tool for developing and optimizing mathematical models based on partial differential equations. The current version of Numerrin uses the finite element method to discretize the equations. Numerrin 2.0 consist of a Fortran 95 library, 2D and 3D mesh generators and a visualization tool. The models are defined by writing short Fortran 95 codes, as will be seen in the next sections.

This paper is linked with the article [8] that concentrates more on automatic differentiation and optimization. It also offers two additional examples implemented using Numerrin 2.0 software.

Remark 1. The above design principles are not limited to any specific numerical method or application area, but they can be applied in designing of a mathematical modeling software in general.

2 IMPLEMENTATION OF THE DESIGN PRINCIPLES

In this section, we demonstrate how the design principles of Section 1 are realized in Numerrin 2.0. First, we use a nonlinear heat equation as an example and then we consider a system of electric and thermal conduction. For the details of the finite element method, we refer to [9, 10, 11].

2.1 Heat conduction

Consider a nonlinear heat equation posed in the geometry of Figure 1

$$-\nabla \cdot (k(T)\nabla T) = f \quad \text{in } \Omega, \qquad T = T_0 \quad \text{on } \Gamma_1, \qquad -k(T)\nabla T \cdot \mathbf{n} = 0 \quad \text{on } \Gamma_2, \tag{1}$$

where $\mathbf{n}$ is the outward unit normal. Since we use the finite element method, we shall work with the variational formulation of (1). First, we define the residual

$$r(T,\phi) = \begin{cases} \displaystyle\int_\Omega k(T)\,\nabla T \cdot \nabla\phi - f\phi\,dx, \\ T|_{\Gamma_1} - T_0. \end{cases} \tag{2}$$

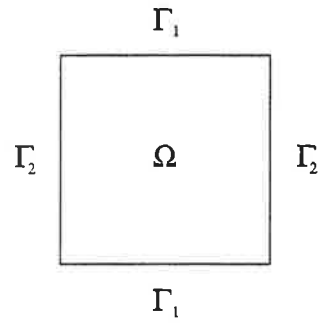

Figure 1: A domain used in examples.

Then, the variational formulation reads: Find $T \in V := H^1(\Omega)$ such that

$$r(T, \phi) = 0 \quad \text{for all } \phi \in \{v \in H^1(\Omega) \,:\, v|_{\Gamma_1} = 0\}. \tag{3}$$

To linearize (3), we use the Newton's method that reads as follows

repeat

Compute the residual $r(T)$ and the Jacobian $\dfrac{\partial r}{\partial T}$

Solve the linear system $\dfrac{\partial r}{\partial T}\delta T = r$

Update the temperature $T = T - \delta T$

until r is small

To present the objects of the model in Numerrin 2.0, we need four basic data types: System vector (SysVec), system matrix (SysMat), system geometry (SysGeom) and system space (SysSpace). The system vectors represent all functions and variables in the model, for example, the residuals and the unknowns of the models. The system matrices represent all linear transformations, like derivatives, interpolants and geometric transformations. System geometry represents a computational mesh or a part of it. System space stands for the function space defined over the geometry.

Remark 2. The basic data types of Numerrin 2.0 and their operations are designed and implemented such that the software design principles of Section 1 are satisfied.

We next describe the heat transfer model with Numerrin 2.0. First, the objects need to be introduced and initialized

```
TYPE(SysMat_t):: drdT
TYPE(SysVec_t):: T, r, dT, f
TYPE(SysGeom_t):: Omega, Gamma1
TYPE(SysSpace_t):: V

Omega = SysGeom('square.msh')
Gamma1 = SysGeom(Omega, boundary='Gamma1')
V = SysSpace(Omega)
T = SysVec(V)
```

```
drdT = SysMat(V, V)
r = SysVec(V)
f = SysVec(V)
dT = SysVec(V)
```

After initializations, the code solving the heat equation reads as

```
! Newton iteration
DO it=1,maxit

  drdT = 0.0_wp; r = 0.0_wp
  drdT = DefaultDerivative(r, T)

  ! Variational formulation
  DO WHILE ( Integrate(Omega) )
    phi => GetBasisFunctionPtr()
    r = k(T) * (grad(T) .DOT. grad(phi)) - f * phi
  END DO

  ! Dirichlet boundary condition
  DO WHILE( Nodes(Gamma1) )
    r = T - T0
  END DO

  ! Solution of the linear system
  dT = LU(drdT, r)
  T = T - dT

  ! Stopping criterion
  IF ( norm2(r) < toler ) EXIT

END DO
```

Basically, this code works like a traditional finite element code; it performs the numerical integration and the element-by-element assembly. However, these often technical details of the finite element method are now completely hidden from the user and the resulting code resembles more the original problem than its discretization. We feel the lack of details does not restrict the user, it only liberates from technical tasks.

Let us next briefly describe how automatic differentiation is used in Numerrin 2.0. We concentrate only on aspects specific to Numerrin 2.0, a more general discussion can be found in [8, 14]. The automatic differentiation is implemented using operator overloading of Fortran 95. The differentiation is applied to local elemental or nodal contributions which are defined inside the `DO WHILE ... END DO` loop. The differentiation is triggered by `DefaultDerivative` command. Here, the term `Default` means that the derivative is computed by default in every local operation onwards. The differentiation can be done with respect to any variable, which is defined before the local operations. For example, in the above code the residual `r` could be differentiated with respect to heat source `f`. This is a very useful aspect in optimization and parameter identification, for example.

The differentiation with respect to geometry is done using the `ShapeDerivative` command. For example, the derivative of function `r` with respect to a geometric parameter `a` is obtained by the command

```
drda = ShapeDerivative(r, G)
```

where G is the derivative of nodal coordinates with respect to a. The user must supply the matrix G which can be produced, for example, inside the mesh generator using automatic differentiation. Internally, the derivative is computed applying the chain rule

$$\frac{\partial r}{\partial a} = \sum_{i=1}^{n} \frac{\partial r}{\partial x_i} \frac{\partial x_i}{\partial a},$$

where n is the dimension of the geometry. We will demonstrate the use of `ShapeDerivative` command in Section 3.

2.2 Coupled electric and thermal conduction

Let us next demonstrate how the model coupling can be done in Numerrin 2.0 environment. As an example, we consider simultaneous electric and thermal conduction in the domain Ω of Figure 1

$$-\nabla \cdot (k\nabla T) = f(u) \quad \text{in } \Omega, \qquad T = T_0 \quad \text{on } \Gamma_1, \qquad -k\nabla T \cdot \mathbf{n} = 0 \quad \text{on } \Gamma_2, \tag{4}$$

$$-\nabla \cdot (\sigma(T)\nabla u) = 0 \quad \text{in } \Omega, \qquad u = u_0 \quad \text{on } \Gamma_1, \qquad -\sigma(T)\nabla u \cdot \mathbf{n} = 0 \quad \text{on } \Gamma_2, \tag{5}$$

where T is temperature and u is electrostatic potential. These equations are coupled, since the current density causes a heat source $f = \sigma\|\nabla u\|^2$ and, on the other hand, the electrical conductivity σ depends on temperature. Here, we assume that σ is proportional to $1/T$, which is an approximation used for metals. The variational residuals of (4)–(5) are defined as

$$r_1(T, u, \phi) = \begin{cases} \displaystyle\int_\Omega k\,\nabla T \cdot \nabla \phi - f(u)\phi \, dx \\ T|_{\Gamma_1} - T_0 \end{cases} \tag{6}$$

$$r_2(T, u, \phi) = \begin{cases} \displaystyle\int_\Omega \sigma(T)\,\nabla u \cdot \nabla \phi \, dx, \\ u|_{\Gamma_1} - u_0 \end{cases} \tag{7}$$

Then, the variational formulation reads as: Find $T, u \in V = H^1(\Omega)$ such that

$$r_1(T, u, \phi_1) = 0, \quad r_2(T, u, \phi_2) = 0, \quad \text{for all } \phi_1, \phi_2 \in \{v \in H^1(\Omega) : v|_{\Gamma_1} = 0\}. \tag{8}$$

Now, the Jacobian is a two-by-two block matrix, and the residual as well as the solution are presented by block vectors

```
TYPE(SysMat_t):: J(2,2)
TYPE(SysVec_t):: q(2), r(2), dq(2), sigma, c, f
TYPE(SysVec_t), POINTER:: T, u
```

Here, q is the two-component solution vector whose first component is associated to temperature and second component is associated to electrostatic potential. Now, the model definition reads as follows

```
DO it=1,maxit

  drdq = 0.0_wp; r = 0.0_wp
  drdq = DefaultDerivative(r, q)
  T => q(1)
  u => q(2)

  ! variational formulations
  DO WHILE ( Integrate(Omega) )
    phi => GetBasisFunctionPtr()
    sigma = c/T
    f = -sigma * (grad(u) .DOT. grad(u))
    r(1) = k * (grad(T) .DOT. grad(phi)) - f * phi
    r(2) = sigma * (grad(u) .DOT. grad(phi))
  END DO

  ! Dirichlet boundary conditions
  DO WHILE( Nodes(Gamma1) )
    r(1) = T - T0
    r(2) = u - u0
  END DO

  dq = LU(drdq, r)
  q = q - dq

  IF ( norm2(r) < toler ) EXIT
END DO
```

Let us now discuss the computer efficiency of Numerrin 2.0 compared to a traditional finite element software. Clearly, there is some overhead in using operator overloading and automatic differentiation. However, these operations only slow down the assembly stage of the linear system. In a test case with a 2D Navier-Stokes code, we observed that the assembly in Numerrin 2.0 took 2.4 times longer than in a traditional FEM code. However, the time used in assembly is proportional to the number of unknowns, which is asymptotically optimal. Thus, for larger problems the efficiency of the assembly is of secondary importance. Secondly, utilizing the exact linearization obtained with automatic differentiation, in many cases Numerrin 2.0 is faster than a traditional partially or incorrectly linearized code.

Remark 3. Finally, note that the above codes are dimension independent; the same codes could be applied to one, two or three dimensional problems simply by changing the definition of the computational geometry `Omega`.

3 EXAMPLE: A FREE BOUNDARY PROBLEM

In this section, we illustrate the Numerrin 2.0 software with a more complicated example. We consider the classical "die-swell" problem modeling free jet flow [12]. This problem has received considerably attention, because the implementation of robust and efficient solvers requires exact linearization. For example, the trial methods [15] are easy to linearize but give linear convergence at best. On the other hand, the total linearization method [12, 16]

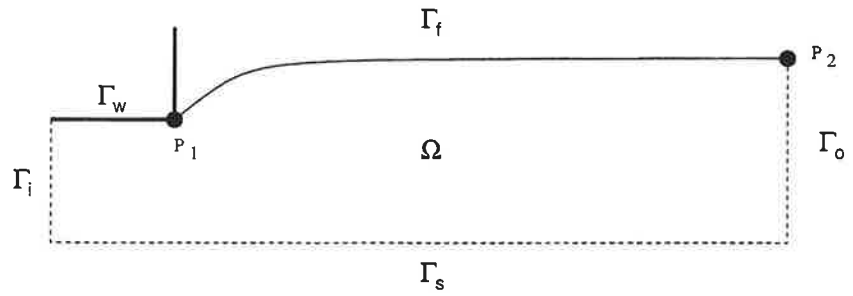

Figure 2: A domain of a "die-swell" problem.

is more complicated to implement and yields superlinear convergence. Finally, the exact linearization without applying automatic differentiation results in quadratic convergence, but it is very complicated to implement. Our approach is to use Newton's method with automatic differentiation in Numerrin 2.0 environment. This gives simple implementation and quadratic convergence.

In the die-swell problem we are interested in determining the velocity $\mathbf{u}$, the hydrostatic pressure p and the free jet surface. The fluid flow is governed by the Navier-Stokes equations

$$-\nabla \cdot \boldsymbol{\sigma} + \rho \mathbf{u} \cdot \nabla \mathbf{u} = 0 \quad \text{in } \Omega, \qquad \nabla \cdot \mathbf{u} = 0 \quad \text{in } \Omega. \tag{9}$$

with

$$\boldsymbol{\sigma} = \mu(\nabla \mathbf{u} + \nabla \mathbf{u}^T) - pI.$$

The geometry is sketched in Figure 2; Γ_f is the unknown free boundary and Γ_s is the symmetry axis. The boundary conditions are chosen as

$$u_1 = \frac{3}{2}U(1 - 2x_2/b)^2, \quad u_2 = 0 \quad \text{on } \Gamma_i, \tag{10}$$

$$\mathbf{u} = 0 \quad \text{on } \Gamma_w, \tag{11}$$

$$\mathbf{n} \cdot \boldsymbol{\sigma} \cdot \mathbf{n} = 0, \quad \mathbf{u} \cdot \mathbf{t} = 0 \quad \text{on } \Gamma_o, \tag{12}$$

$$\mathbf{t} \cdot \boldsymbol{\sigma} \cdot \mathbf{n} = 0, \quad \mathbf{u} \cdot \mathbf{n} = 0 \quad \text{on } \Gamma_s, \tag{13}$$

$$\mathbf{n} \cdot \boldsymbol{\sigma} \cdot \mathbf{n} = \lambda\kappa, \quad \mathbf{t} \cdot \boldsymbol{\sigma} \cdot \mathbf{n} = 0 \quad \text{on } \Gamma_f, \tag{14}$$

where λ is the surface tension, κ is the mean curvature, U is the characteristic speed and b is the inlet height. Here $\mathbf{n}$ and $\mathbf{t}$ refer to surface normal and tangent vectors. On the free boundary Γ_f, we have an additional boundary condition

$$\mathbf{u} \cdot \mathbf{n} = 0. \tag{15}$$

In what follows, we omit the Dirichlet boundary conditions on Γ_i, Γ_o an Γ_w; These conditions are handled as in Section 2.

Now, the variational formulas read as follows

$$r_1 = \int_\Omega \boldsymbol{\sigma}_1 \cdot \nabla\phi \, dx + \int_\Omega \rho \mathbf{u} \cdot \nabla u_1 \, \phi \, dx + \int_{\Gamma_f} \lambda\kappa n_1 \, \phi \, ds = 0, \tag{16}$$

$$r_2 = \int_\Omega \boldsymbol{\sigma}_2 \cdot \nabla\phi \, dx + \int_\Omega \rho \mathbf{u} \cdot \nabla u_2 \, \phi \, dx + \int_{\Gamma_f} \lambda\kappa n_2 \, \phi \, ds = 0, \tag{17}$$

$$r_3 = \int_\Omega \nabla \cdot \mathbf{u} \, \phi \, dx = 0, \tag{18}$$

$$r_4 = \int_{\Gamma_f} \mathbf{u} \cdot \mathbf{n} \, \phi \, dx = 0, \tag{19}$$

where $\boldsymbol{\sigma}_i$ is the i:th row of the tensor $\boldsymbol{\sigma}$. The boundary integral on Γ_f is simplified using the Frenet's formula

$$\kappa n_k = \frac{dt_k}{ds} \tag{20}$$

which gives

$$\int_{\Gamma_f} \lambda\kappa n_k \phi \, ds = \lambda \int_{\Gamma_f} \frac{dt_k}{ds} \phi \, ds = \lambda \left(\int_{\Gamma_f} t_k \frac{d\phi}{ds} \, ds + t_k(P_2)\phi(P_2) - t_k(P_1)\phi(P_1) \right). \tag{21}$$

Here, P_1 and P_2 are the end points of Γ_f. In the last term $\phi(P_1)$ vanishes since $\mathbf{u}(P_1) = 0$.

In the Numerrin 2.0 implementation, we solve simultaneously the fluid flow and the location of the free boundary Γ_f. Thus, we are solving a system of four-by-four blocks, where the unknowns are velocity, pressure and displacement of Γ_f in x_2-direction. The displacement is simultaneously a geometric parameter and the unknown of the system. Hence, the last column of the linearization matrix contains the sensitivities with respect to the displacement. The code describing the model reads as

```
! Mesh coordinates at the initial stage
x0 = mesh

DO it=1,itmax

   drdq = DefaultDerivative(r, q)
   drdq(:,4) = DefaultShapeDerivative(r, G)

   CALL AssembleNavierStokes(r, q)
   CALL AssembleFreeBoundary(r, q)

   dq = LU(drdq, r)
   q = q - dq

   ! Update mesh coordinates
   mesh = G * dq(4) + x0

   IF ( norm2(r) < toler ) EXIT

END DO
```

The Navier-Stokes equations are approximated using the linear elements and the so-called Franca & Frey stabilization, we refer to [13] for the details. The main part of the subroutine `AssembleNavierStokes` reads as

```
u => q(1:dim)
p => q(dim+1)

DO WHILE ( Integrate(Omega) )

   phi => GetBasisFunctionPtr()

   ! Franca & Frey stabilization parameters
   CALL StabFrancFrey(tau,delta,u,rho,mu,it)

   ! Stabilized basis function
   phis = tau * ( u .DOT. grad(phi))

   ! Stress tensor
   DO i=1,dim
      DO j=1,dim
         sigma(i,j) = mu * (grad(u(i),j)+grad(u(j),i))
      END DO
      sigma(i,i) = sigma(i,i) + p
   END DO

   ! Momentum residuals (linear basis)
   DO i=1,dim
      conv(i) = rho * (u .DOT. grad(u(i)))
      Res(i) = conv(i) + grad(p,i)
   END DO

   ! Continuity residual
   ResC = rho * div(u)

   DO i=1,dim
      r(i) = (sigma(i,:) .DOT. grad(phi))  & ! stress
           + conv(i) * phi                 & ! convection
           + delta * ResC * grad(phi,i)    & ! continuity stabilization
           + Res(i) * phis                   ! momentum stabilization
   END DO
   r(dim+1) = - ResC * phi                 & ! continuity
            - tau * (Res .DOT. grad(phi))    ! stabilization

END DO
```

On the free boundary, we need to compute the integral over Γ_f and the point-wise contribution from (21). Here, we assume that the tangent vector at the end point P_2 is $\mathbf{t} = (1, 0)$. The main part of the `AssembleFreeBoundary` reads as

```
! The free boundary integrals
DO WHILE ( Integrate(Gamma_f) )
   nvec => GetNormalVecPtr()
   tvec => GetTangentVecPtr()
   phi  => GetBasisFunctionPtr()

   ! tangential derivative of the basis function
   dphi_ds=grad(phi) .DOT. tvec(1,:)

   ! surface stresses in the momentum equations
   DO i=1,dim
      r(i) = SurfaceTension * tvec(1,i) * dphi_ds
   END DO

   ! the kinematic equation for the free boundary
   r(dim+2) = (u .DOT. nvec) * phi
END DO

! Dirac delta function at the endpoint of the free boundary
P2 = (Gamma_o .INTERSECTION. Gamma_f)
DO WHILE ( DiracNodes(P2) )
   r(1) = -SurfaceTension
END DO
```

Figure 3 shows computed results for various Reynolds and capillary numbers. The surface tension λ and the capillary number Ca are related by $\lambda = \mu U/Ca$. In table 1 we compare the results computed with Numerrin 2.0 to those obtained with a total linearization method [12]. The comparison is done using the so-called die-swell percentage

$$r_s = 100(h(\Gamma_o) - h(\Gamma_i))/h(\Gamma_i),$$

where $h(\Gamma_i)$ and $h(\Gamma_o)$ are the height of the inlet and height of the outlet. The results are essentially the same and the small differences are apparently attributed to the differences in the meshes. The mesh used in computations was not documented in [12]. Figure 4 shows the convergence in two extreme cases: High Reynolds number and high capillary number.

4 CONCLUSIONS

The software can be designed in such a way that the mathematical objects and operations have their counterparts in the software. This leads to a very general software framework where many error-prone stages of modeling can avoided using software abstractions based on mathematical objects. Derivatives with respect to almost any parameter or variable can be computed conveniently using automatic differentiation.

REFERENCES

[1] *FEMLAB home page*, http://www.femlab.com.

[2] *Diffpack home page*, http://www.nobjects.com.

[3] *FlexPDE home page*, http://www.pdesolutions.com.

[4] *deal.II home page*, http://gaia.iwr.uni-heidelberg.de/deal.

Re	$1/Ca$	r_s [Kruyt et. al.]	r_s [Numerrin 2.0]
0.1	0.0	19.28	18.87
1.0	0.0	19.17	18.68
1.0	0.4	16.88	16.04
1.0	1.6	11.76	11.04
1.0	3.6	7.5	7.06
4.0	0.4	15.49	14.51
4.0	1.6	12.44	11.62
4.0	2.4	10.67	10.00
18.0	2.222	1.25	0.91
18.0	4.444	1.95	1.75
75.0	2.0	-11.21	-11.06
300.0	0.0	-15.24	-15.29

Table 1: The comparison of die-swell percentages.

[5] *ELMER homepage*, http://www.csc.fi/elmer.

[6] *Freefem home page*, http://www.freefem.org.

[7] Numerola Oy. *Numerrin 2.0 käyttäjän opas*, 2003.

[8] R. A. E. Mäkinen, K. Hiltunen, M. Laitinen and A. Niemistö. *Exact Linearization in Numerical Simulation and Optimization*, Proceedings of the VIII Finnish Mechanics Days, 2003.

[9] P. Ciarlet. *The Finite Element Method for Elliptic Problems*, North Holland, 1976.

[10] S. Brenner and R. Scott. *Mathematical Theory of Finite Element Methods*, Springer–Verlag, 1994.

[11] C. Johnson. *Numerical Solution of Partial Differential Equations by the Finite Element Method*, Studentlitteratur, 1987.

[12] N. P. Kruyt et.al. *Total Linearization Method for Solving Viscous Free Boundary Flow Problems by the Finite Element Method*, International Journal for Numerical Methods in Fluids, vol. 8, 351–363, 1988.

[13] L. Franca and S. Frey. *Stabilized Finite Element Methods II: The Incompressible Navier-Stokes Equations*, Computer Methods in Applied Mechanics and Engineering, vol. 99, 209–233, 1992.

[14] A. Griewank. *Evaluating Derivatives: Principles and Techniques of Algorithmic Differentiation.* SIAM, 2000.

[15] C. Cuvelier. *Finite Element Methods and Navier-Stokes Equations*, D. Reidel Publishing company, 1986.

[16] C. Cuvelier and R. M. S. M. Schulkes. *Some Numerical Methods for the Computation of Capillary Free Boundaries Governed by the Navier-Stokes Equations*, SIAM Review, vol. 32, 355–423, 1990.

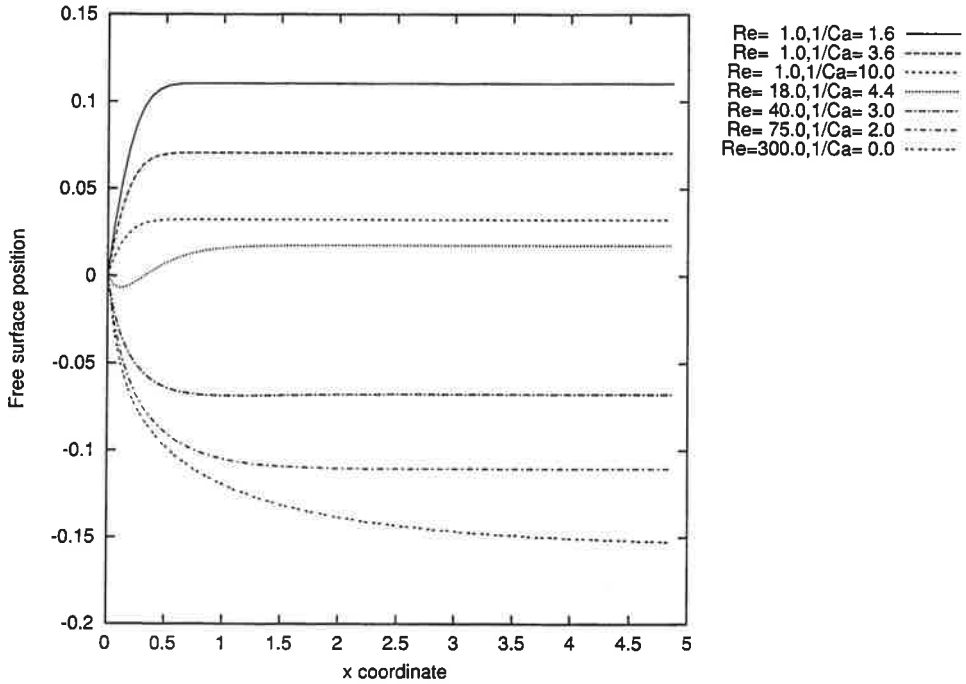

Figure 3: The free surface for various Reynolds and capillary numbers.

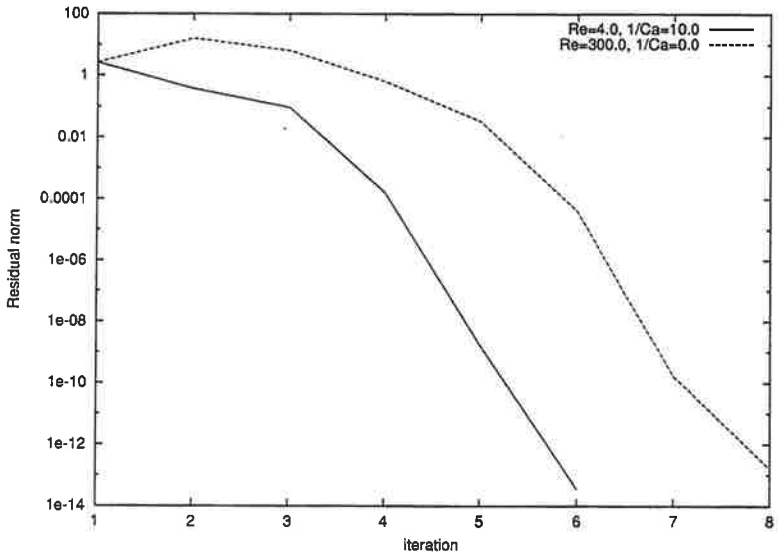

Figure 4: The convergence.

EXACT LINEARIZATION IN NUMERICAL SIMULATION AND OPTIMIZATION

R. A. E. MÄKINEN[1], K. HILTUNEN[2], M. LAITINEN[2], A. NIEMISTÖ[2]

[1]Department of Mathematical Information Technology
P. O. Box 35 (Agora)
FIN-40014 University of Jyväskylä, Finland

[2]Numerola Oy
Väinönkatu 11 A
FIN-40100 Jyväskylä, Finland

ABSTRACT

Simulation of many physical phenomena requires the numerical solution of nonlinear partial differential equations. In addition to simulation, one often wishes to identify or optimize some parameters of the system (including geometry). In this work we present how exact Jacobian can be produced fully automatically for a simulation problem by using the technique of automatic differentiation of computer programs. Under some additional hypothesis, exact gradient can be produced semi-automatically for shape optimization problems, too. The advantages of exact linearization in practical problems of fluid mechanics is demonstrated by numerical examples.

1 INTRODUCTION

Consider the following model problem. Let $\Omega(\boldsymbol{a})$ be a domain defined by a vector of geometric parameters $\boldsymbol{a} = (a_1, \ldots, a_n) \in U^{ad} \subset \mathbb{R}^n$. The domain is occupied by incompressible fluid which is modeled by the Navier–Stokes equations:

$$-\mu\Delta\vec{u} + \nabla p + \rho(\vec{u}\cdot\nabla)\vec{u} = \rho\vec{g}, \qquad \nabla\cdot\vec{u} = 0 \quad \text{in } \Omega(\boldsymbol{a}). \tag{1}$$

We wish to control the fluid flow by changing the geometry of the domain $\Omega(\boldsymbol{a})$. Mathematically this can be formulated as the following combined simulation and optimization problem:

$$\min_{\boldsymbol{a}\in U^{ad}} \left\{ J(\boldsymbol{a}, \vec{u}(\boldsymbol{a})) = \int_{\Omega(\boldsymbol{a})} |\vec{u}(\boldsymbol{a}) - \vec{u}_d|^2 \, dx \right\}, \tag{2}$$

where $\vec{u}(\boldsymbol{a})$ is the the solution of (1) for the given control parameter $\boldsymbol{a}$ and $\vec{u}_d$ is the target flow field. For an introductory treatment of theoretical and computational aspects of shape optimization problems we refer to [5].

Performing a finite element discretization of (1) we obtain the following nonlinear programming problem

$$\min_{\boldsymbol{a}\in U^{ad}} \{\mathcal{J}(\boldsymbol{a}) = J(\boldsymbol{a}, \boldsymbol{u}(\boldsymbol{a}))\} \tag{3}$$

subject to

$$\boldsymbol{K}(\boldsymbol{a}; \boldsymbol{u}(\boldsymbol{a}))\, \boldsymbol{u}(\boldsymbol{a}) = \boldsymbol{f}(\boldsymbol{u}(\boldsymbol{a})). \tag{4}$$

Here (4) is the set of quasi-linear algebraic equations corresponding the discretization of (1). Vector $\boldsymbol{u}(\boldsymbol{a})$ contains the nodal values of approximated velocity and pressure, $\boldsymbol{K}(\boldsymbol{a};\boldsymbol{u}(\boldsymbol{a}))$ is the "stiffness" matrix, and $\boldsymbol{f}(\boldsymbol{a};\boldsymbol{u}(\boldsymbol{a}))$ is the "force" vector.

Let us assume that the mappings $\boldsymbol{a} \mapsto \boldsymbol{u}(\boldsymbol{a})$ and $(\boldsymbol{a},\boldsymbol{u}) \mapsto J(\boldsymbol{a},\boldsymbol{u})$ are continuously differentiable. Principally it would be possible to treat $\boldsymbol{u}$ and $\boldsymbol{a}$ independent variables and iterate them simultaneously until the Kuhn–Tucker optimality conditions of (3)–(4) are satisfied. However, this approach is not convenient if one wants to utilize existing general purpose simulation codes. Instead the state variable $\boldsymbol{u}$ is eliminated from the optimization problem and we have a two level iterative scheme. The outer loop is for optimization of geometry while the inner one solves the simulation problem corresponding to the given (fixed) parameter $\boldsymbol{a}$:

Choose initial guess $\boldsymbol{a}^{(0)}$, $k := 0$
repeat
  Choose initial guess $\boldsymbol{u}_0(\boldsymbol{a}^{(k)})$, $i := 0$
  repeat
    Determine $\Delta \boldsymbol{u}_i$
    $\boldsymbol{u}_{i+1}(\boldsymbol{a}^{(k)}) := \boldsymbol{u}_i(\boldsymbol{a}^{(k)}) + \Delta \boldsymbol{u}_i$ (iterate state solution)
  until $|\Delta \boldsymbol{u}_i|$ is small
  Determine $\Delta \boldsymbol{a}^{(k)}$
  $\boldsymbol{a}^{(k+1)} := \boldsymbol{a}^{(k)} + \Delta \boldsymbol{a}^{(k)}$ (improve design)
until $|\Delta \boldsymbol{a}^{(k)}|$ is small

There are several ways how to realize this abstract algorithm, i.e. how to choose $\Delta \boldsymbol{u}$ and $\Delta \boldsymbol{a}$.

System (4) is usually solved using iteration

$$\boldsymbol{P}(\bar{\boldsymbol{u}})\,\Delta \boldsymbol{u} = -\boldsymbol{r}(\bar{\boldsymbol{u}}), \tag{5}$$

where $\boldsymbol{r}(\boldsymbol{u}) \equiv \boldsymbol{K}(\boldsymbol{u})\boldsymbol{u} - \boldsymbol{f}(\boldsymbol{u})$ is the residual and $\bar{\boldsymbol{u}}$ is the approximate solution from the previous iteration (from here on we omit the dependence on $\boldsymbol{a}$ in most notations). Natural choices for the preconditioner $\boldsymbol{P}(\bar{\boldsymbol{u}})$ are $\boldsymbol{K}(\bar{\boldsymbol{u}})$ ("Picard" linearization) and $\frac{\partial \boldsymbol{r}(\bar{\boldsymbol{u}})}{\partial \boldsymbol{u}}$ (exact or "Newton" linearization).

There are two fundamentally different approaches to realize the optimization loop. In classical descent methods the correction is computed from

$$\boldsymbol{Q}(\bar{\boldsymbol{a}})\,\Delta \boldsymbol{a} = -\nabla_{\boldsymbol{a}} \mathcal{J}(\bar{\boldsymbol{a}}), \tag{6}$$

where $\bar{\boldsymbol{a}}$ a the approximate design from the previous optimization iteration and $\boldsymbol{Q}(\bar{\boldsymbol{a}})$ is a preconditioner (Hessian approximation). In stochastic optimization methods (like Genetic Algorithms, GA) no gradient information is used to generate a set of new candidates for approximate optimum design.

Numerical solution of problems (1) is a computing intensive task even in two spatial dimensions. Adding optimization loop increases the computational burden by an order of magnitude. Therefore it is necessary that the total efficiency and robustness of selected strategy is as good as possible.

Below we discuss on three common approaches to tackle problem (3)–(4) using combination of four numerical methods for nonlinear equations or nonlinear programming problems.

1. *Solve outer (optimization) problem using GA. Solve inner (state) problem using Picard iteration*

$$\boldsymbol{K}(\bar{\boldsymbol{u}})\Delta \boldsymbol{u} = -\boldsymbol{r}(\bar{\boldsymbol{u}}).$$

The advantage of this approach is its robustness (GA has the potential to find global minimum instead of local one) and ease of implementation (no gradients or Jacobians are needed). Moreover, stochastic optimization methods can be applied to more general optimization problems involving discrete variables or nonsmooth cost functions. The obvious disadvantage of this approach is its inefficiency. Picard iteration converges slowly also near the exact solution. As a rule GA needs hundreds or thousands cost function evaluations. Moreover, there is no natural stopping criterion for stochastic optimization method which means that there is no rigorous justification on the accuracy of the results.

2. *Solve outer problem using a descent method. Solve inner problem using the Newton method*

$$\frac{\partial \boldsymbol{r}(\overline{\boldsymbol{u}})}{\partial \boldsymbol{u}} \Delta \boldsymbol{u} = -\boldsymbol{r}(\overline{\boldsymbol{u}}).$$

The advantage of this approach is its accuracy and efficiency (super-linear or even quadratic convergence). The minor disadvantage is that descent methods may find only a local optimum. Moreover the Newton method may fail to converge from a given initial guess. The more important disadvantage is the implementation of gradient and Jacobian computations. In the case of problem (1)–(2) this is the major obstacle.

3. *Solve outer problem with a combination of GA and descent methods. Solve inner problem with a combination of Picard and Newton linearization.*

This hybrid approach obviously shares the good properties of methods 1 and 2, namely robustness and reasonable efficiency (GA is used only to locate region where the global optimum probably is). Unfortunately, one still have to program the derivative formulas.

It is obvious that gradients and Jacobians are useful in large-scale simulation and optimization. Despite this we must admit that people in industry is not willing to spent hours after hours to program and to debug the complicated derivative formulas related to problem (3)–(4). Divided difference approximations of partial derivatives, like

$$\frac{\partial \mathcal{J}(\boldsymbol{a}^0)}{\partial a_i} = \frac{\mathcal{J}(\boldsymbol{a}^0 + \delta \boldsymbol{e}^{(i)}) - \mathcal{J}(\boldsymbol{a}^0)}{\delta} + O(\delta), \tag{7}$$

are a way to utilize derivative information without laborious programming. However, in large-scale simulation/optimization they are very expensive to evaluate in terms of CPU-time. Moreover they suffer accuracy problems as the optimal value of the step length δ is not straightforward to obtain. In many industrial applications, however, difference formulas have been used with success.

2 EXACT LINEARIZATION USING AUTOMATIC DIFFERENTIATION

Automatic differentiation of computer programs is still sometimes confused with finite difference approximation of derivatives using (7) or symbolic differentiation of a single expression using symbolic manipulation packages like Mathematica or Maple. Symbolic manipulation packages are, in general, unable to deal with whole computer programs with subroutines, loops, and branches. It takes a lot of human effort to differentiate a large computer program in small pieces using symbolic manipulator and to reassemble the resulting pieces of derivative code into a new program.

Automatic differentiation (AD) is a technique for augmenting computer programs with derivative computations. It exploits the fact that every computer program executes a sequence of elementary arithmetic operations. By applying the chain rule of derivative calculus repeatedly to these operations, accurate derivatives of arbitrary order can be computed automatically. In this work we consider only the "forward" mode of AD which is implemented using the operator overloading

technique available in Fortran 95 programming language, for example. For more details on AD and its practical implementation, see [3], [5], [10].

We proceed to show how to obtain: fully automatic exact Jacobian for the Newton linearization and semi-automatic exact linearization with respect to geometry. As a simple model problem we consider the minimization of the functional

$$J(\boldsymbol{a},u) = \int_{\Omega(\boldsymbol{a})} (u-u_d)^2\,dx, \tag{8}$$

where $u = u(\boldsymbol{a})$ solves the 2D quasilinear scalar diffusion equation

$$\nabla\cdot(k(u)\nabla u) + f(u) = 0 \quad \text{in } \Omega(\boldsymbol{a}). \tag{9}$$

The Galerkin discretization of (9) with Lagrangian finite elements reads

$$\int_{\Omega} (k(u_h)\nabla u_h\cdot\nabla\varphi_j - f(u_h)\varphi_j)\,dx = 0, \quad j = 1,\ldots,N, \tag{10}$$

where $u_h = \sum_{i=1}^{N} u^i\varphi_i$. Here φ_i are the basis functions, u^i the nodal values of u_h, and N is the number of mesh nodes. System (10) can be written again in the matrix form

$$\boldsymbol{r}(\boldsymbol{a};\boldsymbol{u}) \equiv \boldsymbol{K}(\boldsymbol{a};\boldsymbol{u})\boldsymbol{u} - \boldsymbol{f}(\boldsymbol{a};\boldsymbol{u}) = 0, \tag{11}$$

Differentiating (11) with respect to a design variable a_k implicitly gives

$$\frac{\partial \boldsymbol{r}(\boldsymbol{a};\boldsymbol{u})}{\partial a_k} + \frac{\partial \boldsymbol{r}(\boldsymbol{a};\boldsymbol{u})}{\partial \boldsymbol{u}}\frac{\partial \boldsymbol{u}}{\partial a_k} = 0. \tag{12}$$

By introducing the adjoint state vector $\boldsymbol{p}$ we can eliminate the partial derivative of $\boldsymbol{u}$ from (12) and obtain the following formula for the evaluation of the gradient of the objective function $\mathcal{J}$:

$$\frac{\partial \mathcal{J}(\boldsymbol{a})}{\partial a_k} = \frac{\partial J(\boldsymbol{a},\boldsymbol{u})}{\partial a_k} - \boldsymbol{p}^{\mathrm{T}}\left(\frac{\partial \boldsymbol{r}(\boldsymbol{a};\boldsymbol{u})}{\partial a_k}\right), \tag{13}$$

where $\boldsymbol{p}$ solves the adjoint equation

$$\left(\frac{\partial \boldsymbol{r}(\boldsymbol{a};\boldsymbol{u})}{\partial \boldsymbol{u}}\right)^{\mathrm{T}} \boldsymbol{p} = \nabla_{\boldsymbol{u}} J(\boldsymbol{a},\boldsymbol{u}). \tag{14}$$

Our aim is to utilize the forward mode of AD to calculate the derivatives appearing in (13) and (14). The direct application of AD to calculate e.g. the $N\times N$ matrix $\partial \boldsymbol{r}/\partial \boldsymbol{u}$ is not efficient in terms of computing time and memory. Using the forward mode of AD the computing time and memory consumption would be multiplied by N compared to sheer analysis. Therefore, it is necessary to take into account the sparsity of the derivatives with respect to $\boldsymbol{u}$ and to work on the element level.

We assume that the finite element mesh consists of similar elements Ω_e each having m degrees of freedom. The residual vector $\boldsymbol{r}(\boldsymbol{a};\boldsymbol{u}) \in \mathbb{R}^N$ is obtained using the standard assembly process

$$\boldsymbol{r}(\boldsymbol{a};\boldsymbol{u}) = \overset{\text{ass.}}{\sum_{e}} \boldsymbol{r}^e(\boldsymbol{a};\boldsymbol{u}^e), \tag{15}$$

where

$$\boldsymbol{r}^e(\boldsymbol{a};\boldsymbol{u}^e) \equiv \boldsymbol{K}^e(\boldsymbol{a};\boldsymbol{u}^e)\boldsymbol{u}^e - \boldsymbol{f}^e(\boldsymbol{a};\boldsymbol{u}^e)$$

```
DO iter=1,itmax
   r = 0.0_wp; drda = 0.0_wp; drdu = 0.0_wp
   drdu = DefaultDerivative( r, u )
   drda = ShapeDerivative( r, G )
   DO WHILE ( Integrate(mesh) )
      phi => GetBasisFunctionPtr()
      r = ( (k(u)*grad(u)) .DOT. grad(phi) ) - f(u)*phi
   END DO
   du = LU( drdu, r )
   u = u - du
   if ( norm2(r) < toler ) exit
END DO
!
dJdu = DefaultDerivative( J, u )
dJ = ShapeDerivative( J, G )
J = 0.0_wp
DO WHILE ( Integrate(mesh) )
   phi => GetBasisFunctionPtr()
   J = (u-u_d)**2*phi
END DO
p = LU( drdu, dJdu, trans=.TRUE. )
CALL SysMatVec( drda, p, pt_x_drda, trans=.TRUE.)
dcost = dJ - pt_x_drda
...
```

Figure 1: Piece of Fortran 95 code for the numerical solution of (9) and the calculation of the value and the gradient of the cost functional J in (8).

and $\boldsymbol{u}^e \in \mathbb{R}^m$ is the vector of element degrees of freedom. Also the integral-type cost functional is clearly separable in the following sense:

$$J(\boldsymbol{a};u_h) = \sum_e \int_{\Omega_e} (u_h - u_d)^2 \, dx = \sum_e J_e(\boldsymbol{a};\boldsymbol{u}^e). \tag{16}$$

Now we need to apply automatic differentiation only to local contributions in (15) and (16). Thus, we have to differentiate only scalars and "small" vectors with respect to "small" number of independent variables $a_1,\ldots,a_n,q_1^e,\ldots,q_m^e$. The global terms in (13) and (14) are then obtained using the standard assembly process which contains no automatic differentiation.

If $\boldsymbol{a}$ is a geometric parameter then differentiation with respect to $\boldsymbol{a}$ can be done utilizing the chain rule. We assume that the coefficients $\boldsymbol{G}^{(i)},\boldsymbol{c}^{(i)}$ of the Taylor expansion (linearization)

$$\boldsymbol{X}(:,i) = \boldsymbol{G}^{(i)}\boldsymbol{a} + \boldsymbol{c}^{(i)}, \quad i = 1,2 \tag{17}$$

are available, where $\boldsymbol{X} \in \mathbb{R}^{N\times 2}$ is the matrix of Cartesian coordinates of mesh nodes. Derivatives with respect to $\boldsymbol{a}$ in (13) involve now essentially differentiation with respect to element nodal coordinates. For example the partial Jacobian of $\boldsymbol{r}$ with respect to $\boldsymbol{a}$ is given by

$$\frac{\partial \boldsymbol{r}}{\partial \boldsymbol{a}} = \frac{\partial \boldsymbol{r}}{\partial \boldsymbol{X}(:,1)}\boldsymbol{G}^{(1)} + \frac{\partial \boldsymbol{r}}{\partial \boldsymbol{X}(:,2)}\boldsymbol{G}^{(2)}. \tag{18}$$

Note that linearization (17) is independent on the state problem to be solved and can be done inside the mesh generator using again automatic differentiation.

Numerrin 2.0 is a state of the art software for numerical simulation and optimization which relies on automatic differentiation [4], [7]. In Figure 1 a piece of Numerrin 2.0 code needed to calculate the value of the cost functional and its gradient at a given point $\boldsymbol{a}$ is shown. As we see, the differentiation is almost completely hidden from the user. For the linearization of the state problem the user only has to identify variables representing the state vector, the residual, and the Jacobian.

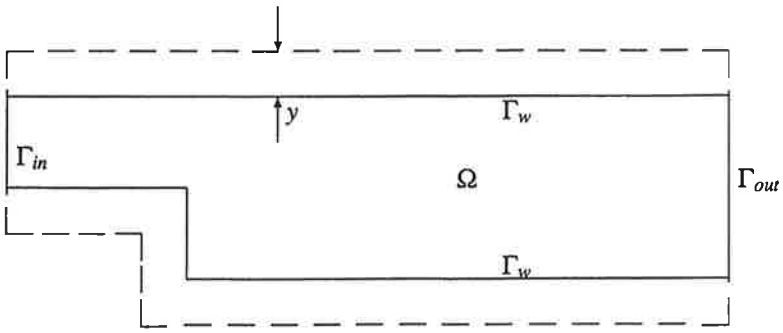

Figure 2: Physical (dashed) and computational (solid) domains

3 APPLICATIONS

We present two examples of the use of automatic derivatives in numerical simulation and optimization in computational fluid dynamics. The first example demonstrates the advantages of exact linearization in the solution of highly nonlinear and complicated state problem. The second one shows the effectiveness of descent methods in determining a local optimum for a complicated shape optimization problem. We would like to emphasize, however, that the technique presented in the previous section is generic and by no means restricted to computational fluid dynamics. Recently, it has been applied e.g. in the multigrid solution of non-equilibrium radiation diffusion problems [2].

4.1. Simulation of turbulent flow in an expanding channel

Simulation of high Reynolds number fluid flows is often done using Reynolds averaged Navier–Stokes equations with the k-ε turbulence model. In this formulation turbulent kinetic energy k and kinetic energy dissipation ε are unknowns in addition to velocity and pressure. For more details on the model, see e.g. [9] and [11].

As the k-ε model is not valid in the boundary layer, the computation is done in the artificial domain Ω shown in Figure 2. The system of PDEs to be solved in Ω reads

$$-\nabla\cdot\boldsymbol{\sigma}+\rho(\vec{u}\cdot\nabla)\vec{u}=\rho\vec{g} \tag{19}$$

$$\nabla\cdot\vec{u}=0 \tag{20}$$

$$-\nabla\cdot((\mu_0+c_1\hat{\mu})\nabla k)+\rho\vec{u}\cdot\nabla k=\hat{\mu}\Phi-\rho\varepsilon \tag{21}$$

$$-\nabla\cdot((\mu_0+c_2\hat{\mu})\nabla\varepsilon)+\rho\vec{u}\cdot\nabla\varepsilon=C_1\hat{\mu}\frac{\varepsilon}{k}\Phi-C_2\rho\frac{\varepsilon^2}{k}. \tag{22}$$

Here

$$\boldsymbol{\sigma}=(\mu_0+\hat{\mu})(\nabla\vec{u}+\nabla\vec{u}^{\mathrm{T}})-pI,\quad \Phi=2\left(\frac{\partial u_1}{\partial x_1}\right)^2+\left(\frac{\partial u_1}{\partial x_2}+\frac{\partial u_2}{\partial x_1}\right)+2\left(\frac{\partial u_2}{\partial x_2}\right)^2 \tag{23}$$

and $\hat{\mu}$ is the turbulent viscosity defined by $\hat{\mu}=C_\mu\rho k^2/\varepsilon$. The empirical constants have the following values: $c_1=1$, $c_2=(1.3)^{-1}$, $C_1=1.44$, $C_2=1.92$, $C_\mu=0.09$.

On the inlet boundary Γ_{in} the values of $\vec{u},k$, and ε are prescribed and on outlet boundary natural boundary conditions are assumed. On the artificial boundary Γ_w near to solid walls we set

$$\sigma_t=-\mathrm{sign}(u_t)\rho(u^\star)^2,\quad u_n=0,\quad k=(u^\star)^2/\sqrt{C_\mu},\quad \varepsilon=\frac{(u^\star)^3}{\kappa y}, \tag{24}$$

where $\sigma_t\equiv n_i\sigma_{ij}t_j$, $u_n\equiv u_in_i$. Here y is the distance from wall, $\kappa=0.41$, and $u^\star$ is solved from the

nonlinear equation

$$u_t = u^\star \Psi(y^+), \quad y^+ = \frac{\rho u^\star y}{\mu}, \tag{25}$$

where Ψ is a given nonlinear wall law function.

The finite element discretization of system (19)–(25) can be done using e.g. stabilized Lagrangian finite elements [1]. The resulting algebraic system is very hard to solve due to complicated boundary conditions (24), (25) and the need to keep k and ε strictly positive as they appear in the denominators of algebraic expressions.

As an example we consider the flow in the backward step with Reynolds number equal to 10^6. The computational domain was discretized using 2300 four-noded elements. We solved the algebraic system with two approaches. In the first approach only Picard iteration was used. In the second approach first 20 iterations were Picard iterations and then we switched to the exact Newton method. In Figure 3 the residual norm histories for both methods are depicted. The latter approach is clearly superior but its implementation would be a tremendous task without automatic differentiation.

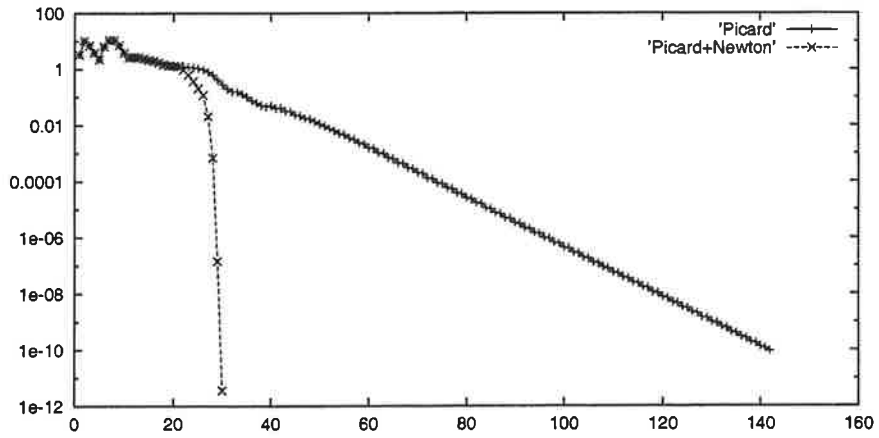

Figure 3: Residual norm vs. iterations

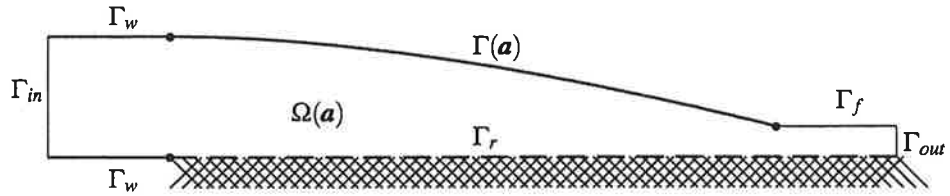

Figure 4: Problem geometry

4.2. Shape optimization in spreading process

Consider a device spreading fluid on the surface of moving porous material shown in Figure 4. The fluid flow in the device $\Omega(\boldsymbol{a})$ is modeled by the equations

$$-\nabla\cdot\boldsymbol{\sigma}+\rho\vec{u}\cdot\nabla\vec{u}=\rho\vec{g} \tag{26}$$

$$\nabla\cdot\vec{u}=0. \tag{27}$$

We assume the following constitutional equation (non-Newtonian power-law fluid)

$$\boldsymbol{\sigma}=\mu(\nabla\vec{u}+\nabla\vec{u}^{\mathrm{T}})-pI,\quad \mu=k_0\Phi^{\frac{n-1}{2}}, \tag{28}$$

where k_0, n are given parameters.

On the inflow boundary Γ_{in} and on the solid walls $\Gamma_w\cup\Gamma(\boldsymbol{a})$ both velocity components are prescribed. On the free fluid surface Γ_f the vertical velocity component is prescribed to zero. On Γ_r the tangential velocity component and the normal forces are prescribed:

$$u_t=u_R\quad \sigma_n=\lambda u_n+f_0\quad \text{on } \Gamma_{out}, \tag{29}$$

where $u_t\equiv u_i t_i$ and $\sigma_n\equiv n_i\sigma_{ij}t_j$.

The aim is to control the filtration profile (normal velocity) on Γ_r by changing the shape of the back wall $\Gamma(\boldsymbol{a})$ of the device to minimize the functional

$$\mathcal{J}(\boldsymbol{a})=\int_{\Gamma_r}|u_n-\hat{u}_n|^2\,dx, \tag{30}$$

where $\vec{u}$ solves problem (26)–(28) in $\Omega(\boldsymbol{a})$ and $\hat{u}_n$ is the target filtration profile.

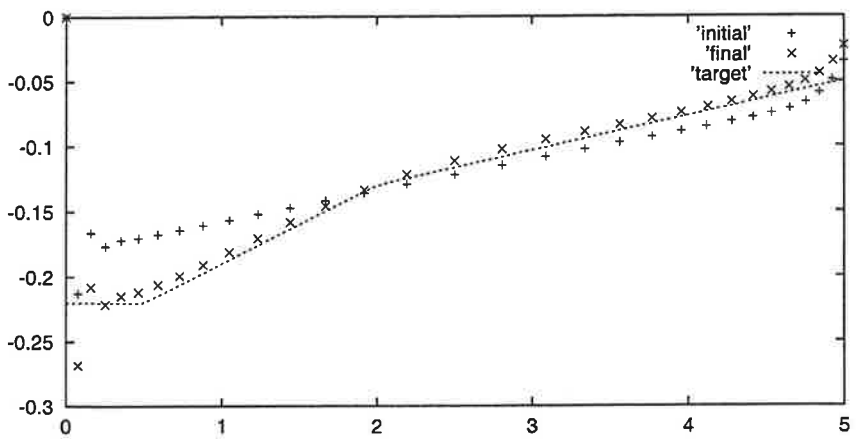

Figure 5: Outflow profiles on Γ_r

We solved the problem with the following values of parameters $k_0=1$, $n=0.5$, $u_R=0.2$, $\lambda=150$, $f_0=-0.5$, and $\vec{u}=(4x_2(1-x_2),0)$ on Γ_{in}. The unknown part of the boundary was parameterized using a Bezier curve with 6 control points. The control points were allowed to move between given move limits. The state problem was discretized using 440 four-noded finite elements. The optimization problem was solved with quasi-Newton method and the nonlinear state problem

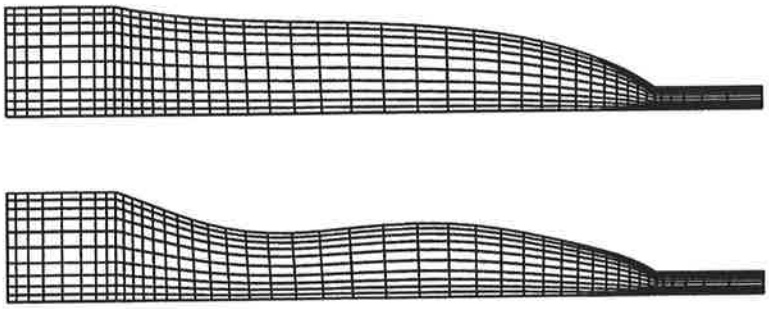

Figure 6: Initial (upper) and optimum (below) designs

with Newton method. In Figure 5 the initial, final, and target filtration profiles are shown. The initial and optimal designs are shown in Figure 6. A similar shape optimization problem was solved in paper [8] using hand-coding of derivatives and classical Fortran 77 programming. The amount of man-hours spent to implement and debug the code was tenfold compared to the approach presented here.

4 CONCLUSIONS

Accurate and robust numerical simulation and optimization of highly nonlinear systems modeled with partial differential equations requires the use of a combination of different type of numerical methods. Robustness (e.g. location the region of convergence to global solution) is usually achieved using more simple derivative-free methods. Also very coarse unstructured meshes may imply non-smoothness in the dependency on geometric parameters. Attaining high accuracy in final solution with acceptable amount of computational work may require numerical methods exploiting exact linearization. For finer meshes the discretization induced nonsmoothness will gradually disappear if the continuous problem is inherently differentiable.

Calculation derivatives by hand is laborious, very error-prone, and sometimes practically impossible. Automatic differentiation of computer programs makes it possible to use exact linearization also in fast-paced industrial projects. In this paper we have shown that it is possible to implement automatic differentiation in such a way that it is a natural, and an almost invisible part of the numerical simulation process itself.

REFERENCES

[1] L. P. Franca and S. L. Frey, Stabilized finite element methods: II. The incompressible Navier–Stokes equations, Comput. Methods Appl. Mech. Engrg., **99**, 209-233, 1992.

[2] R. Glowinski and J. Toivanen, Solution of non-equilibrium radiation diffusion problems using multigrid, Proceedings of Copper Mountain Conference (to appear), 2003.

[3] A. Griewank, Evaluating Derivatives, Principles and Techniques of Algorithmic Differentiation, SIAM, Philadelphia, 2000.

[4] K. Hiltunen, M. Laitinen, A. Niemistö, and P. Tarvainen, Using mathematical concepts in software design of computational mechanics, Proceedings of VIII Finnish Mechanics Days, 2003.

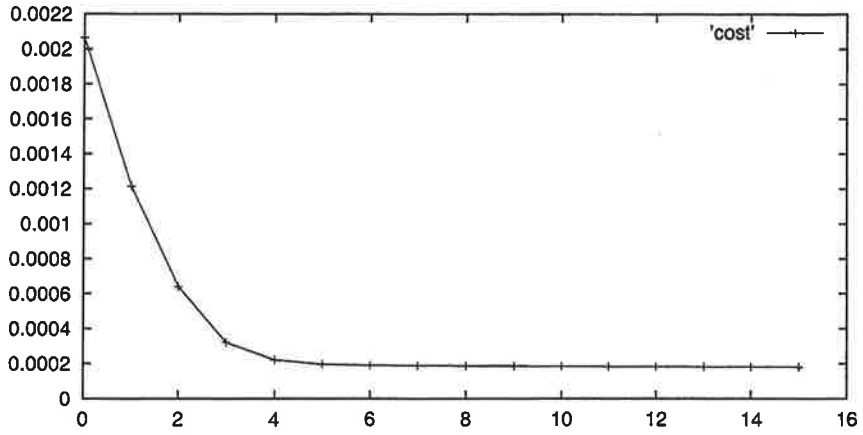

Figure 7: Cost vs. iterations

[5] J. Haslinger and R. A. E. Mäkinen, Introduction to Shape Optimization: Theory, Approximation, and Computation, SIAM, Philadelphia, 2003.

[6] R. A. E. Mäkinen, On automatic derivatives in sensitivity analysis for shape optimization problems, Proceedings of VII Finnish Mechanics Days, J. Koski and S. Virtanen (eds.), Tampere University of Technology, Vol. 1, 63–70, 2000.

[7] Numerrin 2.0 – Käyttäjän opas, Numerola Oy, Jyväskylä, 2003.

[8] J. Hämäläinen, R. A. E. Mäkinen, and P. Tarvainen, Optimal design of paper machine headboxes, Int. J. Numer. Meth. Fluids, **34**, 685–700, 2000

[9] B. Mohammadi and O. Pironneau, Analysis of the K-Epsilon turbulence model, Wiley, Chichester, 1994.

[10] B. Mohammadi and O. Pironneau, Applied Shape Optimization for Fluids, Oxford University Press, Oxford, 2001.

[11] D. C. Wilcox, Turbulence modeling for CFD, DCW Industries, La Cañada (CA), 1993.